Elastic Deformation of Sands in Triaxial Tests

（三軸試験による砂の弾性変形特性）

by

Eqramul Hoque

A thesis submitted in partial fulfilment
of the requirements for the degree of

Doctor of Philosophy

Department of Civil Engineering
University of Tokyo
Tokyo, Japan

September, 1996

Contents

Abstract		i
Acknowledgment		iii
List of the figures		iv
1.	Introduction	1
1.1.	Background	1
1.2.	Elastic deformation characteristics of granular materials	4
1.3.	Testing methods	4
1.4.	Damping ratio and its measurements	8
1.5.	Factors affecting small-strain deformation characteristics of soils	8
1.6.	Objectives of the present study	11
1.7.	Organization of this thesis	13
2.	An automated triaxial system and the performance of LDTs	15
2.1.	Introduction	15
2.2.	Description of the triaxial system	16
2.3.	Accuracy of stress control and measurement	18
2.4.	Operation of the system	19
2.5.	The soft-ware program	21
2.6.	Performance of the automated system	22
2.7.	Performance evaluation of LDTs for the use in triaxial tests	23
2.7.1.	Structure of LDT and data acquisition system	24
2.7.2.	Materials for LDTs	25
2.7.3.	Manufacturing of LDT	28
2.7.4.	Data acquisition system	30
2.7.5.	Resolution of LDT	31
2.7.6.	Effects of temperature change on the LDT output	35
2.7.7.	Small-strain behavior of LDT	35
2.7.8.	Workable range of LDT	38
2.7.9.	Lateral LDTs	39
2.7.10.	Durability of LDT under pressurized submerged condition	39
2.8.	Summaries	40
	Tables	42
	Figures	44
3.	Inherent anisotropy in the elastic deformation of granular materials	69
3.1.	Introduction	69
3.2.	Theoretical background of elasticity	70
3.3.	Experimental setup	73
3.4.	Test program	74
3.5.	Testing method	75
3.6.	Resolutions, errors and countermeasures	75
3.7.	Results and discussions	76
3.7.1.	Inherent anisotropy: Deformation in isotropic stress path	79

3.7.2. Transverse isotropy 81
3.7.3. Inherent anisotropy in small strain stiffness 81
3.8. Summaries 84
Tables 85
Figures 86

4. Cross-anisotropy in the small strain stiffness 103
4.1. Introduction 103
4.2. Summary of the previous chapter 104
4.3. Dependency of Young's moduli on stress states 105
4.4. Test results and discussions 106
4.4.1. Stress-dependency of elastic Young's modulus 106
4.4.2. Poisson's ratio 110
4.5. Cross-anisotropic elasticity model 112
4.6. Stress path-dependency of integrated elastic strains 114
4.7. Summaries 117
Tables 118
Figures 119

5. Effects of stress ratio on Young's modulus for elastic strains during shearing 142
5.1. Introduction 142
5.2. Testing procedure 142
5.3. Test results and discussions 143
5.4. Summaries 149
Tables 150
Figures 151

6. Cyclic prestraining and the elastic deformation properties 166
6.1. Introduction 166
6.2. Description of the testing system 167
6.3. Test procedure 168
6.4. Test program 169
6.5. Test results 170
6.5.1. Axial stress-dependency of E_{max} 171
6.5.2. Effects of aging on E_{max} 174
6.5.3. Equivalent Young's modulus E_{eq} 175
6.5.4. Poisson's ratio 177
6.5.5. Damping ratio 178
6.5.6. Elasto-plasticity of deformation during cyclic loading 180
6.5.7. Effects of CP on the monotonic behavior during triaxial compression tests 185
6.6. Summaries 187
Tables 190
Figures 192

7. Loading rate-dependency of sand deformation in cyclic triaxial tests 241
7.1. Introduction 241
7.2. Description of the apparatus 242
7.3. Testing procedure and test results 244
7.4. Practical applications 252

7.5. Summaries 253
Tables 255
Figures 256

8. Creep behavior of sand in TC test and its effect on the deformation characteristics 272
8.1. Introduction 272
8.2. Test procedure 273
8.3. Test results and discussions 274
8.3.1. Creep tests and the deformation characteristics 274
8.3.2. Elastic deformation properties 277
8.3.3. Existence of elasticity in any stress states during monotonic loading 278
8.3.4. Stress-dilatancy relationship 280
8.3.5. Monotonic TC tests to failure 282
8.4. Summaries 284
Tables 286
Figures 287

9. Summary, conclusions, and recommendations 317
9.1. Introduction 317
9.2. Conclusions 318
9.2.1. Automation and the performance of LDTs 318
9.2.2. Inherent anisotropy in elastic deformation properties 319
9.2.3. Cross-anisotropy in small strain stiffness 320
9.2.4. Effects of stress ratio on Young's modulus for elastic strains during shearing 320
9.2.5. Cyclic prestraining and the elastic deformation properties 321
9.2.6. Loading rate-dependency of deformation properties 322
9.2.7. Creep behavior of sand in TC and its effect on deformation characteristics 323
9.3. Recommendation for future research 325

References 326

Abstract

A comprehensive series of triaxial tests were performed on granular materials to study into anisotropy in small strain stiffness (elastic Young's modulus), Poisson's ratios and some of the factors affecting small strain deformation characteristics. A variety of air-dried materials were used: coarse-grained to fine-grained, subround to subangular, and loose to dense. The first series of tests used a large rectangular-prism specimen (57 cm x 23 cm x 23 cm). Elastic parameters defined for principal strain increments in vertical and horizontal directions were evaluated by applying small amplitude cyclic principal stress in each direction while keeping the other principal stress constant. The tests utilized an automated loading system. For each specimen, the stress state was varied systematically along various stress paths, and small-amplitude cyclic loads were applied at each stress state. Another series of triaxial tests were performed by using a smaller specimen (7.5 cm diameter and 15 cm high) to study into the effects of cyclic prestraining, aging, loading frequency (in the range of 0.005 to 2 Hz) and creep on the small strain deformation characteristics.

The axial deformations were measured locally and externally by using a pair of Local Deformation Transducers (LDT) and a set of proximeters, respectively. For a large triaxial specimen, lateral strains were measured also locally and externally by using, respectively, four pairs of LDTs at three levels of a specimen height and one pair of proximeters at the mid-height of the specimen. For a smaller triaxial specimen, radial strains were measured locally by using six small proximeters, three on each side of the specimen. Both cyclic loading tests with very small to medium strain amplitudes and monotonic loading tests were carried out on over-consolidated, presheared, cyclically prestrained and virgin specimens.

The following conclusions were obtained:

1. The small strain stiffness of granular materials is inherently anisotropic in that the vertical Young's modulus is larger than the horizontal Young's modulus and the lateral elastic normal strain is larger than the vertical elastic normal strain in isotropic compression. They exhibit transverse isotropy in deformation.

2. Elastic Young's modulus is rather a unique function of the normal stress in the direction of the major principal strain increment for which the elastic Young's modulus is defined.

Therefore, the granular materials become inevitably anisotropic as the stress state becomes anisotropic (stress system-induced anisotropy).

3. Elastic Poisson's ratio defined for horizontal strain increment caused by vertical strain increment (ν_{vh}) increases, within a narrow range, with the increase in the ratio of vertical-to-horizontal stresses.

4. As the principal stress ratio exceeds 3 to 4 while the stress condition approaches the failure condition in triaxial compression or extension, both Young's moduli defined for vertical and lateral elastic strain increments decrease at a constant value of vertical or lateral stress.

5. As a result of cyclic prestraining (CP), elastic deformation characteristics of sands become more anisotropic in that the elastic Young's modulus, compared to the respective values measured prior to CP, increases or exhibits the same value at and near the maximum axial stress during CP, while it decreases at and near the minimum axial stress during CP. Damping of sands decreases considerably by CP.

6. The plastic strain increment decreases drastically by cyclic loading along a fixed stress path, but the deformation does not become totally elastic even after the application of a large number of cyclic loading when the amplitude of deviator stress is relatively large. Deformation during a relatively large cycle of isotropic reloading and re-unloading does not become totally elastic either.

7. The Young's modulus and damping of sand at small strains do not change largely by the change in loading rate unless the loading frequency is very low (below 0.05 Hz). Damping ratio at small strains of a virgin specimen increases largely when the loading frequency becomes below 0.05 Hz, while Young's modulus decreases slightly.

8. Elastic deformation properties for sand appear at the restart of loading from any stress state during monotonic loading after the plastic deformation component (related to creep) is allowed to occur.

Acknowledgment

First and foremost, I wish to express my heartfelt appreciation to my supervising professor, Professor Fumio Tatsuoka of the University of Tokyo, who not only ensured to the providence of a conducive academic atmosphere and availed himself whenever I wished to consult with him, but also went a long way in motivating me positively.

I also wish to thank Professors Ikuo Towhata and Hideyuki Horii, and Assoc. Professors Fumio Yamazaki and J. Koseki, all of the University of Tokyo and the members of the examination committee, for their comments and suggestions in preparing this thesis.

My appreciation also goes to the staff: Dr. Y. Kohata, Dr. Takeshi Kodaka, Mr. Takeshi Sato and Ms. Michie Torimitsu of the Geotechnical Engineering Laboratory of the Institute of Industrial Science, University of Tokyo. Dr. Y. Kohata and Mr. T. Sato, assisted me greatly in automating the large triaxial system. Mr. T. Sato's assistance in assembling and explaining both mechanical and electronic components of the Testing apparatus used in the investigation reported in this thesis has been vital. Ms. M. Torimitsu handled the administrative aspects of the final version of the thesis. Dr. T. Kodaka assisted me greatly in preparing summary of this thesis in Japanese. I wish to express my gratitude to my fellow graduate students of the Geotechnical Engineering Laboratory of the Institute of Industrial Science, University of Tokyo, for the diverse ways in which they assisted me during the course of the testing program and the preparation of this thesis.

Special appreciation goes to my family for their support, understanding and encouragement during the study. It is to them — my beloved wife Lima, daughter Lamiya and son Loveen— that I dedicate this thesis.

There are numerous other people who assisted me in various ways. To all those people I hereby wish to express my thanks.

Funding for the graduate work reported in this thesis was provided by the Ministry of Education, Science and Culture, Japan.

Finally, but not least, I would like to express my sincere gratitude to Bangladesh University of Engineering and Technology (BUET) for granting me study-leave to pursue the research.

List of the figures

Chapter 2:

Fig. 2.1a: Large triaxial apparatus used in the present study.

Fig. 2.1b: Large triaxial specimen with local strain measurement.

Fig. 2.1c: Details of lateral LDT for local strain measurement.

Fig. 2.2a: Block diagram of the electro-pneumatic loading system for cell pressure.

Fig. 2.2b: Block diagram of the servo-hydraulic loading system for axial load.

Fig. 2.3a: Principle of the algorithm for some typical stress paths control.

Fig. 2.3b: Block diagram of the software program.

Fig. 2.4: Typical test results to demonstrate the performance of the automated control system in achieving monotonic loading along some stress paths and cyclic loading: a) $\Delta K=0$ stress path with K=0.37, b) $\Delta K=0$ stress path with K=1.0, c) $\Delta\sigma_m=0$ stress path with σ_m=1.665 kgf/cm^2, d) $\Delta\sigma_v=0$ stress path with $\sigma_v=\sigma_h$=1.0 kgf/cm^2, e) Cyclic variation of σ_h, f) Controlling $\Delta\sigma_v=0$ stress path during HCL, and g) Variation of σ_v in a VCL test.

Fig. 2.5: LDT at working condition to measure vertical strains in a triaxial specimen.

Figs. 2.6: Details of the internal connections at the heart of a 4-gage type LDT with (a) front face, and (b) back face.

Fig. 2.7a: The connections of the e.r. strain gages (4-gage type) in the Wheatstone bridge.

Fig. 2.7b: Typical external connector for input-output communication.

Fig. 2.7c: The LDT with two-gage method.

Fig. 2.8: Block diagram of the data acquisition system for LDTs.

Fig. 2.9: Resolution of the combined system of an A-D card and an AC amplifier.

Figs. 2.10: Typical relationships between axial stress and axial deformation in voltage (RV) during one cycle of vertical CL test at isotropic stress states: (a) σ_c= 2.0 kgf/cm^2, and (b) σ_c= 4.5 kgf/cm^2.

Fig. 2.11: Typical calibration characteristics of an LDT.

Fig. 2.12a: 'Creep' of LDTs during a long-term consolidation.

Fig. 2.12b: Relationship between elastic force exerted by LDT strip on the hinges and axial deformation of the LDT (tested by Kim, Y.-S.; 1992).

Fig. 2.12c: Variation of the output voltage (in RV) with time for one minute at a standstill position of LDT.

Fig. 2.13a: Typical 'error-curve' for a given calibration characteristics of an LDT.

Fig. 2.13b: Variation of R (= $\varepsilon_{err}/\varepsilon_a$) with ε_a (current axial strain) along a calibration curve of an LDT.

Figs. 2.14: Typical small unload-reload deformation cycles for (a) $(\varepsilon)_{SA}$=0.143%, and (b) $(\varepsilon)_{SA}$ =0.00476% along a typical calibration curve of an LDT.

Fig. 2.15: Errors in stiffness measurement by the use of LDT in measuring small strains.

Fig. 2.16a: Calibration characteristics of LDT by the conventional method and the finer displacement step method.

Fig. 2.16b: Comparison of the performance of LDT in measuring small-strain stiffness by using two calibration methods.

Fig. 2.17: Long-term stability of LDT at submerged condition under pressurized water in measuring small-strain Young's modulus (tested by Mukabi, J.N., 1995).

Chapter 3:

Fig. 3.1: Test program for vertical and horizontal CL tests at different stress paths ($0.5 \le \sigma_v/\sigma_h \le 2.0$).

Figs. 3.2: (a) $\sigma_v \sim \varepsilon_v$ and $\varepsilon_h \sim \varepsilon_v$ responses in a typical vertical CL test, (b) $\sigma_h \sim \varepsilon_h$ and $\varepsilon_v \sim \varepsilon_h$ responses in a typical horizontal CL test performed on SLK1V specimen.

Figs. 3.3: (a) $\sigma_v \sim \varepsilon_v$ and $\varepsilon_h \sim \varepsilon_v$ responses in a typical vertical CL test, (b) $\sigma_h \sim \varepsilon_h$ and $\varepsilon_v \sim \varepsilon_h$ responses in a typical horizontal CL test performed on TCK1A specimen.

Figs. 3.4: Comparison of external and local (a) ε_v during a vertical CL test, and (b) ε_h during a horizontal test performed on SLK1V specimen.

Figs. 3.5: Comparison of external and local strains during K=1 consolidation on SLK1V specimen (a) for ε_v and (b) for ε_h.

Fig. 3.6: $E_{eq}/(E_{max})_{initial} \sim (\varepsilon_v)_{SA}$ relations for different materials (Ticino sand was tested by Teachavorasinskun (1992)).

Figs. 3.7: Typical relationships obtained from TYK02 specimen between (a) $E_v/f(e)$ and the number of cycle (N), (b) $E_h/f(e)$ and N, and (c) $E_h/f(e)$ and the number of LDTs.

Figs. 3.8: Relationships between volumetric strain (ε_{vol}) and ε_v during isotropic stress states of specimens (a) TYK1A, TCK1A and HGK1A for Cycle 1, (b) SLK1A and SLK1V for Cycle 1, (c) TYK1A, TCK1A and HGK1A for Cycle 2, and (d) SLK1A and SLK1V for Cycle 2.

Figs. 3.9: Relationships between tangent moduli (L_v, L_h) and mean stress (σ_m) during K=1 loading for (a) SLK1V, (b) SLK1A.

Figs. 3.10: Relationships between $d\varepsilon_h/d\varepsilon_v$ and σ_m during reloading along K=1 stress path.

Figs. 3.11: Comparison of (a) local strains during K=1 loading, (b) Young's moduli in two orthogonal horizontal directions.

Figs. 3.12: Relationships between $E_v/f(e)$ and $E_h/f(e)$ and σ_m along isotropic stress states for specimens of (a) Toyoura, (b) SLB sand and (c) Hime gravel and Ticino sand.

Fig. 3.13: Relationships between I ($=1-E_h/E_v$) and A ($=(\varepsilon_h-\varepsilon_v)/(\varepsilon_h-\varepsilon_v)_{ref}$) in the K=1 stress path.

Fig. 3.14: Effects of loading frequency on Young's modulus E_v.

Chapter 4:

Figs. 4.1a~i: $E_v/f(e)\sim\sigma_v$ and $E_h/f(e)\sim\sigma_h$ relations for different out-plane stresses performed on specimens (a) TYK1A, (b) TYISD, (c) TYK02, (d) TCK1A, (e) HGK1A, (f) HGK0A, (g) SLK1A, (h) SLK1V and (I) SLK0A.

Fig. 4.1j: The relationships between E_v / E_h and σ_v / σ_h of different specimens.

Fig. 4.2a: Relationships between $E_v/f(e)$ and σ_h along $\Delta K=0$ stress paths.

Fig. 4.2b: Relationships between $E_v \times K^{m_v}$ / f(e) and σ_h, and $E_h/f(e)$ and σ_h along $\Delta K=0$ stress paths.

Fig. 4.3a: Relationships between the ratio of measured to predicted E_v (based on σ_v dependency of E_v) and σ_h along $\Delta K=0$ stress paths.

Fig. 4.3b: Relationships between the ratio of measured to predicted Young's moduli E_v (based on σ_m dependency of E_v) and σ_h along $\Delta K=0$ stress paths.

Fig. 4.4a: Relationships between the ratio of measured to predicted Young's moduli E_h (based on σ_h dependency of E_h) and σ_h along $\Delta K=0$ stress paths.

Fig. 4.4b: Relationships between the ratio of measured to predicted Young's moduli E_h (based on σ_h dependency of E_h) and σ_h along $\Delta K=0$ stress paths.

Fig. 4.5a: Relationships between the ratio of measured to predicted Young's moduli and σ_v/σ_h along TC at $\sigma_v=\sigma_h=1.0$ kgf/cm^2 of TYK02 specimen.

Fig. 4.5b: Relationships between the ratio of measured to predicted Young's moduli and σ_h/σ_v along TE at $\sigma_v=\sigma_h=1.0$ kgf/cm^2 of TYK02 specimen.

Figs. 4.6: Relationships between Poisson's ratio and stress ratio for specimens (a) TYK1A, (b) TYK02 and (c) TYISD.

Figs. 4.7: Relationships between Poisson's ratio and stress ratio for specimens (a) HGK1A, (b) HGK0A and (c) TCK1A.

Figs. 4.8: Relationships between Poisson's ratio and stress ratio for specimens (a) SLK1A, (b) SLK1V and (c) SLK0A.

Figs. 4.9: Relationships between normalized G_{vh} and normalized stress level for specimens (a) TYK1A, (b) TCK1A, (c) SLK1A and (d) HGK1A.

Fig. 4.10: Schematic diagram of stress path to investigate integrated elastic strains.

Figs. 4.11: Relationships between (a) $d(\Delta\varepsilon_v)/(\Delta\varepsilon_v)_{ave}$ and h (=the length of the side of a square stress path), and (b) $d(\Delta\varepsilon_h)/(\Delta\varepsilon_h)_{ave}$ and h for different values of I_0.

Figs. 4.12: Relationships between (a) $d(\Delta\varepsilon_v)/(\Delta\varepsilon_v)_{ave}$ and h (=the length of the side of a square stress path), and (b) $d(\Delta\varepsilon_h)/(\Delta\varepsilon_h)_{ave}$ and h for different values of ν_0.

Figs. 4.13: Relationships between (a) $d(\Delta\varepsilon_v)/(\Delta\varepsilon_v)_{ave}$ and h (=the length of the side of a square stress path), and (b) $d(\Delta\varepsilon_h)/(\Delta\varepsilon_h)_{ave}$ and h for different values of m.

Chapter 5

Figs. 5.1: The relationships between (a) q ($=\sigma_v-\sigma_h$) and ε_v, (b) volumetric strain (ε_{vol}) and ε_v during TC on Toyoura and Ticino sands specimens.

Figs. 5.2: $q\sim\varepsilon_v$ relationships of Toyoura and Ticino sands specimens at small strain levels up to (a) ε_v= 0.10%, (b) ε_v= 0.01% and (c) ε_v= 0.005%.

Figs. 5.3: The relationships between (a) q ($=\sigma_v-\sigma_h$) and ε_v, (b) volumetric strain (ε_{vol}) and ε_v during TC on Hime gravel specimens.

Figs. 5.4: $q\sim\varepsilon_v$ relationships of Hime gravel specimens at small strain levels up to (a) ε_v= 0.10%, (b) ε_v= 0.01% and (c) ε_v= 0.005%.

Figs. 5.5: The relationships between (a) q ($=\sigma_v-\sigma_h$) and ε_v, (b) volumetric strain (ε_{vol}) and ε_v during TC on SLB sand specimens.

Figs. 5.6: $q\sim\varepsilon_v$ relationships of SLB sand specimens at small strain levels up to (a) ε_v= 0.10%, (b) ε_v= 0.01% and (c) ε_v= 0.002%.

Figs. 5.7 $q\sim\varepsilon_v$ and $\varepsilon_h\sim\varepsilon_v$ relationships of TYISD specimen to demonstrate the existence of bedding error in ε_v and membrane penetration error in ε_h during TC at small strain levels up to (a) ε_v (LDT)= 0.10%, (b) ε_v (LDT)= 0.01%.

Figs. 5.8: $\sigma_v\sim\varepsilon_v$ relationships of typical unload-reload cycles during TC on SLISD specimen at (a) low stress level, (b) at high stress level.

Fig. 5.9: Definition of elastic Young's modulus E^e.

Figs. 5.10: The relationships between the normalized E^e (=E_v) and stress ratio (σ_v/σ_h) during TC performed on specimens (a) TYISD, (b) TYK0D.

Figs. 5.11: The relationships between the normalized E^e (=E_v) and stress ratio (σ_v/σ_h) during TC performed on specimens (a) SLISD, (b) SLK0D.

Figs. 5.12: The relationships between the normalized E^e (=E_v) and stress ratio (σ_v/σ_h) during TCs performed on specimens (a) TYK1A, (b) TCK1A.

Figs. 5.13: The relationships between the normalized E^e (=E_v) and stress ratio (σ_v/σ_h) during TCs performed on specimens (a) HGK1A, (b) HGK0A.

Figs. 5.14: The relationships between the normalized E^e (=E_v) and stress ratio (σ_v/σ_h) during TCs performed on specimens (a) SLK1V, (b) SLK0A.

Fig. 5.15a: The relationships between the normalized E^e (=E_v or E_h) and stress ratio (σ_v/σ_h) during TC at $\sigma_v=\sigma_h=1.0$ kgf/cm^2 performed on TYK02 specimen.

Fig. 5.15b: The relationships between the normalized E^e (=E_v or E_h) and stress ratio (σ_h/σ_v) during TE at $\sigma_v=\sigma_h=1.0$ kgf/cm^2 performed on TYK02 specimen.

Chapter 6

Fig. 6.1a: The triaxial apparatus.

Fig. 6.1b: Block diagram of load-control deviator loading system.

Fig. 6.2a: Block diagram of test program for cyclic prestraining.

Fig. 6.2b: Definitions of E_{eq}, E_{tan}, and h.

Figs. 6.3: $\sigma_a\sim\varepsilon_a$ responses of typical CL tests from TYRA 3 specimen with (a) $(\varepsilon_a)_{SA} \le 0.002\%$ and (b) $(\varepsilon_a)_{SA}$ for CP stress cycle.

Figs. 6.4: $\sigma_a\sim\varepsilon_a$ responses of typical CL tests from HOSTN1 (CP-1) specimen with (a) $(\varepsilon_a)_{SA} \le$ 0.002% and (b) $(\varepsilon_a)_{SA}$ for CP stress cycle.

Fig. 6.5a: σ_a~ε_a and σ_a~ε_r responses of typical large amplitude CL tests at true virgin state of HOSTN5 specimen.

Fig. 6.5b: Variations of the translation of strain axes (ε_a, ε_r, and ε_{vol}) with the number of loading cycles during CP.

Figs. 6.6: Relationships between $E^e/f(e)$ and σ_a along CP stress path for specimens (a) TYRA 3, (b) HOSTN5, (c) HOSTN1 (CP-1), (d) HOSTN1 (CP-2), (e) HOSTN1 (CP-3), (f) HOSTN1 (overlapping data for CP-1, CP-2 and CP-3), and (g) HOSTN3.

Figs. 6.7: Time histories of the variation of E_{max} for specimens (a) TYRA 2, (b) TYRA 3 and (c) HOSTN1 (CP-1).

Fig. 6.8a: E_{eq}~$\log((\varepsilon_a)_{SA})$ relations (before CP) of the specimens of Toyoura sand.

Fig. 6.8b: Normalized E_{eq}~$\log((\varepsilon_a)_{SA})$ relations (before CP) of the specimens of Toyoura sand.

Figs. 6.9. Effects of CP on the relationships between $E_{eq}/(E_{max})_{initial}$ and $(\varepsilon_a)_{SA}$ for specimens (a) TYRA 2 and (b) TYRA 3.

Figs. 6.10: Effects of CP on the relationships between $E_{eq}/(E_{max})_{initial}$ and $(\varepsilon_a)_{SA}$ of HOSTN1 specimen for CP stages (a) CP-1, (b) CP-2 and (c) CP-3.

Fig. 6.10d: Effects of CP on the shape of the normalized decay curve of HOSTN1 specimen.

Figs. 6.11: Effects of CP on the relationships between $E_{eq}/(E_{max})_{initial}$, ν_{eq} and $(\varepsilon_a)_{SA}$ for HOSTN5 specimen.

Fig. 6.12: Effects of the number of loading cycle N at constant stress-amplitude on $(\varepsilon_a)_{SA}$, ν_{eq} and h

Figs. 6.13: Effects of CP on the relationships between ν_{eq} and $(\varepsilon_a)_{SA}$ of HOSTN1 specimen for CP stages (a) CP-1, (b) CP-2 and CP-3.

Figs. 6.14: Effects of CP on the relationships between ν and σ_a/σ_r along CP stress path of HOSTN1 specimen for CP stages (a) CP-1, (b) CP-2, (c) CP-3.

Fig. 6.15: Effects of CP on the relationships between damping ratio (h) and $(\varepsilon_a)_{SA}$ of Toyoura sand.

Figs. 6.16: Effects of CP on the relationships between damping ratio (h) and $(\varepsilon_a)_{SA}$ of Hostun sand for specimens (a) HOSTN1 (CP-1), (b) HOSTN1 (CP-2 and CP-3), and (c) HOSTN5.

Figs. 6.17: (a) σ_a~ε_a and (b) σ_a~ε_r relationships of virgin and prestrained states of specimen HOSTN3 in CP stress path.

Figs. 6.18: (a) σ_a~ε_a and (b) σ_a~ε_r relationships of virgin and prestrained states of specimen HOSTN5 in CP stress path.

Figs. 6.19: σ_a~ε_a relationships at the start and at the end of CP of specimens (a) HOSTN1 (CP-1), (b) HOSTN1 (CP-2), (c) HOSTN1 (CP-3) and (d) TYRA 3.

Figs. 6.20: Variations of (a) axial plastic-to-elastic, (b) radial plastic-to-elastic strains increments with σ_a in CP stress path of HOSTN3 specimen.

Figs. 6.21: Variations of (a) axial plastic-to-elastic, (b) radial plastic-to-elastic strains increment with σ_a in CP stress path of HOSTN5 specimen.

Figs. 6.22a~d: Variations of axial plastic-to-elastic strains increment with σ_a in CP stress path of specimens (a) HOSTN1 (CP-1), (b) HOSTN1 (CP-2), (c) HOSTN1 (CP-3) and (d) TYRA 3.

Figs. 6.22e~h: Variations of total strain components (ε_v, ε_h and ε_{vol}) and elastic strain components (ε^e_v, ε^e_h and ε^e_{vol}) with $\sigma_v=\sigma_a$ ($=\sigma_h$) in isotropic stress path of specimens (e) Toyoura sand (TYK1A), (f) Ticino sand (TCK1A), (g) SLB sand (SLK1V), and (h) Hime gravel (HGK1A).

Figs. 6.23: Relationships between the stress ratio (R) and the dilatancy rate (D) in CP stress path for specimens (a) HOSTN3 and (b) HOSTN5.

Figs. 6.24: Relationships between the stress ratio (R) and the prestrained-to-virgin shear strains rate in CP stress path for specimens (a) HOSTN3 and (b) HOSTN5.

Figs. 6.25a~f: Relationships between tangent modulus (E_{tan}) and σ_a in CP stress path for specimens (a) HOSTN3, (b) HOSTN5, (c) HOSTN1 (CP-1), (d) HOSTN1 (CP-2), (e) HOSTN1 (CP-3), and (f) TYRA 3.

Figs. 6.25g~h: Relationships between E_{tan}/E_{max} and σ_a in CP stress path for specimens (g) HOSTN3, and (h) HOSTN5.

Fig. 6.26a: Relationships between the deviatoric stress (q) and ε_a during TC at $\sigma_a=\sigma_r=0.8$ kgf/cm^2.

Fig. 6.26b: Relationships between the volumetric strain (ε_{vol}) and ε_a during TC at $\sigma_a=\sigma_r=0.8$ kgf/cm^2.

Fig. 6.26c: Relationships between the volumetric plastic-strain (ε^p_{vol}) and q during TC at $\sigma_a=\sigma_r=0.8$ kgf/cm^2.

Fig. 6.26d: Relationships between q and ε_{vol} during TC at $\sigma_a=\sigma_r=0.8$ kgf/cm^2.

Fig. 6.26e~f: Relationships between (e) q~ε^p_{vol}, and (f) q~ ε_{vol} (at low stress level) during TC at $\sigma_a=\sigma_r=0.8$ kgf/cm^2.

Figs. 6.27a~c: $q \sim \varepsilon_a$ relationships during TC at $\sigma_a=\sigma_r=0.8$ kgf/cm^2 for the range of ε_a up to (a) 1.0%, (b) 0.10% and (c) 0.01%.

Figs. 6.27d~e: $\varepsilon_a \sim \varepsilon_{vol}$ relationships during TC at $\sigma_a=\sigma_r=0.8$ kgf/cm^2 for the range of ε_a up to (d) 1.0%, and (e) 0.1%.

Figs. 6.28: (a) $E_{sec}/(E_{sec})_{max} \sim \log(\varepsilon_a)$ and (b) $E_{tan}/(E_{tan})_{max} \sim \log(\varepsilon_a)$ relationships during TC at $\sigma_a=\sigma_r=0.8$ kgf/cm^2.

Figs. 6.29: (a) $E_{sec}/(E_{sec})_{max} \sim \varepsilon_a$ and (b) $E_{tan}/(E_{tan})_{max} \sim \varepsilon_a$ relationships up to $\varepsilon_a=0.5\%$ during TC at $\sigma_a=\sigma_r=0.8$ kgf/cm^2.

Figs. 6.30: (a) $E_{sec}/(E_{sec})_{max} \sim q/q_{max}$ and (b) $E_{tan}/(E_{tan})_{max} \sim q/q_{max}$ relationships during TC at $\sigma_a=\sigma_r=0.8$ kgf/cm^2.

Figs. 6.31: Relationships between (a) $E_{tan}/E^e \sim q/q_{max}$ and (b) $E_{tan}/E^e \sim \log(q/q_{max})$ during TC at $\sigma_a=\sigma_r=0.8$ kgf/cm^2.

Chapter 7:

Fig. 7.1: Block diagram of data acquisition system.

Fig. 7.2: $\sigma_a \sim \varepsilon_a$ (ε_a measured by LDTs) relations for typical cycles with the use of (a) sine-wave form, (b) triangular wave-form.

Fig. 7.3: Relations of E_{eq} and h for very small strain (i.e., $(\varepsilon_a)_{SA} \approx 0.002\%$) with the number of load cycles.

Fig. 7.4: $\sigma_a \sim \varepsilon_a$ (ε_a measured by GS) relations for typical cycles with the use of (a) sine-wave form, (b) triangular wave-form.

Fig. 7.5: Relationship between (a) E_{eq} and f, (b) h and f at $(\varepsilon_a)_{SA} \approx 0.002\%$ performed on HOSTN2.

Fig. 7.5c: Typical axial load and axial displacement relationships of elastic spring during CL tests (time-lag concern).

Fig. 7.5d: Typical axial load and displacement relationships of elastic spring during CL tests (filter-concern in the data acquisition system).

Figs. 7.6: $\sigma_a \sim \varepsilon_a$ (ε_a measured by LDTs) relations for a typical cycle at each frequency obtained from HOS12 specimen at neutral stress states of (a) $\sigma_a=\sigma_r=0.8$ kgf/cm^2, and (b) $\sigma_a=2.0$ kgf/cm^2, $\sigma_r=0.8$ kgf/cm^2.

Figs. 7.6: Relationship between (c) E^e / $E^e_{f=0.1}$ and f, (d) h and f at $(\varepsilon_a)_{SA}$≈ 0.0015% performed on HOS12 at different neutral axial stress states.

Figs. 7.6: Relationship between (e) E_{eq} /f(e) and f, (f) h and f at $(\varepsilon_a)_{SA}$≈ 0.0012% and 0.0038% performed on HOSTN3 at a neutral stress state of σ_a=1.4 kgf/cm^2, σ_r=0.8 kgf/cm^2.

Figs. 7.7: Relationships at near virgin state of HOSTN3 between (a) h and $(\varepsilon_a)_{SA}$, and (b) E_{eq} and $(\varepsilon_a)_{SA}$.

Fig. 7.8: Typical σ_a~ε_a response characteristics during large amplitude axial stress cycles at virgin state and at steady state conditions.

Fig. 7.9: Comparison of σ_a~ε_a responses during large amplitude axial stress cycle between two configurations of arrangement of principal measuring devices at steady state conditions.

Figs. 7.10: Relationships at steady state conditions of HOSTN3 between (a) h and $(\varepsilon_a)_{SA}$, and (b) E_{eq} and $(\varepsilon_a)_{SA}$.

Figs. 7.11: Relationships at steady state conditions (after N=25000 cycles) of HOSTN5 between (a) E_{eq} and $(\varepsilon_a)_{SA}$, and (b) h and $(\varepsilon_a)_{SA}$.

Figs. 7.12: Relationships at steady state conditions (after N=65000 cycles) of HOSTN5 between (a) E_{eq} and $(\varepsilon_a)_{SA}$, and (b) h and $(\varepsilon_a)_{SA}$.

Fig. 7.13: Sensitivity of the number of data points per cycle in the evaluation of h and the resulting relationship between h and $(\varepsilon_a)_{SA}$ at a given frequency.

Chapter 8:

Figs. 8.1: (a) σ_a~ε_a, and (b) σ_a~ε_r relationships during creep tests performed on HOSTN2 specimen.

Figs. 8.2: (a) σ_a~ε_a, and (b) σ_a~ε_r relationships during creep tests performed on HOSTN4 specimen.

Figs. 8.3: (a) σ_a~ε_a, and (b) σ_a~ε_r relationships during creep tests performed on HOS12 specimen.

Figs. 8.4: (a) σ_a~ε_a and σ_a~ε_r relationships, (b) time histories of σ_a, ε_a and ε_r for the test segments (0)-(1)-(2) (of Fig. 8.2a) performed on HOSTN4 specimen.

Figs. 8.5: (a) σ_a~ε_a and σ_a~ε_r relationships, (b) time histories of σ_a, ε_a and ε_r for the test segments (1)-(2)-(3)-(4) (of Fig. 8.2a) performed on HOSTN4 specimen.

Figs. 8.6a through i: Time histories of the variation of σ_a, ε_a and ε_r during creep tests performed at different stress states of HOSTN4 specimen.

Figs. 8.7a through i: Time histories of the variation of σ_a, ε_a and ε_r during creep tests performed at different stress states of HOS12 specimen.

Figs. 8.8a through i: Time histories of the variation of γ and ε_{vol} during creep tests performed at different stress states of HOS12 specimen.

Figs. 8.9: Relationships between σ_a and creep rate in (a) ε_a, and (b) ε_r for different specimens.

Figs. 8.10: Relationships between (a) $E^e/f(e)$ and σ_a, and (b) ν and σ_a/σ_r of HOSTN4 specimen.

Figs. 8.11: Relationships between (a) $E^e/f(e)$ and σ_a, and (b) ν and σ_a/σ_r of HOS12 specimen.

Figs. 8.12: Relationships between $E_{sec}/(E_{sec})_{max}$ and ε_a for different stress segments (Type 1) of specimens (a) HOS12, and (b) HOSTN2.

Figs: 8.12: Relationships between (c) $E_{sec}/(E_{sec})_{max}$ and ε_a, and (d) $E_{tan}/(E_{tan})_{max}$ and ε_a for different stress segments (Type 1) of HOSTN4 specimen.

Figs. 8.13: Relationships between $E_{sec}/(E_{sec})_{max}$ and ε_a for different stress segments (Type 2) of specimens (a) HOS12, and (b) HOSTN2.

Fig: 8.13d: Relationships between (c) $E_{sec}/(E_{sec})_{max}$ and ε_a, and (d) $E_{tan}/(E_{tan})_{max}$ and ε_a for different stress segments (Type 2) of HOSTN4 specimen.

Figs. 8.14: Stress-dilatancy relationships during loading (σ_a increasing), unloading (σ_a decreasing), reloading (σ_a increasing), creep and delayed rebound for specimens (a) HOS12, and (b) HOSTN4.

Fig. 8.14c: Stress-dilatancy relationships during loading (σ_a increasing) and creep for HOSTN2 specimen.

Figs. 8.15: (a) $q\sim\varepsilon_a$ and (b) $\varepsilon_{vol}\sim\varepsilon_a$ relationships of different specimens during TC at $\sigma_a=\sigma_r=0.8$ kgf/cm^2.

Figs. 8.16: $q\sim\varepsilon_a$ relationships during TC at small strain levels with ε_a up to (a) 1.0%, (b) 0.10% and (c) 0.005%.

Figs. 8.17: Relationships between $E_{sec}/(E_{sec})_{max}$ and ε_a for different specimens during TC up to (a) the full range of ε_a, (b) ε_a= 0 5%.

Fig. 8.17c: Relationships between $E_{sec}/(E_{sec})_{max}$ and q/q_{max} for different specimens during TC.

Figs. 8.18: Relationships between (a) $E_{tan}/(E_{tan})_{max}$ and ε_a, (b) $E_{tan}/(E_{tan})_{max}$ and q/q_{max} for different specimens during TC.

Figs. 8.19: Relationships between (a) E_{tan}/E^e and $\log(q/q_{max})$, and (b) E_{tan}/E^e and q/q_{max} for different specimens during TC.

Chapter 1

Introduction

1.1. Background

Elastic deformation characteristics of soil, expressed in terms of shear modulus and bulk modulus (or Young's modulus and Poisson's rato), and material damping in case of cyclic loading, are important parameters for the design of soil-pavement and soil-structure systems subjected to cyclic and dynamic loadings. This is because, in most soil dynamic problems, shear stress levels are relatively low and stresses are repeated, therefore, the elastic deformation stiffness of geomaterials is one of the most important design parameters. In most usual static loading problems, on the other hand, the amount of elastic deformation is relatively small compared to plastic deformation. However, the deformation could be controlled by elastic components when a foundation is constructed on/in stiff soil and subjected to working loads.

In the past, much of the concern on cyclic loading was focused on the behavior of soils during earthquake loading. However, in the recent years, much interest has developed in the area of low-amplitude problems associated with human-made vibrations such as those caused by vehicular traffic, machine vibrations, pile-driving, and blasting. For these issues, the elastic behavior of soils needs to be understood more deeply. The perceived difference between static and dynamic moduli is decreasing as stress and strain measurements at small strains in static loading tests become more accurate. The advent of local strain measuring devices, such as electro-levels (Burland and Symes, 1992), local deformation transducer (LDT) (Goto et al. 1991), etc., helped researchers performing static tests to evaluate the true soil stiffness at small strains. The maximum soil stiffness thus measured is found to agree fairly well with that obtained by dynamic testing methods (e.g., wave velocity measurements, resonant column tests). Burland (1989), with the use of the small-strain stiffness value, predicted well the full-scale deformation of London clay in a real construction site. Bellotti et al. (1989) interpreted the shear moduli obtained from unload/reload responses in pressuremeter tests on sands based on the maximum shear

modulus and the strain level-dependency of shear modulus. Tateyama et al. (1992) found that strains induced in an embankment of the railway track under working loads were very small. In many case histories, the back-calculated values of in-situ Young's modulus agreed well with that obtained from the laboratory test at similar strain levels. A number of examples are available in the literature, such as Jardine et al. (1991), Siddiquee (1995), Tatsuoka and Shibuya (1992), Tatsuoka and Kohata (1995), and so on, which show the importance and essence of the measurements of deformation characteristics at small (10^{-5}% to 10^{-3}) to intermediate (10^{-3}% to 10^{-1}%) strains.

However, moduli at small strains (below 10^{-3}%) from cyclic tests are generally assumed to be independent of strain amplitude, and hysteresis material damping is often assumed to be a certain value which is nearly zero. Clear conclusions in this respect have not been obtained because of the difficulties in measuring accurate stress-strain loops in a cyclic loading test, which is a key factor in the study of deformation characteristics, particularly material damping, at small strains.

It is well established that the deformation characteristics of soil are neither linear nor isotropic. In the field, loading direction (i.e., the principal stress direction) in the ground beneath a foundation is not fixed in a certain direction either. Therefore, three-dimensional (3-D) analysis based on the principles of elasto-plasticity is getting popular. For that purpose both plasticity and elasticity should be dealt with properly. For 3-D characterization of elastic deformation of geomaterials, their possible anisotropy must be well understood. Stokeo et al. (1991), Bellotti et al. (1994), and Lo Presti and O'Neill (1991), among many others, did some work in this field by means of wave velocity method.

The determination of the maximum moduli has become popular in both laboratory and field tests. The most well known method is to measure the velocity of body wave traveling through a soil medium, which can be performed both in the laboratory and in the field. However, the wave velocity measurements are not the only way to determine the elastic modulus of soils. They are not always the most convenient way either. There are some cases where elastic properties should be determined by other laboratory soil testing methods. These are:

(a) Stiffness of soil is strain-dependent and the values of G (or E) at larger strain levels cannot be evaluated from seismic techniques. Strain level-dependency of G (or E) must be determined by other laboratory tests. The resonant-column apparatus has often been employed for this purpose. It has two major limitations: the maximum applicable strains cannot exceed about 10^{-4}, and the number of loading cycles is very difficult to control and too large for many static geotechnical problems. Therefore, the triaxial and torsional shear apparatuses are often used to obtain the deformation properties at strains larger than 0.01% but less than 1%. Thus, to obtain deformation properties for a wide range of strain from about 0.0001% to that exceeding 10% and the peak strength, it conventionally requires three different specimens: one for a resonant-column test (strains less than about 0.01%), one for a special triaxial or torsional shear test (strains between 0.01% to 1%), and the other for a conventional triaxial or torsional shear test (strains larger than 1%). Since each specimen may have different qualities and properties (i.e., fabric, void ratio, bedding plane, etc.), it is difficult to construct a reliable overall stress-strain relationship from the results of these three tests. It is very important, therefore, to obtain the stress-strain relationship of a given soil from very small strains to failure by using a single specimen.

(b) Static loading laboratory test apparatuses are more widely in use than dynamic ones (e.g., ultrasonic wave velocity measurement apparatuses and resonant-column apparatuses). It is convenient if as many fundamental soil parameters as possible can be determined from a test using the most commonly used equipment.

(c) For dynamic problems, the modulus and damping at strains less than 0.01% are accurately measured. However, in many static conventional analyses, much smaller value of the deformation modulus is estimated and used as the maximum stiffness including the elastic Young's modulus. In other words, a large safety factor is always applied to the analysis of the deformation in static problems, which is not realistic. To change this conventional practice, the first of all, the static test apparatuses need modifying aimed at obtaining the similar potential as the dynamic test apparatuses in accurate measurements of the stiffness and damping of soil.

1.2. Elastic Deformation Characteristics Properties of Soils

Deformation of soil is composed of elastic and plastic components. When a material is subjected to stress change, it is strained. Within some region of stress, the strain responds rather linearly. If the stress is reduced, the strain decreases reversibly, and upon the complete removal of stress, the residual strain becomes zero; the material is said behaving elastically. On the other hand, plastic deformation is always accompanied with slippage at inter-particle contacts, and re-arrangement and crushing of particles. Mindlin (1949) showed that slippage at the contact between two elastic spheres must occur even for the smallest tangential force.

It is very difficult to measure any elastic property by using a conventional laboratory test apparatus unless very small strains and stresses can be measured confidently. The elastic deformation may be considered as the total deformation of a mass of sand if its internal structure (i.e., fabric) is kept unchanged. Since the changes in structure are mostly caused by the application of shear force, elastic deformations can be isolated more easily by cyclically loading a sand specimen under the hydrostatic stress condition than by a conventional cyclic triaxial or torsional shear test (Hardin, 1978). Elastic strains can also be isolated in static tests by applying small cyclic shear strains with a strain amplitude less than 0.001% (Chen 1948, and Hardin 1978). This strain value may be called the threshold elastic strain. Moduli defined for this strain range are hardly influenced by (1) stress-strain histories that are small enough to maintain the initial fabric, (2) the type of loading (i.e., monotonic or cyclic) and (3) the rate of shearing (dynamic or static), while the soil deformation at this strain level is recoverable (Tatsuoka and Shibuya 1992; Tatsuoka and Kohata 1995; Jamiolkowski et al. 1991). This static method has been employed in this study to evaluate Young's moduli of sands.

1.3. Testing methods

Field measurements of dynamic soil properties are generally limited to measurements of moduli at small strains (less than 0.001%), where the moduli are independent of strain amplitude. No practical field method is available at this moment for the measurements of material damping at any strain amplitude. Therefore, static cyclic and dynamic laboratory tests are often used to determine moduli and damping of soil over a wide range of strain amplitude. Field and laboratory tests

results are then combined with engineering judgement to obtain the nonlinear properties of soil in-situ.

Various laboratory testing methods have been used to determine the deformation properties of soils. In general, there are two basic groups of laboratory testing devices. One group is cyclic tests, which include (a) cyclic triaxial test, (b) cyclic simple shear test, and (c) cyclic torsional shear test. These tests are based on the measurements of the stress-strain relationships at low frequencies where inertia effects can be neglected. The other group is dynamic tests. Tests in this group are based on measurements of wave or pulse propagation, or the resonance of the system. The present study belongs to the first group, using triaxial apparatuses, which will be described in the foregoing chapters.

Dynamic Tests:

In dynamic laboratory tests, high frequency, transient or steady state excitations are applied to a soil specimen. There are two groups of dynamic tests: one based on resonant methods and the other based on wave or pulse propagation methods. In general, strain amplitudes associated with these tests are significantly less than those associated with conventional static cyclic tests.

Resonant-Column Test

A specimen is subjected to dynamic excitation force at a high frequency, while the frequency is adjusted until the specimen-apparatus system exhibits resonance. The modulus is computed from the resonant frequency and the geometric properties of the specimen and driving apparatus. The resonant-column technique was first applied to soil testing by Ishimoto and Iida (1937) and Iida (1938 and 1940). The early version of the device was used for testing soil under isotropic stress conditions. Hardin and Music (1965) developed a new resonant column apparatus, with which it is able to carry out a test at anisotropic stress states. In a solid cylinder specimen, shear stress and strain along the cross-section vary from zero at the center to the maximum at the edge. To reduce this non-uniformity in shear stress and strain distributions, Drnevich (1972 and 1978) developed a hollow cylinder resonant-column apparatus, in which the average shearing stress and strain on the horizontal cross-section are not greatly different from their maximum and minimum values.

Two specimen configurations have been attempted for the resonant column apparatus; i.e., free-free and fixed-free configurations. The fixed-free configuration has been found better-suited to this technique than the free-free configuration, since the latter is not perfectly free at either end and the degree of freedom is not easy to determine (Richart et al., 1970). Type of vibration can either be longitudinal (for the evaluation of Young's modulus) or torsional (for shear modulus measurement). Since driving and motion monitoring systems must be attached to the free end of the fixed-free arrangement specimen, these change the theoretical end-condition of the specimen. For a first mode of vibration, the compressive and shear wave velocities can be calculated as:

$$V_c = 2\pi f_n \, l / \beta_l \quad \text{(compressional)}$$

$$V_s = 2\pi f_N \, l / \beta_s \quad \text{(shear)}$$

where β_l and β_s are the functions of inertia force and mass polar moment of inertia of the added mass, respectively. The resonant column does not provide direct measurement of the element behavior of soil under tests, since the states of stress and strain vary continuously both with time and in their distributions within the sample (Jardine et al., 1984).

Pulse Tests

By measuring the travel time of shear or compression waves from their point of origin to a detecting sensor, pulse wave velocities can be obtained. From these velocities, moduli can be computed using elastic wave propagation theory. Lawerence (1963) was the first one to use piezoelectric crystals or ceramics to generate and detect wave disturbances in a conventional triaxial test cell. Knox et al. (1982) constructed a large scale triaxial device at the University of Texas and investigated the propagation of body waves under isotropic, biaxial, and triaxial confinements. Lewis (1990) developed a multi-moduli testing device to determine independently the constrained, rod, and shear wave velocities in the same specimen. One of the major drawbacks of pulse tests is the difficulties with the identification and the interpretation of exact wave arrival times.

Elastic Wave Velocity Method

This is the most popular field method for the evaluation of the maximum stiffness of soils and rocks. By propagating shear wave (S-wave) and compression wave (P-wave) through soil mass, the shear modulus, and one dimensional elastic modulus, respectively, can be determined. The difficulty in measuring wave velocity lies principally in the precise determination of very small time intervals. The general formulation for calculating the maximum stiffness from the velocity of propagated waves are:

$$\frac{\partial^2 u}{\partial t^2} = V_L^{\,2} \frac{\partial^2 u}{\partial x^2} \quad and \quad V_L^{\,2} = L / \rho \qquad \text{(longitudinal wave)}$$

$$\frac{\partial^2 u}{\partial t^2} = Vs^2 \frac{\partial^2 u}{\partial x^2} \quad and \quad V_s^{\,2} = L / \rho \qquad \text{(shear wave)}$$

where ρ is the mass density and u is the displacement. The maximum shear modulus, G_{max}, can be directly obtained from the shear wave velocity. However, the longitudinal modulus, L, is neither the bulk modulus nor the maximum Young's modulus, E_{max}. Rather it is often expressed as: $L = \lambda + G = \rho V_L^{\,2}$, where λ= Lame constant. For an isotropic material, $L = E / \{2(1+\nu)(1-2\nu)\}$(Teachavorasinskun, 1992), where E is the Young's modulus.

Wave velocities can be measured in field by downhole, crosshole, or other methods. In the downhole test, waves are generated by an excitor placed on ground surface, and the propagated waves are received by receivers which are located at different depths beneath the excitor. In the crosshole test, excitor and receivers are located at the same horizontal level in at least two different vertical bore-holes. The velocity of wave is in general dependent on the individual stresses within the plane of wave travel. The velocity of the wave propagated through the soil is theoretically the same between the conventional crosshole method with the particle movements in vertical direction and the downhole methods due to the same mode of small shear deformation. However, it should be noted that the velocity of the crosshole wave with horizontal particle movements propagating in different shearing modes is different from the above two methods. Then, the measured shear wave velocity can be different due to inherent anisotropy and stress-induced anisotropy by different individual stress components (Yan et al., 1991).

1.4. Damping ratio and its measurements

When a rodof any material is subjected to a state of free vibration (i.e., the vibration after the causing force has been ceased), the amplitude of vibration will decrease gradually and eventually disappear. This reduction is caused by internal damping of the material. In the resonant-column apparatus, the logarithmic decrement (δ) which is defined to explain the decay in the amplitude of the free vibration system is given by:

$$\delta = \frac{1}{n}\ln\frac{z_1}{z_{1+n}} = \frac{2\pi D}{\sqrt{1-D^2}} \approx 2\pi D$$

where D is the damping ratio, n is the number cycle, Z_1 is the amplitude of vibration at the first cycle, and Z_{1+n} is the amplitude of vibration after n cycles. Hardin (1965) found that for round granular materials, the plot between the amplitude and the number of cycle of oscillation in full logarithmic scale is linear. So the logarithmic decrement can be easily defined from the slope of this line. Another parameter that used to express damping is the decrease in amplitude of vibration with the increase in distance from a source. This is designated as 'coefficient of attenuation.' Damping is often estimated also from the response curve at and near the resonance state.

In a cyclic test, damping can be determined from the ratio of the energy absorbed in one cycle to the potential energy at the maximum displacement in that cycle. In other words, damping is represented by the ratio of the area enclosed by the hysteresis loop to the total area enclosed by the triangle joining three points: two peaks (the maximum and minimum values) of axial strain amplitude and the maximum value of axial stress amplitude of that cycle.

1.5. Factors Affecting Small-Strain Deformation Characteristics of Soils

Hardin and Black (1968) have indicated various factors which influence the maximum shear modulus of soils as:

$$G_{max} = f(\sigma_c, e, H, S, \tau_0, C, A, f, t, \phi, T)$$

where:

σ_c= effective octahedral normal stress,

e= void ratio,

H= ambient stress and vibration history,

S= degree of saturation,

τ_0= octahedral shear stress,

C= grain characteristics: grain shape, size, grading and mineralogy,

A= amplitude of vibration,

f= frequency of vibration,

t= secondary effects that are a function of time,

ϕ= soil structure,

T= temperature including freezing.

Hardin and Drnevich (1972) investigated these factors affecting the shear modulus and damping ratio of soils and grouped them into three categories; very important, less important and relatively unimportant. The five very important factors are strain amplitude, effective mean principal stress, void ratio, number of cycles of loading, and degree of saturation.

Again, the degree of influence of each parameter varies from soil to soil. For clean sands, the degree of saturation and the loading frequency have minor effects on the maximum shear modulus. Also the overconsolidation ratio, which imparts large effects on clayey soils, has a negligible effect on the stiffness of clean sand (Teachavorasinskun 1992). Some factors which were believed to be unimportant in the past are presently going to take an important role: the effects of stress ratio and initial shear on shear modulus (also on Young's modulus in this study), and the effects of grain size on inherent anisotropy in the Young's moduli (in this study). Tatsuoka et al. (1979) showed that in torsional shear tests, the shear modulus of a sand specimen in triaxial compression and extension is not a unique function of the mean effective stress p= $(\sigma_1+\sigma_2+\sigma_3)/3$ for a wide range of strain. Yu and Richart (1984), Roesler (1979), and Yan and Byrne (1991) reported that the elastic shear modulus of sands depends on the two normal stresses in the propagation plane than the mean effective stress p= $(\sigma_1+\sigma_2+\sigma_3)/3$. Jamiolkowski et al. (1991), on the other hand, suggested that the Young's modulus be only a function of the normal stress in the direction of the applied normal stress increment.

Much less research has been performed on the material damping than on the shear modulus of soils. Several investigators (Marcuson and Wahls, 1972a and 1972b; Stokoe and Lodde, 1978; Isenhower, 1979; Stokoe et al., 1980, and Ni, 1987) have investigated the low-amplitude damping ratio (D_{min}) by resonant-column tests. They found that D_{min} is independent of strain amplitude below a shearing strain of about 0.001% and decreases with the increase in the confining pressure and with the increase in the time of confinement at a constant effective pressure.

Silver and Seed (1971) tested crystal silica No. 20 sand at shearing strains between 0.01% and 0.5% using an NGI simple shear device. The shear modulus and hysteretic damping were found to increase and decrease, respectively, with the number of loading cycles. These changes with the number of loading cycles were the greatest in the first ten cycles, after which the changes were relatively small.

Vucetic and Dorby (1991) indicated that the seismic response of soil deposits can be very sensitive to the variation in small-strain damping. They reported that the range in small-strain damping ratios of soils found in the literature is from 0.5% to 5.5%. They recommended that, in an important project, small-strain damping be measured carefully, and more research be needed to determine the influence of different factors on small-strain damping.

Drnevich and Richart (1970) investigated the effect of dynamic prestraining on shear modulus and material damping of dry sand by performing resonant-column tests. They cycled a specimen with a large amplitude of strain (i.e., the single amplitude shear strain up to 0.06%), then reduced the strain amplitude to a value (say, 0.005%) to measure the shear modulus. Prestraining at relatively higher strain levels produced significant increases in shear modulus and damping ratio at relatively smaller to very small strain levels without any significant change in void ratio. They attributed the increase in stiffness to enlargement and improvement of particle contact areas. However, there was no chance to acquire data below 1000 cycles because the number of cycles required to resonate the specimen at a frequency in the range of 30 to 60 Hz is larger. Teachavorasinskun (1992), on the other hand, showed by performing triaxial tests that the elastic Young's modulus of sand is insensitive to cyclic prestraining, but the damping ratio decreases drastically as an effect of cyclic prestraining. He applied cyclic prestraining of a large

number of cycles (as large as 500,000 cycles) at a single amplitude axial strain varying in the range from 0.03% to 0.1%, and measured the elastic Young's modulus and damping ratio at the neutral stress state (isotropic or anisotropic) about which cyclic prestraining was applied.

Each external loading source for a soil-pavement or soil-structure system can be largely of different pattern and varying, which result in loading frequencies to be varied widely: ranging from very low frequency of about 0.05 Hz or below (such as ocean storm waves) to high frequency of above 100 Hz by machine vibrations. In general, soils subjected to cyclic loading typically experience higher rates of loading or strain than they do when characterized as monotonic. Therefore, proper understanding of the effects of loading rate on the deformation characteristics of soils has become an important issue. Researchers do not feel comfortable with this issue since no apparatus is currently available that can be used uniquely to investigate the rate-dependency phenomenon in the entire range of frequency of interest. Laboratory and field testing techniques have limitations in frequency characteristics in their measurements: the resonant-column apparatus is operable in the frequency range typically from 20 to 150 Hz, the torsional shear apparatus and triaxial apparatus are typically below 10 Hz, and the wave velocity methods are up to 400 Hz. Most of the previous works, such as Bolton and Wilson (1989), Graham et al. (1983), Kim and Stokoe (1995), Shibuya et al. (1995) and so on, were performed using simple shear, torsional shear and resonant column apparatuses. A few works using triaxial apparatus (e.g., Tatsuoka and Kohata, 1995) have been reported in the literature.

1.6. Objectives of the Present Study

The purpose of this study is to characterize the small-strain stiffness of granular materials under general stress conditions by using triaxial specimens. Materials tested are dry granular soils; grain size is varied from fine-grained to coarse-grained, while the particle shape is varied from subround to subangular, and the density of specimen is varied from loose to dense. Anisotropy has been investigated by direct measurements of Young's moduli in both vertical and horizontal principal stress/strain directions. Effects of cyclic prestraining and loading frequency on the elastic deformation properties are also critically investigated. To accomplish these purposes, the study has been divided into the following objectives.

1. To develop a methodology for the evaluation of elastic properties in both vertical and horizontal directions by measuring stresses and strains in triaxial testing system. Emphasis is given on the direct measurements of strains, free from any potential errors. For that purpose, some modifications in triaxial testing system are inevitable. On the other hand, complete characterization of elasticity of soil needs evaluating the elastic parameters at various stress states, which can be attained by following different stress paths and by rotating principal stress directions. To accomplish this with reasonable accuracy, an automated loading system is inevitable.

2. To examine extensively the performance of the measuring transducers, especially the Local Deformation Transducers (LDTs), in measuring the small strain stiffness. In this research, LDTs are extensively used to measure both vertical and lateral strains; the measurements are essentially free from many potential errors which are inherent in the conventional method. However, potential errors could come from other sources, such as slope-error in the calibration characteristics, creep, and/or insufficient resolutions and accuracy.

3. To investigate the existence of inherent anisotropy in small strain stiffness as typically measured at isotropic stress states. Their possible link with grain characteristics of particulate materials, strength and deformation anisotropies are to be sought.

4. To investigate the dependency of elastic Young's moduli on stress states at general stress states and, hence, to characterize the stress system-induced anisotropy.

5. To investigate the effects of stress ratio on elastic Young's moduli during triaxial compression and triaxial extension tests.

6. To investigate the effects of cyclic prestraining on the stiffness, anisotropy in elastic Young's modulus, Poisson's ratio and damping ratio of granular materials. Natural soil deposits have been somehow subjected to some degrees of cyclic prestraining by seismic, traffic, wave, and/or machine vibration loadings.

7. To investigate the effects of loading frequency on the deformation characteristics of sand. Test results could severely be affected, especially damping at higher frequencies in triaxial system, by time-lag of any type if exists between the recorded responses of strains and stresses. For that purpose, the data acquisition systems of strains and stresses and their measuring devices need to be verified.

8. To investigate whether granular material exhibits elastic behavior upon the restart of loading from any stress state during shearing after allowing creep deformation to occur at that stress state.

1.7. Organization of this Thesis

A brief review of literature on testing methods for determination of small-strain deformation properties of soils is presented in this chapter (Chapter 1). Then, factors affecting deformation characteristics of soils are discussed.

A large triaxial testing system is described in Chapter 2, along with the modifications required for the characterization of elastic deformation properties of soils. An automated system of loading in both horizontal and vertical directions, the principle of automation, and the performance of this system are also described. Manufacture of LDTs, its major components, modification of its components aimed at improving its performance in the last five years, and its performance in the measurement of very small strain stiffness are described. The performance of LDTs are evaluated in terms of its resolution, accuracy, and workability.

Theoretical background, based on the theory of elasticity, for evaluation of elastic deformation properties from small-strain amplitude unload/reload cycle is described in Chapter 3. Inherent anisotropy in elastic Young's moduli observed at isotropic stress states and elastic deformations observed during isotropic reloading and re-unloading is presented.

Chapter 4 described investigation into the dependency of elastic Young's moduli on stress states, the characterization of stress system-induced anisotropy in elastic Young's moduli, and a new cross-anisotropic elastic model based on experimental results. Hypo-elasticity, based on the observed elastic parameters, is also described.

Effects of stress ratio during triaxial compression and triaxial extension tests are described in Chapter 5. Results obtained from tests using a load-control and a displacement-control loading systems are compared. Elastic Young's modulus (evaluated from a typical unload/reload cycle) for higher shear stress level is redefined.

Effects of cyclic prestraining on elastic Young's modulus, damping, Poisson's ratio and deformation characteristics are described in Chapter 6. A small triaxial apparatus, which was used to obtain test results described in this chapter and Chapters 7 and 8, is also described. Effects of long-term consolidation on moduli and damping ratio are presented. The result of analysis based on the proposed cross-anisotropic elastic model is presented to show whether a granular material could exhibit a true elastic response during an unload-reload cycle of a relatively large stress amplitude after an application of a large number of cyclic prestraining at that amplitude, and during isotropic stress states.

Effects of loading frequency on stiffness and damping ratio are described in Chapter 7. Various attempts aimed at identifying the existence of any time-lag between the pair of measured strains and stress, which could severely affects final conclusion, are also described.

Investigation of whether a granular material exhibits elastic behavior upon the restart of loading at any stress state during shearing is described in Chapter 8. Creep behavior of sand during shearing, effects of previous stress histories on the elastic deformation properties, and dilatancy rate during loading, unloading, re-loading, creep deformation at a constant stress state (during both loading and unloading) are also presented.

Finally, a summary and conclusions of this work with associated recommendations for future studies are presented in Chapter 9.

Chapter 2

An automated triaxial testing system and the performance of LDTs

2.1. Introduction

In most usual static loading problems, the amount of elastic deformation is relatively small compared to plastic deformation. However, deformation can be governed by elastic component when a foundation is constructed on/in stiff soil and subjected to working loads. On the other hand, in most dynamic loading problems, shear stress levels are relatively low and stresses are repeated, therefore, the elastic deformation stiffness of geomaterials has been one of the most important design parameters.

Complete characterization for elasticity of soil needs evaluating the elastic parameters at various stress states attained by following different stress paths and by rotating principal stress directions. An advanced triaxial testing system (Tatsuoka 1988) is capable of controlling stress paths of, for example, constant mean stress $\Delta\sigma_m=0$, constant vertical stress $\Delta\sigma_v=0$, and constant horizontal stress $\Delta\sigma_h=0$ covering a wide region in both triaxial extension and compression stress states. Small-amplitude vertical cyclic loading (CL) with $\Delta\sigma_h=0$ and horizontal CL with $\Delta\sigma_v=0$ are convenient for evaluating elastic parameters — vertical Young's modulus (E_v), horizontal Young's modulus (E_h) and Poisson's ratios — directly from measured elastic deformation properties of a soil specimen. Some of the stress paths stated above need both the axial load and the cell pressure ($p=\sigma_h$) to be controlled simultaneously. Besides, when the inside volume of a triaxial cell is very large (as the one used in this study) and it is filled with air, fast variation of cell pressure as that of the deviator load (i.e., $\sigma_v-\sigma_h$) is difficult. Along a stress path that needs σ_h to be controlled, therefore, a sufficient time is required to attain a steady state for each step of loading (or unloading). The use of an automated system is essential, therefore, to ascertain a uniform rate of loading, to provide sufficient consolidation time at a given stress state, to minimize the deviation from an intended path, and above all, to avoid the tedious, time consuming work of manual control and its negative effects on the test result.

So far, several different types of automated triaxial testing systems have been developed by various researchers. Among others, Ampadu and Tatsuoka (1989), Atkinson (1985) and Pradhan et al. (1989) automated their systems in such a way that an intended stress or strain path is achieved by computer-controlling through one channel feed-back looping scheme for pneumatic pressure loading of σ_h while straining the specimen at a controlled constant rate of axial deformation. On the other hand, Bishop and Wesley (1975), Li et al. (1988) and Sheahan and Germaine (1992), among others, developed auto-loading systems, which can control σ_v and σ_h individually or synchronously to achieve a specified stress or strain path. The former type of control is simpler, but this study used the latter considering that it can control a wider range of stress paths as employed in the test program. This paper describes the automated triaxial testing system using a large specimen and shows several typical test results concerning anisotropic elastic deformation properties of sands.

2.2. Description of the triaxial system

The larger triaxial apparatus which has been in use in the authors' laboratory at the Institute of Industrial Science, University of Tokyo, was modified for the purpose of the present study (Fig. 2.1a). Unlike many other conventional triaxial systems, a) the axial load is measured with a load cell inside the triaxial cell to eliminate the effects of piston friction (Tatsuoka 1988), b) various stress-path tests including anisotropic consolidation can be performed by auto-controlling σ_v and σ_h, and c) axial and lateral deformations which are free from the effects of bedding error and membrane penetration are measured directly on the specimen surface by using local deformation transducers (LDTs) which were developed by Goto et al. (1991). A provision was made also for long-term lubrication, as suggested by Goto et al. (1993), to minimize the effects of end restraint at the cap and pedestal.

An external displacement transducer and two proximity transducers were also used to measure the displacement of the loading piston and the cap. Two proximity transducers were used to detect lateral movement of the specimen lateral surface. Although these external axial and lateral strains included, respectively, the effects of bedding error and membrane penetration (in case the lateral pressure is changed), these were measured to cross-check the general trend obtained from local strain measurements. A pair of vertical LDTs and four pairs

of lateral LDTs were used as shown in Fig. 2.1b. Fig. 2.1c shows the details of a pseudo-hinge attached on the specimen surface at one end of a lateral LDT. To use lateral LDTs, it is imperative to use a specimen having rectangular cross-section. Tatsuoka and Kohata (1995) and the preliminary results showed that the shape (i.e., non-circular) and size of specimen have little effect on the deformation behavior at small strains. A larger number of lateral LDTs were used assuming that the lateral strain distribution could be less uniform in both lateral and vertical directions of the specimen compared with the axial strain distribution.

An electro-pneumatic loading system (Fig. 2.2a) was used to apply the lateral stress (σ_h). Deviator load (i.e., the axial load in excess to that applied by σ_h) was applied by using a servo-hydraulic loading system (Fig. 2.2b) (Tatsuoka 1988; Li et at. 1988). From the functional point of view, the automated system consists of four components; (i) the geotechnical component unit (i.e., a triaxial apparatus and a specimen), (ii) a data acquisition unit which consists of transducers, the data conditioning unit and two analogue-to-digital (A/D) converter cards, (iii) a micro-computer, and (iv) a feed-back control unit which consists of a digital-to-analogue (D/A) converter card, an actuator and an electro-pneumatic (E/P) transducer. The data conditioning unit is armed with dynamic signal receivers, amplifiers and filters.

The micro-computer uses two feed-back control channels; one for the actuator of a servo-hydraulic system for axial load and the other for an electro-pneumatic (E/P) system for the lateral pressure. Both channels can transmit commanding signals individually or synchronously.

As mentioned earlier that Fig. 2.2a shows the details of the electro-pneumatic loading system, where a high pressure line from an air compressor is fed into a 8 kgf/cm^2 capacity regulator to maintain steady pressure in the supplied air. The E/P transducer, whenever receives a commanding signal (or signals) from the computer, converts it into the equivalent air-pressure maintaining a static equilibrium on the torque bar seated inside the E/P transducer. As the air-flow capacity of E/P transducer is relatively small, it was increased by using a 1:1 volume boaster while not changing the pressure value.

Fig. 2.2b shows the working principle of the servo-hydraulic loading system. It is a 50 tonf capacity servo loading system manufactured by Shimadzu Corporation, Japan, bearing the commercial name Servo-Pulser Jackey System. The sub-control system receives driving or input signals from the micro-computer and conveys it to the servo-amplifier in the load control module which was employed in the present study. The servo-amplifier, based on the prefixed maximum capacity (20% of the maximum capacity was used in this study), feeds signals into the servo-valve for the actuator. The servo-valve finally converts the signals into the equivalent axial load by allowing pressurized liquid, to a certain quantity, to enter the upper or lower chamber of the actuator, accordingly, depending on the compressive or tensile nature of current load increment.

2.3. Accuracy of Stress Control and Measurement

The accuracy of stress path control and stress measurements depends mainly on the control and measurement systems used. The accuracy of the feed-back control unit is determined largely by the bit precision of the D/A converter. The E/P transducer, for example, was set to control a full range of 8 kgf/cm^2 pressure over a 10 volt (V) range through a 12-bit D/A converter. Therefore, the smallest controllable pressure in this system is $(8/10)*(10/2^{12})=0.002$ kgf/cm^2. The accuracy of the measurement system, on the other hand, depends on many factors: the resolution of transducers, the extent of errors involved in the measurement, the amplification capacity of transducer signal, and the bit precision of A/D converter. Use of LDTs and an internal load cell helps in restricting the present issue to the last two factors. A number of lateral LDTs with a gage length of 18 cm, for example, were set to measure a maximum deformation of 2.5 mm over a range of -3.2 to +4.4 V. When small strains are to be measured, the output voltage is amplified ten times before being fed into the 12-bit A/D converter. The smallest detectable displacement is, therefore, $(2.5/7.6)x\ (10/2^{12})x\ (1/10)=$ 0.0008 mm (assuming linear calibration characteristics), equivalent to a lateral strain $4.4*10^{-7}$ (cm/cm), which is sufficient to capture elastic deformation properties of a sand specimen. Similarly, for the purpose of measuring small strains during cyclic loading tests, the resolution of the inner load cell transducer should be high enough. The measurable smallest axial load without the secondary amplification is, however, as large as 4.8 kgf, which is equivalent to axial stress of 0.009 kgf/cm^2 for a 23cm x 23cm square cross-section of the specimen. With

this resolution of load cell, at best 15 to 20 discernible data (considering axial stress only) would be available during an unload/reload cycle being applied to measure stiffness for small elastic deformation, which has been considered insufficient. This problem was overcome by amplification of the output voltage ten times before being conditioned by filter and digitized by A/D converter. This amplification was made after the output voltage was shifted to a small value, if necessary.

The resolution of the entire system is governed either by the resolution of the measuring system or by the resolution of the control system or by the convergence criterion used in the stress path control subroutine, whichever the larger. Table 2.1 shows the resolution of the control and measurement units used in this system.

2.4. Operation of the System

The output from the internal load cell was defined as zero when the deviator load at the top of the specimen, which is denoted as LC, is zero;

$$\sigma_v = \sigma_h + \frac{LC}{A_s} \qquad (2.1)$$

where A_s is the current cross-sectional area of the specimen. In the automated system, any desired stress-path, hence stress state, is achieved by varying the axial stress (σ_v) and the lateral stress σ_h (=p) in the desired manner. Since the response of internal load cell, which is free from bearing friction of the loading piston, is used throughout, the measured σ_v by Eq. (2.1) does not need any correction.

Eq. (2.1), which is valid whether σ_v is greater than or less than σ_h, implies that the vertical stress σ_v is dependent on σ_h and LC. Therefore, the working principle of automation is that a stress path with varying σ_h needs both σ_v and σ_h to be controlled simultaneously, which is traced by imposing many small steps of loading. In each step, a very small increment or decrement of $\Delta\sigma_h$ is first applied, which is followed by incremental feed-back to the deviator load until the stress state returns to the intended stress path.

Stress paths employed in the present study are 1) isotropic and anisotropic consolidation stress path, $\Delta K=0$ ($K=\sigma_h/\sigma_v$), 2) constant vertical stress path, $\Delta\sigma_v=0$, 3) constant mean principal stress path, $\Delta\sigma_m=0$ ($\sigma_m=(\sigma_v+2\sigma_h)/3$), 4) constant lateral stress path, $\Delta\sigma_h=0$, 5) vertical cyclic loading stress path with $\Delta\sigma_h=0$, and 6) horizontal cyclic loading stress path with $\Delta\sigma_v=0$.

In the σ_v-σ_h plane (Fig. 2.3a), consider a specimen at a stress state $1(\sigma_{v1}, \sigma_{h1})$ on the K=1 line. During loading along this path, suppose that an incremental voltage provided to the E/P transducer increases the lateral stress by $\Delta\sigma_h$. Because the cross-sectional area of the piston rod is less than A_s and the piston bearing friction exists, the corresponding increase in σ_v is less than $\Delta\sigma_h$. Therefore, the new stress state would be $m(\sigma_{vm}, \sigma_{hm})$ rather than $2(\sigma_{v2}, \sigma_{h2})$ on the K=1 line, where $\sigma_{hm}=\sigma_{h2}$ and $\sigma_{vm}<\sigma_{v2}$. Based on the difference between the measured and desired stress states, σ_{v2}-σ_{vm}, the feedback deviator load is increased or decreased by a finite value through the actuator. Keeping σ_h unchanged, this operation continues until the difference, σ_{v2}-σ_{vm}, reduces to a tolerable limit. A next increment of σ_h is then applied, which is followed by the procedure described above. It continues until the current lateral stress σ_h reaches to a given target value, ULT.

This algorithm was used also for anisotropic consolidation with minor modifications; the stress state 1′ or 2″ (on stress path K= 0.75 or 0.50) moves to the stress state m′ or m″ by the application of $\Delta\sigma_h$, then a deviator stress increment is applied to reach the stress state 2′ or 2″. As $\Delta\sigma_v\neq0$ and $\Delta\sigma_h\neq0$, one can obtain $K=\Delta\sigma_h/\Delta\sigma_v=\Delta\sigma_h/(\Delta\sigma_h+\Delta LC/A_s)$ from Eq. (2.1), where ΔLC is the incremental deviator load. This provides;

$$\Delta LC/A_s = \Delta\sigma_h\left(\frac{1}{K}-1\right) \qquad (2.2)$$

It is worthy to mention that ΔLC is the quantity measured with the internal load cell. The equivalent actuator load must be larger than ΔLC due to piston friction, etc. For the same $\Delta\sigma_h$, according to Eq. (2.2), feed-back to the deviator stress after each increment or decrement in the lateral stress is more-or-less inversely proportional to K. Therefore, to limit the iterative

scheme within a specific time, the incremental value for feed-back needs to be increased as K decreases.

The method described above can be used also for stress paths $\Delta\sigma_v=0$ and $\Delta\sigma_m=0$. Controlling $\Delta\sigma_h=0$ stress path is rather straightforward and is achieved by allowing deviator load to increase or decrease continuously by a finite step until σ_v reaches to a given target value. Stress path control for vertical cyclic loading (CL) is the same as that for a monotonic loading test with $\Delta\sigma_h=0$. The only difference is that the axial stress σ_v is varied sinusoidally with time in a cycle. Similarly, horizontal cyclic loading (CL) is applied by varying σ_h in a triangular wave form at a constant σ_v. The effect of using two different wave forms, sinusoidal and triangular, is considered negligible. In the present study, loading frequencies for vertical and horizontal CL tests were 0.1 and 0.0067 Hz, respectively. Horizontal CL is not possible to apply as fast as vertical CL because of an inherently sluggish response of pneumatic loading system, the large triaxial cell size and the feed-back iteration scheme.

2.5. The Software Program

A program, HOQ.BAS, was written in BASIC, which consists of two major parts (Fig. 2.3b); a Control routine and a Performer routine. The Control routine consists of two main sub-control routines; CONTINUE and MULTI.TEST. It (the Main, Fig. 2.3b) first initializes A/D-card, D/A-card and other necessary internal variables, and transfers the control to CONTINUE. The subroutine CONTINUE actually does all the managerial action for the Control routine. It receives the value of on-screen control-flag, MULTI (0/1), from the operator to a take decision whether a test series will be performed as one-test-per-time basis (MULTI=0) or as a continuous process (MULTI=1). In the former case, CONTINUE will then receive on-screen test variables such as PATH (to define the stress path), ULT (the target stress), K ($=\sigma_h/\sigma_v$ for consolidation stress path), and so on, depending on the type of test to be followed next. After confirmation and re-confirmation of the variables, the control is transferred to 'Performer routine.' For MULTI=1, on the other hand, the control is transferred to another sub-routine, MULTI.TEST, to perform a series of unattended continuous tests. This routine reads test variables of one test from an input-file, transfers the control to

'Performer routine' for performing the test, reads test variables for the next test when the control returns, and so on until the end of input-file appears. To get commands to be executed next, the control is transferred to the operator via CONTINUE routine.

The Performer routine finally materializes a specific test into reality. It consists of sub-routines for different stress path tests and CL tests. Each sub-routine can be activated by assigning a specific value to the flag PATH. Thus, Performer routine transfers the control to the specific subroutine according to the value of PATH to have the specified test performed. The control returns to either CONTINUE or MULTI.TEST subroutine depending on the flag value MULTI.

2.6. Performance of the automated system

Partial vacuum was applied to the specimen before the mold was dissembled and was replaced by the equivalent cell pressure before the automated system was being in use. Figs. 2.4a~g show typical test results which demonstrate the typical performance of the system in achieving monotonic loading along different stress paths and cyclic loading, obtained from a test on dense Ticino sand (e=0.58). Ticino sand is a poorly graded, silica-dominant sand. Its physical properties are; G_s=2.68, D_{50}=0.502 mm, e_{max}=0.96, and e_{min}=0.59. While following stress paths such as $\Delta K=0$, $\Delta\sigma_v=0$ and $\Delta\sigma_m=0$, the vertical stress was adjusted so that the variation was within ±0.005 kgf/cm^2, which determines the overall accuracy of the system. The accuracy for $\Delta K=0$ stress path was within $\Delta K = \pm 0.003$, while it was within $\Delta\sigma_v = \pm 0.005$ kgf/cm^2 and $\Delta\sigma_m = \pm 0.006$ kgf/cm^2 for the stress paths $\Delta\sigma_v=0$ and $\Delta\sigma_m=0$, respectively. Fig. 2.4e shows the cyclic variation of the horizontal stress obtained from a horizontal CL test performed with $\Delta\sigma_v=0$ for the purpose of evaluating the elastic Young's modulus E_h in the lateral direction, while the variation of σ_v in the same test is shown in Fig. 2.4f. Fig. 2.4g shows the variation of $\Delta\sigma_v$ in a vertical CL test.

2.7. Performance evaluation of LDTs for the use in Triaxial tests

The small strain behavior of soil is of great importance in various geotechnical engineering practices where pre-failure ground deformations are considered. In particular for the case of relatively stiff soils (e.g., dense sands and hard clays) and soft rocks, strain levels in the ground under working load conditions are less than about 0.1% (e.g., Burland, 1989; Jardine et al., 1991; Tatsuoka and Kohata, 1995; Tatsuoka et al., 1995). On the other hand, precise determination of soil stiffness at strains less than about 0.1% is difficult to achieve in routine laboratory triaxial tests. In triaxial test, conventional external measurements of specimen deformation of hard soils and soft rocks can include large effects of the compliance of the loading system and load measuring system as well as the so-called bedding error at both ends of specimen, resulting in the underestimation of the true stiffness. For a triaxial specimen, therefore, it is crucial to measure 'local strains' to exclude those potential errors. A number of local strain measuring devices have been developed in the past two decades, such as electrolevel gauge by Burland and Symes (1982) and Jardine et al. (1984), Hall effect transducer by Clayton et al. (1986, 1989), non-contact type proximeter by El-Hosri et al. (1981) and Hird and Yung (1987, 1989), and local deformation transducer (LDT) by Goto et al. (1991). In many laboratories, it is now possible to measure with confidence axial strains smaller than 0.01%.

Seismic methods have been popular in evaluation of the elastic deformation properties of geomaterials (e.g., Stokoe et al., 1991; Bellotti et al., 1994). However, the maximum Young's modulus (E_{max}) of a given geomaterial under given conditions in the range of 0.001% of a single amplitude axial strain evaluated by applying small unload/reload cycles is comparable to the corresponding value obtained by field body wave velocity measurements (e.g., Tatsuoka and Shibuya, 1992; Tatsuoka and Kohata, 1995). This finding is in agreement with the fact that the deformation characteristics at those small strain levels are essentially recoverable and strain-rate independent in triaxial tests on clays, sands, gravels and artificial and sedimentary soft rocks (Tatsuoka and Kohata, 1995; Tatsuoka et al., 1995). Consequently, the advent of those local strain measuring devices allows geotechnical engineers to measure elastic properties of geomaterials for a wide range of shear strains and stresses up to the peak failure

condition (Tatsuoka and Kohata, 1995), which is very important for proper modeling of geomaterials.

Since the first use in the Geotechnical laboratory of the Institute of Industrial Science, the University of Tokyo, LDTs have been improved continuously. This section summarizes improvements to LDTs made after the publication of Goto et al. (1991). The sensitivity (or resolution) of LDT measurements has increased noticeably by those improvements. On the other hand, measuring elastic deformation properties in the course of triaxial compression testing by applying a series of small unload/reload cycles has become the standard testing procedure in the Geotechnical laboratory (IIS) (Tatsuoka et al. 1994a, 1994b). For this type of testing, hysteretic properties of LDTs should be minimized. Axial strain is obtained by substituting the responses of LDT in voltage observed during each unload/reload cycle into the respective calibration curve (i.e., the nonlinear relationships between the output voltage and the axial compression for a given LDT established for monotonic loading). Therefore, elastic Young's moduli evaluated from small axial strain amplitudes may include errors due to the hysteresis effects.

Discussed herein are recent developments in the structure and calibration procedures of the current version of LDT, the resolution and the largest measurable axial strain, the hysteretic characteristics, and the durability when used in pressurized water, together with some limitations (Scholey et al., 1995).

2.7.1 Structure of LDT and Data Acquisition System

Reliable small-strain values can be obtained only by a good combination of sensitive transducers (e.g., LDTs) and a stable high-resolution data acquisition system. The instrument consists of a pair of thin phosphor bronze strain-gaged strips bridging a given gage length as shown in Fig. 2.5. Each strip is in contact with the surface of a specimen at each end of the gage length, and is balanced by its own elastic force against a pair of pseudo-hinges that are attached to the surface of a specimen. Axial deformation of a specimen causes relative displacement of the hinges, and thus the arching of the strips. Bending of each strip is detected

by small electric-resistant strain gages attached to both sides of the strip. The output can be related directly to the axial deformation of the specimen.

2.7.2 Materials for LDTs

(a) Heat-treated phosphor-bronze strip: Normal bronze (i.e., untreated) cannot withstand axial buckling without permanent deformation, but heat-treated phosphor-bronze strip does. This highly elastic behavior is imperative for the reliable use of LDT since its working principle is based on the elastic buckling deformation of the carrier strip. Stainless steel is not used because its carbon content, even in the smallest quantity, accelerates corrosion by carbonation with the oxygen present in air or water.

The gage length varies with the specimen size (i.e., the specimen height for axial strain measurements). Table 2.2 is the list of sizes being used successfully at the Geotechnical laboratory (IIS). The width and thickness and, hence, the self-weight should be as small as possible within the operational limit. Therefore, the width should at least be just sufficient to provide an area for electric resistant strain gages (e.r.s.gs.) and terminals to be attached at the central height. Elastic force during buckling exerted by the strip on the pseudo-hinges increases with the increase in the thickness and the width. The effect of elastic force is usually negligible.

(b) Electric resistant strain gages (e.r.s.gs.): Table 2.3 lists the foil type e.r. strain gages manufactured by Kyowa Electronic Instruments Co., Ltd., Japan, that are in use for LDTs. The carrier matrix uses a polyimide resin that provides superlative adhesion and moisture-proof properties. The extra thin backing guarantees a high flexibility so that accurate strain measurements are possible within the entire measuring range up to a nominal strain limit equal to 5% at the room temperature. Other important catalogue technical properties are: operating temperature from -196 to $+150^0$C and a fatigue life of $2*10^6$ cycles at a strain level of ± 1500 με (micro-strain).

Normally, an individual e.r. strain gage is affected not only by changes in gage strains but also by changes in resistance caused by temperature variations. For LDTs, the sources of 'temperature-induced apparent strains' are of two types: (a) the temperature effect on the carrier strip, i.e., the effects of length change of the carrier strip appears as strain directly in the measurement, and (2) the temperature effect on leadwire resistance. These problems can be solved essentially by means of a full Wheatstone bridge (as has been done for LDTs). The former problem has also been overcome by the 'self-temperature-compensating' (S-T-C) capability engineered into each e.r.s.g.. By S-T-C, the temperature coefficient of resistivity of the e.r. strain gage's resistance element is compensated for the coefficient of linear expansion of the object being measured (i.e., the LDT strip) so as to reduce the temperature change-induced strains of the object. The e.r. strain gages with this S-T-C capacity which have been developed for the use with stainless steel are currently in use for LDTs (Table 2.3). Phosphor-bronze has a coefficient of linear expansion equal to $\pm 16 \mu\varepsilon/^0C$, which is similar to that for stainless steel (i.e., $\pm 18 \mu\varepsilon/^0C$). As a result, the apparent strain due to temperature changes becomes much smaller to the order of $\pm 1.0 \mu\varepsilon/^0C$. However, the effects of temperature change cannot be totally eliminated because of the curved shape of LDT at working condition (as described later).

Two or four e.r. strain gages are used for each LDT (Table 2.2). Previously, each of all the LDTs with a length range from 6 cm to 50 cm used four e.r. strain gages, since the two-e.r. strain gage type is less sensitive than the four-gage type under otherwise the same condition. However, the latest version of LDT with a length of 6 cm or 8 cm utilizes two e.r. strain gages, one in compression side and the other in tension side. This new configuration is based on the following facts;

(i) The output from e.r.strain gages for a given normal strain to be measured is proportional to the ratio t/l, where t and l are the thickness and length of each phosphor-bronze strip, respectively. Therefore, with a constant t, LDTs become more sensitive with the decrease in length. At the same time, the elastic force increases, which may increase the creep deformation of adhesive and rubber membrane at each pseudo-hinge. Therefore, it is required to reduce the width of a strip, which results in a reduction in the area available for attaching e.r. strain gages.

(ii) Due to the recent advantages in the e.r. strain gage technology in addition to the point described above, a sufficiently high resolution can be realized by using only two active gages.

When four active e.r. strain gages are used, they are connected to each other via terminals to form a Wheatstone bridge (see Figs. 2.6 and 2.7). When two active e.r. strain gages are used, two additional dummy resistors (120Ω) — feigning gages — are used to form a full bridge (Fig. 2.7c). A pair of dummy resistors D1 and D2 is placed either inside or outside the triaxial cell. Even when the temperature is different between the pairs of active e.r. strain gages (Nos. 1 and 2) and the two dummy resistors, the effect of this difference on the output of the bridge is theoretically none. The bridge formation and purpose will be described later.

(c) Adhesive: To obtain high quality data, e.r. strain gages must be firmly fixed to the measurement material — the LDT strip. The optimum adhesive should be selected depending on the measurement material, the material of the carrier matrix (of the micro-e.r. strain gages) and the specific measurement conditions. Adhesive Kyowa CC-33A has been used as the cementing agent for LDTs. It is a single-component cyanoacrylate with the operating temperature from -196^0 to $+120^0$C and clamping pressure in the range of 0.5 to 1.0 kgf/cm^2 (50~100 kPa) to be applied with a thumb. A curing time of about one minute at the room temperature, which is usually followed by post-curing for about four hours at the room temperature without clamping pressure.

(d) Gage terminals: Gage terminals, as denoted by solid circles in Fig. 2.6b, are used to connect e.r. strain gages to instrument leadwires. They prevent force exerted directly to the e.r. strain gage if the leadwires are slightly pulled. Kyowa T-F7 with the operating temperature is -196^0 to $+120^0$C is suitable terminal for foil-type e.r. strain gages, since the dimensions are very small, the weight is very light, and the applicable adhesive is also CC-33A. For a four-gage type LDT as shown in Figs. 2.6a and b, four gage terminals on each side (eight terminals in total for each LDT) are used.

(e) Protective coating: Sealant KE47RTV or KE45RTV (manufactured by Shin-Etsu Chemical Co., Ltd., Japan) is usually used, together with surface treatment agents (Primer FA and FB), to seal the e.r. strain gages and gage terminals. The sealant is a silicone compound, which has

high heat resistance and outstanding elastic properties (rubber springiness). The primers are used to ensure a good contact between phosphor bronze and silicone sealant. The water-proofing properties of the sealant keeps the e.r. gages and terminals from coming in contact with cell water and thus facilitates the under-water use of LDTs.

(f) Leadwires: As the electric resistance of the leadwires connecting the e.r. strain gage and the measuring instrument greatly affect the accuracy of the measurements to be taken, they should be of minimum length. Another consideration, which is unique for LDTs, is that the instrument leadwire should be as small in diameter and as light in weight as possible. Since the wire is attached on and hangs from the heart of the LDT (Fig. 2.5), even a slightest disturbance caused by air, vibration, etc. can result in shaking of the instrument leadwire under working condition. This eventually disturbs the measurement by desultory voltage output. This inherent problem for LDTs, which is more serious for the shorter and the lighter LDTs, has been greatly reduced recently by using an ultra-thin sophisticated type leadwire. Table 2.4 compares the two types of leadwires. The use of the new type leadwire, instead of a conventional relatively thick type, greatly improves the performance of short LDTs. Long LDTs, however, do not exhibit any problem with the use of conventional thick type leadwires. The improvement demands some sacrifice; that is, the use of thin leadwire increases the electric resistance in series, since the resistance is inversely proportional to the diameter of wire. However, the problem becomes serious only when a LDT undergoes a wide temperature variation (about 10^0C or more) during testing.

2.7.3. Manufacturing of LDT

Manufacture of LDT is outlined below with reference to one with four e.r. strain gages.

Preparing phosphor bronze (PB) strip: It consists of cutting a PB strip into a desirable length, smoothing and shaping the edges with a fine file, and filing the central part with fine-grained sand paper. Fats, oils and dirts are removed from the surface of the strip by wiping with a gauze having absorbed acetone (i.e., a volatile solvent, which dissolves oils and fats) firmly in one direction.

Fixing e.r. strain gages on the PB strip: Four gage terminals are arranged into a 2x2 matrix and glued by using an adhesive (Kyowa CC-33A) slightly off-centered within the width of the PB strip. Two e.r. strain gages are arranged side-by-side across the length of LDT strip and their back faces are affixed to the PB strip by using the same adhesive, also slightly off-centered but in the opposite direction to the gage terminals (Fig. 2.6a and b). After allowing sufficient time (at least four hours at the room temperature) for full strength mobilization of the glue, the similar procedure on the reverse side is followed. Fixing e.r. strain gages is the most important step to ensure:

- a very good contact between the PB strip and the e.r. strain gages so that the conjugate will function as an itegrated unit, and
- 'no slackness' to both the e.r. strain gages and the PB strip while bonding; for that, they must be glued to each other under perfectly unstretched and unbended conditions.

Wiring: To avoid confusion, the strain gages and terminals are named (or numbered) as shown in Figs. 2.6a and b. As mentioned earlier, four e.r. strain gages (or two strain gages plus two dummy gages) are connected into a Wheatstone bridge (Fig. 2.7a). For that purpose, each e.r. strain gage is connected by soldering to two adjacent terminals (one near terminal and the other far terminal) on the respective face (tension or compression) of a PB strip. The e.r. strain gage No. 1, for instance, is connected to the terminal B′ (near one) with the outer gage lead and to the terminal A (far one) with the inner wire; for the latter, the central part of the gage leadwire is covered with teflon tube for safety purpose. Then each corresponding terminals bearing the same lettered-name (primed and unprimed) are short-circuited (e.g., A and A′).

The instrument leadwires from the terminals A, B, C, and D are then connected to, for example, a 7-pin receptacle (i.e., a plug, PRC03-12A-10-7M-10, Tajimi Musen Co., Ltd.) as shown in Fig. 2.7b. The receptacle is to be connected to a dynamic strain measuring device for input-output purposes.

As the gage leadwires and the instrument leadwires become longer, variations in leadwire resistance caused by temperature changes (as augmented by the variation in length) may occur

in the form of apparent strain, resulting in measurement error. By adopting a Wheatstone bridge, such temperature influence can largely be eliminated.

Coating: After cleaning the surface of application (i.e., the central part of LDT containing e.r. strain gages, terminals, connecting leadwires, the tie of leadwires, etc.), the primers are spread on that area. When they get dry, silicone (KE47RTV or KE45RTV) is applied as final coating. It has sufficiently high flow property to spread by itself to the edge of the strip as well as to cover the interested small but important parts.

2.7.4. Data Acquisition System

Fig. 2.8 shows the block diagram of the data acquisition (DA) system for LDTs. The LDT's bridge is energized by 2V AC supply from a dynamic strain amplifier, which is Kyowa DPM-600 series, through the input terminals A and C (Fig. 2.6a). The AC amplifier receives continuous output signals through the bridge terminals B and D, measuring the signals in terms of voltage, which is controlled by the gain (i.e., the amplification ratio) and zero-shift value. As each LDT has a particular non-linear relationship between the axial compression and the output (i.e., calibration characteristics, CC), the gain values must be preset and fixed once the CC has been determined. The gain should be set at a proper value so as to obtain the optimum resolution depending on the maximum axial deformation to be measured. A calibration signal [CAL], 100~200$\mu\varepsilon$, can be used occasionally to confirm the gain value. Zero-shifting can be made arbitrarily when necessary as described below. A DC amplifier is used to increase the gain value exactly ten times to increase the resolution, which is necessary to measure very small strain increments. In that case, zero-shifting often becomes necessary, but this shift-value should be recorded to use later to get back the actual voltage before zero-shifting. In order to eliminate unwanted high frequency noise components involved in the input to the DC amplifier, the AC amplifier is armed by a built-in low-pass filter. A cut-off frequency equal to 10 Hz is used for LDT. The output from the DC amplifier is directed to another low-pass filter (33 Hz cut-off frequency) to increase a signal-to-noise ratio. Finally, data is fed into a 16-bit micro-computer through a 12-bit A-D card, which is set for a voltage range of -5 to +5 V. The other line from the DC amplifier is connected to a digital voltmeter (Fig. 2.8), which is used for visual purposes, particularly during zero-balancing and zero-shifting.

2.7.5. Resolution of LDT

The evaluation of the resolution (and hence sensitivity) of an LDT is an essential but a painstaking task as the system of LDT incorporates an AC amplifier and an A-D card, both of which have their own resolutions, which may control the actual resolution of the LDT.

Before evaluating the resolution of the whole measuring system of LDT, it is necessary to evaluate the smallest resolutable voltage (or deformation) during sampling data through a DA unit. Fig. 2.9 shows the variation of voltage output with time at an arbitrary setting of an LDT at a standstill condition. The output voltage was expressed in terms of the resolution voltage (RV) of A-D card, which is 10 V/2^{12} = 2.441 mV. Pseudo-hinges of LDT were fixed directly on a rigid steel plate by using high strength glue. The normalized voltage is always an integer and varies within the range of 0 to +1 RV (or 0 to -1 RV). In other words, a combination of an AC amplifier and an A-D card exhibits a resolution of 1 RV with an accuracy of ±1 RV. The values of resolution and accuracy were confirmed as exactly the same as those for the A-D card according to the manufacturer. Therefore, it is clear that the resolution of A-D card (1 RV) is the governing factor when that of AC amplifier is smaller. Consequently, an AC amplifier should possess a resolution higher than or at least equal to 1 RV, which can be set by adjusting the gain and vernier of the AC amplifier. Therefore, in any case, the resolution of an LDT (more precisely, a system comprising of an LDT, AC amplifier and A-D card) would be nRV, where $n \geq 1$ (an integer). The e.r. strain gages used in manufacturing an LDT possess an infinite resolution. Even so, one cannot get a value of n less than unity because of the lower-bound resolution, 1 RV.

Figs. 2.10a and b show a typical response in a sine-wave form cyclic loading (CL) test (load-controlled) performed on a large specimen of dry Toyoura sand (57 cm high and 23 cm × 23 cm in cross-section) isotropically consolidated at stress states σ_c= 2.0 kgf/cm^2 (196 kPa) and 4.5 kgf/cm^2 (441 kPa), respectively (Fig. 2.1b). Toyoura sand is a fine-grained, sub-angular, quartz-dominant Japanese sand with D_{50}=0.16 mm, U_c=1.46, e_{min}=0.61, e_{max}=0.97 and G_s=2.64. A pair of vertical LDTs of 50 cm long were used to measure locally axial strains. The single amplitude axial strains were 0.0014% (at σ_c=2.0 kgf/cm^2) and 0.001% (at σ_c=4.5 kgf/cm^2) for Fig. 2.10a and Fig. 2.10b, respectively. For convenience, axial stresses were

plotted directly against axial strains in terms of voltage output (in RV), which had been amplified 10 times. Arbitrary zero-shifting has been made in both axes directions. The shift values were, for instance in Fig. 2.10a, +210 RV along the horizontal voltage axis equally for both loading and unloading, and +0.02 kgf/cm^2 along the axial stress axis for unloading only. It can be seen that the LDT was able to respond for very small increments of axial strain. This point can be noted from the data obtained when the loading rate was small at and near the two extreme stress condition (see the encircled data in Fig. 2.10a and b). At these locations, data was sampled even at an interval of 1 RV. At other locations, where loading rate was high and non-uniform, data was sampled at a regular interval of 3 to 6 RV (see the data in the dotted polygon). Note that sinusoidal wave-form cyclic load was applied at a frequency of 0.1 Hz during which loading rate (absolute value) was varied between 0 to 1.885 kgf/cm^2/minute. As data passes through an A-D card, which has an accuracy of ±1 RV, one may expect two dissimilar (unequal) data at a particular standstill position of an LDT (Fig. 2.9). Considering this, it can be said that LDTs can respond to a displacement which is equivalent to at least 2 RV. The scatter in the data shown in Figs. 2.10a and b are due to not only these factors (i.e., the resolution of LDT, accuracy of A-D card - AC amplifier system, and the loading rate) but also the resolution of the axial load measuring system. The latter factor is equally important to accurately measure the stiffness of specimen at small strains.

Showing the equivalent axial strain (e.a. strain) to 2 RV as the resolution of LDT is more appealing in the performance evaluation of LDT in small strain behavior of geomaterials. Since the calibration curve of an LDT is non-linear (Fig. 2.11), the e.a. strain also varies with the slope (=dy/dx; Fig. 2.11) as the output voltage varies with the change in deformation of LDT. For that, 'nominal' axial strain (N) based on a fictitious linear calibration curve joining the two extreme ends of the actual calibration curve could be a good way for representation. In such a case, the range of variation due to non-linearity must be defined. Nominal axial strain (N) can be defined as

$$1N = 2RV * (dy/dx)_{linear} * (1/LL) * 100\% \qquad (2.3)$$

where the entities LL and $(dy/dx)_{linear}$ stand for the length of LDT (more precisely the gage length) and the slope of fictitious linear calibration curve. Using LL=105 mm and

$(dy/dx)_{linear}$=0.38 (see Fig. 2.11), the resolution of LDT becomes 0.0018% nominal axial strain (without amplification). The actual equivalent strain can be obtained by replacing $(dy/dx)_{linear}$ of Eq. 2.3 with dy/dx, the actual slope at a given point. The value of dy/dx varies in the range of $0.18 \leq dy/dx \leq 0.59$ for the calibration curve shown in Fig. 2.11. Therefore, the maximum resolution of the LDT is equal to 0.00085% of axial strain (without amplification). A better resolution (less than 0.0005% of axial strain without amplification) can be obtained by utilizing the full scale output voltage (-5 V to +5 V) for the same deformation range. For example, Fig. 2.11 utilizes 5.7 V, out of full scale range of 10 V, to measure a 2.2 mm total deformation. If the total 10 V range was utilized, the resolution could have become 0.00085*(5.7/10)% = 0.00048% of axial strain. It can be achieved by adjusting the gain and the zero-shift of the AC amplifier.

In the foregoing discussion, the assumptions that have been employed implicitly are: (1) there was 'no creep' deformation in the rubber membrane and the glue which was used to fix the pseudo-hinges on the membrane; (2) the rotation at the hinge was perfectly smooth. Since both the phenomena may be interrelated, it is not easy to evaluate the effect of each factor on the measured deformation. An attempt was made to evaluate the combined effects with time (herein it will called as 'creep') at different 'standstill positions' on the calibration curve (Fig. 2.11) of an LDT (10.5 cm long). 'Standstill positions' were -1.424 V, +3.882 V, and +6.056 V (on the extended part of the calibration curve). At each 'standstill position', two tests—Type 1 and Type 2, which are defined in Fig. 2.12a—were performed after each 'resetting' of the LDT. That is, after each test the LDT had been removed from the hinges by the 'catching fish' method and after a while, it had been re-anchored against the hinges immediately before the next test was started. The hinges were fixed once at the beginning of these tests. Fig. 2.12a shows the variation of voltage output with time at different standstill positions of the LDT. To bring the results into one plot, curves for +6.056 V and +3.882 V standstill positions were shifted down along the voltage axis for amounts of +4.259 V and +7.426 V, respectively. For convenience, Type 1 and Type 2 tests at different standstill positions will be called by the names given in Fig. 2.12a. Test group Type 1 (chronologically V_2, V_3, V_1) was performed first and was followed by the test group Type 2 (chronologically V_{11}, V_{22}, V_{33}).

The test results show the following trends. (a) 'Creep' exists and increases with time for both types (Type 1 and Type 2) except for test V_1. The maximum creep strains $(\varepsilon_{cr})_{max}$, which was defined as 100*the maximum creep deformation/gage length, are indicated for each test in the figure. (b) At a given elapsed time, creep for Type 2 tests (i.e., V_{ii} (i=1~3) series) is larger than the corresponding one for Type 1 tests (i.e., V_i series). This result indicates that the observed creep deformation is largely due to the creep deformation of the latex membrane. (c) Creep rate is quite high (for example, average rate was 0.00024%/minute in test V_{33}) at the beginning of a test for a couple of hours, after which the rate decays out gradually. Fifty percent of the total creep occurs within an hour immediately after setting an LDT. After about two hours, the creep rate becomes very small (for example, average rate was 0.00004%/minute in the second couple of hours in test V_{33}). (d) The values of $(\varepsilon_{cr})_{max}$ for test series V_{ii} and V_i are in the ascending order of $V_{33}>V_{22}>V_{11}$ and $V_3>V_2>V_1$, respectively, which indicates that creep increases as the elastic force imparted by LDT on pseudo-hinges increases. The elastic force imparted by an LDT after having been set against the hinges does not change largely by further deformations of the LDT (Fig. 2.12b). Before recording any data, the LDT should be allowed to set in position against the hinges for at least about 60 minutes so as to allow the initial creep (about 50% of $(\varepsilon_{cr})_{max}$, Fig. 2.12a) to occur. This time duration is usually required after setting the LDTs on a specimen and before starting any test (cyclic or monotonic) on that specimen. In most tests in the Geotechnical laboratory of IIS, about an half-day is allowed between the set of LDTs and the start of test.

With the effects of creep, the measured strain will be underestimated during compression test and overestimated while following an unloading (swelling) stress path. In a cyclic loading (CL) test, loading and unloading stress paths follow sequentially. Therefore, creep strain may bring about some errors in the measured soil parameters (especially, damping) evaluated by CL tests. To examine this problem, a similar test of Type 2 of Fig. 2.12a was conducted with the same LDT, which was only about 60 minutes after the set of the LDT to the calibration table. Fig. 2.12c shows the variation of output voltage in RV (after amplified 10 times) with elapsed time at an arbitrary position of LDT during the calibration test. Data was recorded for one minute, a long duration compared to the time used to apply one cyclic load to evaluate small strain soil parameters. The creep was about 3 RV (total 4 RV of which 1 RV could be due to accuracy of A-D card; see Fig. 2.9), which produced an apparent axial strain increment of as

small as less than about 0.0001%. The problem of creep will have to be investigated more in details.

2.7.6. Effects of Temperature Change on the LDT Output

The dimensions of a specimen change upon temperature changes. Usually, this change cannot be detected correctly by LDTs, since LDTs may have a different response against temperature change. This is due to many factors, which include: (a) the change in the length of the PB strip due to temperature change which can be compensated partially by the e.r. strain gauges by means of S-T-C mechanism (described earlier), and (b) the change in the bending strain in LDT due to temperature change; differential temperature coefficients between soils and metal (i.e., PB strip) and temperature effects on membrane (especially the part of membrane between the hinges) are attributing to erroneous bending strains. This second factor can be illustrated by the following case. Suppose the dimensions of a test specimen are nearly insensitive to temperature changes, which means nearly no change in the gauge length of LDT. Then, temperature changes cause the length change in a LDT strip resulting in the change in bending strains in the LDT strip, which certainly does not reflect zero strains in the specimen. For this reason, tests should be performed in a temperature control room for accurate strain measurements by using LDTs.

The changes in temperature in the specimen and LDT strips may be caused not only by the changes in the room temperature, but also by introducing water into the triaxial cell which has originally a different temperature. Therefore, the LDTs should be left for a sufficient duration (until the temperature in the triaxial cell stabilizes) after having been set on the specimen lateral surface, and after introducing the cell water. This procedure may also help the rate of creep deformation at the hinges to become negligible before starting any soil test.

2.7.7. Small Strain Behavior of LDT

Fig. 2.11, as mentioned before, shows typical calibration characteristics (the relationship between the axial compression and the output voltage) of a 10.5 cm long LDT. The calibration method was the same as described by Goto et al., 1991 (see the figure inset in Fig. 2.11). That

is, the displacement was applied at the one end of the LDT by using a micrometer at a 0.05 mm/step. The load-unload relations exhibit visible but small hysteresis. Calibration coefficients are usually obtained by fitting unload-reload data together by defining a unique two-degree nonlinear curve as represented by an equation given in Fig. 2.11. Fig. 2.13a shows the corresponding typical 'error curve' of the LDT. Deformation error at a given state, ε_{err}, was defined by the difference between calibrated and real displacements from Y=0.0 mm divided by the length of the LDT in percent and plotted against the output voltage. For example, the calibrated displacement Y during loading was 0.1 mm (Fig. 2.11) and the deformation error was 0.008% (Fig. 2.13a). The true compression of LDT between the hinges at that state was 0.1 - (0.008*10.5*10)/100 = 0.0916 mm. Note, however, that the most important is the errors involved in the measured axial strain as the ratio to the true axial strain ε_a, which is obtained as:

$$R = \frac{\varepsilon_{err}}{\varepsilon_a} = \frac{(cd - rd)/gl}{rd/gl} = \frac{cd - rd}{rd} \tag{2.4}$$

where the entities cd, rd and gl are defined in Fig. 2.13a, and ε_a is the current 'true' strain depending on the origin defined on the calibration curve (Fig. 2.11). Fig. 2.13b shows the relationships between R and ε_a defined with the origin at point a during loading shown in Fig. 2.13a. Errors in a strain increment between the given two points can be obtained from the difference between the corresponding values of R. The largest error will be involved at and near the beginning and ending parts of the calibration curve. In the actual tests, however, LDTs are used to measure axial strain increments not from the point a, but from another point, for example, a′ or b, and not to the end point h, but to another point, for example, f or g. In these cases, the errors are much smaller, for example, the errors between the points a′ and c is not larger than 1% of the measured total actual strain increment of about 1.2%.

The evaluation of errors in a small strain amplitude applied during a unload-reload cycle is one of the important parts of this study, and needs another type of analysis. In an actual test on a soil specimen, the maximum Young's modulus (E_{max}) or equivalent Young's modulus (E_{eq}) is evaluated usually by applying a small strain amplitude cyclic loading. The deformation characteristics of LDT during such a unload-reload cycle is usually assumed to be similar to

the calibration curve obtained by a large load/unload cyclic test (e.g., Fig. 2.11). However, there exists a noncompatibility between the real and the simulated variations in LDT deformation, which is different from strain-errors described in Figs. 2.13a and b.

The behavior of LDT during a small unload/reload cycle was evaluated directly by applying a series of small-amplitude cycles to an LDT in the range of 0.004~0.15% of single amplitude axial strain, $(\varepsilon)_{SA}$, at arbitrary locations of the respective calibration curve. An LDT was set against hinges on a calibration table (Type 1 test, as described in Fig. 2.12a). Similar tests were performed using other LDTs having different lengths. Fig. 2.14a and b show typical results for a 10.5 cm long LDT, where the average values of $(\varepsilon)_{SA}$ were 0.143% and 0.0048%, respectively. The axial displacement was plotted against the output voltage. Two types of errors can be observed; drift error by a nearly parallel shifting of calibrated variation from the real data, and the slope-error. Drift error does not have any effect on the measured strain amplitude, but the slope error directly affects the measured stiffness. For example, for the case of the data shown in Fig. 2.14b, the use of the slope of the calibrated curve equal to 0.32114, compared to the correct value of 0.31945, leads to an under-estimation of (1-0.31945/0.32114)*100 = 1.38% of the correct stiffness. Note that the error in the stiffness measurement depends on the compression of the LDT (i.e., Y values in Fig. 2.11). The largest error for each different $(\varepsilon)_{SA}$ value obtained from similar CL tests using LDTs having different lengths are shown in Fig. 2.15. In all cases, the correct stiffness is under-estimated. The error, however, does not exceed 2%.

To date, LDTs have been calibrated by an incremental displacement method, where in each step, an axial displacement of 0.5 mm for a 50 cm long LDT or 0.025 mm for a 10.5 cm long LDT is applied. The corresponding strain increments are 0.05% for a 10.5 cm long LDT and 0.1% for a 50 cm long LDT. This strain increments could be too large to obtain the actual calibration curve for a small strain range. To examine this point, a 50 cm long LDT was calibrated by fine steps, 0.02% axial strain per step, which was five times finer than the usual method. Fig. 2.16a shows the calibration characteristics (set 1), together with the another obtained for the same LDT by the conventional method (set 2). The calibration coefficients do not show any appreciable change that could be attributed as a meaningful improvement over the conventional method.

For a small unload-reload displacement cycle with $(\varepsilon)_{SA}$=0.0075% (Fig. 2.16b), the overall calibrated relations obtained by set 1 and set 2 calibrations showed a negligible change in the slope; one could observe an 1.39% error in the stiffness measurement by the new method (set 1; fine stepping method), whereas it was 1.41% by the conventional method (set 2). Therefore, it can be concluded that the size of the displacement increments in the calibration method is not responsible for the errors involved in the small-strain stiffness evaluation. It seems that these intrinsic hysteresis behavior of LDT may come from effects of wiring, soldering, sealing, etc. at the central part of LDT, and/or imperfect movement at the hinges.

2.7.8. Workable Range of LDT

It is desirable to measure locally the axial strains as large as possible, since the effect of bedding errors does not necessarily decay as the axial strain increases. Lo Presti et al. (1995) used LDTs to more than 3% of axial strain without any damage to the LDTs. However, the use of LDT for more than 2% of axial strain (with full-scale calibration; -5 to +5 V) needs sacrificing the accuracy and resolution, in particular for the measurements of very small-strain behavior. For example, Tables 2.5a and b show the relationship between the measuring range, the corresponding resolution based on 2 RV and the theoretical maximum number of data points that could be discernible during an unload-reload cycle with $(\varepsilon_a)_{SA}$= 0.001% by the use of two LDTs (a 50 cm long LDT and a 10.5 cm long LDT). The calibration curves shown in Fig. 2.11 and Fig. 2.16a were used for this evaluation. The analysis shows that the use of a 10 time DC amplifier is imperative while evaluating small-strain stiffness since the number of discernible data points during a small unload-reload cycle greatly decreases with the increase in the measuring range. The type of wave-form and frequency also have an influence on the number of data discernible. Strain-controlled CL tests at a very small constant strain rate can provide the maximum number of discernible data points, while stress-controlled sinusoidal CL tests, on the other hand, provide the minimum number of discernible data because of non-uniform loading rate in each cycle. Besides, large axial deformation of LDT may affect phosphor-bronze strip, which could impair performance by increasing hysteretic behavior.

2.7.9. Lateral LDTs

One of the latest development of LDT for the use in a triaxial test is its successful use for lateral strain measurements. For this purpose, the soil specimen should have a rectangular or square cross-section. Fig. 2.1b shows such an instrumented triaxial specimen. In total eight lateral LDTs at different heights were used to measure lateral strains along the lateral faces of the specimen. The principle of strain measurement is the same as that of vertical LDTs except the supporting hinges. Fig. 2.1c shows the details of a hinge for a lateral LDT. Usually, lateral LDTs are set at the central width (or breadth) of a specimen, excluding 1.5~2.0 cm space at either ends. Like vertical LDTs, any change in the gage length between the hinges in course of testing is detected by small e.r. strain gauges. Therefore, measured strains are free from any membrane penetration errors. Lateral strain at any instant is the average of strains obtained from the eight LDTs. With the use of lateral LDTs, the evaluation of reliable values of horizontal Young's modulus (E_h) directly from the deformation properties of the particulate materials is possible by applying small amplitude horizontal CL test at constant axial stress Typical results will be presented in Chapters 3 to 5.

2.7.10. Durability of LDT under Pressurized Submerged Condition

Sealant CC-33A has been used to seal electric components of LDT at its central part of length to impart water-proof properties. Typical long-term performance of LDTs under pressurized cell water can be observed in Fig. 2.17, which shows the influence of consolidation time for a duration of 41 days on E_{max} of a stiff clay specimen (Mukabi, 1995). The test was performed on a saturated over-consolidated (OCR= 1.86) specimen (11.5 cm high and 5.0 cm in diameter) of Osaka Aminity Past (OAP) clay at an effective consolidation pressure of σ_c = 3.68 kgf/cm^2 (361 kPa) with effective principal stress ratio K = 0.53, while the back pressure was 2.0 kgf/cm^2 (196 kPa). The specimen was retrieved from a depth of 79 m below the ground surface by means of a Denison sampler. The E_{max} values was evaluated at different consolidation periods by applying strain-controlled small unload-reload cycles with $(\varepsilon_a)_{SA} \leq$ 0.001% under drained conditions. The LDTs were completely immersed into the pressurized cell water. The E_{max} value reached to a stable value within a couple of hours almost at the same time when the specimen attained 100% consolidation state (t_{100}). Differences in the E_{max}

values measured by using LDTs and a gap sensor were due to the bedding error since the gap sensor measured the axial compression between the specimen cap and pedestal.

2.8. Summaries

(1) A triaxial testing system is automated to study into the anisotropic deformation characteristics in the small strain range of geomaterials using a large rectangular-prism specimen. Stress states can be changed along stress paths with a constant value of either axial stress or lateral stress or mean principal stress or stress ratio. Small amplitude vertical and horizontal cyclic loading tests while keeping the other principal stress constant can also be performed with this automated system.

(2) The details of the manufacturing method of local deformation transducer (LDT) have been described together with its components that are essential for high performance of LDT. Some aspects of the behavior of LDT also were outlined. Resolution was observed at least 2 RV, where RV is the resolution of a 12-bit A-D board currently used in the data acquisition system. For a full scale maximum strain range of 2%, the current version of LDT is able to detect a strain as small as 0.0005% and 0.00005% without and with, respectively, ten times amplification of the output from the AC strain amplifier. The hysteresis of LDT was not totally negligible. However, the effect does not become a serious problem for usual purposes. While evaluating small strain stiffness during otherwise monotonic loading, an LDT was observed to under-estimate stiffness by a maximum of about 2%. This error was found un-related with the present calibration method of LDT. An LDT with a full-scale axial strain range more than 2% was found unfavorable in evaluating stiffness at very small strain range (say, $(\varepsilon_a)_{SA} \leq 0.001\%$), since the number of discernible data could decrease largely with the increase in the maximum measuring range. The effects of creep deformation of glue and rubber membrane were found noticeable immediately after the set of LDT, but became negligible after having been left over-night. The effect of creep on small-strain stiffness was found negligible. LDT can also be used to measure local lateral strains, which are free from membrane penetration errors, of a triaxial specimen having a rectangular prismatic cross-section. The performance of LDT under

pressurized cell water for a long duration (about 41 days) was observed to be satisfactorily stable.

Table 2.1: Resolution of the control and measurement systems

Secondary amplification (times)	Control system		Measurement system			
	E/P transducer (kgf/cm^2) [kPa]	Actuator load (kgf/cm^2) [kPa]	Lateral LDT (m/m)	Vertical LDT (m/m)	Axial stress (kgf/cm^2) [kPa]	Lateral stress (kgf/cm^2) [kPa]
1	0.002 [0.2]	0.0045 [0.44]	$4.4*10^{-6}$	$6.8*10^{-6}$	0.009 [0.9]	0.002 [0.2] or less
10	--	--	$4.4*10^{-7}$	$6.8*10^{-7}$	0.0009 [0.09]	

Table 2.2: List of the dimensions of LDTs used in IIS

Triaxial specimen size [diam. (mm) × height (mm)]	Width × Length × Thickness (mm × mm × mm)	Number of electric-resistant strain gages on one LDT
35 × 80	3.0 × 60 × 0.20	2 or 4
50 × 100	3.5 × 80 × 0.20	2 or 4
75 × 150	3.5 × 105 × 0.30 4.0 × 120 × 0.30	4
100 × 200	4.0 × 170 × 0.30 4.5 × 170 × 0.30	4
300 × 600	5.0 × 500 × 1.0 6.0 × 500 × 1.0	4

Table 2.3: List of the electric resistant strain gauges.

Gage type	Resistance (Ω)	Gage factor	Dimensions: mm				Remarks
			Gage length	Grid width	Matrix length	Matrix width	
KFG-1N-120-C1-16	120	2.1	1	0.68	4.2	1.4	Narrow grid pattern
KFG-2N-120-C1-16	120	2.1	2	0.84	5.3	1.4	Narrow grid pattern

Table 2.4: Comparison of the properties of leadwires.

	Conventional type	New type
Physical description	Four-wire shielded. Besides, each wire has teflon protection.	Four-single wires. Each is shielded by teflon.
Overall largest diam./wire[Ψ]	0.7 mm	0.35 mm
Weight/meter length (4-wire)	4.0 gf (excluding outer shield)	1.2 gf
Cross-sectional area (4-wire)[♀]	0.5 sq.mm	0.05 sq.mm

[Ψ] cross-section is not circular
[♀] supplied by the manufacturer

Table 2.5a: Availability of the number of discernible data based on resolution (50 cm LDT)

Full scale displacement range (mm)	Resolution in percent of nominal axial strain, based on 1 RV	No. of data discernible in one complete cycle of $(\varepsilon_a)_{SA}$=0.001% based on resolution of LDT (2 RV)	
		Without amplification	With 10 times amplification
5 (ε_a = 1%)	$3.5*10^{-4}$	6	57
10 (ε_a = 2%)	$7*10^{-4}$	3	28
12 (ε_a = 2.4%)	$8.3*10^{-4}$	3	24
15 (ε_a = 3%)	$10.5*10^{-4}$	2	19

Table 2.5b: Availability of the number of discernible data based on resolution (10.5 cm LDT)

Full scale displacement range (mm)	Resolution in percent of nominal axial strain, based on 1 RV	No. of data discernible in one complete cycle of $(\varepsilon_a)_{SA}$=0.001% based on resolution of LDT (2 RV)	
		Without amplification	With 10 times amplification
1 (ε_a = 0.95%)	$5.16*10^{-4}$	4	38
1.50 (ε_a = 1.4%)	$7.75*10^{-4}$	3	26
2.25 (ε_a = 2.1%)	$8.72*10^{-4}$	3	24
3 (ε_a = 2.9%)	$11.62*10^{-4}$	2	17
4 (ε_a = 3.8%)	$15.4*10^{-4}$	1	13

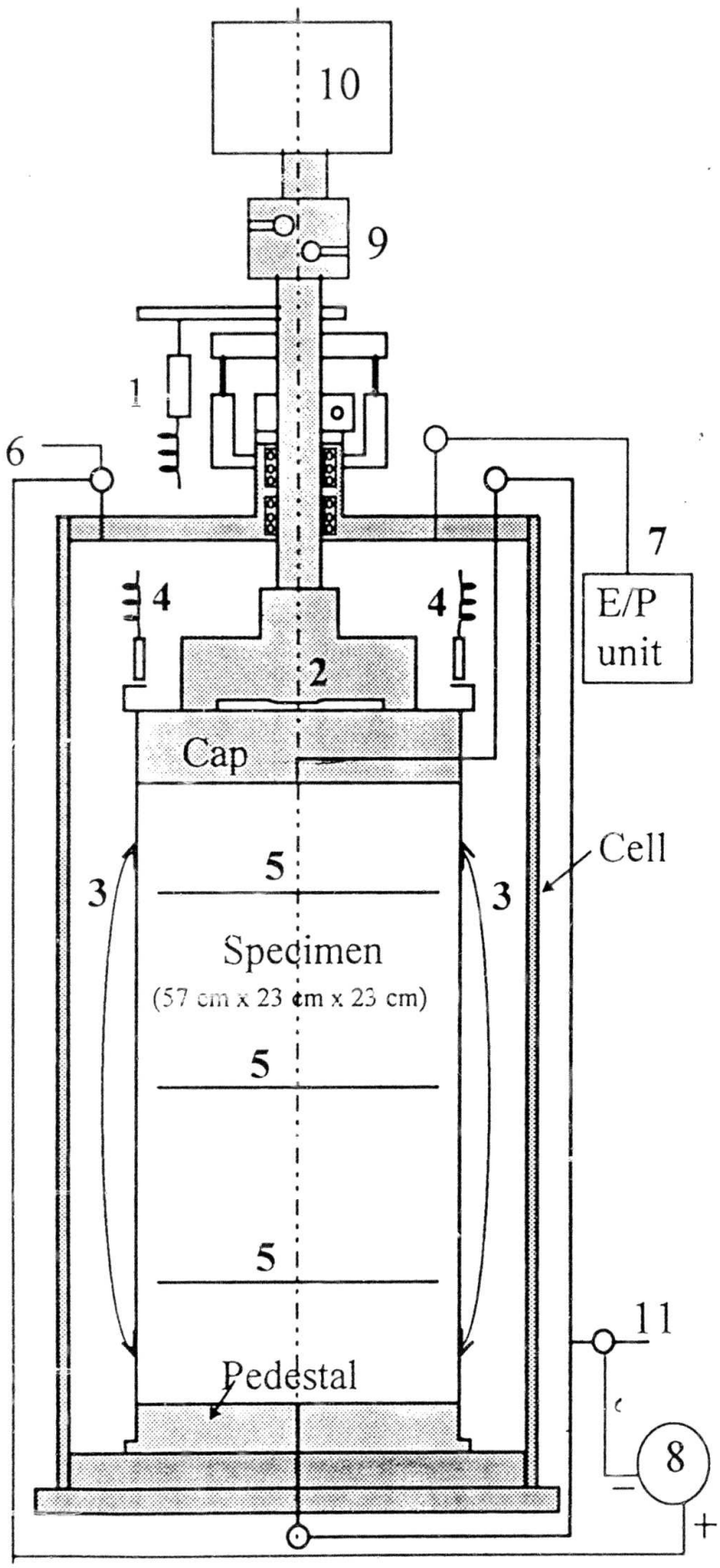

1 : External displacement transducer
2 : Inner load cell
3 : Vertical LDTs
4 : Vertical proximeter
5 : Lateral LDTs
6 : Cell pressure supply
7 : Electro-pneumatic (E/P) pressure transducer
8 : High capacity differential pressure transducer
9 : Outer load cell
10: Actuator unit
11: Back pressure (vacuum or positive pressure)

(Not in scale)

Fig. 2.1a: Large triaxial apparatus used in the present study.

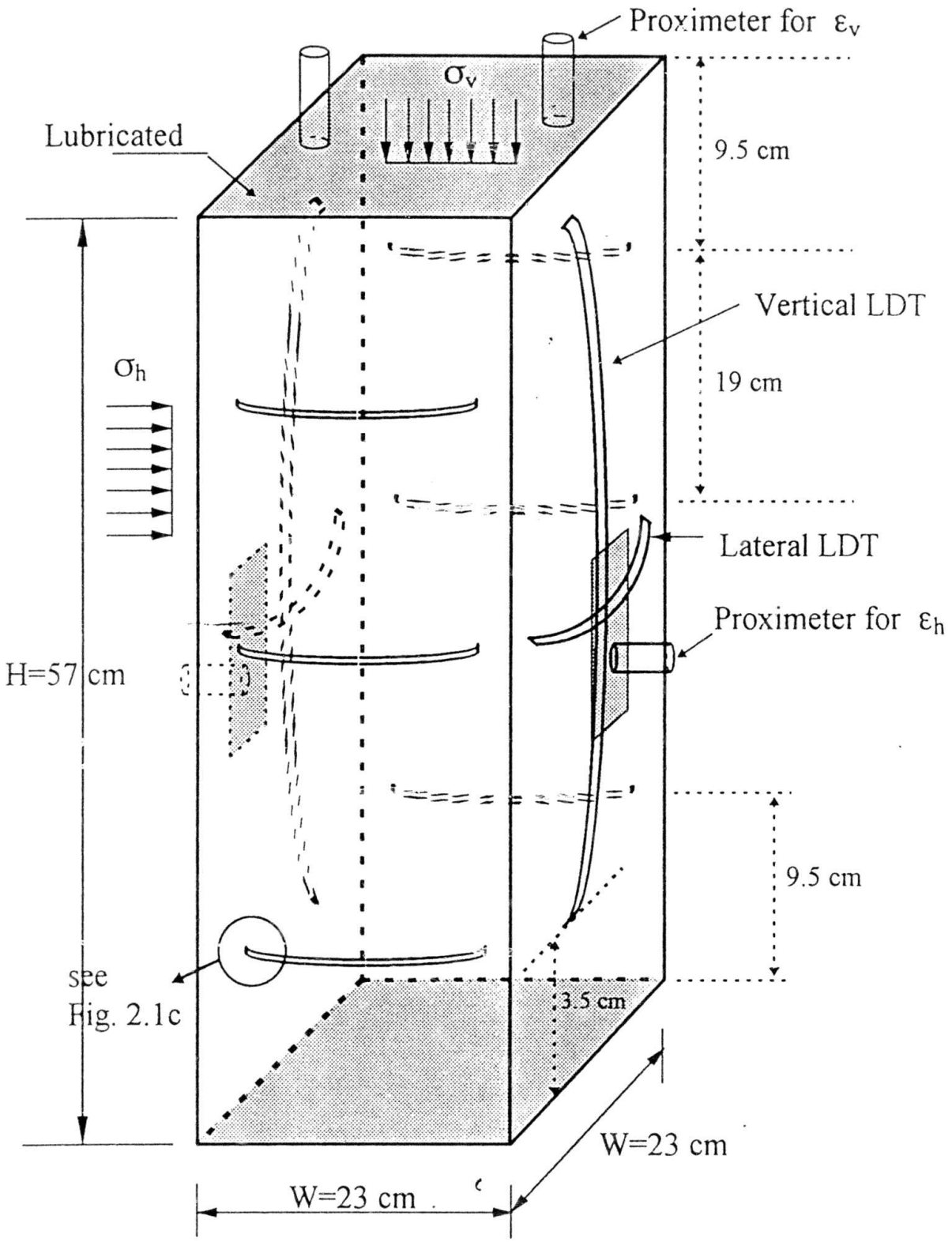

Fig. 2.1b: Large triaxial specimen with local strain measurement.

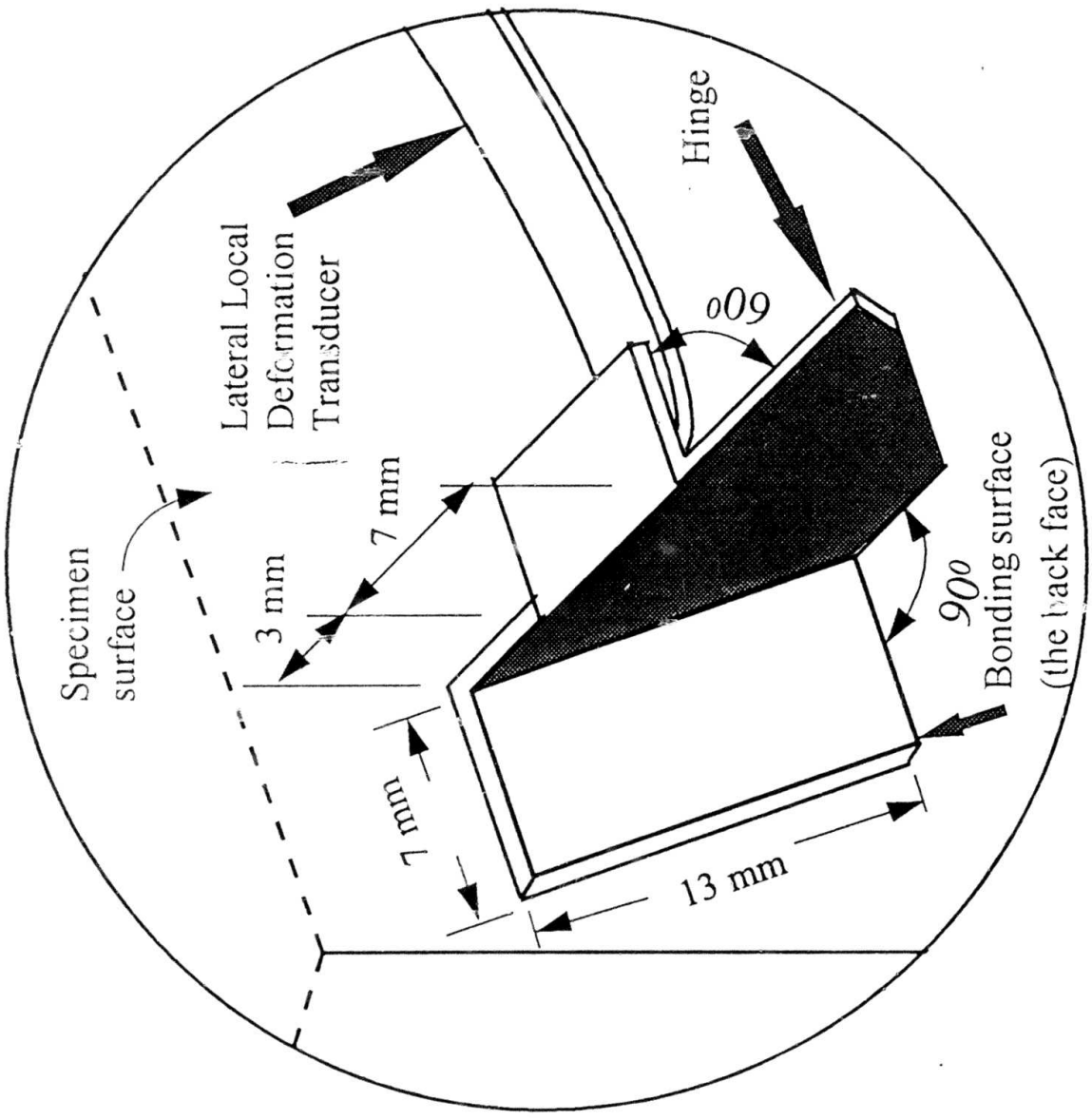

Fig. 2.1c: Details of lateral LDT for local strain measurement.

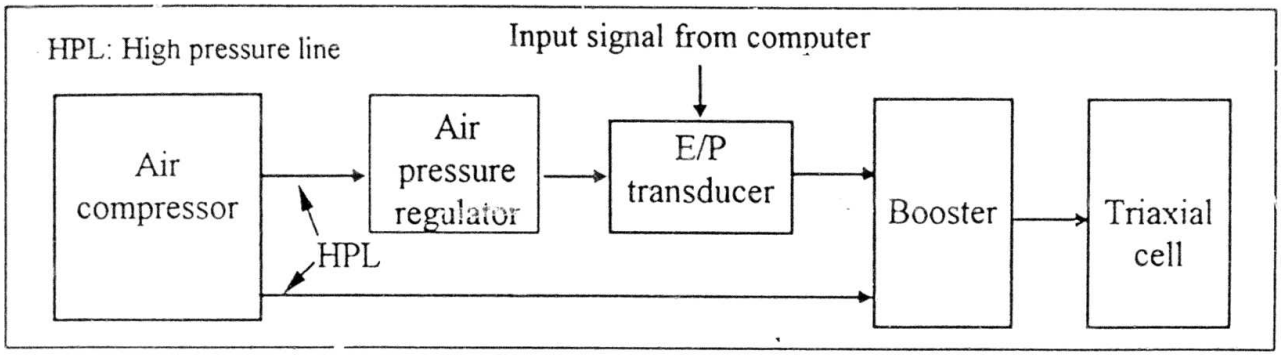

Details of electric-to-pneumatic loading system

Fig. 2.2a: Block diagram of the electro-pneumatic loading system for cell pressure.

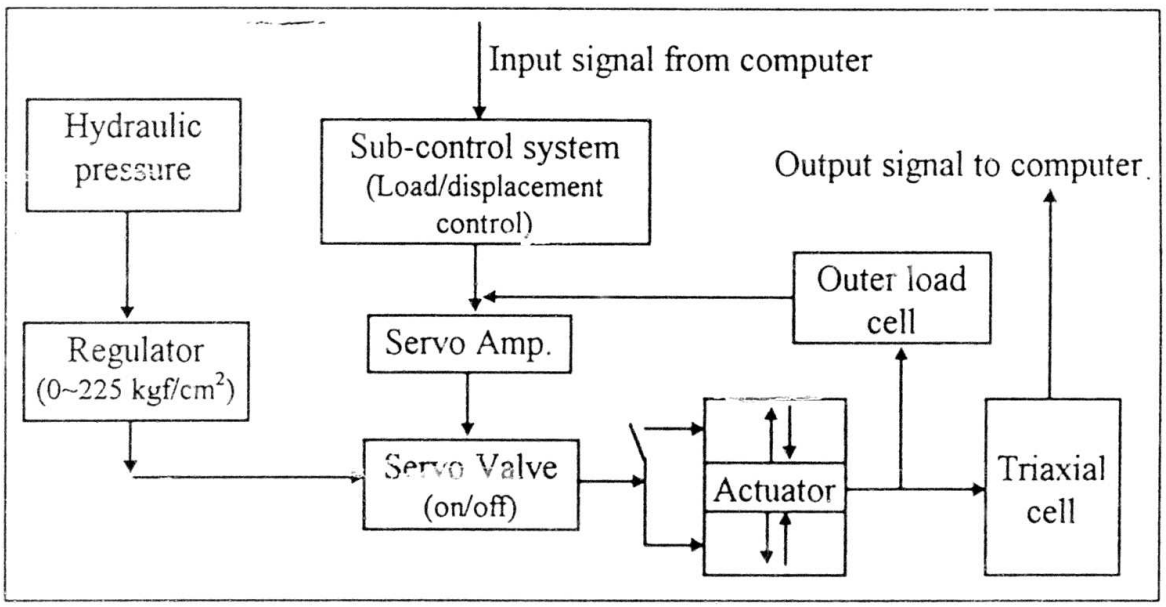

Details of Servo-hydraulic loading system for axial loading

Fig. 2.2b: Block diagram of the servo-hydraulic loading system for axial load.

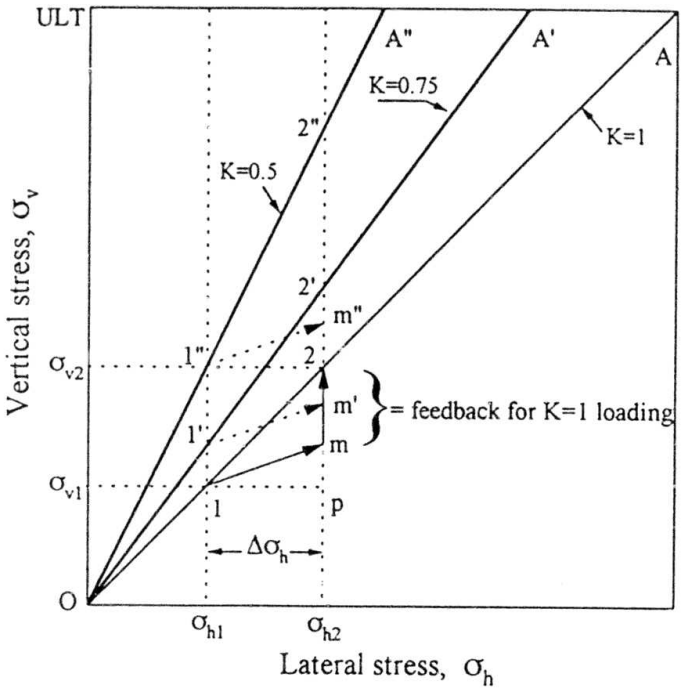

Fig. 2.3a: Principle of the algorithm for some typical stress paths control.

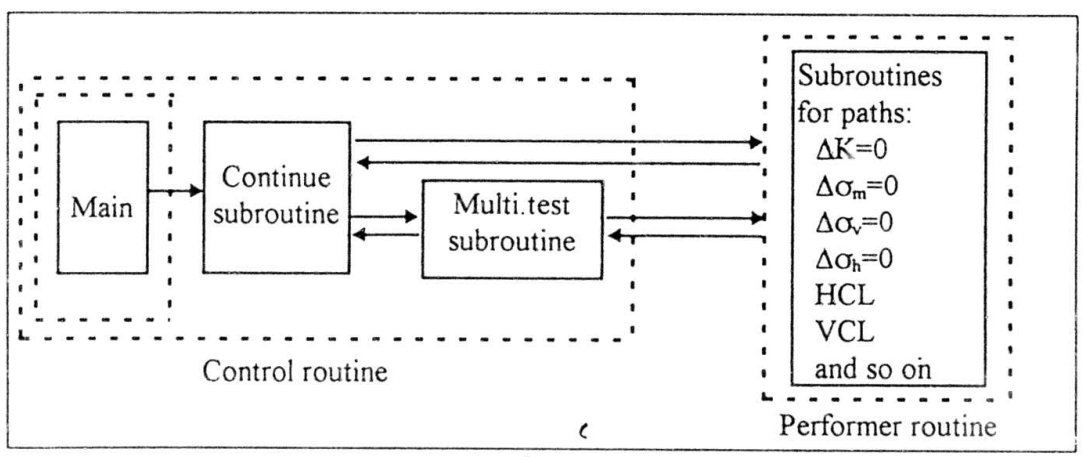

Fig. 2.3b: Block diagram of the software program.

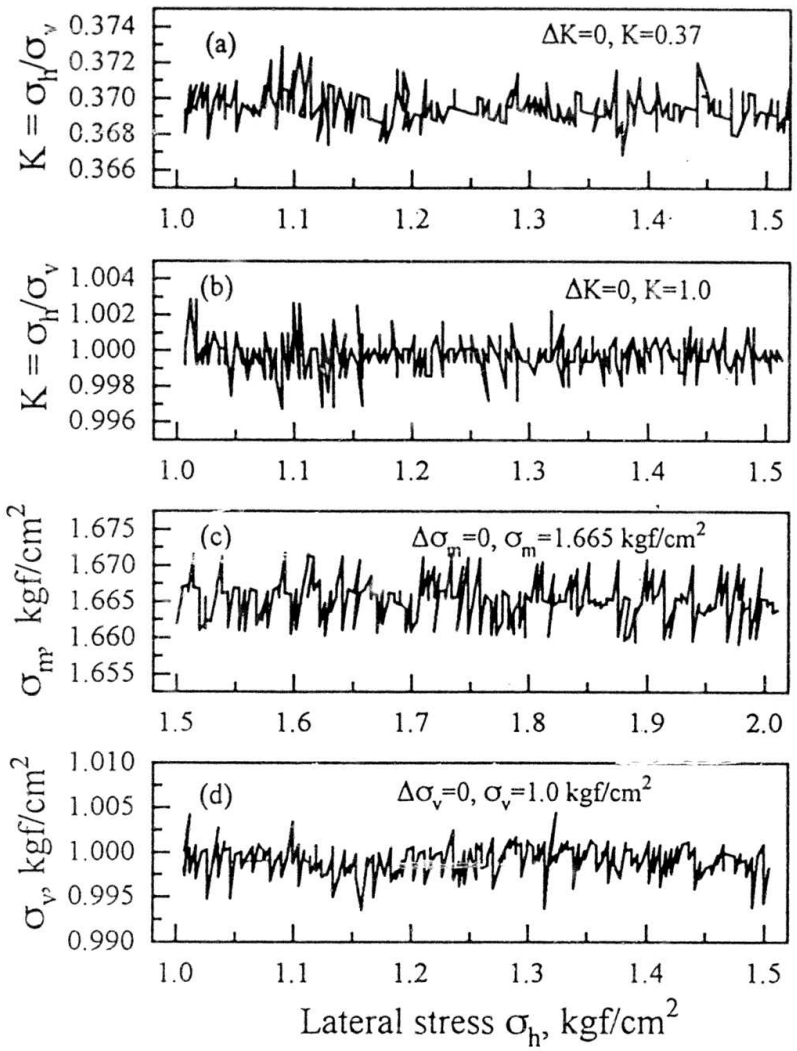

Fig. 2.4: Typical test results to demonstrate the performance of the automated control system in achieving monotonic loading along some stress paths and cyclic loading: a) $\Delta K=0$ stress path with K=0.37, b) $\Delta K=0$ stress path with K=1.0, c) $\Delta\sigma_m=0$ stress path with $\sigma_m=1.665$ kgf/cm^2, d) $\Delta\sigma_v=0$ stress path with $\sigma_v=\sigma_h=1.0$ kgf/cm^2.

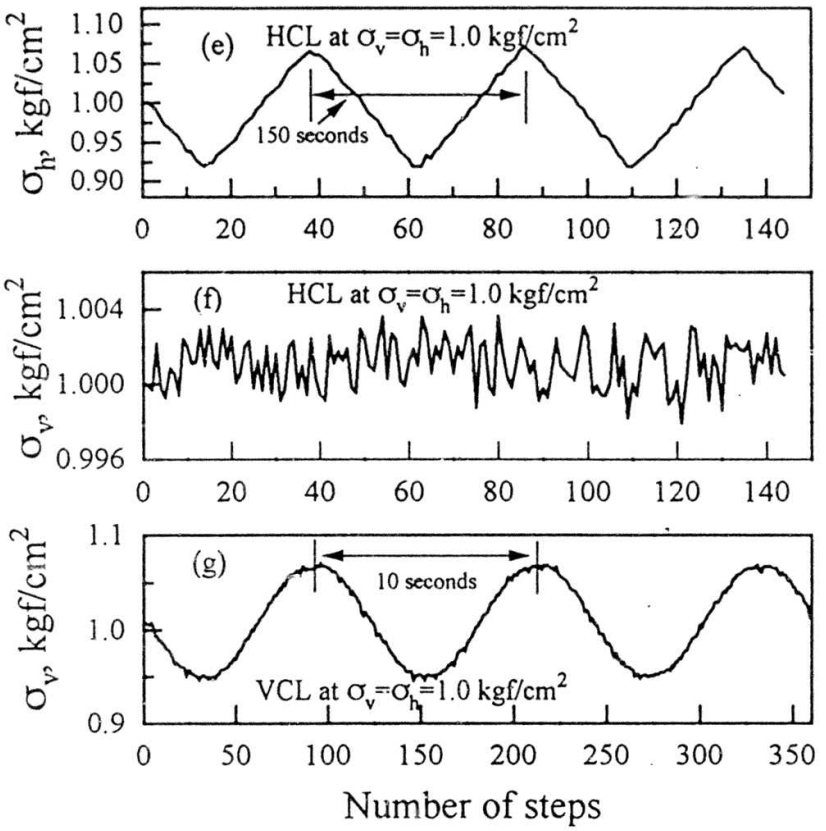

Fig. 2.4: Typical test results to demonstrate the performance of the automated control system in achieving monotonic loading along some stress paths and cyclic loading: e) Cyclic variation of σ_h, f) Controlling $\Delta\sigma_v=0$ stress path during HCL, and g) Variation of σ_v in a VCL test.

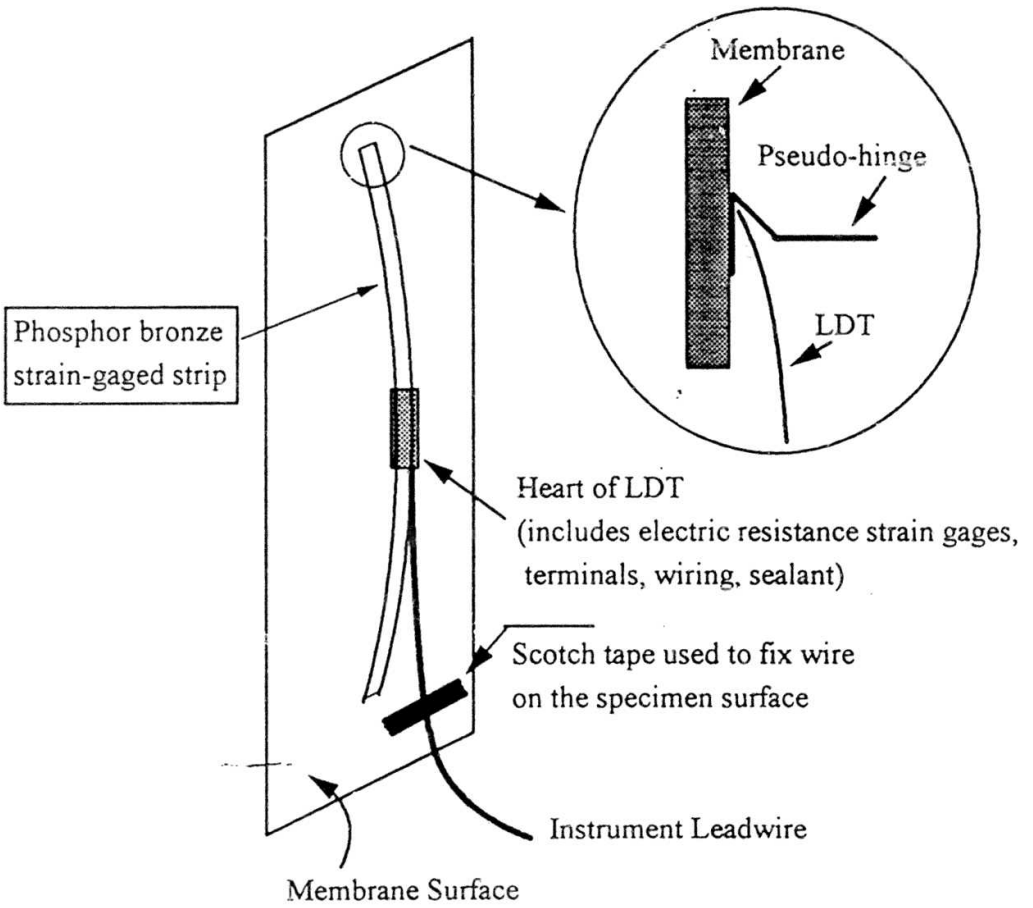

Fig. 2.5: LDT at working condition to measure vertical strains in a triaxial specimen.

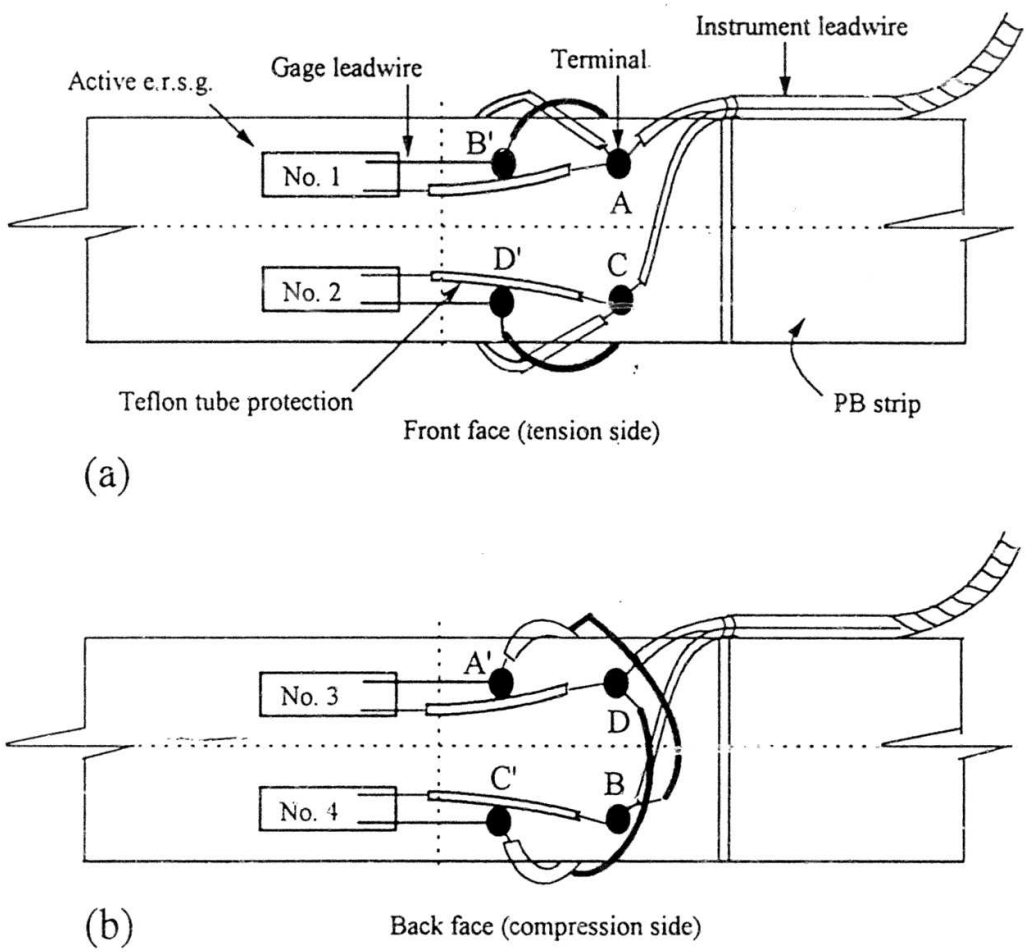

Figs. 2.6: Details of the internal connections at the heart of a 4-gage type LDT with (a) front face, and (b) back face.

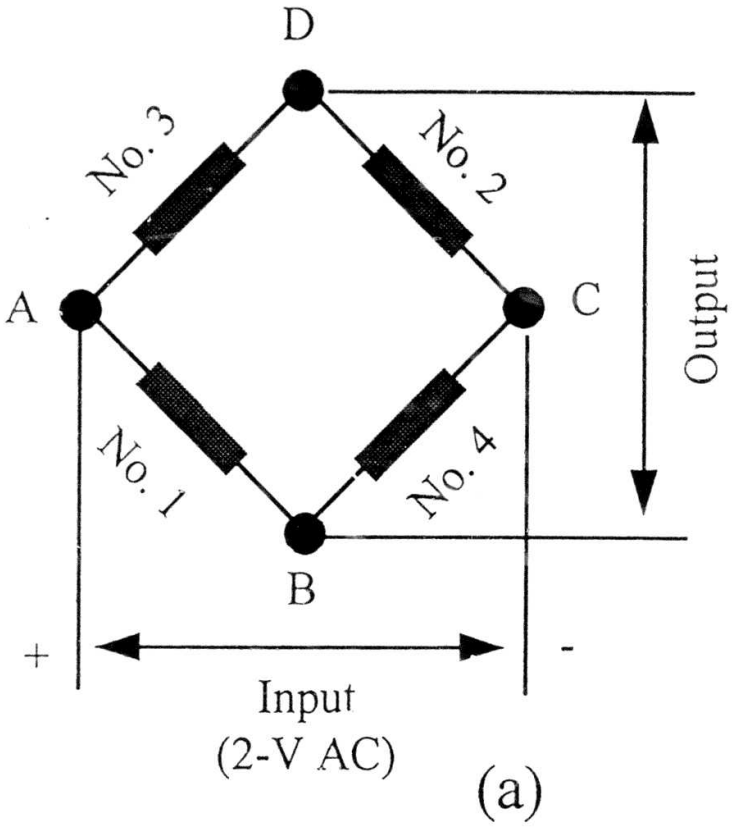

Fig. 2.7a: The connections of the e.r. strain gages (4-gage type) in the Wheatstone bridge.

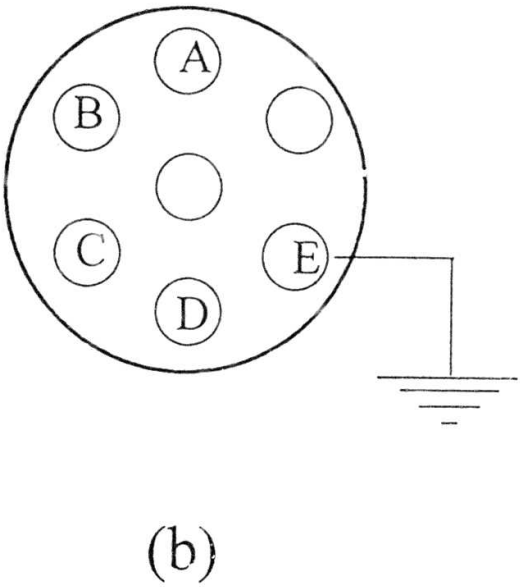

Fig. 2.7b: Typical external connector for input-output communication.

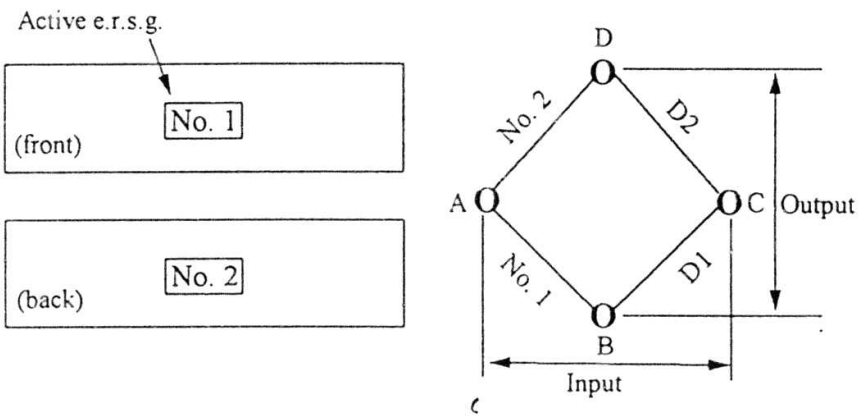

Fig. 2.7c: The LDT with two-gage method.

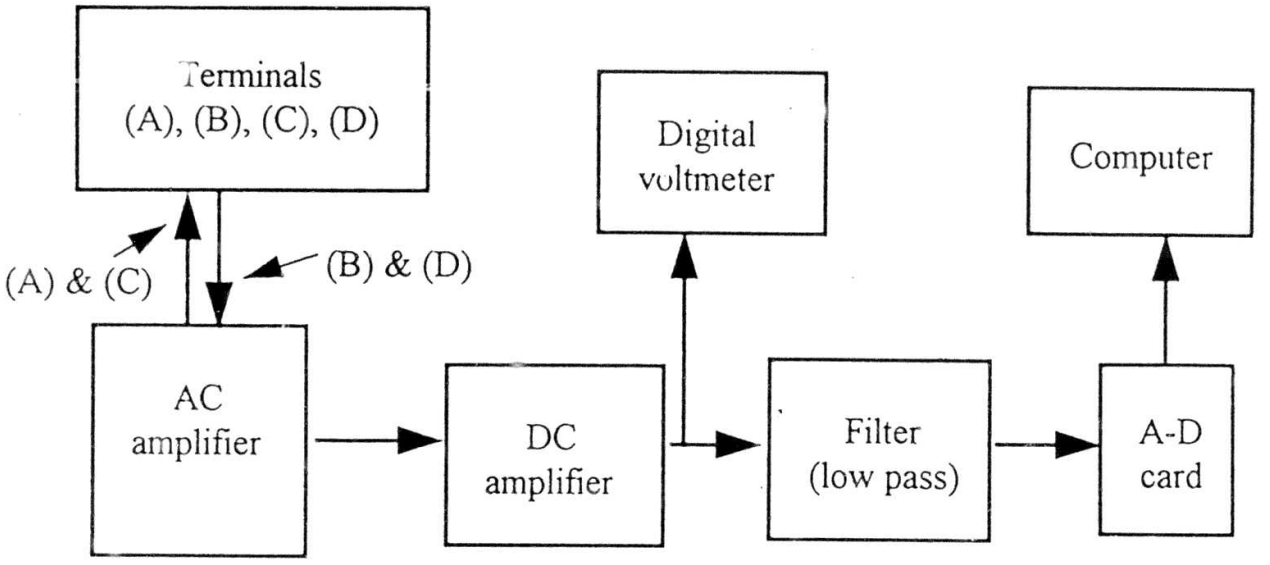

Fig. 2.8: Block diagram of the data acquisition system for LDTs.

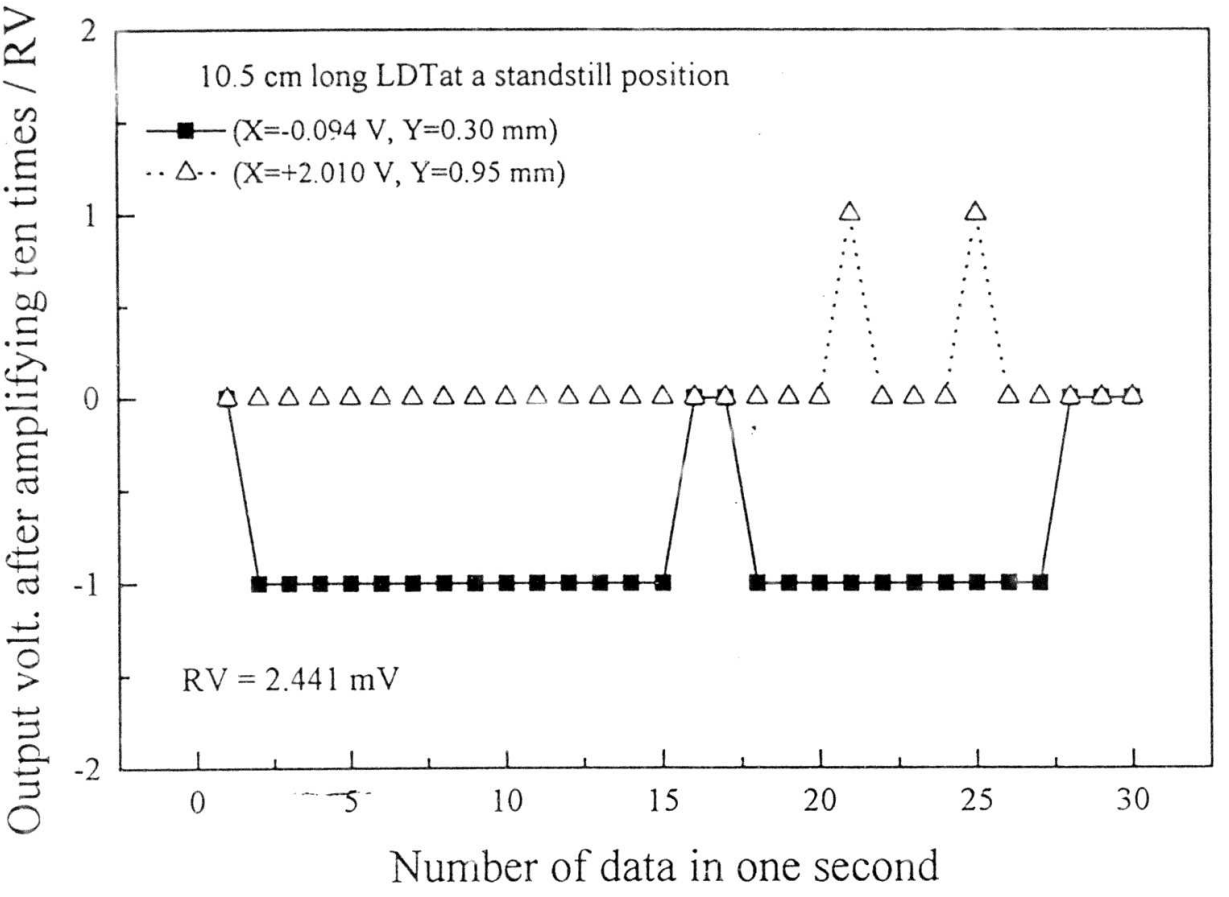

Fig. 2.9: Resolution of the combined system of an A-D card and an AC amplifier.

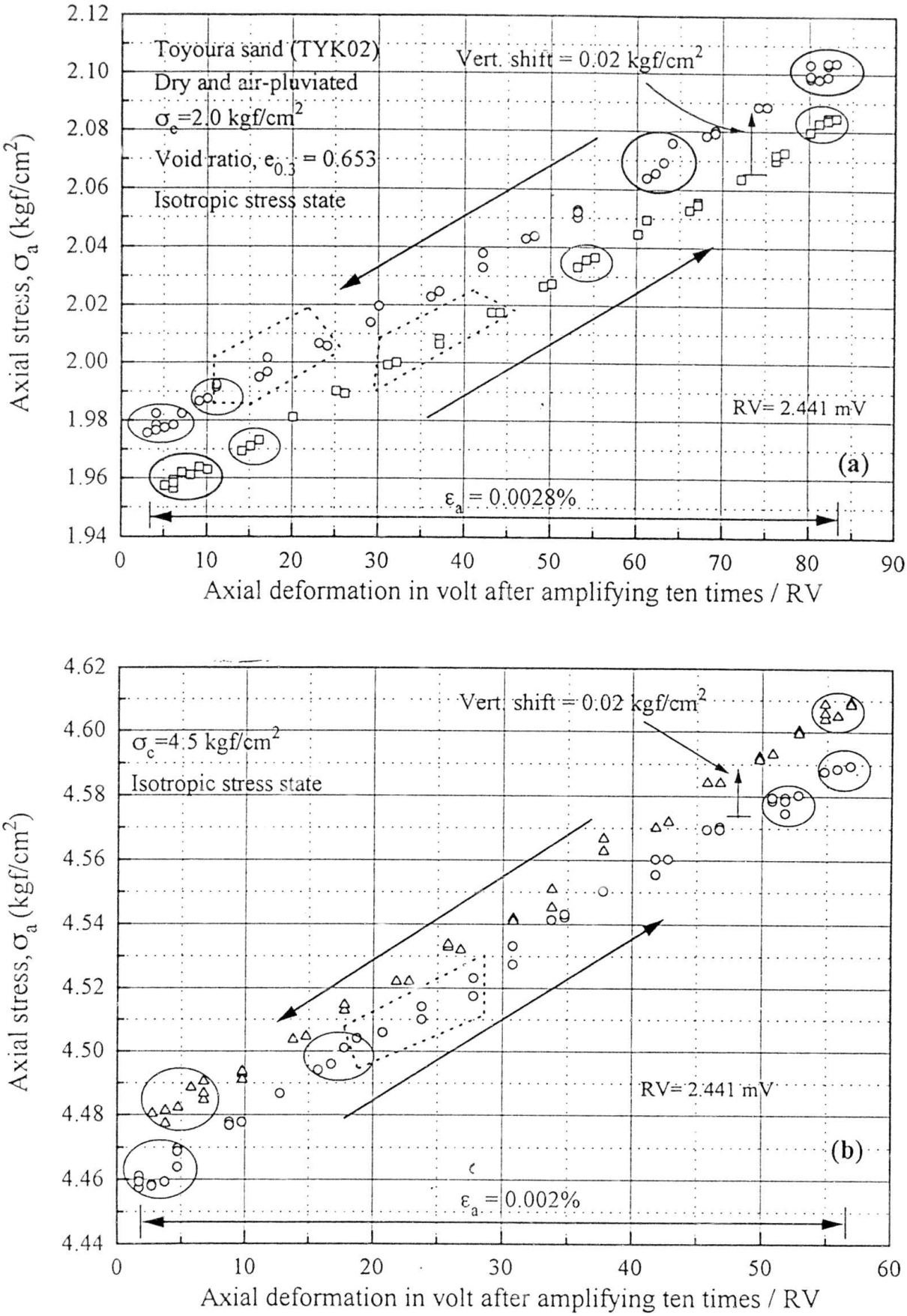

Figs. 2.10: Typical relationships between axial stress and axial deformation in voltage (RV) during one cycle of vertical CL test at isotropic stress states: (a) σ_c= 2.0 kgf/cm^2, and (b) 4.5 kgf/cm^2

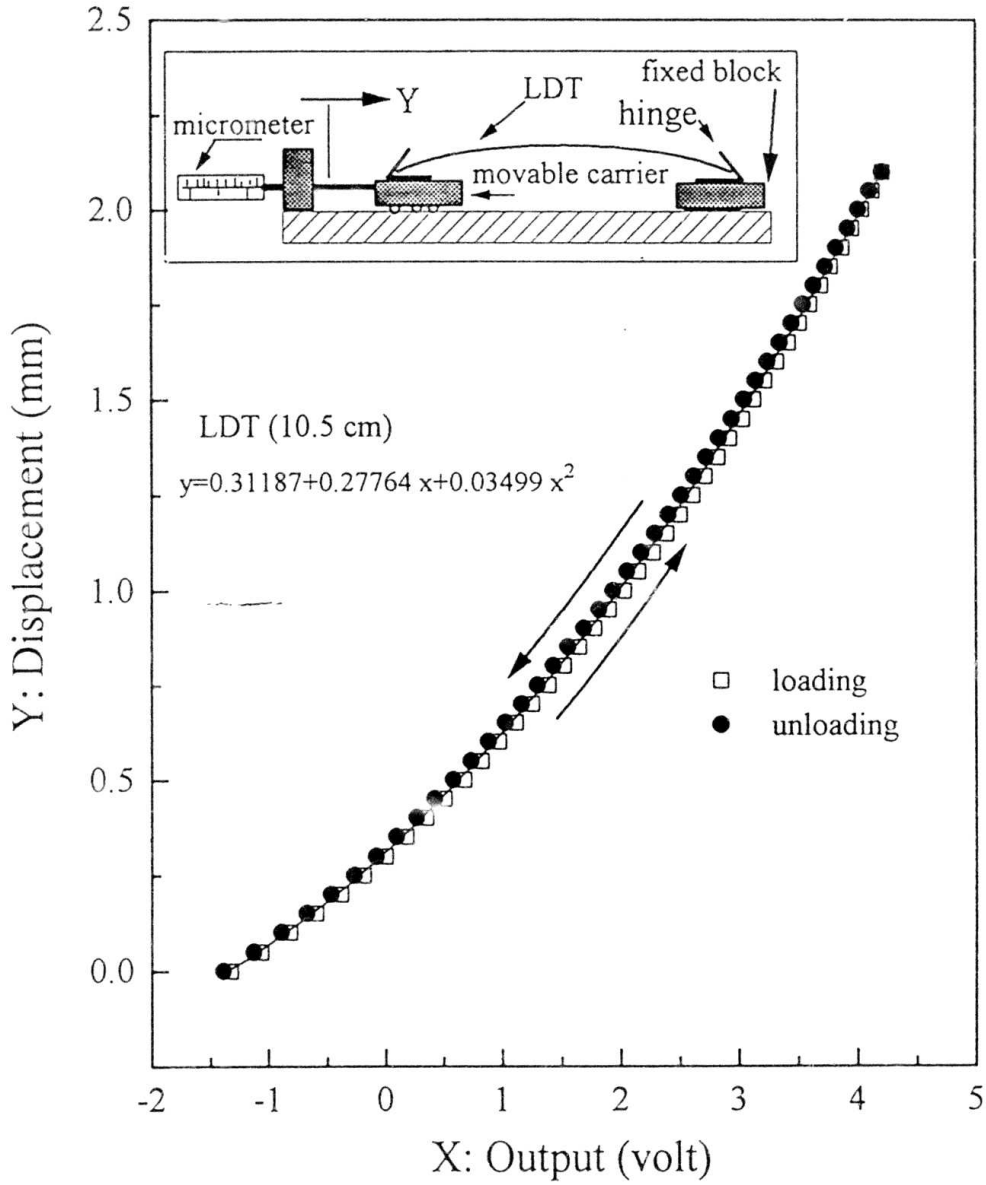

Fig. 2.11: Typical calibration characteristics of an LDT.

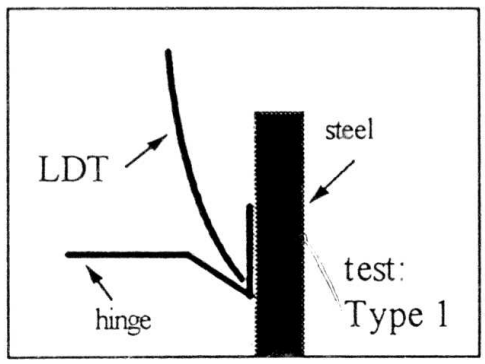

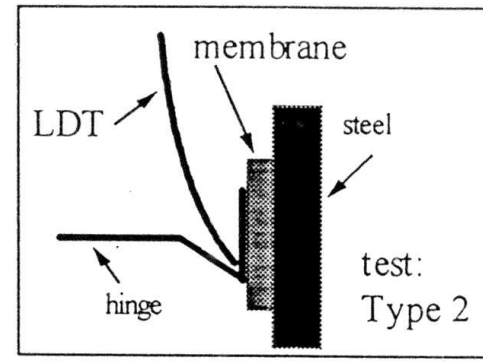

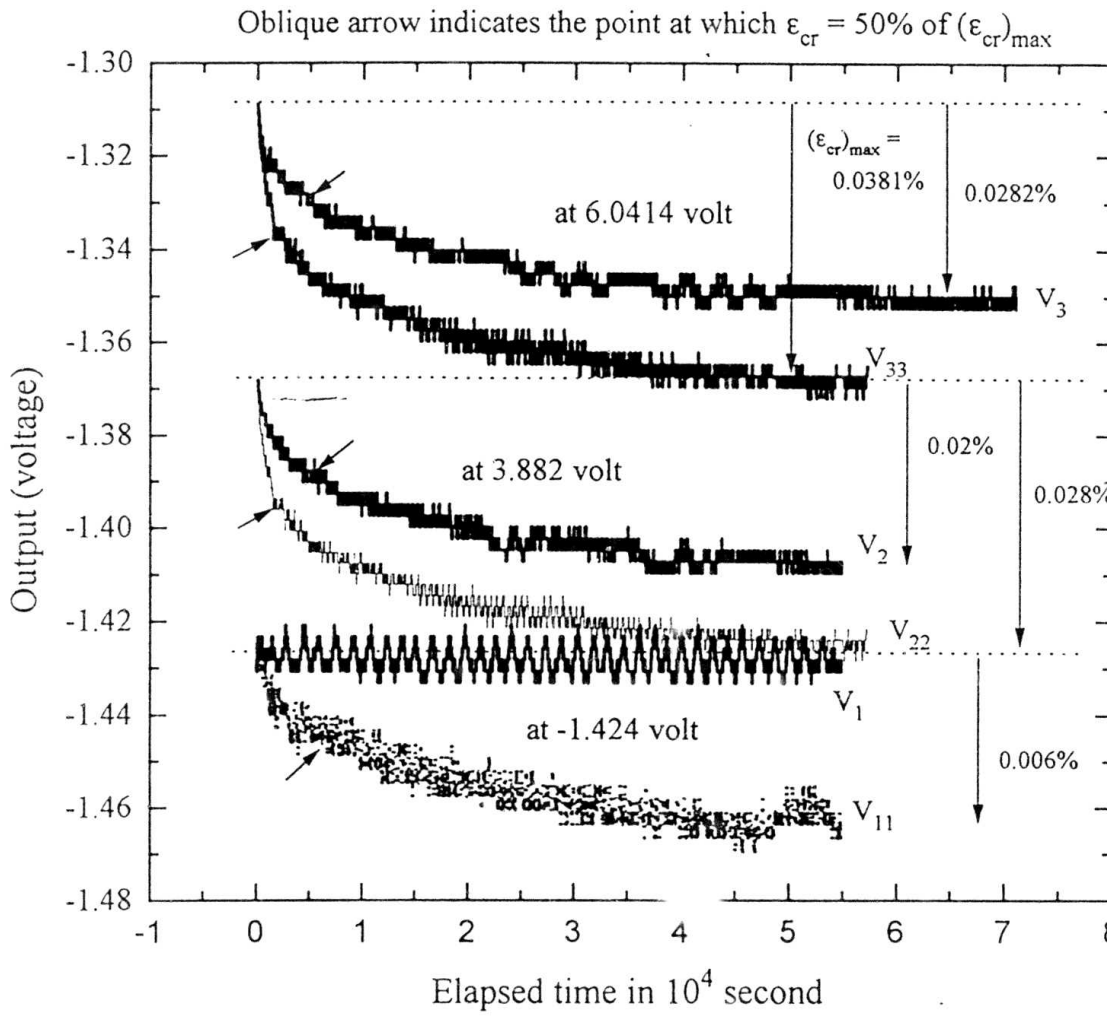

Fig. 2.12a: 'Creep' of LDTs during a long-term consolidation.

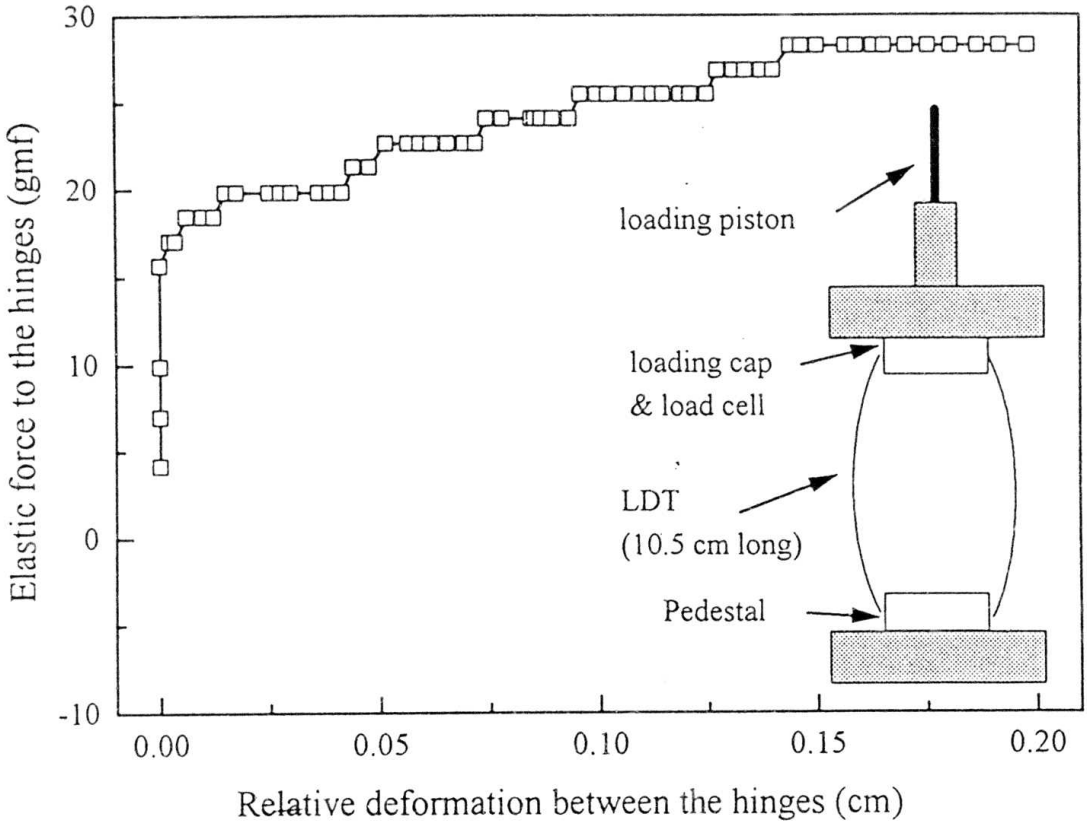

Fig. 2.12b: Relationship between elastic force exerted by LDT strip on the hinges and axial deformation of the LDT (tested by Kim, Y.-S., 1992).

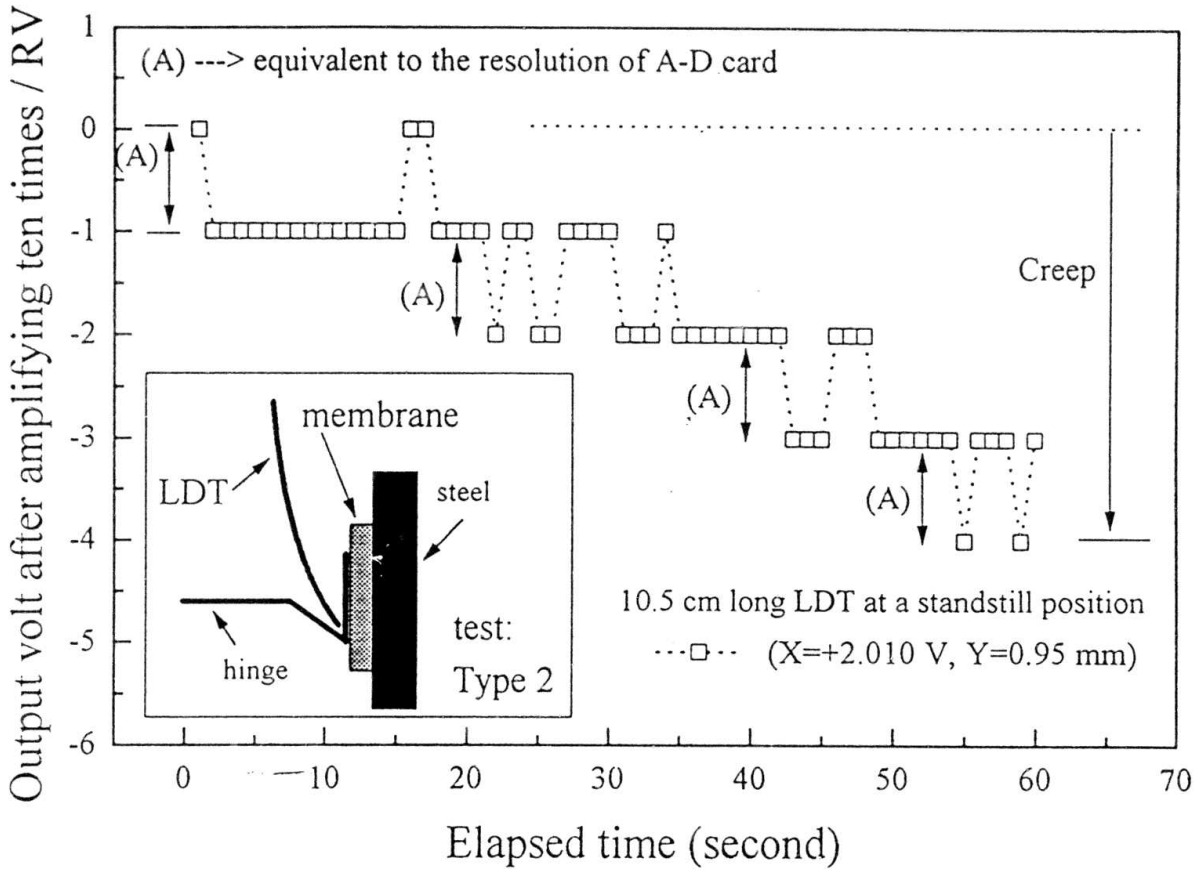

Fig. 2.12c: Variation of the output voltage (in RV) with time for one minute at a standstill position of LDT.

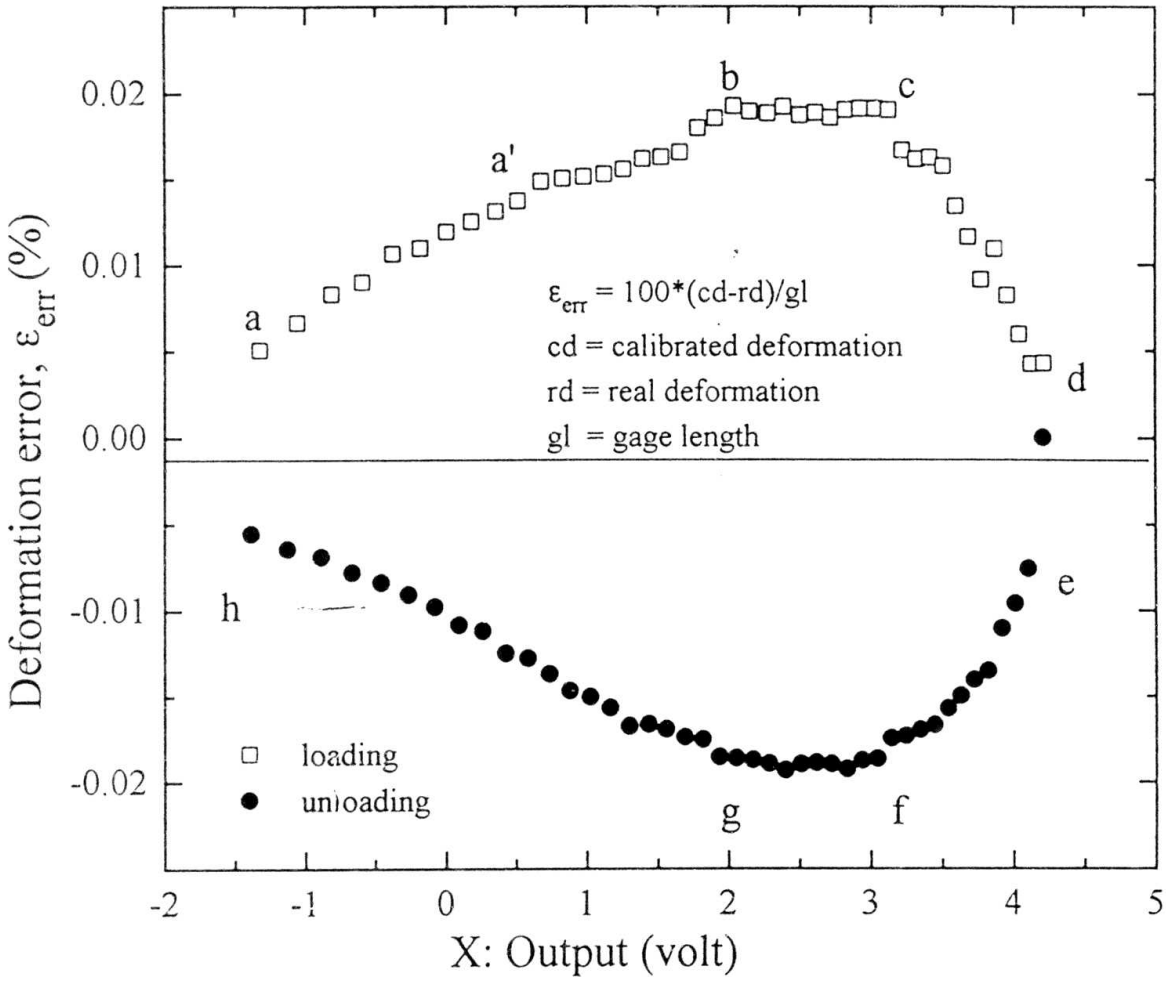

Fig. 2.13a: Typical 'error-curve' for a given calibration characteristics of an LDT.

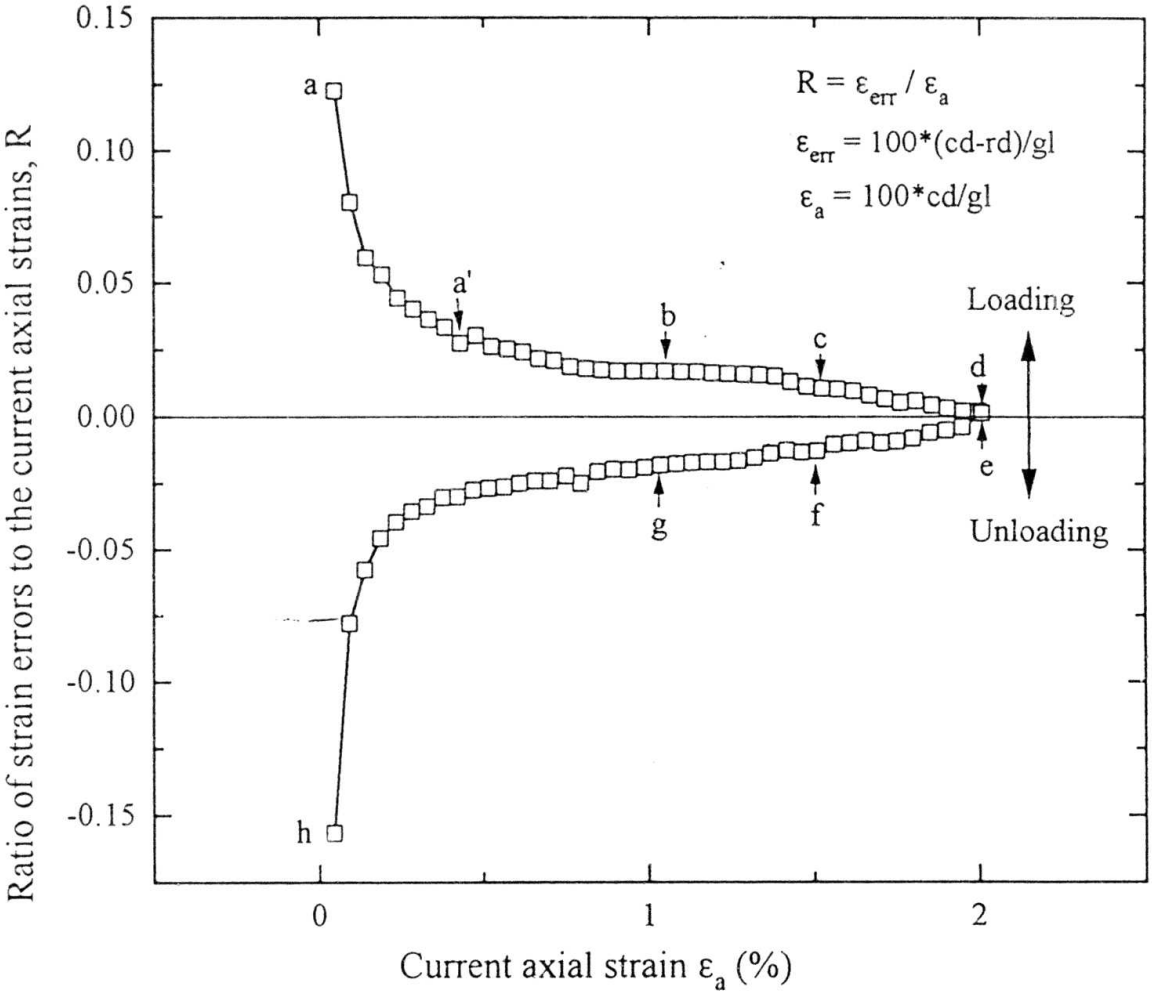

Fig. 2.13b: Variation of R (= $\varepsilon_{err}/\varepsilon_a$) with ε_a (current axial strain) along a calibration curve of an LDT.

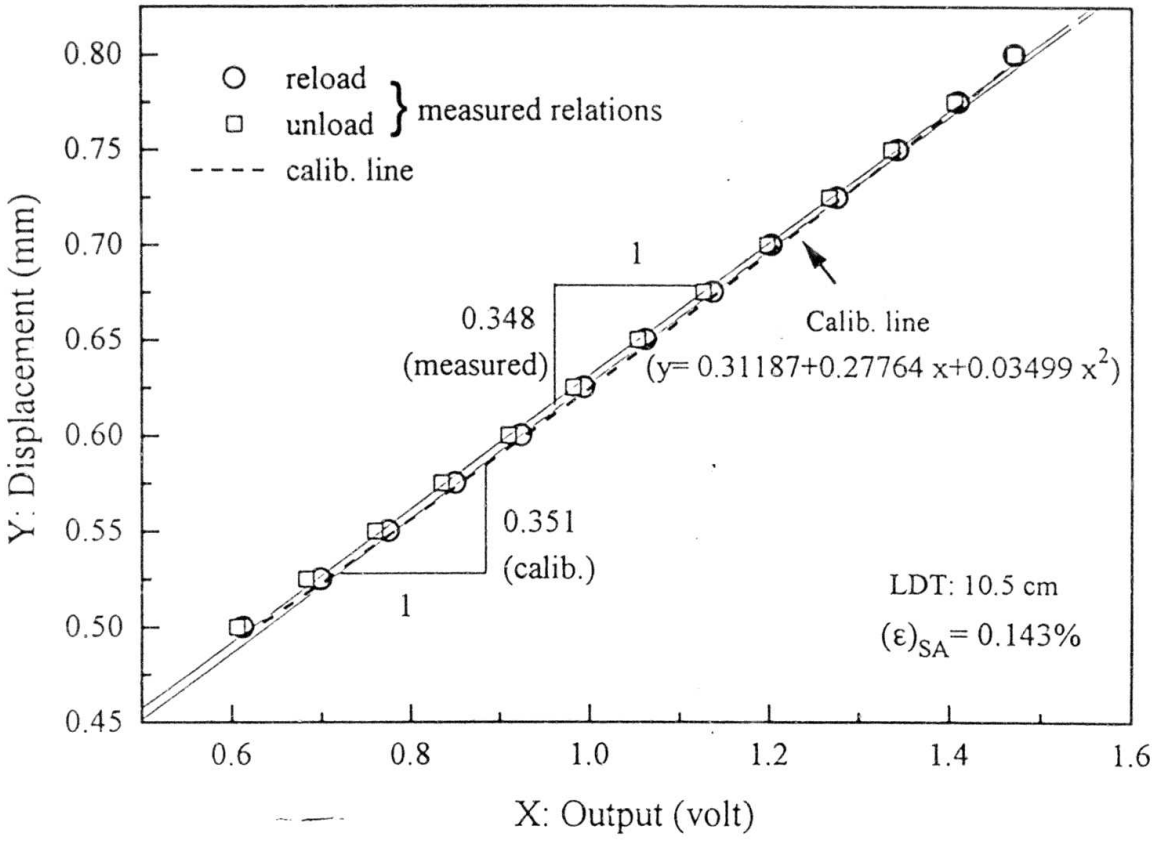

Fig. 2.14a: Typical small unload-reload deformation cycles along a typical calibration curve of an LDT for $(\varepsilon)_{SA}$=0.143%.

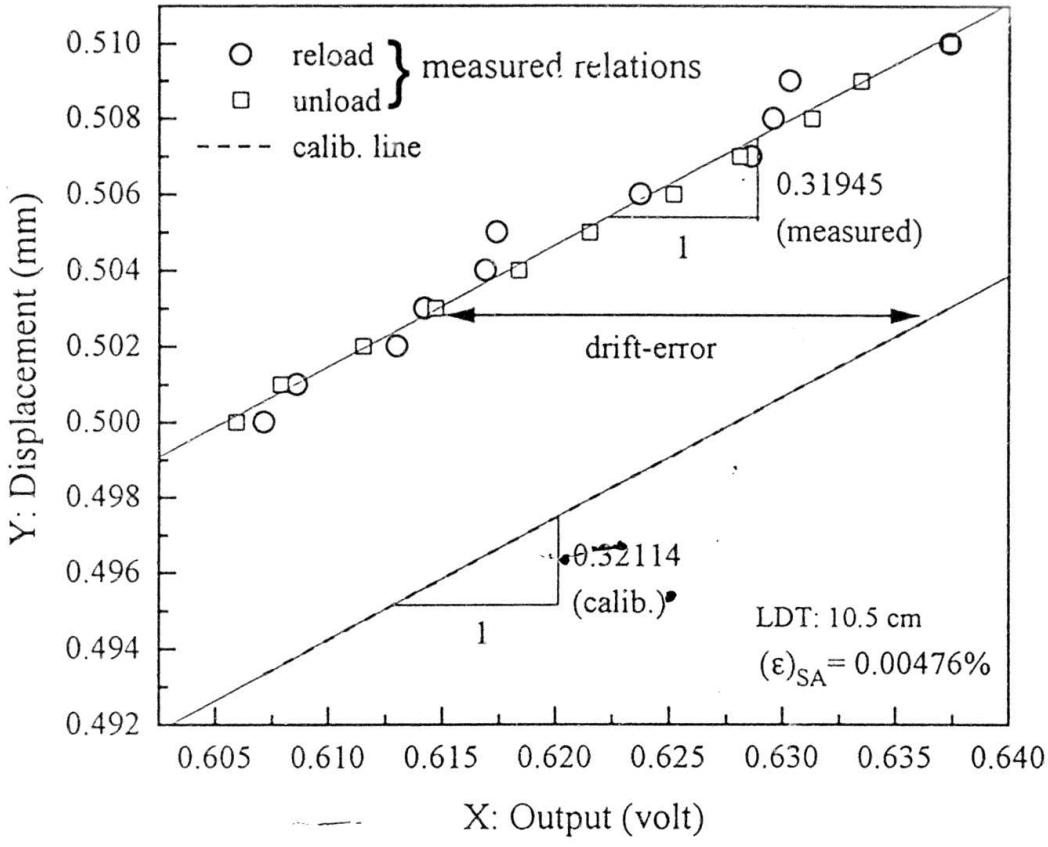

Fig. 2.14b: Typical small unload-reload deformation cycle for $(\varepsilon)_{SA}$= 0.00476% along a typical calibration curve of an LDT.

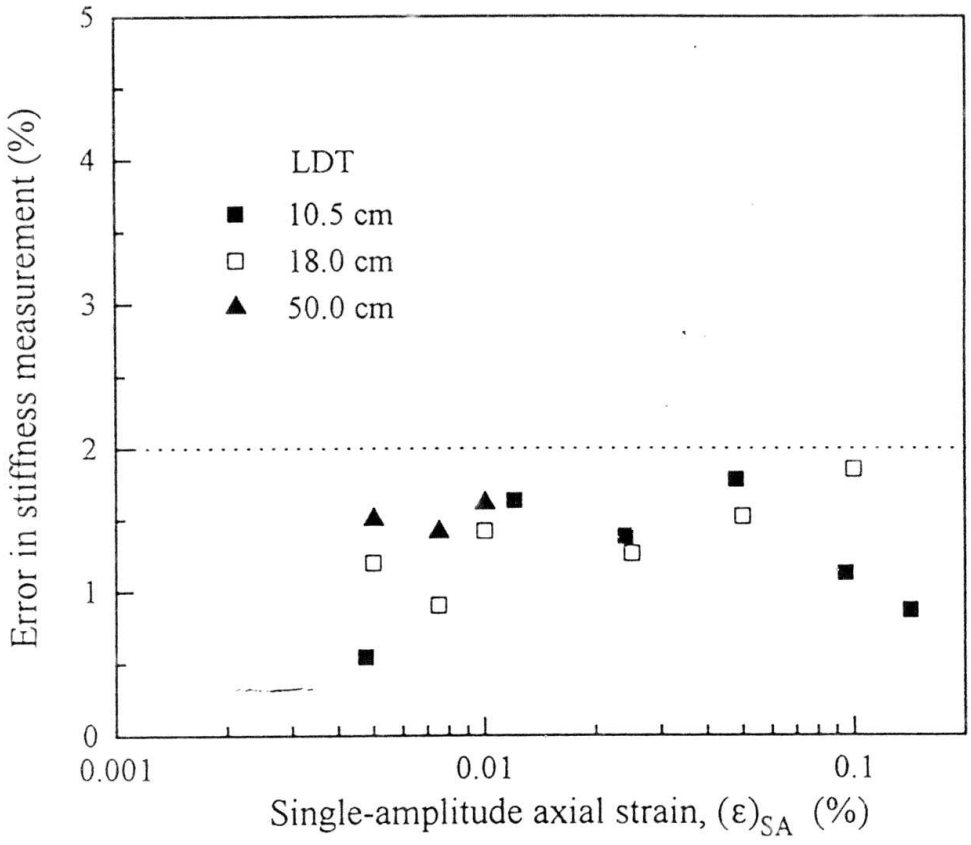

Fig. 2.15: Errors in stiffness measurement by the use of LDT in measuring small strains.

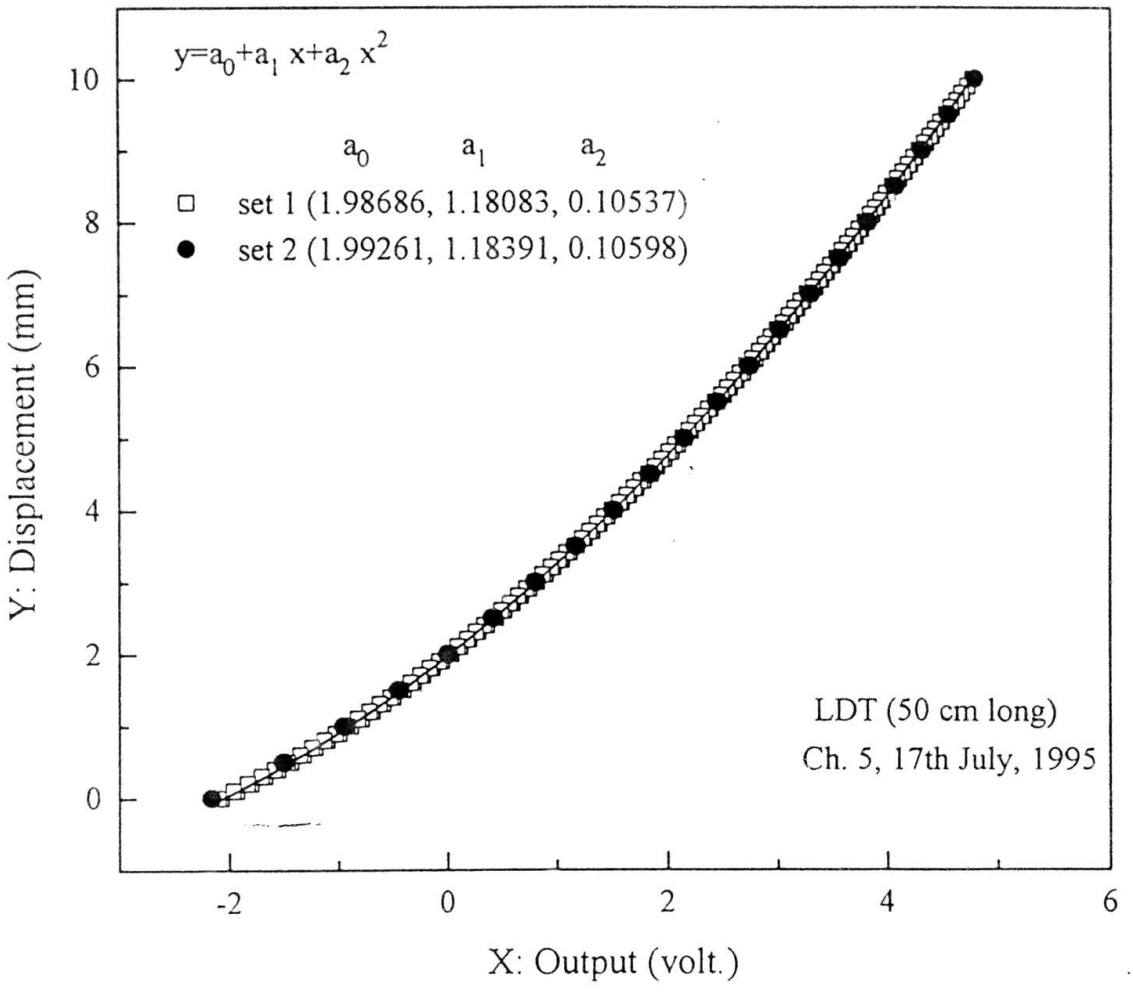

Fig. 2.16a: Calibration characteristics of LDT by the conventional method and the finer displacement step method.

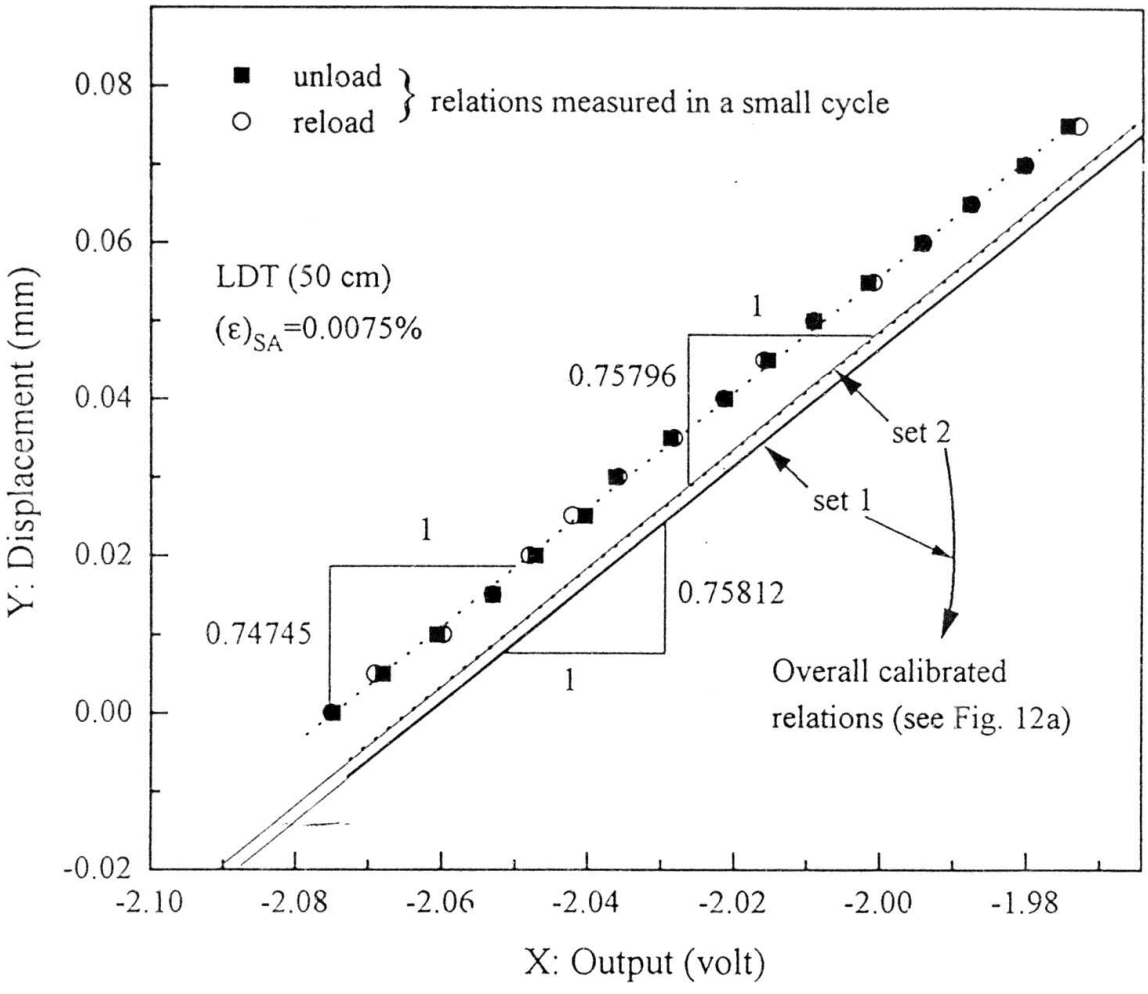

Fig. 2.16b: Comparison of the performance of LDT in measuring small-strain stiffness by using two calibration methods.

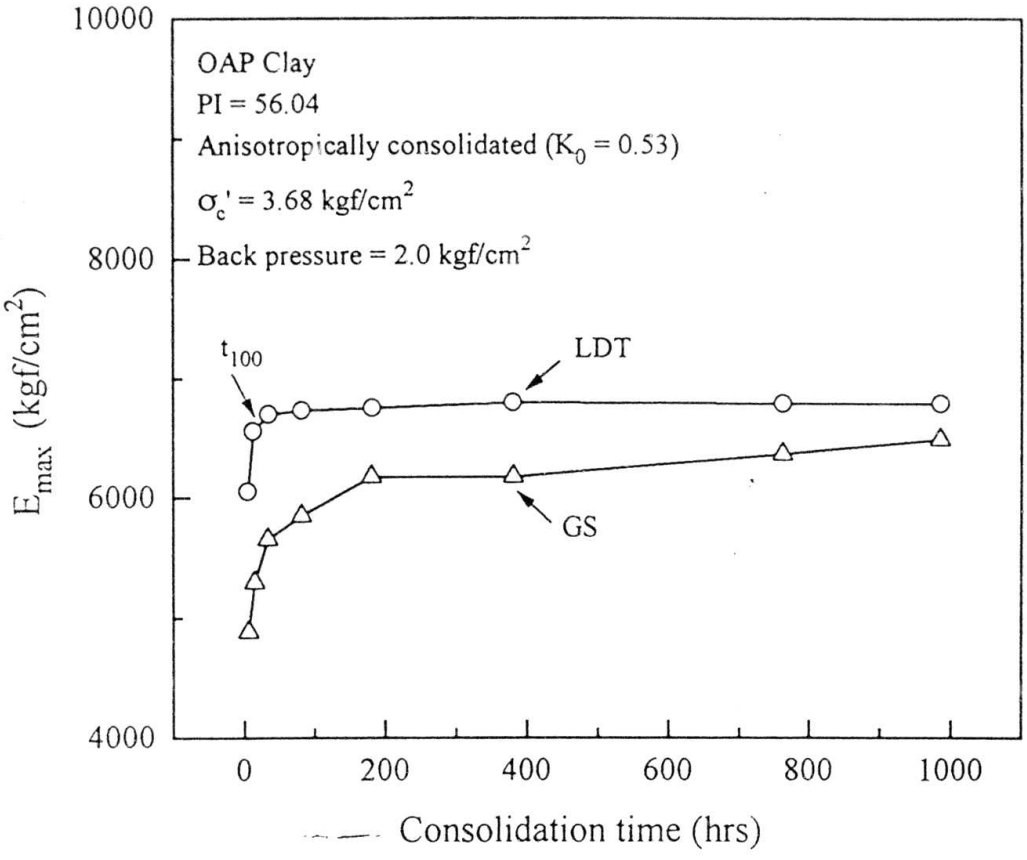

Fig. 2.17: Long-term stability of LDT at submerged condition under pressurized water in measuring small-strain Young's modulus (tested by Mukabi, J.N., 1995).

Chapter 3

Inherent Anisotropy in the Elastic Deformation of Granular Materials

3.1. Introduction

Deformation and strength characteristics of most soils are not isotropic in many respects. Most geotechnical problems are three-dimentional (3-D), for which elasto-plastic analyses are getting popular. For these analyses, both plasticity and elasticity should be dealt with properly. For 3-D characterization of elastic deformation of geomaterials, their possible anisotropy must be properly accounted for. It can be classified into the following three categories;

a) inherent anisotropy produced when deposited in air or under water, or when compacted;
b) stress state-induced anisotropy developed by current anisotropic stress-states; and
c) strain history-induced anisotropy produced by dominant shear (monotonic or cyclic) strain in a certain direction.

Symes et al. (1984) showed that for sand specimens produced by pluviation in water and subsequent vibration, the initial stiffness in the loading direction decreases with the rotation of major principal axis direction from 0^0 (i.e., the vertical direction) through 45^0 to the horizontal direction. Ko and Scott (1967), Parkin et al. (1968) and Siddiquee (1994) showed that the deformation of sand specimens produced by air-pluviation subjected to hydrostatic compression is anisotropic with strains in the lateral/radial direction (ε_h) being larger than that in the vertical direction (ε_v). Inherent strength anisotropy of sand specimens has been investigated by many researchers. For air-pluviated specimens of Silver Leighton Buzzard (SLB) and Toyoura sands tested in drained triaxial compression, the strength of a specimen with $\theta=0^0$ (i.e., the pluviation direction and the major principal stress direction are the same) was always stronger than that of a specimen with $\theta=90^0$ (i.e., the pluviation direction and the minor principal stress direction are the same), while strain value at the same shear stress is always smaller for a specimen with $\theta=0^0$ (Arthur and Menzies, 1972; Oda 1972a and 1972b). This finding was substantiated by Oda (1981), Tatsuoka et al. (1990) and Park and Tatsuoka (1994) in plane strain compression tests on a number of sands including Toyoura sand.

Particle orientation in air- or water-pluviated cohesionless soil has been investigated by many researchers. Parkin et al. (1968) investigated the orientations of the long axes of grains in a thin section by impregnating air-pluviated samples as formed with resin, and by using photographic enlargements of vertical and horizontal sections. They observed that the maximum dimension tended to be aligned in the horizontal plane and was symmetrically disposed about the vertical axis. Oda (1972a, 1972b) and Symes (1983) also confirmed that there was a strong horizontal bias to the long axis directions of the grains and the directions of inter-particle contact planes, which makes a air- or water-pluviated specimen softer and weaker when compressed in the horizontal direction.

On the other hand, inherent anisotropy in elastic deformation characteristics are not well understood. Among the previous works by wave velocity measurements, Stokoe et al.(1991), Bellotti et al. (1994), Lo Presti and O'Neill (1991) showed that elastic deformation characteristics of granular material produced by pluviation in air are inherently anisotropic. They showed that at isotropic stress states, the elastic Young's modulus in the horizontal direction (E_h) is always larger than the vertical value (E_v). These results are apparently not consistent with the anisotropy in deformation characteristics at relatively large strains and peak strength as described above.

Inherent anisotropy observed in the elastic Young's moduli is described in this chapter. The investigation was carried out in large triaxial square-prismatic specimens of cohesionless soils by measuring local strains.

3.2. Theoretical Background of elasticity

For an elastic body, strains ε_{ij} defined from a stress-free condition are related uniquely to stresses σ_{kl}; that is, strains are stress-path independent. A general anisotropic body has 36 independent elastic constants. When there exists a potential energy function, such as

$$W = \int \sigma_{ij}\, d\varepsilon_{ij} = \int \sigma_{ij}\, C_{ijkl}\, d\sigma_{kl} \tag{3.1a}$$

then the compliance matrix C_{ijkl} becomes symmetric (i.e., $C_{ijkl} = C_{klij}$). This is because

$$\varepsilon_{kl} = \partial W / \partial \sigma_{kl}\,; \qquad C_{ijkl} = \partial \varepsilon_{kl} / \partial \sigma_{ij} = \partial^2 W / \partial \sigma_{ij} \partial \sigma_{kl} \tag{3.1b}$$

$$\varepsilon_{ij} = \partial W / \partial \sigma_{ij} \; ; \qquad C_{klij} = \partial \varepsilon_{ij} / \partial \sigma_{kl} = \partial^2 W / \partial \sigma_{kl} \partial \sigma_{ij} \tag{3.1c}$$

Such a material is called a hyper-elastic body, which has 21 independent elastic constants. On the other hand, when only strain increments $d\varepsilon_{ij}$ are related uniquely to stress increments $d\sigma_{kl}$; that is, $d\varepsilon_{ij}$ are independent of the path of stress increment, $d\varepsilon_{ij}$ are related to $d\sigma_{kl}$ as $d\varepsilon_{ij} = C_{ijkl} d\sigma_{kl}$, this material is called a hypoelastic body. Generally, C_{ijkl} is a function of current stress state σ_{kl}. When strains ε_{ij} obtained by integrating $d\varepsilon_{ij}$ becomes stress path-independent, the hypo-elastic body is an ordinary elastic body. Generally, ε_{ij} are stress path-dependent for most soils. In this case, $d\varepsilon_{ij} = C_{ijkl} . d\sigma_{kl}$ is not a total differential, which means that $d\varepsilon_{ij}$ can be integrated partially only when a stress path is defined. This is the case with granular materials.

Most of the granular materials deposited naturally or artificially, or compacted vertically exhibit cross-anisotropic deformation properties, which are symmetric about the vertical axis. Cross-anisotropy requires only six elastic parameters for the characterization. The incremental relationship between stress and strain (Hooke's law) is:

$$\begin{bmatrix} \delta\varepsilon_{xx} \\ \delta\varepsilon_{yy} \\ \delta\varepsilon_{zz} \\ \delta\gamma_{yz} \\ \delta\gamma_{zx} \\ \delta\gamma_{xy} \end{bmatrix} = \begin{bmatrix} \frac{1}{E_h} & \frac{-\nu_{hh}}{E_h} & \frac{-\nu_{vh}}{E_v} & 0 & 0 & 0 \\ \frac{-\nu_{hh}}{E_h} & \frac{1}{E_h} & \frac{-\nu_{vh}}{E_v} & 0 & 0 & 0 \\ \frac{-\nu_{hv}}{E_h} & \frac{-\nu_{hv}}{E_h} & \frac{1}{E_v} & 0 & 0 & 0 \\ 0 & 0 & 0 & \frac{1}{2G_{vh}} & 0 & 0 \\ 0 & 0 & 0 & 0 & \frac{1}{2G_{vh}} & 0 \\ 0 & 0 & 0 & 0 & 0 & \frac{(1+\nu_{hh})}{E_h} \end{bmatrix} \begin{bmatrix} \delta\sigma_{xx} \\ \delta\sigma_{yy} \\ \delta\sigma_{zz} \\ \delta\tau_{yz} \\ \delta\tau_{zx} \\ \delta\tau_{xy} \end{bmatrix} \tag{3.1d}$$

where the stress and strain increments are referred to rectangular Cartesian axes x(=h), y(=h), and z(=v) with the z axis being vertical; E_v and E_h are the vertical and horizontal elastic Young's moduli; ν_{vh}, ν_{hh}, ν_{hv} are the Poisson's ratios; G_{vh} is the shear modulus.

When we can assume that for small stress increments $\Delta\sigma_{ij}$, the potential strain energy $\Delta W = \int \Delta\sigma_{ij} d(\Delta\varepsilon_{ij})$ exists, then the compliance matrix becomes symmetric, which requires $\nu_{vh}/E_v = \nu_{hv}/E_h$. Accordingly, five individual constants are left to be determined. Note that it has not been verified that the function ΔW always exists for a given soil element under a given stress-strain condition. Furthermore, even if the function ΔW exists for a given small stress increments

$\Delta\sigma_{ij}$, this does not mean that a potential strain energy function $\Delta W'$ also exists for larger stress increments $\Delta\sigma'_{ij}$.

In a given uncemented soil, the Young's moduli, E_v and E_h, within the elastic threshold strain, depend on the following factors:

- the soil state expressed by a combination of current void ratio (e) and the current stress state (σ_{ij}),
- the soil fabric reflecting the depositional environment and post-depositional processes such as aging, diagenesis, cementation, etc.

It is the objective of this investigation to characterize inherent and stress-induced anisotropy in the elastic deformation properties of cohesionless soil as observed at very small strains in the case where the axes of symmetry for both types of anisotropy are identical (i.e., air-pluviated sands under triaxial compression and extension stress conditions). In this case, Eq.(3.1d) becomes:

$$\begin{bmatrix}\delta\varepsilon_h\\ \delta\varepsilon_v\end{bmatrix}=\begin{bmatrix}(1-\nu_{hh})/E_h & -\nu_{vh}/E_v\\ -2\nu_{hv}/E_h & 1/E_v\end{bmatrix}\begin{bmatrix}\delta\sigma_h\\ \delta\sigma_v\end{bmatrix} \qquad (3.2)$$

The matrix in Eq. 3.2 is unsymmetric, because the stress and strain vectors used in Eq. 3.2 have not been chosen in such a way that the product of the corresponding stress and strain increments gives the input work increment.

Elastic parameters can be obtained by static triaxial cyclic loading (CL) tests with a single amplitude principal strain $(\varepsilon)_{SA}$ less than about 0.002% (Hardin 1978; Jamiolkowski et al., 1991; Tatsuoka et al., 1994a, 1994b; Tatsuoka et al., 1995). In this strain range, moduli are hardly influenced by stress-strain histories that are small enough to maintain the initial fabric, type of loading (montonic or cyclic), wave-form during cyclic loading and rate of shearing (dynamic or static) (Tatsuoka and Kohata, 1995; Jamiolkowski et al, 1991). For vertical CL tests at constant lateral stress (i.e., $\Delta\sigma_h=0$ and $\Delta\sigma_v\neq0$), Eq. 3.2 provides:

$$E_v=\Delta\sigma_v/\Delta\varepsilon_v,\ and\ \upsilon_{vh}=-\Delta\varepsilon_h/\Delta\varepsilon_v \qquad (3.3a)$$

For horizontal CL tests at constant vertical stress (i.e., $\Delta\sigma_v=0$ and $\Delta\sigma_h\neq0$), Eq. 3.2 provides:

$$E_h = (1-\upsilon_{hh})\Delta\sigma_h/\Delta\varepsilon_h, \text{ and } \Delta\varepsilon_v/\Delta\varepsilon_h = -2\upsilon_{hv}/(1-\upsilon_{hh}) \quad (3.3b)$$

The two parameters, ν_{vh} and E_v (Eq. 3.3a) can be determined from vertical CL tests. On the other hand, E_h cannot be determined only from horizontal CL test without adopting one assumption, which however will not sacrifice much the final outcome. The assumption used is that ν_{hh}="ν_{vh} at isotropic stress state."

3.3. EXPERIMENTAL SETUP

The tests were performed using a large triaxial apparatus in which a square-prismatic specimen, 23 cm in side and 57 cm in height, which can be subjected to a wide variety of stress states by controlling boundary stresses. Table 3.1 lists the cohesionless materials used in this investigation. A variety of materials in terms of grain size and particle shape were selected to study into their influences (if any) on elasticity. The materials are poorly graded.

All specimens were tested at air-dried conditions. The specimens were reconstituted by pluviation through air, except the one specimen of SLB sand, which was prepared by vertical vibratory compaction with use of a vibrator. Each specimen was tested at air-dried conditions. The specimens were reconstituted by pluviation through air, maintaining a constant height of fall, into a split mold from multiple sieves, except the one specimen of SLB sand. The latter one was prepared by vertical vibratory compaction with use of a vibrator, which applied vertical vibrations on the surface of each of 14 layers. The top and bottom ends of each specimen were well lubricated by the method suggested by Goto et al. (1993). After each specimen was set in the triaxial cell, a partial vacuum of 0.2 or 0.3 kgf/cm^2 was applied before any instrumentation.

A load cell that is sensitive enough to measure very small load was placed inside the triaxial cell. Local Deformation Transducers (LDTs) were used in both vertical and horizontal directions, running parallel to the principal stress directions, to measure normal strains locally. A pair of 50-cm long LDTs were set vertical (3 to 4 cm away from top and bottom ends) to measure vertical strains, ε_v, and a total eight 18-cm long LDTs were set horizontal to measure lateral

strains, ε_h (Figs. 2.1 and 2.2a, Chapter 2). Lateral LDTs (i.e., LDTs used to measure lateral LDTs) were also set at the center of width (or breadth) of a specimen, excluding 1.5 to 2.0 cm at both edges. In measuring local strains by LDTs, the specimen ends, which are very vulnerable for including bedding errors (Tatsuoka and Kohata, 1995; Jardine et al, 1984) in both principal strain directions, were avoided to include as part of gage length of LDT. Any change in the gage length of LDT in course of testing is detected by the small electric-resistant strain gauges at the center length of an LDT. Therefore, the measured strains by LDTs are free from any bedding errors. Besides, a pair of proximeters were used to measure vertical displacement of the specimen cap and another pair to measure the lateral displacements of rubber membrane (0.8 mm in thickness) at diagonally opposite faces of the specimen (Fig. 2.2a, Chapter 2).

To load the specimen along a specified stress path as well as to perform CL test, the automatic system described in Chapter 2 was used, which controls both a hydraulic axial actuator and a cell air-pressure. The latter was controlled by using a regulator and an electro-pneumatic pressure transducer. In each test, vacuum was replaced with cell air pressure before using the stress path control system.

3.4. TEST PROGRAM

The experimental program consisted of small cyclic loading, both vertical and horizontal, at many selected stress states. The program consisted of the following steps sequentially:

1. Isotropic compression, or anisotropic compression at a constant stress ratio ($K=\sigma_h/\sigma_v=0.37$), up to a cell pressure of 5.0 kgf/cm^2, followed by rebounding to 0.5 kgf/cm^2 (Cycle 1). Another cycle (Cycle 2) of reloading and re-unloading in the same path mentioned above was applied to confirm the results obtained from Cycle 1.
2. Isotropic compression up to 4.5~5.0 kgf/cm^2, during which 11 cycles of small vertical CL followed by 3 cycles of small horizontal CL were applied at various stress states.
3. CL tests were performed at stress states shown in Fig. 3.1 in the sequence of the numbers indicated.
4. Similar CL tests were performed at different stress states of the same range of σ_h described in step 2, but following different $\Delta K=0$ (in addition to $K=1$) stress paths, while K was varied in the range between 0.5 to 0.75. This step was performed for some specimens.

5. For some specimens, multiple stages triaxial compression (TC) were applied from $\sigma_v=\sigma_h=C_1$ to a stress ratio $\sigma_v/\sigma_h=C_2$ with small unload/reload cycles at various stress states with subsequent unloading from C_2 to the previous isotropic stress.The range of C_1 was varied from 0.5 to 1.0 kgf/cm^2, while for C_2 ($=\sigma_v/\sigma_h$), it was varied from 3.0 to 4.0.

6. Finally, triaxial compression to failure was performed from the isotropic stress state of $\sigma_v=\sigma_h=0.8$ kgf/cm^2.

Part of the results which is relevant to describe inherent anisotropy in the small strain stiffness is described in this chapter. The rest will be described in the foregoing chapters.

3.5. TESTING METHOD

Each test was performed by using a auto-control testing system in which both vertical load and lateral stress were controlled independently. Stress path tests such as $\Delta\sigma_v=0$, $\Delta\sigma_h=0$, $\Delta\sigma_m=0$, and $\Delta K=0$, together with vertical and horizontal CL tests are possible to be performed by using this system. The details of the system is described in Chapter 2. To control a stress path, such as $\Delta\sigma_v=0$ (also horizontal CL with $\Delta\sigma_v=0$), $\Delta\sigma_m=0$ or $\Delta K=0$, which needs simultaneous controlling of σ_v and σ_h, a very small increment (or decrement) of cell pressure is applied first, followed by incremental feed back to the deviator load to maintain the intended stress path. For these stress paths, a finite time, Δt, is set up for each step of loading. Before proceeding to the next step, Δt allows the cell pressure to attain a steady state and/or creep deformation to cease, and σ_v to be brought to the intended stress path by feed-back close-loop scheme. Therefore, Δt prohibits horizontal CL to apply as fast as vertical CL. In this investigation, vertical and horizontal CL tests were performed at constant frequencies (f) of 0.1 Hz and 0.0066 Hz, respectively. Loading rate effect on the test results was also investigated, which will be described later.

3.6. Resolutions, Errors & Countermeasures

None of the LDTs was used for a full scale maximum strain range of more than 2%. The LDTs were able to detect a strain as small as 0.00005% (with 10 times amplification) with confidence. The gap-sensors also possessed the similar resolution. Other principal measuring devices also possess sufficiently enough resolution to measure small strain stiffness (Table 2.2). Typically, 100 and 50 data points were recorded in each hysteresis loop of vertical and horizontal CL,

respectively. Due to the existence of small hysteresis, an LDT can under-estimate stiffness by a maximum of about 2%. Data presented herein is not corrected for this probable under-estimation. To reduce the effects of creep deformation of glue (used to fix an LDT on the membrane) and rubber membrane (at the vicinity of hinge shoe) to a negligible value, LDTs were left for at least 3 hours after setting it on the specimen surface. After this treatment, the effects of creep on the deformation was negligible. On the other hand, load cell did not show any hysteresis in a small unload/reload cycle, and neither did a small unload/reload cycle show any slope difference with the calibrated response, which is usually obtained by a monotonic load/unload cycle for the full scale range.

3.7. Results and Discussions

Specimen designations are listed in Table 3.2. Figs. 3.2a and b show typical responses during one cycle of small-amplitude vertical and horizontal CL tests, respectively, obtained from the specimen of SLB sand (SLK1V, Table 3.2). Similar responses for Ticino sand (TCK1A) specimen are shown in Figs. 3.3a and b. Fig. 3.4a compares externally and locally measured axial strains from a vertical CL test (see also Fig. 3.2a). Fig. 3.4b compares externally and locally measured lateral strains from a horizontal CL test (see also Fig. 3.2b). Axial strains are largely over-estimated by external measurements due to bedding error, and the deformation of load cell and loading piston. A low resolution of external measuring device (external gage located outside of the triaxial cell) was also partially responsible for the big difference with that obtained by gap-sensors (GS). Because it was used to measure large strains (say, up to 5%) during shearing and therefore, it could not measure strain increments less than 0.002%. The lateral strains (Fig. 3.4b) measured by GS during a horizontal CL test is also unreliable due to two reasons: bedding error in lateral direction and the rotation of the rods which support the GSs caused by the bending deformation of the base plate of the triaxial cell caused by changes in the cell pressure. Figs. 3.5a and b show the effects of bedding error on ε_v (in vertical direction) and ε_h (in lateral direction), respectively, during isotropic compression tests (loading and unloading of Cycle 1) on the same specimen (SLK1V). The effects of membrane penetration on lateral strain during isotropic and anisotropic compression tests on SLB sand are also demonstrated in Fig. 20 of Tatsuoka and Kohata (1995). Herein data obtained by using LDTs will be presented if not specified otherwise.

From the responses of Figs. 3.2a and b, the elastic parameters (Eqs. 3.3a and b) were evaluated by linear regression. The strain increments $d\varepsilon_v$ and $d\varepsilon_h$ were obtained by averaging the readings of the pair of vertical LDTs and four pairs of lateral LDTs, respectively. The single-amplitude major principal strain, $(\varepsilon)_{SA}$, was less than 0.002% in most of the cases, while in a few cases, $(\varepsilon)_{SA}$ exceeded the above value. In the previous studies (e.g., Tatsuoka et al., 1994a), a large amount of cyclic triaxial tests on various types of sands, in which symmetrical cyclic axial stresses were applied to isotropically consolidated specimens with increasing $(\varepsilon)_{SA}$ in steps show that the value of E_v is essentially constant for a range of $(\varepsilon)_{SA}$ less than about 0.002%. This strain value may be called the threshold elastic strain. The E_v and E_h values defined for $(\varepsilon)_{SA} \leq 0.002\%$ may be called the quasi-elastic Young's moduli. In the following, however, they will be called simply the elastic Young's moduli. The measured values of E_v and E_h were corrected for $(\varepsilon)_{SA}$ whenever it exceeded the threshold elastic strain. In that case, the corrected Young's modulus, E_{cor}, was obtained as $E_{cor} = E_{measured}/C$, where C is the ratio of Young's modulus at $(\varepsilon)_{SA}$ to that at $(\varepsilon)_{SA} \leq 0.002\%$. The relationship between C and $(\varepsilon)_{SA}$ was constructed by using the relationship between the equivalent Young's modulus (E_{eq}) and the single amplitude vertical strain $(\varepsilon_v)_{SA}$ obtained from a series of conventional cyclic triaxial tests on the relevant type of geomaterials (e.g., Fig. 3.6). The amount of correction was 4% at the largest. To evaluate E_h, it was assumed for Eqs. 3b that ν_{hh}="$\nu_{hv}=\nu_{vh}$ at isotropic stress states" (note that the values of ν_{vh} at isotropic stress states, ν_0, for different specimens are given in Table 3.2).

On the other hand, the reliable values of ν_{hv} and ν_{hh} could not be obtained by the present test program. Rather these (ν_{hv} and ν_{hh}) can be evaluated only by tests in which horizontal stress in one direction is changed. In the present study, however, the horizontal stresses in two orthogonal directions are always identical. Using a $\varepsilon_v \sim \sigma_h$ response as shown in Fig. 3.2b during a horizontal CL test, one may be able to make an estimation of ν_{hh}. However, it was not done in this investigation due to lack of reliability, because σ_v during a horizontal CL test fluctuated a bit during feed-back scheme (Fig. 2.4f, Chapter 2).

However for the time being, suppose that the $\varepsilon_v \sim \varepsilon_h$ response shown in Fig. 3.2b is reasonably correct, which indicates $\Delta\varepsilon_v/\Delta\varepsilon_h = -0.081$. Using the measured values of E_v= 5780 kgf/cm^2, E_h= 3100 kgf/cm^2, and ν_{vh}= 0.13 (Fig. 3.2a and b), the energy conservation principle yields $\nu_{hv} = \nu_{vh}(E_h/E_v) = 0.07$. Then Eq. 3.3b yields $\nu_{hh} = 1+2\nu_{hv}/(\Delta\varepsilon_v/\Delta\varepsilon_h) = -0.73$. Theoretically,

this value of ν_{hh} is possible for a material considering the bounding values of the elastic parameters in 3-D space, which can be obtained from Eq. 3.1 by setting the right-hand-side compliance matrix product equal to zero as follows (Pickering, 1970):

$$\begin{aligned} &E_v > 0.0 \\ &E_h > 0.0 \\ &-1 < \upsilon_{hh} < 1 \\ &(1-\upsilon_{hh})E_h / E_v > 2\upsilon_{vh}^2 \end{aligned} \tag{3.4}$$

Within the space obtained by Eqs. 3.4, any given material is represented by a point and points in certain regions represent particular types of material. Now if we assume E_v=E_h (i.e., isotropic) and use the same values of the other entities (i.e., E_v, E_h, etc.) as before, it will yield ν_{hh}=-2.2, which is impossible to occur. Besides to-date, no evidence can be available in the literature which shows that a soil may exhibit a negative Poisson's ratio. Rather the value of ν lies somewhere between 0.0 and 0.20 (among many others, Hardin 1978). The assumption adopted to evaluate E_h may not influence the outcome dramatically.

The measured Young's moduli were stable with the number of loading cycles N as shown in Fig. 3.7a and b for a Toyoura sand specimen (TYK02). The variation of the coefficient of correlation r, a statistical quantity defined as Eq. 3.5 (below), with N is also plotted in the inset to Figs. 3a and b.

$$r = \pm \frac{\sum(xy)}{\sqrt{\sum(x^2)\sum(y^2)}} \tag{3.5}$$

Eq. 3.5 is applied on the data of each cycle of $\sigma_v \sim \varepsilon_v$ relation (e.g., Fig. 3.2a) with x=ε_v and y=σ_v. For r=+1, all data points lie on the single linear regressed line, which would be the expectable value for moduli evaluation. On the other hand, r= -1 is the expected value whlie evaluating Poisson's ratio from each cycle of data (e.g., $\varepsilon_h \sim \varepsilon_v$ relation of Fig. 3.2a). Therefore, elastic Young's moduli evaluation from the data of each cycle can be said to be perfectly positively (r=+1) correlated since r varies in the range between 0.995 and 1.0 (Figs. 3.2a and b). However,

while evaluating ν_{vh}, the value r typically varies in the range of -0.75 to -0.9 (negatively correlated) because of relatively large scatter.

For the cycles applied at a stretch at a given stress state, the E_v or E_h values never exceeded ±1% of the mean value. Fig. 3.7c shows the values of E_h evaluated based on the readings of each of eight lateral LDTs at the fifth cycle for the case shown in Fig. 3.7b. The scatter of these E_h values is not large. In some cases, however, particularly in tests at low pressure levels, E_h value evaluated based on the individual reading from some of the top- and bottom-height LDTs became larger than 1.1 or smaller than 0.9 of the average of the others. In such cases, these data were discarded while averaging to define E_h value. On the other hand, E_v values evaluated separately by two vertical LDTs never deviated more than ±3.5% from the mean value. This results indicate the existence of the distribution of non-uniform 'local density' pockets in both directions in a specimen. Bhatia and Soliman (1990) reported non-uniform density distribution. By a computer-controlled image analyzer, they examined thin vertical and horizontal sections through a series of triaxial specimens prepared by air-pluviation and compaction methods. They observed that the frequency distributions of void ratio were skewed towards the denser void ratios. Many others such as Arthur and Menzies (1972) and Kirkpatrick and Belshaw (1968) also reported nonhomogeneous strain distribution by radiographic methods. In a stress controlled apparatus with flexible boundaries where stress is uniform, the material response is strain which is in no way constrained to uniform.

3.7.1. Inherent Anisotropy: Deformation in Isotropic Stress Path

Fig. 3.8a and b show the relationships between volumetric strain ε_{vol} ($=\varepsilon_v+2\varepsilon_h$) and ε_v obtained from isotropic loading and unloading (Cycle 1) of different granular materials. The volumetric strain should be three times the axial strain for isotropic behavior. Therefore, for all the four materials, deformations of air-pluviated specimens were anisotropic during primary loading with ε_h greater than ε_v (Ko and Scott, 1967; Parkin et al., 1968), whereas the behavior was less anisotropic during unloading and reloading. The specimens of SLB sand (Fig. 3.8b) exhibited strong anisotropy, almost to the same extent, in primary loading, unloading, reloading and re-unloading. Data for reloading and re-unloading was shown in Figs. 3.8c and d. Residual strains of Cycle 1 were neglected during second loading in Cycle 2. Range of σ_m during Cycle 2 was from

0.5 to 5.0 kgf/cm^2, except for TYK1A specimen in which σ_m was increased up to 6.0 kgf/cm^2. Due to virgin loading from 5.0 to 6.0 kgf/cm^2 during Cycle 2, TYK1A specimen exhibited more hysteresis (Fig. 3.8c). Although denser, the compacted specimen (SLK1V, Fig. 3.8b) was slightly less anisotropic in virgin loading than the air-pluviated one (SLK1A). But during unloading of SLK1V, anisotropy slightly increased. The reason could be due to more passive sliding during unloading, together with elastic rebound as a result of the withdrawal of restraining forces, that makes the particles interlocked during compaction method.

Figs. 3.9a and b show the variations of tangent moduli L_v (in vertical direction) = $dp/d\varepsilon_v$ and L_h (in horizontal direction)= $dp/d\varepsilon_h$, respectively, with the mean stress $p(=\sigma_m)$ of specimens SLK1A and SLK1V, respectively. A similar behavior was observed for the other specimens. General features observed are:

a) For loading ($dp>0$), the modulus is larger in Cycle 2 (i.e., reloading) than in Cycle 1 due to reduced plastic strains in Cycle 2;

b) For unloading ($dp<0$), the modulus is similar between Cycles 1 and 2 due to essentially elastic deformation;

c) For unloading ($dp<0$), the value of L_v is larger than the corresponding value of L_h during both loading and unloading, indicating that elastic deformation stiffnesses at isotropic stress states were anisotropic;

d) Stiffness immediately after the start of unloading was affected by continuous creep deformation;

For first loading, where both elastic and plastic strains are involved, these sand specimens had greater stiffness in the axial than in the lateral direction. Also for unloading, reloading and re-unloading, where the strains are primarily elastic (Ko and Scott, 1967; Rowe, 1971), the stiffnesses were noticeably anisotropic. Therefore, the inherent anisotropy of deformation results not only from plastic strains but also from elastic strains. Fig. 3.10 shows the relationship between the horizontal-to-vertical strain increments (i.e., $d\varepsilon_h/d\varepsilon_v$) and the confining pressure $p(=\sigma_m)$ during reloading path (Cycle 2) for different materials. The value of $d\varepsilon_h/d\varepsilon_v$ should be equal to unity for isotropic deformation. It can be seen that SLB sand (SLK1A) was more anisotropic in all, which was followed by Hime gravel, Toyoura sand and Ticino sand in the descending order. Anisotropic deformation increased with pressure level for air-pluviated SLB (SLK1A) sand, whereas it

decreased slightly for the others with the increase in p. The elastic deformation anisotropy described are reflected in the small strain stiffness measured by small cyclic loading tests as described in the next section.

3.7.2. Transverse Isotropy

The lateral strains (ε_h) measured in two orthogonal directions during isotropic consolidation (primary loading and unloading) of Ticino (TCK1A) and Toyoura (TYK1A) sands are shown in Fig. 3.11a, which are typical of the similar test results. In the figure, the ε_h value measured at a given stress state in each horizontal direction (x or y) was divided by the corresponding maximum average value, $(\varepsilon_h)_{max}$= [$(\varepsilon_y)_{max}$+$(\varepsilon_x)_{max}$] / 2, measured at σ_m= 5.0 kgf/cm^2, which is listed in Fig. 3.11a. A nearly 1:1 relationship can be observed, which indicates the transverse isotropy in the deformations of triaxial specimens.

Fig. 3.11b shows the relationship of E_h between two orthogonal horizontal directions. The values of E_h were obtained in each of the two horizontal directions at isotropic stress states (i.e., K=1, σ_v=0.5~4.5 kgf/cm^2) and anisotropic stress states (i.e., 0.5 $\leq\sigma_h/\sigma_v \leq$2.0) under isotropic stress conditions in the horizontal plane. Therefore, air-pluviated (e.g., TYK1A) and compacted (SLK1V) depositions of granular materials are transversely isotropic in the small strain stiffness. This finding is in agreement with that obtained by Stokoe et al., 1991, Bellotti et al., 1994, etc. by calibration chamber tests measuring body wave velocities.

3.7.3. Inherent Anisotropy in Small Strain Stiffness

In Figs. 3.12a~c, the elastic Young's modulus have been divided by the void ratio function f(e)= $(2.17\text{-}e)^2/(1+e)$ [Hardin and Richart, 1963]. Based on the function f(e), the changes in E_v or E_h due to the changes in void ratio during tests on a given specimen were less than 1%. Variations of E_v/f(e) and E_h/f(e) for the tested materials obtained from the series of vertical and horizontal CL tests performed at various stress states along the isotropic stress path are shown in Figs. 3.12a~c in full logarithmic scale. The following important trends can be observed:

(a) E_v and E_h are proportional to σ_c^m with $m<1.0$, or more rigorously to $\sigma_c^{m_v}$ and $\sigma_c^{m_h}$, respectively. The values of m_v and m_h for different tests are listed in Table 3.2. It was found that $m_v>m_h$ in most cases.

(b) The m_v values were very stable among the different specimens for Toyoura sand (m_v=0.49) and Hime gravel (m_v=0.51). For the latter case, m_v was independent of initial consolidation stress ratio (i.e., K=1.0 and 0.37; Table 3.2). On the other hand, m_v values varied in the range of 0.45 to 0.51 among different specimens for SLB sand; this variation could be due to the effects of initial consolidation stress ratio (K=1 or 0.37) and different sample preparation methods. For Ticino sand, the value of m_v was 0.53.

(c) The m_h values were generally more scattered than m_v values. This is due to that the accuracy of E_h measurements was less than that of E_v measurements.

(d) Some degree of inherent anisotropy with $E_v>E_h$ is noticeable. This finding is opposite to that $E_h>E_v$ obtained by body wave velocity measurements (e.g., Stokoe et al., 1991, Bellotti et al., 1994). The reasons are not known to the present authors.

(e) For the same void ratio and at the same isotropic stress state, among the air-pluviated specimens, SLB sand exhibited the largest vertical Young's modulus E_v, while Ticino sand exhibited the smallest value. On the other hand, Toyoura and SLB sands exhibited the largest horizontal Young's modulus E_h, while Hime gravel exhibited the smallest value. The ratio of the largest to the smallest E_v values is about 2.0, while that of E_h values is about 1.5 (see Table 3.2). Further, the specimen of SLB sand prepared by compaction method (SLK1V) exhibited a vertical Young's modulus that is higher by 11% than that of the other prepared by the air-pluvial method (SLK1A), while the horizontal Young's modulus was not affected by the different sample preparation methods. These results indicate that the elastic modulus of granular materials in vertical direction is more sensitive to the particle and structure properties of granular materials than that in the horizontal direction.

An attempt was made to correlate the degree of inherent anisotropy in small strain stiffness "I," defined as $I=1-E_h/E_v$, with that of elastic deformation anisotropy (A) during isotropic re-compression (Cycle 2). The values of "I" at $\sigma_v=\sigma_h=1.0$ kgf/cm^2, which is named after I_0, are listed in Table 3.2. For ε_h and ε_v at a given stress state during second loading, A is defined as $A=(\varepsilon_h-\varepsilon_v)/(\varepsilon_h-\varepsilon_v)_{ref}$ after initialization of ε_h and ε_v to zero at the start of reloading, $(\varepsilon_h-\varepsilon_v)_{ref}$ being the

value of ε_h-ε_v at a reference σ_m (here σ_m=4.5 kgf/cm^2). The relationship is shown in Fig. 3.13. Although a unique relationship was not obtained, the following trends can be observed:

(1) "I" increases with the increase in A (i.e., with the increase in pressure level).
(2) Coarse-grained soil (SLB sand having D_{50}=0.62 mm and Hime gravel having D_{50}=1.73 mm) exhibits significant stiffness anisotropy than Toyoura (fine-grained having D_{50}=0.162 mm) and Ticino (medium-grained having D_{50}=0.502 mm) sands. Therefore, inherent anisotropy in small strain stiffness could be affected by particle size.
(3) Particle shape also seems to have some effect on "I" as the sand consisted in subround particle (e.g., SLB sand) exhibits more significant anisotropy than a sand having subangular particle (Ticino sand) although the mean grain sizes (d_{50}) are not very different.

Thus, inherent anisotropy observed in the small strain stiffness may be affected by particle size, shape, orientation, and so on. This anisotropy (i.e., E_v>E_h) is consistent with the observed elastic deformation anisotropy (ε_h>ε_v) observed in compression along the isotropic stress path. It is also consistent with inherent strength anisotropy observed by Arthur and Menzies (1970), Oda (1981), and Park and Tatsuoka (1994). Micro-mechanical studies by Symes (1983), Parkin et al. (1968) are also in agreement with the present observations.

As mentioned earlier, most of the vertical and horizontal CL tests were performed at frequencies 0.1 and 0.0066 Hz, respectively. Effects of loading frequency (or strain rate) on the response during small-amplitude cyclic loading were investigated by performing vertical CL tests also at a frequency equal to that of horizontal CL tests, mostly under isotropic stress conditions on some of the specimens in Table 3.2. Fig. 3.14 shows that the effect of different loading frequencies is negligible except for one case (Hime gravel at σ_m=0.5 kgf/cm^2; see also Fig. 3.12b). Kim et al. (1991) and Shibuya et al. (1995) observed similar results on granular materials and normally consolidated clay, respectively. It can be concluded, therefore, that the inherent anisotropy observed in small strain stiffness is not due to strain rate effects.

3.8. Summaries

(1) Inherent anisotropy has been investigated into the small strain stiffnesses and elastic deformation in isotropic stress path on large rectangular-prismatic triaxial specimens by measuring local strains in vertical and horizontal directions. A variety of cohesionless materials, medium-dense to dense, fine-grained to coarse-grained, subround to subangular, have been investigated.

(2) Materials were anisotropic both in small strain stiffnesses with E_v being larger than E_h and in elastic deformation with ε_h being larger than ε_v in isotropic compression. The degree of inherent anisotropy increased with the increase in the degree of elastic deformation anisotropy as the stress level increases in isotropic compression.

(3) Anisotropy in small strain stiffness seems to be influenced by particle size, shape, orientation, etc. of the particulate materials. Coarse grained and subround materials were more anisotropic compared to those fine grained and subangular materials.

(4) All the materials exhibited transverse anisotropy both in small strain stiffness and deformation.

(5) Elastic parameters were independent of frequency of loading (or rate of shear) within the range examined (i.e., f= 0.0066~0.1 Hz). The observations described above were common to both air-pluviated and vibrator-compacted specimens.

Table 3.1: List of test materials.

Material (Origin)	D_{50} (mm)	U_c	G_s	e_{max}	e_{min}	Grain shape
Toyoura sand (Japan)	0.162	1.46	2.64	0.973	0.612	Subangular
Ticino sand (Italy)	0.502	1.33	2.68	0.96	0.59	Subangular
Silver Leighton Buzzard sand (UK)	0.62	1.11	2.66	0.79	0.49	Subround
Hime gravel (Japan)	1.73	1.33	2.65	0.48	0.709	Subround

Table 3.2: List of the test specimens and some results.

Materials	Specimen name	Initial void ratio		Preloading stress ratio ($K=\sigma_h/\sigma_v$)	$^{\Psi}E_1$ (kgf/cm^2)	m_v	m_h	$I_0=1-E_h/E_v$ at $\sigma_v=\sigma_h=1$ kgf/cm^2	ν_0 at $\sigma_v/\sigma_h=1$	[a]Change in void ratio (Δe)
		e	measured at σ_c (kgf/cm^2)							
Toyoura sand	TYK1A	0.641	0.2	1.0	2030	0.486	0.410	0.12	0.170	-0.011
	TYK02	0.653	0.3	1.0	1820	0.494	0.453	0.10	0.163	-0.012
	TYISD	0.681	0.2	1.0	1905	0.491	0.486	0.08	0.172	-0.014
Hime gravel	HGK1A	0.510	0.3	1.0	2080	0.511	0.450	0.38	0.144	-0.004
	HGK0A	0.490	0.3	0.37	2188	0.509	0.489	0.44	0.158	-0.004
SLB sand	SLK1A	0.540	0.2	1.0	2890	0.474	0.300	0.37	0.110	-0.003
	[b]SLK1V	0.524	0.3	1.0	3220	0.452	0.420	0.46	0.130	-0.002
	SLK0A	0.520	0.3	0.37	2810	0.510	0.475	0.55	0.180	-0.004
Ticino sand	TCK1A	0.580	0.2	1.0	1510	0.530	0.440	0.05	0.163	-0.008

[a]: the change in void ratio ('-' indicates a decreases) is for steps (2) to (5) of test program.
[b]: the specimen was reconstituted by vibrator-compaction method.
$^{\Psi}$: $E_v = E_1 f(e).\sigma_c^{m_v}$; E_1 is the value of E_v at $\sigma_v=\sigma_h=1.0$ kgf/cm^2 when $f(e)=1$.

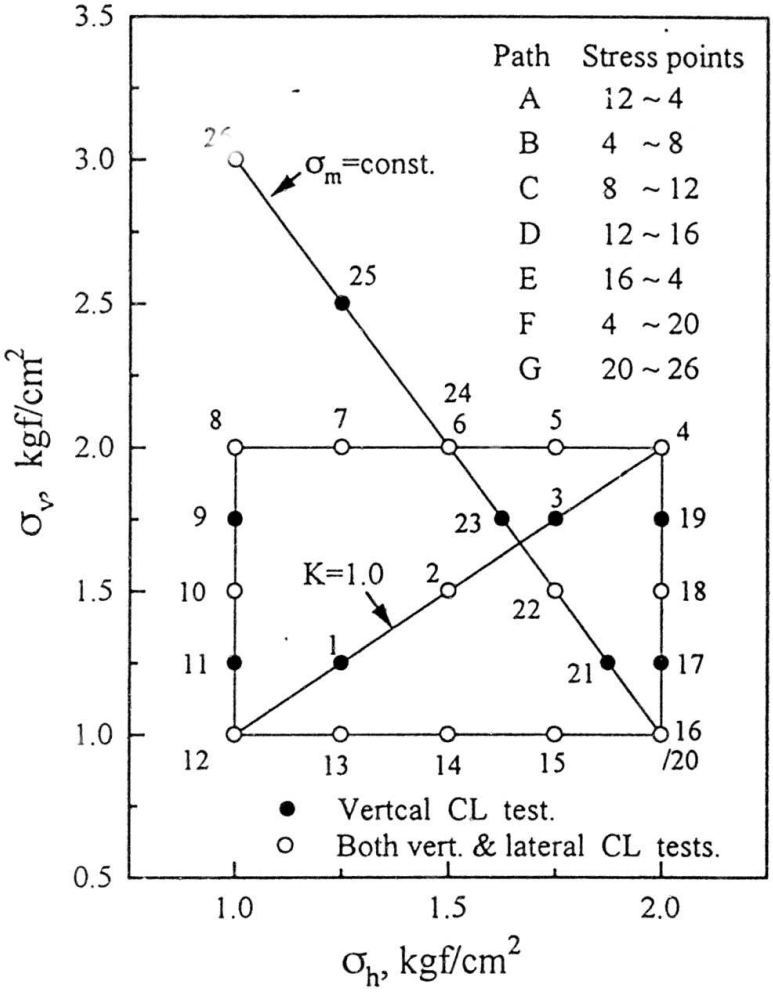

Fig. 3.1: Test program for vertical and horizontal CL tests at different stress paths ($0.5 \leq \sigma_v/\sigma_h \leq 2.0$).

Fig08.org/inherent/D1

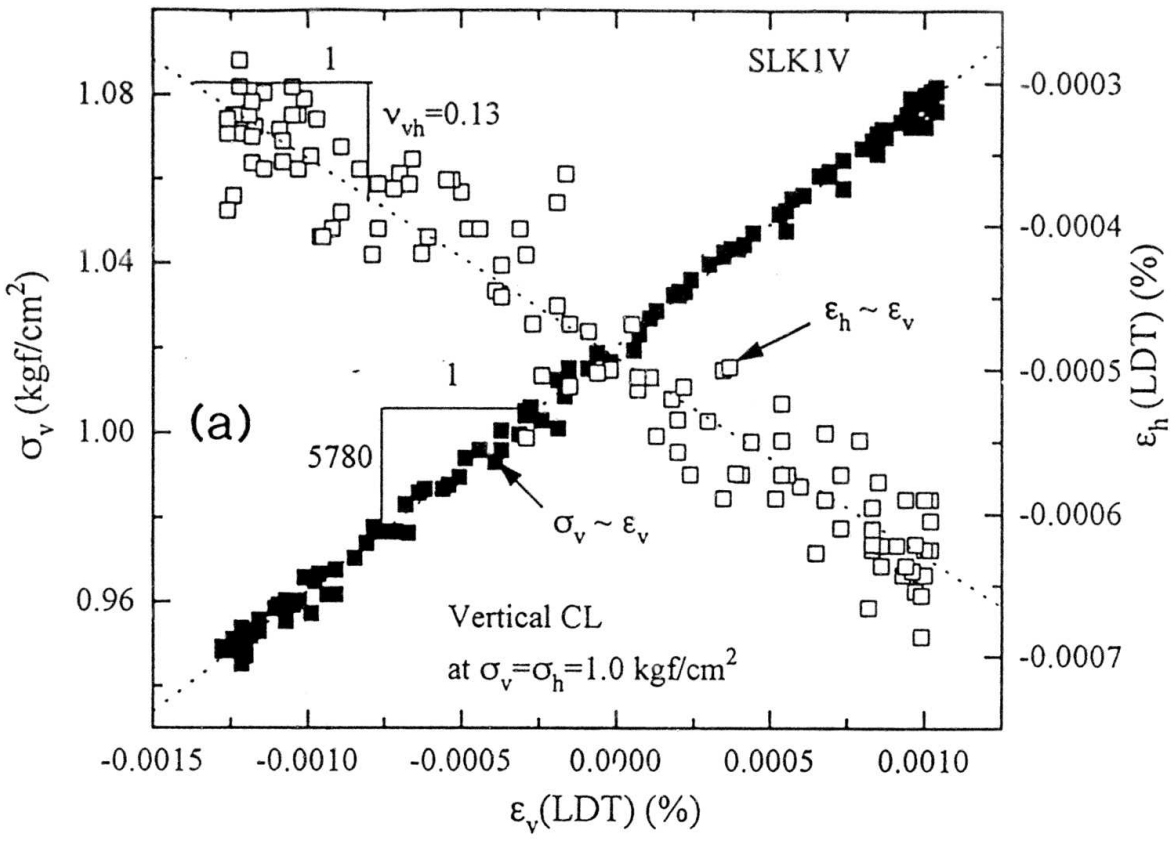

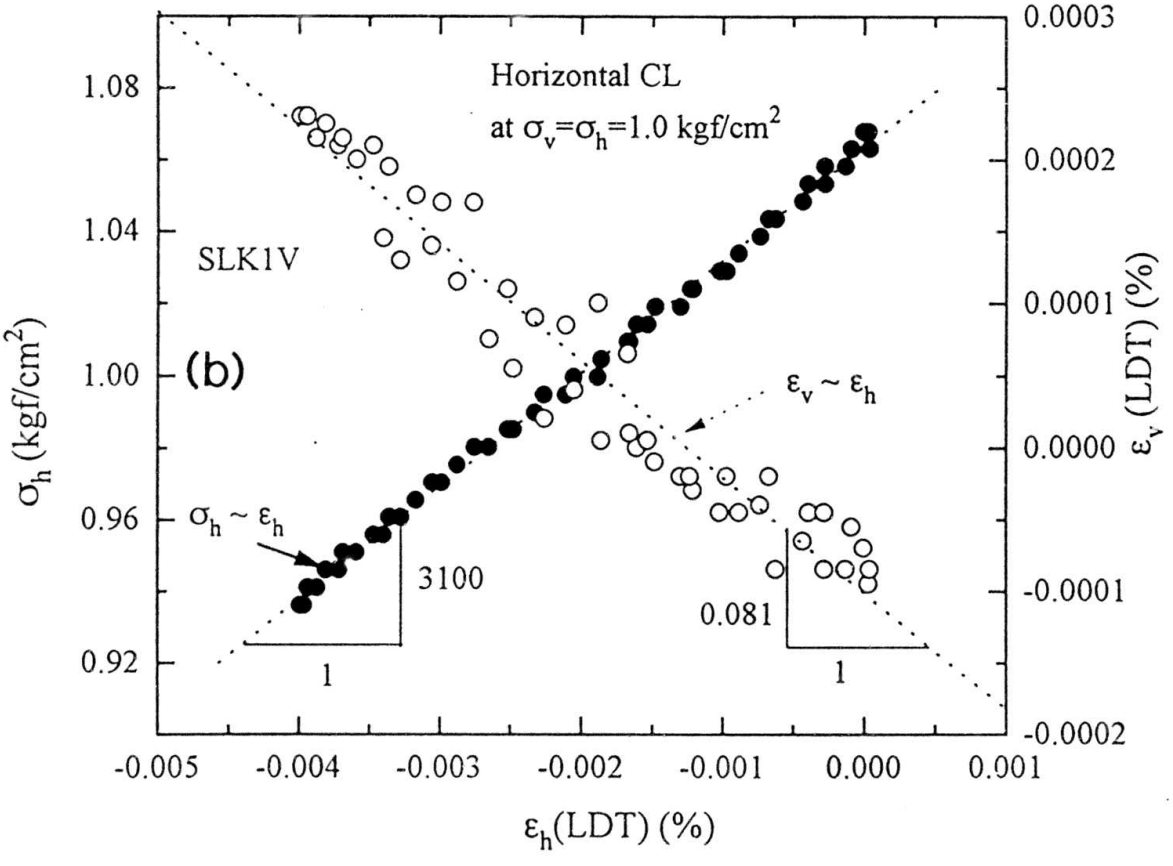

Figs. 3.2: (a) σ_v~ε_v and ε_h~ε_v responses in a typical vertical CL test, (b) σ_h~ε_h and ε_v~ε_h responses in a typical horizontal CL test performed on SLK1V specimen.

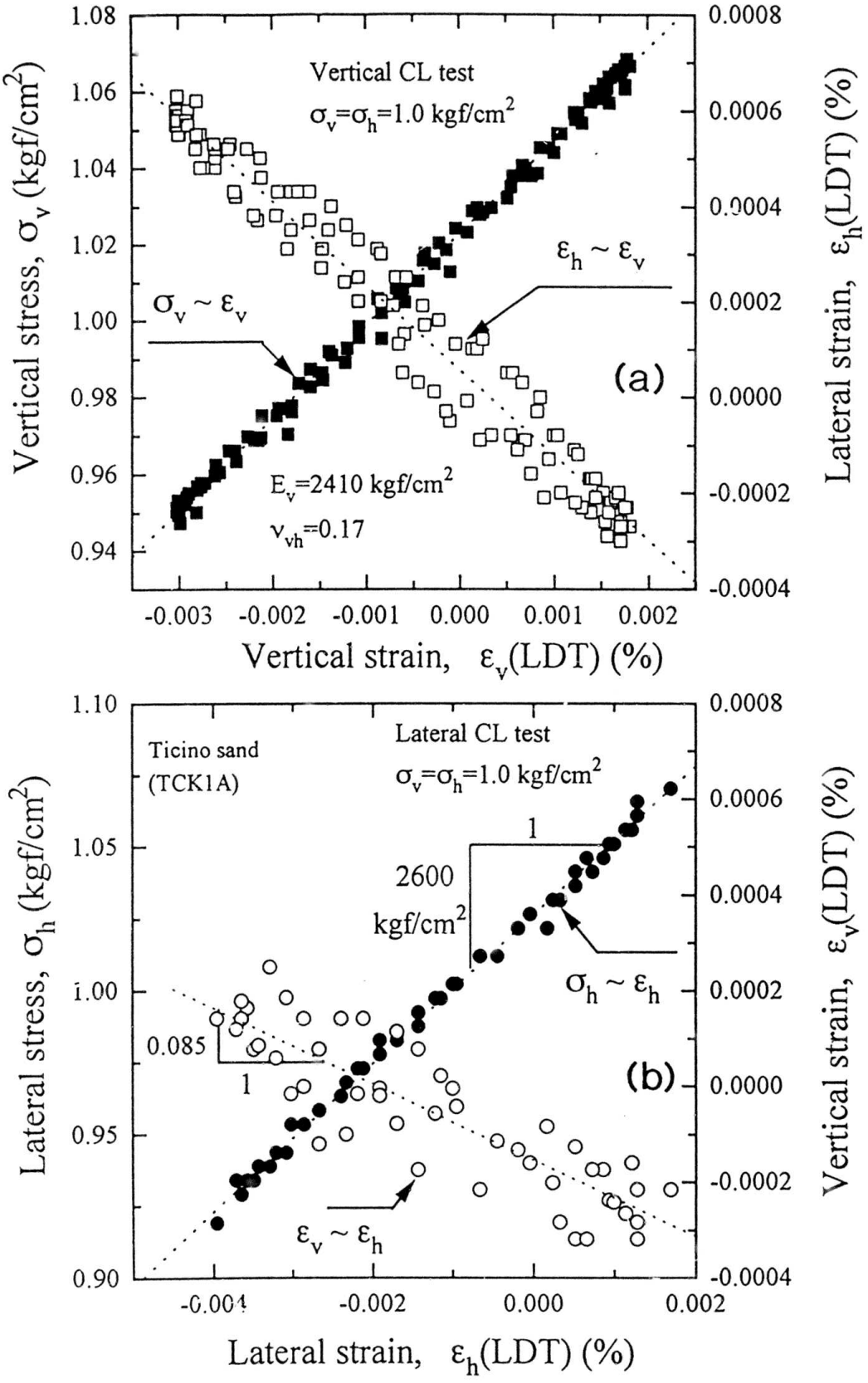

Figs. 3.3: (a) σ_v~ε_v and ε_h~ε_v responses in a typical vertical CL test, (b) σ_h~ε_h and ε_v~ε_h responses in a typical horizontal CL test performed on TCK1A specimen.

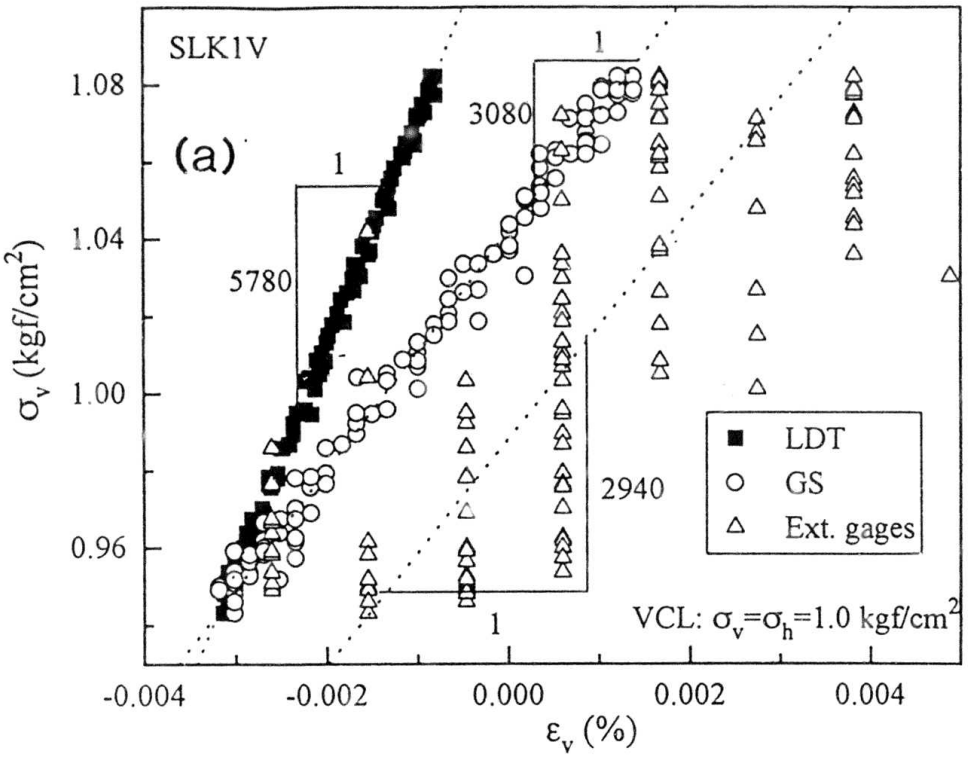

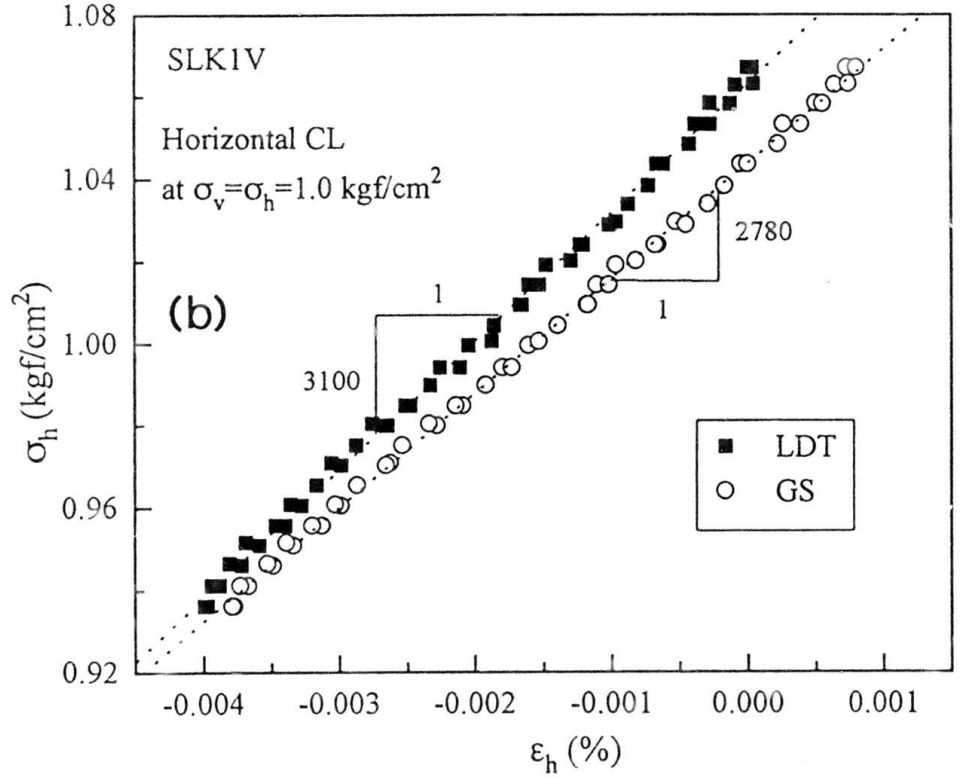

Figs. 3.4: Comparison of external and local (a) ε_v during a vertical CL test, and (b) ε_h during a horizontal test performed on SLK1V specimen.

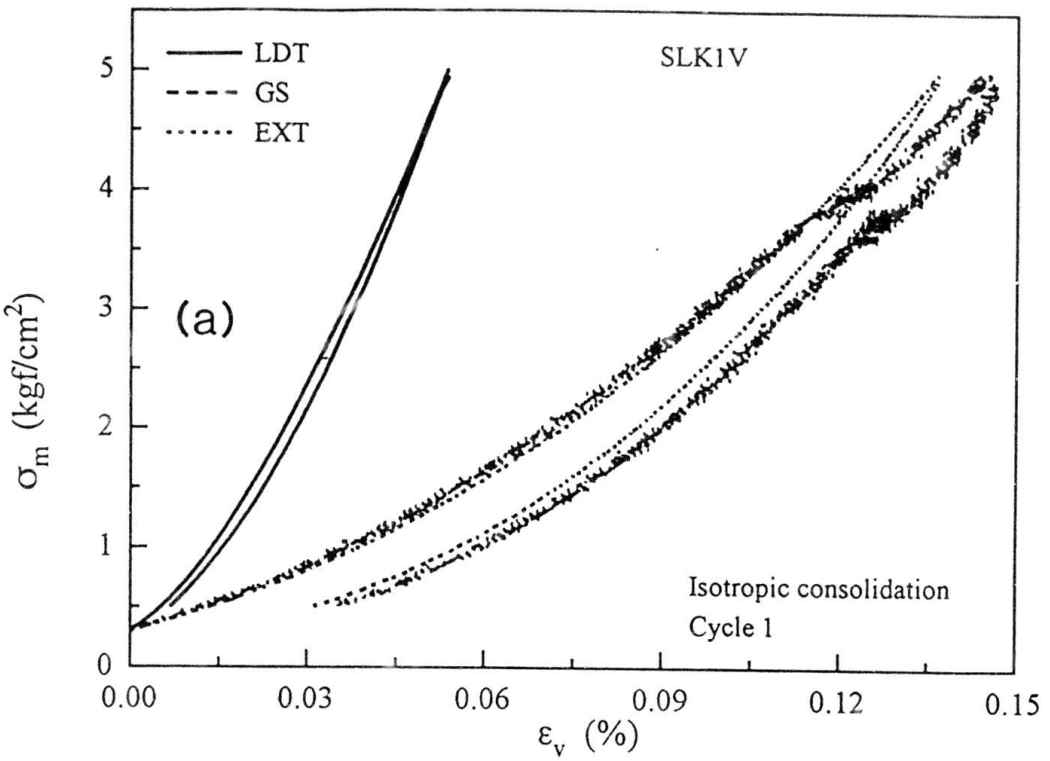

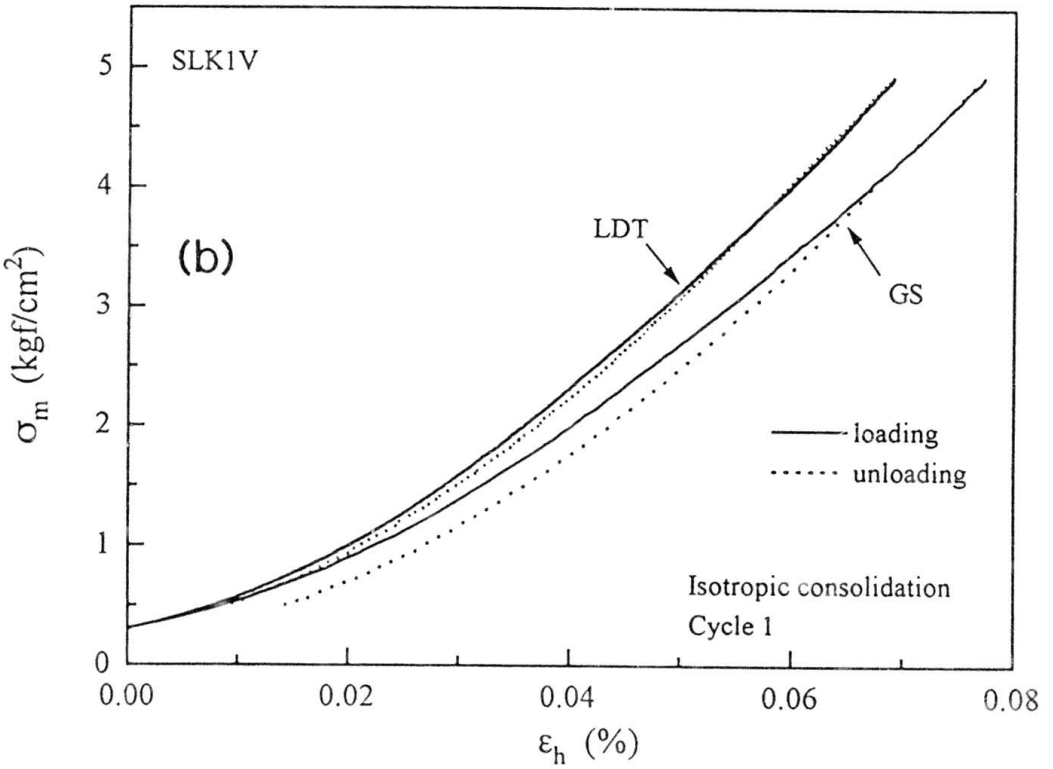

Figs. 3.5: Comparison of external and local strains during K=1 consolidation on SLK1V specimen (a) for ε_v and (b) for ε_h.

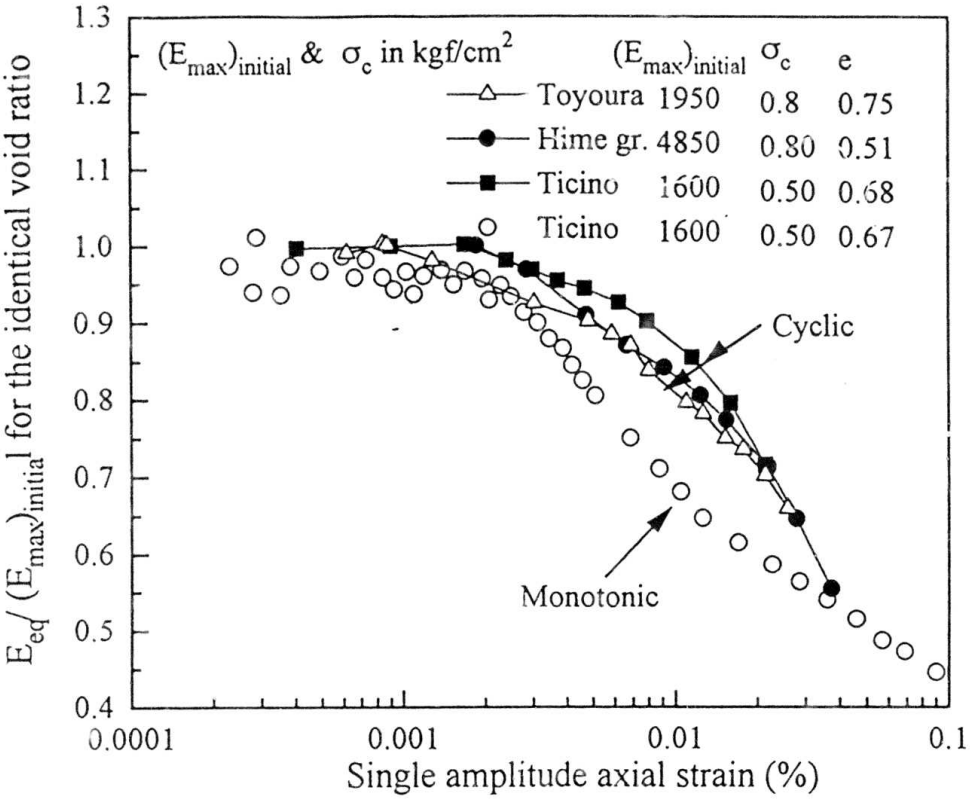

Fig. 3.6: $E_{eq}/(E_{max})_{initial}$~$(\varepsilon_v)_{SA}$ relations for different materials (Ticino sand was tested by Teachavorasinskun (1992)).

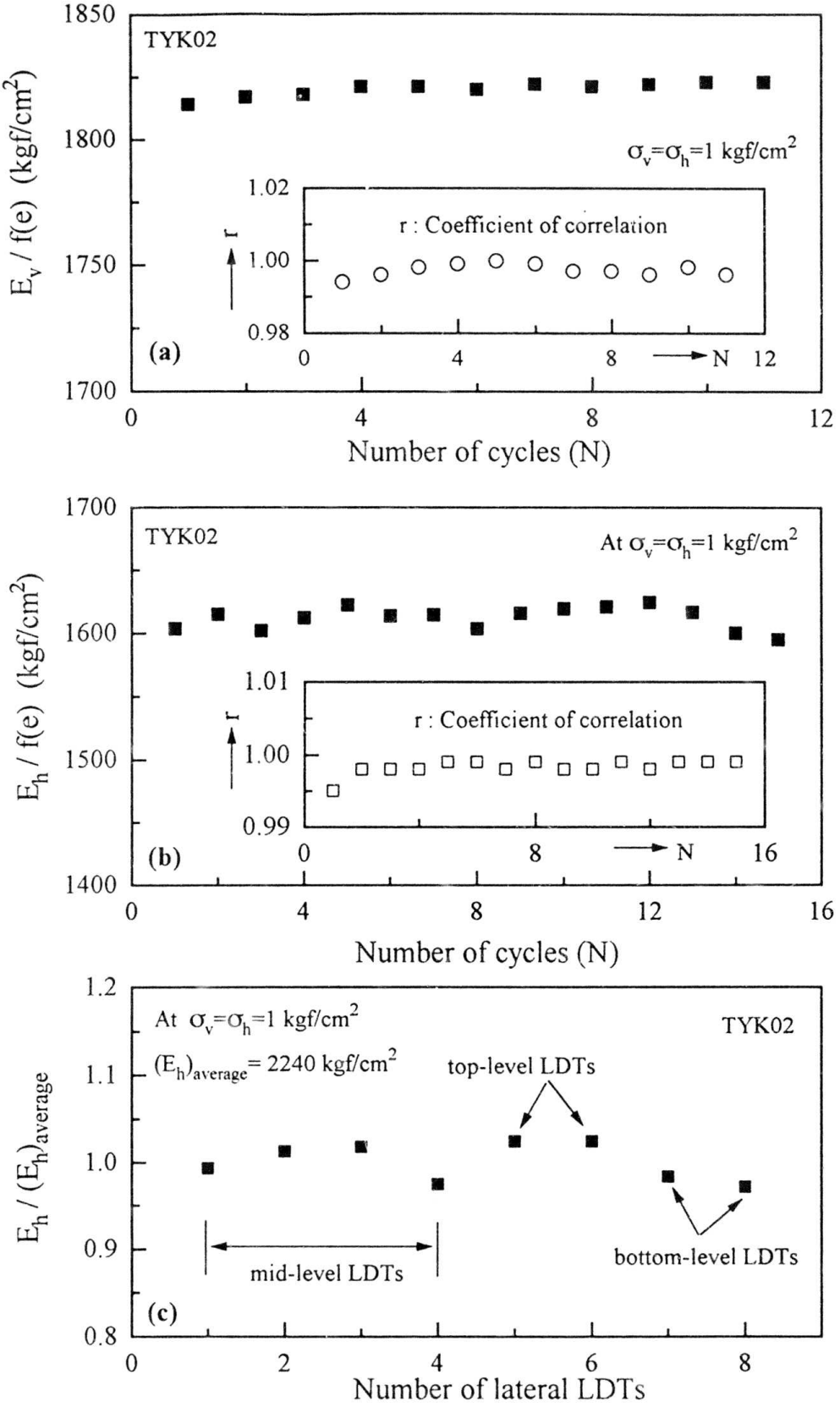

Figs. 3.7: Typical relationships obtained from TYK02 specimen between (a) E_v/f(e) and the number of cycle (N), (b) E_h/f(e) and N, and (c) E_h/f(e) and the number of lateral LDTs.

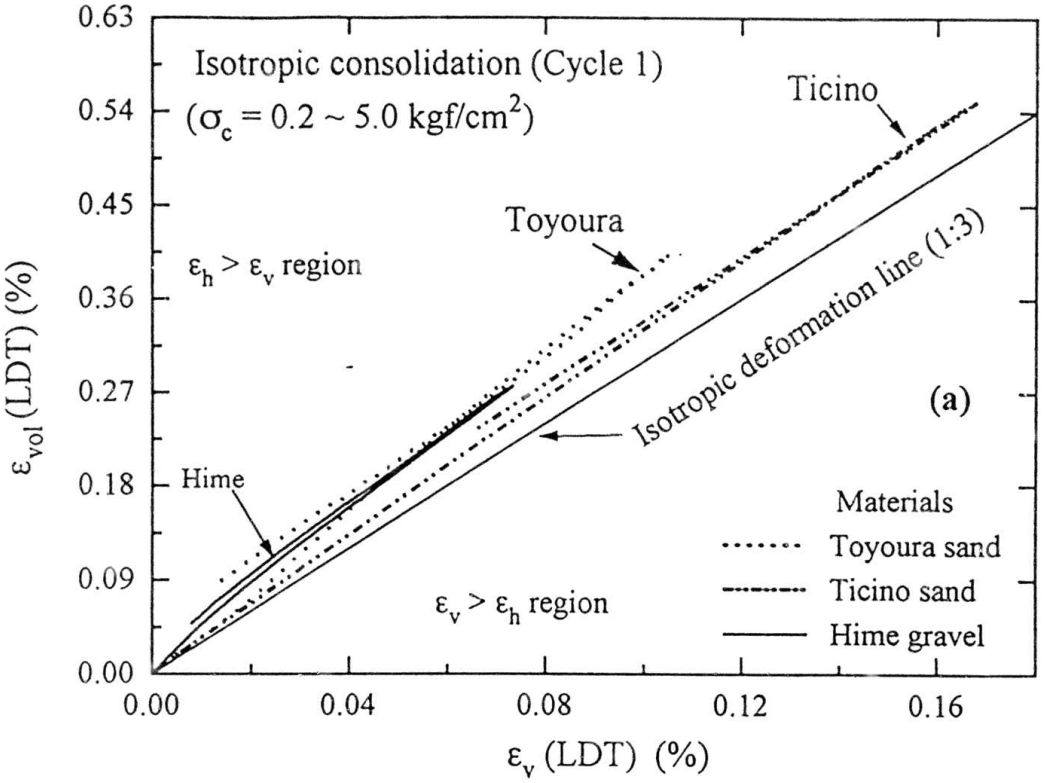

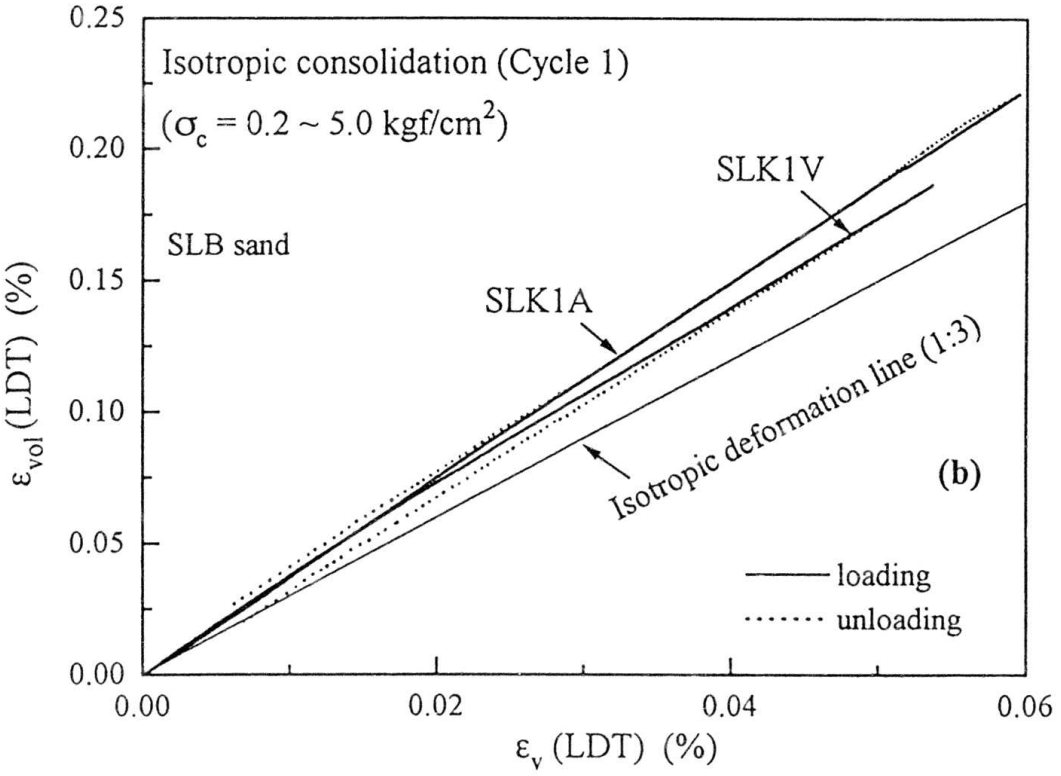

Figs. 3.8: Relationships between ε_{vol} and ε_v during isotropic loading and unloading (Cycle 1) of specimens (a) TYK1A, TCK1A and HGK1A, and (b) SLK1A and SLK1V.

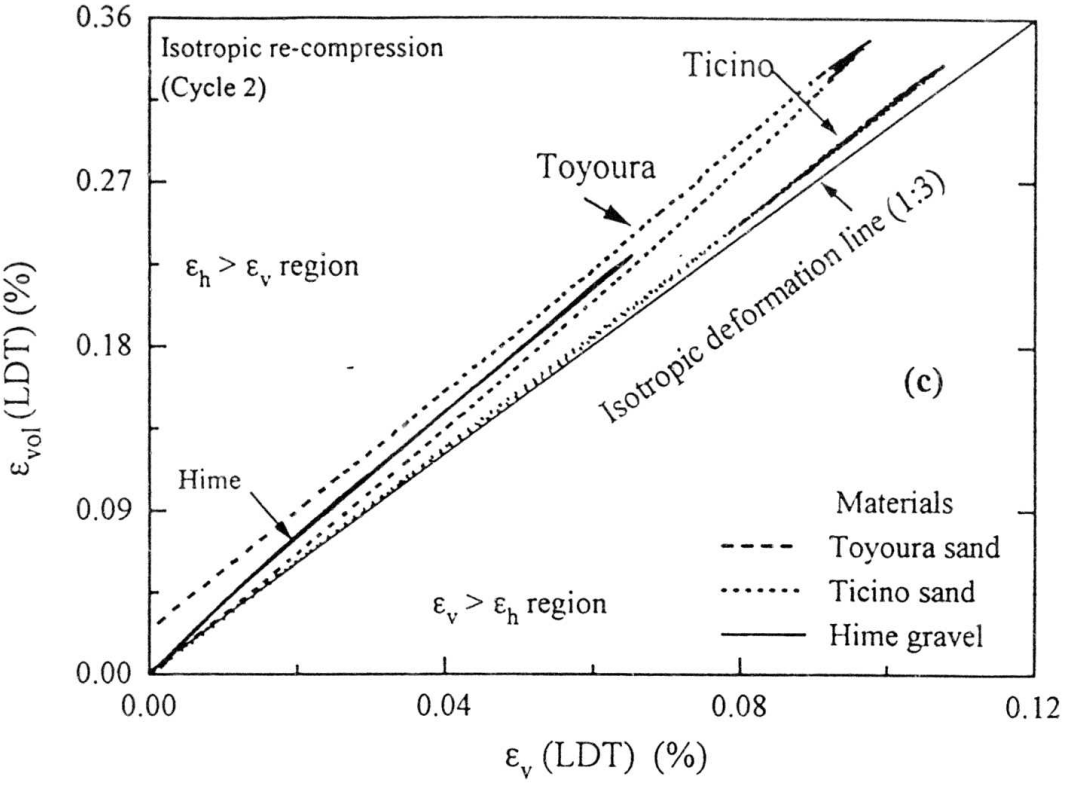

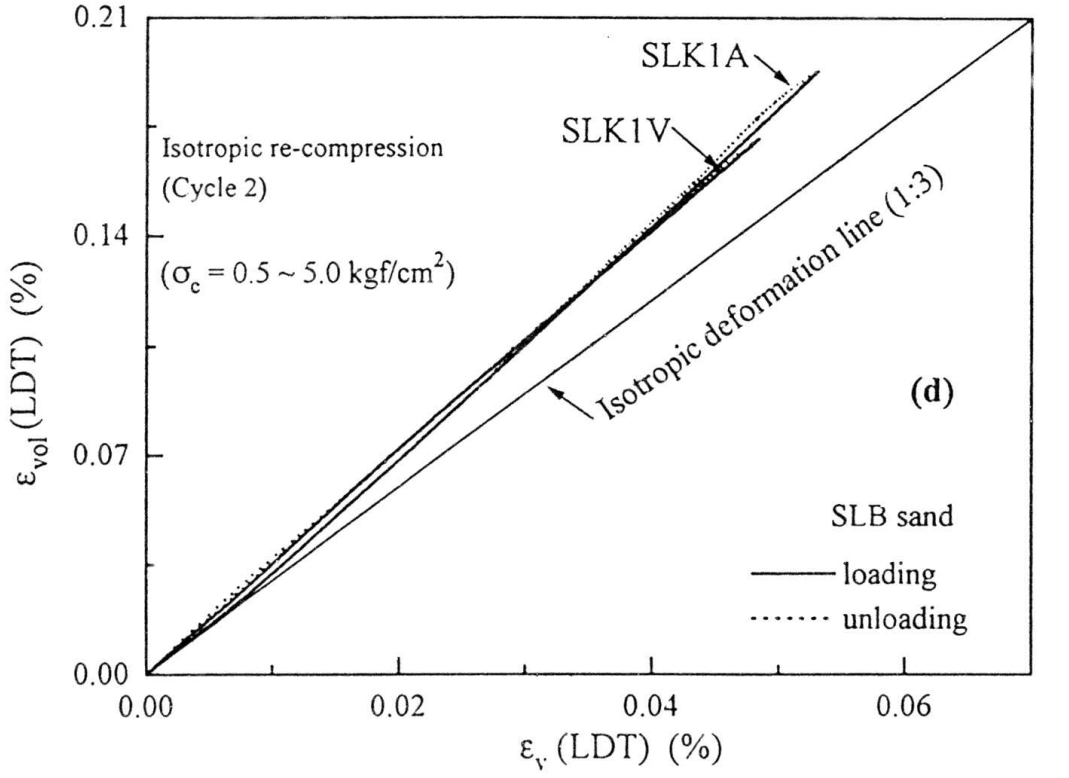

Figs. 3.8: Relationships between ε_{vol} and ε_v during isotropic reloading and re-unloading (Cycle 2) of specimens (c) TYK1A, TCK1A and HGK1A, and (d) SLK1A and SLK1V.

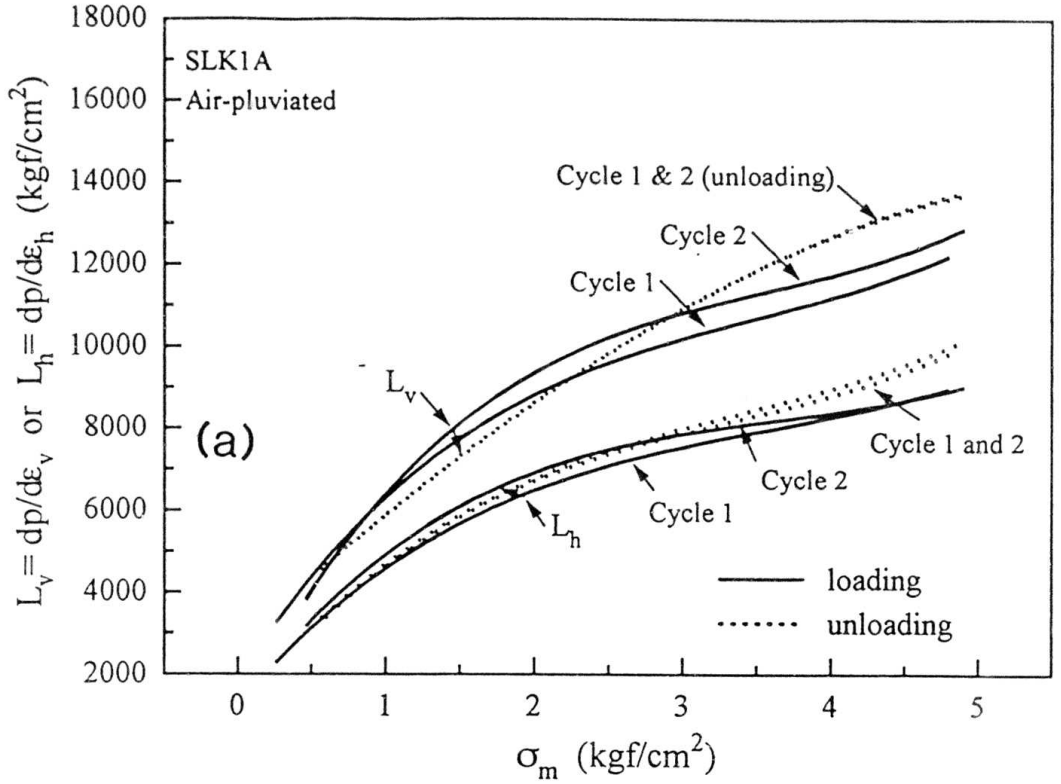

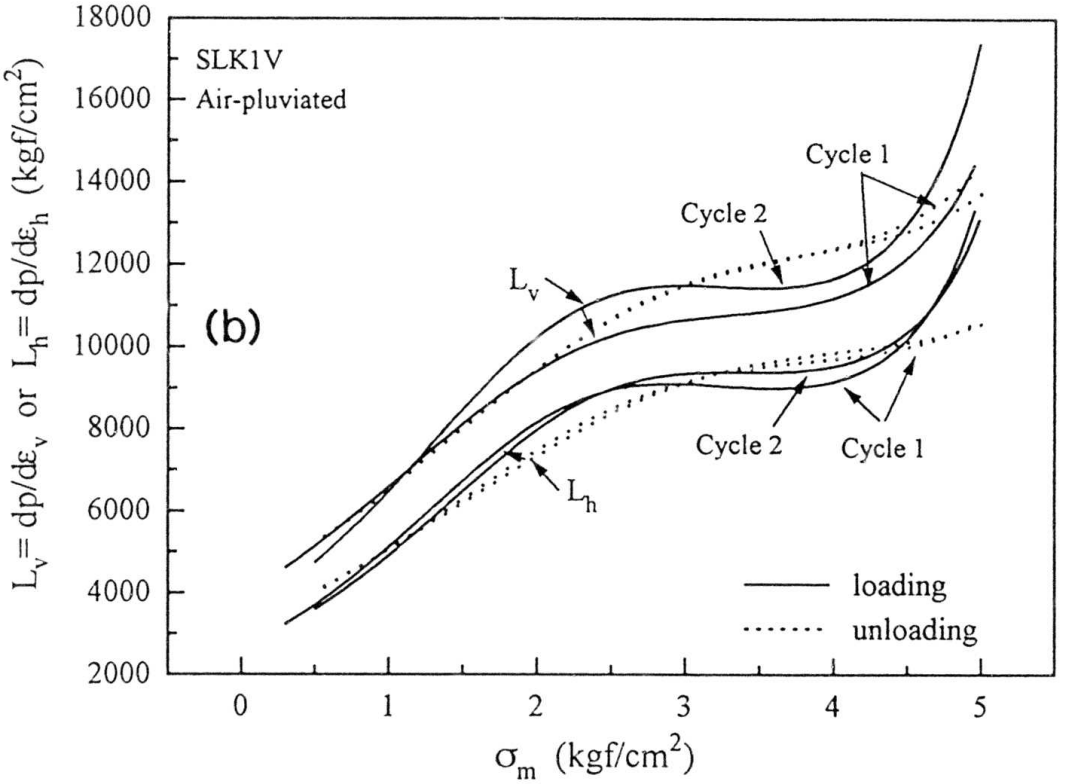

Figs. 3.9: Relationships between tangent moduli (L_v, L_h) and mean stress (σ_m) during K=1 loading for (a) SLK1V, (b) SLK1A.

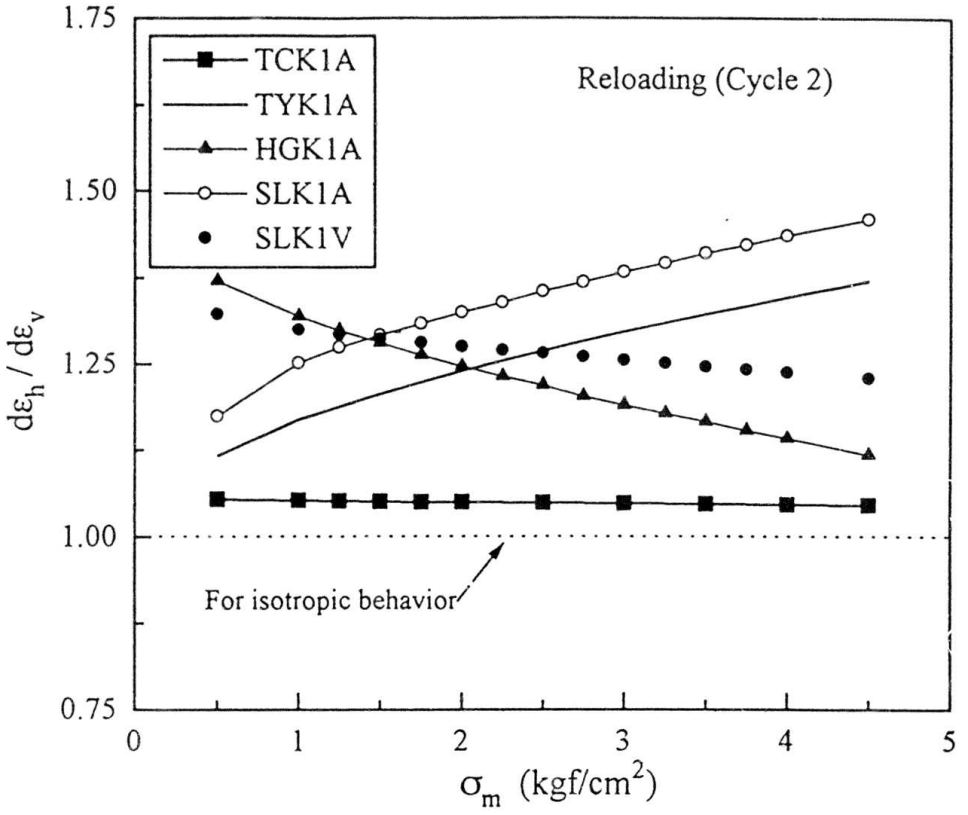

Figs. 3.10: Relationships between $d\varepsilon_h/d\varepsilon_v$ and σ_m during reloading along K=1 stress path.

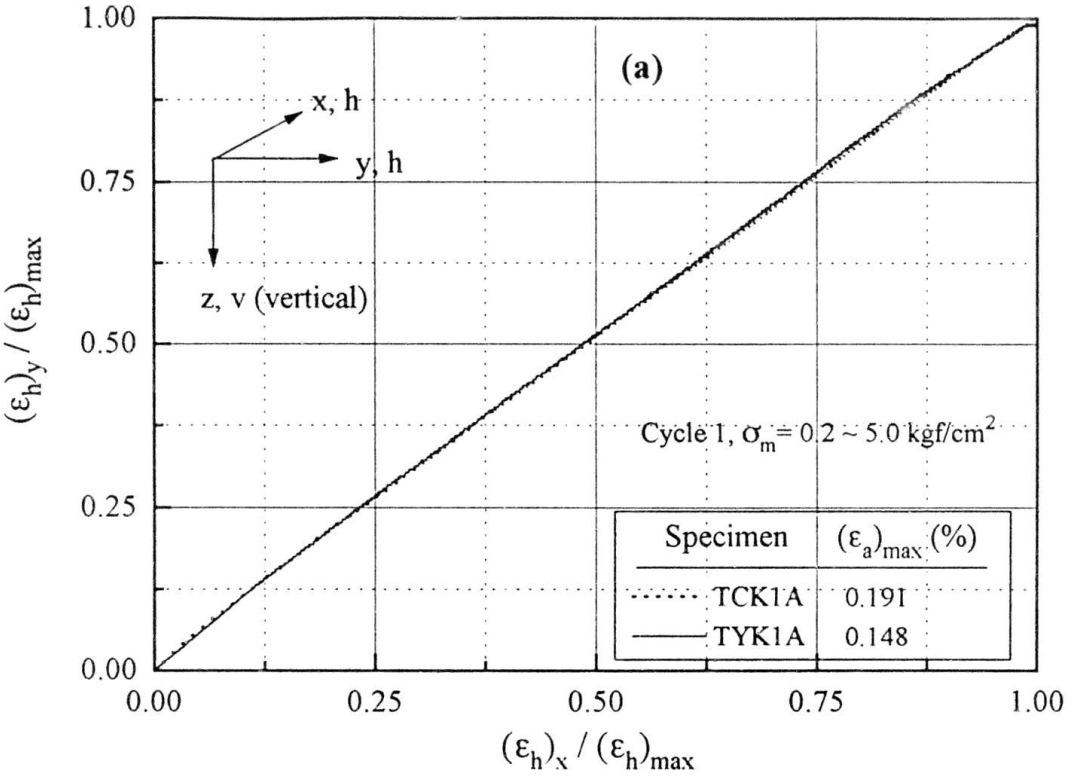

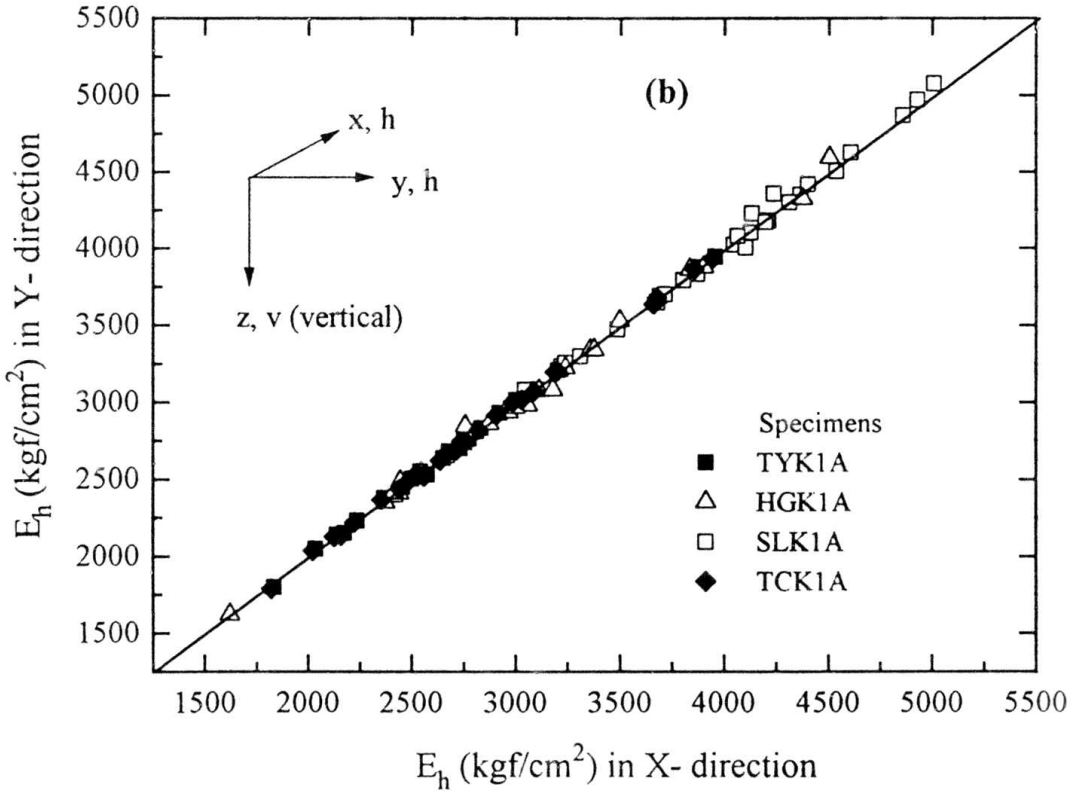

Figs. 3.11: Comparison between (a) local strains during K=1 loading, (b) Young's moduli in two orthogonal horizontal directions.

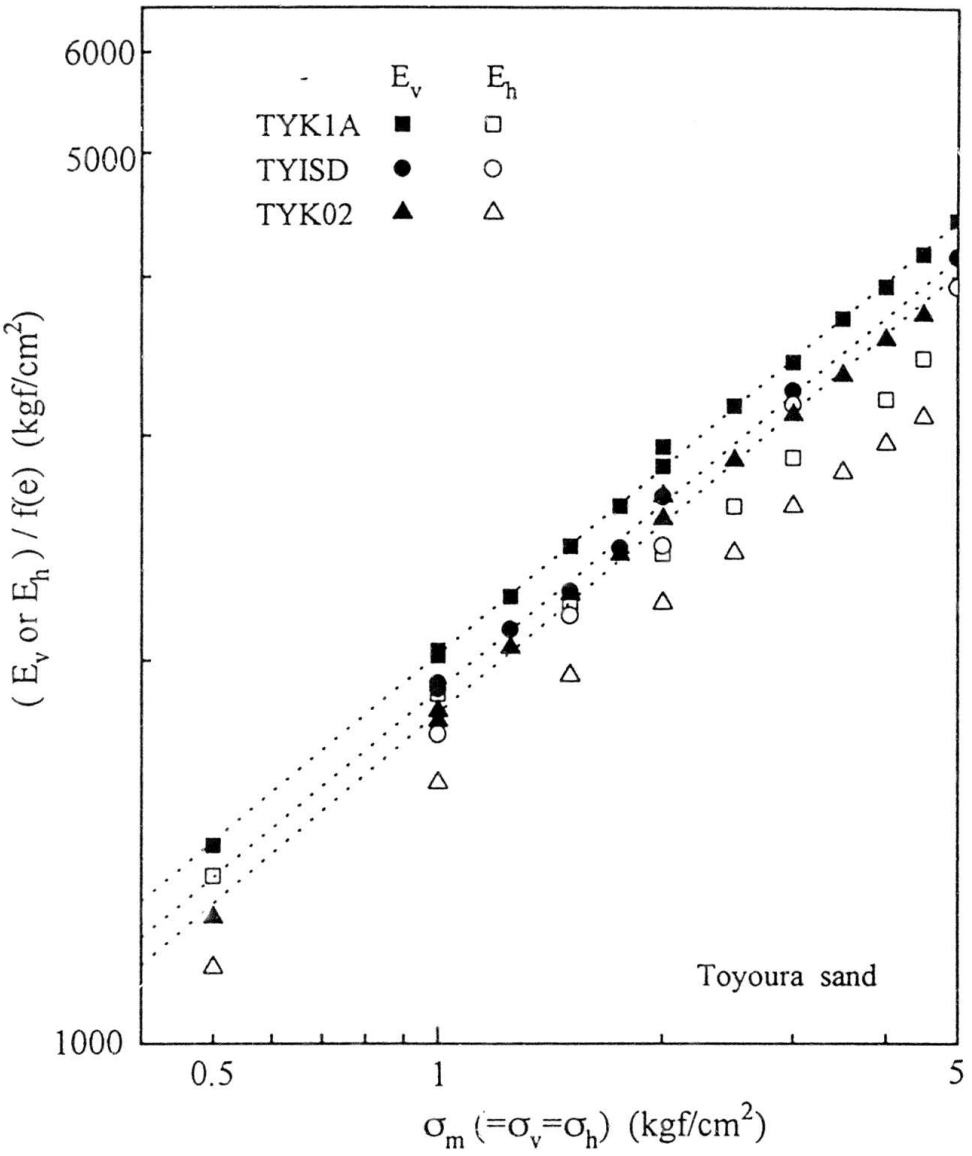

Figs. 3.12a: Relationships between $E_v/f(e)$ and $E_h/f(e)$ and σ_m along isotropic stress states for specimens of Toyoura sand.

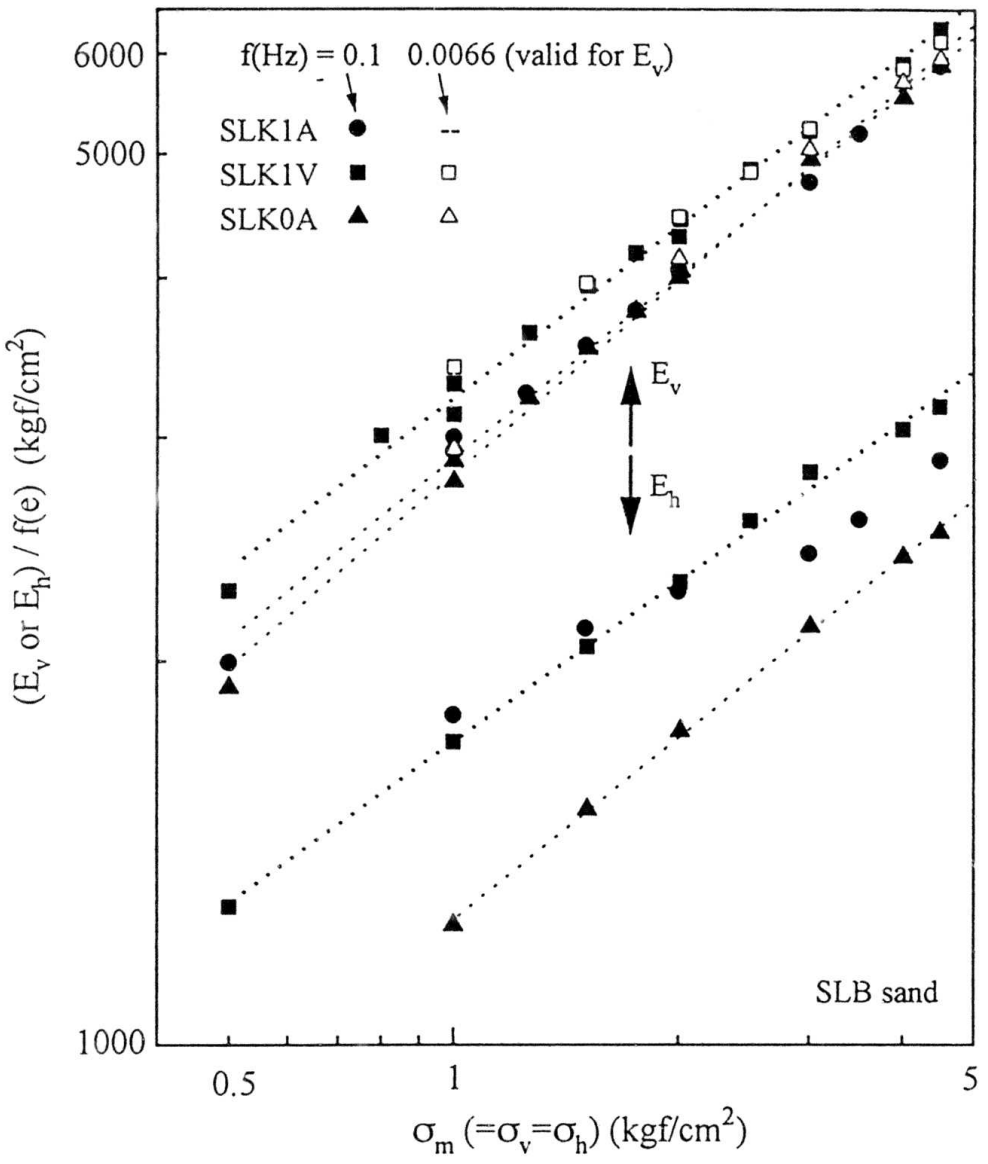

Figs. 3.12b: Relationships between $E_v/f(e)$ and $E_h/f(e)$ and σ_m along isotropic stress states for specimens of SLB sand.

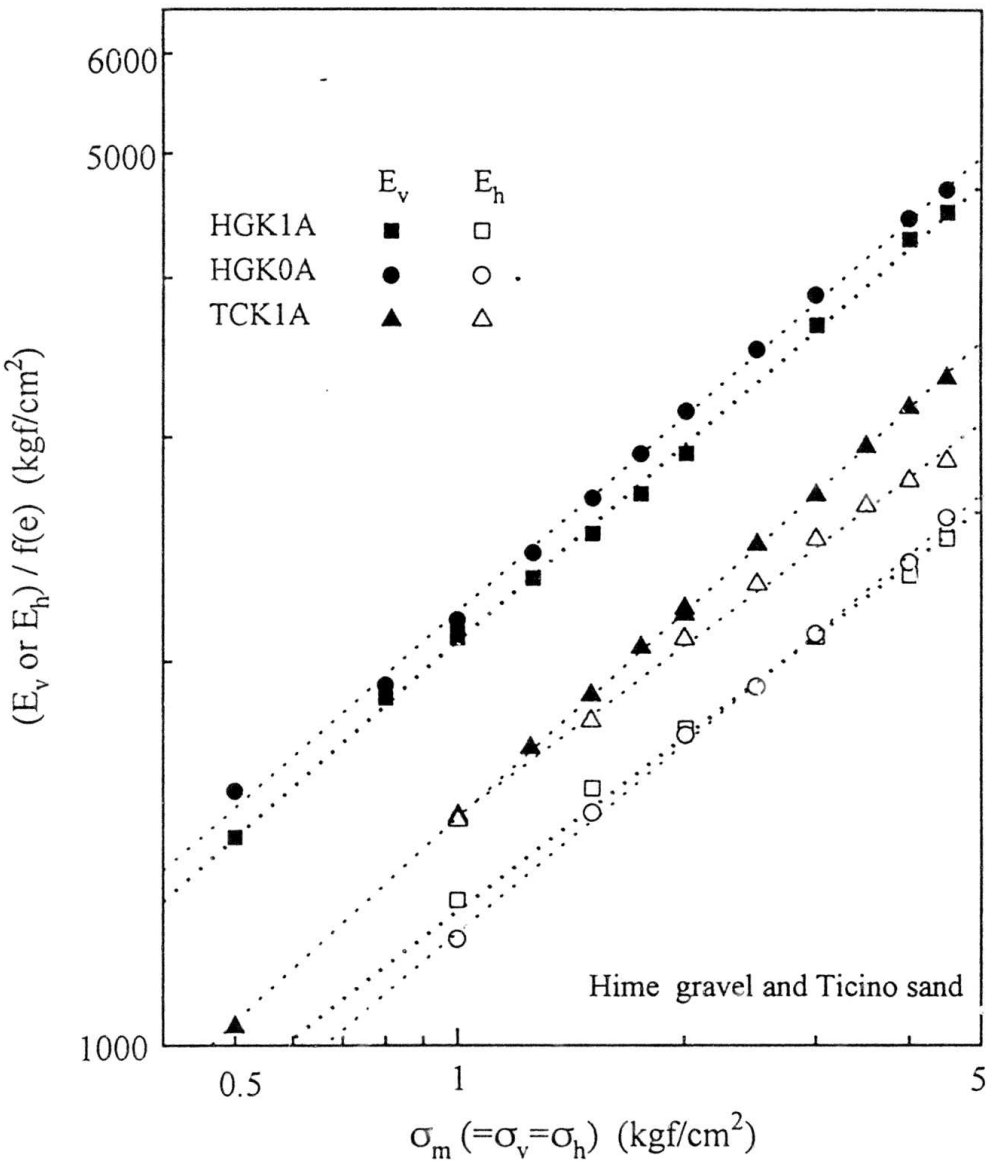

Figs. 3.12c: Relationships between $E_v/f(e)$ and $E_h/f(e)$ and σ_m along isotropic stress states for specimens of Hime gravel and Ticino sand.

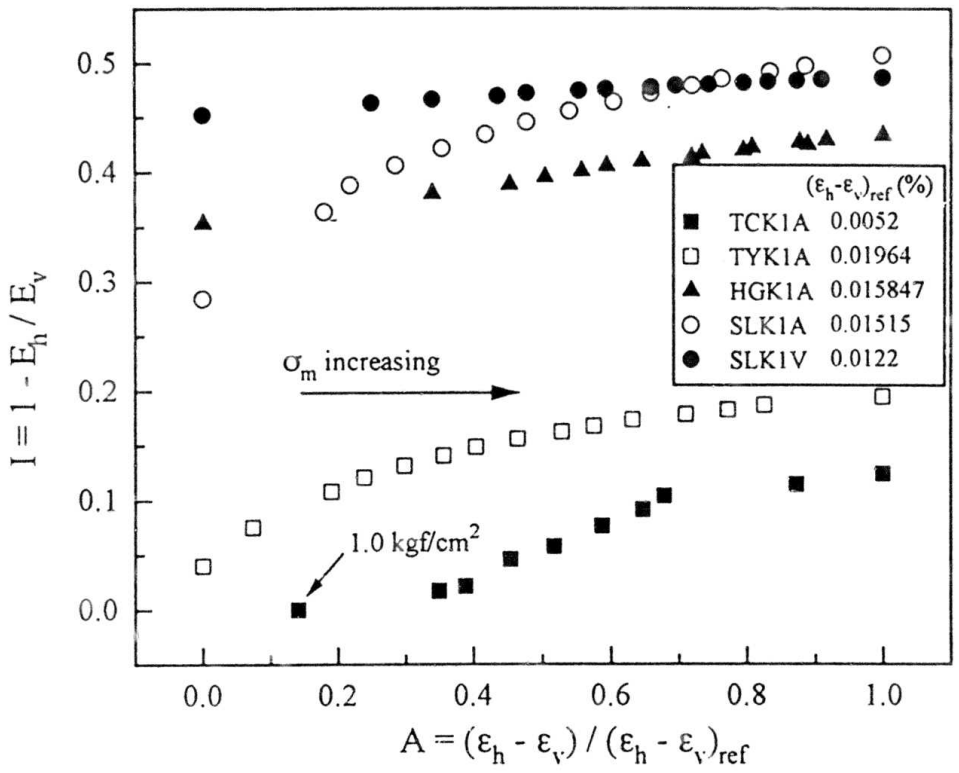

Fig. 3.13: Relationships between I (=1-E_h/E_v) and A [=$(\varepsilon_h-\varepsilon_v)/(\varepsilon_h-\varepsilon_v)_{ref}$] in the K=1 stress path.

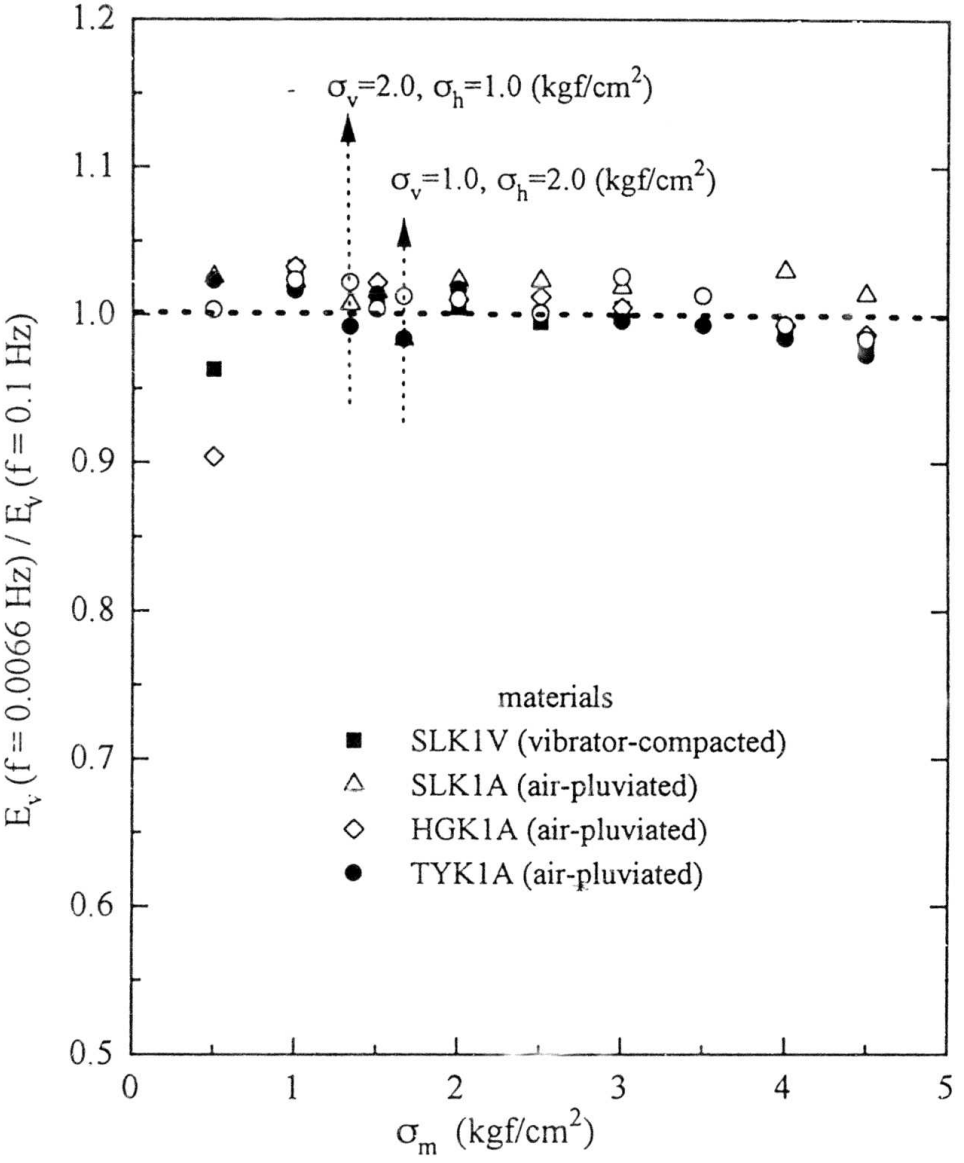

Fig. 3.14: Effects of loading frequency on Young's modulus E_v.

Chapter 4

Cross-Anisotropy in the Small Strain Stiffness

4.1. Introduction

For the evaluation of stress state-induced anisotropy, it is essential to investigate into the dependency of Young's moduli on the current stress state. That is, how does Young's modulus in a particular direction vary with the change of 'stress state.' Here 'stress state' can be represented by either the mean stress and/or deviator stress, principal stress in the direction of principal strain increment for which the Young's modulus is defined, or both. In the early stages of research into the elastic deformation properties and the stiffness at relatively small strains, many resonant-column tests, cyclic triaxial tests and torsional shear tests were performed on isotropically consolidated specimens. In most cases, the results obtained by these testing procedures were usually applied to field cases under anisotropic stress states by assuming that the maximum shear modulus G_{max} and shear moduli at relatively small strains are a function of the mean principal stress p ($=\sigma_m$) (e.g., Hardin and Black, 1968). Later, it was found that for clean sands, the isotropic assumption mentioned above is valid only for a small range of the stress ratio ($K=\sigma_h/\sigma_v$) in triaxial compression near the isotropic stress state (Tatsuoka et al., 1979; Tatsuoka, 1985).

Aiso, Yu and Richart (1984) by means of resonant-column tests on clean sands, and Roesler (1979), Jamiolkowski et al. (1991), Lo Presti and O'Neill (1991) and Stokoe et al. (1991) by measuring body wave velocities in a large clean sand specimen commonly showed that the shear modulus in a given plane (say, x-y plane) is essentially a unique function of the two orthogonal normal stresses working in that plane (i.e., the normal stress in the wave propagation direction and the normal stress in the particle displacement direction), while independent of the normal stress working in the direction orthogonal to that plane. Note that as shown later, this finding already indicates the stress system-induced anisotropy of the elastic deformation properties of sands. This property can be represented as:

$$\left(G_{max}\right)_{ij} = f\left(\sigma_i, \sigma_j\right) \tag{4.1a}$$

or more specifically,

$$(G_{max})_{ij} = f(\sigma_i)\,g(\sigma_j) \tag{4.1b}$$

On the other hand, Hardin (1978), Hardin and Bladford (1989) and later Chang (1994) suggested that the Young's modulus defined for elastic principal strain increments in a certain direction be a unique function of the normal stress in that direction. Some data which support stress system-induced anisotropy of G_{max} and E_{max} described above have been obtained by measuring body wave velocities in different directions in a large specimen of sand under controlled anisotropic stress conditions (Jamiolkowski et al., 1991; Lo Presti and O'Neill, 1991; Stokoe et al., 1991). Furthermore, Lo Presti et al. (1995) showed that in monotonic loading triaxial compression (TC) tests with compression being in the vertical direction, the initial Young's moduli E_{max} of Toyoura sand and a much more crushable sand (Quiou sand) are a function of the initial axial stress (σ_v) at the start of TC loading, while independent of the initial lateral pressure σ_h for a wide range of anisotropic consolidation stress ratio σ_h/σ_v from 0.46 to 2.04 and from 0.34 to 1.0, respectively.

Described herein are the test results, which were obtained from cyclic triaxial tests on large specimens of granular materials performed to investigate into the dependency of small strain Young's moduli on stress state. Stress system-induced anisotropy of Young's moduli is described from the characteristics of stress state-dependency of Young's modulus, which is followed by a cross-anisotropic formulation of elastic behavior for granular materials.

4.2. Summary of the Previous Chapter

The investigation was carried out on large triaxial specimens (for dimension see Figs. 2.1a and b) of four granular materials (Table 3.1). Small strain amplitude vertical cyclic load (VCL) at $\Delta\sigma_h=0$ and horizontal cyclic load (HCL) at $\Delta\sigma_v=0$ were applied by using the automated system (described in Chapter 2) to evaluate elastic parameters. Elastic parameters were evaluated with the use of local strains. Local lateral strain (ε_h) and local vertical strain (ε_v) were measured by local deformation transducers (LDTs). The strains measured by LDTs in both principal strain directions were free from bedding errors. Although other strain measuring devices (e.g., gap sensors, external gages) were used (Fig. 2.1a), the data obtained by those will not be presented as they need corrections for 'bedding error.' The word 'bedding error' is equally applicable to ε_v and ε_h measured by using gap sensors and external gages. The resolutions of LDTs, inner load cell to

measure deviator load and pressure transducer to measure lateral stress (σ_h) were sufficiently high to capture the respective responses of small unload/reload cycles being applied to measure the elastic parameters (Chapter 2).

4.3. Dependency of Young's Moduli on Stress States

As discussed in the previous chapter (see Figs. 3.12a to c), the Young's moduli (E_v, E_h) obtained by small-amplitude CL tests at isotropic stress states can be represented as follows;

$$E_v = E_1 . f(e) . \sigma_m^{m_v} \qquad 4.2a$$

$$E_h = (1 - I_0) . E_1 . f(e) . \sigma_m^{m_h} \qquad 4.2b$$

where the parameters (E_1, I_0, m_v, m_h) for the tested materials are listed in Table 3.2 (Chapter 2); the entity $(1-I_0).E_1$ is equal to normalized E_h (by f(e)) measured at the stress state of $\sigma_v=\sigma_h=1.0$ kgf/cm^2.

Now, the most difficult work is to apportion the exponent m (i.e., m_v and m_h) while taking into account properly the effects of major and minor principal stresses at state on Young's modulus in a particular direction. Since the factor σ_m^m at isotropic stress states can be divisible in various forms, such as $\sigma_m^m=\sigma_v^{m1}.\sigma_h^{m2}$ (where, m1+m2= m and m1xm2 ≥0.0), without violating Eq. 4.2a and b, there could be a number of probable solutions to represent the dependency of Young's modulus. Certainly, all of them cannot be valid for general stress paths. Of them the following forms, which are used by other previous researchers and which were supported, to some extent, by data for a limited stress paths, will be examined by using the results from a systematic series of small-amplitude CL tests.

Case 1 dependency: At any stress path, E_v and E_h are unique functions of σ_m, which can be represented by Eq. 4.2a and b, respectively.

Case 2 dependency: Young's moduli are directionally dependent. That is, Young's modulus in a particular direction is a function of principal stress in the direction of principal strain for which the Young's modulus is defined (Stokoe et al., 1991; Lo Presti and O'Neill). King (1970) and Wu et

al. (1991) also observed by the wave propagation method that this form of characterization of elastic moduli holds good also for intact hard rock. The mathematical definition is as follows:

$$E_v = E_1 . f(e) . \sigma_v^{m_v} \quad 4.3a$$

$$E_h = (1 - I_0) . E_1 . f(e) . \sigma_h^{m_h} \quad 4.3b$$

Case 3 dependency: Young's moduli are functions of all the principal stresses, but their dependency is more pronounced to the principal stress in the direction of principal strain for which they are defined. It can be represented by;

$$E_v = E_1 . f(e) . \sigma_v^{m1} . \sigma_h^{m2} \quad 4.4a$$

$$E_h = (1 - I_0) . E_1 . f(e) . \sigma_h^{m1} . \sigma_v^{m2} \quad 4.4b$$

where, m1+m2= m (=m_v or m_h) at isotropic stress states. Since $m_v \neq m_h$ in most of the cases (Table 3.2), different values of m_v and m_h need to be considered to represent E_v and E_h, respectively.

4.4. Test Results and Discussions

4.4.1. Stress-dependency of elastic Young's modulus

Small-amplitude CL tests (both vertical and horizontal) were performed at various stress states (Fig. 3.1, Chapter 3) in the range of $0.5 \leq \sigma_v/\sigma_h \leq 2.0$ to investigate the dependency of small strain stiffness on principal stresses. The small circular points (both open and dark symbols) in Fig. 3.1 indicate the stress states where small unload/reload cycles of axial stress were applied while keeping $\Delta\sigma_h=0$. At about two-third of measuring stress points (i.e., open circle symbols) horizontal CL tests (HCL) with $\Delta\sigma_v=0$ were performed. Stress states were selected symmetrically in compression and extension sides along stress paths $\Delta\sigma_v=0$, $\Delta\sigma_h=0$ and $\Delta\sigma_m=0$ to obtain a sufficient variation of Young's moduli for various combinations of σ_v and σ_h. This testing program can therefore provide the sensitivity of Young's modulus to principal stresses.

The results obtained from all the tests specimens (Table 3.2) are shown in Figs. 4.1a to i. The values of E_v and E_h are plotted after dividing by the void ratio function $f(e)= (2.17-e)^2/(1+e)$

(Hardin and Richart, 1963) to account for a slight variation in void ratio during performing CL tests at different stress states. Total changes in void ratio for Steps 2 to 5 [see Test Program, Chapter 3] were very small and are given in Table 3.2. Therefore, the correction for the change in void ratio was well below 1% of the respective uncorrected Young's modulus. In the same figures, the variations of $E_v/f(e)$ with σ_v for different lateral stresses σ_h and the variations of $E_h/f(e)$ with σ_h for different vertical stresses σ_v are plotted. In the $E_v/f(e)\sim\sigma_v$ relationships, a small scatter of data for different σ_h at each σ_v is noticeable. More significantly, however, E_v increases consistently with σ_v. Similar behavior can be observed in the $E_h/f(e)\sim\sigma_h$ relations. That is, the vertical Young's modulus E_v is rather independent of σ_h, while E_h is rather independent of σ_v. Therefore, these data sets support the stress-dependency of Young's moduli represented by Eqs. 4.3a and b. The curves based on these two equations using the respective elastic parameters (m_v, m_h, I_0 and E_1) have been plotted in Figs. 4.1a to i, which reasonably fit the data obtained in the stress range of $0.5 \leq \sigma_v/\sigma_h \leq 2.0$.

From Eqs. 6a and b, we obtain;

$$\frac{E_v}{E_h} = \frac{1}{1-I_0}\left(\frac{\sigma_v^{m_v}}{\sigma_h^{m_h}}\right) \tag{4.4c}$$

When $m_v = m_h = m$, Eq. 4.4c becomes;

$$\frac{E_v}{E_h} = \frac{1}{1-I_0}\left(\frac{\sigma_v}{\sigma_h}\right)^m \tag{4.4d}$$

in which the term $1/(1-I_0)$ represents the inherent anisotropy and the term $(\sigma_v/\sigma_h)^m$ represents the stress system-induced anisotropy. Fig. 4.1j shows the plot based on Eq. 4.4d. For a given specimen, the vertical offset at $\sigma_v/\sigma_h = 1$ indicates the effect of inherent anisotropy, while the variation of E_v/E_h with σ_v/σ_h represents the effect of stress system-induced anisotropy.

Let us assume that the stress-dependency of Young's moduli represented by Eqs. 4.3a and b be true for general stress paths, including anisotropic stress paths (i.e., for $\Delta K=0$ stress paths with $K \neq 1$). If we replace σ_v of Eq. 4.3a with σ_h/K then the following equation, which is parallel to Eq. 4.3a is obtained;

$$E_v = E_1 . f(e) . \frac{1}{K^{m_v}} . \sigma_h^{m_v} \qquad 4.5$$

Along isotropic stress path (K=1), the quantity $1/K^{m_v}$ becomes unity and Eq. 4.5 becomes Eq. 4.3a.

To verify the validity of Eq. 4.5, a series of CL tests were performed in some of the specimens of Table 3.2 along anisotropic stress paths [Step 4; Testing program of Chapter 3]. The value of K was varied in the range of 0.50~0.70 other than K=1 stress path. In all $\Delta K=0$ stress paths, the range of σ_h was kept constant (i.e., from 0.5 to 5.0 kgf/cm^2) while σ_v was varied to get the required variation in K. Fig. 4.2a show typical variations of $E_v/f(e)$ obtained from a specimen of SLB sand (SLK1V) with σ_h (according to Eq. 4.5) for different K values in full logarithmic scale. As the value of K decreases (i.e., σ_v increases), the $E_v/f(e)$~σ_h relation shifts upward showing the increase in Young's modulus with the increase in σ_v at constant σ_h. The relationships between $E_v/f(e)$ after dividing by f(K) and σ_h are shown in Fig. 4.2b. The normalization by using f(K) brings $E_v/f(e)$ values for the different values of K into a unique relation in full logarithmic plot, which is the same with the relationship between $E_v/f(e)$ and σ_m ($=\sigma_v=\sigma_h$) in K=1 stress path. In the same figure (i.e., Fig. 4.2b), the relationships between $E_h/f(e)$ and σ_h for $\Delta K=0$ stress paths are also shown. A unique variation can also be seen for different constant K (=1.0, 0.70 and 0.5) stress paths.

The parameters [E_1, m_v, m_h, I_0] for various specimens were evaluated for different $\Delta K=0$ stress paths based on Eq. 4.5 and Eq. 4.3b, and are listed in Table 4.1. For a given specimen, slight variation is noticeable among the sets of elastic parameters, [E_1, m_v, m_h, I_0] listed in Table 4.1, obtained from different $\Delta K=0$ stress paths. However, the variation is very small.

Figs. 4.3a and b show the relationships between the 'normalized' E_v and σ_h, where Young's moduli evaluated along all the $\Delta K=0$ stress paths for specimens SLK1V, HGK1A, TYK1A and TCK1A are used. In Fig. 4.3a, E_v was 'normalized' by the right hand side term (r.h.s) of Eq. 4.5 (similar form of Eq. 4.3a), while in Fig. 4.3b it was normalized by r.h.s. of Eq. 4.2a (i.e., considering E_v is a function of mean stress σ_m). Similarly, Figs. 4.4a and b show the corresponding relationships between the 'normalized' E_h and σ_h, where E_h was 'normalized' by the

r.h.s. of Eqs. 4.3b and 4.2b, respectively. In the normalization, the elastic parameters [E_i, m_v, m_h, I_0] obtained from K=1 stress path were used for all the $\Delta K=0$ stress paths. It can be seen that the more the K value decreases, the more the data deviates from normalized unit stiffness line if it is assumed that the Young's modulus is a unique function of the mean principal stress $\sigma_m = (\sigma_v+2\sigma_h)/3$. In this case, Young's modulus is under-estimated or over-estimated depending on (1) the direction for Young's modulus being concerned (i.e., E_v or E_h) and (2) stress paths being considered. A deviation of 5 to 8% from the measured value may be resulted even if the Young's moduli are predicted based on Eqs. 4.3a and b (i.e., Case 2 dependency).

Stress-dependency Case-3 (represented by Eqs. 4.4a and b) was also examined by performing CL tests (both vertical and horizontal) on a specimen of Toyoura sand (TYK02) along the following stress paths sequentially: (a) triaxial compression (TC) from an isotropic stress state $\sigma_c=\sigma_v=\sigma_h=1.0$ kgf/cm^2 to $\sigma_v/\sigma_h=3.5$ by increasing σ_v while keeping σ_h constant with unload/reload cycles at various stress states, which was followed by unloading to $\sigma_c=1.0$ kgf/cm^2 and (b) triaxial extension (TE) from $\sigma_c=1.0$ kgf/cm^2 to $\sigma_h/\sigma_v=3.5$ by increasing σ_h while keeping σ_v constant with unload/reload cycles at various stress states followed by unloading to $\sigma_c=1.0$ kgf/cm^2. Figs. 4.5a and b show the variations of the ratio of the measured E^e (=E_v and E_h) values to the predicted values with stress ratio, while the ratio is set equal to 1.0 when $\sigma_h/\sigma_v=1.0$. The Young's moduli were predicted separately by using the three probable forms of stress state-dependency (i.e., by Case 1, Case 2 and Case 3). In the figures, they are represented by the respective number in brackets For example, the predicted E_v by using Case 1 dependency is denoted simply as E_v [1]. When predicted based on Eqs. 4.4a and b (Case 3), m1 was assumed as 0.8 of the m (=m_v or m_h) and m2= 0.2m. Fig. 4.5a shows the relationship obtained for the TC stress path, while Fig. 4.5b shows the relationship for the TE stress path. Both figures show that the prediction by Case 2 is by far the best representation of the stress-state dependency of Young's moduli, which is followed by Case 3, and then Case 1. Even in Case 2, however, the measured variations of Young's moduli at stress ratios (σ_v/σ_h in Fig. 4.5a and σ_h/σ_v in Fig. 4.5b) greater than 2.50 are not predicted well. This could be related to the 'damage' to Young's modulus at relatively higher shear stress level, which will be described in Chapter 5.

In summary, the test results indicate that Young's modulus in a particular direction is essentially a unique function of the normal stress in the direction of the major principal elastic

strain increment for which the Young's modulus is defined. This implies that small strain elastic moduli and, hence, the initial stiffnesses become anisotropic as the stress state becomes anisotropic, as represented by Eqs. 4.3a and b. This anisotropy at any given anisotropic stress state can be quantified by a parameter A_s as follows;

$$A_s = \sigma_h^{m_h} / \sigma_v^{m_v} \tag{4.6}$$

4.4.2. Poisson's ratio

The values of ν_{vh} (as defined by Eq. 3.3a; Chapter 3) for all the particulate materials (Table 4.1) obtained from vertical CL tests were plotted against σ_v/σ_h in Figs. 4.6a to 4.8c. The values of ν_{vh} are obtained based on locally measured $\Delta\varepsilon_v$ and $\Delta\varepsilon_h$ by LDTs. As mentioned before, the reliable values of ν_{hv} could not be obtained by the current test program; it can be evaluated only by tests in which horizontal stress in one direction is changed while keeping the other unchanged. On the other hand, the values of ν_{hv} obtained by using Eq. 3.3b (Chapter 3) (note that ν_{hh}= "ν_{vh} at isotropic stress state" was assumed; see Chapter 3) were found much less reliable compared to ν_{vh} value because of relatively large scatter in ε_v during horizontal CL test (Fig. 2.4f, Chapter 2), as mentioned in Chapter 3. So these data were not used.

It was found that within the investigated stress range, the value of ν_{vh} was not sensitive to the change in either σ_v or σ_h at a fixed σ_v/σ_h, but ν_{vh} increases with the increase in σ_v/σ_h within a narrow range of ν_{vh} for each specimen. For example, the range of ν_{vh} was from 0.14 to 0.21 for TYK1A and from 0.08 to 0.13 for SLK1A. This tendency is in accordance with the following theoretical prediction.

The test results shown above indicate that the Young's moduli E_v and E_h can be modeled reasonably as:

$$E_v = (E_v)_0 \cdot (\sigma_v/\sigma_{v0})^{m_v} \tag{4.7}$$

$$E_h = (E_h)_0 \cdot (\sigma_h/\sigma_{h0})^{m_h} \tag{4.8}$$

where $(E_v)_0$ and $(E_h)_0$ are the values of E_v and E_h when $\sigma_v=\sigma_{v0}$ and $\sigma_h=\sigma_{h0}$, respectively. On the other hand, if the potential energy increment function $\Delta W= 1/2.C_{ijkl}.\Delta\varepsilon_{ij}.\Delta\varepsilon_{kl}$ exists for a hypo-elastic medium, it requires the following relation (also mentioned in Chapter 3) to be satisfied;

$$\upsilon_{vh}/E_v = \upsilon_{hv}/E_h \qquad 4.9$$

Adopting $\sigma_{v0}=\sigma_{h0}$, Eqs. 4.7, 4.8 and 4.9 yield;

$$\frac{\upsilon_{vh}}{\upsilon_{hv}} = \frac{E_v}{E_h} = \frac{(E_v)_0.\sigma_v^{m_v}}{(E_h)_0.\sigma_h^{m_h}} \qquad 4.10$$

When $m_v=m_h=m$, as one of the possible relations, we can obtain;

$$\upsilon_{vh} = \upsilon_{\psi}.\sqrt{(E_v)_0/(E_h)_0}\,(\sigma_v/\sigma_h)^{m/2} \qquad 4.11$$

$$\upsilon_{hv} = \upsilon_{\psi}.\sqrt{(E_h)_0/(E_v)_0}\,(\sigma_h/\sigma_v)^{m/2} \qquad 4.12$$

where ν_ψ is the Poisson's ratio ν_{vh} and ν_{hv} when $\sigma_v/\sigma_h = \{(E_h)_0/(E_v)_0\}^{1/m}$ for Eq. 4.11 and $\{(E_h)_0/(E_v)_0\}^m$ for Eq. 4.12, respectively. In other words, $\nu_\psi.\{(E_v)_0/(E_h)_0\}^{0.5}$, for example, is the Poisson's ratio $\nu_{vh}=\nu_0$ at isotropic stress states. For an inherently isotropic material, ν_ψ is the Poisson's ratio under isotropic stress conditions. In Figs. 4.6a to 4.8c, the relations based on Eq. 4.11 with $m=m_v$ are presented, which fit the data reasonably. The values of m_v and ν_0 are given in Table 3.2 (Chapter 3). In the same figures, the values of ν_{hv} predicted based on Eq. 4.12 are also plotted assuming ν_{hv}="ν_0 at isotropic stress states" and $m=m_v$. Note that when the particulate materials are inherently anisotropic, the values of ν_0 and ν_ψ are not the same. In case Eqs. 4.11 and 4.12 are valid, isotropic behavior $\nu_{vh}= \nu_{hv}$ is obtained when $\sigma_v/\sigma_h= \{(E_h)_0/(E_v)_0\}^{1/m}$. It may be more reasonable to assume that ν_{hh} is equal to the values of $\nu_{vh}=\nu_{hv}$ at this stress ratio. Further discussion should be made after experimental data of ν_{hv} and ν_{hh} are obtained.

4.5. Cross-anisotropic elasticity model

So far, several different models of stiffness for elastic strain increments have been proposed. Duncan and Chang (1970) assumed that the E_{max} (Young's modulus) value for elastic axial strain increments $d\varepsilon_a$ in a TC test of sand performed at a certain confining pressure σ_h is a unique function of σ_h. In the model of Lade and Nelson (1987), the E_{max} value is isotropic with respect to the direction of the elastic normal strain increment concerned, while it is a function of $(I_1^2+\alpha.J_2^2)$, in which I_1 and J_2 are the first and second stress invariants and α is a parameter which is a function of the elastic Poisson's ratio. Its modification for inherently cross-anisotropic materials has been proposed by Yu and Dakoulas (1992). Further modification will, however, be needed to capture the stress-induced anisotropy of sands.

A stiffness matrix for an inherently cross-anisotropic material was proposed by Barden (1963) based on theoretical considerations. This model was modified by Graham and Houlsby (1983) to explain the anisotropic deformation of a natural clay (note that the deformation of clay analysed by Graham and Houlsby was small, but not of a purely elastic one). In these models, the stress-system induced anisotropy was not dealt with either.

By compiling the results of the current investigation with respect to the inherent and stress-system induced anisotropy, and also combined with the models proposed by Barden (1963) and Graham and Houlsby (1983), the following stiffness matrix for the elastic deformation of a drained inherently cross-anisotropic geomaterials (particularly cohesionless soil) under axially symmetric stress conditions (i.e., $\sigma_x=\sigma_y$ and $\tau_{xz}=\tau_{zy}=\tau_{xy}=0$) may be proposed (Tatsuoka and Kohata, 1995) as shown in Eq. 3.1 (Chapter 3). This stiffness matrix has seven independent parameters; E_h, E_v, ν_{vh}, ν_{hv}, ν_{hh}, G_{vh} and G_{hh}. Of them, five elastic parameters E_h, E_v, ν_{vh}, ν_{hv} and ν_{hh} at any stress states can be obtained by knowing I_0, E_1, m_v, m_h and ν_0 of a particular material and then by using the Eqs. 4.3b (or 4.8), 4.3a (or 4.7), 4.11, 4.12 and 4.13 (given below).

$$\upsilon_{hh}=\upsilon_0 \qquad 4.13$$

It was mentioned in Chapter 3 that the assumption given by Eq. 4.13 was used to evaluate E_h from horizontal CL test with $\Delta\sigma_v=0$.

From inherent isotropy in the horizontal planes, we can obtain;

$$G_{hh} = E_h / \{2(1+\upsilon_0)\} \qquad 4.14$$

The only remaining parameter that cannot be obtained directly by triaxial testing system is G_{vh}=G_{hv}. Rather it can be evaluated with sufficient accuracy by torsional shear apparatus (Teachavorasinshun, 1992). However, we can make an estimation of G_{vh} by assuming that in the case of not very strong anisotropy, as the shear stress increment $\delta\tau_{hv}$ is applied, principal strain increments are induced in the two orthogonal directions at an angle of ±45 degrees relative to the vertical. In terms of the principal stress and principal strain increments, the following relation is obtained:

$$G_{hv} = G_{vh} = E_{45} / \{2(1+\upsilon_0)\} \qquad 4.15$$

where E_{45} is the Young's modulus for the major principal strain increments in the directions at an angle of ±45 degrees from the vertical. Here, the same E_{45} and the basic isotropic Poisson's ratio v_0 are used for these principal strain increments, since in these two orthogonal directions, both the inherent structure and the normal stress σ_n are the same with σ_n=(σ_v+σ_h)/2. Therefore, the value of E_{45} may be assumed as:

$$E_{45} = (E_{45})_0 \cdot (\sigma_n / \sigma_0)^m \qquad 4.16a$$

where $(E_{45})_0$ is E_{45} when σ_n is equal to σ_0, which may be assumed as:

$$(E_{45})_0 = \{(E_h)_0 + (E_v)_0\} / 2 \qquad 4.16b$$

Figs. 4.9a to d show the relationships between the 'normalized' G_{vh}, which was evaluated based on the discussions stated above, and the 'normalized' stress ratio for the four specimens TYK1A, TCK1A, SLK1V and HGK1A, respectively. For each specimen, three stress paths such as K=1, $\Delta\sigma_v$=0 at σ_v=1 kgf/cm^2 and $\Delta\sigma_h$=0 at σ_h=1.0 kgf/cm^2 have been investigated with the maximum value of major principal stress equal to 5.0 kgf/cm^2. G_{vh} can also be evaluated in the following form of Eq. 4.16c:

$$G_{vh} = G_1 . f(e) . \sigma_n^m \qquad 4.16c$$

where m is assumed as $(m_v+m_h)/2$ and G_1 is the shear modulus at σ_n=1 kgf/cm^2 at isotropic stress state (i.e., at $\sigma_n=\sigma_v=\sigma_h$=1.0 kgf/cm^2), which was evaluated based on Eqs. 4.15, 4.16a and 4.16b. Thereafter, G_{vh} evaluated for different σ_n by using Eq. 4.16c may be assumed as 'true' shear modulus. This 'true' shear modulus was compared with those obtained for other stress paths, such as K=1, $\Delta\sigma_v$=0 and $\Delta\sigma_h$=0. For the latter cases, the values of E_v and E_h for each value of σ_n (=$(\sigma_v+\sigma_h)/2$) were evaluated by Eqs. 4.3a and 4.3b, and then the corresponding G_{vh} was evaluated using the Eqs. 4.15 and 4.16b (rather than using Eq. 4.16c). In the Figs. 4.9a~d, G_{vh} values evaluated for three stress paths, including the so-called 'true' values, were normalized by the r.h.s. of Eq. 4.16c (the same G_1 and m values were used as those evaluated to calculate the 'true' values). In those figures, stress axis was normalized by p_0, where p_0=1 kgf/cm^2 representing the pivotal isotropic stress at which G_1 was measured. It can be seen that G_{vh} exhibits stress path dependency to some extent. For materials not inherently strong anisotropic (Toyoura and Ticino sands), G_{vh} (normalized) values estimated along $\Delta\sigma_h$=0 and K=1 stress paths fit reasonably with the normalized unit 'true' modulus line, while those evaluated along $\Delta\sigma_v$=0 stress path exhibit about 10% under-estimation at the maximum shear stress level (i.e., at σ_h=5.0 kgf/cm^2 or σ_n=3.0 kgf/cm^2). On the other hand, for materials which exhibit inherently very strong anisotropy (i.e., SLB sand and Hime gravel), G_{vh} (normalized) values estimated along $\Delta\sigma_h$=0 stress path exhibit about 5% under-estimation whereas those estimated along $\Delta\sigma_v$=0 stress path exhibit about 17% over-estimation. The larger deviation in $\Delta\sigma_v$=0 stress path is due to the larger biasness of σ_n to σ_h values (rather than σ_v) and due to inherent anisotropy with $E_h < E_v$.

4.6. Stress path-dependency of integrated elastic strains

Elastic strain increments $d\varepsilon_v$ and $d\varepsilon_h$ in triaxial stress conditions are given, according to the proposed model, as follows:

$$d\varepsilon_v = 1/E_v \, d\sigma_v - 2\nu_{hv}/E_h \, d\sigma_h \qquad 4.17a$$

$$d\varepsilon_h = (1-\nu_{hh})/E_h \, d\sigma_h - \nu_{vh}/E_v \, d\sigma_v \qquad 4.17b$$

E_v and E_h are given by Eqs. 4.3a and 4.3b, while ν_{hv} and ν_{vh} are given by Eqs. 4.11 and 4.12, and $\nu_{hh}= \nu_0$. Then, the integration of $d\varepsilon_v$ and $d\varepsilon_h$ is stress path-dependent; i.e., the integrated elastic strains $\Delta\varepsilon_v$ and $\Delta\varepsilon_h$ are not a unique function of the stress states before and after loading (see Fig. 4.10). In the following discussion, $m= m_v$ and $\nu_{vh}= \nu_{hv}= \nu_0$ at $\sigma_v=\sigma_h$ are assumed.

For the stress path A→B→C (Fig. 4.10), $\Delta\varepsilon_v$ is given as;

$(\Delta\varepsilon_v)_{ABC} = (\Delta\varepsilon_v)_{AB} + (\Delta\varepsilon_v)_{BC}$, where

$$(\Delta\varepsilon_v)_{AB} = -\int_{\sigma_{ho}}^{\sigma_{ho}+\Delta\sigma_h} 2\nu_{hv}/E_h \, d\sigma_h = -\frac{2\nu_0}{(1-I_0).f(e).E_1.\sigma_{vo}^{m/2}} \int_{\sigma_{ho}}^{\sigma_{ho}+\Delta\sigma_h} \frac{d\sigma_h}{\sigma_h^{m/2}}$$
$$= -\frac{2\nu_0}{1-m/2} \frac{\sigma_{h0}}{(1-I_0).E_1.f(e)} \frac{1}{(\sigma_{v0}\sigma_{h0})^{m/2}} \left\{(1+h)^{1-m/2}-1\right\} \qquad 4.18$$

where $h= \Delta\sigma_h/\sigma_{h0}$.

$$(\Delta\varepsilon_v)_{BC} = -\int_{\sigma_{vo}}^{\sigma_{vo}+\Delta\sigma_v} 1/E_v \, d\sigma_v = \frac{1}{f(e).E_1} \int_{\sigma_{vo}}^{\sigma_{vo}+\Delta\sigma_v} \frac{d\sigma_v}{\sigma_v^{m}}$$
$$= -\frac{1}{1-m} \frac{\sigma_{v0}}{E_1.f(e)} \frac{1}{(\sigma_{v0})^{m}} \left\{(1+r)^{1-m}-1\right\} \qquad 4.19$$

where $r = \Delta\sigma_v/\sigma_{v0}$. On the other hand, for the stress path A→D→C (Fig. 4.10), $\Delta\varepsilon_v$ is given as;

$(\Delta\varepsilon_v)_{ADC} = (\Delta\varepsilon_v)_{AD} + (\Delta\varepsilon_v)_{DC}$, where $(\Delta\varepsilon_v)_{AD} = (\Delta\varepsilon_v)_{BC}$

$$(\Delta\varepsilon_v)_{AD} = -\frac{2\nu_0}{1-m/2} \frac{\sigma_{h0}}{(1-I_0).E_1.f(e)} \frac{1}{(\sigma_{v0}\sigma_{h0})^{m/2}} \frac{\left\{(1+h)^{1-m/2}-1\right\}}{(1+r)^{m/2}} \qquad 4.20$$

Here, we define the difference in $d(\Delta\varepsilon_v)$ between $(\Delta\varepsilon_v)_{ABC}$ and $(\Delta\varepsilon_v)_{ADC}$ and their mean $[(d\varepsilon_v)_{ave}]$ as follows:

$$d(\Delta\varepsilon_v) = (\Delta\varepsilon_v)_{ABC} - (\Delta\varepsilon_v)_{ADC} = (\Delta\varepsilon_v)_{AB} - (\Delta\varepsilon_v)_{DC}$$
$$= -\frac{2\nu_0}{1-m/2} \frac{\sigma_{h0}}{(1-I_0).E_1.f(e)} \frac{1}{(\sigma_{v0}\sigma_{h0})^{m/2}} \left\{(1+h)^{1-m/2}-1\right\} \left\{1-\frac{1}{(1+r)^{m/2}}\right\} \qquad 4.21$$

$(\Delta\varepsilon_v)_{ave} = [(\Delta\varepsilon_v)_{ABC} + (\Delta\varepsilon_v)_{ADC}]/2 = (\Delta\varepsilon_v)_{BC} + \{ (\Delta\varepsilon_v)_{DC} + (\Delta\varepsilon_v)_{AB} \}/2.$

Then the ratio $S_v = d(\Delta\varepsilon_v) / (\Delta\varepsilon_v)_{ave}$ is obtained as

$$\frac{d(\Delta\varepsilon_v)}{(\Delta\varepsilon_v)_{ave}} = \frac{-\frac{4(1-m)}{2-m}\frac{\nu_0}{1-I_0}\left(\frac{\sigma_{h0}}{\sigma_{v0}}\right)^{1-m/2}\left\{(1+h)^{1-m/2}-1\right\}\left\{1-\frac{1}{(1+r)^{m/2}}\right\}\left\{\frac{1}{(1+r)^{1-m}-1}\right\}}{1-\frac{2(1-m)}{2-m}\frac{\nu_0}{1-I_0}\left(\frac{\sigma_{h0}}{\sigma_{v0}}\right)^{1-m/2}\left\{(1+h)^{1-m/2}-1\right\}\left\{1+\frac{1}{(1+r)^{m/2}}\right\}\left\{\frac{1}{(1+r)^{1-m}-1}\right\}} \quad 4.22$$

Similarly, for strains in lateral direction, we obtain the ratio S_h as:

$$\frac{d(\Delta\varepsilon_h)}{(\Delta\varepsilon_h)_{ave}} = \frac{-\frac{2(1-m)\nu_0(1-I_0)}{2-m}\frac{}{1-\nu_0}\left(\frac{\sigma_{v0}}{\sigma_{h0}}\right)^{1-m/2}\left\{(1+r)^{1-m/2}-1\right\}\left\{1-\frac{1}{(1+h)^{m/2}}\right\}\left\{\frac{1}{(1+h)^{1-m}-1}\right\}}{1-\frac{(1-m)}{2-m}\frac{\nu_0(1-I_0)}{1-\nu_0}\left(\frac{\sigma_{v0}}{\sigma_{h0}}\right)^{1-m/2}\left\{(1+r)^{1-m/2}-1\right\}\left\{1+\frac{1}{(1+h)^{m/2}}\right\}\left\{\frac{1}{(1+h)^{1-m}-1}\right\}} \quad 4.23$$

Note that when the ratio $S_v = d(\Delta\varepsilon_v) / (\Delta\varepsilon_v)_{ave}$ (and S_h) is equal to zero, the material is a general elastic body, while the ratio is non-zero, the material is a hypo-elastic one. In this case, the ratio S_v and S_h are functions of $h = \Delta\sigma_h/\sigma_{h0}$ and $r = \Delta\sigma_v/\sigma_{v0}$ and others (i.e., I_0, n_0, m, etc.).

When h=r and $\sigma_{v0}=\sigma_{h0}$, the relations between S_v (and S_h) and h=r are obtained as shown in Figs. 4.11 through 4.13. While keeping the other variables constant, Figs. 4.11a, 4.12a and 4.13a show the relationships between S_v and h=r for different I_0, ν_0 and m values, respectively. On the other hand, similar relationships between S_h and h=r are shown in Figs 4.11b, 4.12b and 4.13b. From these figures, the following trends can be observed. Granular materials exhibit hypo-elastic deformation characteristics in a finite strain range. Hypo-elasticity in ε_v direction (Fig. 4.11a) increases with the increase in the degree of inherent anisotropy in the small strain stiffness I_0 (=1-E_h/E_v), but contemporarily it decreases in ε_h direction (Fig. 4.11b). In both ε_v and ε_h directions (Figs. 4.12a to 4.13b), at a constant I_0, hypo-elasticity increases with the increase in m and ν_0 values while the either is held constant.

4.7. Summaries

(1) Stress-dependency of Young's modulus is critically examined for three cases: Elastic Young's modulus is i) mean stress dependent (Case 1), ii) directionally stress-dependent (Case 2), and (iii) dependent on both principal stresses (Case 3).

(2) Large volume of data shows that the elastic Young's modulus is rather a unique function of the normal stress in the direction of the major principal strain increment (Case 2). Case 1 and 3 types of dependency of Young's modulus may underestimate or overestimate the true values depending on the stress path being followed and the magnitude of stress states.

(3) Poisson's ratio (ν_{vh}) was observed to increase within a narrow range with the increase in stress ratio (σ_v/σ_h).

(4) Based on the experimental observation, a cross-anisotropic elastic model has been proposed and evaluated. In the model, G_{vh} is estimated based on the elastic parameters [E_1, I_0, m_v, m_h] for different stress paths and is observed that G_{vh} is stress-path dependent for the materials which show strong inherent anisotropy in Young's moduli.

(5) Elasticity of granular materials is of hypo-elastic type. Hypo-elasticity increases in both principal strain directions with the increase in ν_0 and m values; it increases in the ε_v direction with the increase in I_0, but at the same time it decreases in the ε_h direction.

Table 4.1: List of the elastic parameters obtained from $\Delta K=0$ stress paths.

Material	Specimen name	$K=\sigma_h/\sigma_v$	[a]E_1 (kgf/cm^2)	m_v	[b]I_0	m_h
Toyoura sand	TYK1A	1.00	2030	0.490	0.096	0.412
		0.70	2016	0.457	0.071	0.408
		0.50	1990	0.463	0.071	0.410
SLB sand	SLK1A	1.00	2890	0.474	0.363	0.440
		0.70	2790	0.486	0.485	0.460
	SLK0A	1.00	2806	0.506	0.552	0.471
		0.75	2715	0.493	0.531	0.475
	SLK1V	1.00	3220	0.446	0.462	0.418
		0.75	3198	0.440	0.454	0.437
		0.50	3107	0.404	0.423	0.443
Hime gravel	HGK1A	1.00	2075	0.512	0.380	0.452
		0.75	2011	0.514	0.349	0.424
		0.50	2027	0.501	0.344	0.438
	HGK0A	1.00	2188	0.514	0.440	0.490
		0.75	2175	0.503	0.440	0.510
		0.50	2113	0.515	0.427	0.518
Ticino sand	TCK1A	1.00	1510	0.53	0.000	0.440
		0.70	1471	0.54	0.003	0.456

[a] : $E_v = E_1.f(e).(1/K^{m_v}).\sigma_h^{m_v}$ (along $\Delta K=0$ stress path)
[b] : $E_h = (1-I_0).E_1.f(e).\sigma_h^{m_h}$

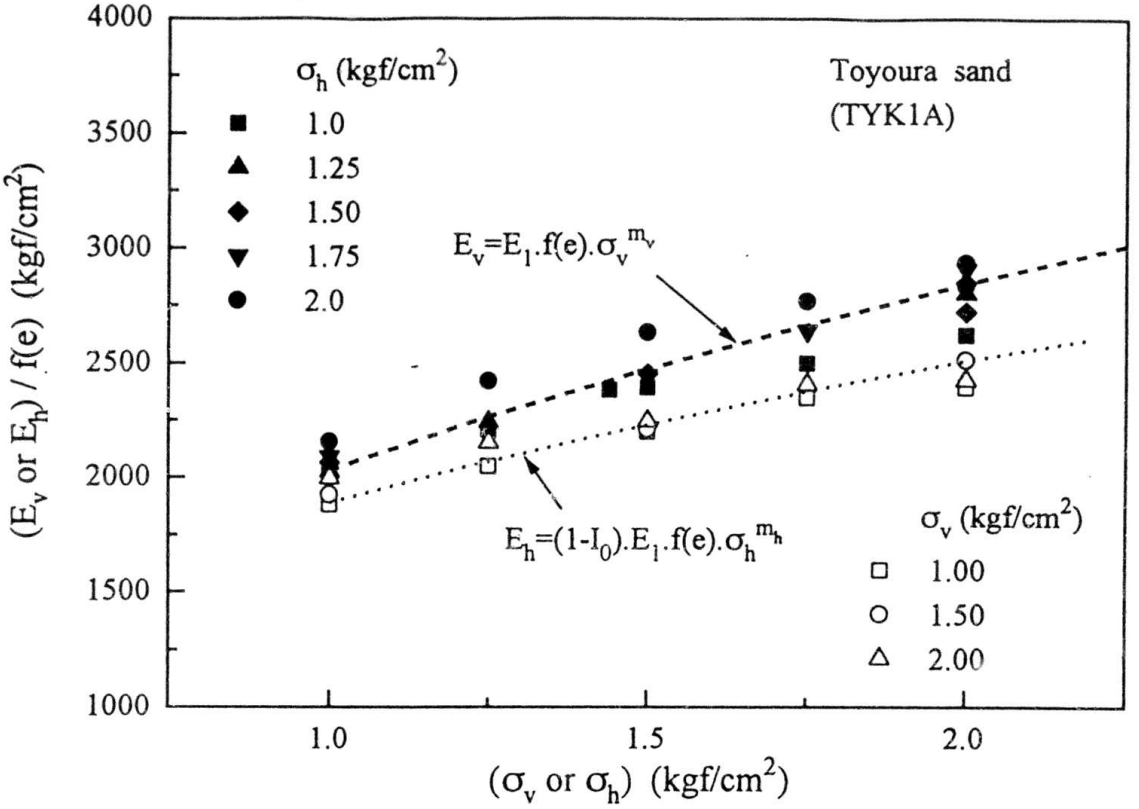

Fig. 4.1a: $E_v/f(e)\sim\sigma_v$ and $E_h/f(e)\sim\sigma_h$ relations for different out-plane stresses performed on TYK1A specimen.

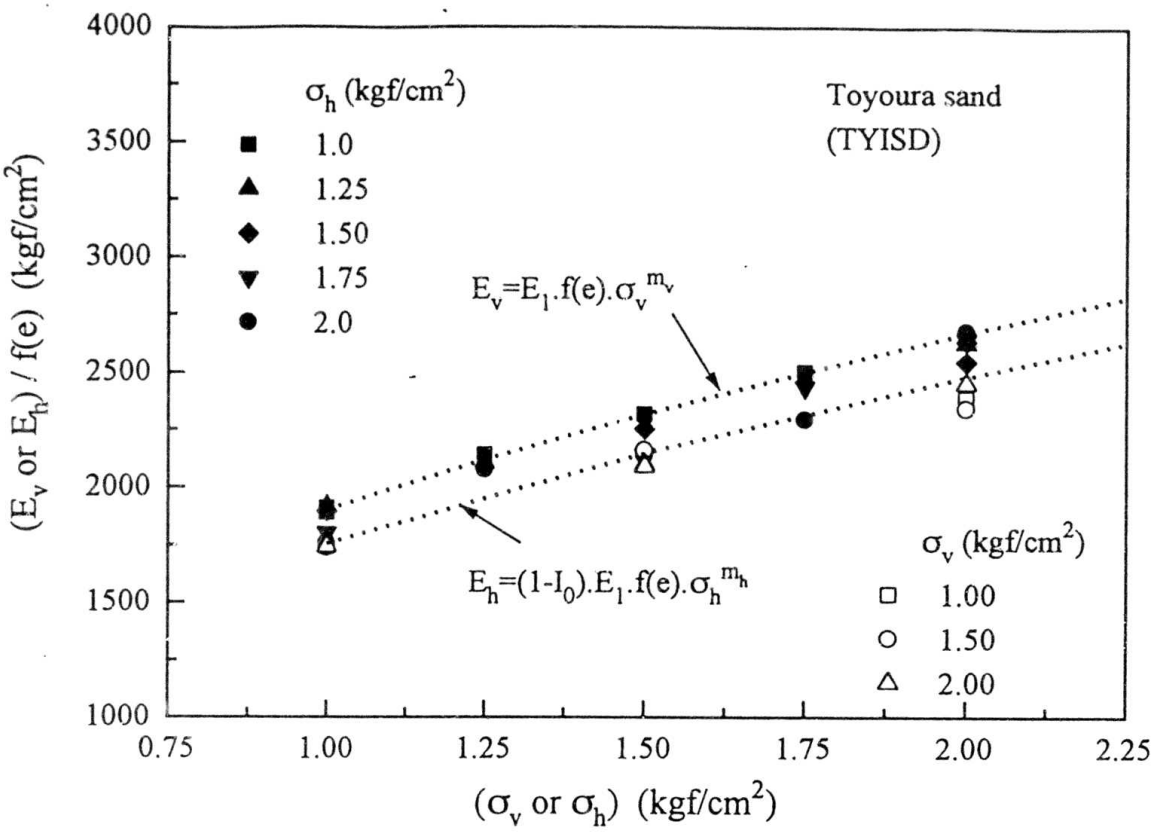

Fig. 4.1b: $E_v/f(e)\sim\sigma_v$ and $E_h/f(e)\sim\sigma_h$ relations for different out-plane stresses performed on TYISD specimen.

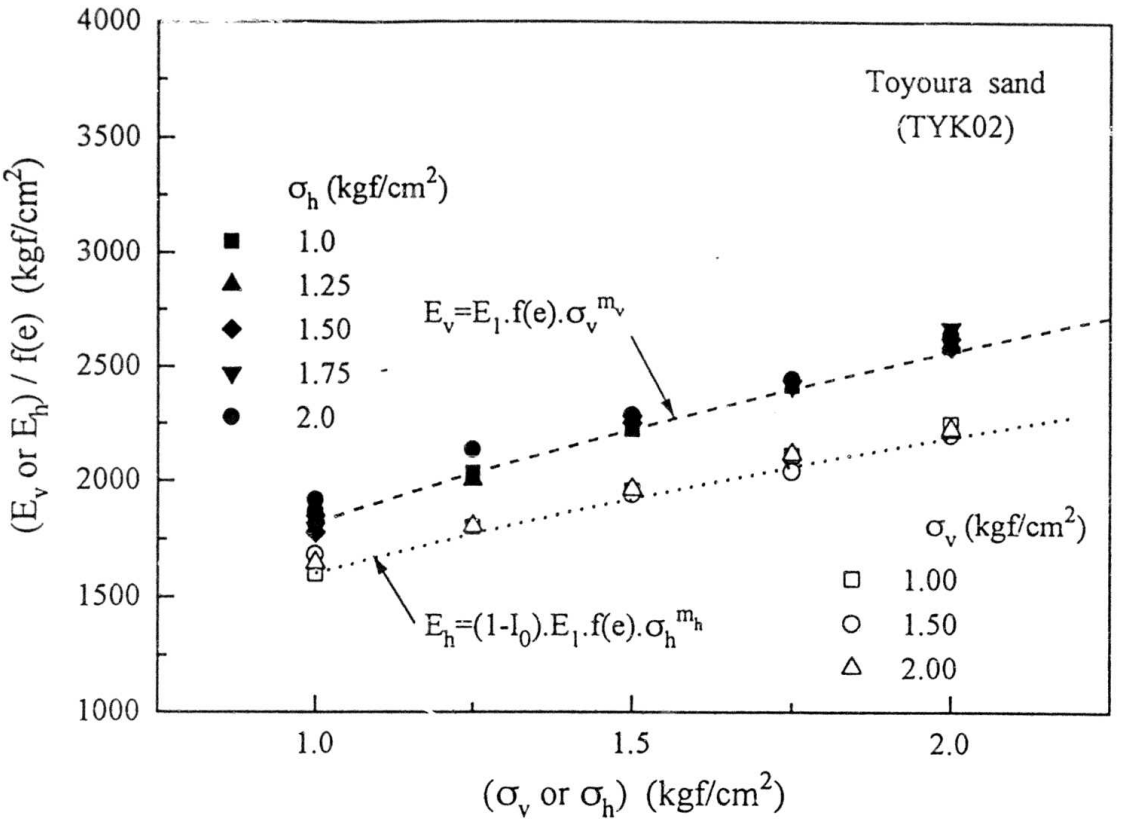

Fig. 4.1c: $E_v/f(e)\sim\sigma_v$ and $E_h/f(e)\sim\sigma_h$ relations for different out-plane stresses performed on TYK02 specimen.

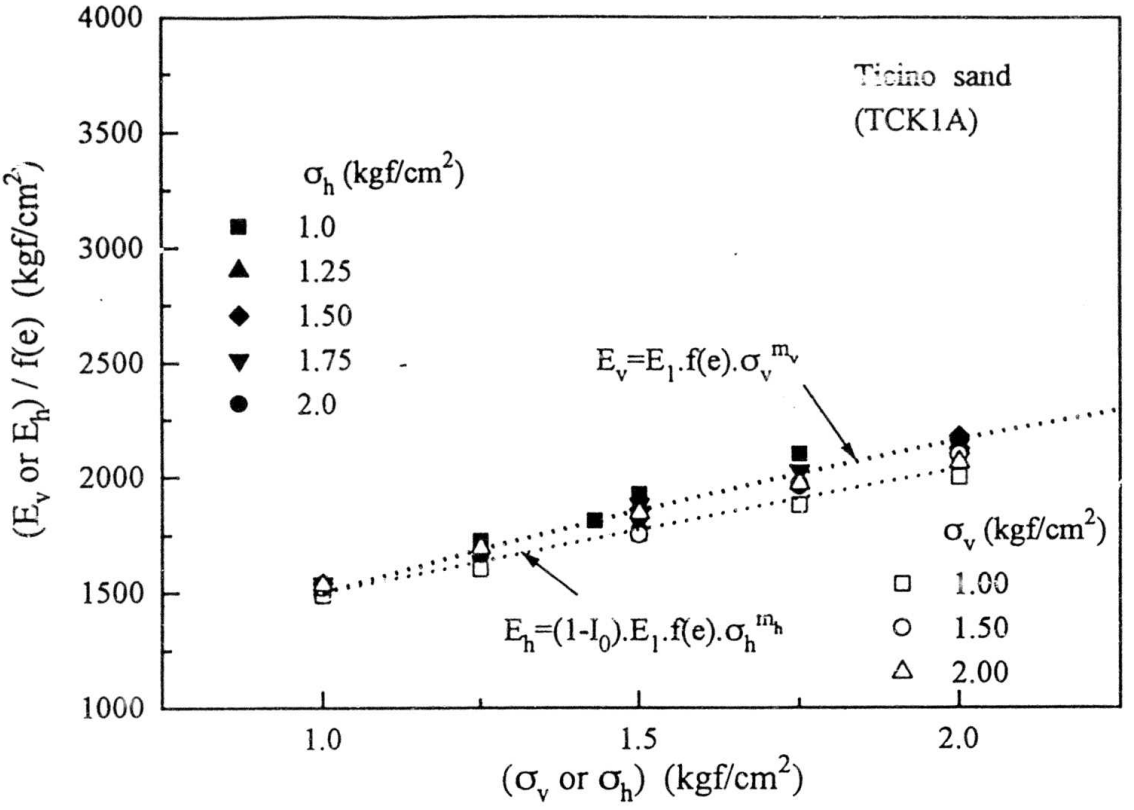

Fig. 4.1d: $E_v/f(e)\sim\sigma_v$ and $E_h/f(e)\sim\sigma_h$ relations for different out-plane stresses performed on TCK1A specimen.

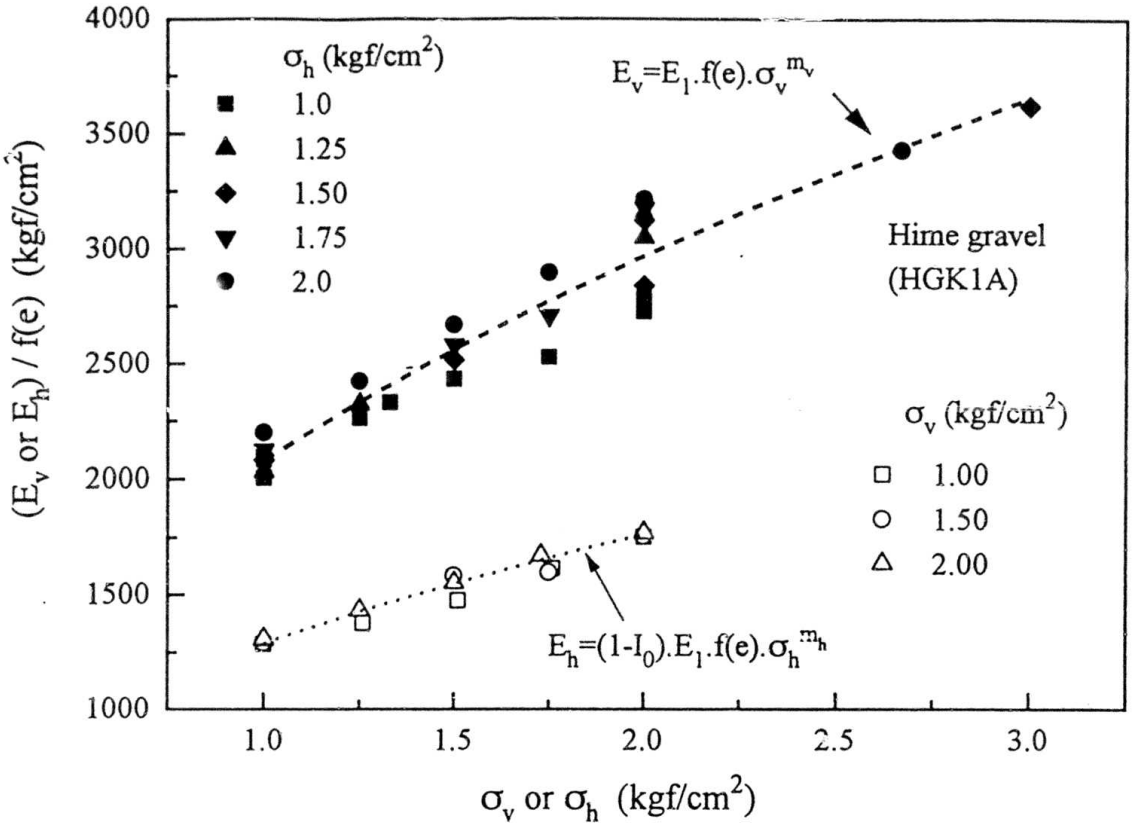

Fig. 4.1e: $E_v/f(e)\sim\sigma_v$ and $E_h/f(e)\sim\sigma_h$ relations for different out-plane stresses performed on HGK1A specimen.

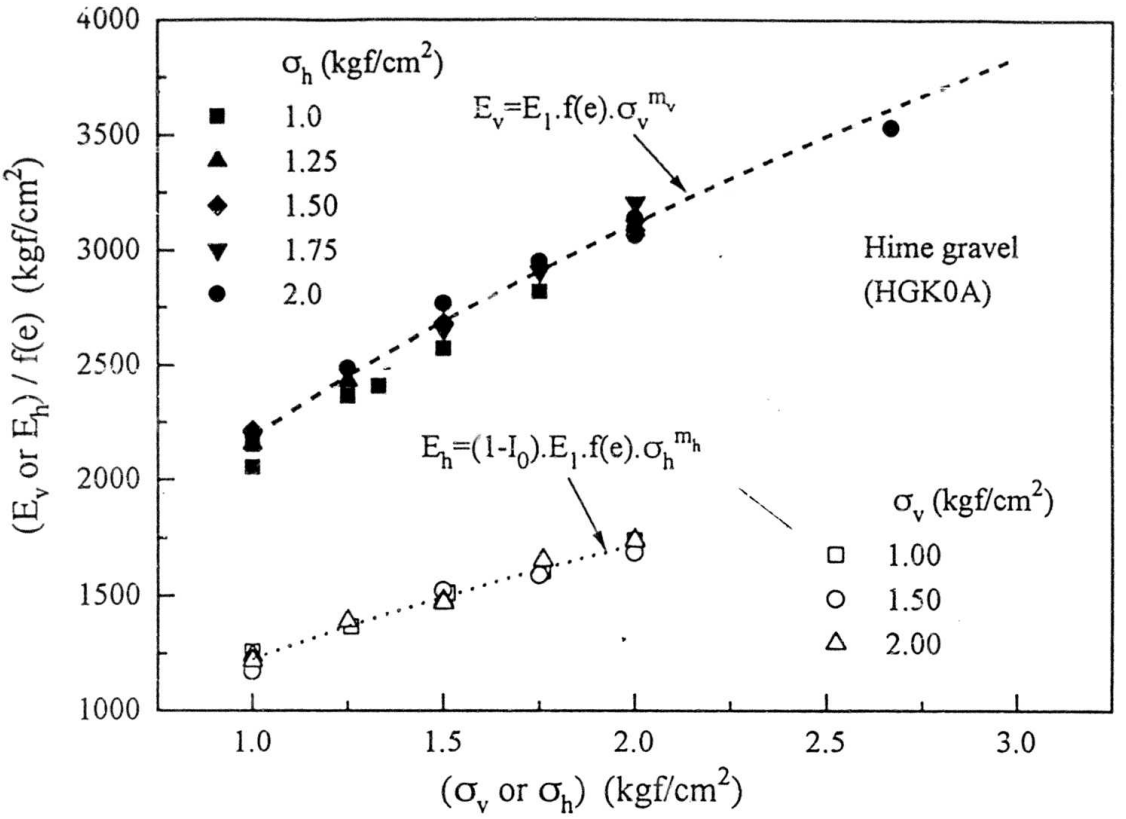

Fig. 4.1f: $E_v/f(e)\sim\sigma_v$ and $E_h/f(e)\sim\sigma_h$ relations for different out-plane stresses performed on HGK0A specimen.

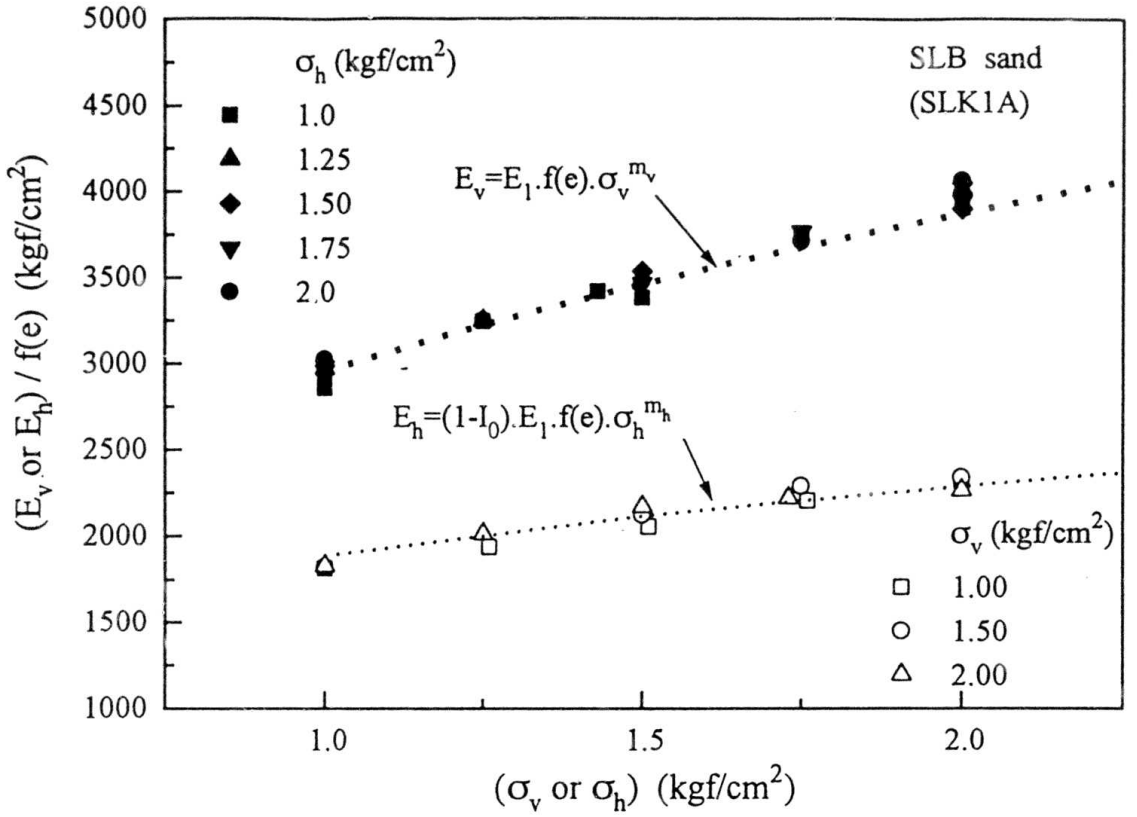

Fig. 4.1g: $E_v/f(e)\sim\sigma_v$ and $E_h/f(e)\sim\sigma_h$ relations for different out-plane stresses performed on SLK1A specimen.

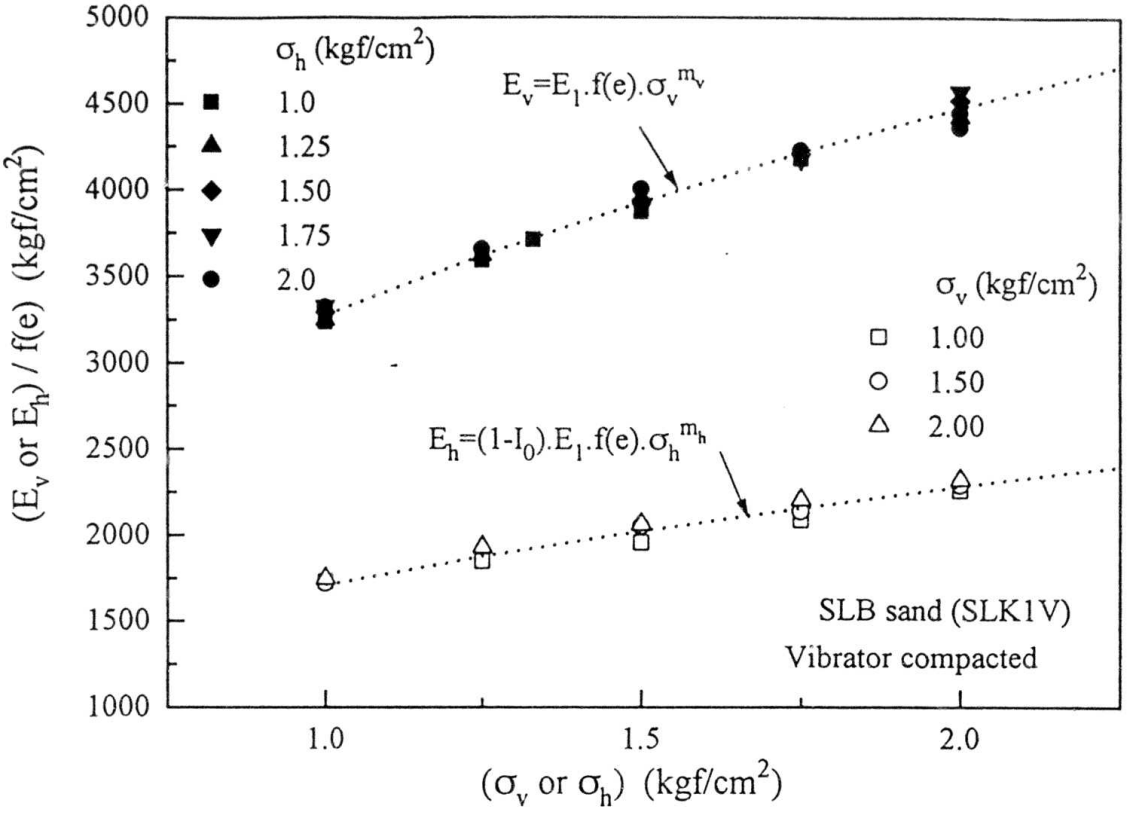

Fig. 4.1h: $E_v/f(e)\sim\sigma_v$ and $E_h/f(e)\sim\sigma_h$ relations for different out-plane stresses performed on SLK1V specimen.

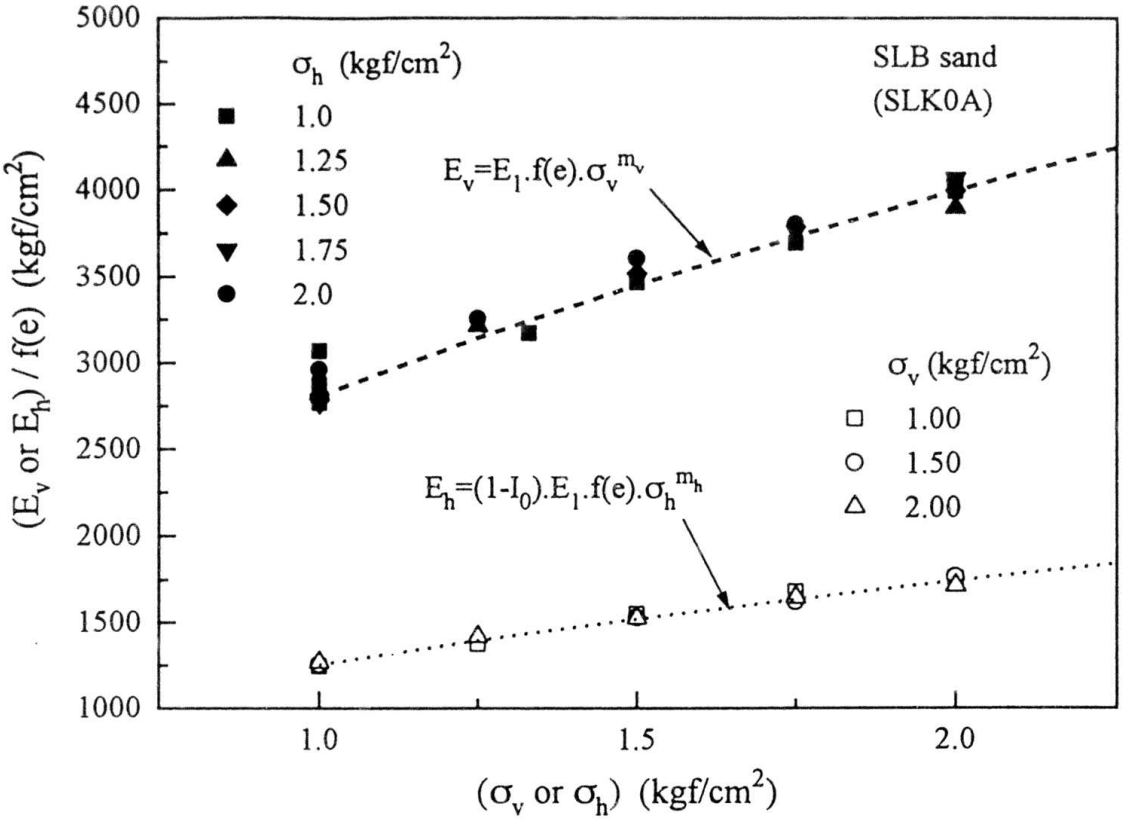

Fig. 4.1i: $E_v/f(e)\sim\sigma_v$ and $E_h/f(e)\sim\sigma_h$ relations for different out-plane stresses performed on SLK0A specimen.

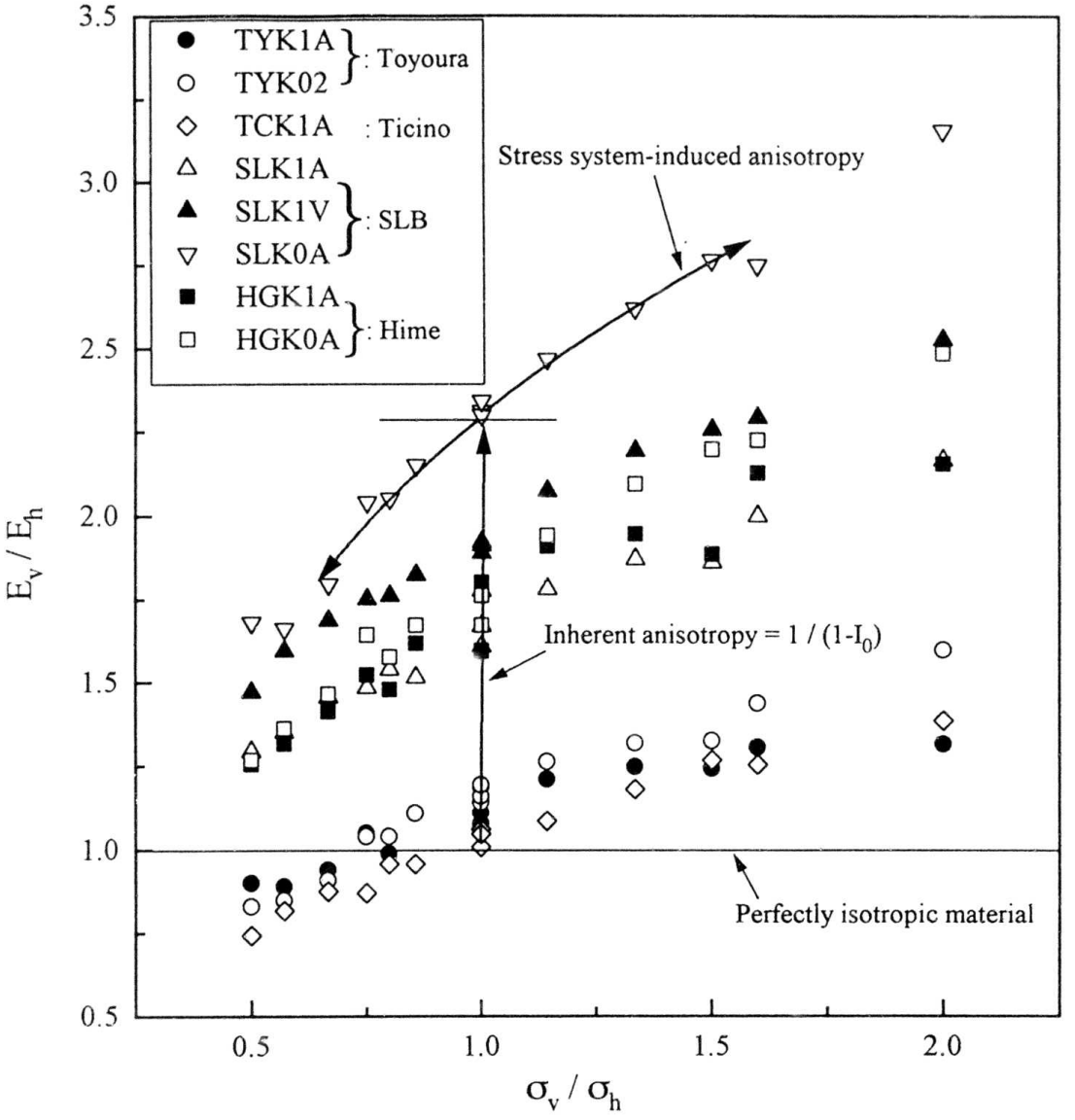

Fig. 4.1j: The relationships between E_v/E_h and σ_v/σ_h of different specimens.

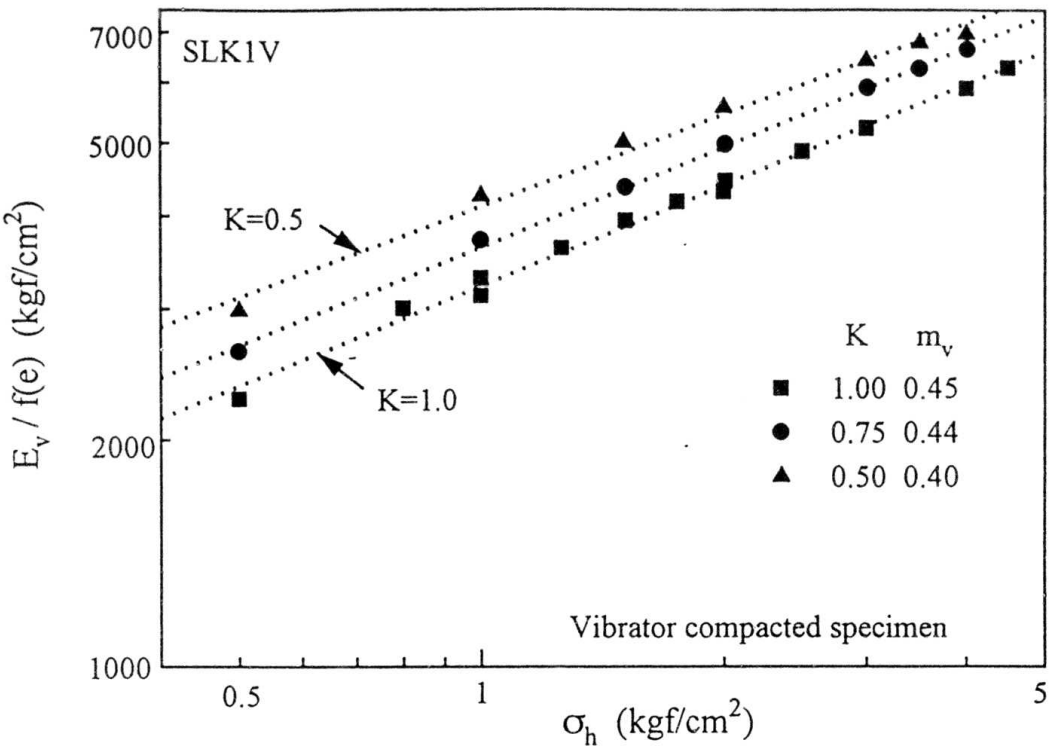

Fig. 4.2a: Relationships between $E_v/f(e)$ and σ_h along $\Delta K=0$ stress paths.

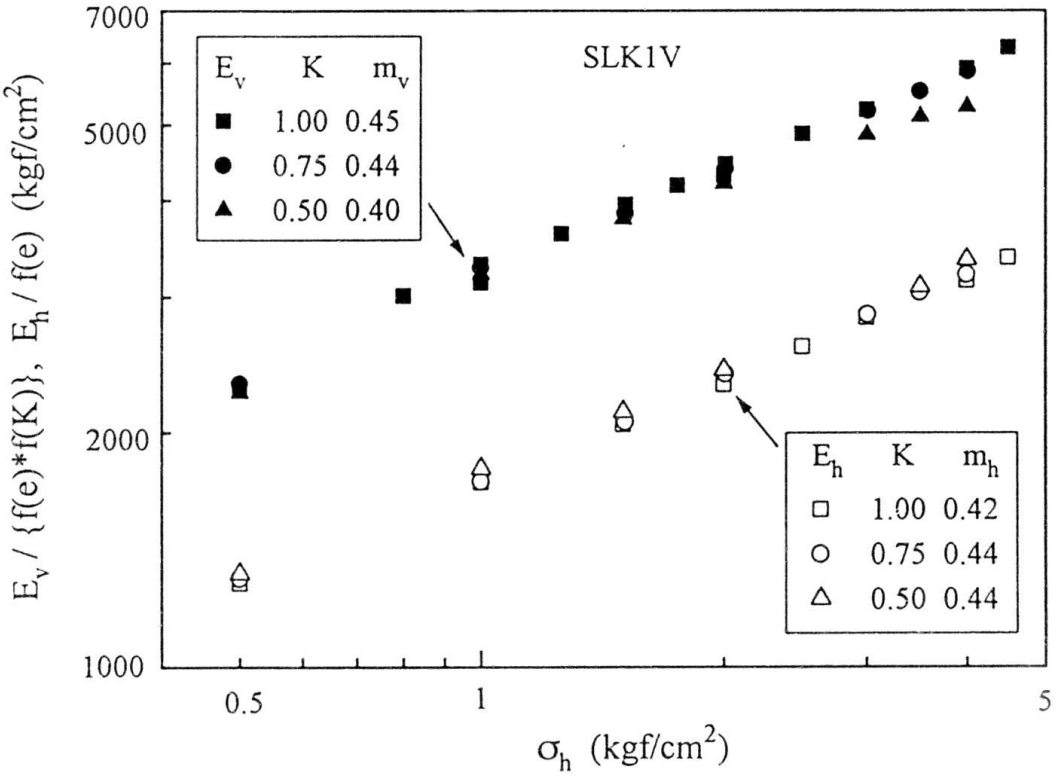

Fig. 4.2b: Relations between $E_v/\{f(e)xf(K)\}$ and σ_h, and $E_h/f(e)$ and σ_h along $\Delta K=0$ stress paths.

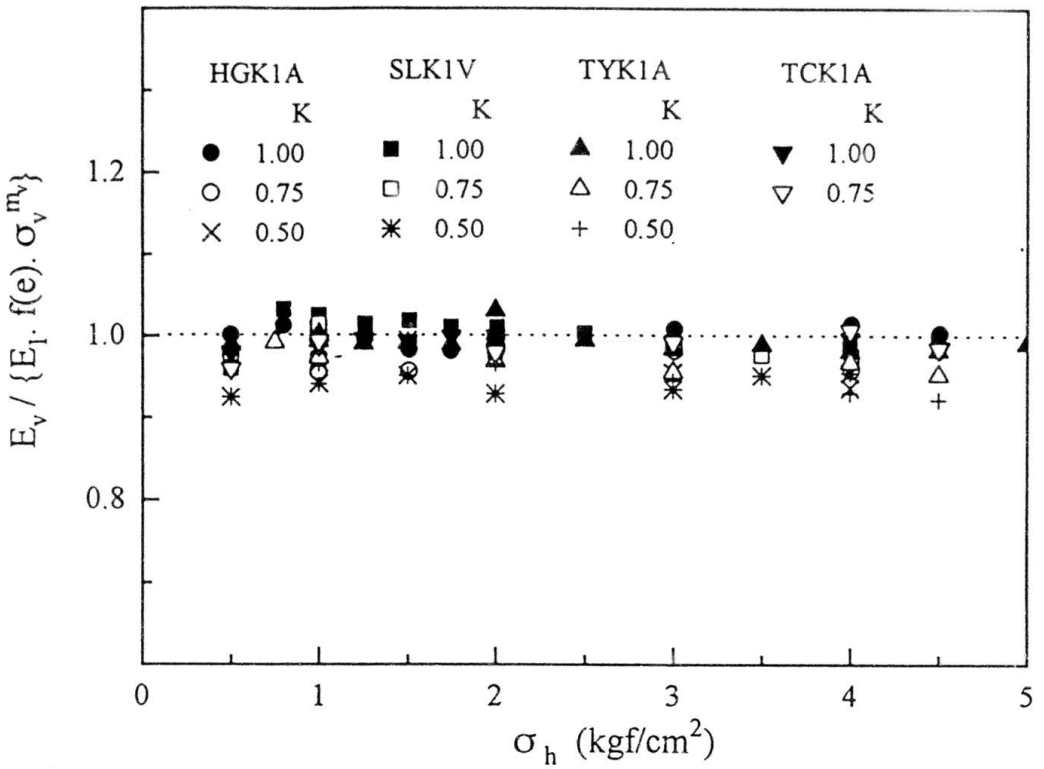

Fig. 4.3a: Relationships between the ratio of measured to predicted E_v (based on σ_v dependency of E_v) and σ_h along $\Delta K=0$ stress paths.

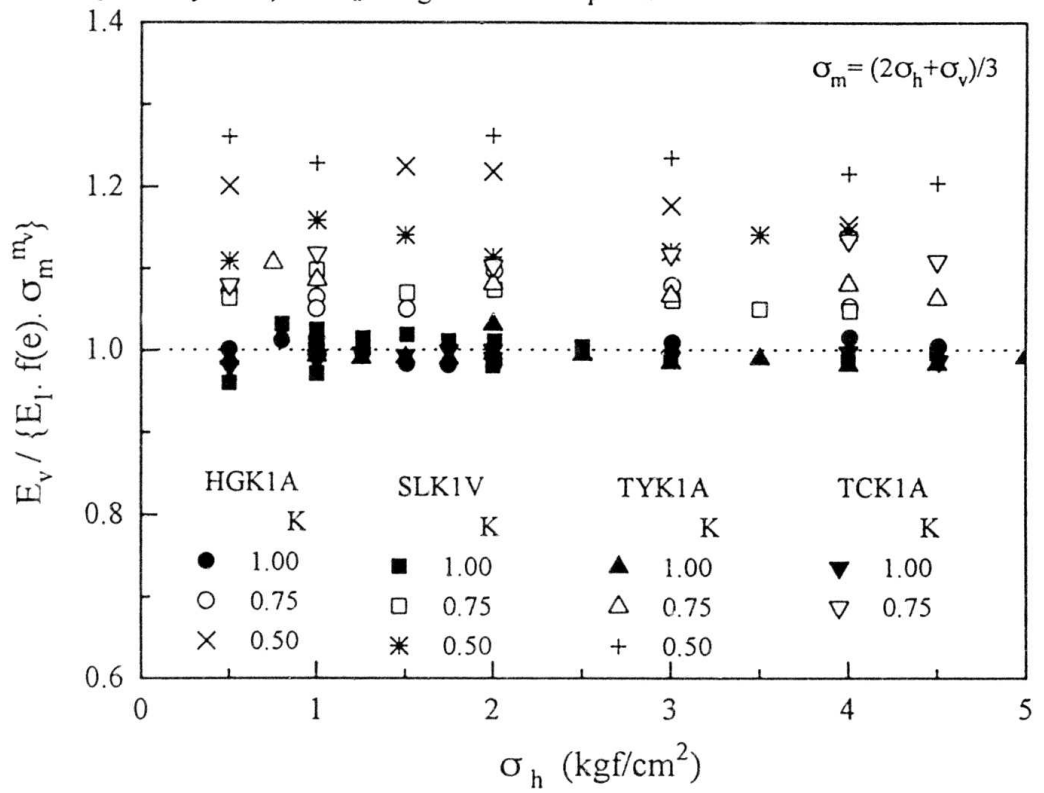

Fig. 4.3b: Relationships between the ratio of measured to predicted Young's moduli E_v (based on σ_m dependency of E_v) and σ_h along $\Delta K=0$ stress paths.

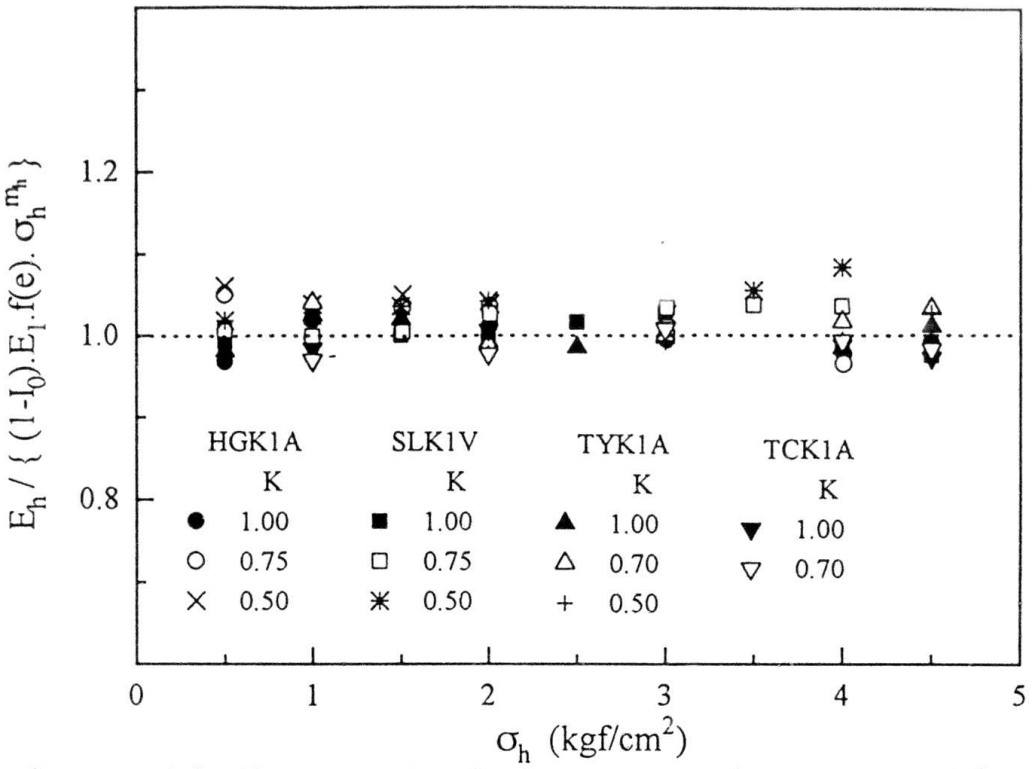

Fig. 4.4a: Relationships between the ratio of measured to predicted Young's moduli E_h (based on σ_h dependency of E_h) and σ_h along $\Delta K=0$ stress paths.

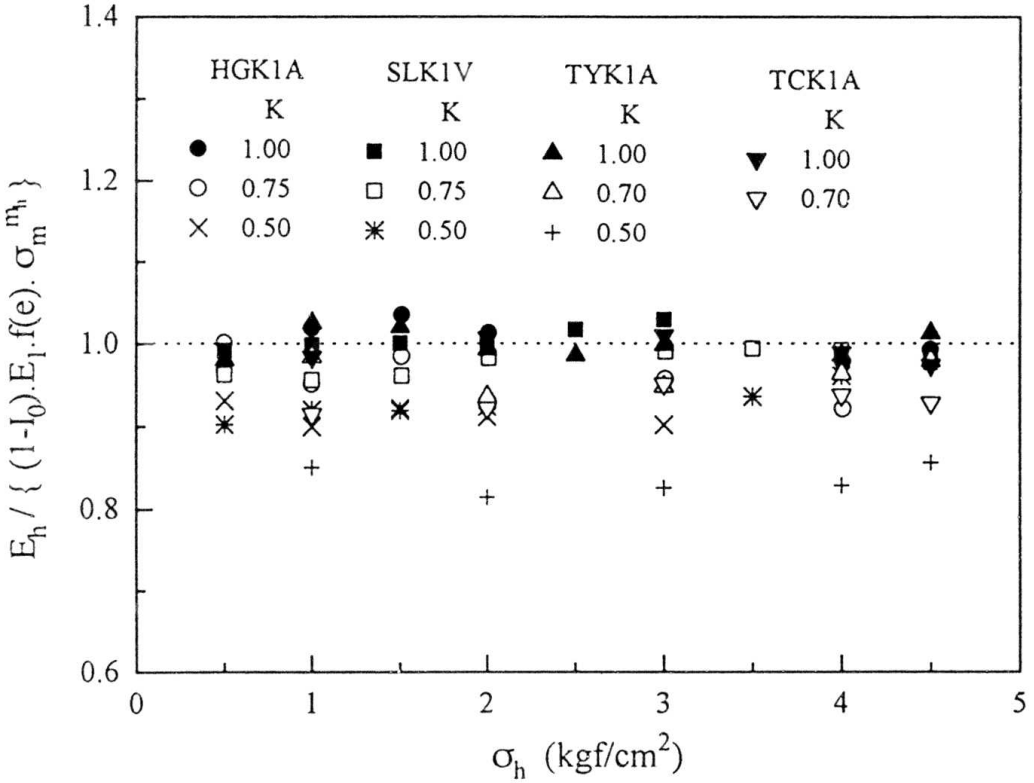

Fig. 4.4b: Relationships between the ratio of measured to predicted Young's moduli E_h (based on σ_h dependency of E_h) and σ_h along $\Delta K=0$ stress paths.

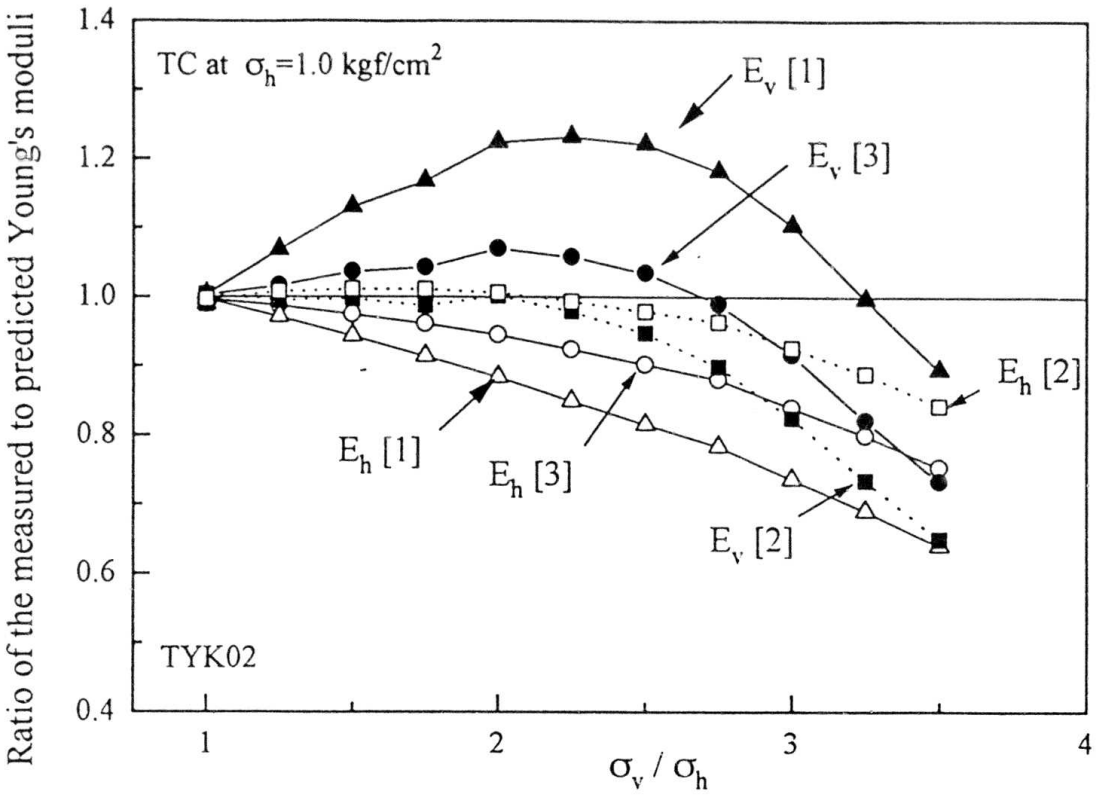

Fig. 4.5a: Relationships between the ratio of measured to predicted Young's moduli and σ_v/σ_h along TC at $\sigma_v=\sigma_h$=1.0 kgf/cm^2 of TYK02 specimen.

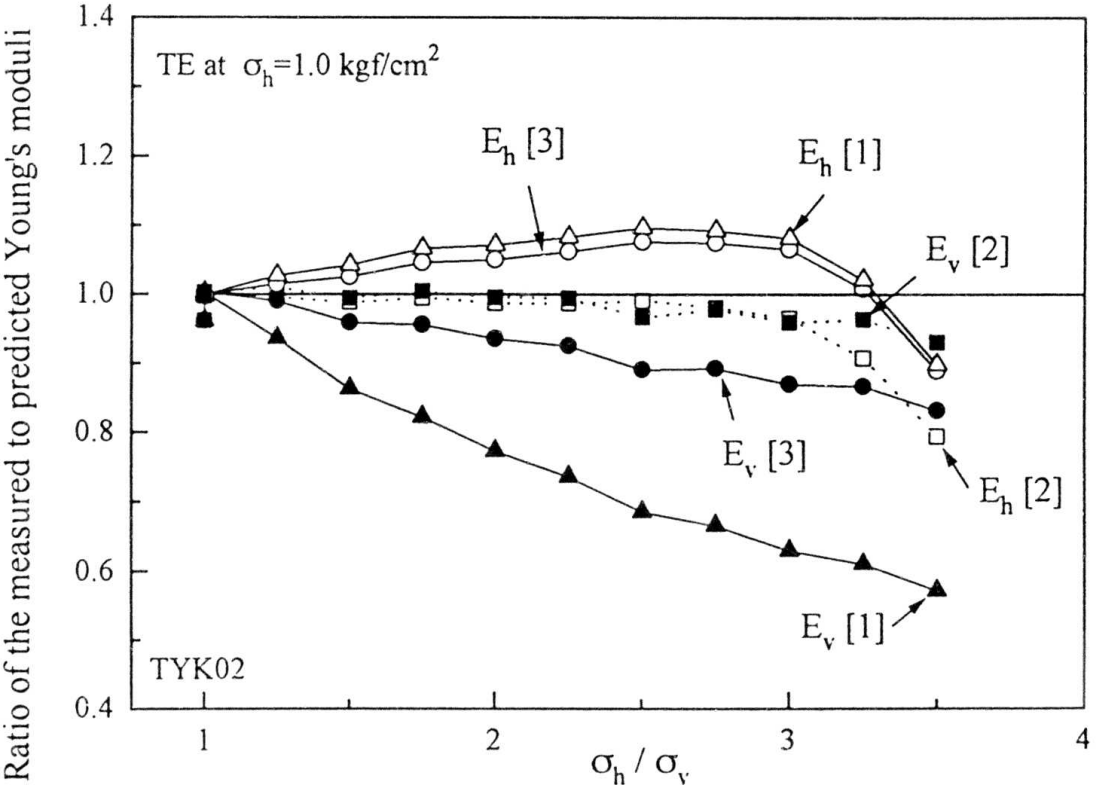

Fig. 4.5b: Relationships between the ratio of measured to predicted Young's moduli and σ_h/σ_v along TE at $\sigma_v=\sigma_h$=1.0 kgf/cm^2 of TYK02 specimen.

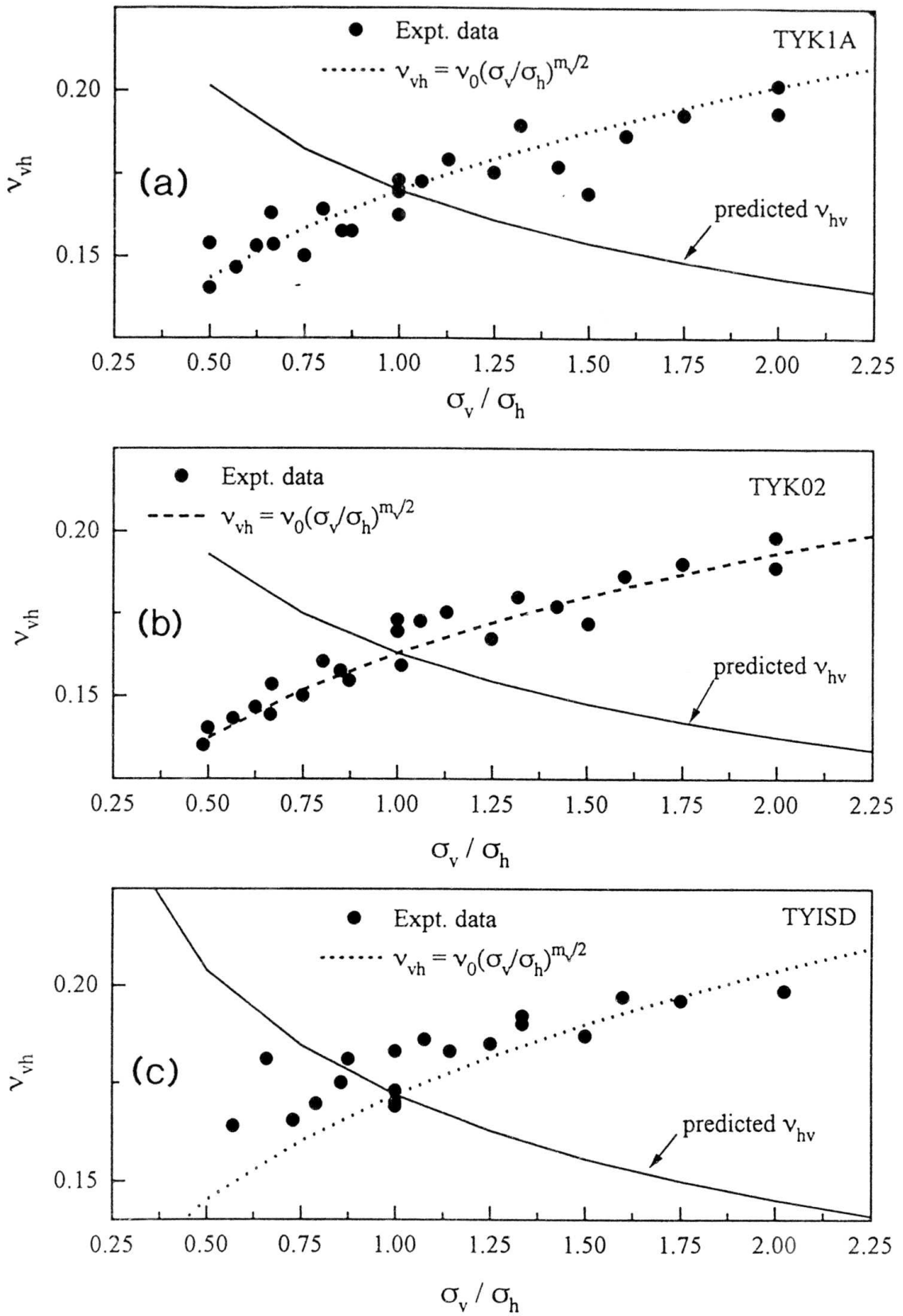

Figs. 4.6: Relationships between Poisson's ratio and stress ratio for specimens (a) TYK1A, (b) TYK02 and (c) TYISD.

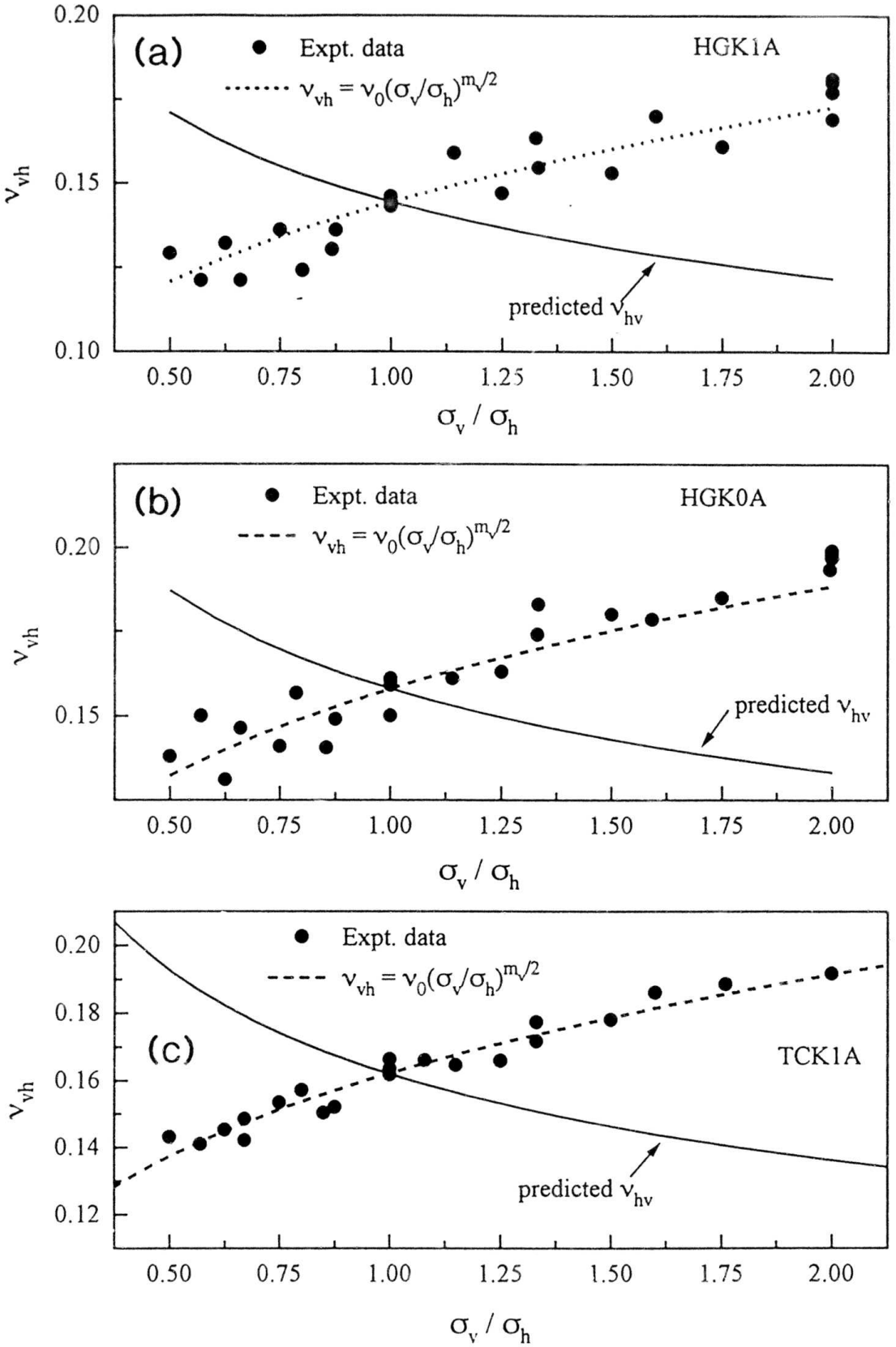

Figs. 4.7: Relationships between Poisson's ratio and stress ratio for specimens (a) HGK1A, (b) HGK0A and (c) TCK1A.

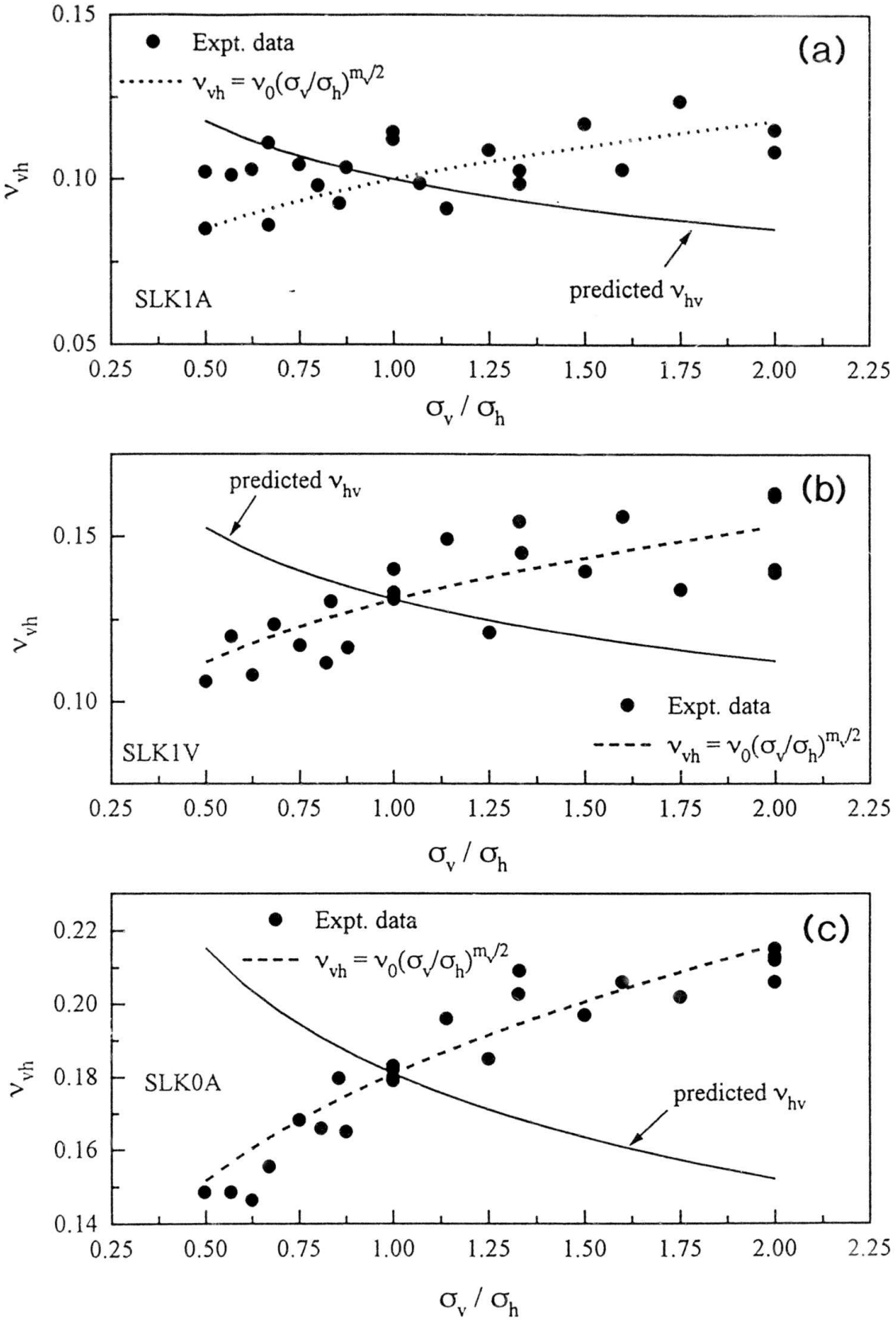

Figs. 4.8: Relationships between Poisson's ratio and stress ratio for specimens (a) SLK1A, (b) SLK1V and (c) SLK0A.

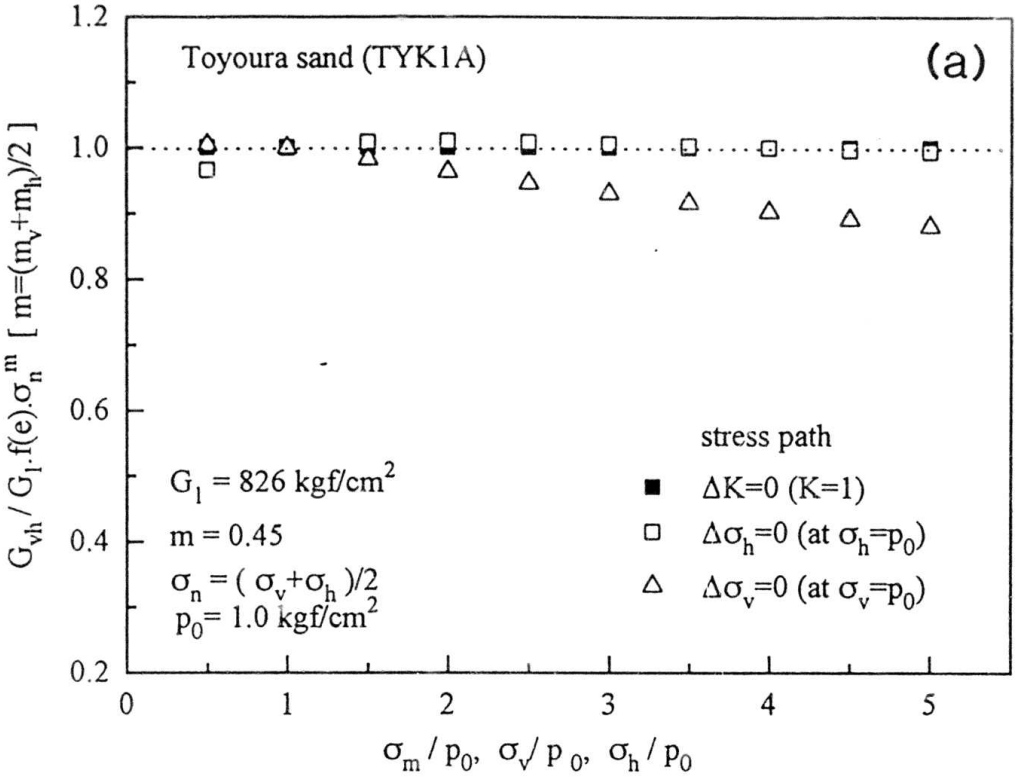

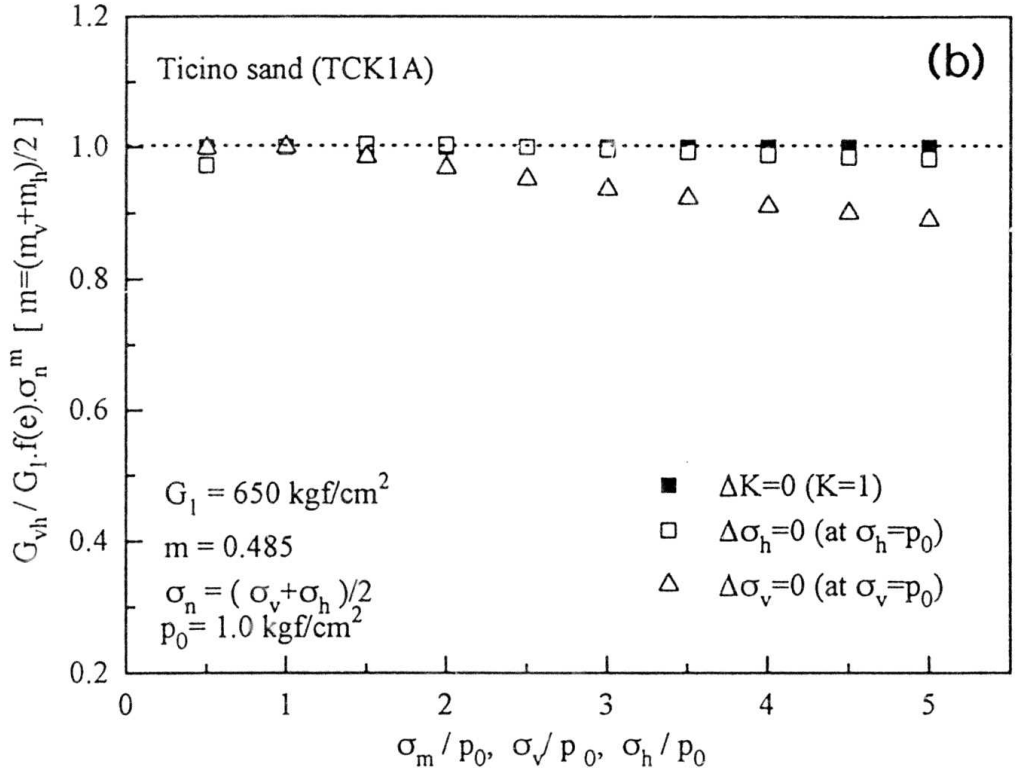

Figs. 4.9: Relationships between normalized G_{vh} and normalized stress level for specimens (a) TYK1A and (b) TCK1A.

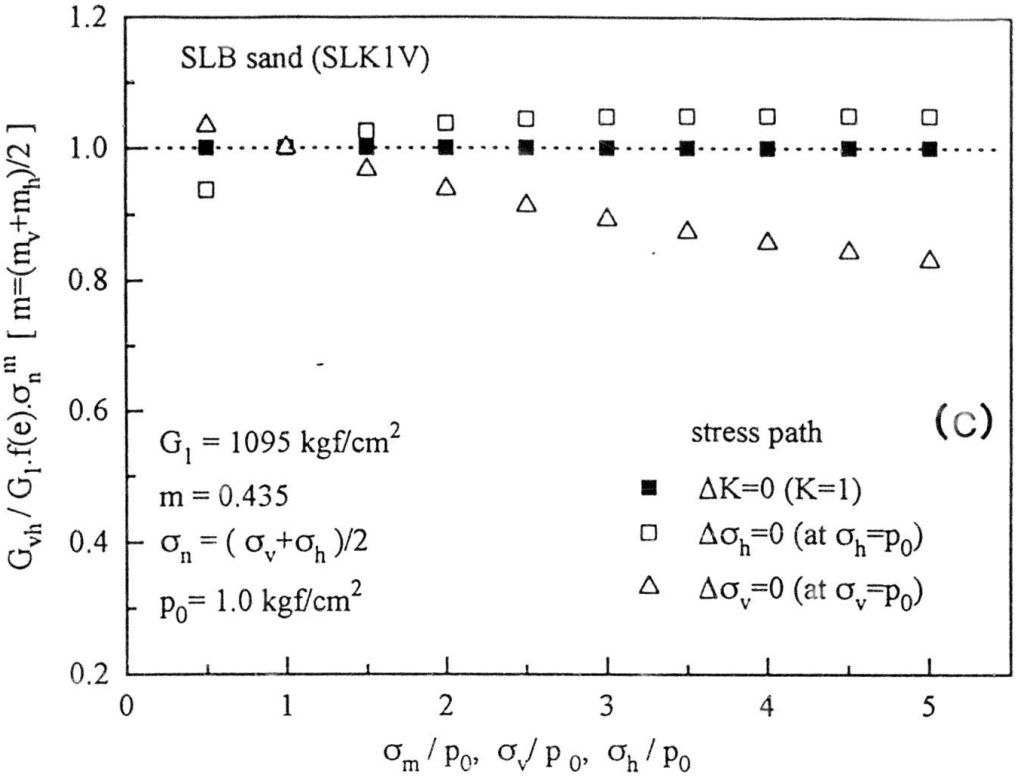

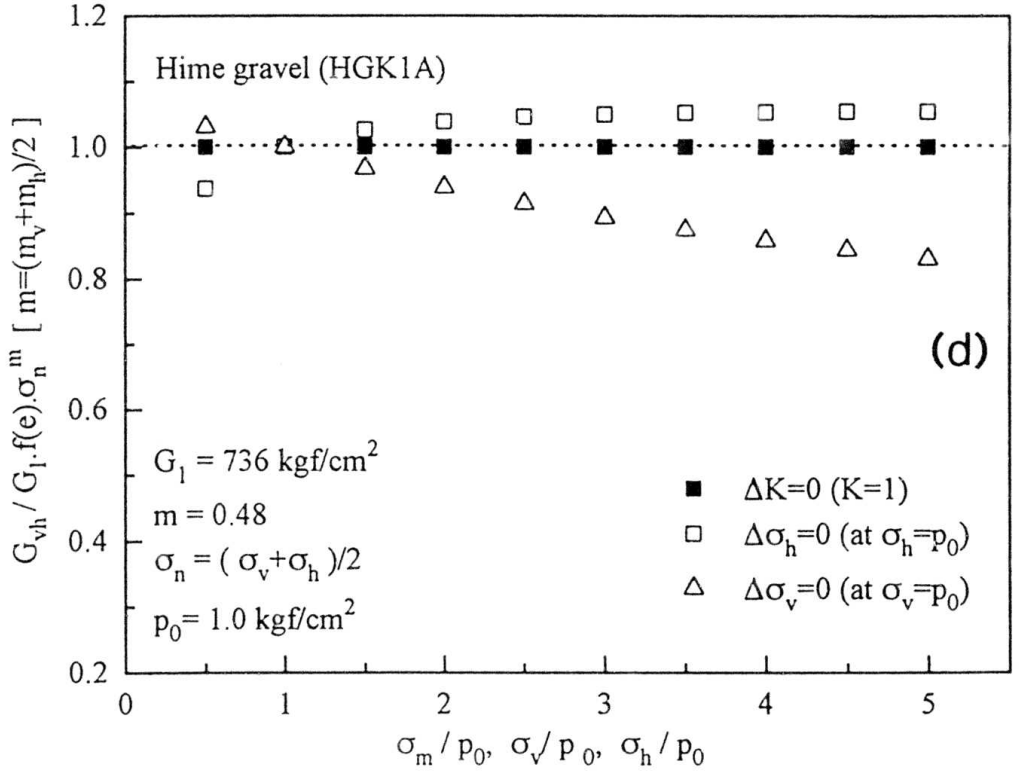

Figs. 4.9: Relationships between normalized G_{vh} and normalized stress level for specimens (c) SLK1A and (d) HGK1A.

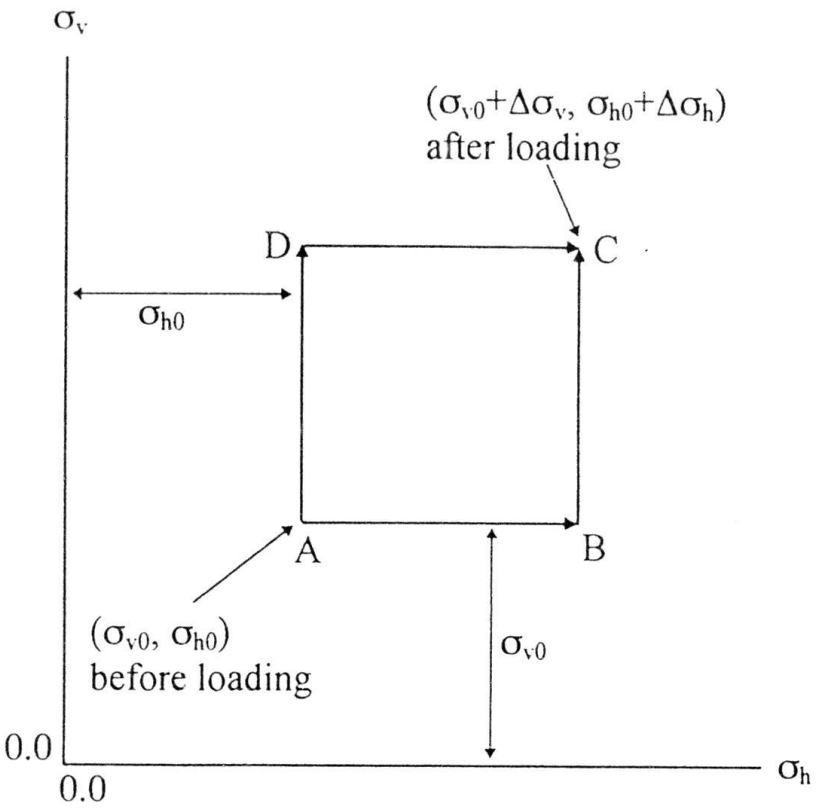

Fig. 4.10: Schematic diagram of stress path to investigate integrated elastic strains.

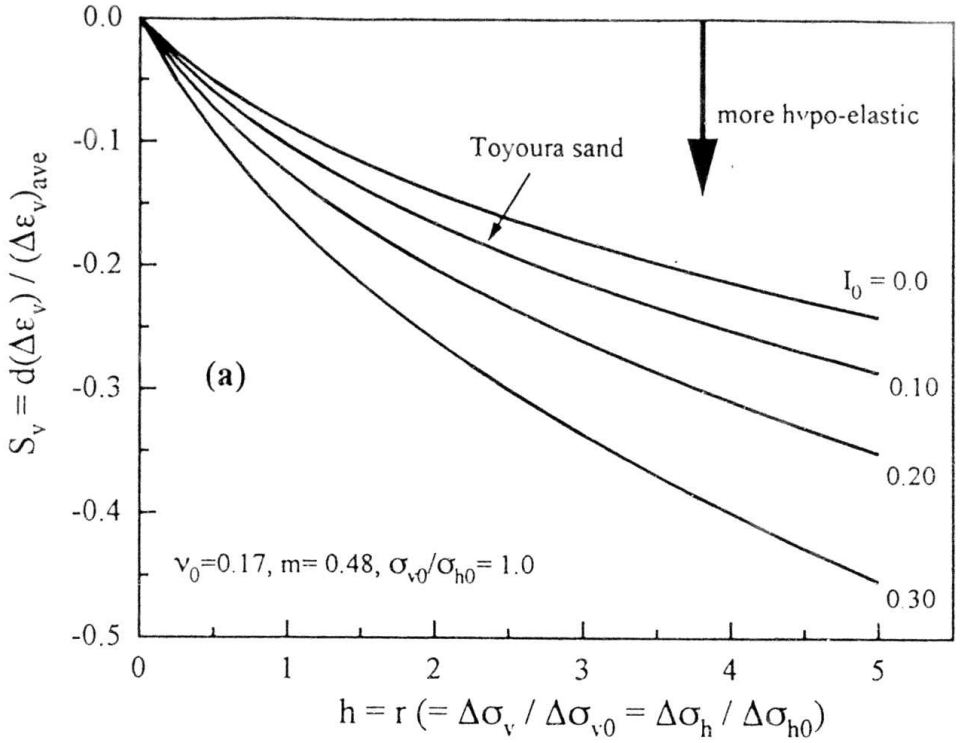

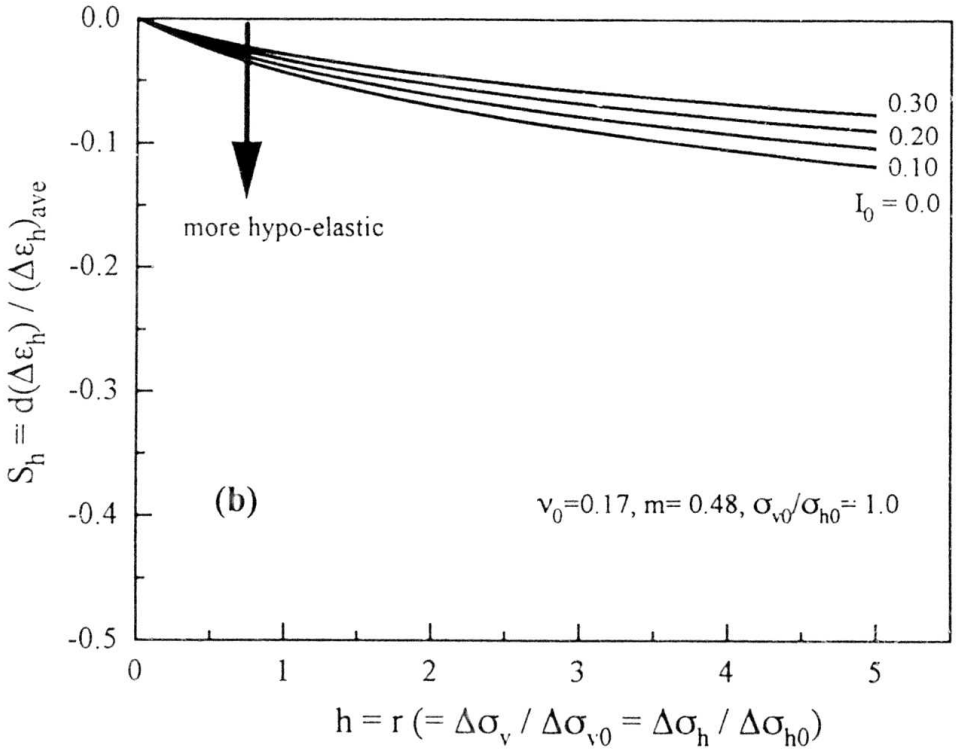

Figs. 4.11: Relationships between (a) S_v and h (= the length of the side of a square stress path), and (b) S_h and h for different values of I_0.

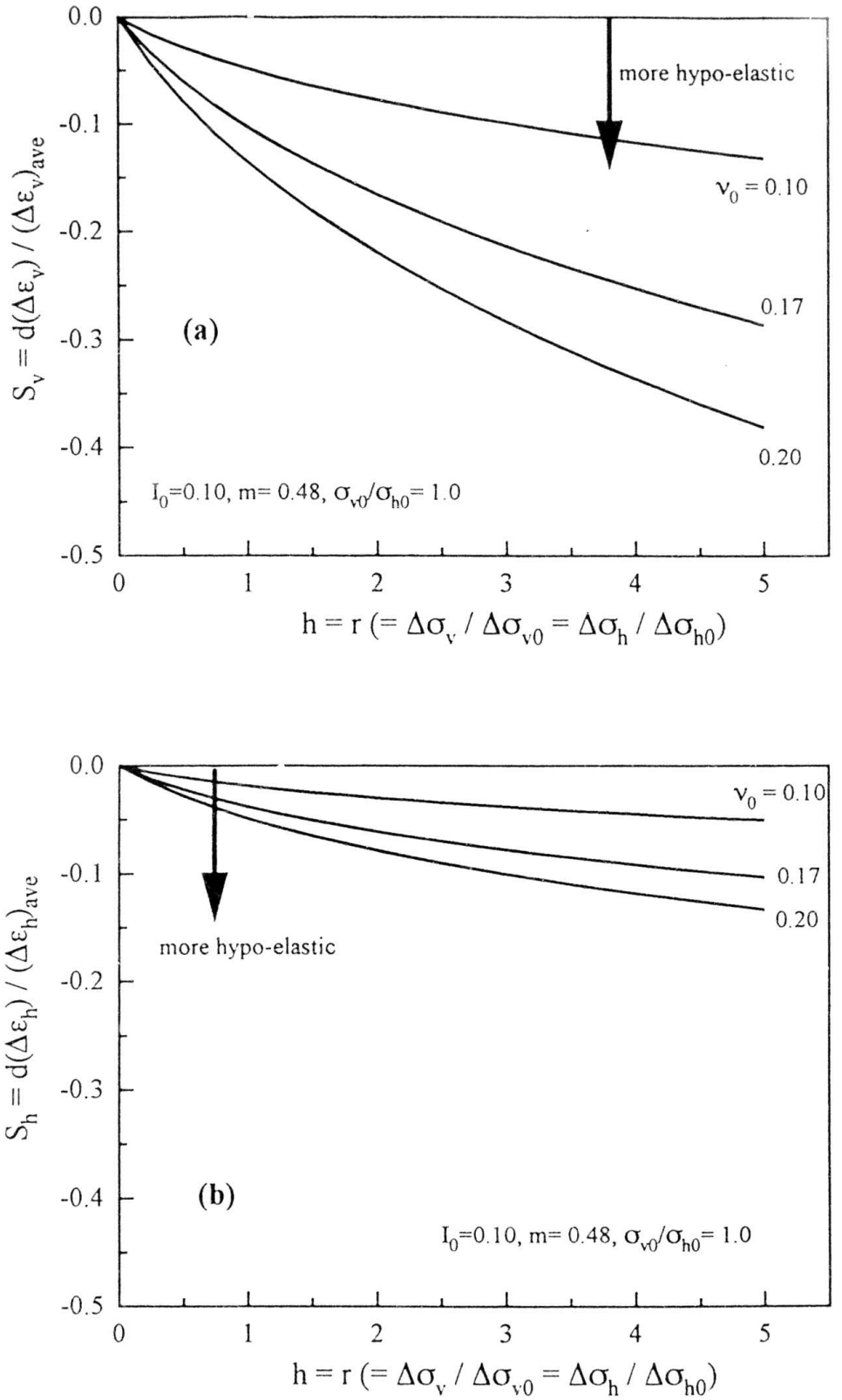

Figs. 4.12: Relationships between (a) S_v and h (= the length of the side of a square stress path), and (b) S_h and h for different values of ν_0.

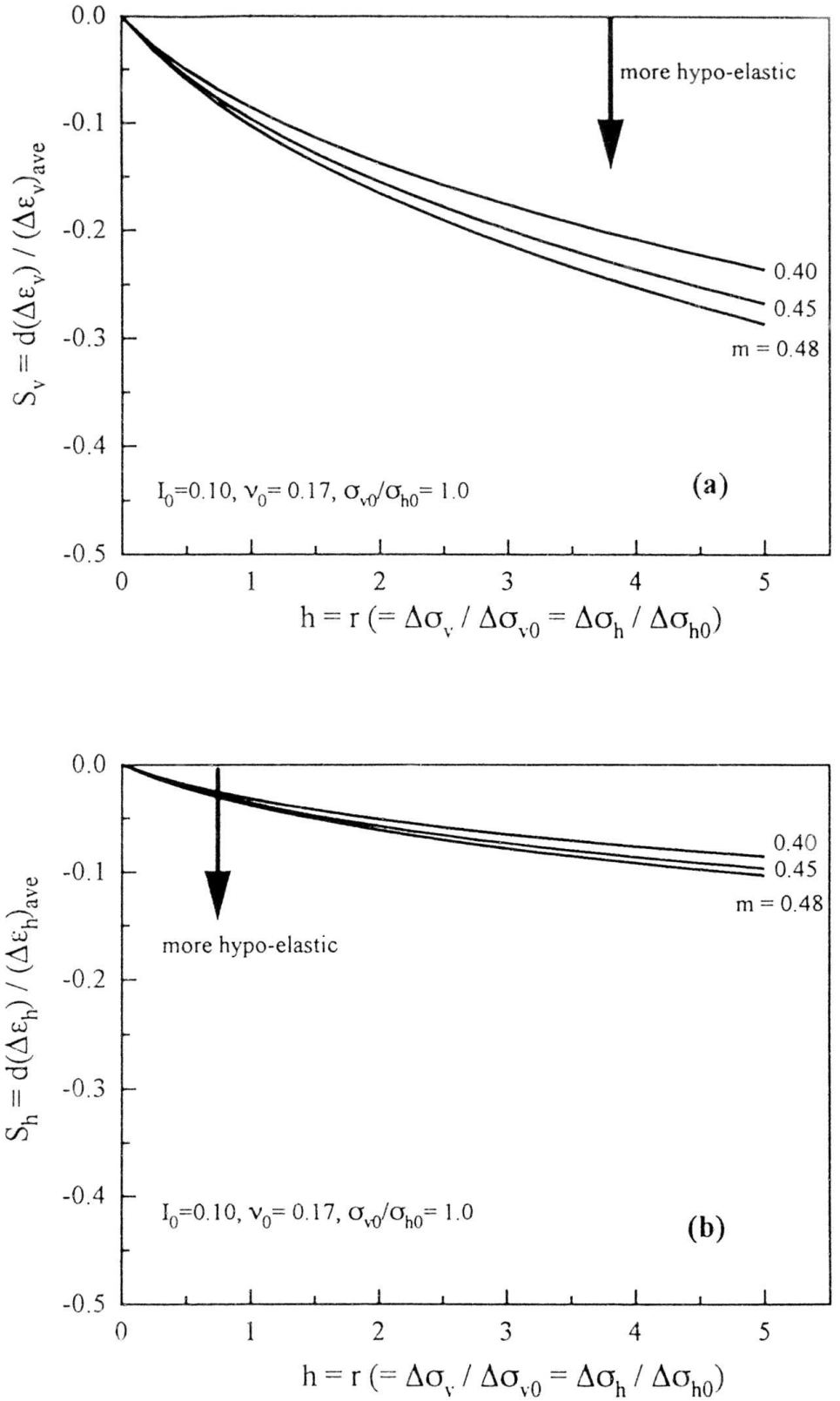

Figs. 4.13: Relationships between (a) S_v and h (= the length of the side of a square stress path), and (b) S_h and h for different values of m (= m_v).

Chapter 5

Effects of stress ratio on Young's modulus for elastic strains during shearing

5.1. Introduction

The Young's modulus E^e of cohesionless soils for elastic major principal strain increment ($d\varepsilon_1^e$) in a certain direction is a rather unique function of the normal stress in the direction of $d\varepsilon_1^e$. Similar results have been observed in various types of static tests (e.g., triaxial tests, plain strain compression tests, torsional shear tests, etc.) and dynamic tests (e.g., body wave test, resonant column test, etc.). Corresponding to the above, the value of E^e defined for axial strain increments in very small unload/reload cycles applied during a triaxial compression (TC) test at a constant lateral stress increases with the increase in the axial stress (Kohata et al. 1994). On the other hand, under a constant mean stress (i.e., $\sigma_v+\sigma_h$= constant), the shear modulus G_{vh}^e decreases as the stress ratio σ_v/σ_h approaches to the peak values [i.e., $(\sigma_v/\sigma_h)_f$ and $(\sigma_h/\sigma_v)_f$] in a torsional shear test and a torsional resonant-column test at a constant confining pressure (Tatsuoka, 1985; Yu and Richart, 1984). The reduction of G_{vh}^e evaluated under anisotropic stress conditions from elastic shear wave velocity measured through a 30-cm large triaxial specimen of undisturbed gravel (taken by means of in-situ freezing method) was even larger at higher stress level (Nishio and Tamaoki, 1990). Yet, they showed that when the principal stress ratio was less than about three, the reduction of G_{vh}^e was rather small. In this chapter, the variation of E^e mostly during a TC test bringing a sand specimen to failure was experimentally examined.

5.2. Testing Procedure

In total thirteen preloaded specimens of four granular materials (Toyoura sand, Ticino sand, Hime gravel and SLB sand), each having a height of 57 cm and a 23 cm x 23 cm in square cross-section, were used for this investigation. Table 5.1 lists the test specimens with some results obtained from TC tests. The specimen SLK1V was reconstituted by vibrator compaction. All the others were prepared by air-pluviation. LDTs were used to measure axial strains, ε_v, free from bedding error as well as lateral strains, ε_h, free from membrane penetration error. Each specimen

was first subjected to one or two unload/reload cycles along isotropic ($K=\sigma_h/\sigma_v=1$) or anisotropic ($K=0.37$) stress path with lateral stress (σ_h) varying in the range between 0.5 kgf/cm^2 to 5.0 kgf/cm^2. Subsequently the specimen was subjected to vertical and horizontal very small cyclic loading (CL) tests at several stress points along the various stress paths: $\Delta K=0$, $\Delta\sigma_v=0$, $\Delta\sigma_h=0$ and $\Delta\sigma_m=0$ (Chapter 3 and 4). Finally, each specimen was sheared (displacement-control test) to failure by TC at $\sigma_v=\sigma_h=0.8$ kgf/cm^2 while applying very small unload-reload cycles at several stress states to determine elastic parameters. Two specimens, TYK0D and SLK0D, were sheared to failure from anisotropic stress state (i.e., $K=0.37$ and $\sigma_h=0.8$ kgf/cm^2). Before final shearing, all other specimens except TYK0D, SLK0D, TYISD, SLISD and HGISD (Table 5.1) were also subjected to stress-control shearing by TC with unload/reload cycles at different stress states from an isotropic stress state (e.g., 0.5, 0.8, and/or 1.0 kgf/cm^2) to a stress ratio R ($=\sigma_v/\sigma_h$) equal to 3.5 to 4.0 (safely below the peak).

In all specimens, the stress states along a given stress path were varied by using the automated system described in Chapter 2, except for TYISD, TYK0D, SLISD, and SLK0D. For the specimens stated latter, stress states were varied manually by controlling σ_v and σ_h simultaneously.

5.3. Test Results and Discussions

Figs. 5.1 to 5.6 show the stress-strain relationships during TC shearing of the test specimens listed in Table 5.1. Of them, Figs. 5.1a, 5.3a and 5.5a show the relationships between the deviatoric stress q ($=\sigma_v-\sigma_h$) and the axial strain ε_v, while Figs. 5.1b, 5.3b and 5.5b show the corresponding relationships between the volumetric strain ε_{vol} ($=\varepsilon_v+2\varepsilon_h$) and ε_v. $q\sim\varepsilon_v$ relationships at lower to very small strain levels are shown in Figs. 5.2, 5.4 and 5.6. For example, Figs. 5.2a, b and c show the $q\sim\varepsilon_v$ relationships (corresponding to Fig. 5.1a) for ε_v= up to 0.1%, 0.01% and 0.005%, respectively. The value of ε_v of each specimen was measured by using LDTs up to 1.25~1.5% of axial strain, while the rest was measured by external gauges. On the other hand, ε_h was measured by lateral LDTs. Table 5.1 lists the peak strength for each specimen in terms of internal friction angle ϕ_{max} [$=\arcsin\{(\sigma_v-\sigma_h)/(\sigma_v+\sigma_h)\}_{max}$]. The initial void ratios of the specimens were measured at a confining pressure of 0.2 or 0.3 kgf/cm^2. Assuming this difference has negligible effects on the test results, the following trends are noticeable.

(a) For a given material, ϕ_{max} increases with the decrease in the void ratio. Three specimens of Toyoura sand (TYISD, TYK0D and TYK1A) and three specimens of Hime gravel (HGISD, HGK0D and HGK1A) show the similar trend.

(b) Despite similar void ratios, the specimens of SLB sand exhibit noticeable difference in ϕ_{max}; the difference was about 2 degrees at the largest. The reason for this was not clear. On the other hand, SLK1V and SLK1A showed similar peak although they were reconstituted by different methods.

(c) Volume change of specimen was dilative (i.e., ε_{vol} is negative) in all cases except the very initial part in some cases.

(d) Preloading (along complicated stress paths) increased linearity in the stress-strain relationship (Figs. 5.2c, 5.4c and 5.6c).

Figs. 5.7a and b show the effects of bedding error and membrane penetration error during TC performed on TYISD specimen for the axial strain ranges up to ε_v= 0.12% and 0.01%, respectively. The $q\sim\varepsilon_v$ relationships are plotted for ε_v measured by both LDTs (locally) and gap-sensors (GS) (externally). In the same figures, the respective $\varepsilon_h\sim\varepsilon_v$ relationships are also plotted, where the values of ε_h were measured locally by LDTs and externally by GSs. The lateral strains measured along the planar surface of specimen by LDTs are free from the bedding (i.e., membrane penetration) error effects, but those measured with GS placed in the direction normal to the specimen surface involved bedding error. Figs. 5.7a and b show that despite a large size of the specimen, the externally measured strains (both vertical and lateral) are unreliable, and the effects of bedding error due to membrane penetration is not negligible even during TC at a constant confining pressure. Membrane penetration error is usually more severe in a test when the confining pressure changes (e.g., isotropic consolidation test, horizontal CL test) and the coarser the material the larger the error. The effects of this error during consolidation test are described in Tatsuoka and Kohata (1995).

Small Strain Stiffness During TC

Though the primary loading curves (as seen in Figs. 5.1 to 5.6) may be noticeably affected by preloading, it is considered that the behavior during small unload/reload cycles are not. Figs. 5.8a and b show two typical $\sigma_v\sim\varepsilon_v$ relations in unload/reload cycles at lower and higher stress levels,

respectively, of SLISD specimen (see Fig. 5.5a). During a typical unload/reload cycle, the unloading and reloading parts at low shear stress level (Fig. 5.8a) are indistinguishable, whereas the difference is clear at high shear stress level (Fig. 5.8b). The latter behavior is due to the involvement of noticeable plastic/creep strains. This phenomena was observed more-or-less in all cyclic test data. Therefore, the slopes of unload/reload variations were obtained separately by linear regression for the same amplitude of vertical stress for unloading and reloading. Further, the true elastic Young's modulus E^e was obtained as illustrated in Fig. 5.9, namely;

$$E^e = 2/\left(1/E_{unload} + 1/E_{reload}\right) \tag{5.1}$$

This is obtained from the following Eqs. (5.2) to (5.4). For an axial stress change $\Delta\sigma_v$, the elastic strain amplitude is:

$$\Delta\varepsilon_v^{\ e} = \Delta\sigma_v / E^e \tag{5.2}$$

When the same plastic axial strain increment $\Delta\varepsilon_v^p$ is involved during unloading and reloading, the axial strain increments are obtained, respectively, as:

$$\left(\Delta\varepsilon_v\right)_{unload} = \Delta\varepsilon_v^{\ e} - \Delta\varepsilon_v^{\ p} = \Delta\sigma_v / E_{unload} \tag{5.3}$$

$$\left(\Delta\varepsilon_v\right)_{reload} = \Delta\varepsilon_v^{\ e} + \Delta\varepsilon_v^{\ p} = \Delta\sigma_v / E_{reload} \tag{5.4}$$

The values of E^e (=E_v), E_{unload} and E_{reload} for each test were normalized by dividing the Young's modulus for elastic axial strains obtained from the empirical relationship established based on the results of the small cyclic tests performed at a range of stress ratio $1/2 \le \sigma_v/\sigma_h \le 2.0$ (Chapters 3 and 4);

$$E^e = E_1 f(e) \sigma_v^{\ m} \tag{5.5}$$

where $f(e) = (2.17-e)^2 / (1+e)$, and E_1 and m are the elastic parameters given in Table 5.1 for each specimen. The normalized (after being divided by the right hand side term of Eq. (5.5)) Young's moduli are plotted against the stress ratio σ_v/σ_h in Figs. 5.10a and b for specimens TYISD and TYK0D, respectively, and in Figs. 5.11a and b for SLISD and SLK0D, respectively. In each case, the variation of a constant Young's modulus E^e, which was the initial Young's modulus at the

start of shearing, divided by the corresponding value of E^e from Eq. 5.5 was also plotted for comparison. The following trends may be noted:

(i) The difference between the measured values of E_{unload} and E_{reload} becomes more noticeable as σ_v/σ_h increases probably due to the involvement of larger creep deformation in an unload/reload cycle. This result suggests that the use of E_{unload} overestimate the true Young's modulus E^e.

(ii) The measured Young's modulus E^e increases with σ_v/σ_h to its maximum value at a certain level of σ_v/σ_h, followed by a noticeable decrease. Therefore, Eq. (5.5) overestimates the elastic Young's modulus E^e measured during TC as approaching the peak stress state.

(iii) Use of constant E^e is unrealistic, and is always under-estimating the true Young's modulus.

Load-control TC tests with very small unload-reload cycles (also load-control) at various stress states were performed on the rest of the specimens listed in Table 5.1 to investigate into the effects of the following factors on the E^e~σ_a/σ_v relationship:

- the mode of loading (i.e., load-control or displacement control).
- the initial stress state from which TC was performed.
- the creep rate during shearing.

Each specimen was subjected to load-control multi-stage TC tests. Each stage included a TC test starting from an isotropic stress state (σ_{str}) to a stress state at σ_v/σ_h equal to 3.5 to 4.0, followed by unloading to the previous isotropic stress state σ_{str}. The specimen was loaded (or unloaded) isotropically to the new σ_{str} to perform the next stage TC, and so on. For the first stage, σ_{str} was 0.8 kgf/cm^2, then it was 1.0 kgf/cm^2, and at last, it was 0.5 kgf/cm^2. Six cycles of very small axial stress amplitude unloading-reloading (without loading to virgin state) were applied at various stress states during each TC. At each stress state, a specified time, forty seconds, was allowed to elapse right before the application of the unload/reload cycles that helped reducing the creep effect (if any) on the measured E^e. All the above tests during a given TC were performed continuously at a single run by using the automated system described in Chapter 2. During shearing, load was applied at a constant rate of 0.05 kgf/cm^2/minute, while very small CL tests were performed at a frequency of about 0.1 Hz. After the completion of load-control multi-stage TC tests, each specimen was brought to the neutral stress state at $\sigma_v=\sigma_h=0.8$ kgf/cm^2. The load-control system was then replaced with the displacement-control system to continue the final

shearing to failure (and also to apply the unload/reload cycles on the way). Tests were performed at a constant rate of axial straining of 0.03%/minute during which no time was dedicated to creep deformation to occur.

Figs. 5.12 through 5.14 show the relationships between the measured Young's modulus E^e divided by the E^e value obtained from the empirical equation (Eq. 5.5) and the stress ratio (σ_v/σ_h). Of them, Figs. 5.12a and b show the relationships for TYK1A and TCK1A, respectively; Figs. 5.13a and b for HGK1A and HGK0A, respectively, and Figs. 5.14a and b for SLK1V and SLK0A, respectively. The following trends can be observed.

(i) TC loading of previous stages had little effect on the E^e values evaluated at the current TC stage. However, in some cases, E^e at a given stress state decreased by a maximum of about 7% of the initial value, but even though the respective measured E^e~σ_v relationship follows essentially the empirical rule of Eq. (5.5) with the current value of E^e at a reference σ_v.

(ii) The measured E^e~σ_v/σ_h relationships obtained from two modes of loading (load- and displacement-controlled) are very similar to each other.

(iii) The measured E^e~σ_v/σ_h relationships are very similar during TC at different σ_{str}. That is, E^e increases with σ_v, attains a maximum at a particular σ_v/σ_h (which is around at 3 to 4), and then starts decreasing due to the effects which can be termed as 'damage.' Damage is probably due to a microscopic change in the fabric as that the number of inter-particle contacts in the axial direction decreases drastically as approaching the failure state. The effects of damage on E^e were very clear when deformation became large near the peak state in the displacement-control tests. Because of safety purpose, load-control shearing was not continued for large deformation at near peak stage where damage in E^e should be significant; otherwise failure of such a large specimen during a load-control test could be catastrophic with subsequent damage to the measuring devices. Nevertheless, in some instances (e.g., Fig. 5.14a), initiation of the damage to E^e can be seen more-or-less at the same stress level as was observed from a displacement-control test.

Figs. 5.15a and b show the relationships between the normalized E^e (=E_v or E_h) and the principal stress ratio obtained from the specimen TYK02 that subjected to both vertical and

horizontal very small CL tests at a given stress state during load-control triaxial compression and extension tests. The preloaded specimen was sheared first in triaxial compression (TC) from $\sigma_v=\sigma_h=1.0$ kgf/cm^2 to $\sigma_v/\sigma_h=3.5$ at a constant σ_h. After unloading to $\sigma_v=\sigma_h=1.0$ kgf/cm^2, the specimen was subjected to triaxial extension (TE) up to $\sigma_h/\sigma_v=3.5$ at a constant $\sigma_v=1.0$ kgf/cm^2. During TC and TE, six vertical unload/reload cycles at constant σ_h and three horizontal unload/reload cycles at constant σ_v were applied at each of the various stress states to evaluate E_v and E_h, respectively. For evaluating E_h, the Poisson's ratio ν_{hh} was assumed a constant (= 0.163), which was equal to the average of ν_{vh} values measured along the isotropic stress path (Chapter 3). Fig. 5.15a shows the relationship between normalized measured E^e (=E_v or E_h) and σ_v/σ_h during TC, where E_v was normalized by Eq. (5.5) and E_h by dividing it with 'E_h at $\sigma_v=\sigma_h=1.0$ kgf/cm^2' (since according to the empirical equation (Eq. 5.5), E_h is independent of the variation of σ_v during TC). On the other hand, Fig. 5.15b shows the similar relationship during TE. The normalized measured E^e was plotted against σ_h/σ_v; here, the measured E_h values were normalized by dividing it with $E_h= E_1.f(e).\sigma_h^{m_h}$ — a similar form of Eq. 5.5. For E_h~σ_h variation, $E_1= E_h/f(e)=1595$ kgf/cm^2 at $\sigma_v=\sigma_h=1.0$ kgf/cm^2 and $m= m_n= 0.453$. The value of E_v obtained during TE was divided by 'E_v at $\sigma_v=\sigma_h=1.0$ kgf/cm^2' (since E_v is independent of the variation of σ_h during TE).

Like E_v~σ_v/σ_r relationship during TC, E_h also increases with σ_h during TE; the rate of increase in E_h gradually decreases as σ_h/σ_v approaches to peak, E_h attains the maximum at around $\sigma_h/\sigma_v \approx 3.0$ beyond which E_h starts decreasing. Damage to E_h during TC at constant σ_h (similarly E_v during TE at constant σ_v) was also observed at the same stress level where E_v during TC (E_h during TE) starts experiencing. In both cases, the rate of damage was less than that occurred to the Young's modulus in the direction of the major principal stress.

Dominating plastic behavior at higher stress levels could be the major reason for damage to E^e. In all cases, the damage to Young's modulus was invariably observed at a major-to-minor principal stress ratio in the range of 3 to 4. If we look back to Figs. 5.1a, 5.3a and 5.5a, it was the range of stress ratio (i.e., $\sigma_v/\sigma_h= 3$ to 4 for TC) at which plastic strain started increasing at a high rate for all the stress-strain curves, beyond which the stress-strain relationships became more non-linear at an increasing rate. It is likely that continuously re-orientation of grains associated with large plastic strains keeps going on while destroying the initial fabric. Alone creep

deformation is not responsible for the observed damage as similar trends were observed even after allowing major portion of creep to occur at a given stress level before the evaluation of E^e. On the other hand, plastic flow also occurs simultaneously in the minor principal strain direction as plastic major strain increases, which can be realized from the rather linear ε_{vol}~ε_v relationships shown in Figs. 5.1b, 5.3b and 5.5b. As a result, E^e (either E_h or E_v) evaluated in the minor stress direction during either TC or TE also experienced damage, to some extent, at the similar higher stress ratio where E^e value in the major principal directions was damaged.

5.4. Summaries

(1) The peak angle of friction of all the specimens (medium dense to dense) of all four particulate granular materials is observed to vary in a narrow range of 4 deg. (i.e., ϕ_{max}= 40 to 44 deg.). Within this narrow range, the specimens of Toyoura sand and Hime gravel exhibit a tendency of increasing ϕ_{max} with density. However, SLB sand shows that ϕ_{max} can be varied for about 2 deg. for a given void ratio.

(2) Linear elastic range in the stress-strain relationships during TC was observed to increase as a result of preloading.

(3) Young's modulus E^e defined for elastic major principal strain increments $d\varepsilon_1^e$ is found to increase with the normal stress in the direction of $d\varepsilon_1^e$. However, the rate of increase in E^e diminishes gradually as the major-to-minor principal stress ratio during TC and TE exceeds 3 to 4, and eventually E^e starts decreasing as approaching the failure.

(4) Young's modulus in the minor stress direction during TC and TE also exhibits the similar tendency. That is, according to the model for elastic Young's modulus discussed in Chapter 4, the Young's modulus E^e in the direction of σ_3 is independent of increase in the major principal stress σ_1 during TC and TE. However, this rule holds good up to a similar major-to-minor principal stress ratio (i.e., 3 to 4), beyond which E^e starts decreasing due to damage to the initial fabric caused by large increment of plastic straining.

Table 5.1: List of the materials.

Material	Specimen	[a]σ_c kgf/cm^2	[b]e	[*]e_1	E_1 kgf/cm^2	m	ϕ_{max} deg.
Toyoura sand	TYISD	0.2	0.68	0.662	2040	0.49	43.56
	[c]TYK0D	0.2	0.70	0.691	1920	0.49	42.50
	TYK1A	0.2	0.64	0.624	2030	0.486	44.64
	TYK02	0.3	0.65	--	1820	0.494	--
Hime gravel	HGK1A	0.3	0.51	0.503	2080	0.511	40.12
	HGK0A	0.3	0.49	0.479	2188	0.509	42.80
	HGISD	0.2	0.47	--	--	--	41.20
SLB sand	SLISD	0.2	0.52	0.516	2875	0.42	43.33
	[c]SLK0D	0.2	0.52	0.511	2800	0.42	42.70
	SLK1A	0.3	0.52	0.515	2890	0.474	40.70
	[d]SLK1V	0.3	0.524	0.518	3220	0.452	40.90
	SLK0A	0.3	0.52	--	2810	0.475	--
Ticino sand	TCK1A	0.2	0.58	0.571	1510	0.530	44.50

[a]: initial confining pressure at which void ratio (e) was measured.
[b]: initial void ratio.
[*]: void ratio immediately before TC to failure.
[c]: specimens were sheared to failure from σ_h=0.8 kgf/cm^2 with K=0.37.
[d]: specimen was reconstituted by vibrator-compaction.
--: reliable data was not obtained due to instrumental problem.

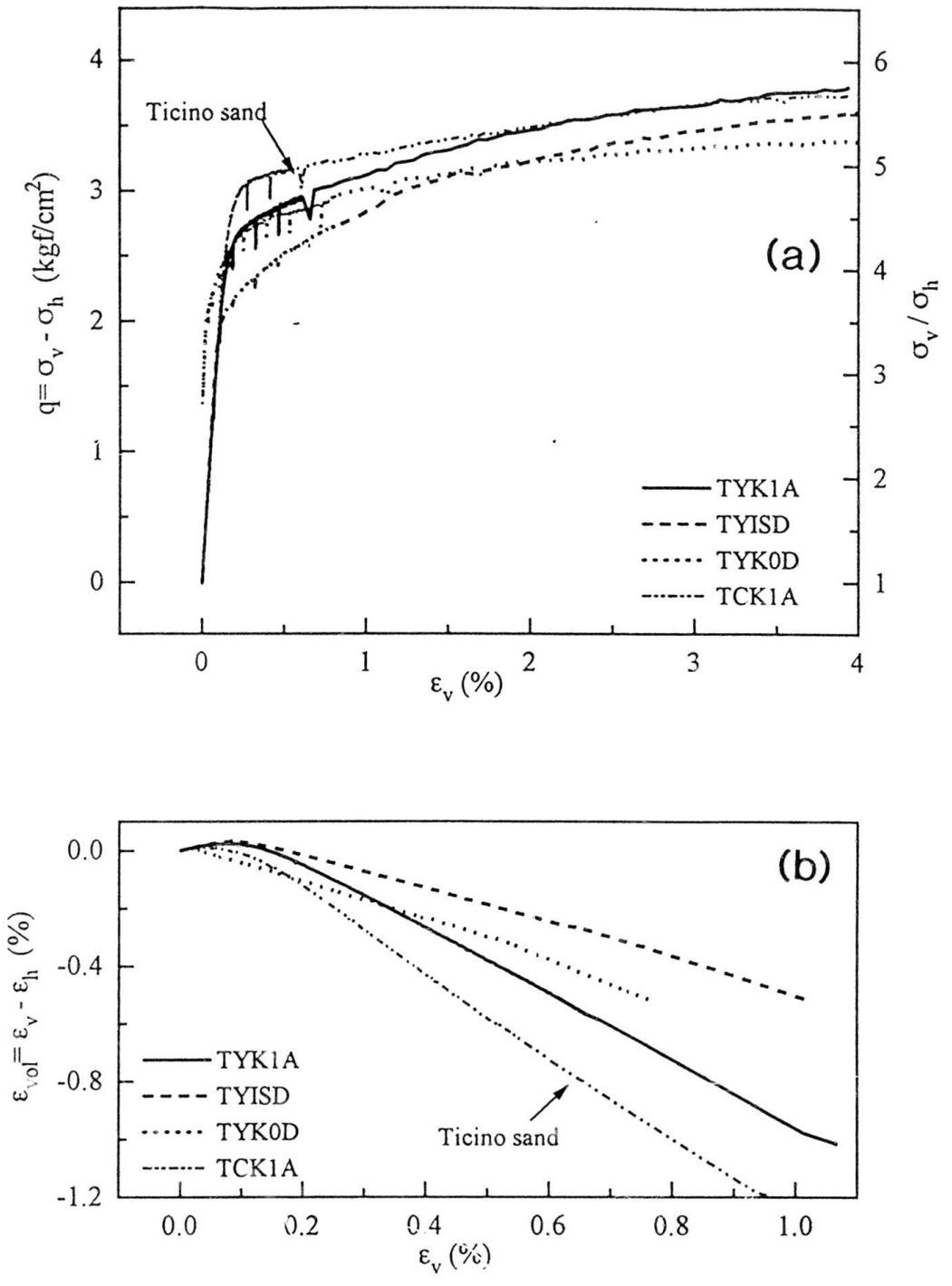

Figs. 5.1: The relationships between (a) q ($=\sigma_v-\sigma_h$) and ε_v, (b) volumetric strain (ε_{vol}) and ε_v during TC on Toyoura and Ticino sands specimens.

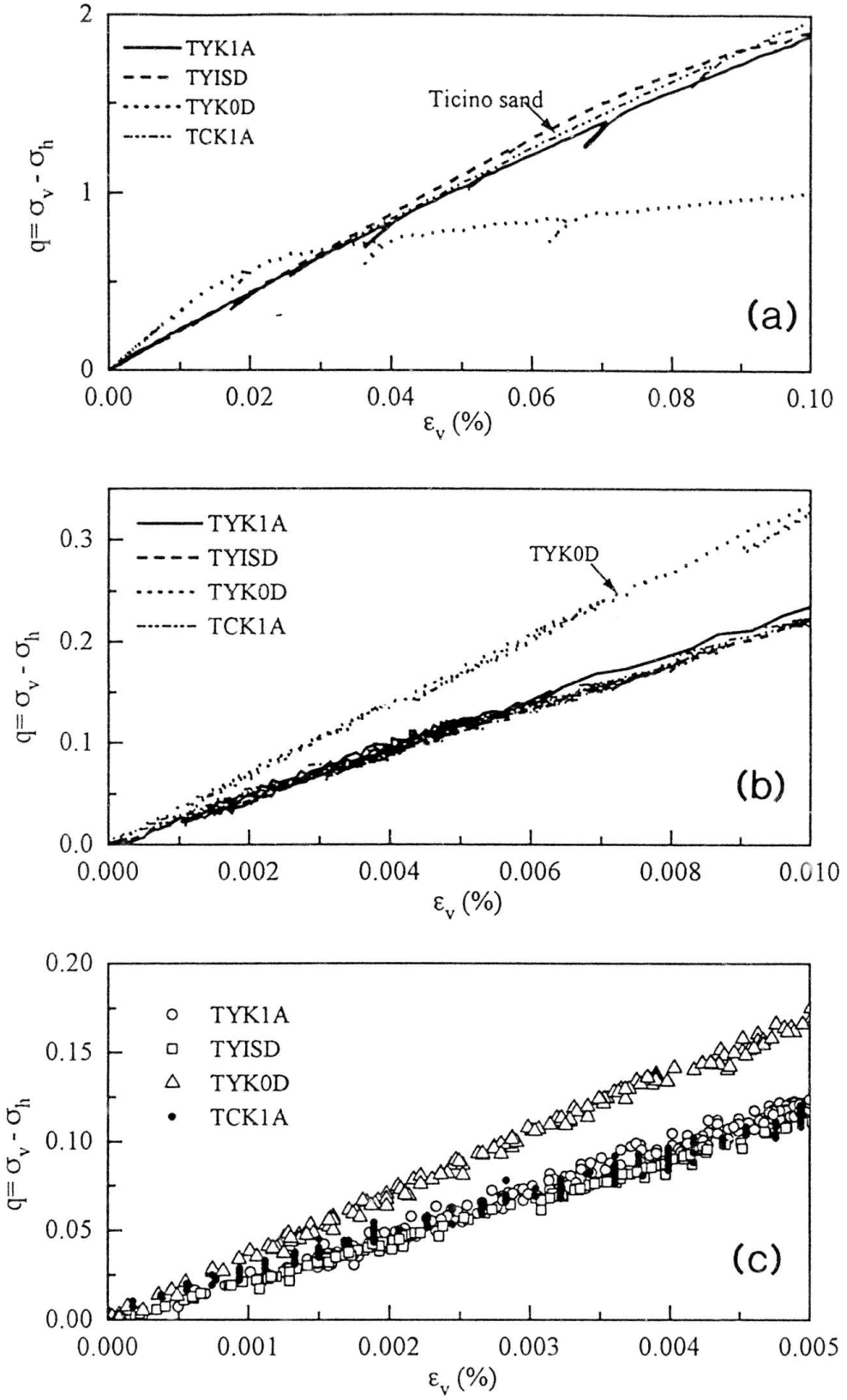

Figs. 5.2: $q \sim \varepsilon_v$ relationships of Toyoura and Ticino sands specimens at small strain levels up to (a) $\varepsilon_v = 0.10\%$, (b) $\varepsilon_v = 0.01\%$ and (c) $\varepsilon_v = 0.005\%$.

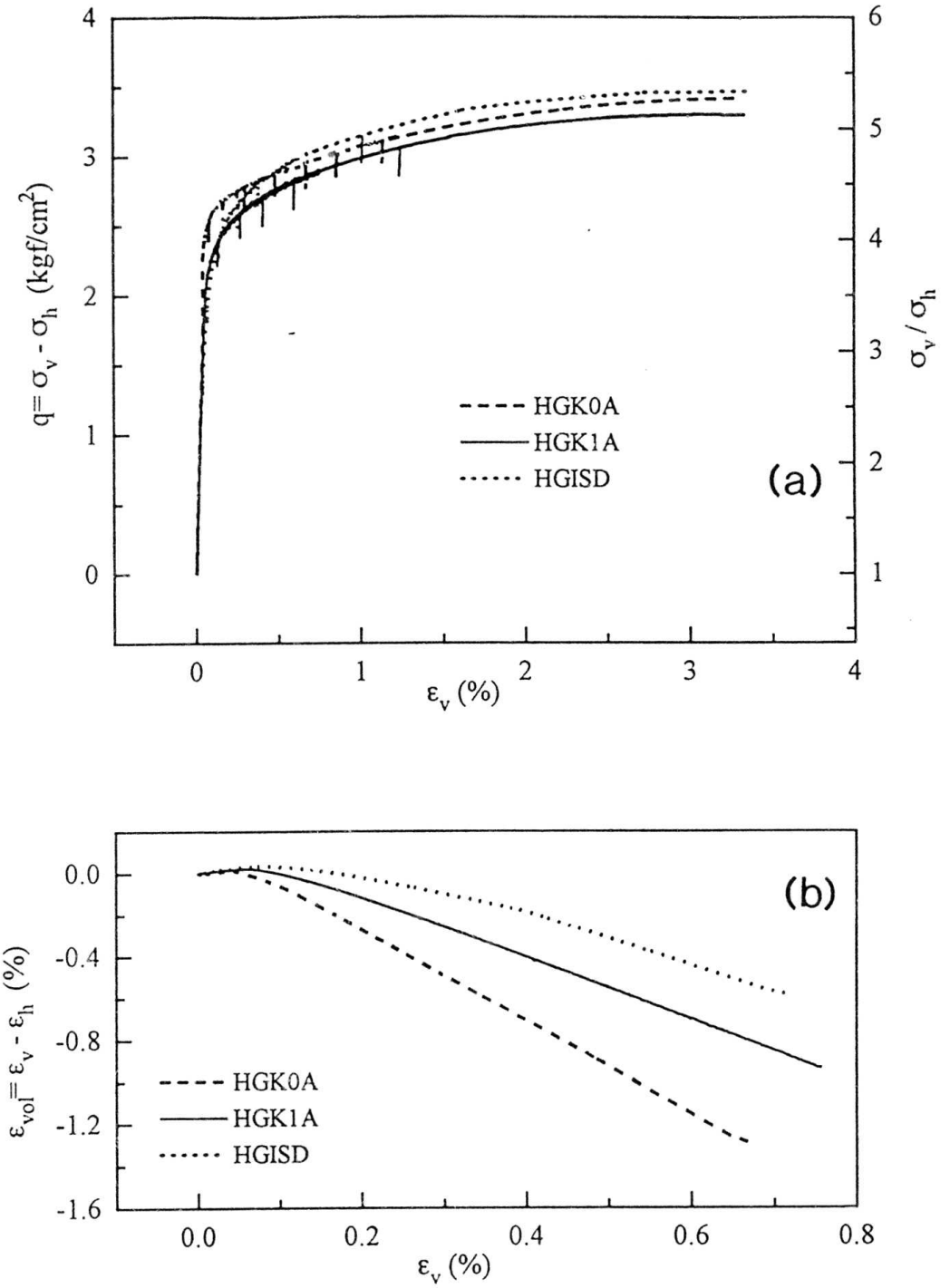

Figs. 5.3: The relationships between (a) q ($=\sigma_v-\sigma_h$) and ε_v, (b) volumetric strain (ε_{vol}) and ε_v during TC on Hime gravel specimens.

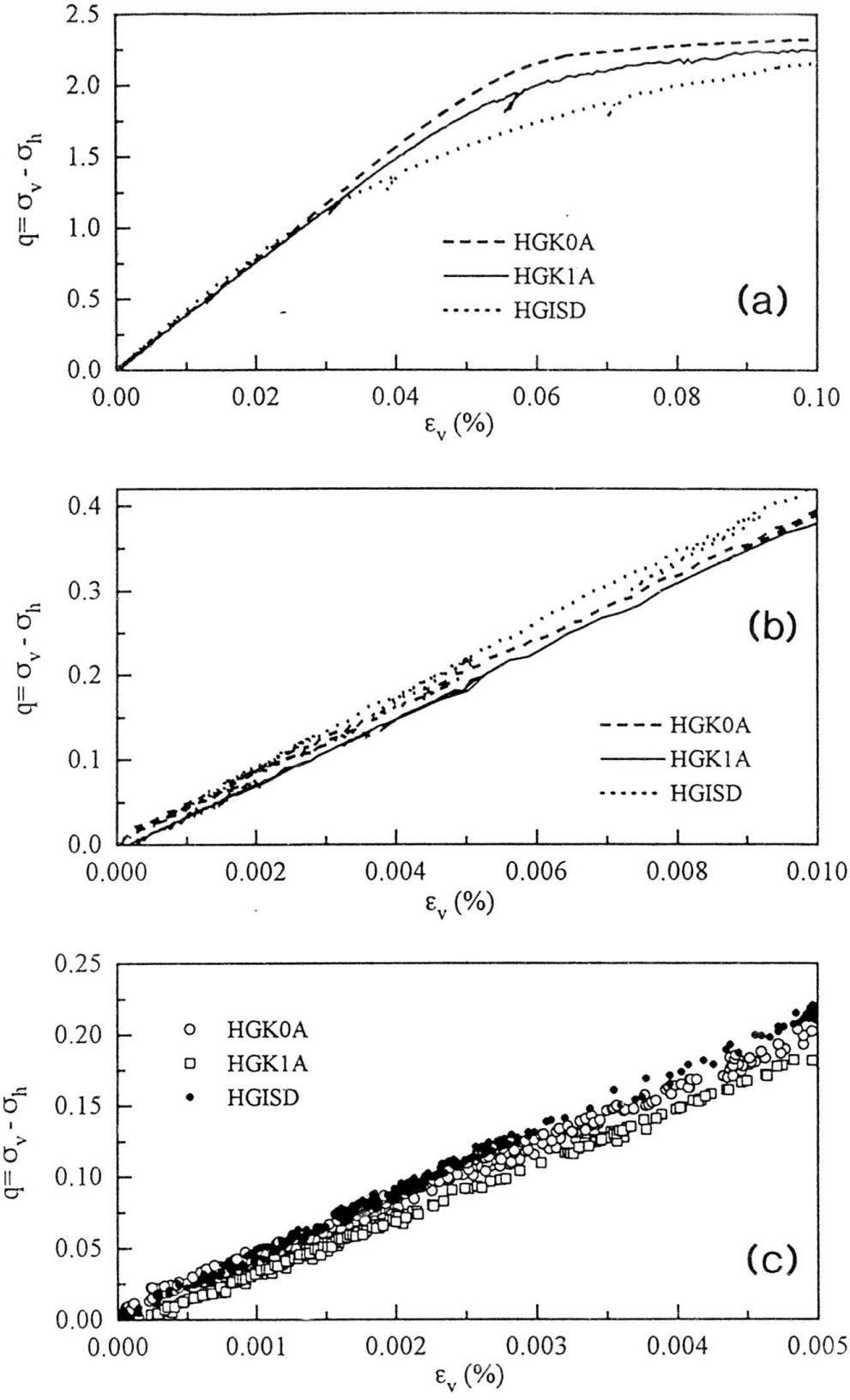

Figs. 5.4: $q \sim \varepsilon_v$ relationships of Hime gravel specimens at small strain levels up to (a) ε_v= 0.10%, (b) ε_v= 0.01% and (c) ε_v= 0.005%.

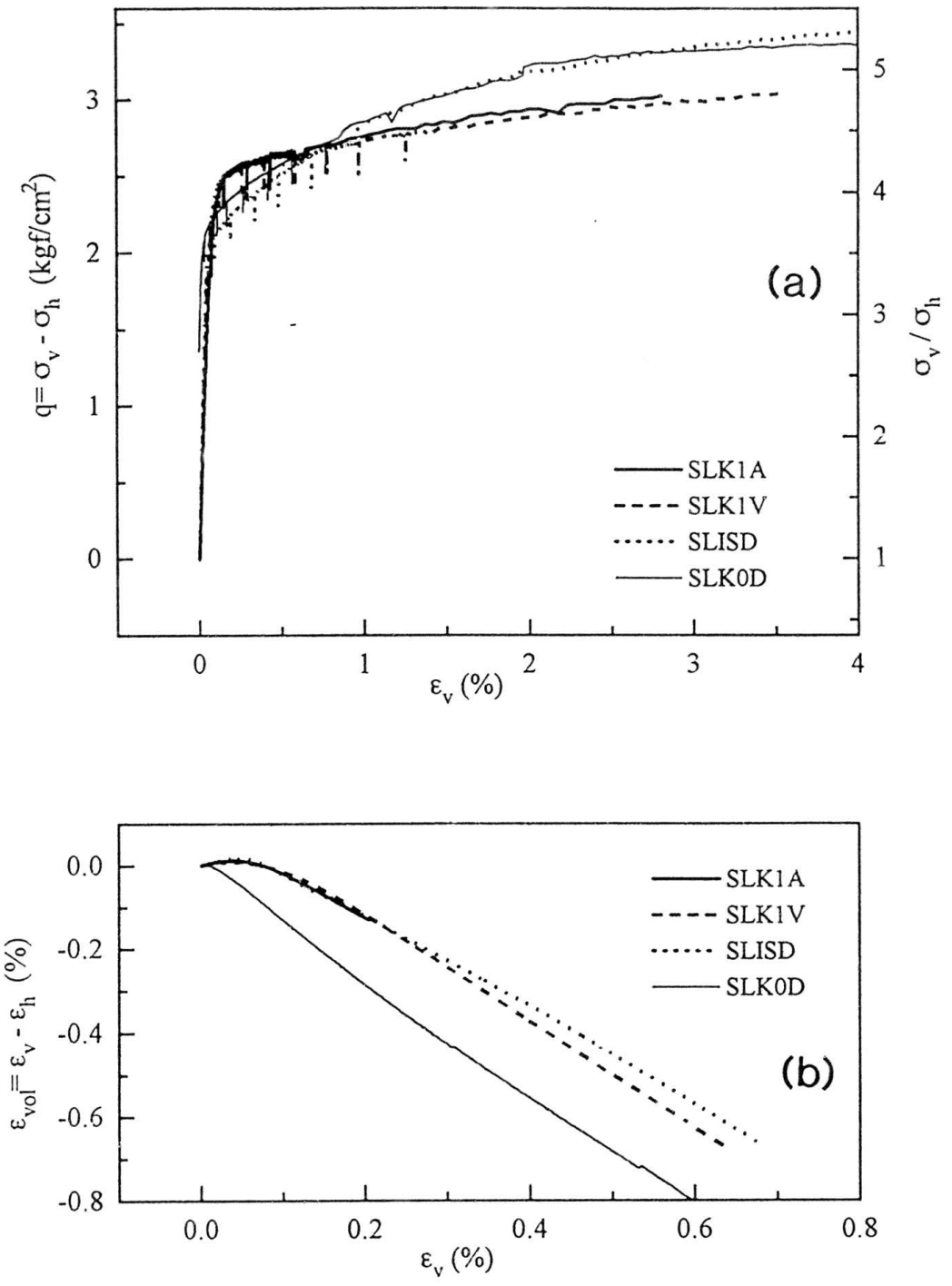

Figs. 5.5: The relationships between (a) q ($=\sigma_v-\sigma_h$) and ε_v, (b) volumetric strain (ε_{vol}) and ε_v during TC on SLB sand specimens.

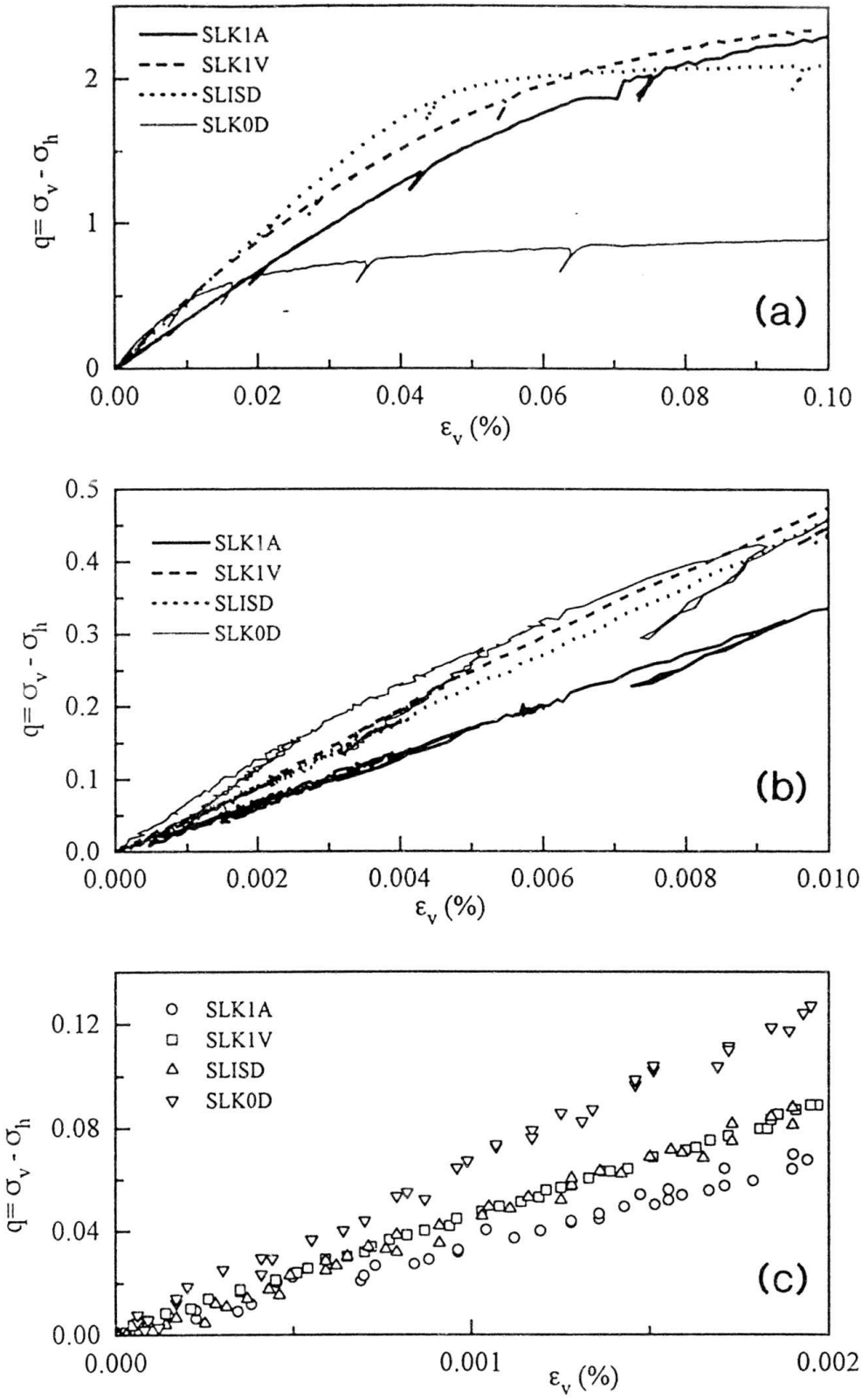

Figs. 5.6: $q \sim \varepsilon_v$ relationships of SLB sand specimens at small strain levels up to (a) ε_v= 0.10%, (b) ε_v= 0.01% and (c) ε_v= 0.002%.

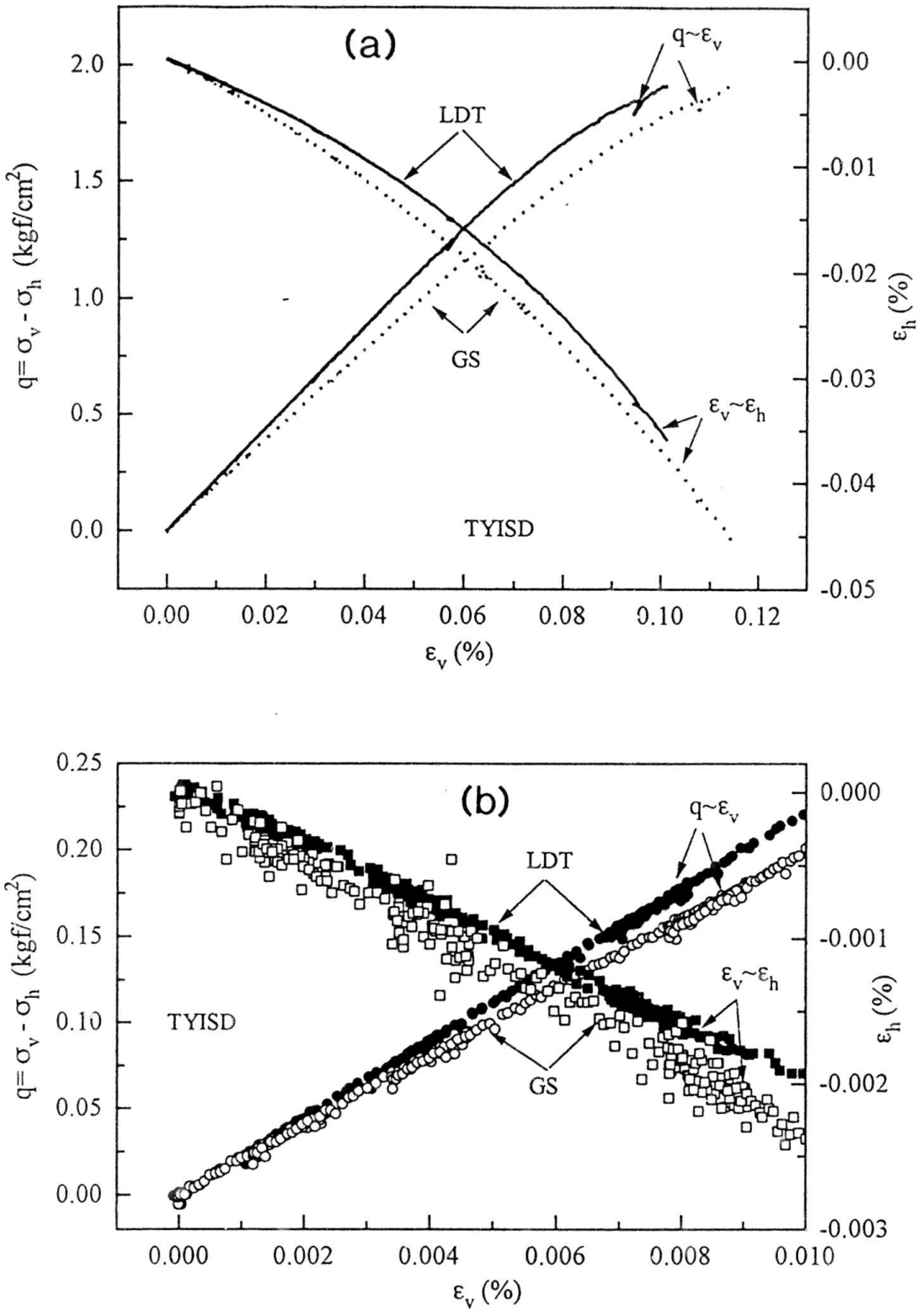

Figs. 5.7 $q\sim\varepsilon_v$ and $\varepsilon_h\sim\varepsilon_v$ relationships of TYISD specimen to demonstrate the existence of bedding error in ε and membrane penetration error in ε_h during TC at small strain levels up to (a) ε_v (LDT)= 0.10%, (b) ε_v (LDT)= 0.01%.

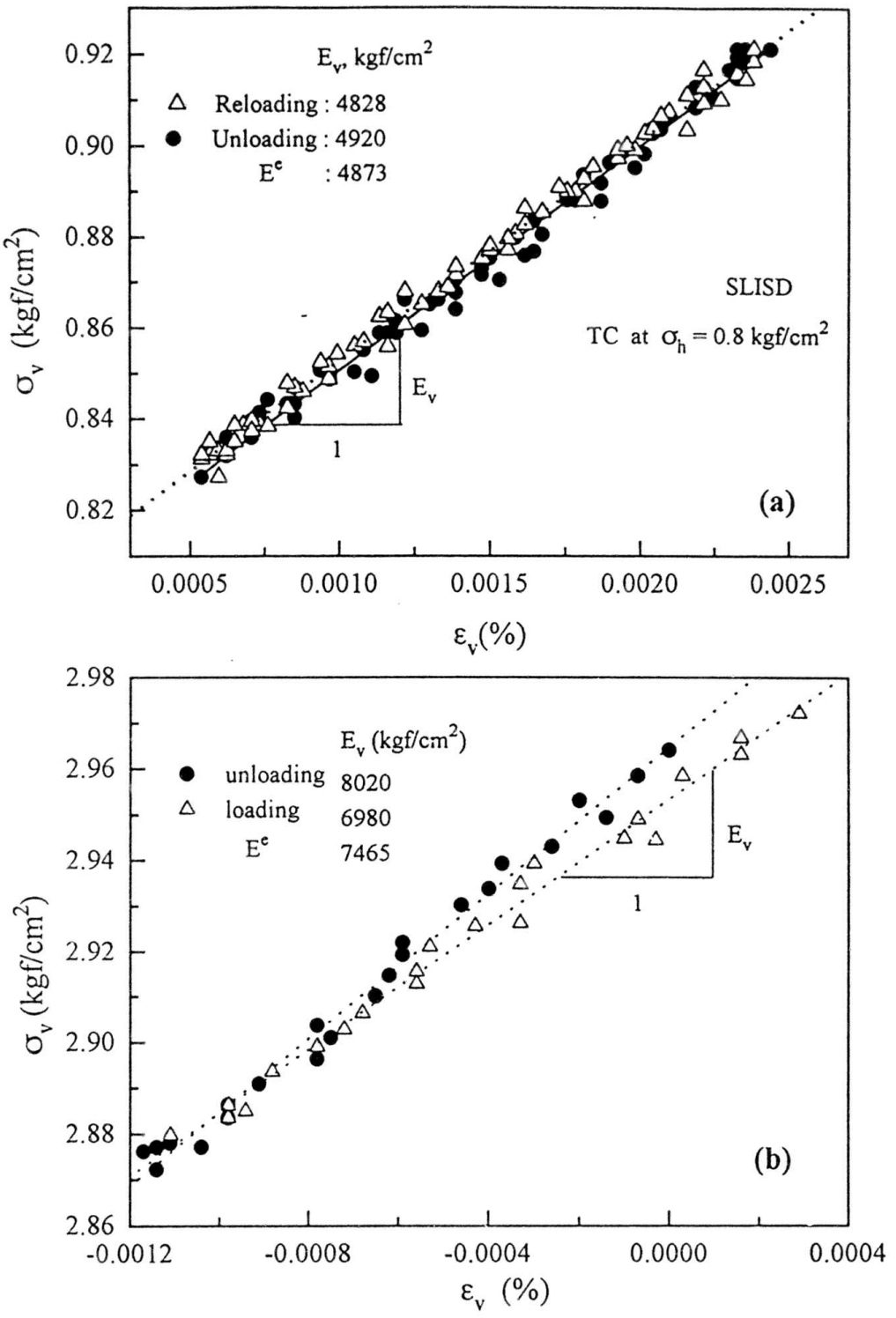

Figs. 5.8: σ_v~ε_v relationships of typical unload-reload cycles during TC on SLISD specimen at (a) low stress level, (b) at high stress level.

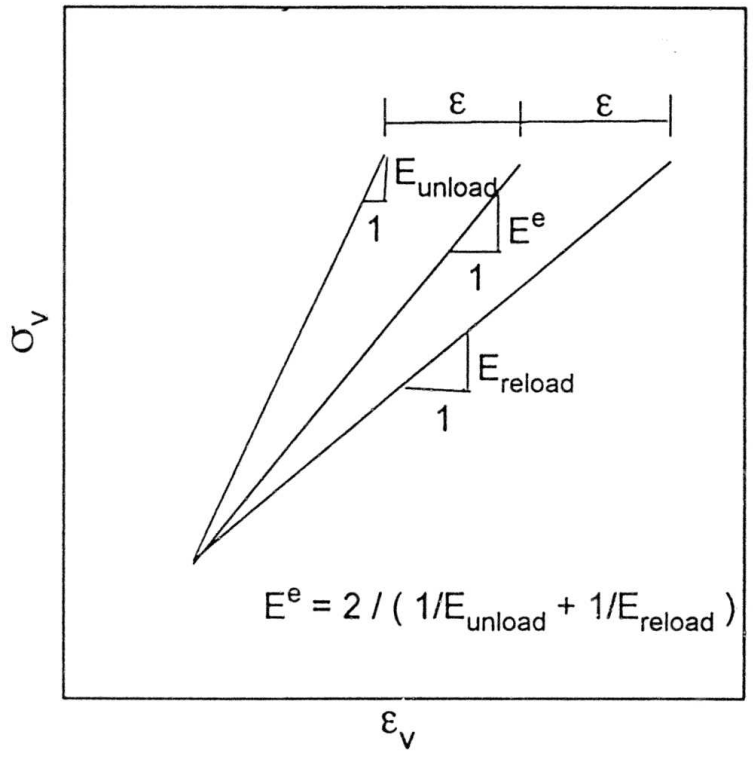

Fig. 5.9: Definition of elastic Young's modulus E^e.

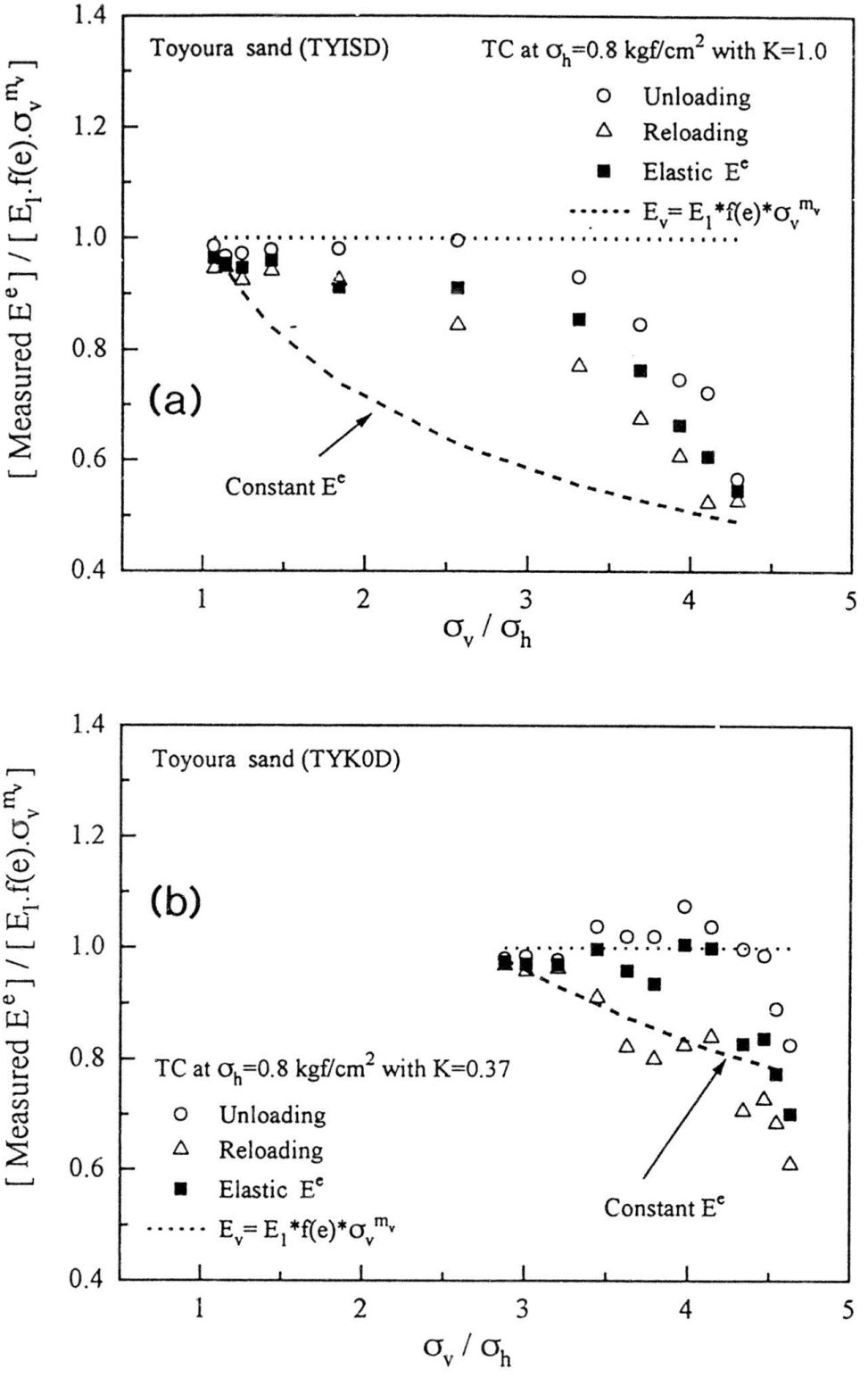

Figs. 5.10: The relationships between the normalized E^e ($=E_v$) and stress ratio (σ_v/σ_h) during TC performed on specimens (a) TYISD, (b) TYK0D.

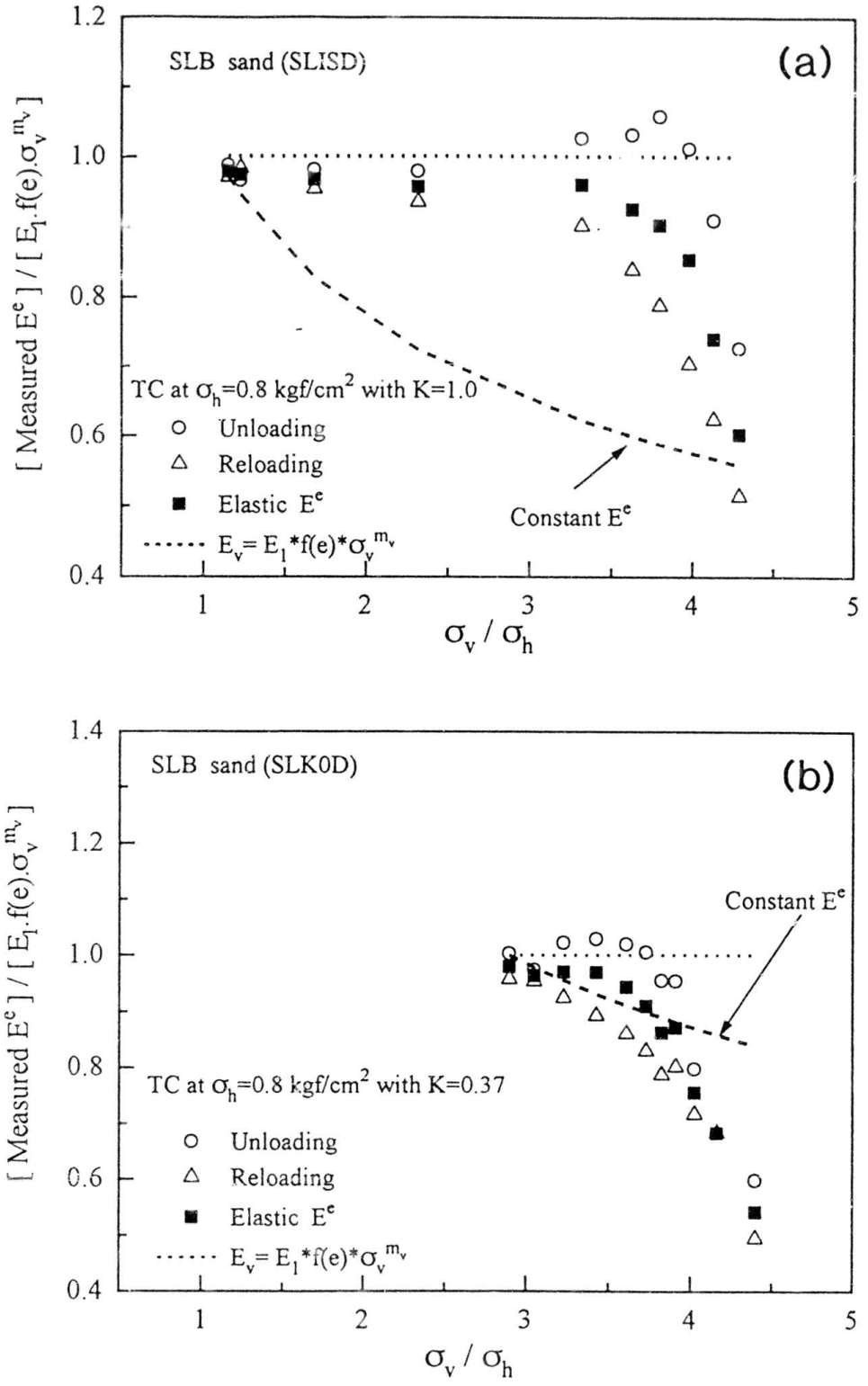

Figs. 5.11: The relationships between the normalized E^e ($=E_v$) and stress ratio (σ_v/σ_h) during TC performed on specimens (a) SLISD, (b) SLK0D.

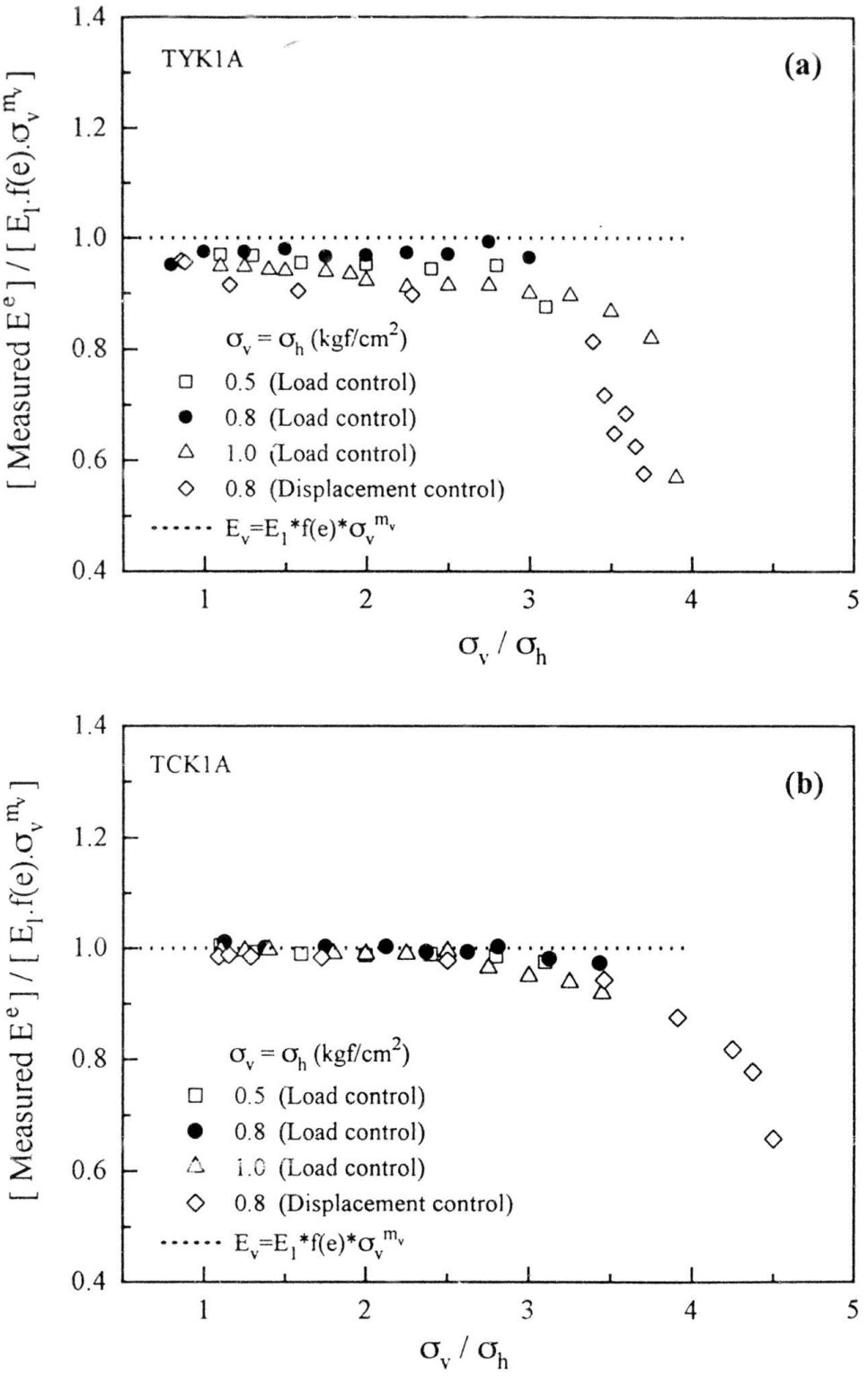

Figs. 5.12: The relationships between the normalized E^e ($=E_v$) and stress ratio (σ_v/σ_h) during TC performed on specimens (a) TYK1A, (b) TCK1A.

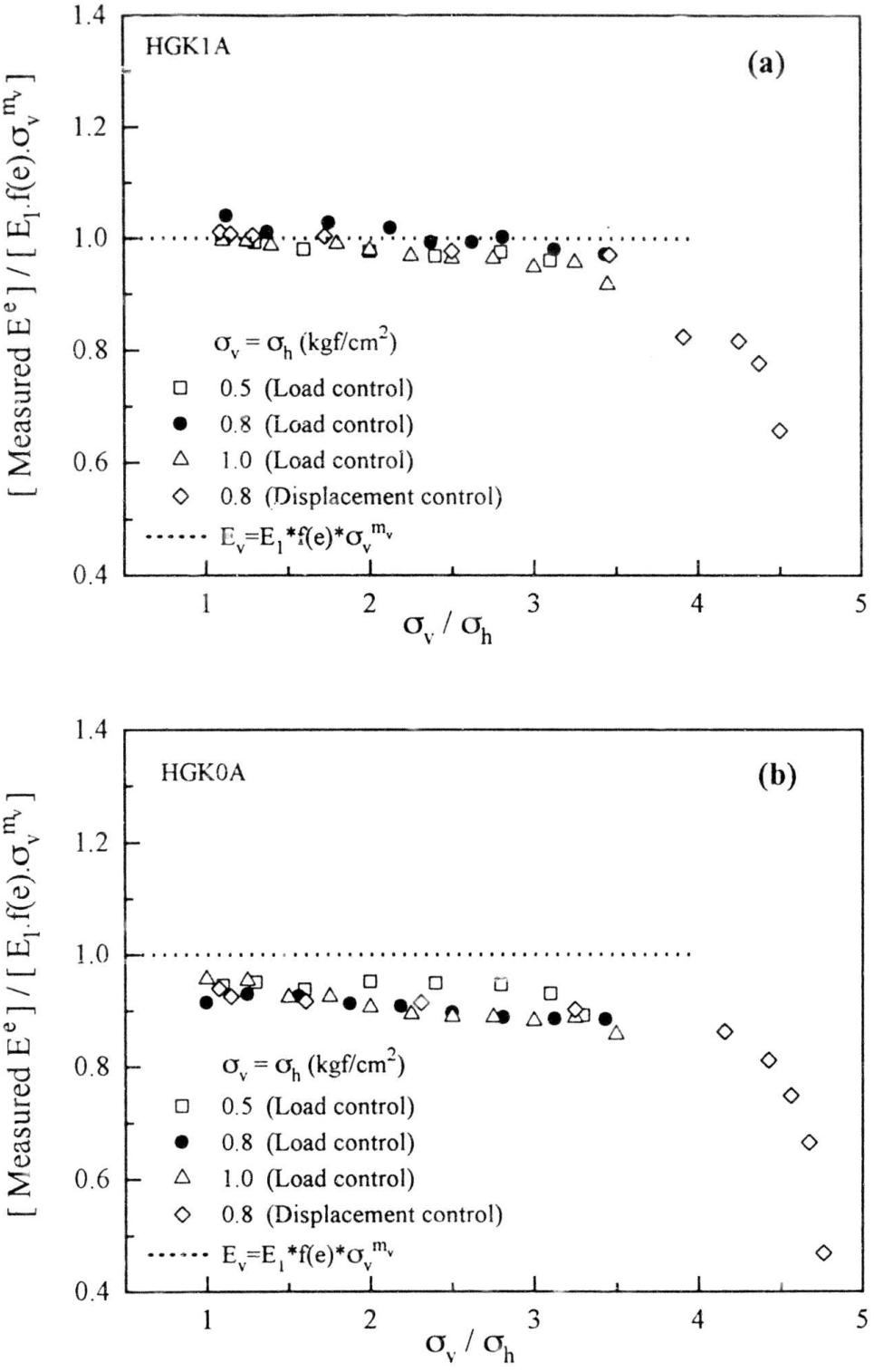

Figs. 5.13: The relationships between the normalized E^e ($=E_v$) and stress ratio (σ_v/σ_h) during TC performed on specimens (a) HGK1A, (b) HGK0A.

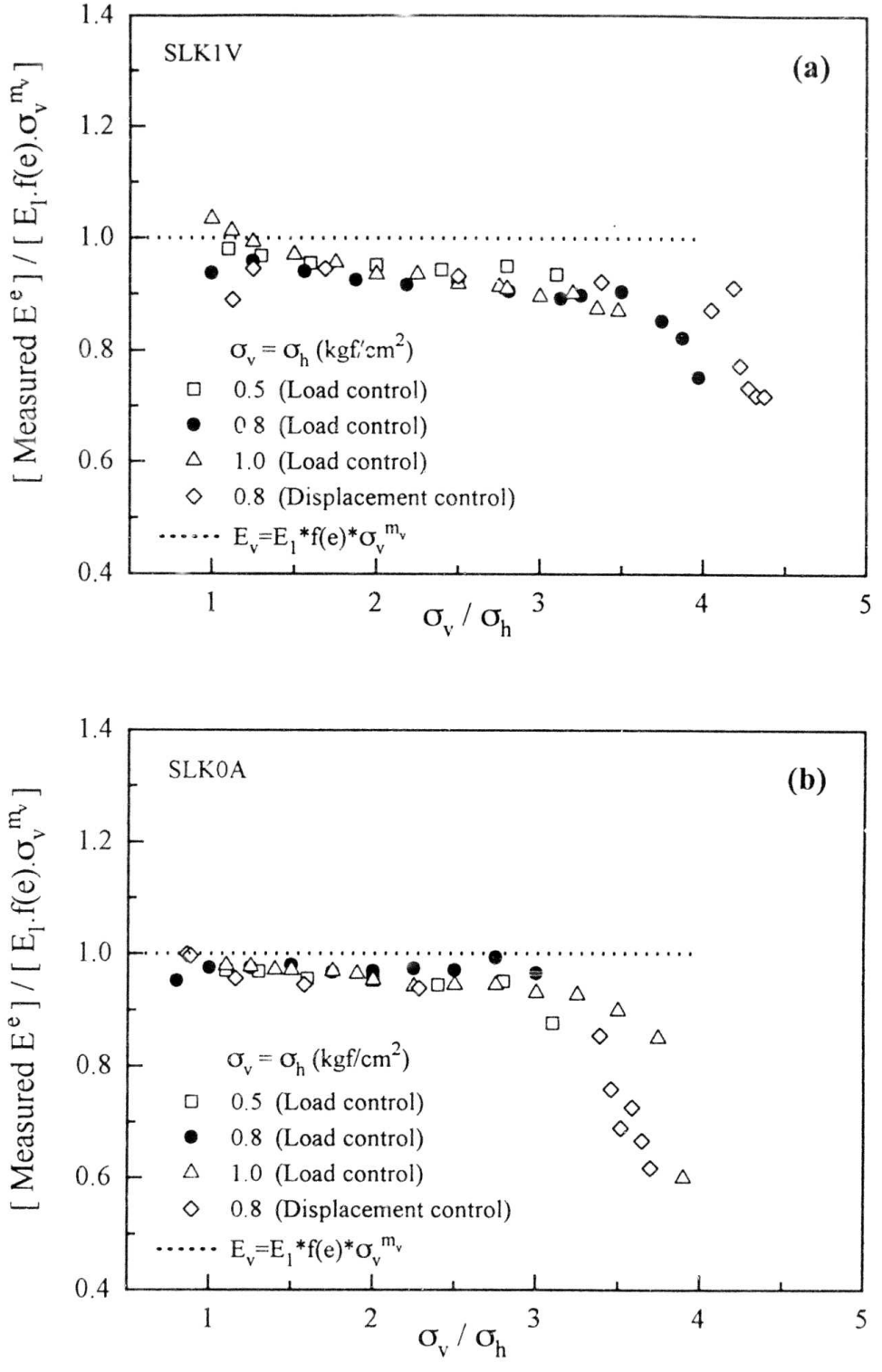

Figs. 5.14: The relationships between the normalized E^e (=E_v) and stress ratio (σ_v/σ_h) during TC performed on specimens (a) SLK1V, (b) SLK0A.

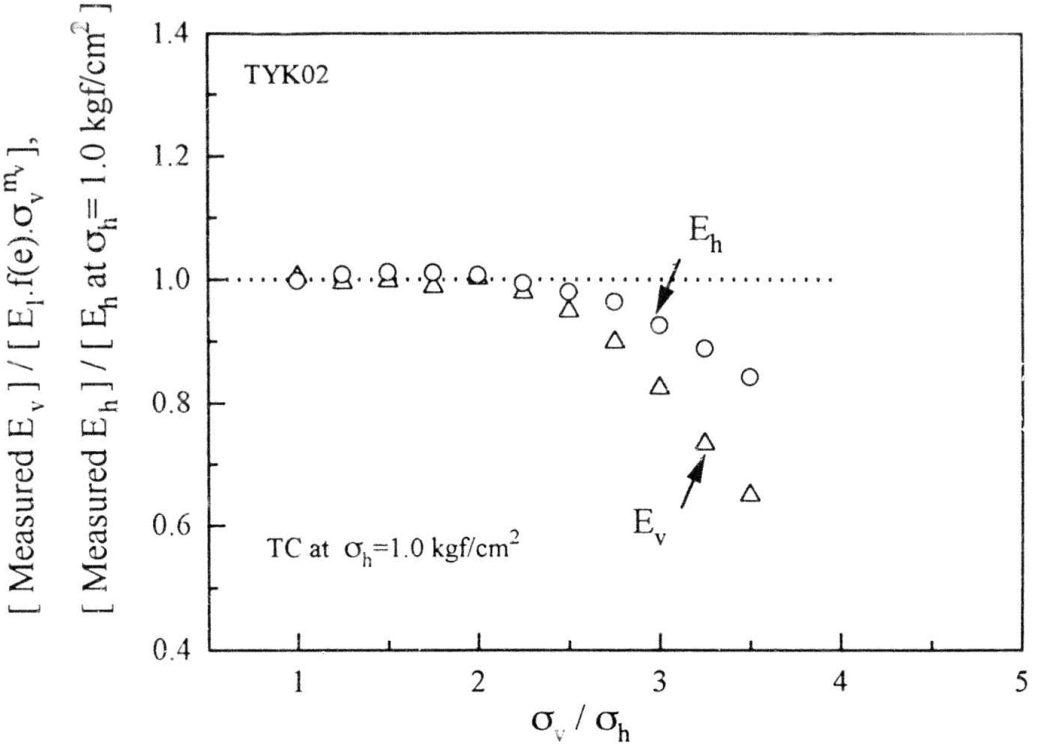

Fig. 5.15a: The relationships between the normalized E^e (=E_v or E_h) and stress ratio (σ_v/σ_h) during TC at $\sigma_v=\sigma_h=1.0$ kgf/cm^2 performed on TYK02 specimen.

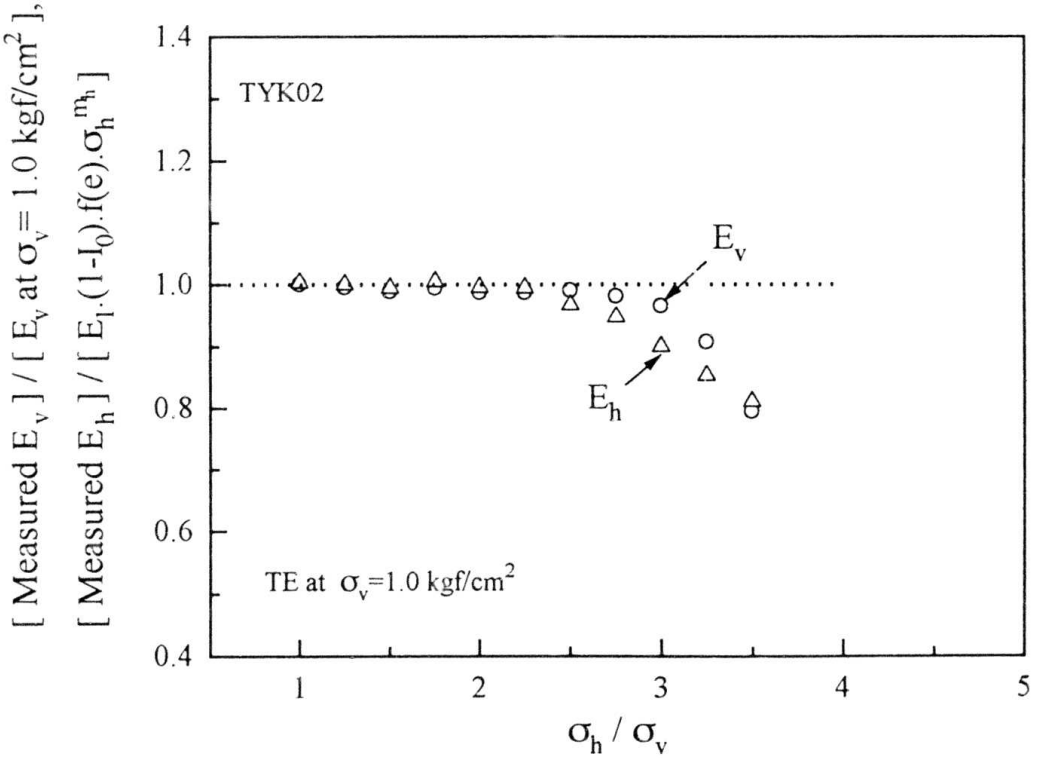

Fig. 5.15b: The relationships between the normalized E^e (=E_v or E_h) and stress ratio (σ_h/σ_v) during TE at $\sigma_v=\sigma_h=1.0$ kgf/cm^2 performed on TYK02 specimen.

Chapter 6

Cyclic Prestraining and the Elastic Deformation Properties

6.1. Introduction

A soil mass upon which a structure is founded often experiences cyclic loading caused by fluctuations in loading intensity. For instance, in the case of wave loading on offshore structures, traffic loading on pavements and heavy machine vibrations on foundations, the number of cyclic loading is very large although the magnitude of the non-constant component of loading is relatively small. The effects of a series of small seismic loading may also be included in this category. In such a case, the effects on the deformation characteristics of soil may not be negligible. Therefore, cyclic loading should be rationally accounted for whenever it is likely to improve safety and/or efficiency in design purpose. Each situation will of course be to some extent unique. Therefore, engineering judgment is required to decide whether, and to what degree, the effects of cyclic loading phenomena ought to be accounted for.

Effects of cyclic prestraining (CP) and consolidation time on the elastic modulus and some other deformation parameters at relatively small strains of less than, say, 0.1% of granular materials are still poorly understood. Drnevich et al. (1970) showed that a large number of loading cycles with a high shear-strain amplitude increases the values of shear modulus and damping ratio of a clean sand with the greater increase occurring at shear strains which are lower than those applied during CP, while the increase in the shear modulus and damping due to CP continues with the number of loading cycles during CP. Tokimatsu et al. (1986) showed that the elastic shear modulus G_{max} for an aged in-situ sand deposit can be reproduced in the laboratory by applying an appropriate amount of cyclic loading followed by consolidation for an appropriate period to an 'undisturbed' sample that may have been disturbed during sampling, transportation, etc. However, some other researchers (De Alba et al., 1984; Alarcon et al., 1989; Teachavorasinskun, 1992) showed that G_{max} of a clean sand is rather insensitive to CP. On the other hand, Hardin et al. (1972) indicated that shear modulus increases noticeably with consolidation time even for a clean sand.

Described herein are the effects of CP on (1) the elastic deformation properties, and (2) their dependency on the current stress or strain state. The effects of aging on some of those parameters in the light of the results from a comprehensive series of triaxial tests are also described.

6.2. Description of the Testing System

The triaxial apparatus used in this study (Fig. 6 1a) is one of the modified apparatuses which has been in use in the Geotechnical laboratory at Institute of the Industrial Science, University of Tokyo. Unlike many other conventional triaxial systems, it includes facilities for a) measurements of axial load by using a sensitive and rigid load cell installed within the triaxial cell to eliminate the effects of piston friction, b) automated anisotropic consolidation by controlling σ_v and σ_h independently, c) bedding-error-free 'on-sample' direct measurements of axial deformation by using local deformation transducers (LDTs) (Goto et al., 1991), and d) local measurements of radial deformations of dry specimen by using 3 pairs of proximity transducers mounted on an attachment system.

One proximity transducer and one dial gage were also used to measure the displacements of the loading cap and the loading piston, respectively. The external strains obtained from the above may include large effects of bedding error. Radial strains were measured at three heights (2.5-, 7.5- and 12.5-cm from the bottom) of a specimen (15 cm high and 7.5 cm diameter) assuming that radial strain distribution could be less uniform in the vertical direction compared with axial strain distribution. Two sets of proximeters, each set consisting of three, were mounted on a pair of two-direction micrometer tables so that they can be effectively moved along the vertical and horizontal directions at any stage of test if required; horizontal movement/shifting is often required when repeated loading test is performed, since such a test usually brings about large plastic deformations.

Tests were performed by using a stress-controlled loading system (Fig. 6.1b). From the functional point of view, the system has two basic components: a static pressure component and a cyclic pressure component, both being fed into from a house pressure unit. The house pressure

unit consists of (a) an air compressor, which supplies high air pressure; (b) a regulator, which, based on the maximum pressure, provides constant house pressure from the air-compressor; and (c) an accumulator and filter tank unit, which filters and then accumulates supplied air. The static pressure unit, fed by a high pressure line from the accumulator, supplies static pressure via a regulator to the lower chamber of a double-action Bellofram cylinder. On the other hand, cyclic pressure is controlled by an electro-pneumatic (E/P) transducer through its two inlets. One inlet is connected to the high pressure line from the accumulator. The other receives driving signals for cyclic loading from a control unit. The control unit could be either a software-guided micro-computer or an auto-function generator. Both control units were used in the present study. The E/P transducer receives continuous signals, depending on the amplitude and frequency of a cyclic loading (CL) test, from the function generator or computer; it converts the commanding signals into an equivalent pressure through maintaining a static equilibrium on the torque bar seated inside the E/P transducer. Finally, the equivalent pressure after having been amplified in volume by using another regulator (boaster) is conveyed to the upper chamber of the Bellofram cylinder. A specimen is directly connected to the Bellofram cylinder through a loading piston. Any change in pressure, static or cyclic, in the Bellofram cylinder results in the corresponding change in the axial stress of the specimen. The confining stress was applied by partial vacuum. Using a 12-bit 16 channel analogue-to-digital (A/D) converter card, the data acquired by using the transducers is fed into a 16-bit micro-computer.

6.3. Test Procedure

A solid, cylindrical specimen (7.5 cm diameter and 15 cm high), was reconstituted by raining air-dried sand particles through air into a split mold. Regular ends (i.e., non-lubricated ends using porous stones) were used at both ends of the specimen. A partial vacuum of 0.1 kgf/cm^2 was applied to a specimen which was completely enclosed within a rubber membrane before the mold was dissembled. A free-standing specimen was then consolidated isotropically to a pressure σ_c (= 0.8 kgf/cm^2 for all specimens in this study), at which the specimen dimensions were measured before any instrumentation. Cyclic loading tests were then performed symmetrically about a neutral axial stress state.

Elastic Young's modulus (E^e) was evaluated by applying very small cyclic axial load for which the single-amplitude axial strain, $(\varepsilon_a)_{SA}$, was kept within 0.001%. The Young's modulus of a specimen of clean sand evaluated at this strain level is observed rather independent of the type of loading (cyclic or monotonic), rate of shearing (static or dynamic), load-history and the degree of over-consolidation as long as the initial fabric remains essentially unchanged (Tatsuoka and Shibuya, 1992; Tatsuoka and Kohata, 1995; Jamiolkowski et al., 1991). This feature has been validated particularly by the fact that a Young's modulus value thus obtained is essentially similar to that obtained by measuring body wave velocities. So, this value can be considered to be the maximum Young's modulus E_{max} ($=E^e$) which a soil element can exhibit in its current state. Equivalent Young's moduli E_{eq} were evaluated from the response during a CL test at constant radial stress (σ_r) performed by varying the axial stress amplitude, and hence the value of $(\varepsilon_a)_{SA}$. The range of $(\varepsilon_a)_{SA}$ was varied from 0.001% to a value corresponding to CL with the axial stress amplitude (CP_{str}) at which the prestraining stress-cycle was applied. The value of E_{eq} at $(\varepsilon_a)_{SA}$ less than 0.001% is the same as E_{max}.

Cyclic loading, including CP, was applied symmetrically about either an isotropic or an anisotropic stress state at σ_r= 0.8 kgf/cm^2. The loading frequency (f) for CP was in the range of 0.1 to 0.5 Hz, while it was 0.1 Hz in the CL tests performed for evaluating soil parameters. f=0.1 Hz was employed to assist a micro-computer to sample a sufficient number of data-per-cycle for analytical purposes. A prescribed number of cyclic loading was applied during CP at CP_{str} for which the value of $(\varepsilon_a)_{SA}$ was varied in the range of 0.025 to 0.06% (after the CP application) from a specimen to another. Note that during CP at CP_{str} on a given specimen, the value of $(\varepsilon_a)_{SA}$ is not a constant value; rather it decreases with the number of loading cycles.

6.4. Test Program

The tests were performed on specimens of Toyoura (Batch E) and Hostun sands (Table 6.1), both being fine-grained sand, quartz-dominant and sub-angular in grain shape. Hostun sand is a French sand provided by Prof. di Benedetto (Ecole Nationale des Travaux Publics de l' Etat).

Test program on a given specimen consisted of CL tests at various amplitudes, which was repeated at different instants of testing (such as 'immediately before CP' and 'immediately after

CP applications), to investigate the effects of cyclic prestraining (CP) on the maximum Young's modulus (E_{max}), the peak-to-peak secant Young's modulus (E_{eq}), Poisson's ratio and the damping ratio. Table 6.2 lists the test specimens with some test results. Specimen HOSTN1 was subjected to CP at three stages, which are designated as CP-1, CP-2 and CP-3 (Table 6.2); CP-1 was applied first and followed by CP-2 and CP-3, respectively. Effects of aging on E_{max}, E_{eq} and h were investigated by measuring these quantities before and after CP applications for some specimens (e.g., HOSTN1:CP-1, TYRA 3, TYRA 2 and TYRA 1). Fig. 6.2 shows the test program employed in this investigation. Not all the specimens followed all the steps in Fig. 6.2. For example, the specimens HOSTN1 (CP-1) and TYRA 3 (Table 6.2) were subjected to all the steps, whereas only the effects of aging on E_{max} (at $\sigma_a=\sigma_r=0.8$ kgf/cm^2) before CP application was investigated in TYRA 1 because the specimen was failed in extension in a few cycles while CP was being applied about isotropic neutral stress state. HOSTN3 and HOSTN5 were used for the evaluation of the effects of CP and loading rate (or frequency of CL) on E_{eq} and h. However, the latter effect will be described in Chapter 7.

6.5. Test Results

Figs. 6.3a and b show the typical axial stress (σ_a) versus axial strain (ε_a) relationships obtained, respectively, from four small-amplitude and two large-amplitude CL tests performed on a Toyoura sand specimen TYRA 3. The responses shown in Fig. 6.3a are those obtained 'long before', 'immediately before', 'immediately after' and 'long after' CP application, while Fig. 6.3b shows those obtained 'immediately before' and immediately after' the CP application. Figs. 6.4a and b show, respectively, the similar small-amplitude and large-amplitude cyclic responses obtained from HOSTN1 (CP-1) specimen performed at anisotropic neutral stress state (i.e., σ_a= 1.4 kgf/cm^2 and σ_r=0.8 kgf/cm^2). The elapsed time is defined as the cumulative time initialized at the beginning of cyclic loading test. Therefore, zero elapsed time indicates that the sample had been consolidated at the neutral stress state (isotropic or anisotropic) for about an hour before starting any CL test. Figs. 6.3a and 6.4a show that the responses were essentially linear and recoverable while the slope after CP was slightly different from that before CP, indicating an existence of the influence of CP on the small-strain stiffness. The Young's moduli evaluated by using gap-sensor (GS) measurements are slightly larger than the respective value by LDTs (Fig. 6.3a). This would be due to that the specimen was denser near both ends. The difference is, however, very small. Note that

this trend is not general, but for a dense sample, the Young' modulus is usually noticeably larger when based on local strains than external strains (Tatsuoka et al., 1995). In particular, the use of a local gage such as LDT is imperative in triaxial tests on a coarse grained material. In tests to evaluate the maximum Young's modulus E_{max}, the single-amplitude axial strain, $(\varepsilon_a)_{SA}$, was less than 0.001% in most of the cases, while in a few tests, it exceeded slightly the above value (but less than 0.002%). The results of a large amount of cyclic triaxial tests on various types of sands, in which isotropically consolidated specimens were cyclically loaded with increasing $(\varepsilon_a)_{SA}$ in steps (e.g., Tatsuoka et al., 1995), show that the Young's modulus is essentially constant for $(\varepsilon_a)_{SA}$ less than about 0.002%.

Figs. 6.3b and 6.4b show the typical σ_a~ε_a relationships for a relatively large strain amplitude obtained during prestraining cycles, at the beginning and at the end of the application of a large amount of CP for the same specimens TYRA 3 and HOSTN1 (CP-1), respectively. The peak-to-peak secant Young's modulus evaluated from such responses was the Equivalent Young's modulus E_{eq}. It can be seen that although the hysteresis area, and hence the damping ratio (h), decreased drastically by CP, the peak-to-peak secant modulus E_{eq} did not change noticeably. It should be noted that the σ_a~ε_a responses at the beginning of CP in Figs. 6.3b and 6.4b do not indicate a virgin state. They are mostly those obtained at the 10th cycle at that axial stress amplitude with having the effects of previously performed CL tests also at the lower strain amplitudes. Herein such responses will, however, be designated as virgin one if not stated otherwise. A typical true virgin (i.e., the first cycle) relationship between σ_a and ε_a and ε_r of HOSTN5 is shown in Fig. 6.5a, together with the similar responses for Cycle 2, 200 and 25000 (at the end of CP) during CP application at CP_{str}= 0.8~2.0 kgf/cm^2 (nominal). In the stress-strain relationships of each cycle, ε_a and ε_r were initialized at the start of loading (or reloading). True values of ε_a and ε_r at the start of any cycle during CP can be obtained from Fig. 6.5b. Drastic changes in the deformation characteristics and the size of the hysteresis loop can be observed even between Cycles 1 and 2 (Fig. 6.5a).

6.5.1. Axial Stress-Dependency of E_{max}

Herein the Young's moduli evaluated from axial strains measured locally (by LDT) will be presented. Figs. 6.6a through f show the relationships between the E_{max} $(=E^e)/f(e)$ value and the

axial stress (σ_a) for air-dried specimens TYRA 3, HOSTN5, HOSTN1 and HOSTN3 (Table 6.2) in full logarithm scale. These E_{max} values were evaluated from the responses of small-amplitude CL tests applied along and within the CP stress path. The values of E_{max} were measured while increasing σ_a (i.e., loading) (Fig. 6.6a) and also while decreasing σ_a (i.e., unloading) (Fig. 6.6b), and have been divided by a void ratio function $f(e)=(2.17-e)^2/(1+e)$ (Hardin and Richart, 1963) to account for the slight change in void ratio which occurred during the course of testing. In Figs. 6.6b to f, $E^c/f(e)\sim\sigma_a$ relationships, which were obtained from isotropic stress conditions at $\sigma_a=\sigma_r$ varying from 0.8 kgf/cm^2 to 3.0 kgf/cm^2 during both loading (i.e., σ_a increasing), and unloading (i.e., σ_a decreasing), are plotted for HOSTN5 specimen at virgin state.

Due to CP, the $E_{max}\sim\sigma_a$ relation was rotated counterclockwise direction. As a result, the isotropically consolidated specimen of Toyoura sand (TYRA 3), for example, suffered a large reduction in E_{max} in the extension side while E_{max} near the peak axial stress during CP was nearly unchanged. However, the trend was not similar to the anisotropically consolidated (i.e., at σ_a= 1.4 kgf/cm^2 and σ_r= 0.8 kgf/cm^2) specimens of Hostun sand subjected to CP only in triaxial compression with CP_{str} in the range of σ_a between 0.8 to 2.0 kgf/cm^2. That is, HOSTN5 (Fig. 6.6b) experienced some increase at larger σ_a while it suffered a decrease at the lower end of σ_a in CP stress path. The similar trend can be observed in HOSTN3 (Fig. 6.6g) and HOSTN1 (CP-1; Fig. 6.6c), which were subjected to CP with the same CP_{str} in triaxial compression. Besides, it is noticeable in case of the looser specimen (HOSTN5; Fig. 6.6b) that within the CP_{str} range, the stress range with the negative effect (or decreasing E_{max}) was more extended (i.e., $0.8\leq\sigma_a\leq1.6$ kgf/cm^2) than that for the positive effect (i.e., increasing E_{max}) (i.e., $1.6\leq\sigma_a\leq2.0$ kgf/cm^2), which was opposite to the trend for the other two specimens of Hostun sand. This difference could be attributable to the fact that the looser specimen, HOSTN5, suffered very large drifts in both axial and radial strain directions during CP compared to those of a denser one (Table 6.2), and hence suffered more damage as a result of fabric alteration.

To investigate the effects of CP_{str} and the location of neutral stress on E_{max} during CP, HOSTN1 was further subjected to the 2nd (CP-2) and the 3rd (CP-3) stages CP with different CP_{str} (Table 6.2) after the completion of the first stage CP (i.e., CP-1). Figs. 6.6d and e show the results for CP-2 and CP-3, respectively. Fig. 6.6f is made by overlapping Figs. 6.6c, d and e; For each CP stage, two plots were drawn— one for the $E^c/f(e)\sim\sigma_a$ relationship obtained at the start of

CP and the other for the similar relationship obtained at the end of CP. For each plot, E_1 and m values are the similar values (or the average values obtained during loading and unloading) as shown in Table 6.2. It can be seen from Fig. 6.6d (also from Fig. 6.6f) that Young's modulus more-or-less increased all through the range of CP_{str} with the maximum increase at the head of CP_{str} and the minimum at the tail. During CP-2, σ_a was cycled between the peak compression state at 2.0 kg/cm^2 (i.e., major-to-minor principal stress ratio $R=\sigma_v/\sigma_h=2.5$) and the peak extension stress state at 0.4 kgf/cm^2 (i.e., $R=\sigma_h/\sigma_v=2.0$). Therefore, σ_a was cycled maintaining approximately an equidistant from both failure states in compression and extension and hence the specimen suffered deformations which were approximately similar but opposite in sign. As a result, total deformations (i.e., translation of strain axes) were not significant (see Table 6.2) as would be expected because of virgin loading in extension stress states for CP-2. This could be the reason of why E_{max} values did not suffer any decrease at the extension stress states. Damage in E_{max} could be associated with larger deformations during CP causing destruction to the initial fabric. Deformations during CP-3 (CP_{str}= 1.4~0.25 kgf/cm^2) were much less (Table 6.2) compared to that would be expected for $R=\sigma_h/\sigma_v$ >3.0 in extension, because of the previously performed CP (i.e., CP-2). Therefore, CP-3 might not bring about any fabric change, which was reflected in Fig. 6.6e as no noticeable change in E_{max} values was observed due to CP-3.

In all cases, CP resulted in the change (decrease or increase) in the parameter E_1, where $E_{max}=E_1 \cdot f(e) \cdot \sigma_a^m$, while increasing the value of the exponent m. Elastic parameters E_1 and m for events at the beginning of CP and at the end of CP are listed in Table 6.3; these parameters were evaluated separately (if applicable) for extension and compression stress-states from the respective E_{max}~σ_a relation. E_1 is one of the so-called elastic parameters of granular materials. The exponent m is another elastic parameter representing nonlinear-dependency of the small strain elastic modulus on σ_a. Both parameters depend generally on the fabric, the particle size, shape, angularity and orientation in a given mass and so on. Therefore, a change in E_1 implies the change in the fabric. Before CP, the elastic parameters E_1 and m in compression stress states differed noticeably from those in extension stress states (TYRA 3, HOSTN1: CP-2 and CP-3) — producing two distinct E_{max}~σ_a relations. In particular, m is always smaller in TC than in TE. Flora et al. (1995) observed similar results on a virgin specimen of well-compacted and well-graded gravel.

As a result of CP, on the other hand, the pair of E_1 and m were changed further noticeably compared to their respective values measured before or at the beginning of CP. The Young's modulus E_{max} of a granular material depends essentially on the principal stress in the direction of the major principal strain increment for which the E_{max} value is defined. By this property, the elasticity of granular material becomes anisotropic under anisotropic stress conditions (i.e., stress state-induced anisotropy) (Chapter 4; Stokoe et al., 1991). Therefore, the change in the exponent m implies a corresponding change in the value of σ_a^m — which, in turn, affects directly the stress-induced anisotropy characteristics. Table 6.3 shows that the state of anisotropy was not similar for extension and compression stress states. Thus, the specimen attained a new state of anisotropy, which may be called 'CP-induced anisotropy.' At this state, the pair of E_1 and m values obtained separately in extension and compression stress states became rather similar—exhibiting almost a unique E_{max}~σ_a relation for extension and compression stress states with the value of exponent m close to unity. This large value of m≈1.0 suggests that the elastic deformation characteristic become more anisotropic at the anisotropic stress states. The conclusion can be obtained, however, only after both E_v~σ_v and E_h~σ_v relations are measured and compared before and after CP.

On the other hand, in the case of test with TYRA 3, in which E_{max} in TE decreased by CP, a tendency of partial recovery (i.e., to get back to the previous E_{max} value that existed before the application of the latest CP) of E_{max} during the post-CP long-term consolidation can also be observed, which was maximum at the smallest σ_a. The reason could be a partial decrease of the effects of the CP-induced anisotropy with time.

6.5.2. Effects of aging on E_{max}

Figs. 6.7a through c show the variation of E_{max} (after correction for the changes in void ratio by f(e)) at a given stress state for the entire time history of each specimen. Two specimens of Toyoura sand, TYRA 2 (Fig. 6.7a) and TYRA 3 (Fig. 6.7b) at an isotropic neutral stress state (i.e., at σ_a=σ_r=0.8 kgf/cm^2), and one specimen of Hostun sand, HOSTN1 (CP-1) at an anisotropic neutral stress state (i.e. at σ_a=1.4 kgf/cm^2, σ_r=0.8 kgf/cm^2), were tested. The figures show: (a) a marginal increase with time involving some scatter in E_{max} prior to CP application; (b) in the case of Toyoura sand specimens, a sudden drop (positive damage) by CP of E_{max} of about 20% in the

looser specimen, while for HOSTN1 specimen, an increase (negative damage) of about 11% in E_{max} due to CP; (c) partial recovery from 'damage' (positive or negative) to the Young's modulus in the initial part of post-consolidation period, followed by a very slow increase in E_{max} with time. In the tests, void ratio did not change noticeably as given in brackets in the respective figures.

Summarizing the above, it can at least be concluded that the E_{max} values does not change substantially due to CP applied at strains largely exceeding the elastic threshold strains. Furthermore, E_{max} value does not increase at a very large rate under sustained long-term consolidation.

6.5.3. Equivalent Young's modulus E_{eq}

Fig. 6.8a shows the E_{eq}~$\log(\varepsilon_a)_{SA}$ relationships of tests performed on three air-dried specimens of Toyoura sand. The relationships were constructed by using the data obtained by increasing the stress-amplitude symmetrically about an isotropic neutral stress condition (i.e., $\sigma_a=\sigma_r=0.8$ kgf/cm^2) in steps to a maximum value (i.e., $\sigma_a=0.4$~1.2 kgf/cm^2), which was the range of CP_{str} for specimens TYRA 2 and TYRA 3. The E_{eq} values are clearly influenced by strain-amplitude and void ratio. Fig. 6.8b shows the decay curves before the application of CP; here E_{eq} values of each specimen have been normalized by using the respective E_{max} ($=(E_{eq})_{max}$) to eliminate the effects of void ratio. The normalized E_{eq} values, thus obtained, exhibit rather a unique variation with $(\varepsilon_a)_{SA}$.

The effects of CP on the E_{eq}~$\log(\varepsilon_a)_{SA}$ relations are shown in Figs. 6.9a through 6.11. In all cases, the values of E_{eq} were normalized by the E_{max} value that had existed immediately before the particular CP application, $(E_{max})_{initial}$, except for Fig. 6.10d. Figs. 6.9a and b show such decay relationships for specimens TYRA 2 and TYRA 3, respectively. Due to CP, E_{eq} at a specific $(\varepsilon_a)_{SA}$ decreased except near and at the strain amplitude $(\varepsilon_a)_{SA}$ before CP corresponding to CP_{str}, with the maximum reduction at the smallest $(\varepsilon_a)_{SA}$. Figs. 6.10a to c show similar relationships obtained before and after CP stages CP-1, CP-2 and CP-3, respectively, of HOSTN1 specimen. For the cases of CP-1 and CP-2, the values of E_{eq} increased for all values of $(\varepsilon_a)_{SA}$ with the maximum increase at the minimum value of $(\varepsilon_a)_{SA}$ and vice versa. For CP-3 (Fig. 6.10c), practically noticeable change due to CP was not observed except the shape of the decay curve. That is, the slight decrease at smaller $(\varepsilon_a)_{SA}$ and the slight increase at relatively larger $(\varepsilon_a)_{SA}$ (i.e., $(\varepsilon_a)_{SA}>0.01\%$)

made the shape of the decay curve different from the one obtained immediately before CP. Fig. 6.11 shows the similar relationship for HOSTN5 specimen, which also shows the negative influence of CP like TYRA 2 and TYRA 3. It is likely that CP only in TC stress conditions tends to increase E_{max} measured at the neutral stress state during CP, while CP symmetrical in both TC and TE does not. This would be due to that the structure becomes more stable against loading by CP only in TC, while the structure is repeatedly perturbed when loaded alternately in TC and TE. The discussion above resembles the effects of CP on the E_{max} values measured along CP stress path described in the previous section. That is, the E_{max} value at a given stress state along CP stress path after CP application, in comparison to the corresponding value immediately before CP application, seems to determine the relative location of decay curve after CP. That means, for CP-1 and CP-2 of HOSTN1 specimen, the decay curves show an overall increase due to CP, which was the reflection of the increase of E_{max} values at the neutral stress states about which CP had been applied. Similar explanation holds for other cases where the decay curves show an overall decrease.

The effects of CP on the shape of the decay curve is shown in Fig. 6.10d. For that purpose, E_{eq} values of each E_{eq}~log($(\varepsilon_a)_{SA}$) relations of HOSTN1 specimen obtained before CP and after CP of CP-1, CP-2 and CP-3 stages are normalized by the values of E_{max} (=$(E_{eq})_{max}$) of the respective relation (i.e., For a particular CP, different E_{max} values, if so, are considered for before CP and after CP). The following trends can be observed.

(a) Before CP event, the relationship was unique for CP-1 and CP-2 but for CP-3, the relationship was more softening, which could be attributable to the weaker response of granular materials in extension than in compression and that the specimen came closer to extension failure state during CP-3.

(b) A rather unique relationship was obtained after CP for all the three stages of CP and the normalized decay curve lies in between the other two sets of decay curves obtained immediately before CP.

Figs. 6.9b and 6.10a also show the effects of post-straining long-term consolidation on the decay relationships. If we call the decrease in the E_{max} value due to CP as positive damage (Fig.

6.9b) and that the increase as negative damage (Fig. 6.10a), partial recovery of stiffness from the damage due to CP was observed in the post-straining consolidation period. The recovery in terms of the increment of E_{eq} was rather constant for the range of $(\varepsilon_a)_{SA}$ examined except near and at $(\varepsilon_a)_{SA}$ corresponding to CP_{str} (Fig. 6.9b).

Variation of $(\varepsilon_a)_{SA}$ at a constant CP_{str} during CP of HOSTN5 specimen with the number of stress cycles N is shown in Fig. 6.12. Some of the stress-strain relations are presented in Fig. 6.5. Here N equal to 1 indicates the true virgin cycle, which does not include any effects of previous stress cycles. This relationship was obtained by an automatic stress-controlled system using a micro-computer. For the given axial stress amplitude, the value of $(\varepsilon_a)_{SA}$ is not a constant value; rather it decreases sharply in the first few cycles, after which the decreasing rate decreases gradually, and diminishes at around N=100 cycles. The value of $(\varepsilon_a)_{SA}$ was rather constant for N≥100 cycles. This tendency is more-or-less common to granular materials. This result indicates that for a given stress-amplitude (confining the discussion for relatively larger stress-amplitude), E_{eq} will increase gradually with the increase in N up to at least 100 cycles. Therefore, the value of E_{eq} for a given stress-amplitude after N=25000 must be larger than that after N=10.

At the same time, for the given stress-amplitude, $(\varepsilon_a)_{SA}$ is also decreasing with N (mentioned earlier). Therefore, during CP, the E_{eq} value for a given stress-amplitude is continuously moving leftward (i.e., towards the direction of lower value of $(\varepsilon_a)_{SA}$ axis) in the decay curve (i.e., E_{eq}~$(\varepsilon_a)_{SA}$) compared to its previous position. Whether the location of E_{eq} during and/or after CP would be above or below the decay curve obtained immediately before CP depends on (1) the current value of $(\varepsilon_a)_{SA}$, which is always lower than the previous one, and (2) the effects of the CP-induced anisotropy in the small-strain stiffness, which may increase or decrease the E_{eq} value. Fig. 6.12 also shows the variations of ν_{eq} and h with N, which will be described later.

6.5.4. Poisson's ratio

Fig. 6.12 shows that the equivalent Poisson's ratio (ν_{eq}) decreases with the increase in N for a constant stress-amplitude (i.e., CP_{str}= 0.8~2.0 kgf/cm^2). The trend is similar to that $(\varepsilon_a)_{SA}$~N relation described earlier. The ν_{eq} value became constant after N≈8000 cycles, while $(\varepsilon_a)_{SA}$ attained

steady state at around N=100 cycles. It indicates that the value of ν_{eq} may decrease with the increase in N for a given $(\varepsilon_a)_{SA}$. This was reflected in the relationships between ν_{eq} and $(\varepsilon_a)_{SA}$ shown in Fig. 6.11 for HOSTN5, and Figs. 6.13a and b for HOSTN1. For a given $(\varepsilon_a)_{SA}$, the value of ν_{eq} (evaluated both before CP and after CP) depends on the value of neutral stress about which CL was applied symmetrically. Besides, CP decreased ν_{eq}, while the rate of decrease was larger at larger $(\varepsilon_a)_{SA}$ and vice versa.. On the other hand, at very small axial strain-amplitude $(\varepsilon_a)_{SA}\approx 0.001\%$, the effects of CP on Poisson's ratio was not noticeable. The latter point was investigated further by analyzing ε_r~ε_a data obtained during small-amplitude CL tests performed at various stress states along the CP stress path. The relationships between the small strain-amplitude Poisson's ratio (ν^e) (for events 'before CP' and 'after CP') and stress ratio (σ_a/σ_r) for CP-1, CP-2 and CP-3 of HOSTN1, respectively, are shown in Figs. 6.14a, b and c. For a given stress ratio, slight differences can be observed in the values of ν^e measured before CP during σ_a increasing (loading) and σ_a decreasing (unloading) for the case of CP-1. This could be due to the accumulation of some plastic strain increments in the measured strains in small cycles applied during loading. Although data was slightly scattering, a subtle but noticeable decreasing tendency can be observed in the value of ν^e at a give stress ratio due to CP. However, the difference at a given σ_a/σ_r was practically insignificant. The ν^e~σ_a/σ_r variations were fitted reasonably by the theoretical relation $\nu^e = \nu_0.(\sigma_a/\sigma_r)^{m/2}$ (dotted lines in each figure), where ν_0 being the value of ν^e measured before CP at $\sigma_a/\sigma_r=1.0$ and m being the exponent of E^e~σ_a relation obtained before CP. The values of ν_0 and m used for each case are given in the respective figures. These results indicate that although the small-strain stiffness was observed to be changed by CP, the corresponding ν^e values are very insensitive to CP.

6.5.5. Damping Ratio (h)

In this investigation, the hysteretic damping ratio (h) was evaluated from each hysteresis loop (e.g., Figs. 6.3a and b) obtained from CL tes:, which is defined as;

$$h = \frac{1}{2\pi}\left(\frac{\Delta w}{w_1 + w_2}\right) \qquad 6.1$$

where Δw is the area of hysteresis loop (i.e., dissipated energy) and $w=w_1+w_2$ is the elastic work done during an unload-reload cycle between the maximum and minimum axial stresses (Fig. 6.2b). A typical relationship between h and N of specimen HOSTN5 during CL at CP_{str} is also shown in

Fig. 6.12 (mentioned earlier). Continuous decrease in h with the increase in N can be observed. The rate of decrease was very high at the initial stage of CP, which gradually decreased with the increase in N. The changes in h become very small at N larger than 1000. The CP application of a specified number of cycles at relatively larger CP_{str} brought about similar effects on h value obtained by applying symmetric axial stress cycle with amplitude that was smaller than CP_{str}. The center of cyclic stresses are the neutral axial stress during applying CP. The results are shown in Figs. 6.15, 6.16a through c. The relationships between h and $(\varepsilon_a)_{SA}$ of TYRA 2 and TYRA 3 specimens obtained before and after CP are shown in Fig. 6.15. Fig. 6.16a shows similar relationships of HOSTN1 (CP-1), while the results of the other CP stages (CP-2 and CP-3), in addition to those at stage CP-1, of the same specimen are shown in Fig. 6.16b. The effects of Post-CP long term consolidation on the $h\sim(\varepsilon_a)_{SA}$ relationship is also shown in Fig. 6.16a. The effects of the amount of prestraining on the $h\sim(\varepsilon_a)_{SA}$ relation obtained from HOSTN5 are shown in Fig. 6.16c. The figures show that the effects of CP on damping are very large. In summary, the following trends can be observed;

a) For the 'virgin' specimen (i.e., before the application of particular CP), the value of h increases very slowly with the increase in strain up to $(\varepsilon_a)_{SA}\approx 0.005\%$ and then it increases very sharply after $(\varepsilon_a)_{SA}$ exceeds about 0.01%. For HOSTN1 specimen, CP-1 had been applied first, which was followed by CP-2 and CP-3. Therefore, the stage CP-1 must have influenced on the relationships between h and $(\varepsilon_a)_{SA}$ measured at stages CP-2 and CP-3 (note that stage CP-3 was further affected by the stage CP-2).

b) CP increases the size of so-called quasi-elastic range in which the value of h is very small; Fig. 6.15, for instance, shows that even at $(\varepsilon_a)_{SA}$ larger than 0.01%, the rate of increase in h with the increase in $(\varepsilon_a)_{SA}$ was very small after the application of CP compared to that for the virgin specimen; Particularly, a drastic decrease in the value of h was observed at or near $(\varepsilon_a)_{SA}$ corresponding to CP_{str}.

c) A larger number of loading cycles during CP results in a larger quasi-elastic threshold strain (Fig. 6.16c).

Therefore, CP has a diminishing effect on the hysteresis damping values. This may be due mostly to the restructuring of sand particles which occurred during the application of CP. The application of CP may bring some loose and unstable groups of particles into stable and dense positions at the micro-level. More stable structure can withstand cyclic reversals without a change in micro-structure, thus with less energy loss. The test results discussed above exhibits a trend opposite to that obtained by Drnevich and Richart (1970). They showed that in resonant column tests on Ottawa sand, damping ratio increases with the increase in the number of loading cycles during CP, where the increase is greater at the lower value of $(\varepsilon_a)_{SA}$. On the other hand, Tatsuoka et al. (1978), Kim and Stokoe (1991), Teachavorasinskun (1992) reported that the damping of sand decreases as the number of loading cycles increases. Although small, long-term consolidation after CP further decreases h at a given $(\varepsilon_a)_{SA}$ (Fig. 6.16a), especially at $(\varepsilon_a)_{SA} \geq 0.008\%$.

6.5.6. Elasto-Plasticity of Deformation during cyclic loading

Precise separation of elastic and plastic components of deformation is essential for proper elasto-plastic modeling of sand deformation subjected to a wide variety of strain history. In this study, this was attempted by measuring elastic strain increment components frequently during shearing (as described in the earlier part of this chapter). The importance of the above was confirmed by comparing the elasto-plastic deformation characteristics of a prestrained specimen with those of a virgin one. Effects of cyclic prestraining (CP) on the deformation of soil is very important also for structures subjected to heavy traffic, seismic activity, machine vibration, and other dynamic loading such as off-shore structures. A large number of loading cycles (of the order of single amplitude axial strain $(\varepsilon_a)_{SA}=0.02\sim0.1\%$) on dry sand has been observed to increase the elastic limit strain and tangent stiffness both in cyclic and monotonic loadings and to decrease significantly damping at relatively large strain levels (say, $(\varepsilon_a)_{SA} \geq 0.01\%$), with relatively smaller effects on the elastic Young's modulus (E^e) (Teachavorasinskun, 1992). Therefore, the deformation characteristics of a prestrained specimen differ noticeably from that of a virgin one not because of changes in elasticity but because of large changes in plasticity including dilatancy characteristics. Modeling of such a prestrained specimen should, therefore, require proper characterization of those aspects.

Figs. 6.17a through 6.19d show the stress-strain relationships of CL tests along CP stress path. Of them, Figs. 6.17a, 6.18a and 6.19a to d show the relationships between σ_a and ε_a, and Figs. 6.17b and 6.18c show the relationships between σ_a and ε_r for virgin and prestrained specimens. The ε_a and ε_r axes for the prestrained specimen were shifted arbitrarily. The actual values of strains (ε_a and ε_r) at the bottom ends of the curves for the prestrained specimen (denoted as S_p) are given in Table 6.2. The number of prestraining cycles and the axial stress amplitude CP_{str} are also listed in Table 6.2. CP were applied at a frequency f between 0.1 to 0.5 Hz.

Elastic strains for the whole stress range of CP_{str} were obtained by integrating $d\varepsilon_a^e = d\sigma_a/E^e$ and $d\varepsilon_r^e = -\nu^e . d\varepsilon_a^e = -\nu^e . d\sigma_a/E^e$ ($\nu^e = \nu$ in Fig. 6.14a~c) by using the relations for E^e ($=E_1 . f(e) . \sigma_a^m$) and ν^e ($=\nu_0 . (\sigma_a/\sigma_r)^{m/2}$) (mentioned earlier) together with the respective elastic parameters (E_1, m, ν_0) listed in Table 6.3 (note; these values are affected by CP). The relationships between σ_a and the elastic axial and radial strains (ε_a^e, ε_r^e) were arbitrarily plotted with the origins denoted as S_v and S_p at the bottom end (e.g., at σ_a=0.8 kgf/cm^2 for HOSTN3) of the respective σ_a~ε_a and σ_a~ε_r relation for the range of CP_{str}. A drastic changes in the σ_a~ε_a and σ_a~ε_r relations were caused by a substantial reduction in the plastic strain components ($\varepsilon_a^p = \varepsilon_a - \varepsilon_a^e$, $\varepsilon_r^p = \varepsilon_r - \varepsilon_r^e$) due to CP, while the σ_a~ε_a^e relation changed very slightly. Now we can understand why the stress-strain relations after CP concave upward with a small hysteresis area. It is interesting to note that the ε_r^e and σ_a relation happens to be very linear. The behavior described above is due to the intrinsic elastic property of sand.

A considerable decrease in the plastic-to-elastic strain increment ratio due to CP can also be seen from Figs. 6.20 through 6.22. The plastic-to-elastic strain increment ratio, both before and after CP, was larger in the radial direction than in the vertical (i.e., principal strain) direction (Figs. 6.20a and b, Figs. 6.21a and b). The relationships were similar in loose and medium-dense specimens of Hostun sand, while the plastic strain components were more dominating in loose specimen (Figs. 6.21a and b). Before CP, the elastic-to-plastic strain increment ratio varied largely and nonlinearly with σ_a, whereas after CP, it varied slightly and more-or-less linearly with σ_a during loading and unloading. The axial plastic-to-elastic strain ratio varied in much wider ranges in Figs. 6.20a and 6.21a than in Figs. 6.22a through d, because the responses before CP in the former cases were based on true virgin state (cycle 1), while in the latter cases, the previous stress histories (as described in the earlier) had reduced the axial plastic strain component.

It is important to note that the deformation, in no cases, for the whole range of σ_a (CP_{str}) which was applied as CP has not become totally elastic even after the application of a very large number of CP stress cycles. On the other hand, cyclic prestraining by 30,000 and 40,000 cycles did not show any difference for medium dense specimen (HOSTN3, Figs. 6.20a and b), whereas some differences could be observed between the responses after 25000 and 65000 cycles in loose specimen (HOSTN5, Figs. 6.21a and b).

Neither was the deformation purely elastic during isotropic reloading and re-unloading (Cycle 2) for the same range of stresses which was applied during primary loading and unloading (Cycle 1), as can be seen from Figs. 6.22e through h. The figures show the relationships between stress (σ_v=σ_h) and strains (axial strain ε_v, radial strain ε_h and volumetric strain ε_{vol}). Figs. 6.22e and f show the stress-strain relationships of Toyoura (TYK1A) and Ticino (TCK1A) sands, respectively, whereas Figs. 6.22g and h for SLB sand (SLK1V) and Hime gavel (HGK1A), respectively. Tests were performed on large triaxial specimens (Chapter 3). Test conditions are listed in Table 3.2 (Chapter 3). In each of the figures (i.e., Figs. 6.22e to h), the relationships between stress and elastic strains (ε^e_v, ε^e_h, ε^e_{vol}) are shown. Strains, both total and elastic, were initialized at the start of reloading point. Elastic strains were evaluated by integrating the following equations:

$$d\varepsilon_h = \frac{1-\nu_{hh}}{E_h}\sigma_h - \frac{\nu_{vh}}{E_v}\sigma_v \quad \text{and} \quad d\varepsilon_v = -\frac{2\nu_{hv}}{E_h}\sigma_h + \frac{1}{E_v}\sigma_v \tag{6.1}$$

In the evaluation of elastic strains, the following rules (as described in the proposed cross-anisotropic elastic model in Chapter 4) were used:

$$E_v = E_1 . f(e) . \sigma_v^{m_v} ; \quad E_h = E_1 . (1-I_0) . f(e) . \sigma_h^{m_h} ;$$
$$\nu_{vh} = \nu_0 . (\sigma_v / \sigma_h)^{m/2} ; \quad \nu_{hv} = \nu_0 . (\sigma_h / \sigma_v)^{m/2} \quad \text{and} \quad \nu_{hh} = \nu_0 \tag{6.2}$$

where the elastic parameters (E_1, I_0, m_v, m_h and ν_0) are given in Table 3.2 (Chapter 3) and $m=m_v$ was assumed. The figures (Fig. 6.22e to h) show that in no cases, deformation during isotropic reloading and re-unloading was totally elastic, except the variation of ε^e_{vol} in Figs. 6.22g and h.

SLB sand and Hime gravel are highly inherently anisotropic in the elastic Young's moduli (Chapter 3). In both cases, the reloading and re-unloading stress-strain relationships were very close to each other, but the predicted ε^e_v was less than measured ε_v, while it was opposite in the lateral strain direction. As a result, the predicted ε^e_{vol} and the measured ε_{vol} were very close to each other.

Figs. 6.23a and b show the relationships, respectively, of HOSTN3 and HOSTN5 between the stress ratio ($R=\sigma_a/\sigma_r$) and the dilatancy rate (defined as $D=-2d\varepsilon_r^p/d\varepsilon_a^p$). The relation during loading at the virgin states follow closely the Rowe's stress-dilatancy relation $R=KD$ with $K=2.95$ for HOSTN3 and $K=2.7$ for HOSTN5, but the other relations do not. Before CP, the relations approach to the non-plastic volumetric strain increment condition (i.e., $D=1.0$) for both loading ($d\sigma_a>0$) and unloading ($d\sigma_a<0$). The relations after CP show a different trend; during loading more contractive behavior ($D>1.0$) with the increase in $R=\sigma_a/\sigma_r$, whereas during unloading more dilative behavior ($D<1.0$). This behavior is much more complicated than the behavior predicted by Pradhan and Tatsuoka (1989).

Figs. 6.24a and b show the relationships between R ($=\sigma_a/\sigma_r$) and plastic prestrain-to-virgin shear strain increment ratio (PPVS) for specimens HOSTN3 and HOSTN5, respectively. PPVS decreases for both loading ($\Delta\sigma_a>0$) and unloading ($\Delta\sigma_a<0$), while a large discontinuity along PPVS axis exists at the point of stress reversal. With the increase in loading cycle (i.e., CP), the value of PPVS for a given σ_a gradually decreases in such a way that the σ_a~PPVS relation for a particular cycle (during loading or unloading) remains parallel to the similar relation at the virgin state.

Figs. 6.25a~f show the relationships between the tangent Young's modulus ($E_{tan}=d\sigma_a/d\varepsilon_a$) and the axial stress ($\sigma_a$) obtained from the hysteresis curves shown earlier in the previous section (Figs. 6.17a, 6.18a, 6.19a through d). Variation of E_{max} (see also Figs. 6.6a through f) along the CP stress cycle is also plotted for comparison. For Figs. 6.25a (HOSTN3) and b (HOSTN5), the corresponding responses 'before CP' were obtained when the specimens were in the true virgin state, while in the remaining cases, the responses (before CP) were affected by previous stages of CP, smaller amplitude CL, and/or at least the previous ten load-cycles of the same stress-amplitude. The values of E_{tan} during both reloading (σ_a increasing) and unloading (σ_a decreasing)

phases of the virgin specimen (i.e., 'immediately before CP) were greatly influenced by continuous plastic deformation (Fig. 6.25f; TYRA 3). The effect of creep was large at the vicinity of the lowest and the highest stress states during the CP stress cycle (i.e., the segments ef and gh of the unloading curve while ab and cd of the reloading curve in Fig. 6.25f). That is, due to this creep effect, the E_{tan} values observed immediately after reversing the loading direction (i.e., those near the point a and e) are noticeably larger than the respective elastic Young's modulus E_{max} measured under otherwise the similar condition. For all cases, the E_{tan} value decreases compared with the respective E_{max} value both with the increase in σ_a during reloading and with the decrease in σ_a during unloading. These results show that plastic strain increments take place similarly during reloading and unloading. Prestrained specimen, on the other hand, exhibits rather similar values of E_{tan} at a given σ_a for both reloading and unloading phases (with the maximum 20% difference betwen them), while the difference between the corresponding E_{tan} and E_{max} values is much smaller than it is before CP except for HOSTN1: CP-1 (Fig. 6.25c). This is due to a substantial decrease in plastic strain increments during CP. Yet the average of unloading E_{tan} and reloading E_{tan} at a given σ_a along the CP stress cycle of the prestrained specimen was lower than the corresponding value of E_{max} of the same specimen. This difference between the values of E_{tan} and E_{max} is due to the ratio of plastic-to-elastic strain increment (during unloading and reloading) of the same prestrained specimen (for instance, Fig. 6.20a). Due to CP-induced anisotropy, the value of E_{tan} at a given σ_a (especially at the lower value of σ_a) of the prestrained specimen was lower than the corresponding value of the virgin specimen in spite of reduced plastic strain increments. Fig. 6.25c is the best example for CP-induced anisotropy: E_{tan} for any σ_a (more-or-less) after CP along the CP stress path was smaller than that the corresponding value before CP.

The relationships between the ratio E_{tan}/E_{max} and σ_a are shown in Figs. 6.25g and h for specimens HOSTN3 and HOSTN5, respectively. Both E_{tan} and E_{max} values were measured at the same time. The effects of CP on the ratio $d\varepsilon_a^p$ / $d\varepsilon_a^c$ are more directly reflected in these relations. By CP, the ratio E_{tan}/E_{max} increases for the whole range of σ_a during both loading and unloading, except at the start of loading and at the start of unloading of HOSTN3 specimen. Also, similarly during loading and unloading, the ratio E_{tan}/E_{max} decreases as loading or unloading continues in the same direction.

6.5.7. Effects of CP on the monotonic behavior during triaxial compression tests

The results of both virgin and prestrained specimens of Hostun sand tested under the triaxial compression condition at air-dried conditions are presented and discussed. Cyclic prestraining was applied at a frequency in the range between 0.1 and 0.5 Hz by constant but different amplitude cyclic axial load (CP_{str}). CP was applied symmetrically about a neutral stress state (see Table 6.1), which was either anisotropic or isotropic with confining pressure at σ_c=0.8 kgf/cm^2. However, the subsequent monotonic triaxial compression (TC) tests were started at isotropic stress state (i.e., σ_a=σ_r=0.8 kgf/cm^2). One test was performed on a virgin specimen (HOSTN6) having a void ratio $e_{0.8}$= 0.76.

Table 6.4 lists the specimens with some results. Fig.6.26a shows the relationships between the deviatoric stress, $q=\sigma_a-\sigma_r$, and ε_a up to near peak of the all the specimens of Table 6.3. The axial strains were measured by using a pair of LDTs and a proximeter. After LDTs stopped functioning (i.e., at around ε_a=1.5%), ε_a values measured by proximeter are considered. The stress-strain relationships for the entire axial strain range measured are affected by the multi-stages CP. The specimens, HOSTN1, HOSTN5 (both prestrained) and HOSTN6 (virgin), having the similar void ratios (Table 6.4) show similar peak, which indicates that CP has no effect on the peak deviatoric stress, q_{max}. Teachavorasinskun (1992) observed similar results.

Fig. 6.26b shows the relationships between the volumetric strain (ε_{vol}= ε_a+2ε_r) and ε_a. The amount of maximum contraction is clearly reduced by CP if we compare specimens HOSTN1, HOSTN5 and HOSTN6. Although density is different, HOSTN3 also shows more dilation than HOSTN6. Teachavorasinskun (1992) also showed that the prestrained specimens tend to dilate more than the virgin specimen. Fig. 6.26c shows the relationships between plastic volumetric strain ε^p_{vol} and q of HOSTN6 (virgin) and HOSTN3 (prestrained) specimens. For comparison, the $q\sim\varepsilon_{vol}$ relationships are also shown in Fig. 6.26d. The value of ε^p_{vol} was obtained by the following Eqs. 6.3.

$$\varepsilon^p_{vol} = \int d\varepsilon^p_{vol} \;;\quad d\varepsilon^p_{vol} = d\varepsilon^p_a + 2d\varepsilon^p_r$$

$$d\varepsilon^p_a = d\varepsilon_a - d\varepsilon^e_a \;;\quad d\varepsilon^e_a = d\sigma_a / E^e \qquad (6.3)$$

$$d\varepsilon^p_r = d\varepsilon_r - d\varepsilon^e_r \;;\quad d\varepsilon^e_r = -\nu^e d\varepsilon^e_a$$

No appreciable difference is noticeable between the figures when plotted for the full range of q. However, the effects of CP on ε^{p}_{vol} can be seen more clearly than on ε_{vol}, when the corresponding relationships are plotted for smaller range of q (Figs. 6.26e and f).

Figs. 6.27a through c show the $q\sim\varepsilon_a$ relationships at small strain levels, and Figs. 6.27d and e show the $\varepsilon_a\sim\varepsilon_{vol}$ relationships, which correspond to Figs. 6.27a and b, respectively. The $\varepsilon_a\sim\varepsilon_{vol}$ relationship, which corresponds to Fig. 6.27c, is not shown because ε_{vol} was affected by large scatter resulting from ε_r measurements (by proximeters due to low resolution). It is clear that CP increased the linearity in the stress-strain relationship up to about $\varepsilon_a\approx0.01\%$ (Fig. 6.27c). For a wider strain range, however, the stress-strain relationships become concave upward due to CP (Figs. 6.27a and b). This kind of behavior can be observed usually during unloading, and theoretically also in an elastic material having a tangent Young's modulus that increases with the axial stress. That is, as seen in the previous Chapter 4 and also earlier in this chapter that the elastic Young's modulus in the vertical (axial) direction of granular material increases with the increase in the axial stress and due to CP, on the other hand, the deformation becomes nearly elastic at least in the stress range of CP_{str} without the elastic parameters being altered significantly. It is important to note that HOSTN1 exhibits weaker response than the virgin specimen (HOSTN6) (Figs. 6.27b and c). It could be an effect of the latest CP (i.e., CP-3) during which the specimen HOSTN1 came closer to the failure state in extension than in compression. In the cases of other specimens (HOSTN3 and HOSTN5), the latest CP (or the only CP) was entirely compression bias.

Fig. 6.28a compares the relationship between the secant Young's modulus (E_{sec}) after dividing by (i.e., normalization) the maximum E_{sec} (i.e., $(E_{sec})_{max}$) and ε_a (in logarithmic scale). Fig. 6.28b shows the variation of E_{tan} after normalization by the maximum E_{tan} (i.e., $(E_{tan})_{max}$) with ε_a (in logarithmic scale). The values of $(E_{tan})_{max}$ and $(E_{sec})_{max}$, together with E^e (for prestrained specimens, the latest E^e), are given in Table 6.4. Figs. 6.29a and b show the relationships of normalized E_{sec} and normalized E_{tan}, respectively, with ε_a at small strain level (i.e., ε_a up to 0.5% in normal scale). Figs 6.30a and b compare the relationships of normalized E_{sec} and normalized E_{tan}, respectively, with the stress level, which was defined as the ratio of q to q_{max}. It is clear that at intermediate strain and stress levels, the prestrained specimens are much stiffer than virgin

specimens. The elastic threshold limit of the prestrained specimens has been enlarged. The concave upward shape of the stress-strain relationships as observed in Figs. 6.27a and b is reflected in the E_{tan} and E_{sec} variations, especially with q/q_{max}. That is, both E_{tan} and E_{max} increase with stress level up to certain range due to elastic deformation characteristics as described before.

A relationship which may be applicable to more general types of stress path (other than the TC stress path at a constant σ_h ($=\sigma_r$) would be the relationship between E_{tan} / E^e and q/q_{max} (Figs. 6.31a and b). The stiffness E^e ($=E_1.f(e).\sigma_a^m$) is the value that was determined by small cyclic tests along isotropic stress state or along a constant σ_r ($=0.8$ kgf/cm^2) stress path. Damage to E^e value as the stress level approaches to the peak (Chapter 5) was not considered. Here, the respective Current E_1 and m values are used, which were obtained immediately before shearing for specimens HOSTN1, HOSTN3 and HOSTN5 (i.e., the effects of CP-induced anisotropy are included in the particular specimens). $E_{tan}/E^e \sim q/q_{max}$ relationship based on the elastic parameters obtained at the virgin state (i.e., obtained before any CP application) for specimen HOSTN5 was also shown in Figs. 6.31a and b. For the virgin specimen HOSTN6, m=0.45 is an assumed value, while E_1 is based on a single measured value of E^e at $\sigma_a=\sigma_r=0.8$ kgf/cm^2. The figures show that although the trends are different, E_{tan} / E^e decreases with q/q_{max} in both virgin and prestrained specimens.

6.5.8. Summaries

(a) The elastic deformation characteristics of granular soil become anisotropic as a result of the application of a large amplitude cyclic axial loading with a large number of cycles (as called CP) in addition to the stress system-induced anisotropy. That is, CP was observed to affect the dependency on the axial stress σ_a of the elastic Young's modulus E_{max} evaluated based on very small increments of axial stress and strain; The dependency of E_{max} on σ_a increases by CP. This kind of anisotropy may be called the CP-induced anisotropy. As a result, E_{max} measured at the neutral stress state (isotropic or anisotropic) during CP was observed to scatter in the range of 0.78~1.20 time the initial value depending on different stress-strain conditions during CP.

(b) Similar effects of CP were observed on the decay curve between E_{eq} and $(\varepsilon_a)_{SA}$. That is, E_{eq}~$\log((\varepsilon_a)_{SA})$ relationship after CP was observed to change in that E_{eq} increases or decreases for the whole strain range compared to the corresponding relation obtained immediately before CP.

Therefore, the shape of the normalized decay curves obtained before and after CP were observed to become different from each other.

(c) Equivalent Poisson's ratio at relatively large strains also decreased as a result of CP, while the Poisson's ratio (ν^e) at very small elastic strains $(\varepsilon_a)_{SA}$ ($\approx 10^{-5}$ or less) was insensitive to CP. Despite CP-induced anisotropy observed in the small strain stiffness, CP did not bring about any change in the dependency of ν^e on stress ratio (σ_a/σ_r).

(d) Damping ratio at strains exceeding the elastic limit strain decreased drastically by the application of a large number of large amplitude axial strain during CP, which leads to the enlargement of the so-called elastic limit; the limit increased with the increase in the number of loading cycles during CP.

(e) When the E_{max} value decreased or increased by CP, a slight increase or decrease in the E_{max} value with elapsed time was observed during post-CP consolidation period, which means a gradual decrease in the effects of CP-induced anisotropy with time. Similar effect was reflected on the E_{eq}~$\log((\varepsilon_a)_{SA})$ relationship. Damping ratio also decreased slightly during the post-CP consolidation period. The E_{max} value increased slightly during pre-CP long-term consolidation period.

(f) The plastic strain increment decreases drastically with cyclic loading along a fixed stress path, but the deformation does not become totally elastic even after applying a large amount of CP with a relatively large amplitude of axial stress cycle. The elastic deformation characteristics are much more stable compared to plastic deformations, but they also changes slightly showing cyclic strain-induced anisotropy. Therefore, the deformation of sand cannot be modeled precisely by a simple elasto-plastic model having fixed range of elasto-plastic behavior which is independent of repeated loading. The stress-dilatancy relation is also changed by cyclic loading in a complicated manner.

(g) Cyclic prestraining increases stiffnesses (tangent and secant moduli) largely at intermediate strain (and stress) levels during monotonic triaxial compression (TC) test although the initial stiffness does not change significantly. Consequently, the E_{tan} value of a cyclically prestrained specimen can increase with the increase in the axial stress in triaxial compression. On the other

hand, even for CP specimens, the ratio of E_{tan} to the current elastic Young's modulus always decreases with the increase in the axial stress. CP does not bring about any change in the peak strength.

Table 6.1: List of the materials

Sand	D_{10}(mm)	D_{50}(mm)	U_c	G_s	e_{max}	e_{min}
Toyoura	0.11	0.162	1.46	2.64	0.97	0.61
Hostun	0.17	0.31	1.94	2.65	0.95	0.55

Table 6.2: List of the specimens subjected to cyclic prestraining and some test results.

Material (sand)	Specimen	[a]$e_{0.8}$	CP No.	CP_{str} (kgf/cm^2)	[b]$(\varepsilon_a)_{SA}$ (%)	N (x1000)	Δe	Translation of strain (%)	
								[c]$\Delta\varepsilon_a$	[c]$\Delta\varepsilon_r$
Hostun	HOSTN1	0.75	CP-1	0.8~2.0	0.033	25	0.749~0.747	+0.225	-0.031
			CP-2	0.35~2.0	0.061	30	0.744~0.744	-0.077	+0.017
			CP-3	0.22~1.4	0.052	120	0.744~0.744	-0.012	+0.003
	HOSTN3	0.72	-	0.8~2.0	0.031	40	0.720~0.719	+0.102	-0.026
	HOSTN5	0.78	-	0.8~2.0	0.030	25~65	0.779~0.773	+0.982	-0.203
Toyoura	TYRA 3	0.75	-	0.35~1.3	0.025	25	0.750~0.749	-0.107	+0.022

[a]: The subscript indicates the value of confining stress (kgf/cm^2) at which the void ratio e was measured first.
[b]: It represents the single amplitude strain observed when nominal stress amplitude CP_{str} was applied after CP.
[c]: the sign + indicates compression and - indicates extension.

Table 6.3: List of the elastic parameters.

Specimen	CP Designation	[a]Elastic parameters [E_1 (kgf/cm^2): m]				
		At the beginning of CP		At the end of CP		State of stresses
		Loading	Unloading	Loading	Unloading	
HOSTN1	CP-1	1930 : 0.38	2005 : 0.47	1853 : 0.82	1875 : 0.93	Compression
	CP-2	1640 : 0.62	1810 : 0.64	2276 : 0.59	-	Compression
		1674 : 0.67	1916 : 0.73	2436 : 0.99	-	Extension
	CP-3	2091 : 0.78	-	2124 : 0.81	2150 : 0.83	Compression
		2198 : 0.96	-	2113 : 1.00	-	Extension
HOSTN3	-	1964 : 0.43	2096 : 0.48	1878 : 0.78	1920 : 0.80	Compression
HOSTN5	-	*1800 : 0.47	-	1536 : 0.81	-	Compression
TYRA 3	-	1704 : 0.40	-	1580 : 0.81	-	Compression
		1894 : 0.80	-	1626 : 0.95	-	Extension

[a] : $E^e = E_1.f(e).\sigma_a^m$: $f(e) = (2.17-e)^2 / (1+e)$; The sign '-' indicates that either CP designation is not required or data is not available.

*: data obtained from isotropic stress states between 0.8 to 3.0 kgf/cm^2.

Table 6.4: Listed of the specimens subjected to TC test.

Specimen	$e_{0.8}$	[b]e_{sh}	ϕ_{max} (degree)	$(E_{tan})_{max}$ (kgf/cm^2)	$(E_{scc})_{max}$ (kgf/cm^2)	E^e (kgf/cm^2)
HOSTN1	0.75	0.745	39.8	2080	2310	2100
HOSTN3	0.72	0.719	42.8	1875	2040	1910
HOSTN5	0.78	0.774	39	1505	1570	1400
HOSTN6	0.76	0.760	39.5	1690	1730	1640

[b]: Void ratio at the start of the final TC to failure.

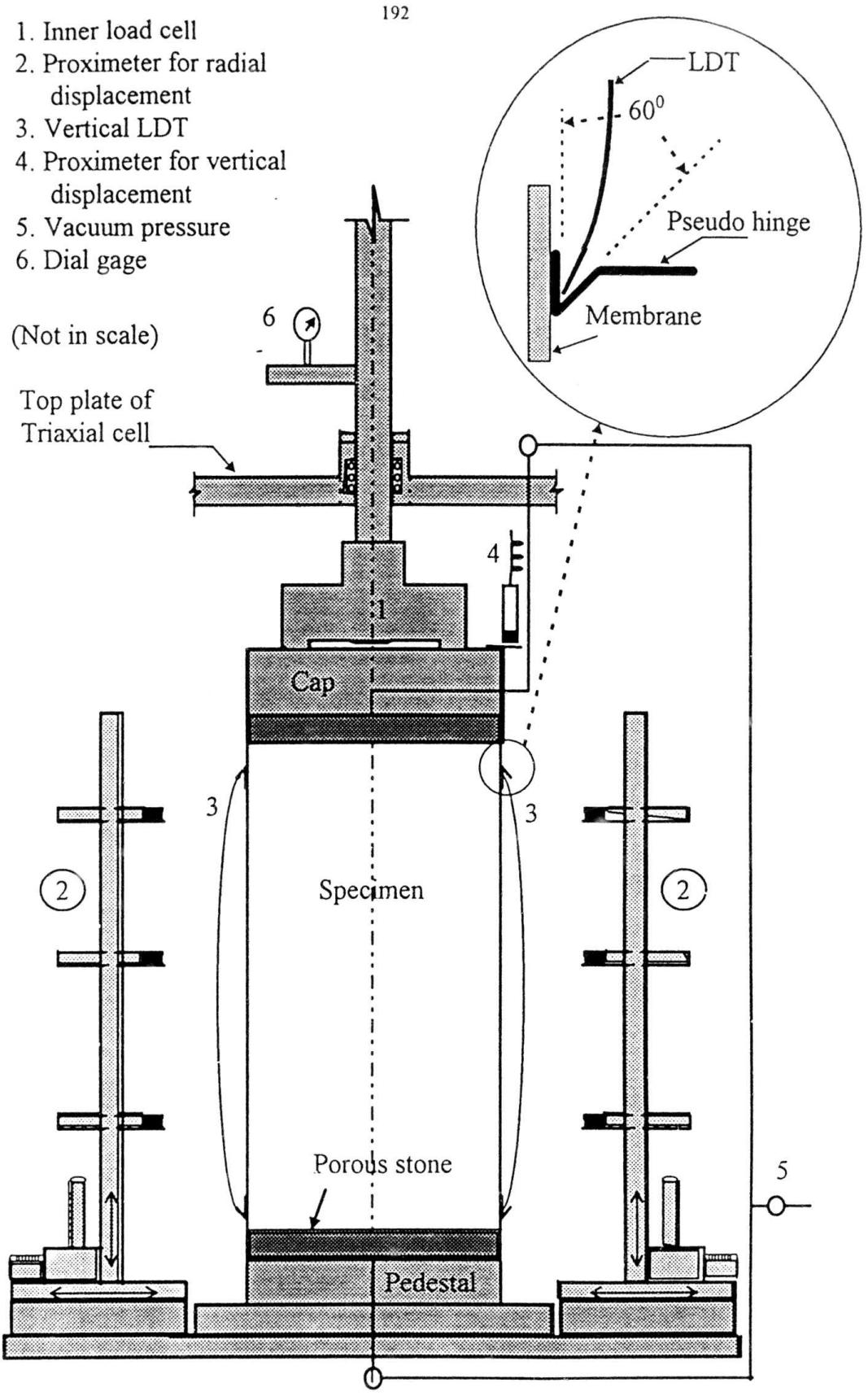

Fig. 6.1a: The triaxial apparatus.

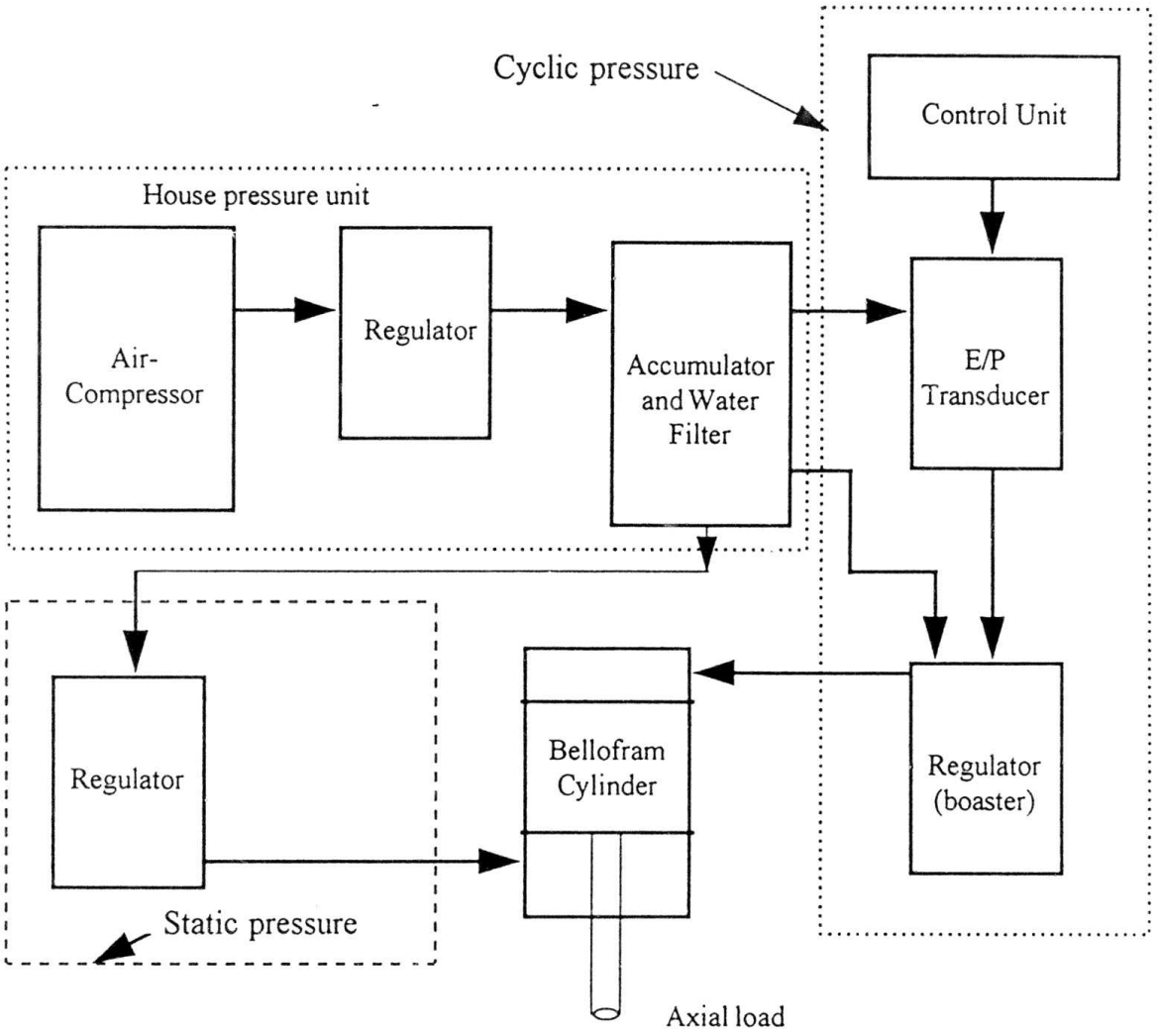

Fig. 6.1b: Block diagram of load-control deviator loading system.

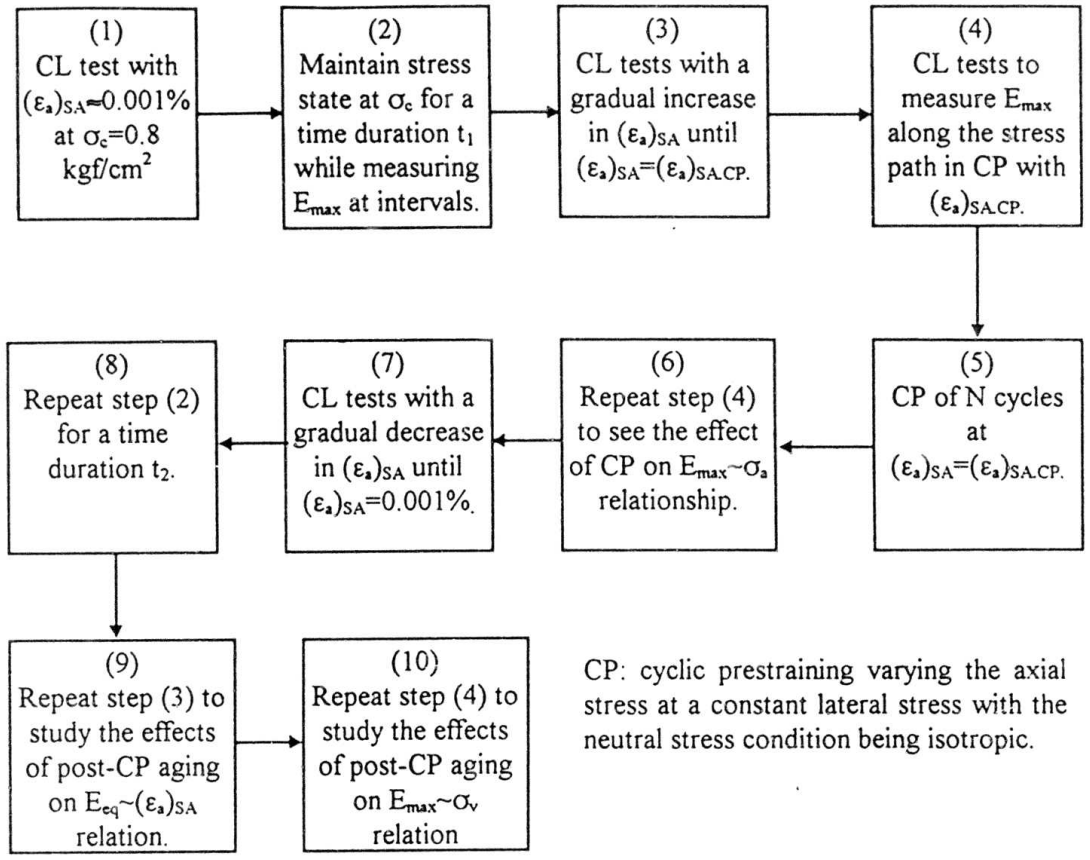

Fig. 6.2a: Block diagram of test program for cyclic prestraining.

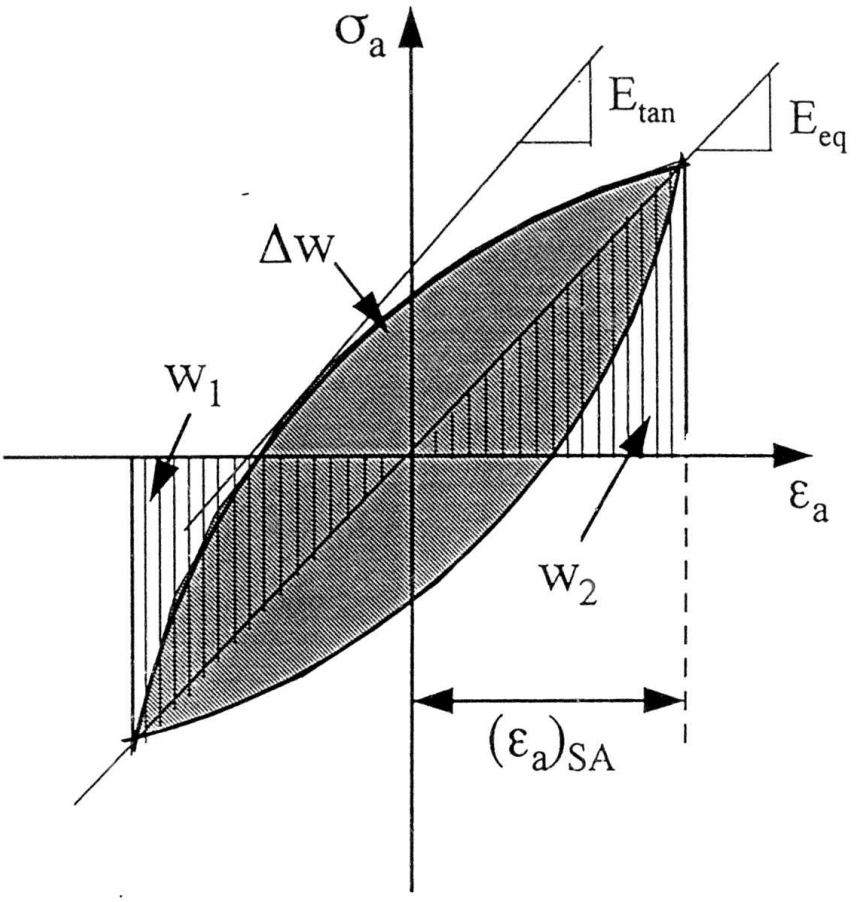

Fig. 6.2b: Definitions of E_{eq}, E_{tan}, and h.

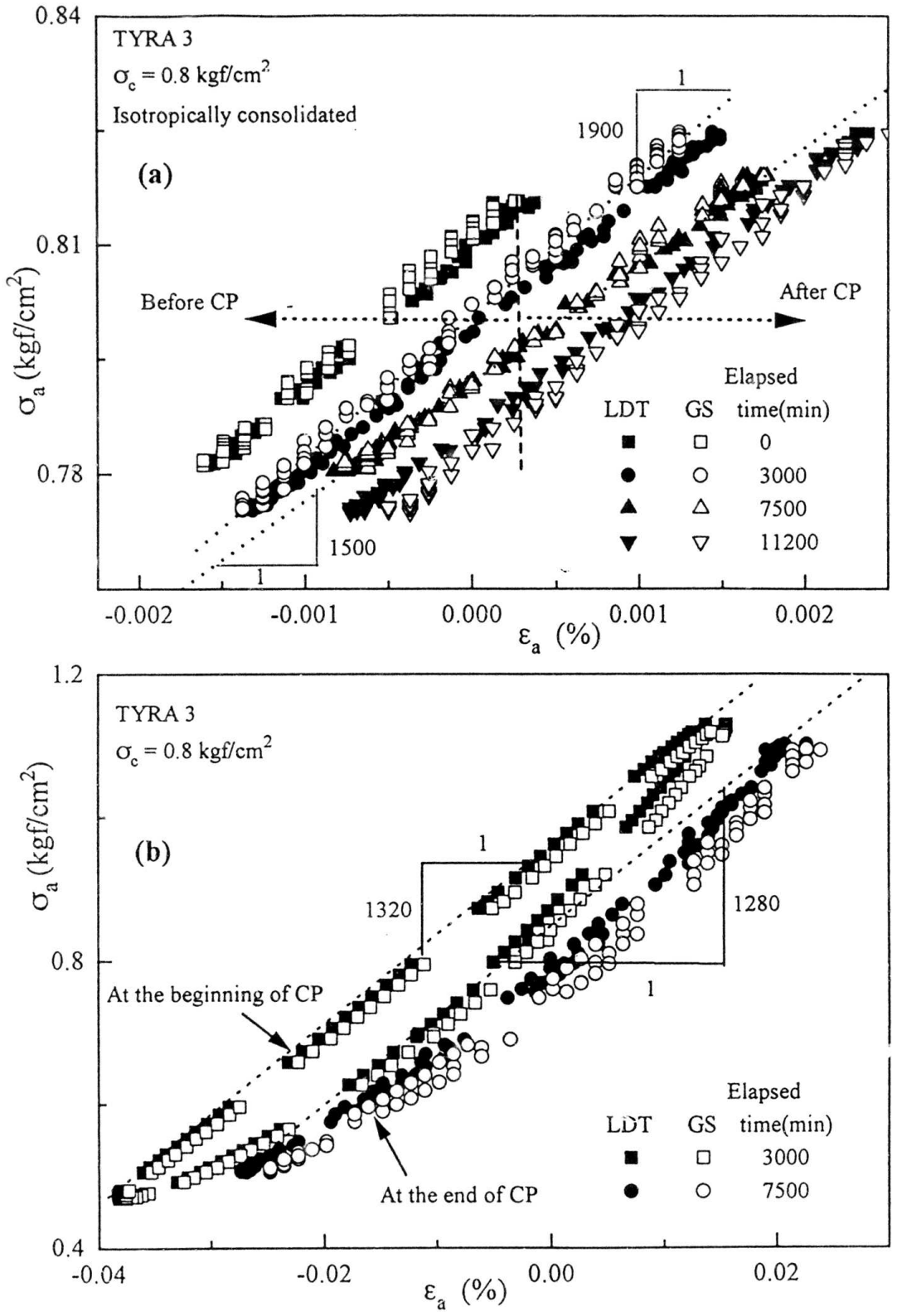

Figs. 6.3: σ_a~ε_a responses of typical CL tests from TYRA 3 specimen with (a) $(\varepsilon_a)_{SA}$ <= 0.002%, and (b) $(\varepsilon_a)_{SA}$ for CP stress cycle.

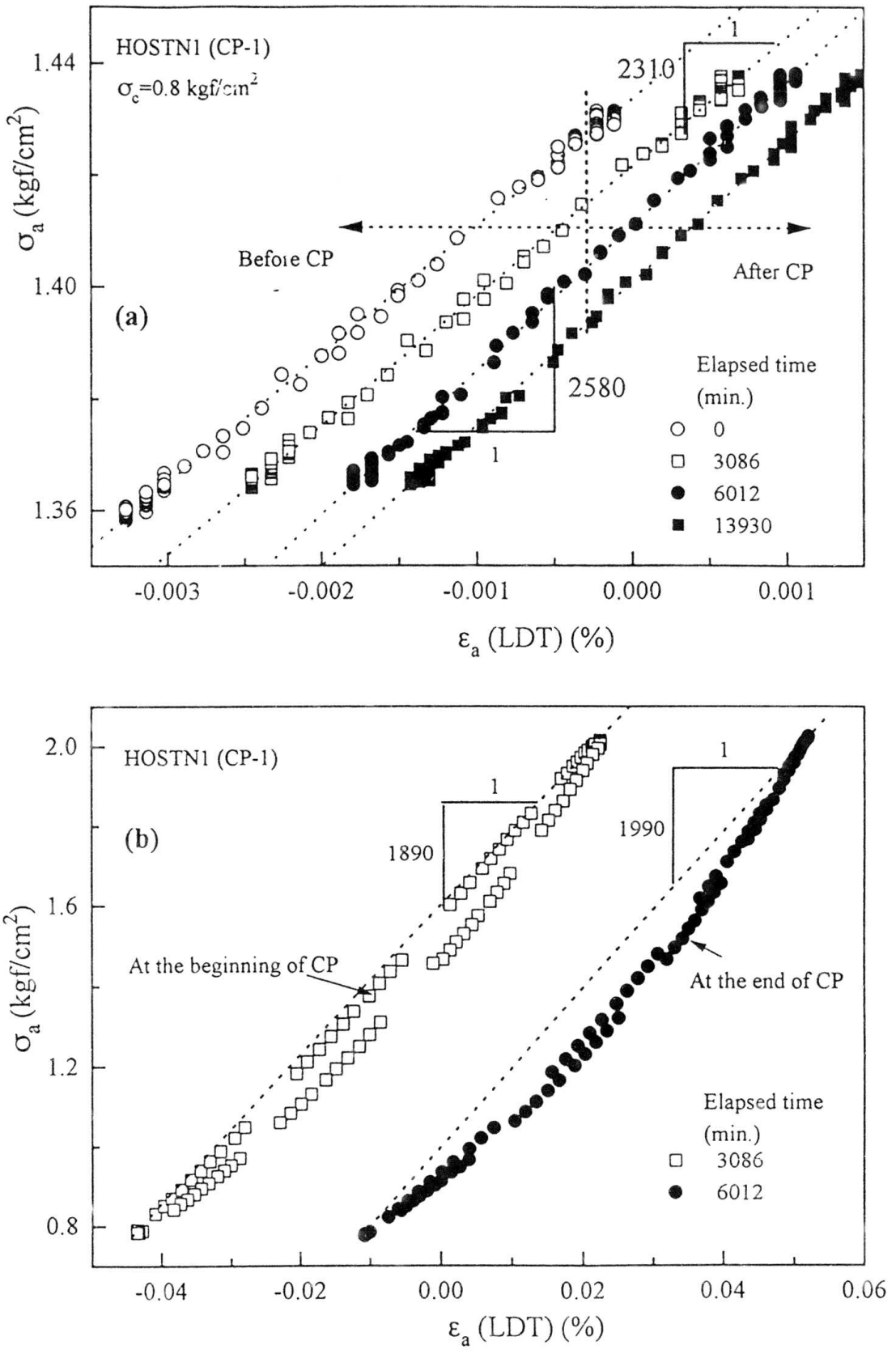

Figs. 6.4: σ_a~ε_a responses of typical CL tests from HOSTN1 (CP-1) specimen with (a) $(\varepsilon_a)_{SA}$ <= 0.002%, and (b) $(\varepsilon_a)_{SA}$ for CP stress cycle.

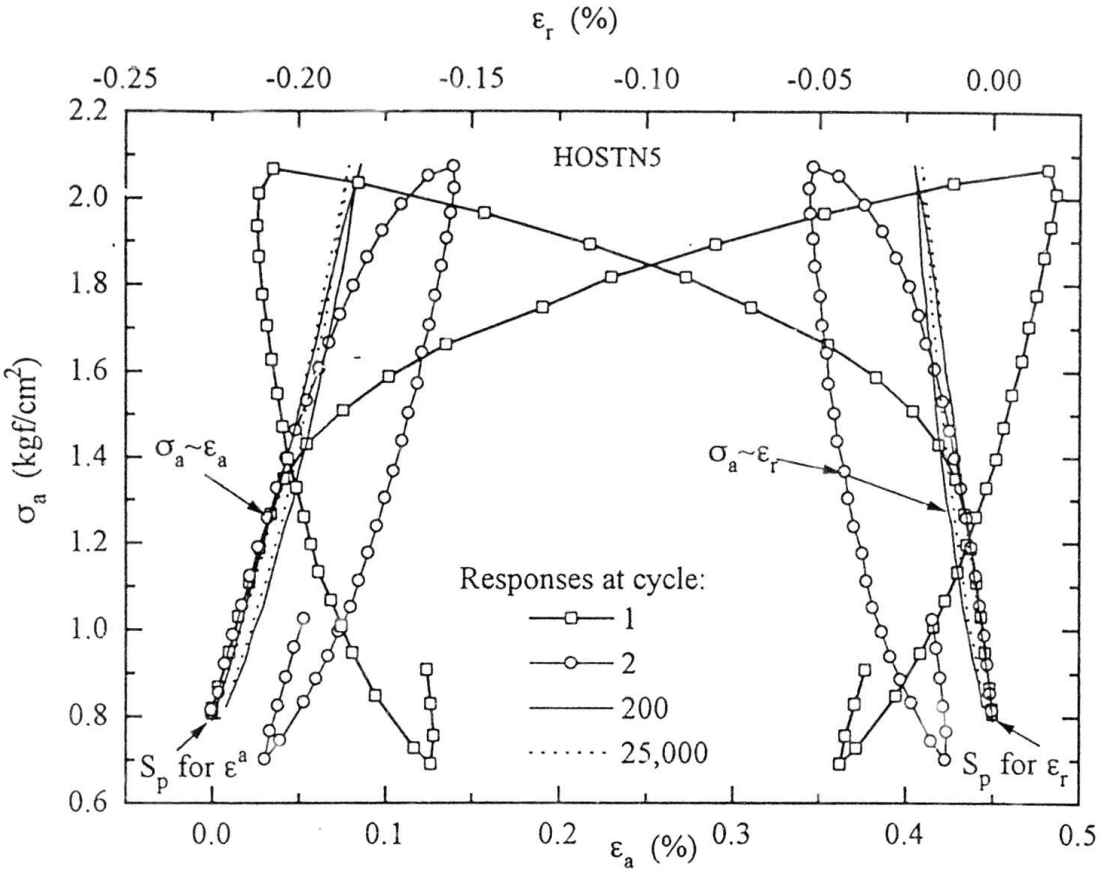

Fig. 6.5a: σ_a~ε_a and σ_a~ε_r relationships of typical large amplitude CL tests at true virgin state of HOSTN5 specimen.

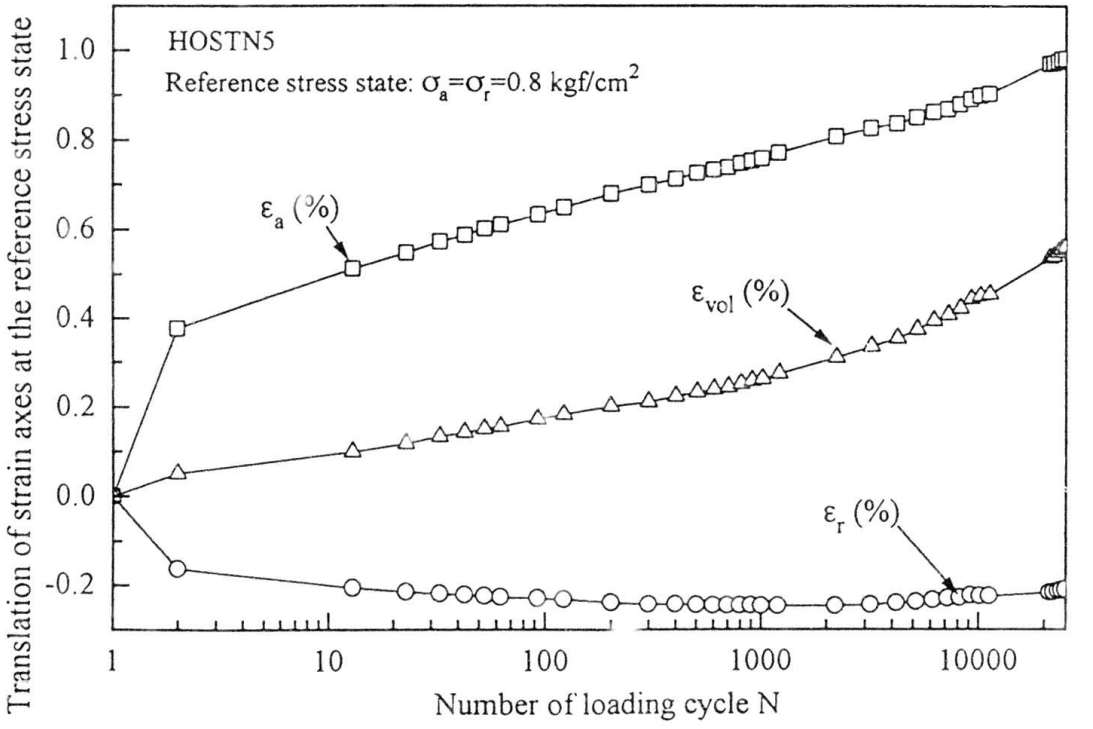

Fig. 6.5b: Variations of the translation of strain axes with the number of loading cycle during CP.

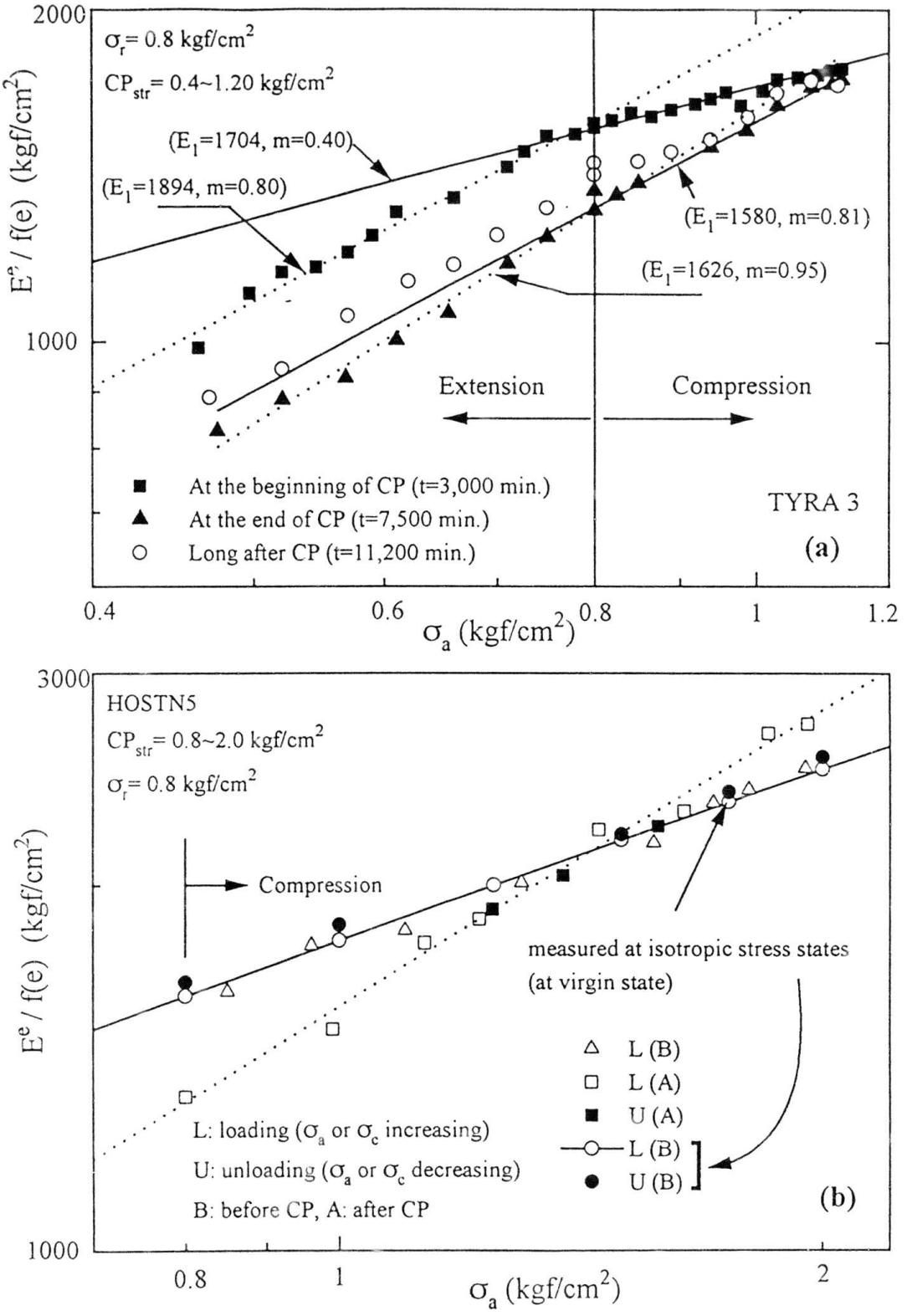

Figs. 6.6: Relationships between $E^e/f(e)$ and σ_a along CP stress path for specimens (a) TYRA 3, and (b) HOSTN5.

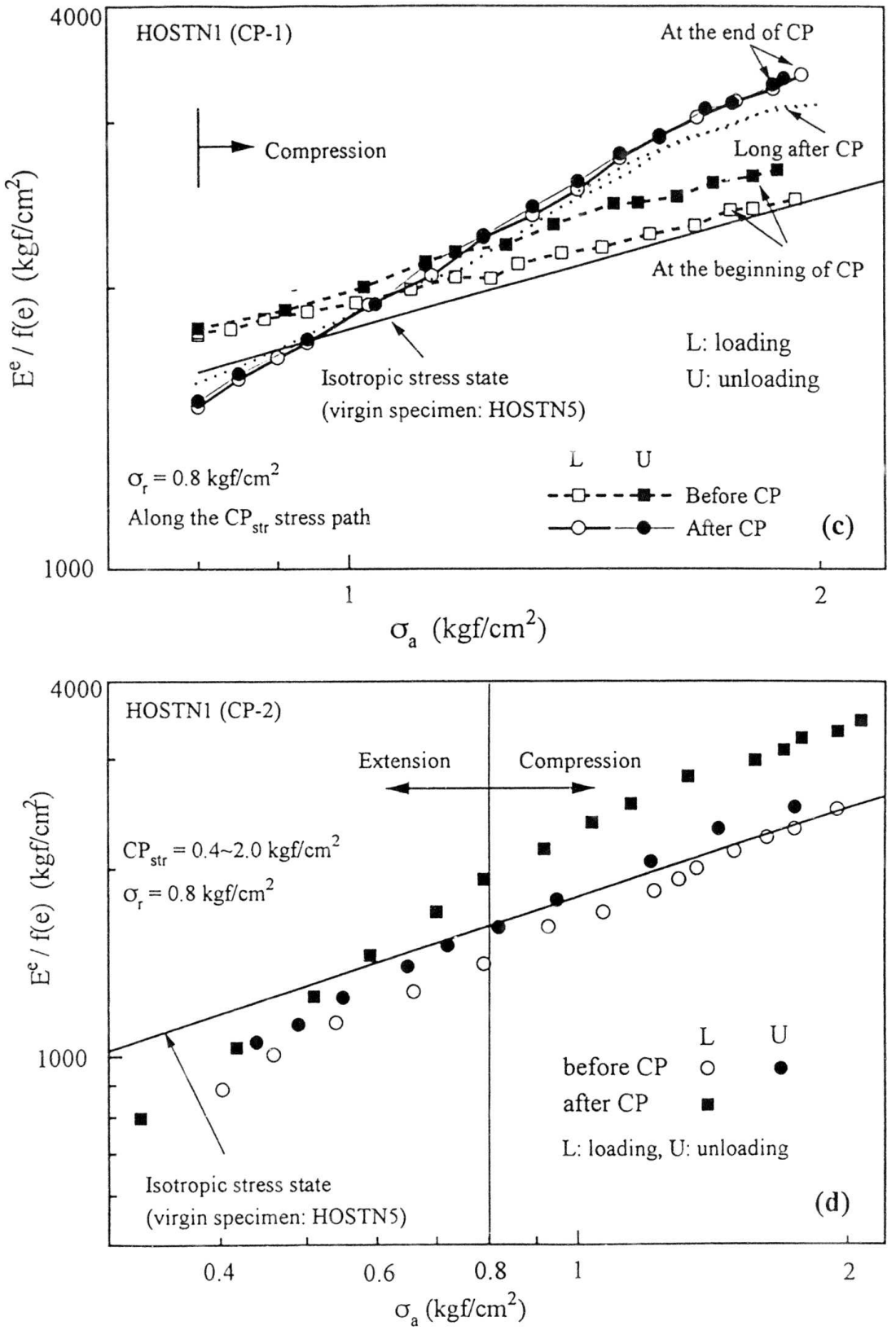

Figs. 6.6: Relationships between $E^e/f(e)$ and σ_a along CP stress path of HOSTN1 specimen for (c) CP-1, and (d) CP-2.

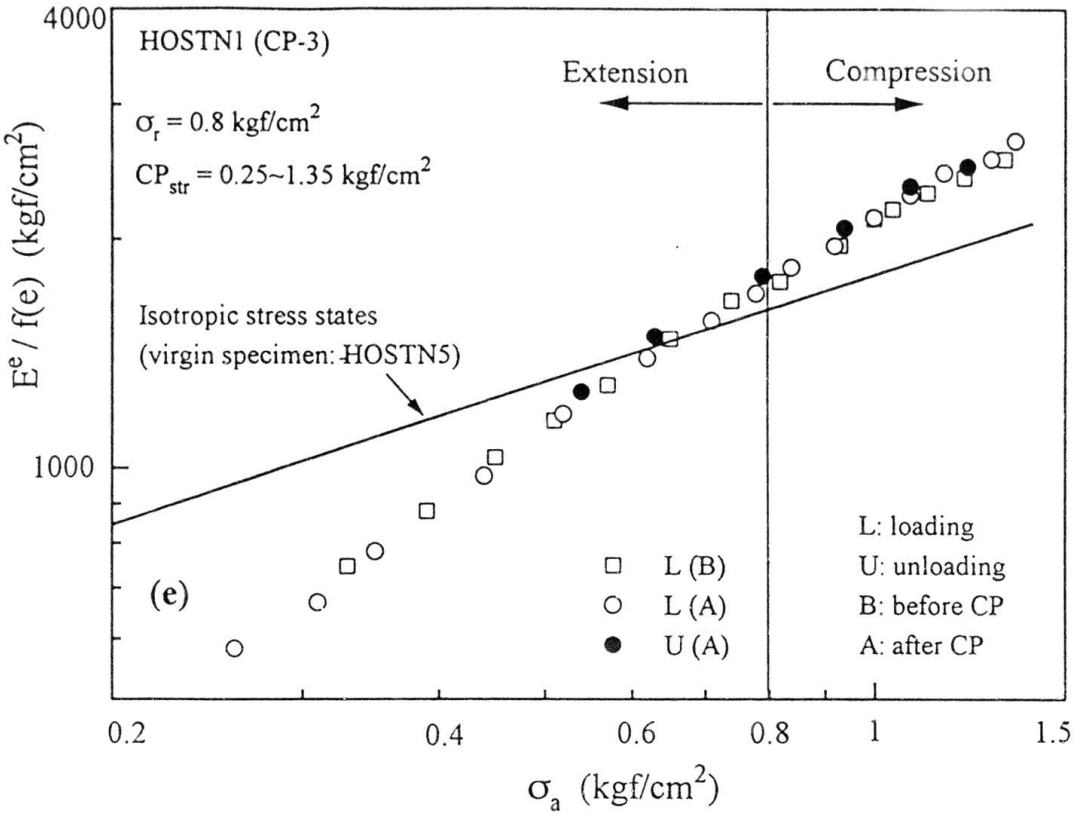

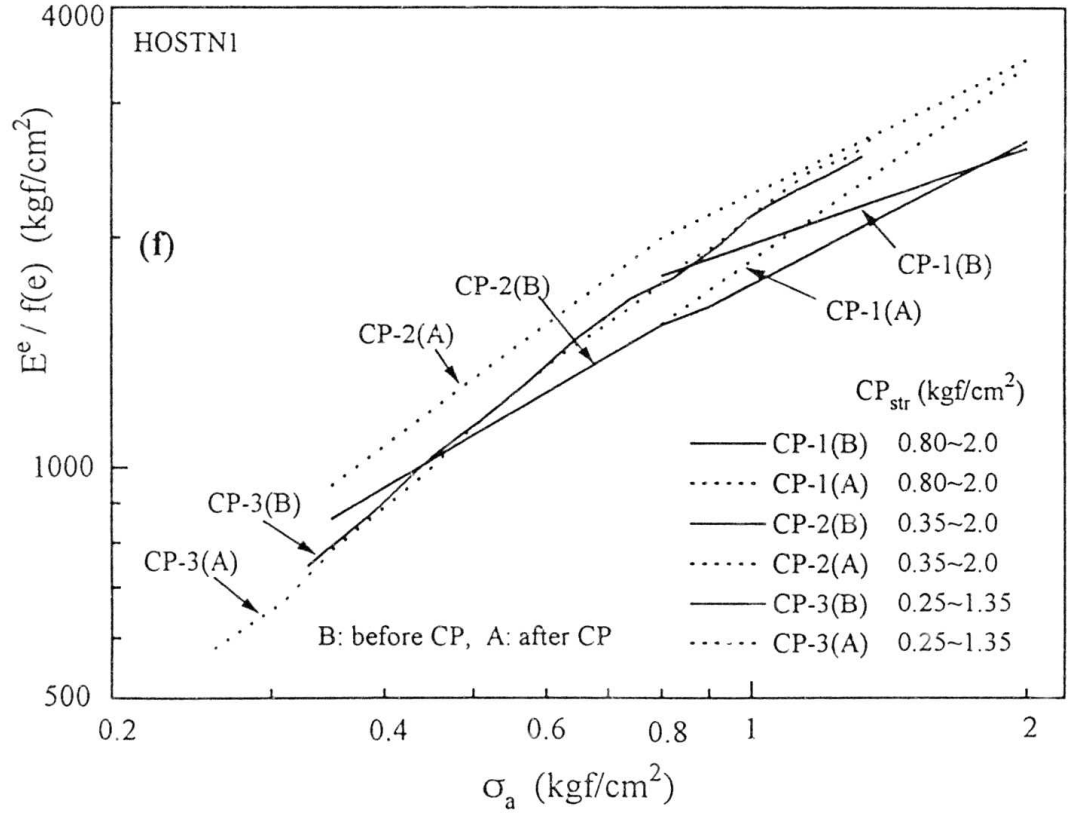

Figs. 6.6: Relationships between $E^e/f(e)$ and σ_a along CP stress path of HOSTN1 specimen for (e) CP-3, and (f) CP-1, CP-2 and CP-3 (overlapping).

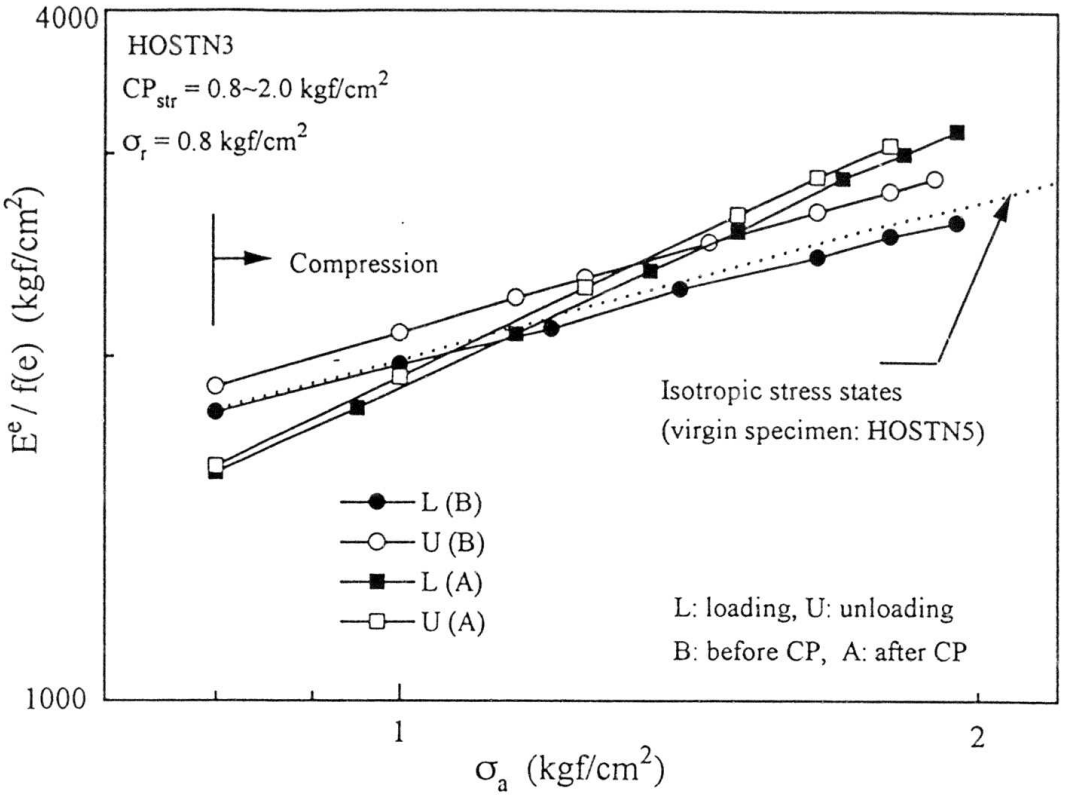

Fig. 6.6g: Relationships between $E^e/f(e)$ and σ_a along CP stress path of HOSTN3 specimen.

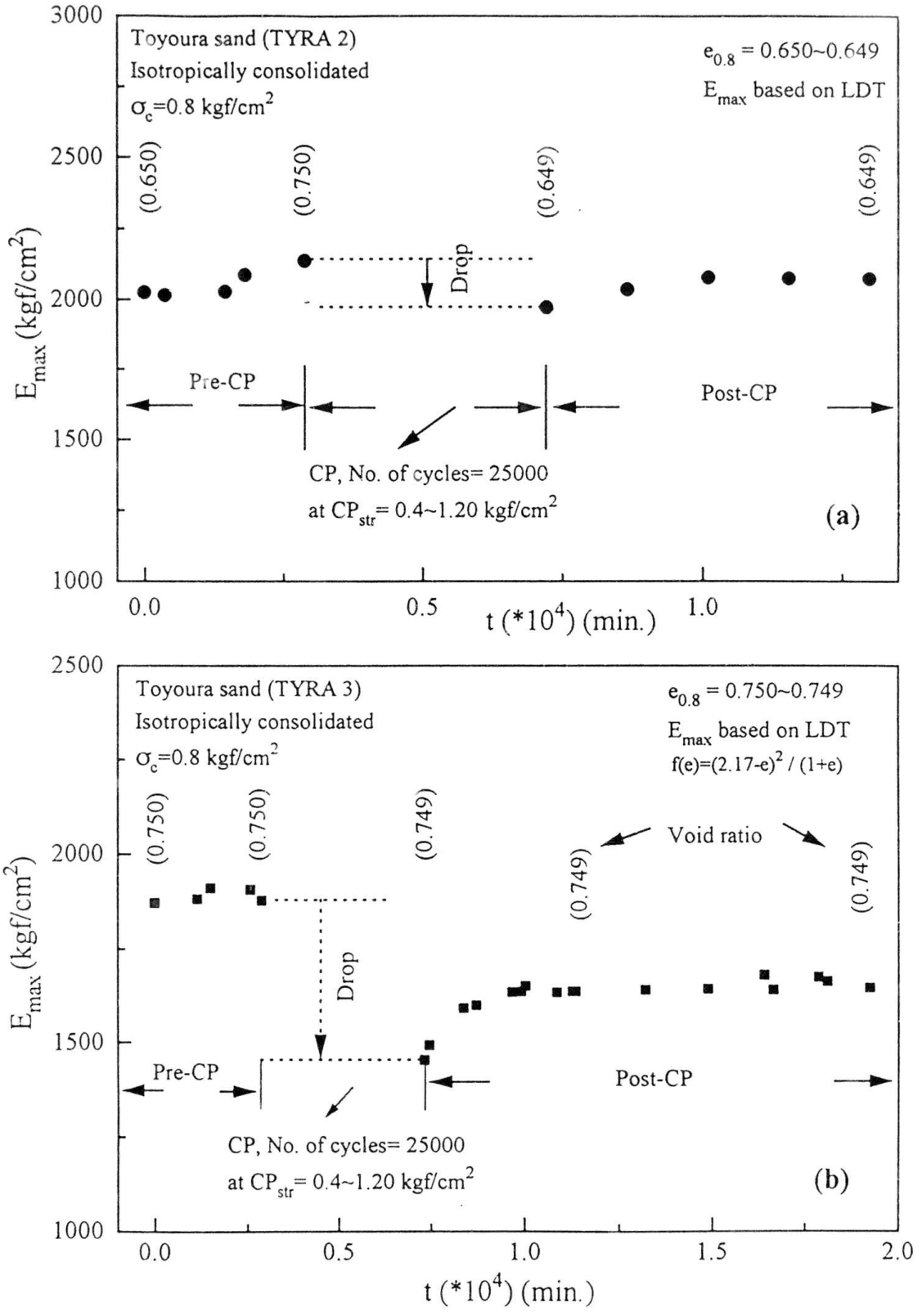

Figs. 6.7: Time histories of the variation of E_{max} for specimens (a) TYRA 2 and (b) TYRA 3.

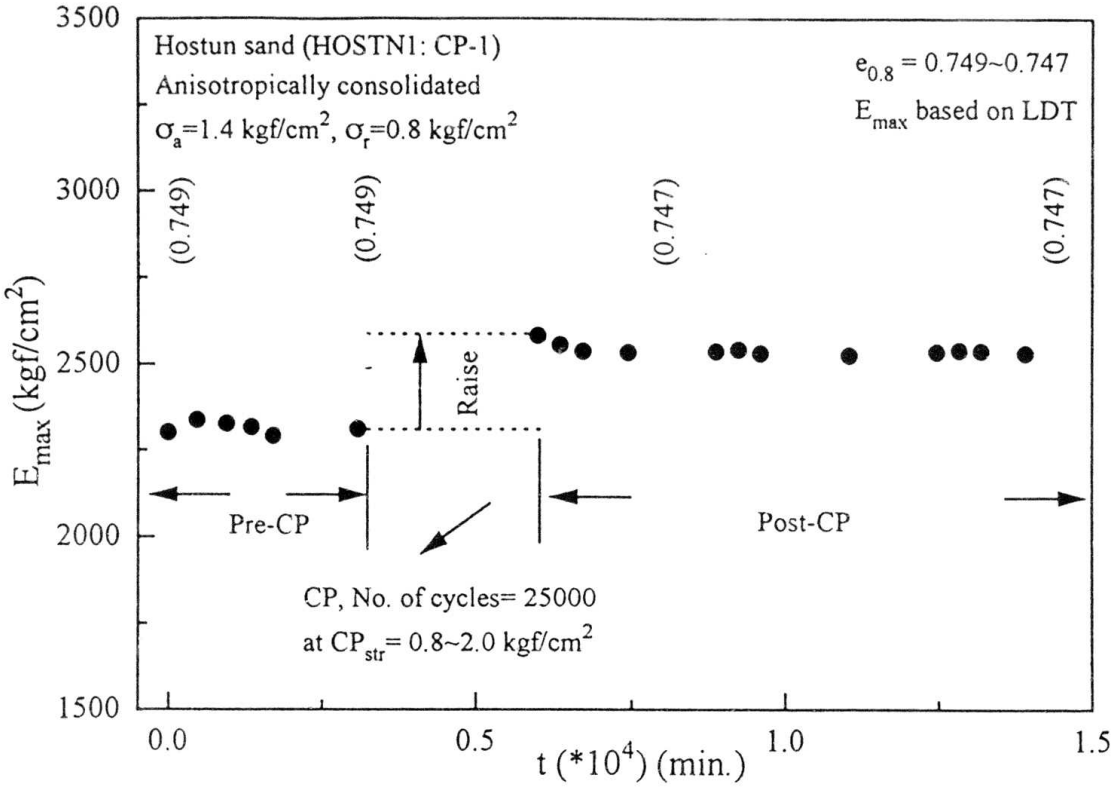

Fig. 6.7c: Time histories of the variation of E_{max} for HOSTN1 (CP-1) specimen.

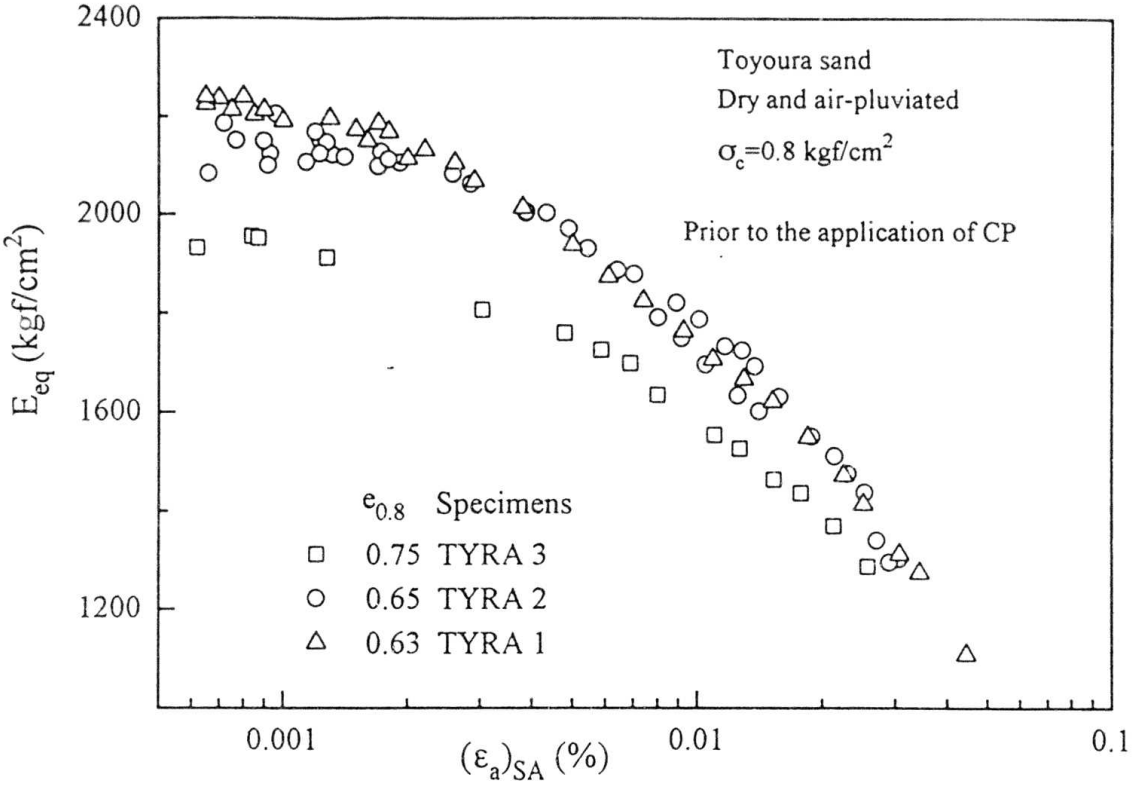

Fig. 6.8a: E_{eq}~log($(\varepsilon_a)_{SA}$) relations (before CP application) of the specimens of Toyoura sand.

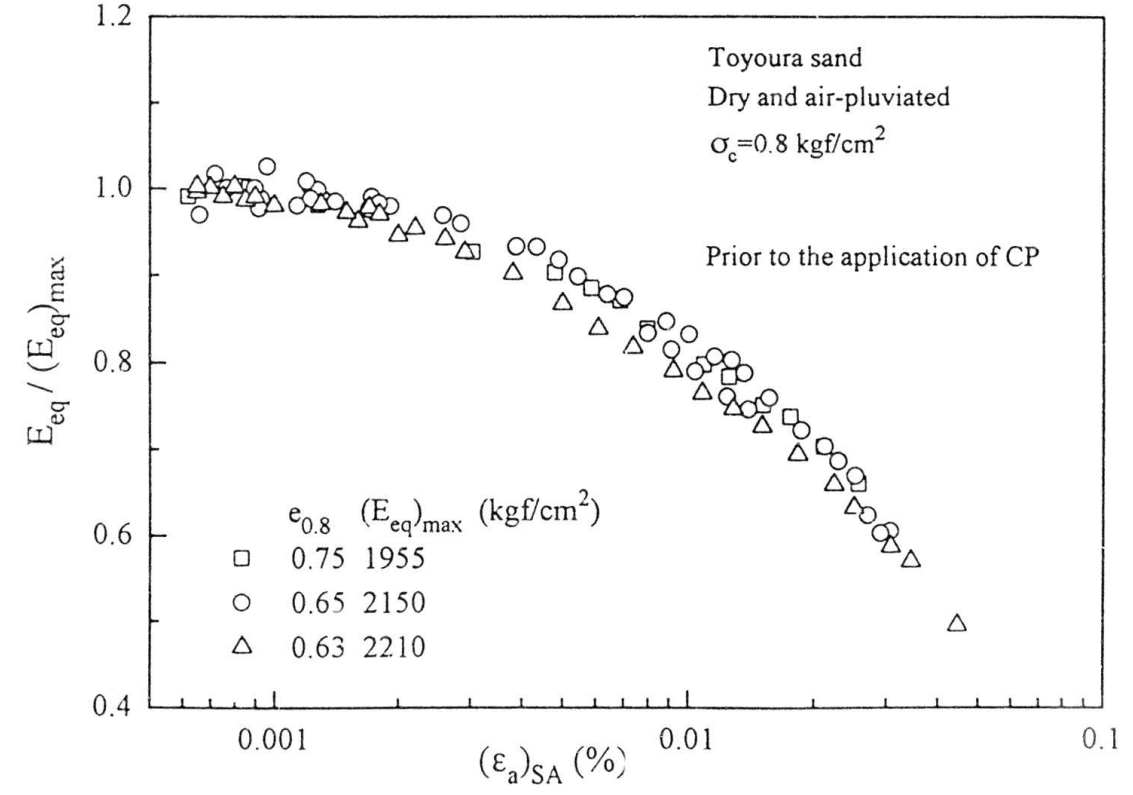

Fig. 6.8b: $E_{eq}/(E_{eq})_{max}$~log($(\varepsilon_a)_{SA}$) relations of the specimens of Toyoura sand.

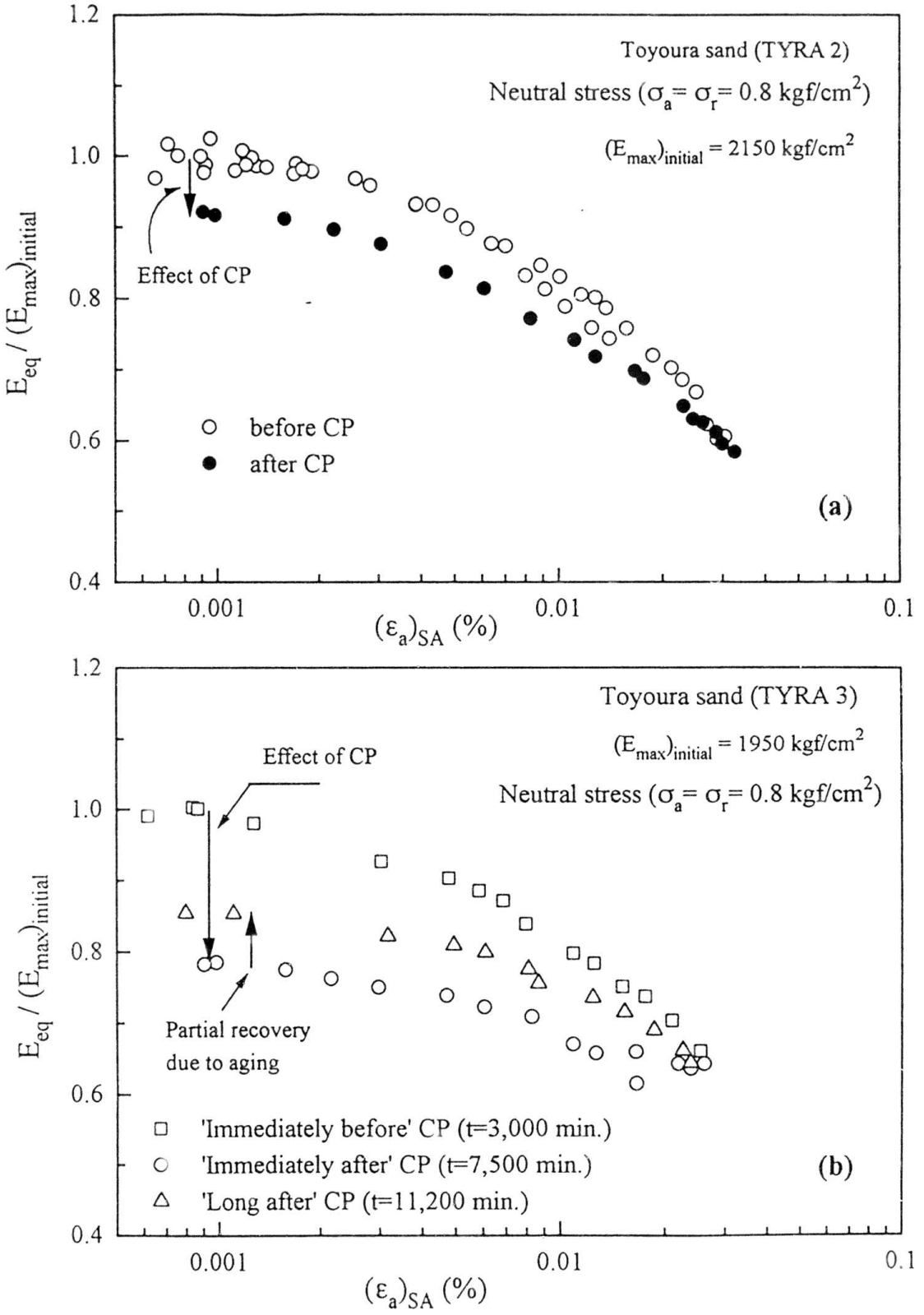

Figs. 6.9: Effects of CP on the relationships between $E_{eq}/(E_{max})_{initial}$ and $(\varepsilon_a)_{SA}$ for specimens (a) TYRA 2, and (b) TYRA 3.

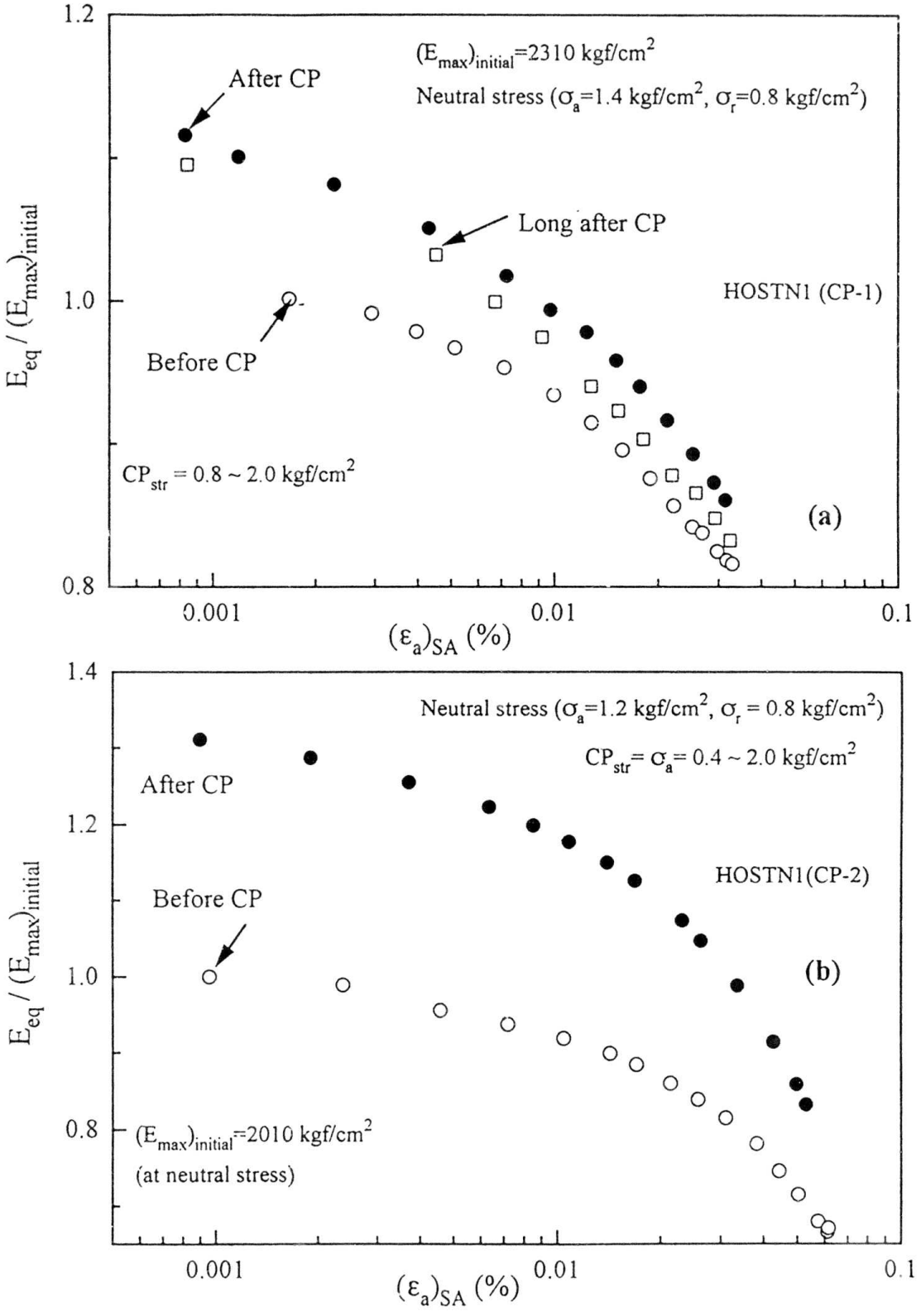

Figs. 6.10: Effects of CP on the relationships between $E_{eq}/(E_{max})_{initial}$ and $(\varepsilon_a)_{SA}$ of HOSTN1 specimen for CP stages (a) CP-1, and (b) CP-2.

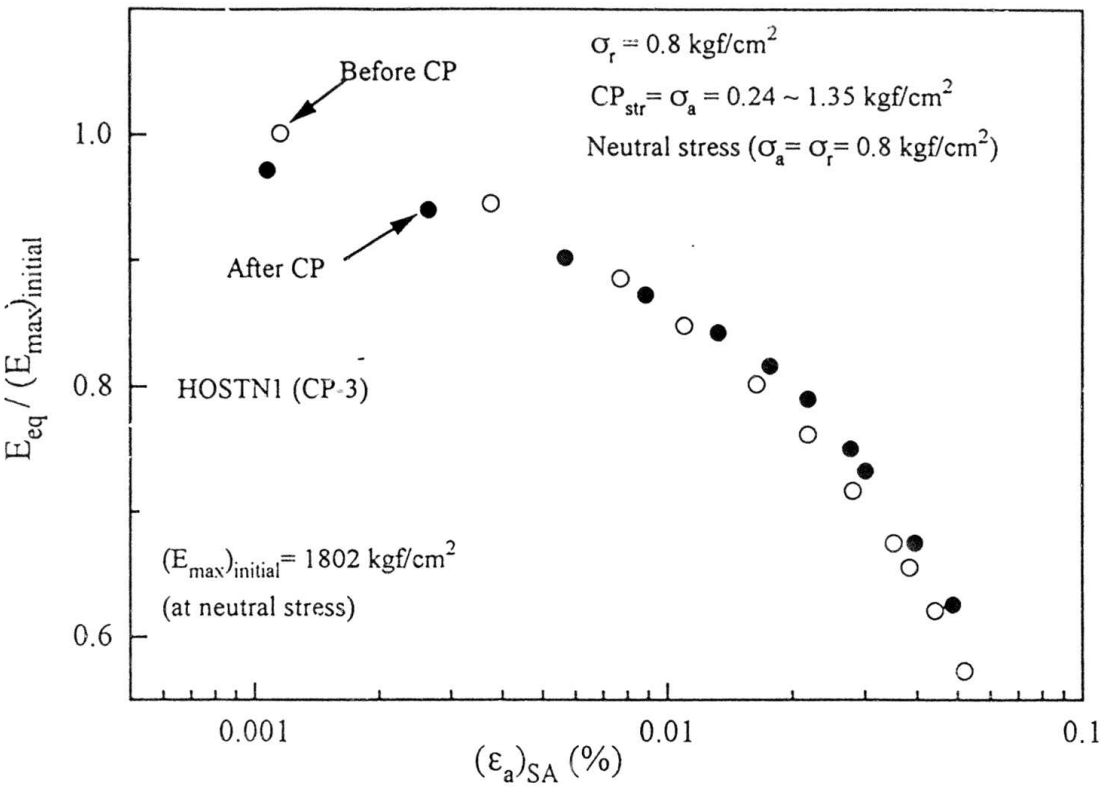

Fig. 6.10c: Effects of CP on the relationships between $E_{eq}/(E_{max})_{initial}$ and $(\varepsilon_a)_{SA}$ of HOSTN1 specimen for CP-3.

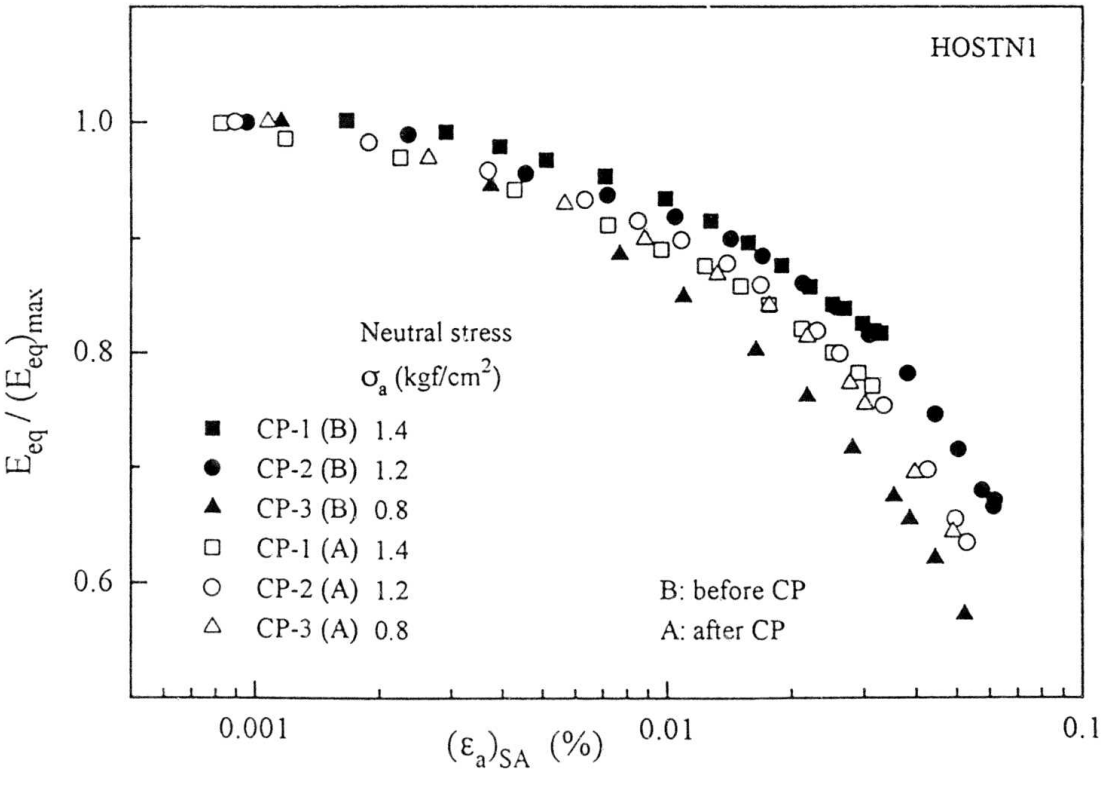

Fig. 6.10d: Effects of CP on the shape of the normalized decay curve of HOSTN1 specimen.

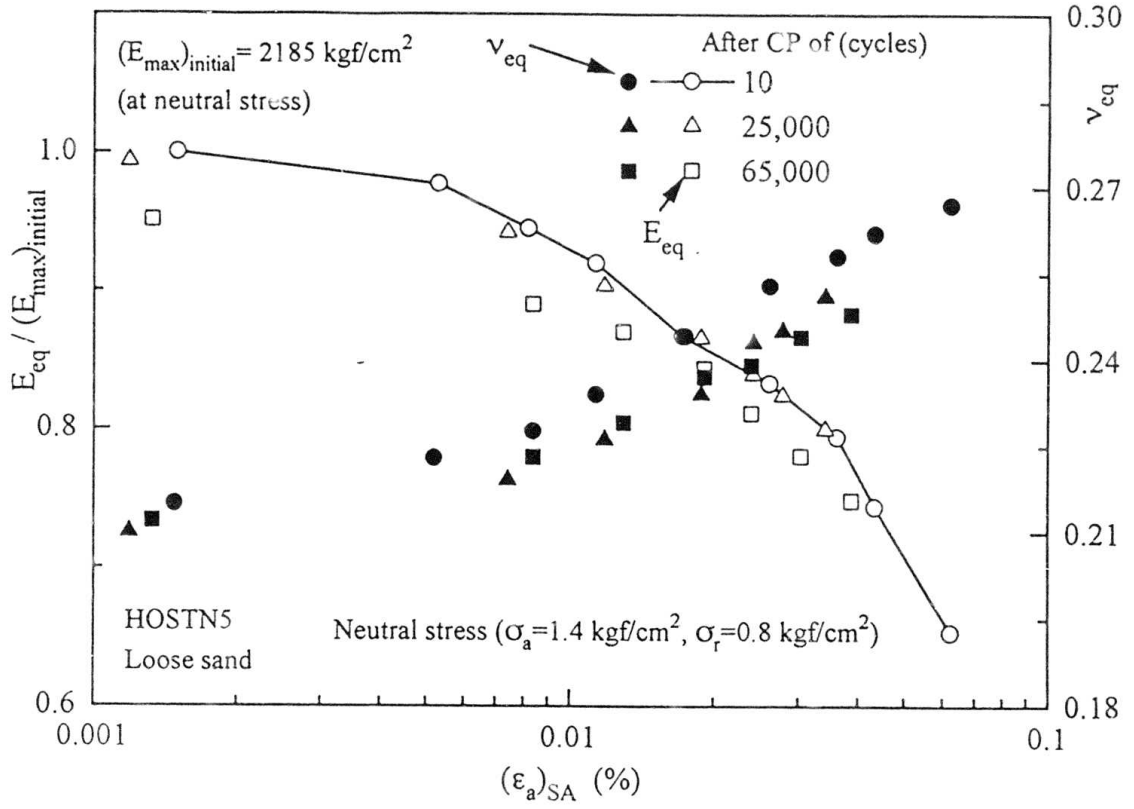

Fig. 6.11: Effects of CP on the relationships between $E_{eq}/(E_{max})_{initial}$, ν_{eq} and $(\varepsilon_a)_{SA}$ of HOSTN5 specimen.

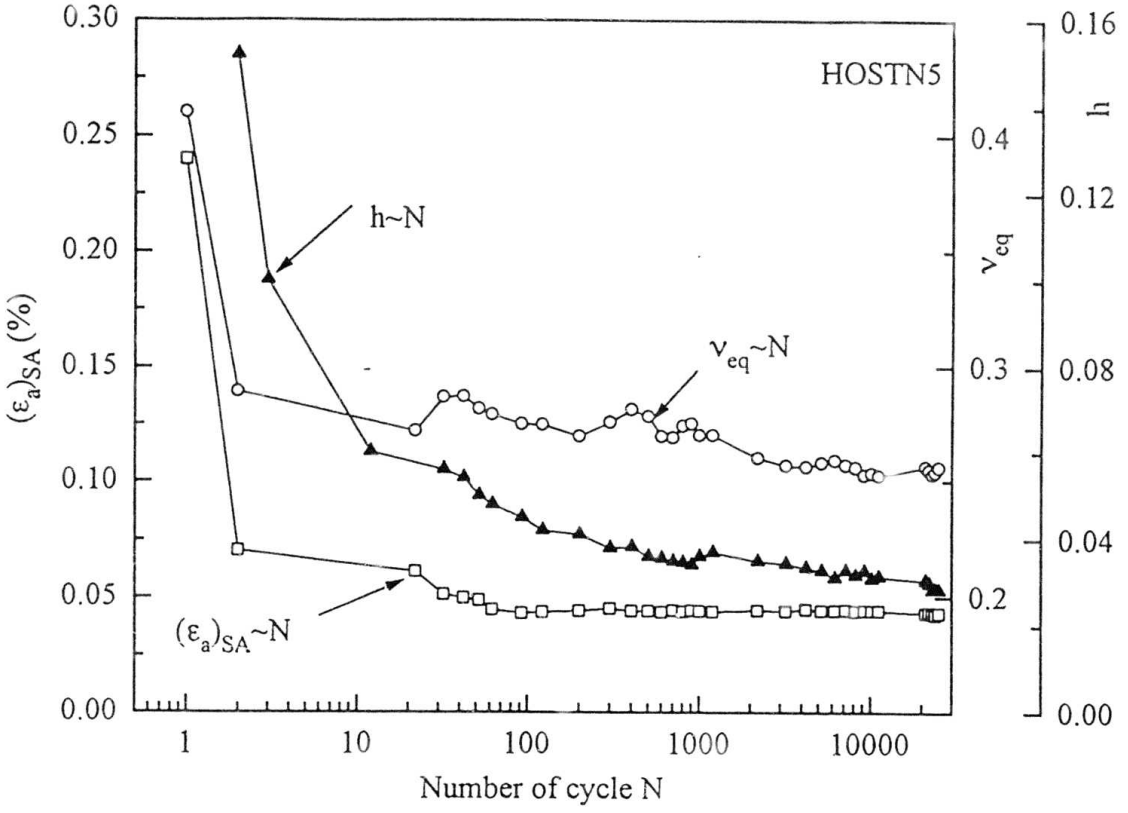

Fig. 6.12: Effects of the number of loading cycle N during cyclic loading at a constant stress-amplitude on $(\varepsilon_a)_{SA}$, ν_{eq} and h.

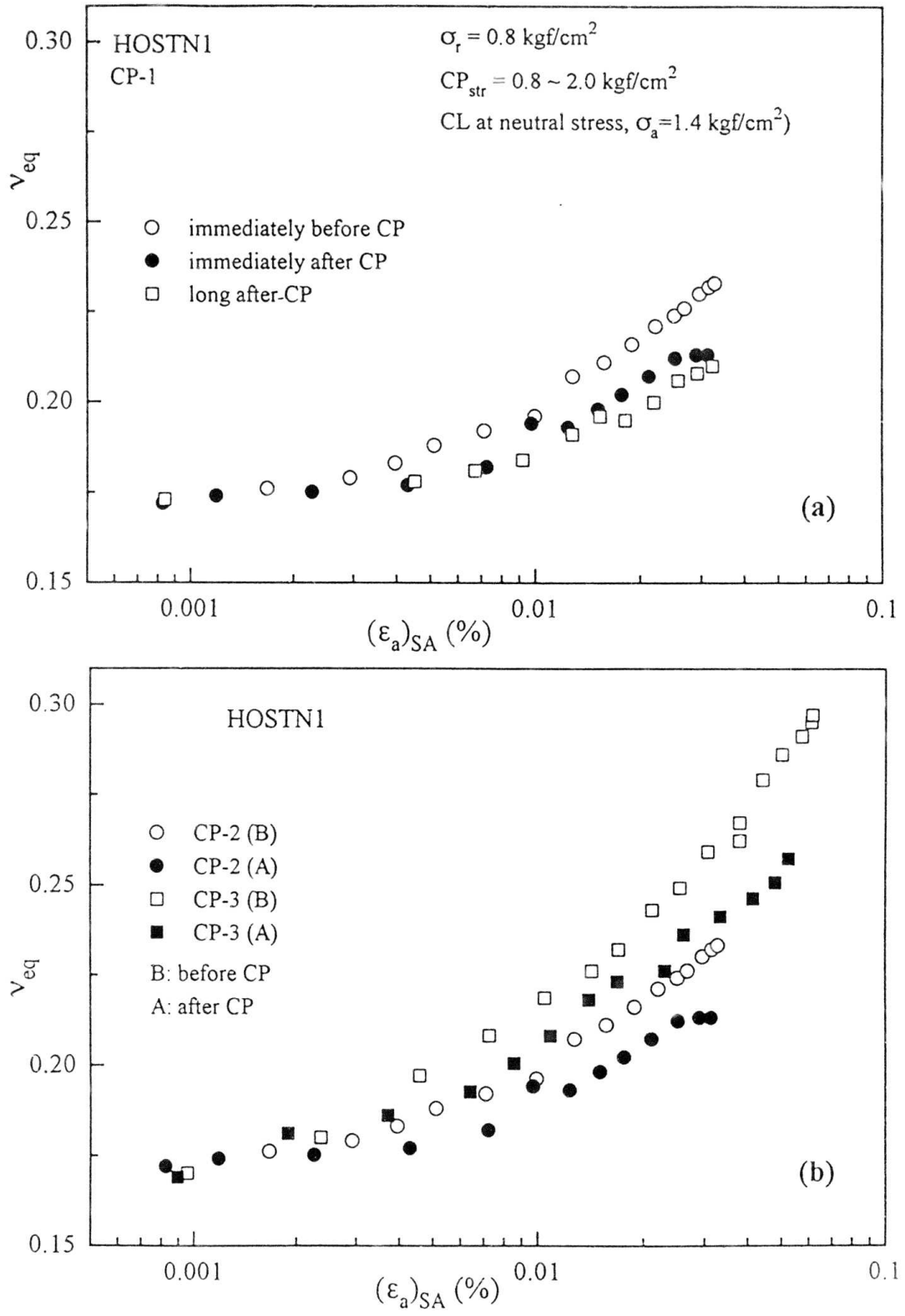

Figs. 6.13: Effects of CP on the relationships between ν_{eq} and $(\varepsilon_a)_{SA}$ of HOSTN1 specimen for CP stages (a) CP-1, (b) CP-2 and CP-3.

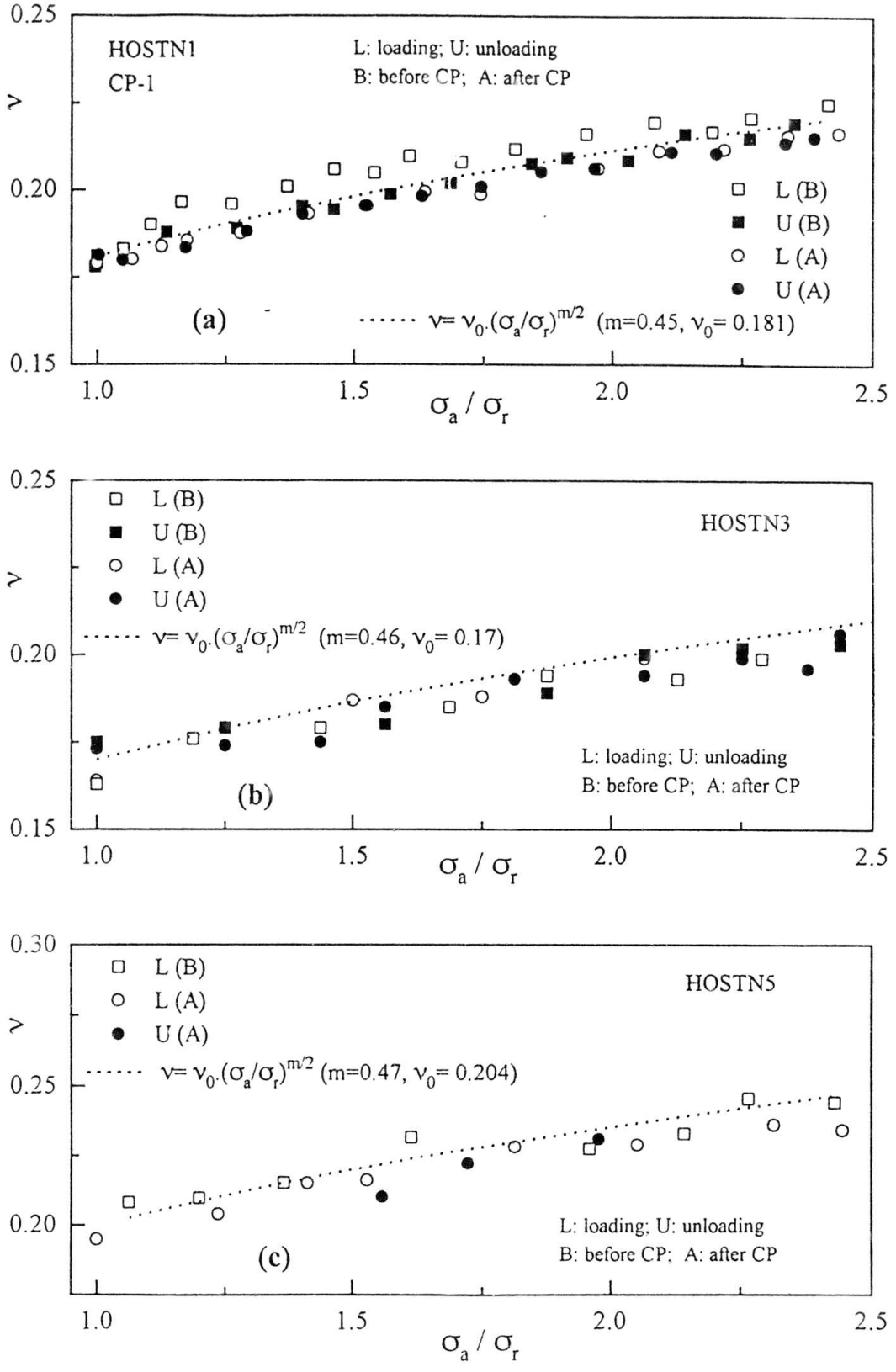

Figs. 6.14: Effects of CP on the relationships between ν ($=\nu^e$) and σ_a/σ_r along CP stress path of HOSTN1 specimen for CP stages (a) CP-1, (b) CP-2, and (c) CP-3.

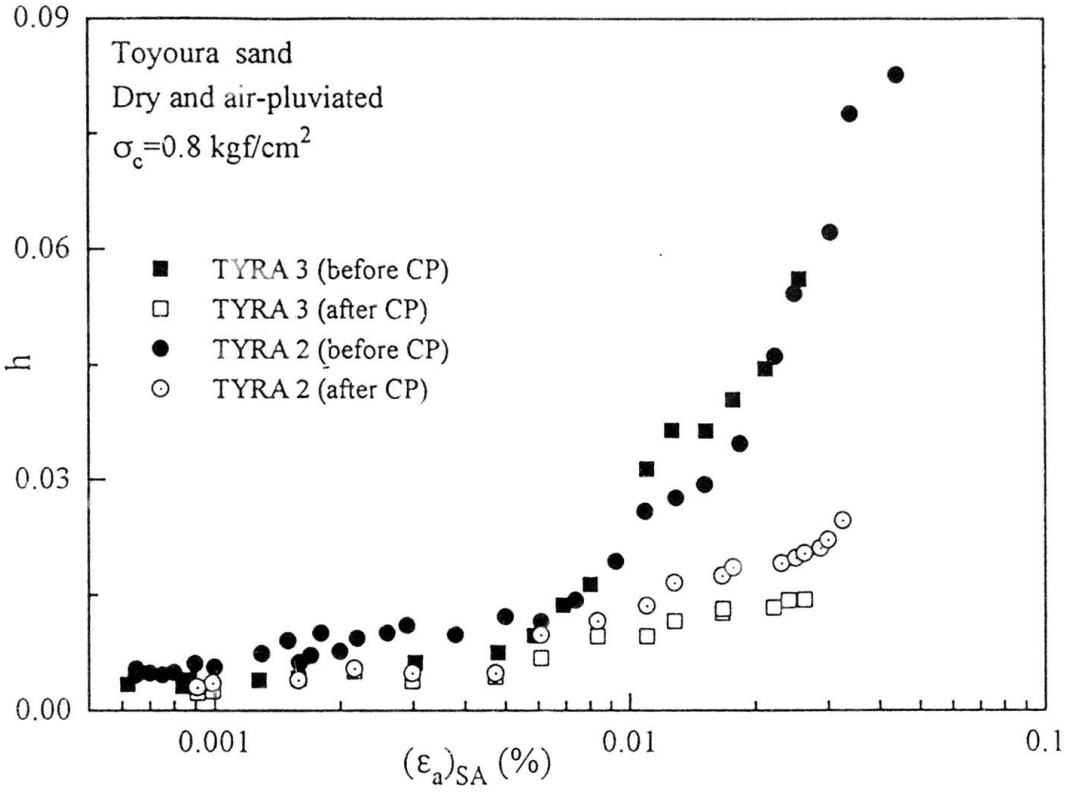

Fig. 6.15: Effects of CP on the relationships between damping ratio (h) and $(\varepsilon_a)_{SA}$ of Toyoura sand.

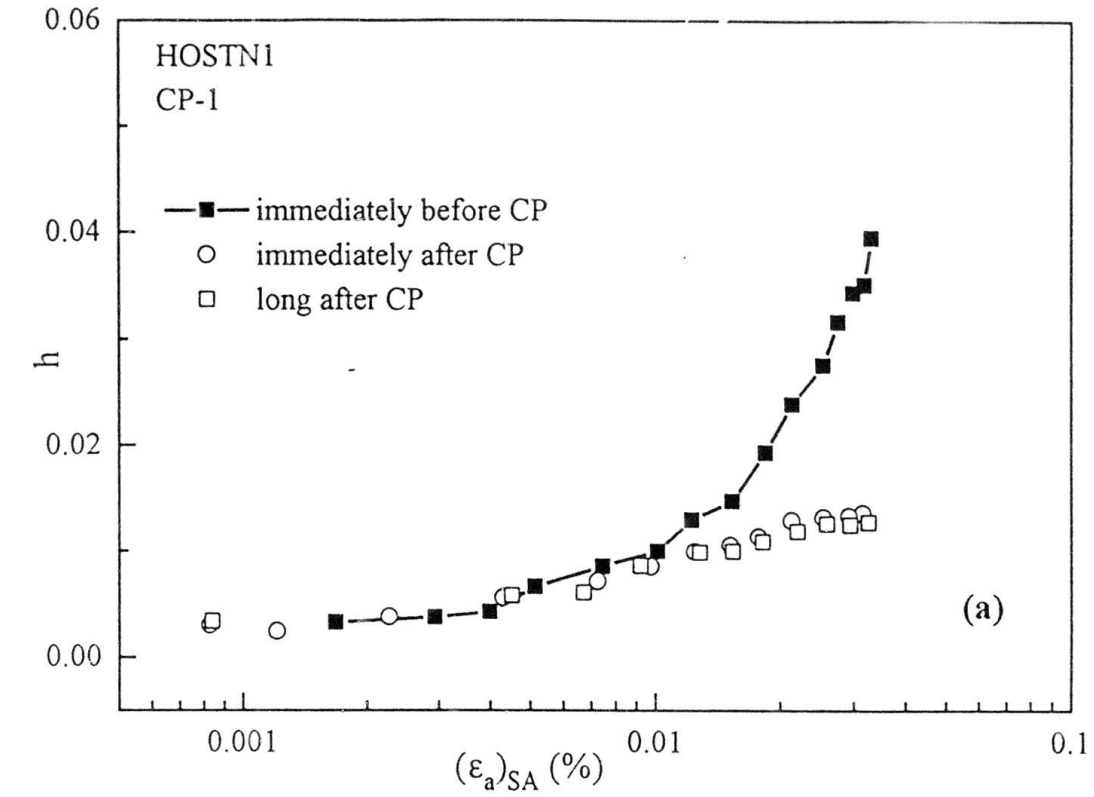

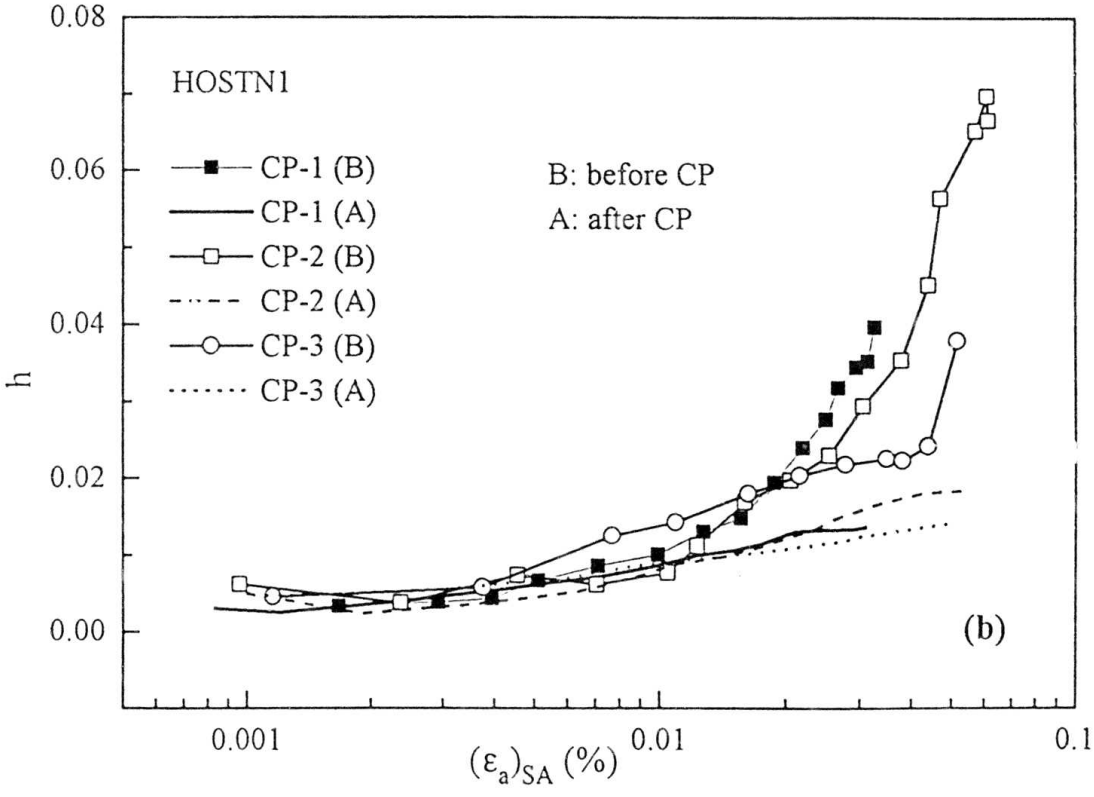

Figs. 6.16: Effects of CP on the relationships between damping ratio (h) and $(\varepsilon_a)_{SA}$ for HOSTN1 specimen for CP stages (a) CP-1, (b) CP-2 and CP-3.

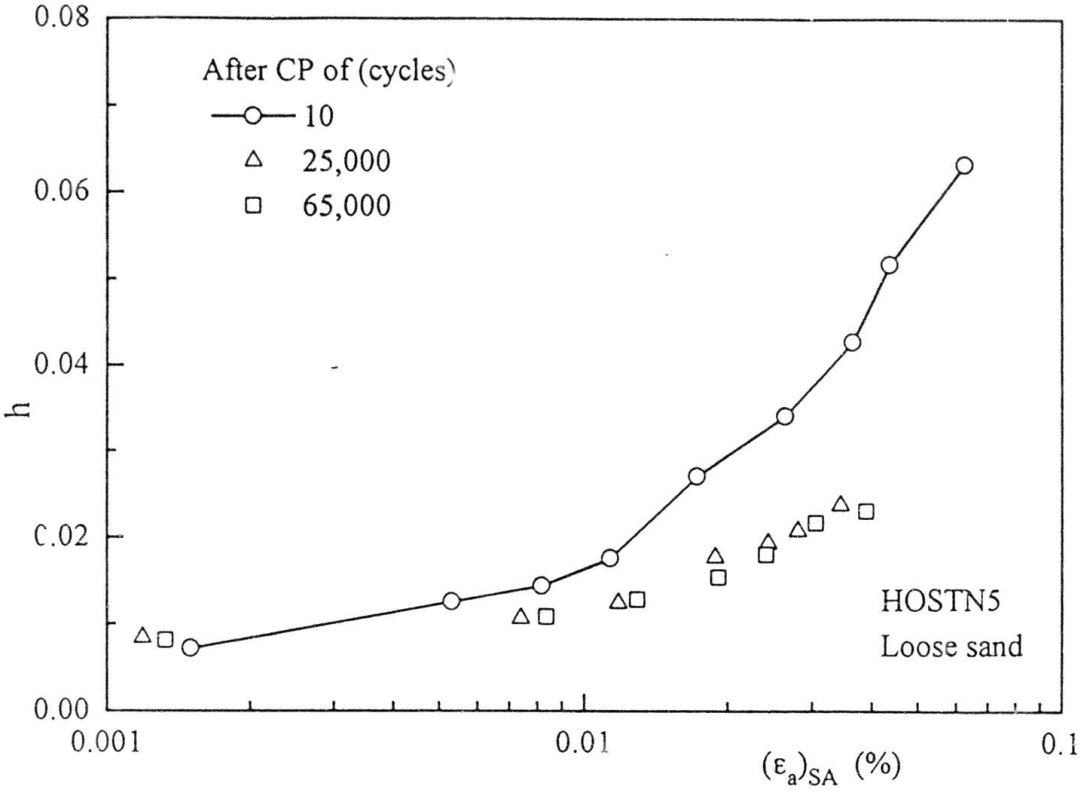

Fig. 6.16c: Effects of CP on the relationships between h and $(\varepsilon_a)_{SA}$ of HOSTN5 specimen.

Fig01.org/CP/D2

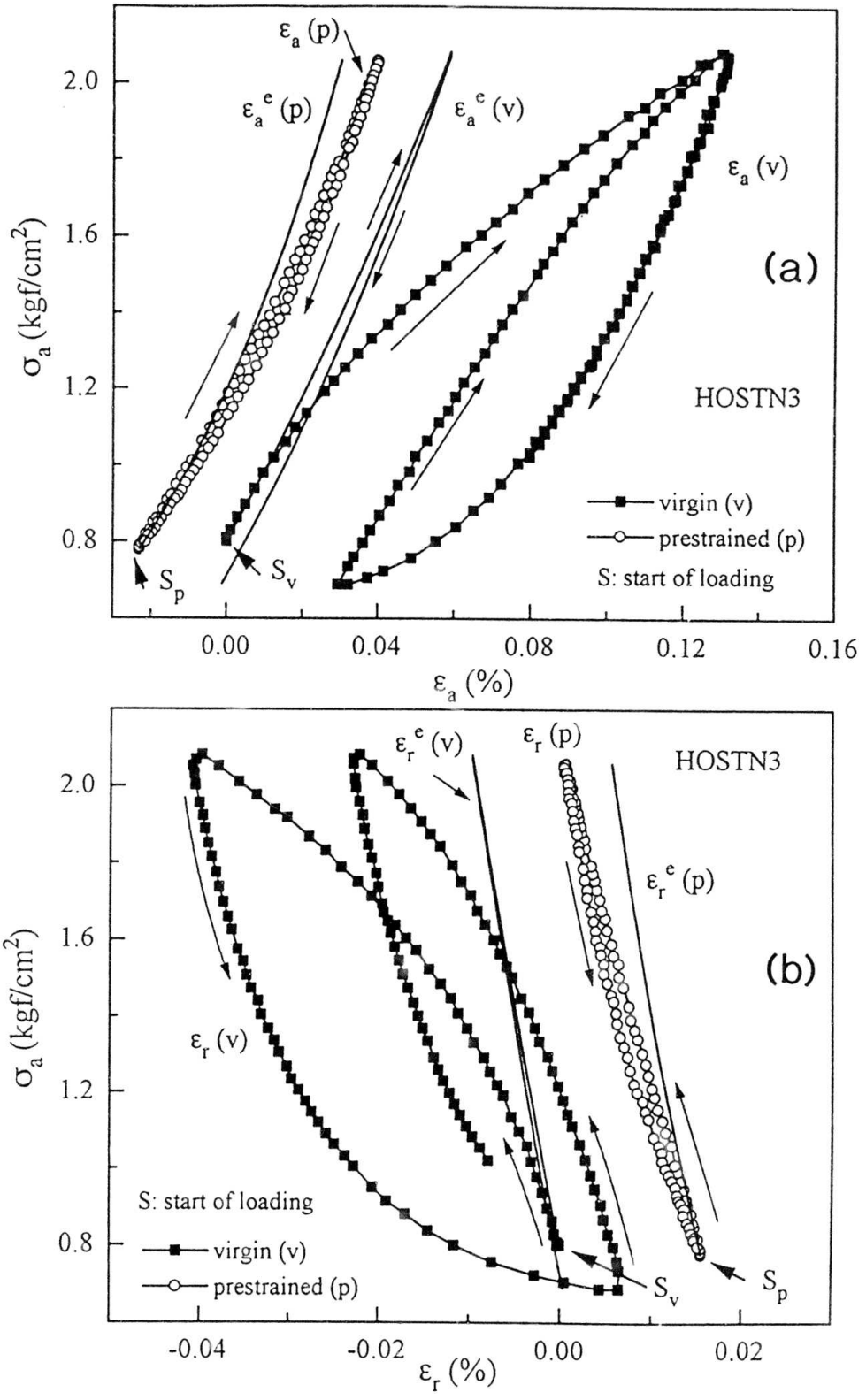

Figs. 6.17: (a) σ_a~ε_a and (b) σ_a~ε_r relationships of virgin and prestrained states of specimen HOSTN3 in CP stress path.

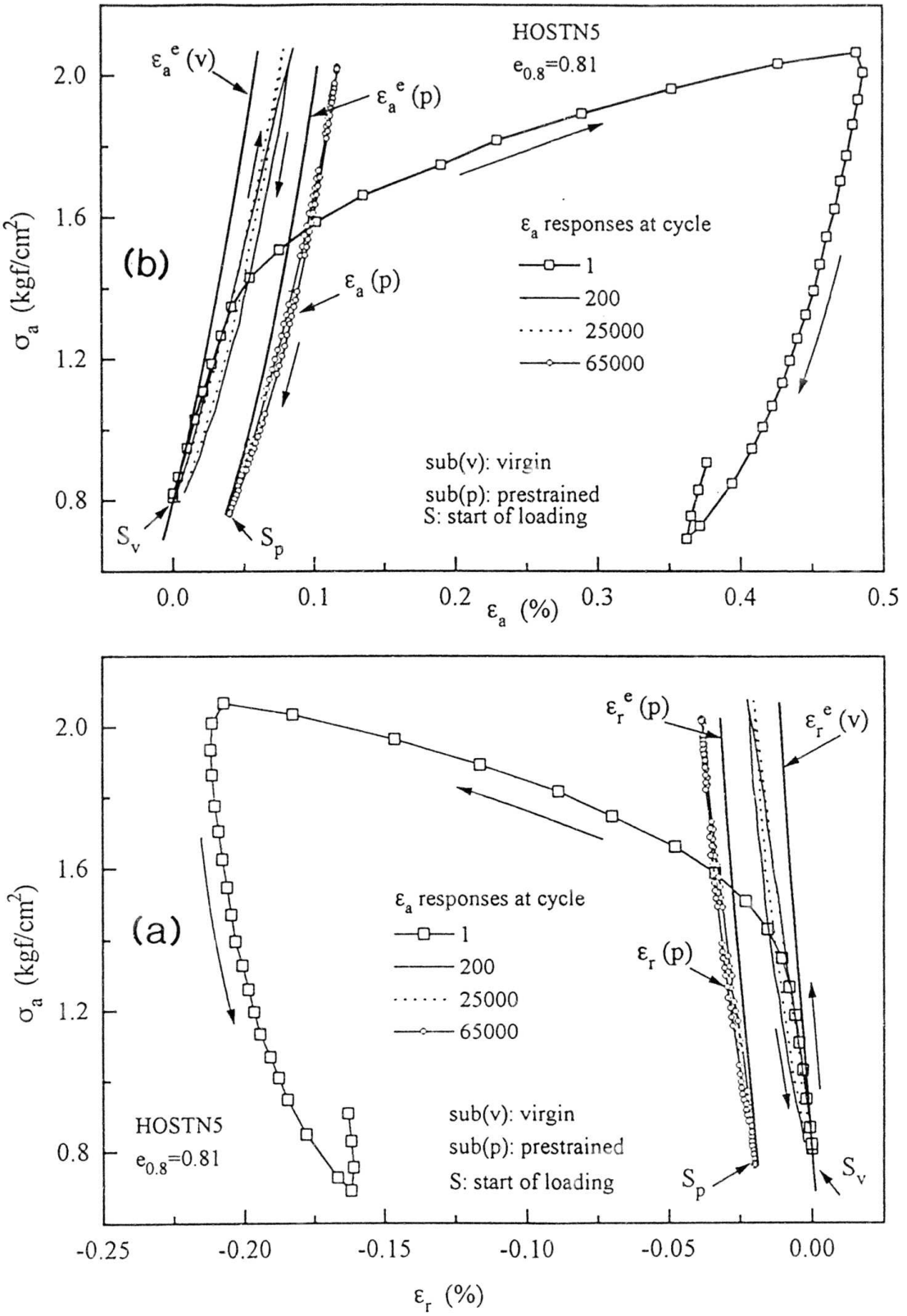

Figs. 6.18: (a) σ_a~ε_a and (b) σ_a~ε_r relationships of virgin and prestrained states of specimen HOSTN5 in CP stress path.

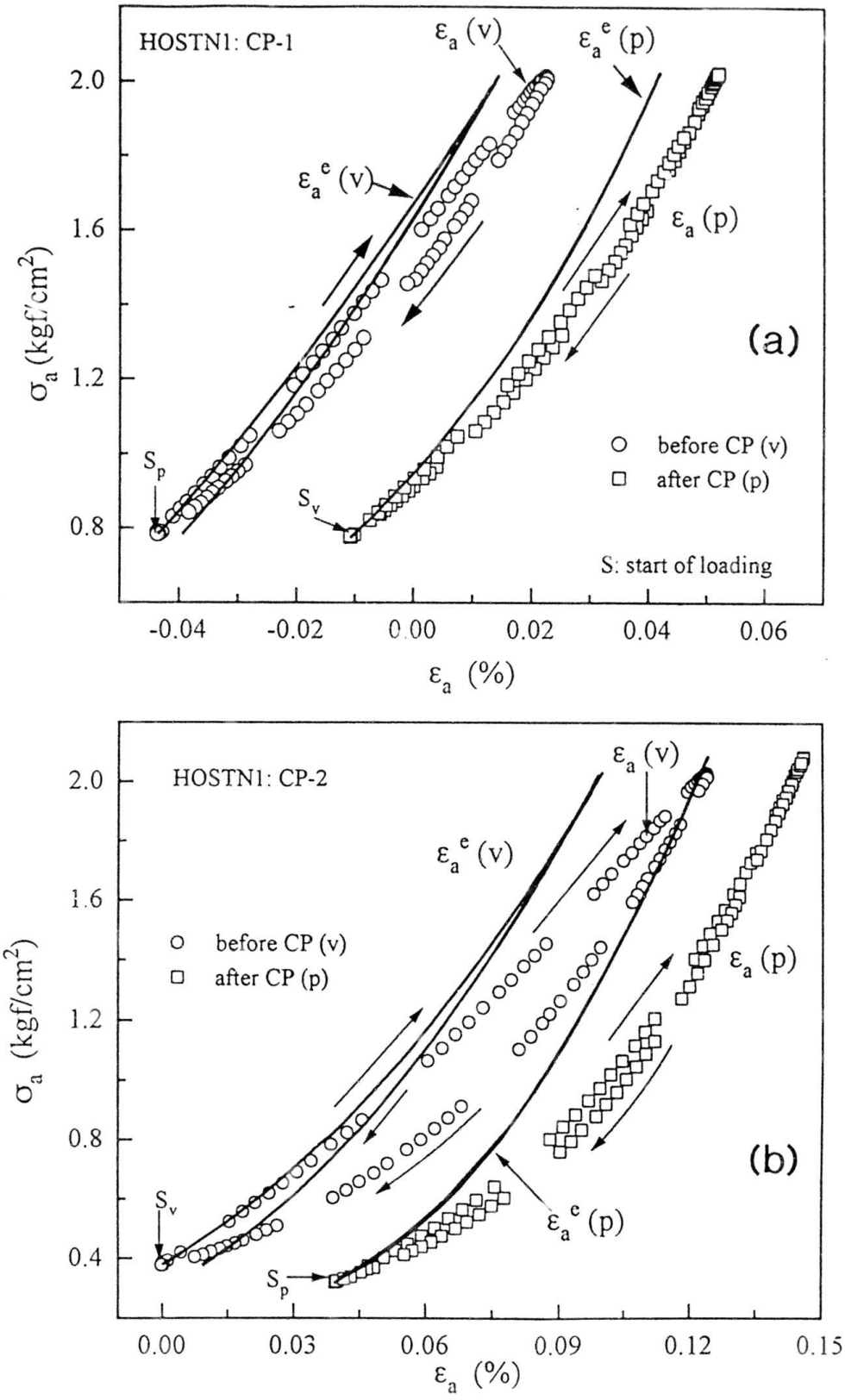

Figs. 6.19: σ_a~ε_a relationships at the start and at the end of CP of specimens (a) HOSTN1 (CP-1) and (b) HOSTN1 (CP-2).

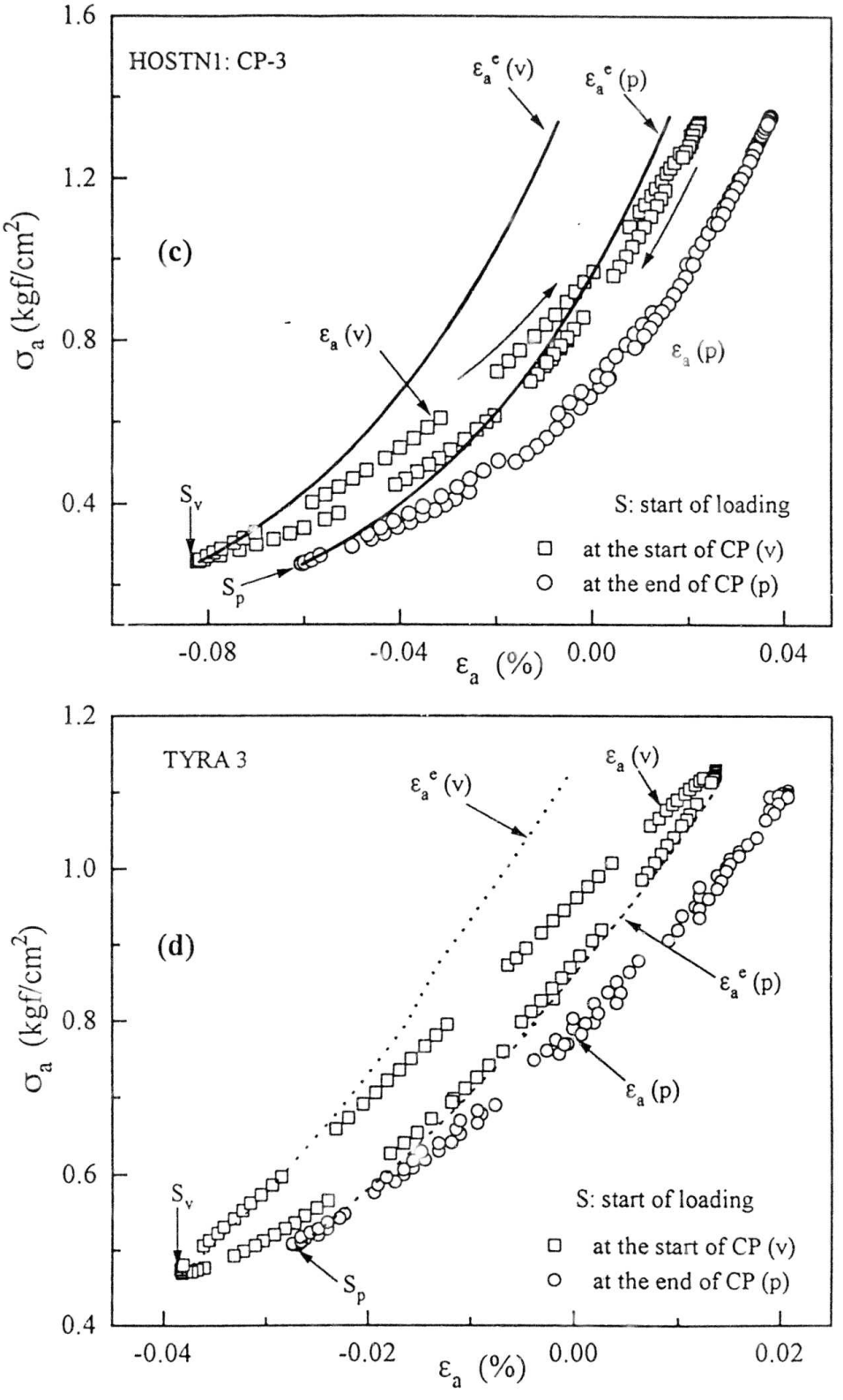

Figs. 6.19: σ_a~ε_a relationships at the start and at the end of CP of specimens (c) HOSTN1 (CP-3), (d) TYRA 3.

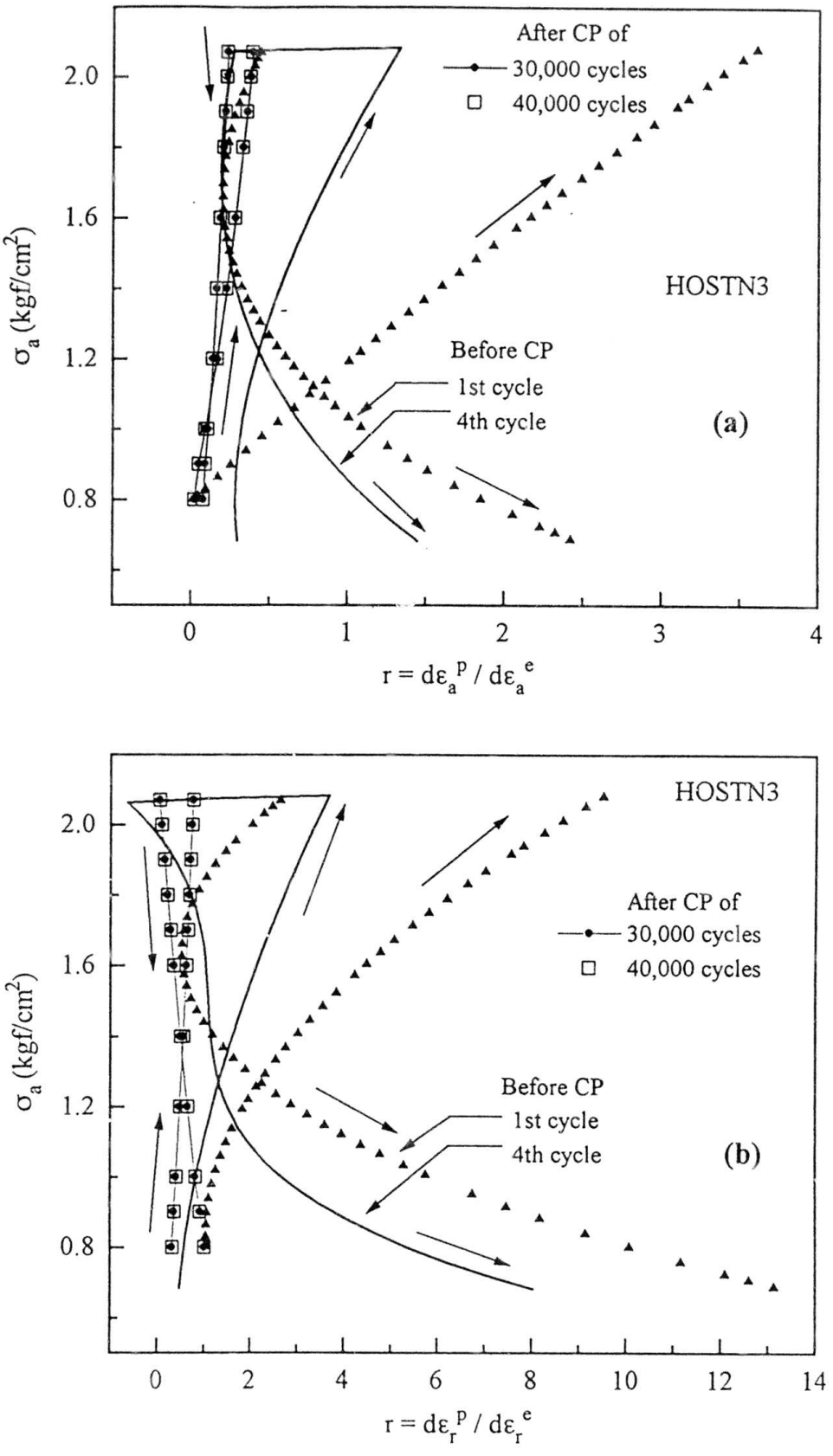

Figs. 6.20: Variations of (a) axial plastic-to-elastic, and (b) radial plastic-to-elastic strain incremens with σ_a in CP stress path of HOSTN3 specimen.

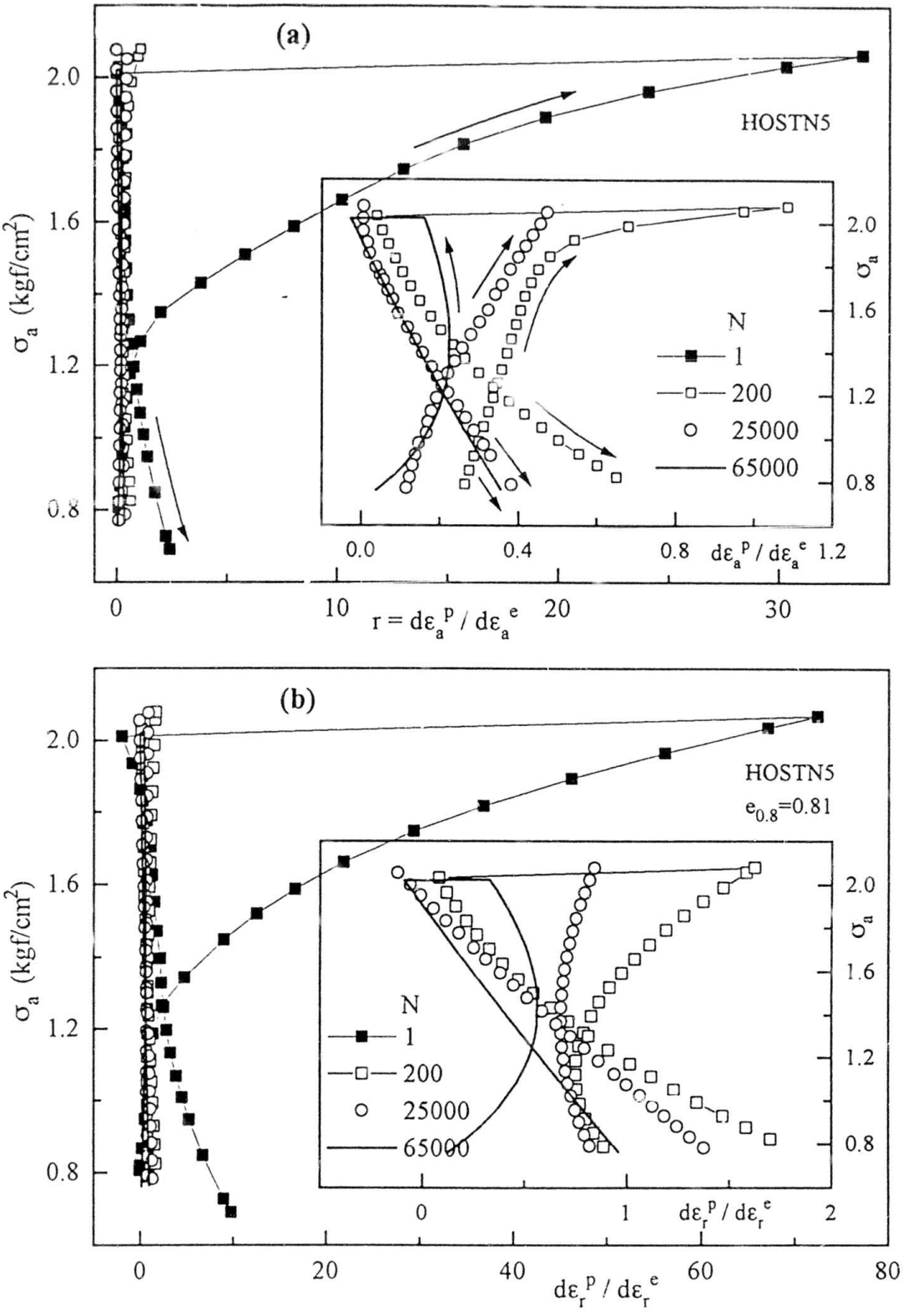

Figs. 6.21: Variations of (a) axial plastic-to-elastic, and (b) radial plastic-to-elastic strain incremens with σ_a in CP stress path of HOSTN5 specimen.

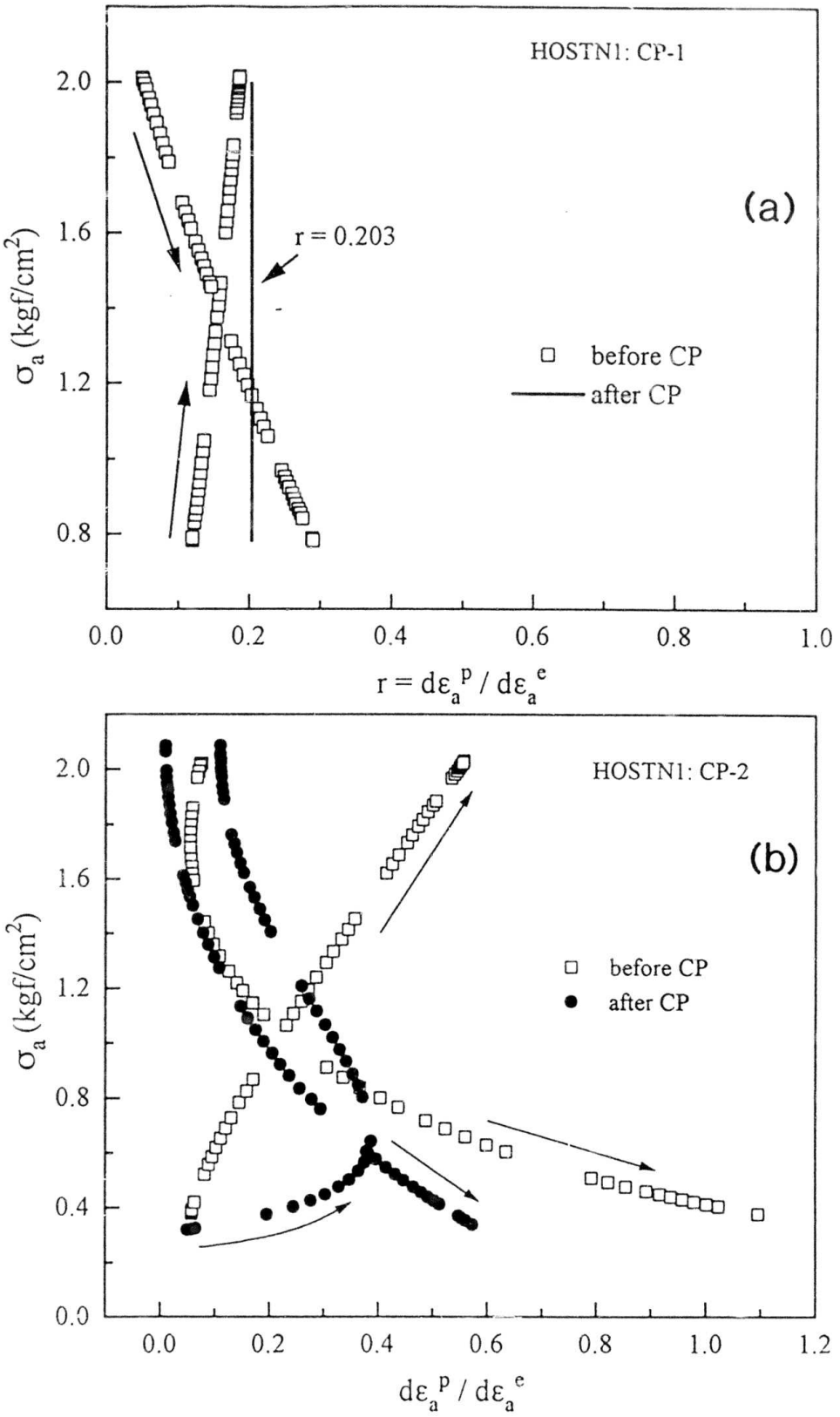

Figs. 6.22: Variations of axial plastic-to-elastic strains increment with σ_a in CP stress path of specimens (a) HOSTN1 (CP-1) and (b) HOSTN1 (CP-2).

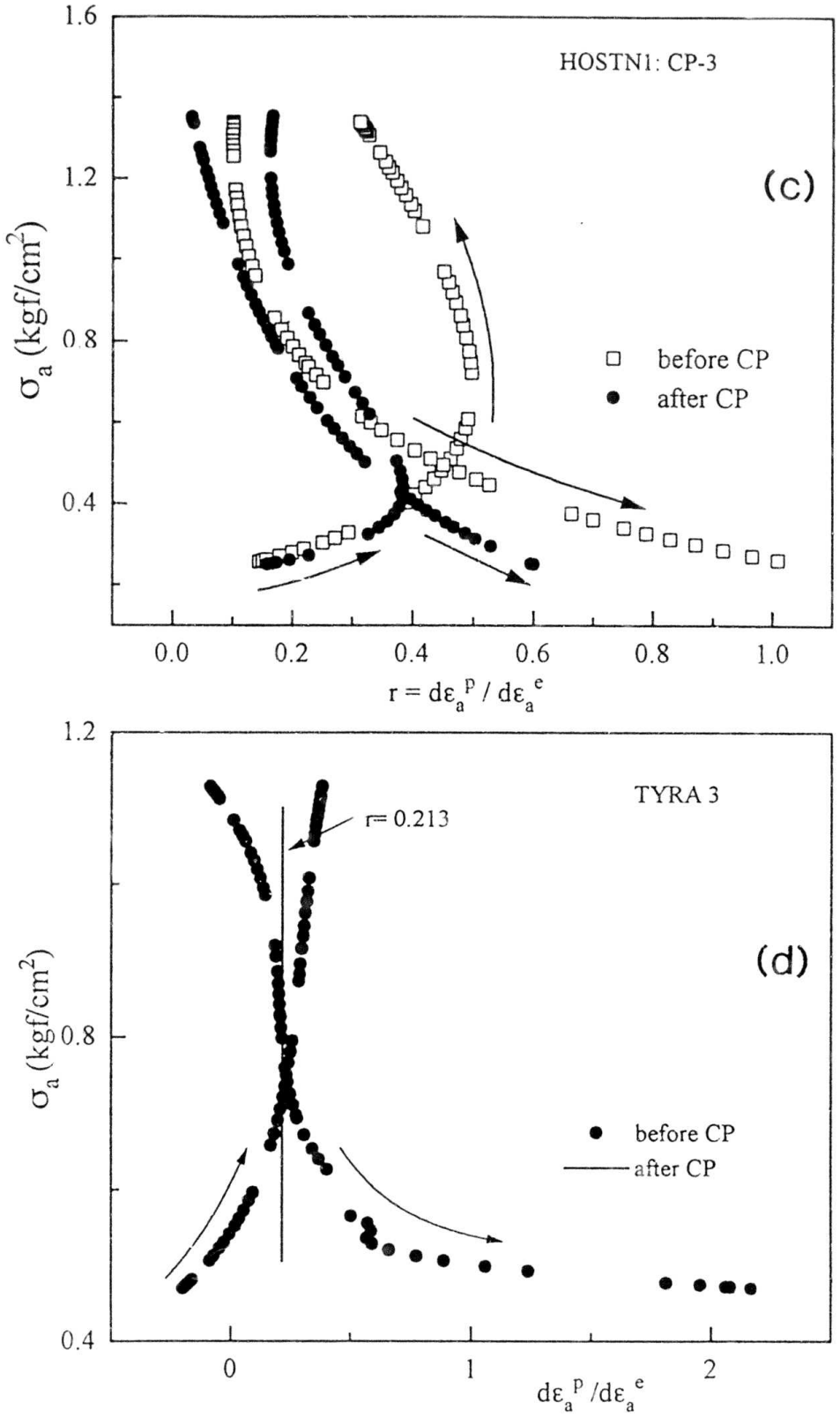

Figs. 6.22: Variations of axial plastic-to-elastic strains increment with σ_a in CP stress path of specimens (c) HOSTN1 (CP-3) and (d) TYRA 3.

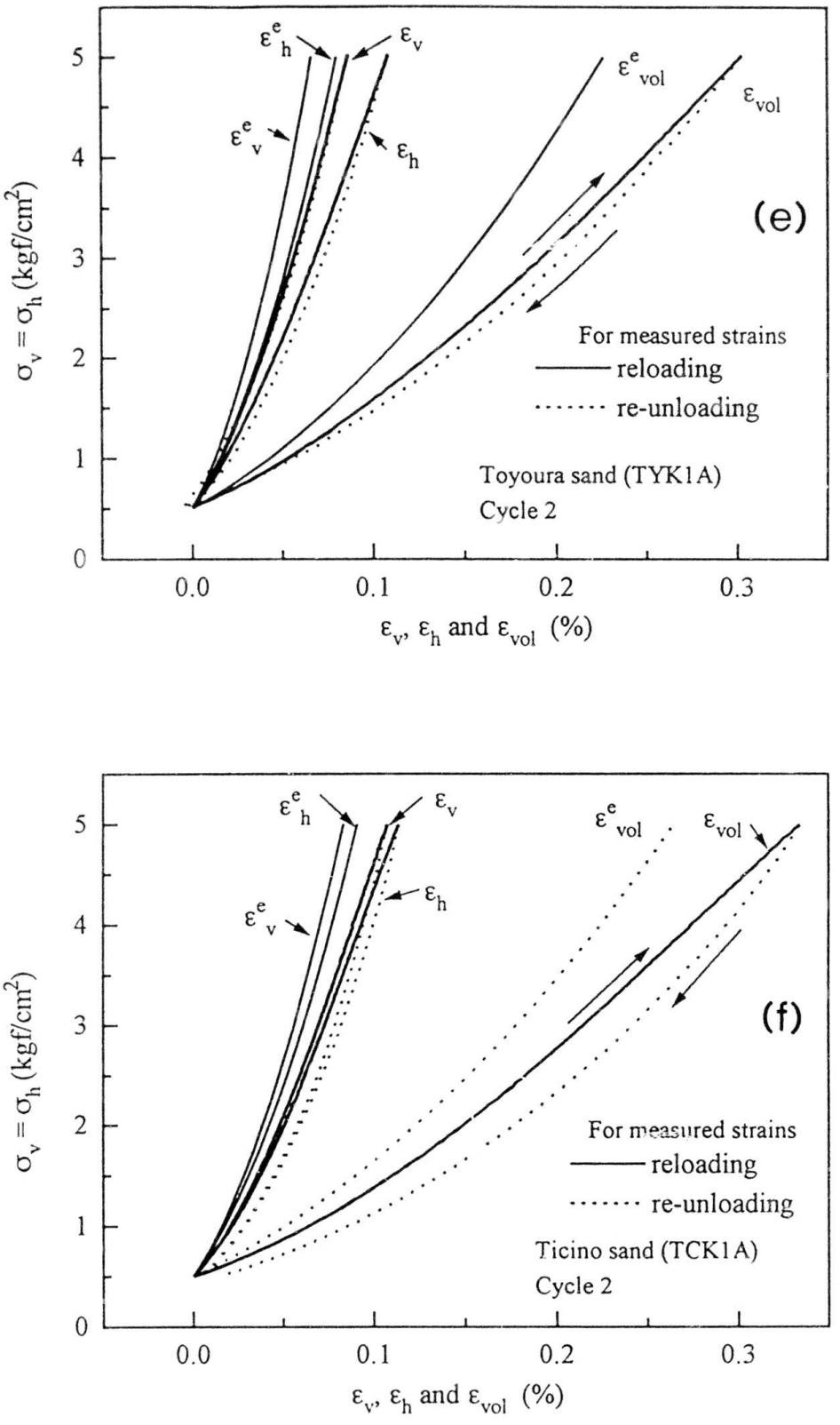

Figs. 6.22: Variations of total strain components (ε_v, ε_h and ε_{vol}) and elastic strain components (ε^e_v, ε^e_h and ε^e_{vol}) with σ_v=σ_a (=σ_h) in isotropic stress path of specimens (e) Toyoura sand (TYK1A) and (f) Ticino sand (TCK1A).

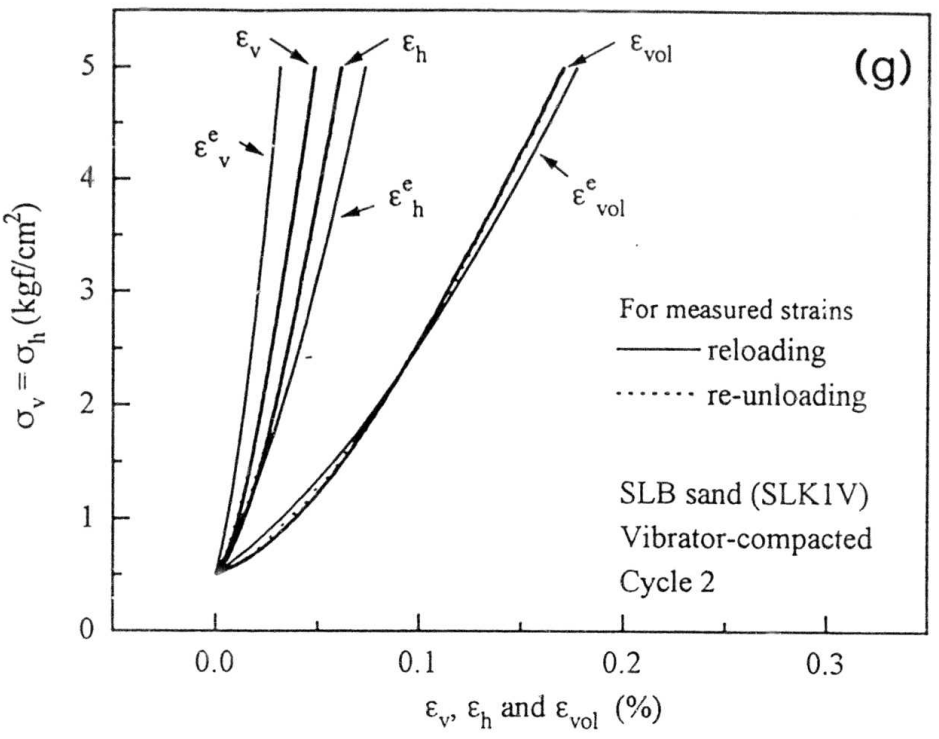

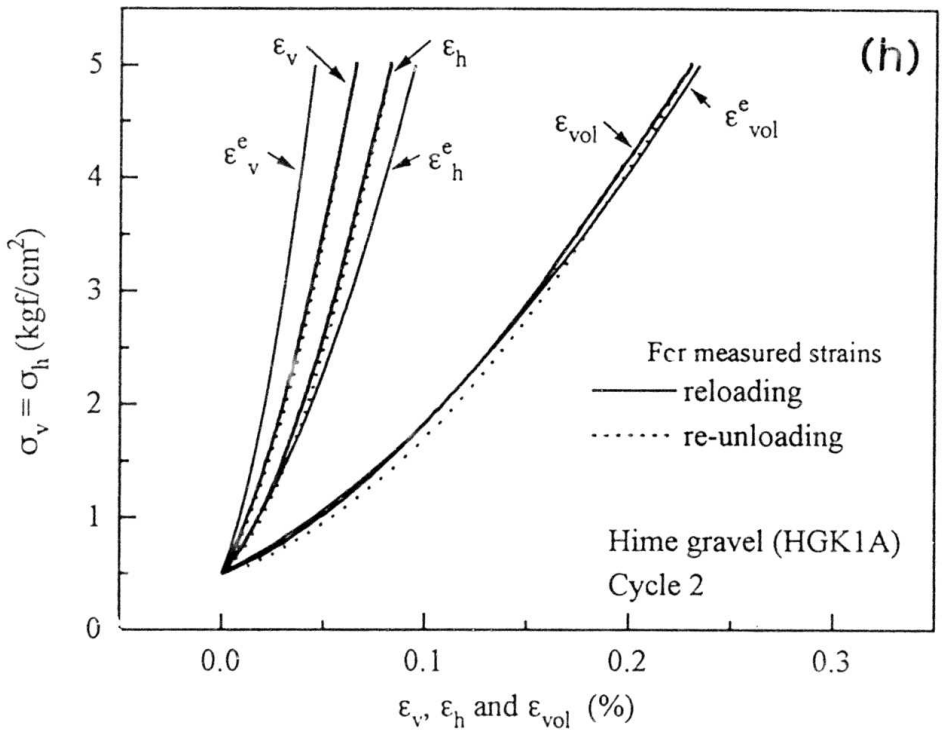

Figs. 6.22: Variations of total strain components (ε_v, ε_h and ε_{vol}) and elastic strain components (ε^e_v, ε^e_h and ε^e_{vol}) with $\sigma_v=\sigma_a$ ($=\sigma_h$) in isotropic stress path of specimens (g) SLB sand (SLK1V) and (h) Hime gravel (HGK1A).

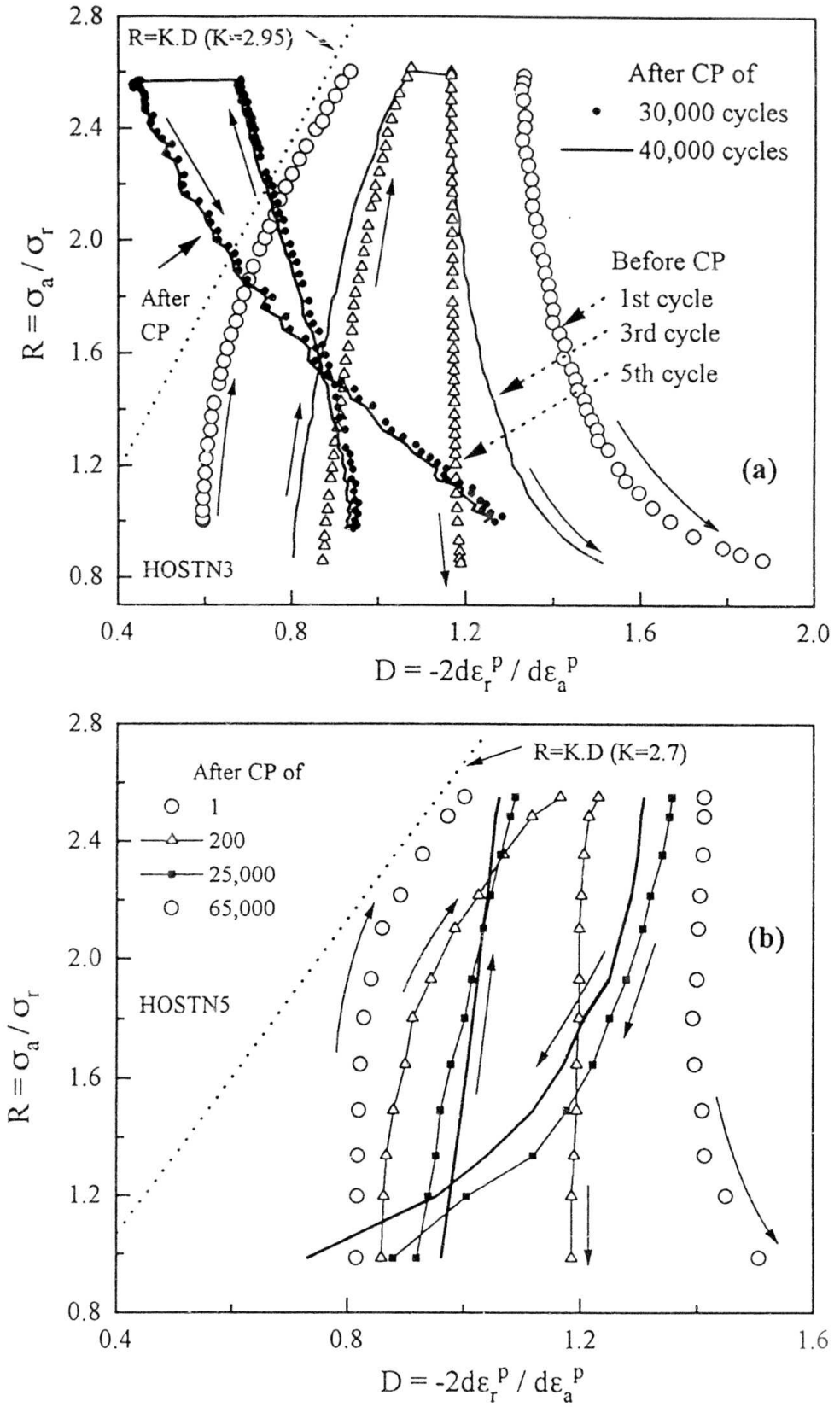

Figs. 6.23: Relationships between the stress ratio (R) and the dilatancy rate (D) in CP stress path for specimens (a) HOSTN3 and (b) HOSTN5.

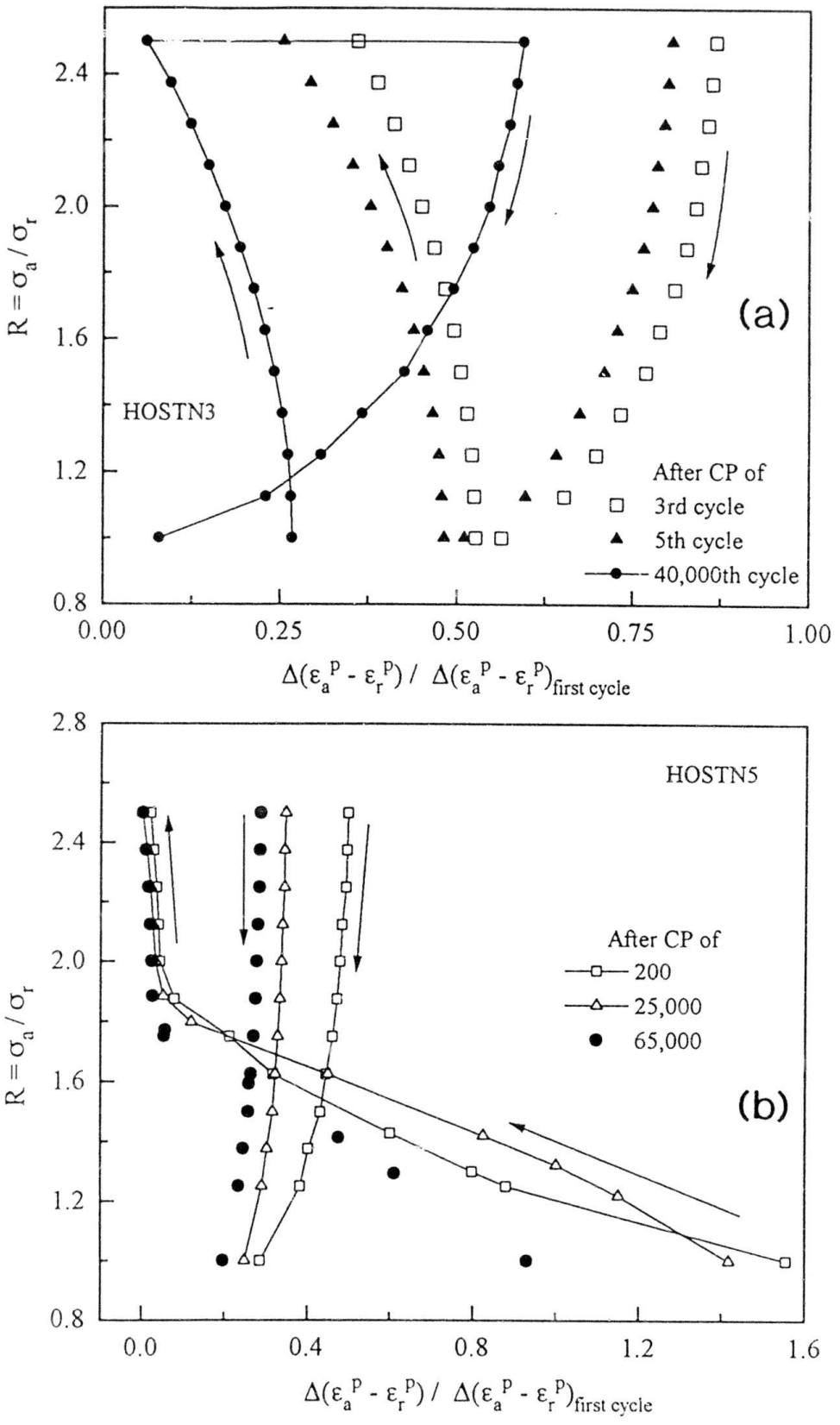

Figs. 6.24: Relationships between the stress ratio (R) and the prestrained-to-virgin shear strains rate in CP stress path for specimens (a) HOSTN3 and (b) HOSTN5.

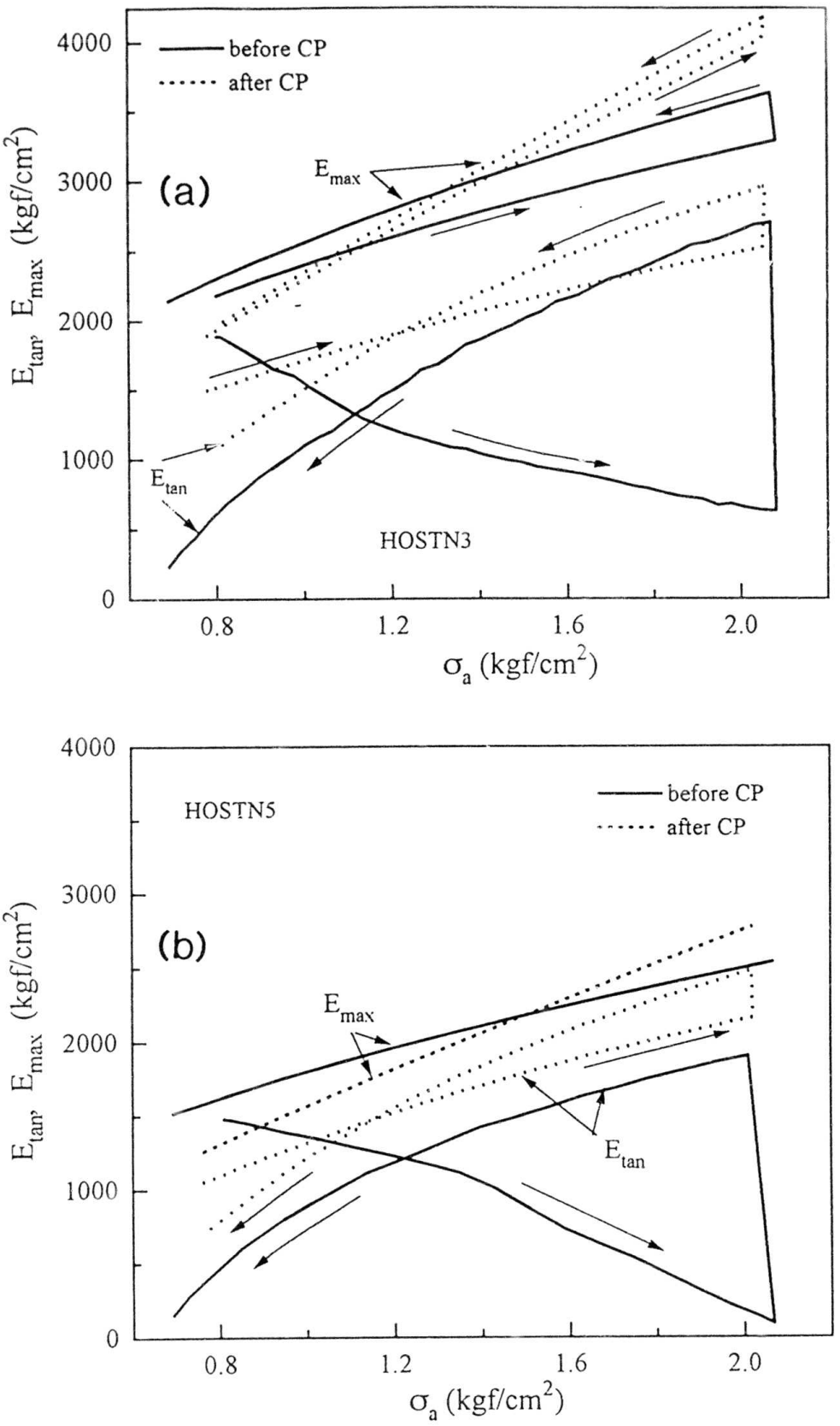

Figs. 6.25: Relationships between tangent modulus (E_{tan}) and σ_a in CP stress path for specimens (a) HOSTN3 and (b) HOSTN5.

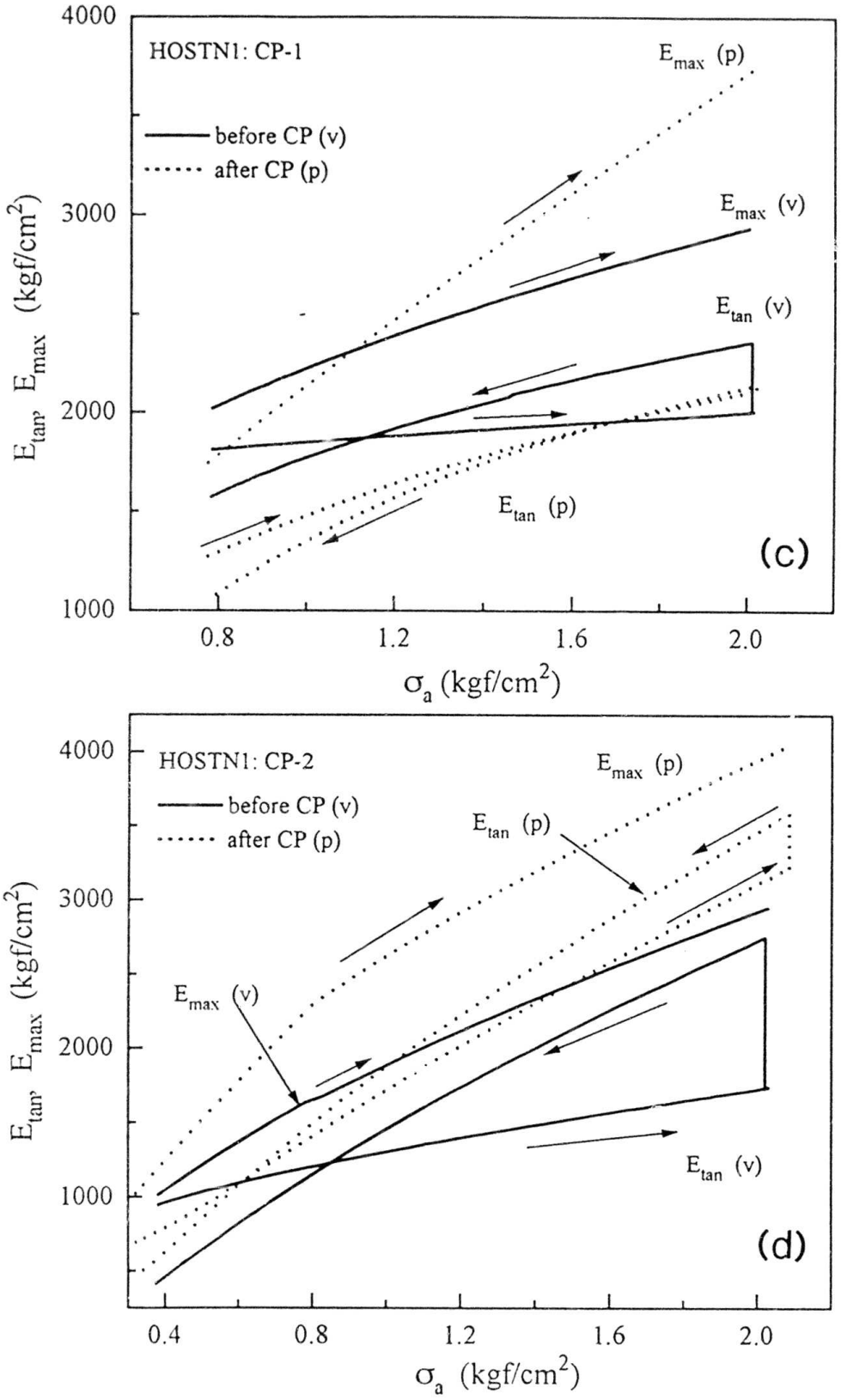

Figs. 6.25: Relationships between tangent modulus (E_{tan}) and σ_a in CP stress path for specimens (c) HOSTN1 (CP-1) and (d) HOSTN1 (CP-2).

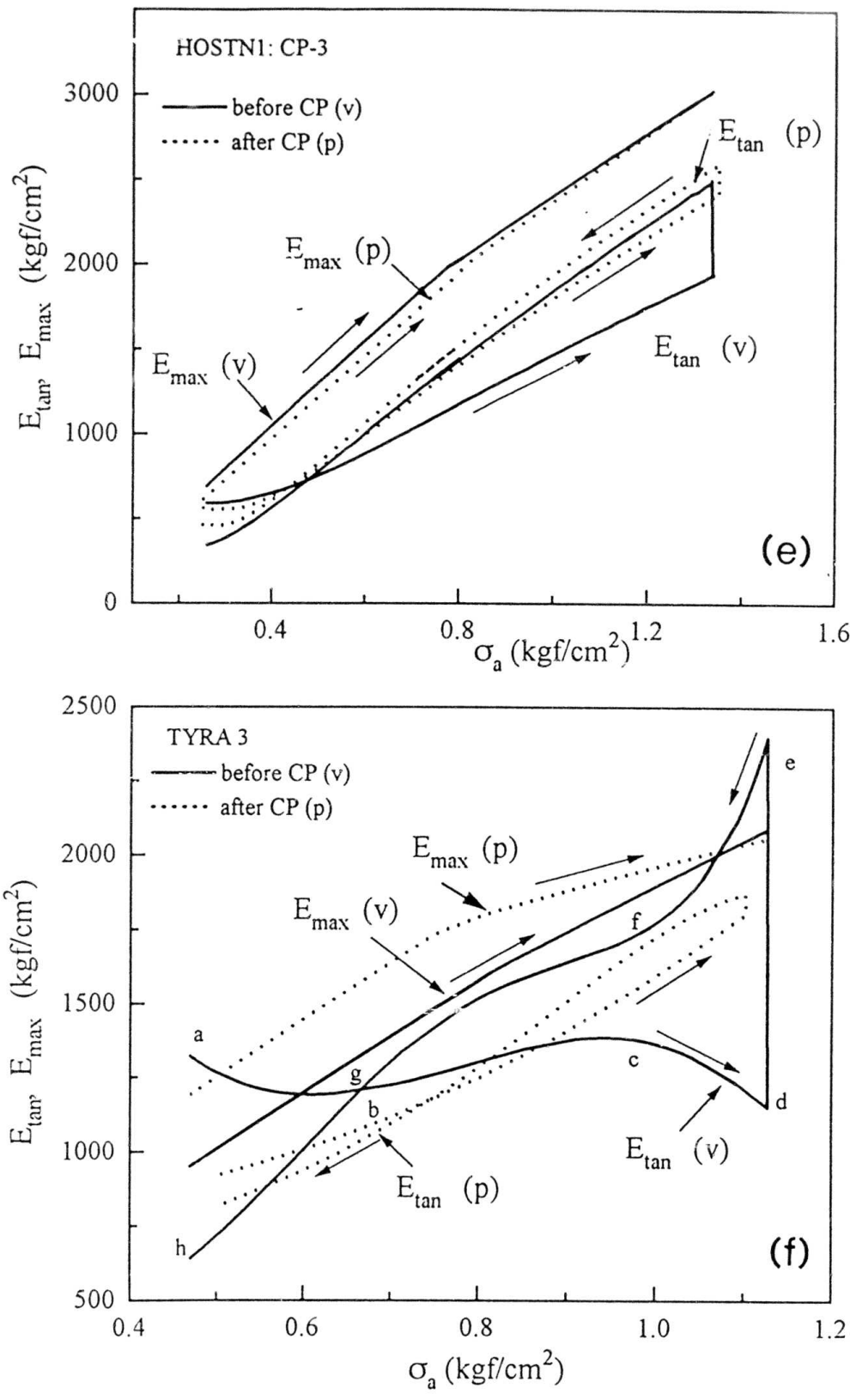

Figs. 6.25: Relationships between tangent modulus (E_{tan}) and σ_a in CP stress path for specimens (e) HOSTN1 (CP-3) and (f) TYRA 3.

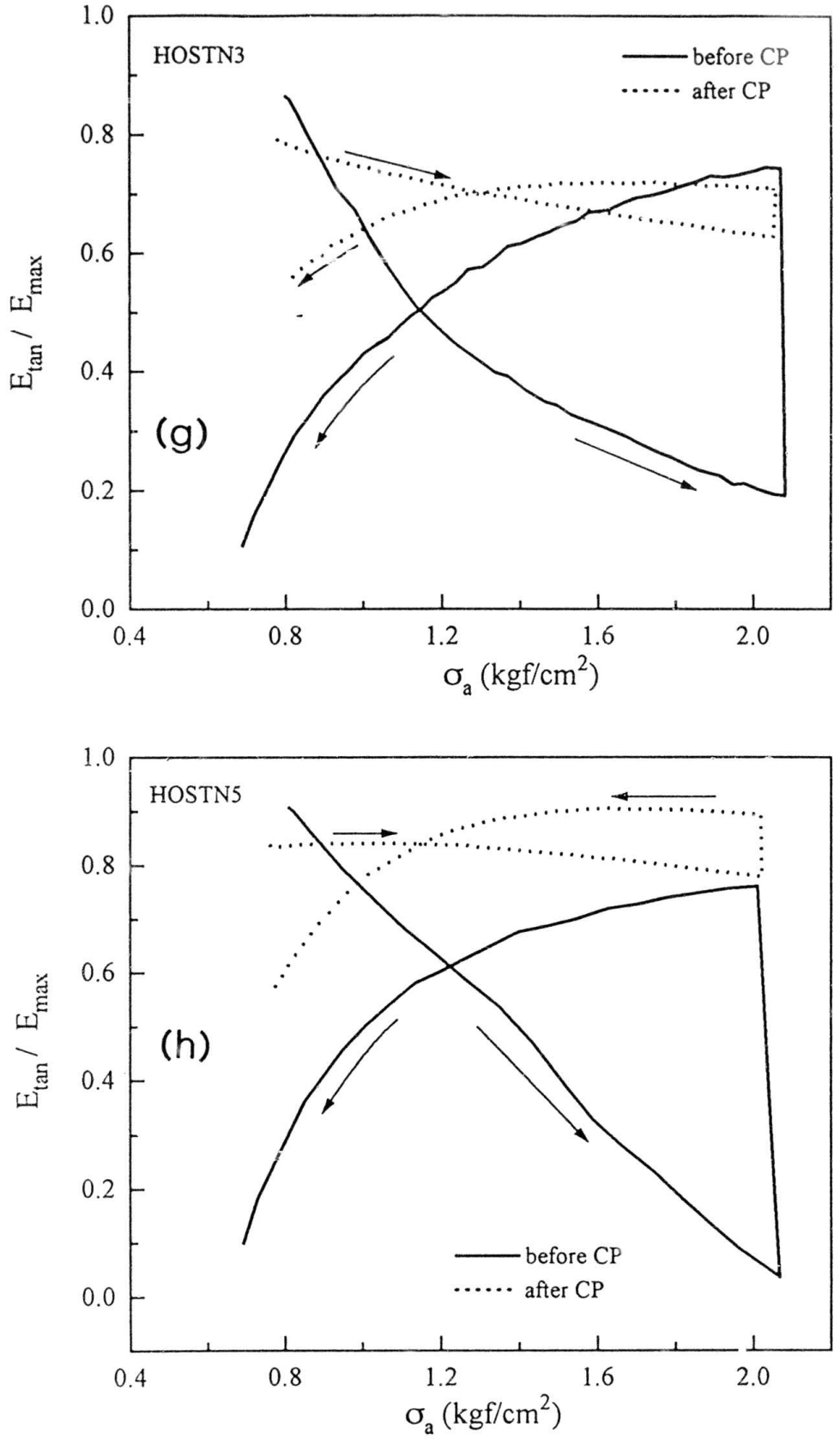

Figs. 6.25: Relationships between E_{tan}/E_{max} and σ_a in CP stress path for specimens (g) HOSTN3, and (h) HOSTN5.

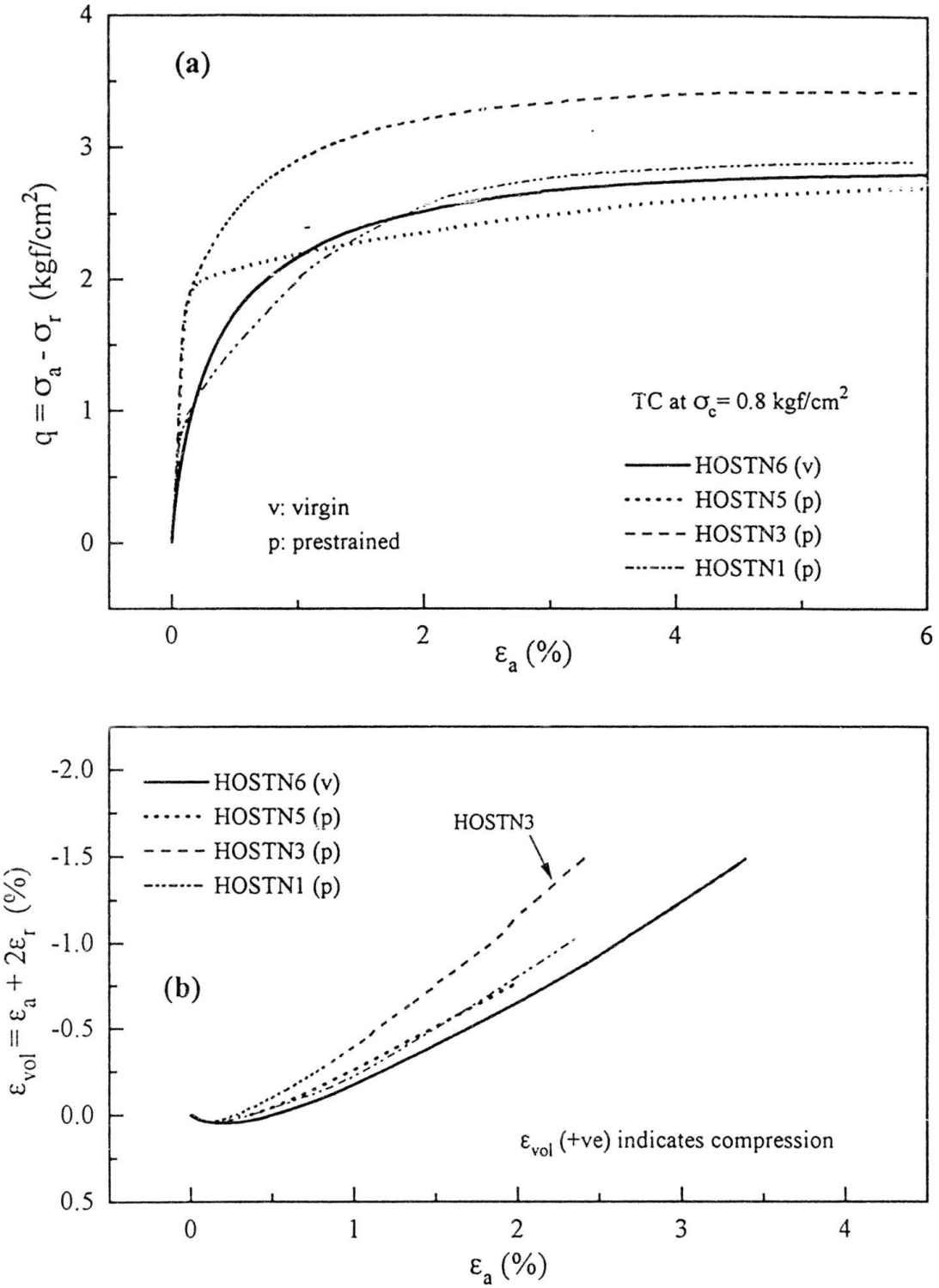

Figs. 6.26: Relationships between (a) q and ε_a, and (b) ε_{vol} and ε_a during TC at σ_a=σ_r=0.8 kgf/cm^2.

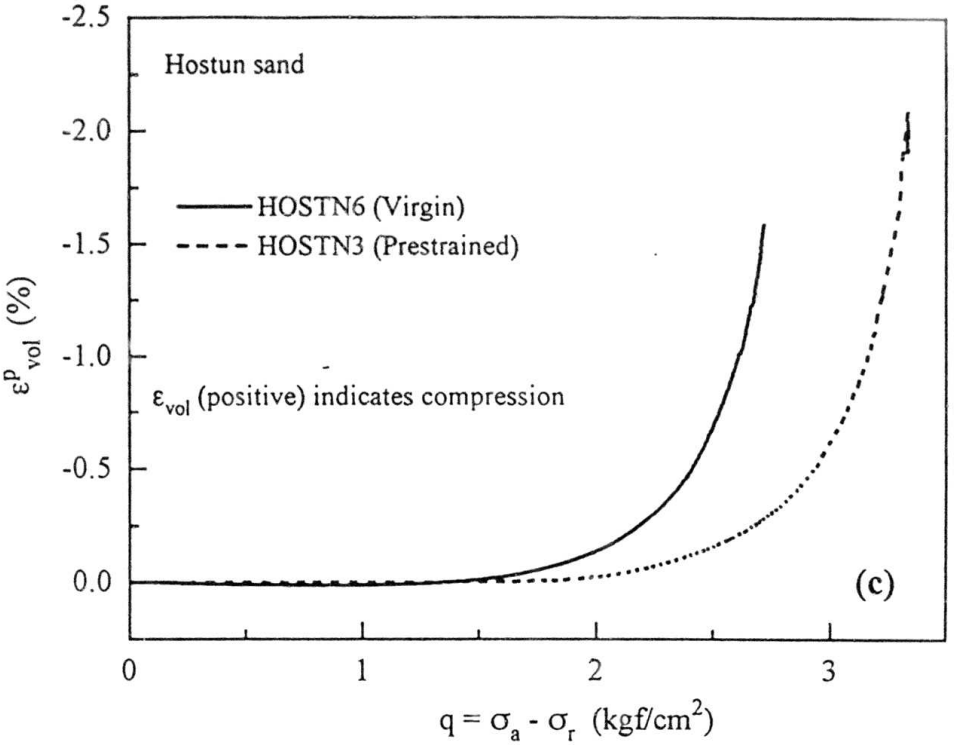

Fig. 6.26c: Relationships between the volumetric plastic strain ε^p_{vol} and q during TC at $\sigma_a=\sigma_r=0.8$ kgf/cm^2.

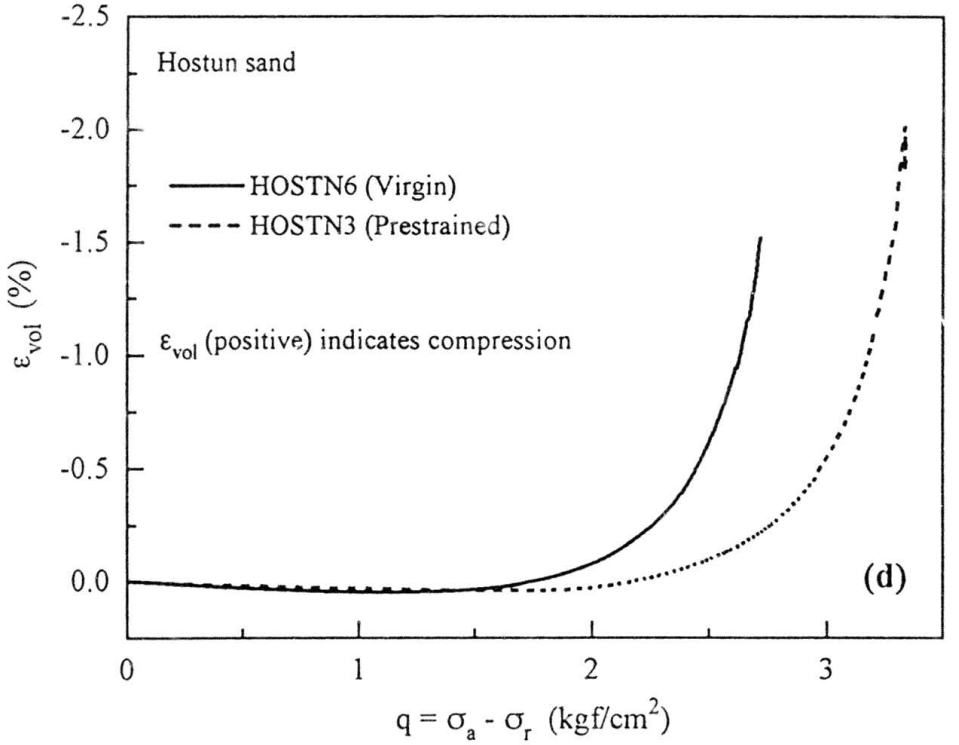

Fig. 6.26d: Relationships between q and ε_{vol} during TC at $\sigma_a=\sigma_r=0.8$ kgf/cm^2.

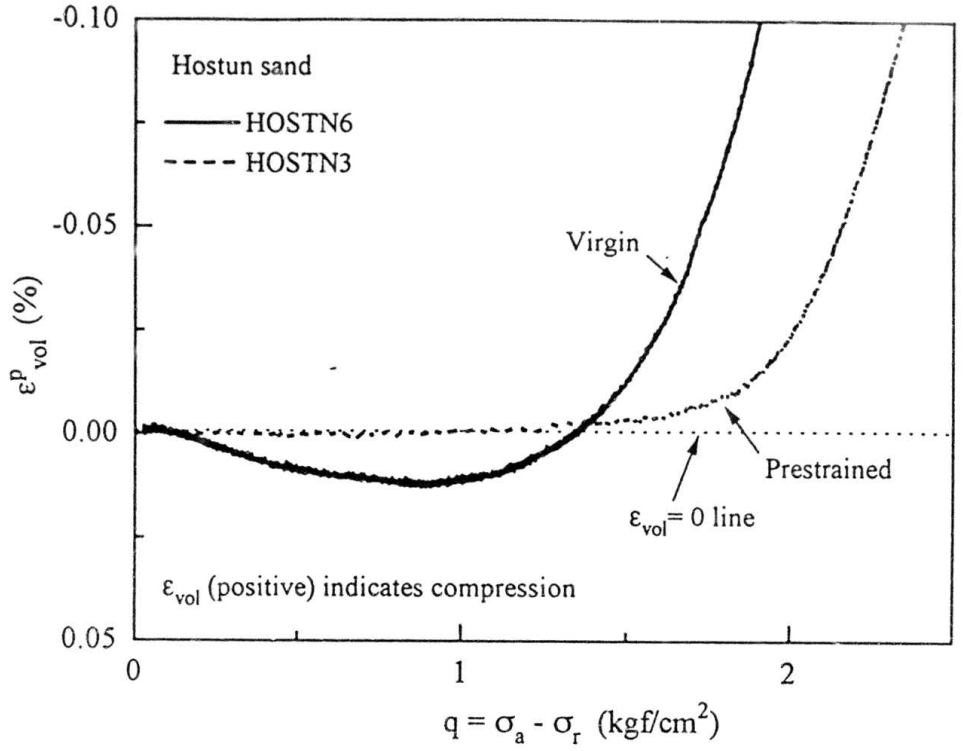

Fig. 6.26e: Relationships between q and ε^{p}_{vol} (at low stress level) during TC at σ_a=σ_r=0.8 kgf/cm^2.

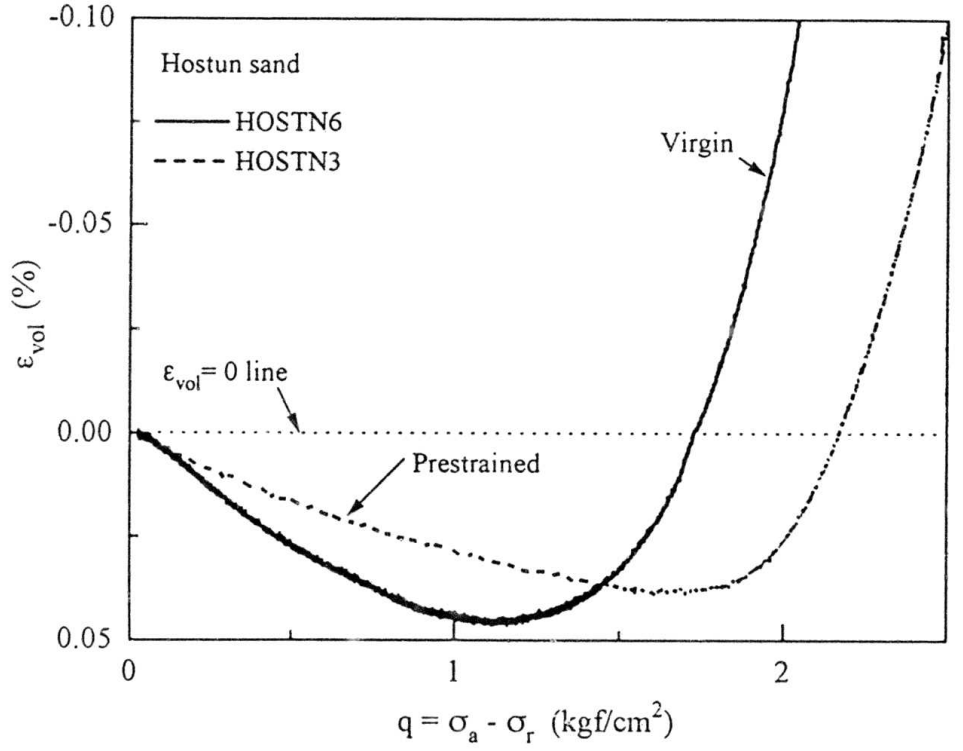

Fig. 6.26f: Relationships between q and ε_{vol} (at low stress level) during TC at σ_a=σ_r=0.8 kgf/cm^2.

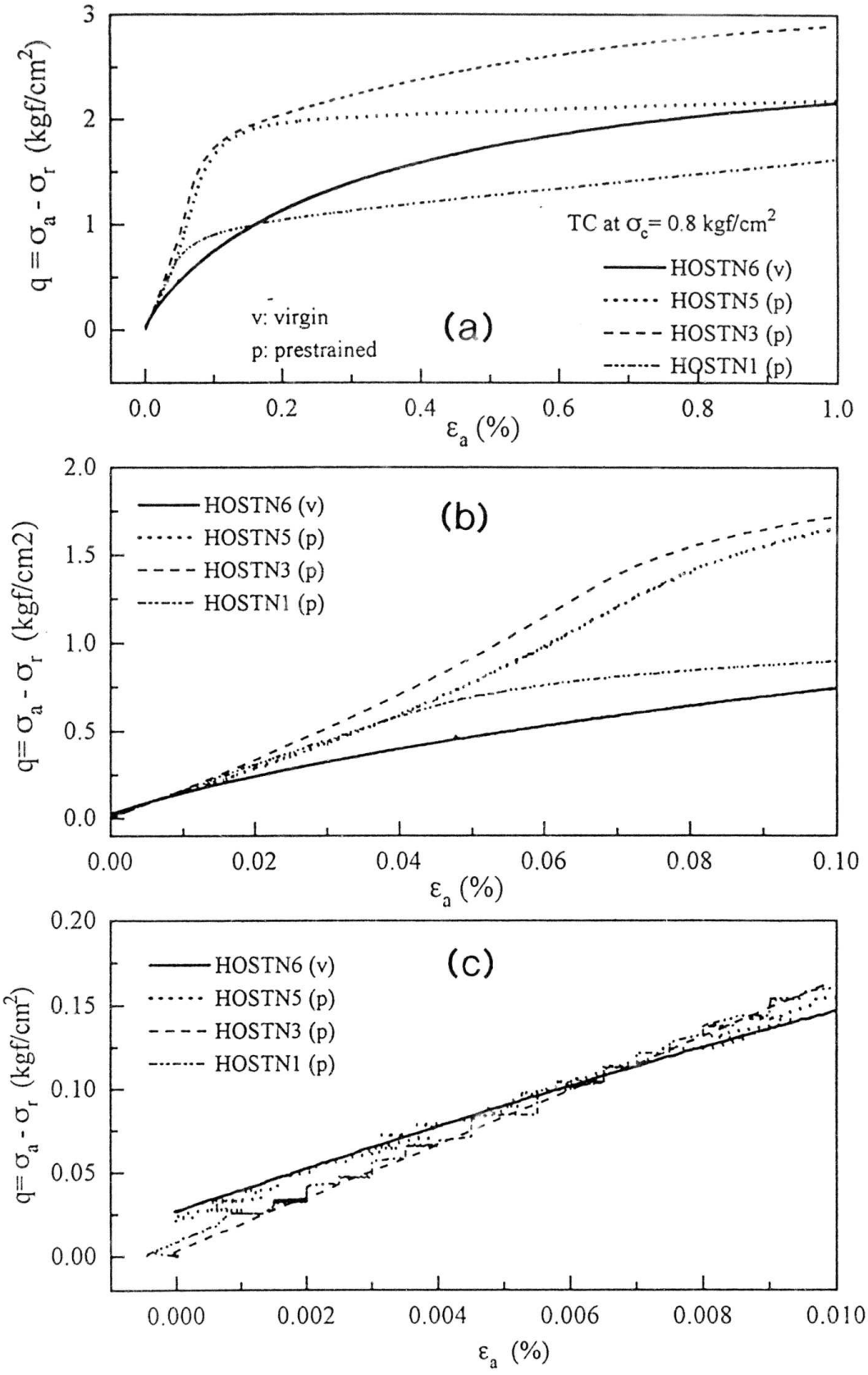

Figs. 6.27a~c: q~ε_a relationships during TC at σ_a=σ_r=0.8 kgf/cm^2 for the range of ε_a up to (a) 1.0%, (b) 0.10% and (c) 0.01%.

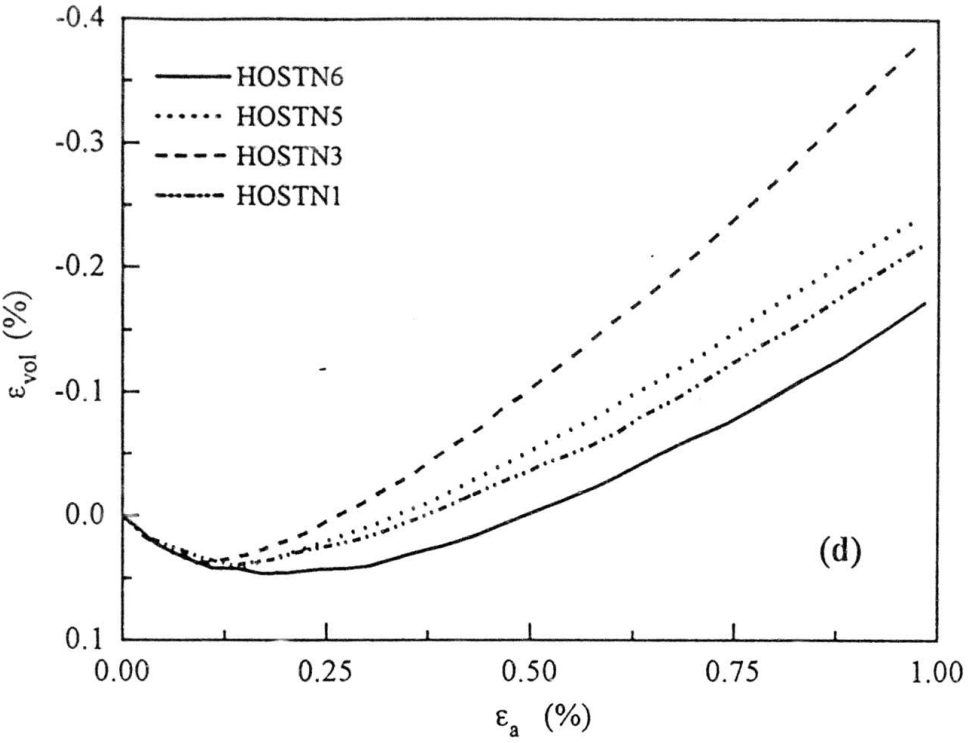

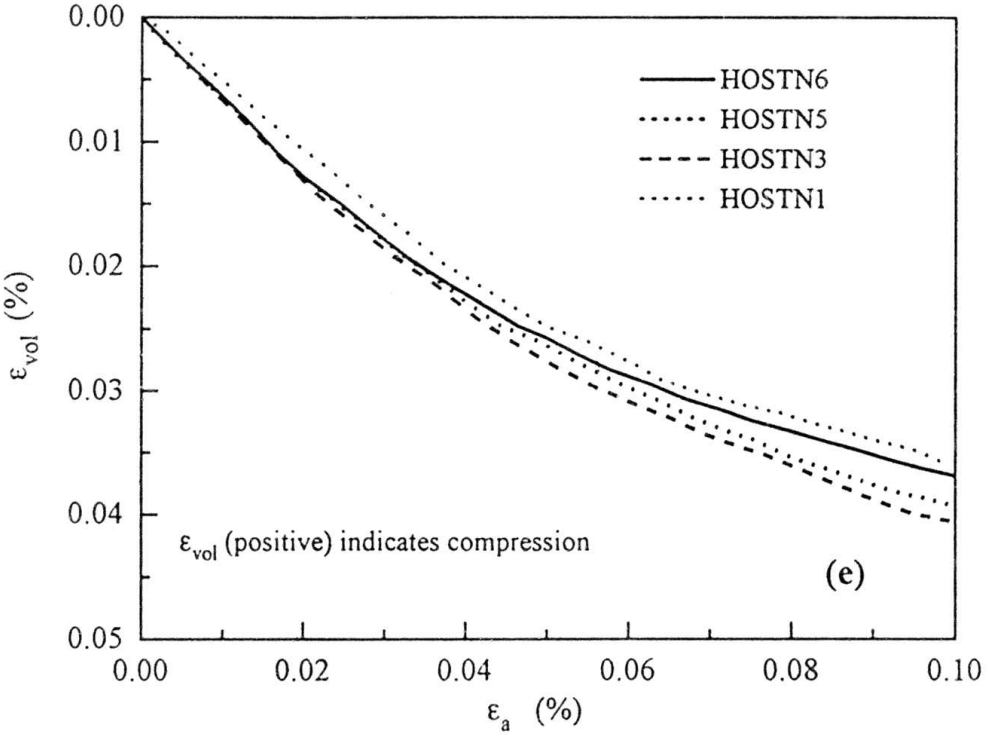

Figs. 6.27: ε_a~ε_{vol} relationships during TC at σ_a=σ_r=0.8 kgf/cm^2 for the range of ε_a up to (d) 1.0% and (e) 0.1%.

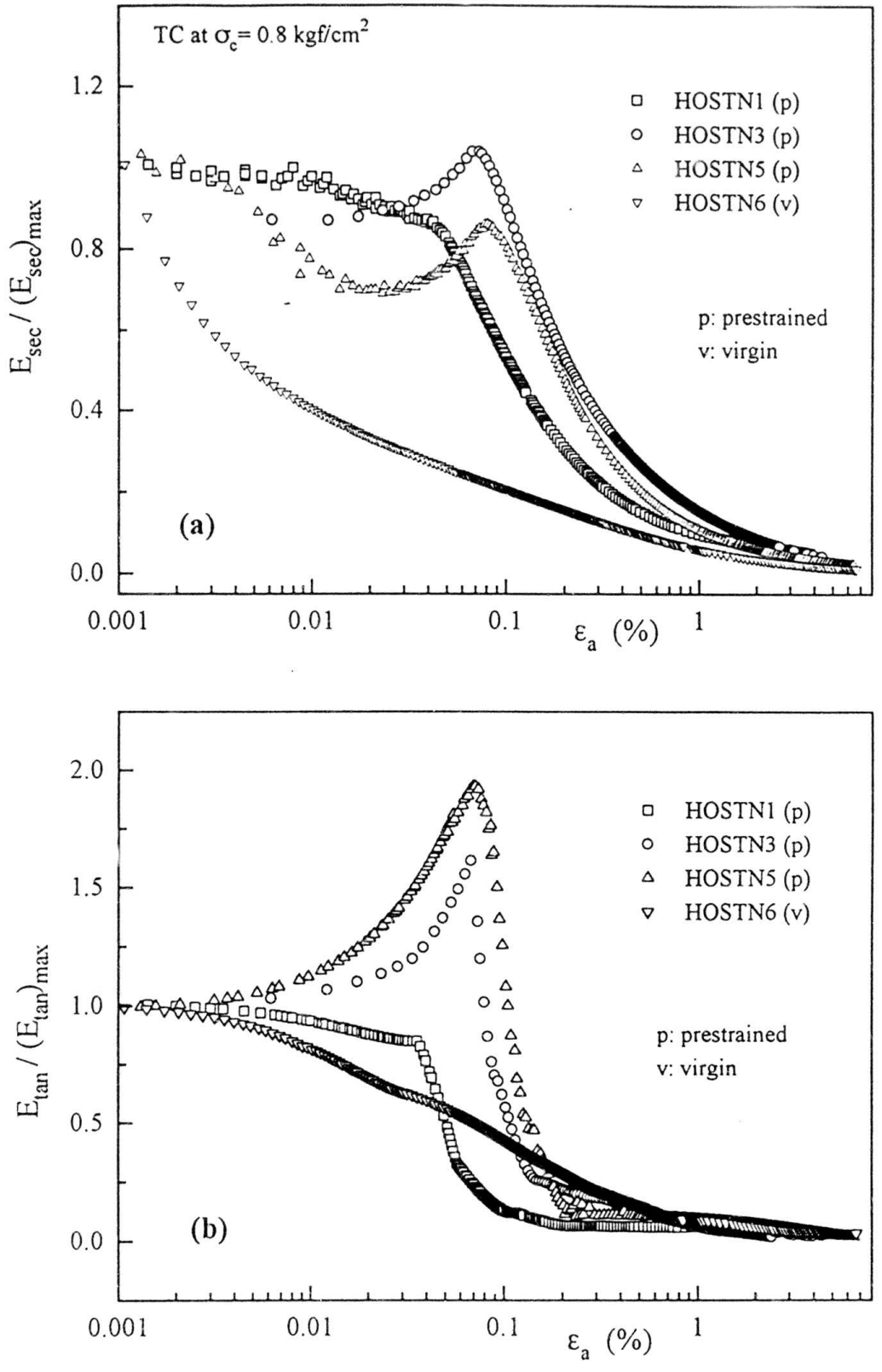

Figs. 6.28: (a) $E_{sec}/(E_{sec})_{max} \sim \log(\varepsilon_a)$ and (b) $E_{tan}/(E_{tan})_{max} \sim \log(\varepsilon_a)$ relationships during TC at $\sigma_a=\sigma_r$=0.8 kgf/cm^2.

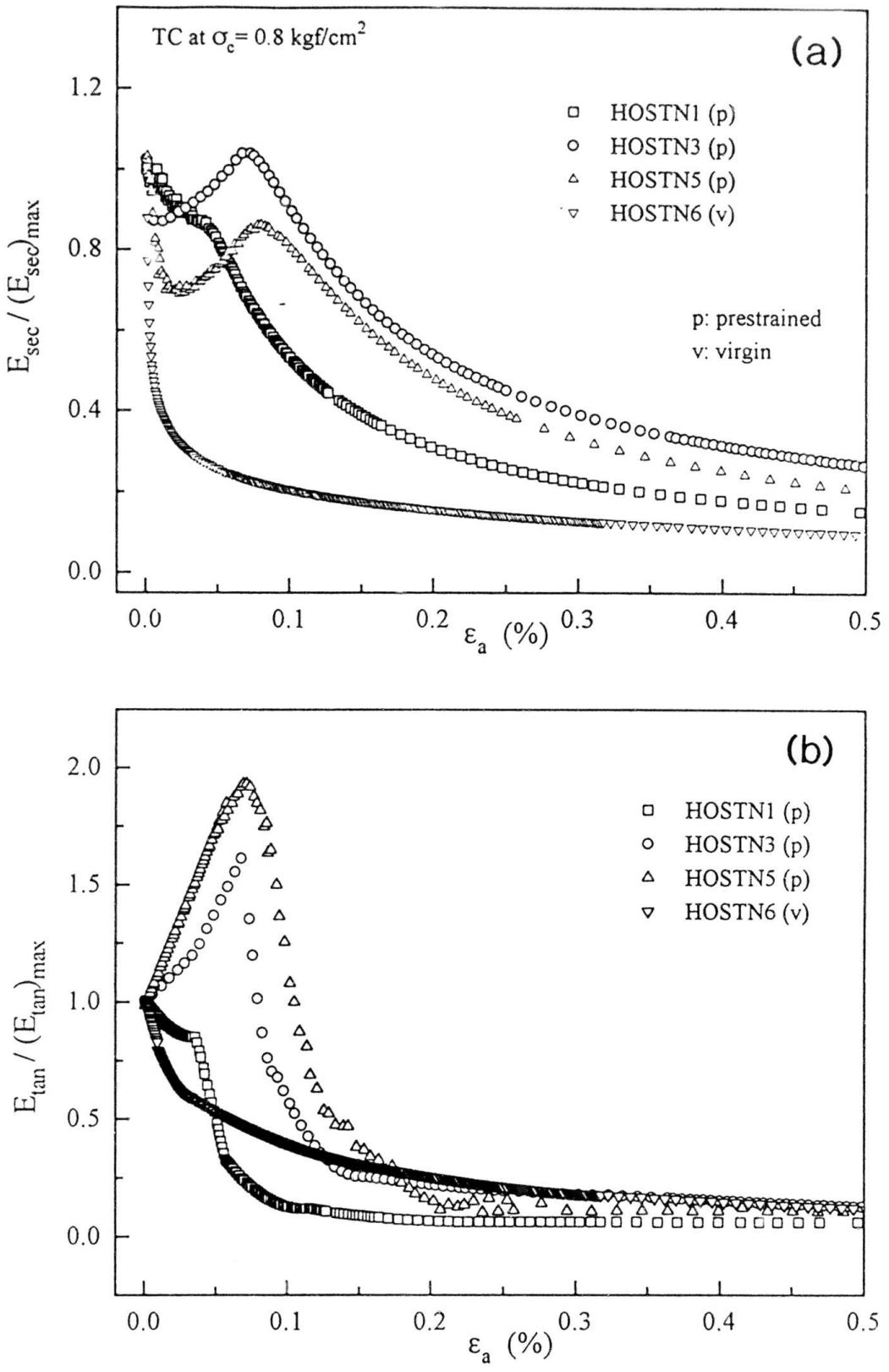

Figs. 6.29: (a) $E_{sec}/(E_{sec})_{max}$~ε_a and (b) $E_{tan}/(E_{tan})_{max}$~ε_a relationships up to ε_a=0.5% during TC at σ_a=σ_r=0.8 kgf/cm^2.

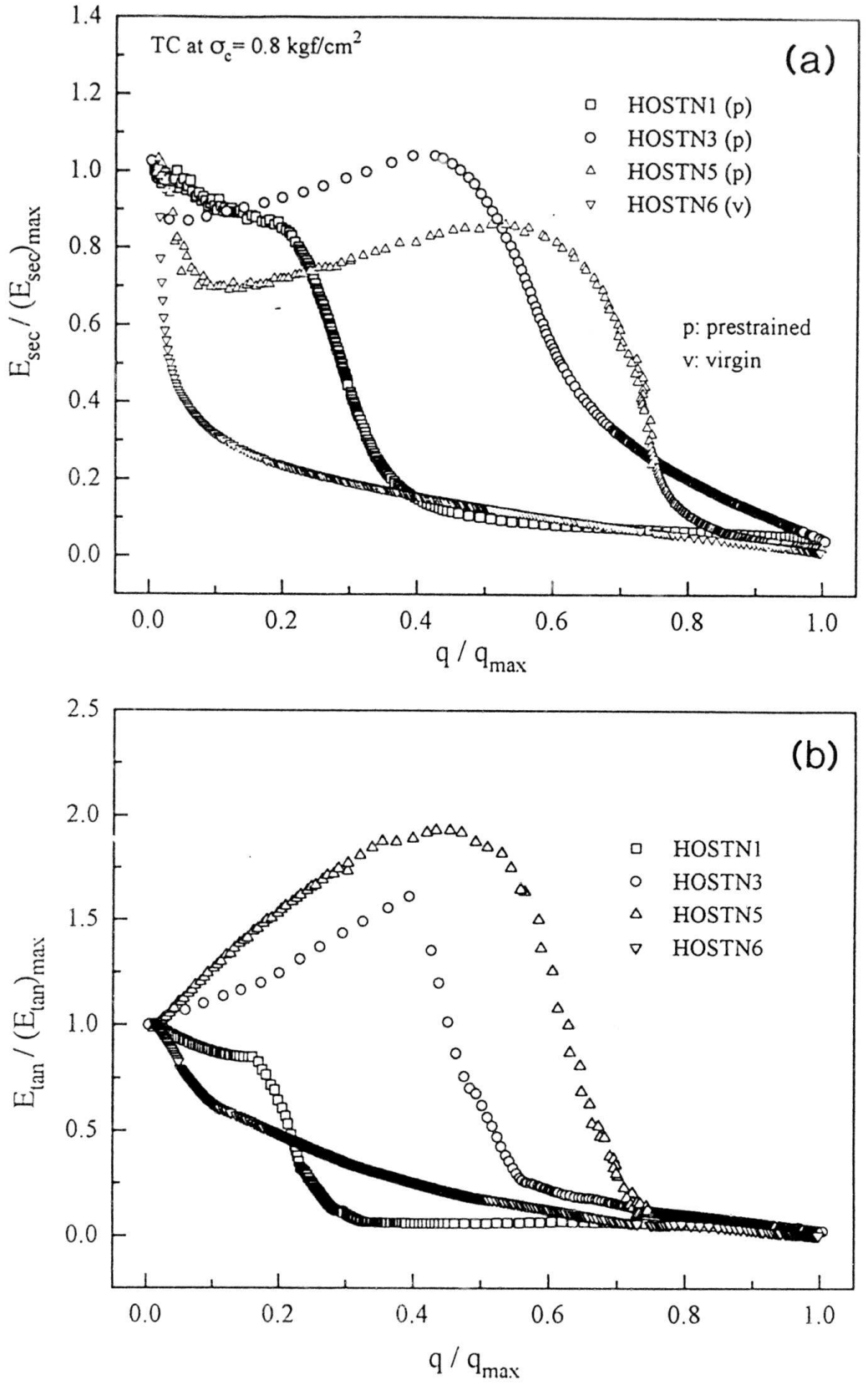

Figs. 6.30: (a) $E_{sec}/(E_{sec})_{max}$~q/q_{max} and (b) $E_{tan}/(E_{tan})_{max}$~q/q_{max} relationships during TC at σ_a=σ_r=0.8 kgf/cm^2.

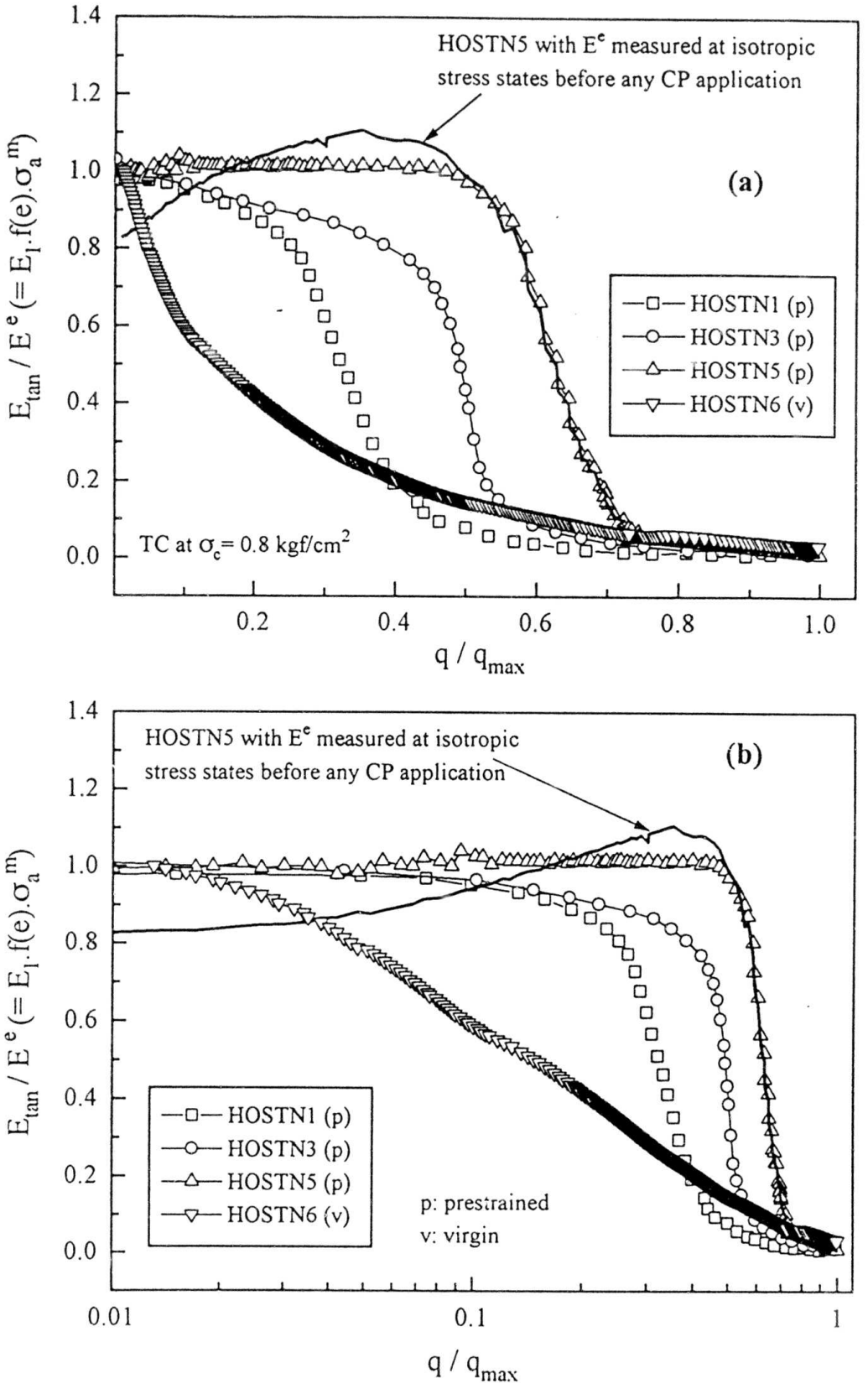

Figs. 6.31: Relationships between (a) E_{tan}/E^e~q/q_{max} and (b) E_{tan}/E^e~$\log(q/q_{max})$ during TC at $\sigma_a=\sigma_r=0.8$ kgf/cm^2.

Chapter 7

Loading-Rate Dependency of Sand Deformation in Cyclic Triaxial Tests

7.1. Introduction

Deformation characteristics of soils are often expressed in terms of shear moduli (or Young's moduli) and material damping ratios, which are important parameters in determining the performance of geotechnical materials under loading condition, and which are necessary to describe the simple shear behavior of a soil element of known mass. Structural loading could be static (monotonic or cyclic), transient, dynamic and vibratory in nature. In general, soils subjected to cyclic loading (static, transient, dynamic or vibratory in nature) typically experience higher rates of loading or strain than systems characterized as monotonic. For example, traffic, machine, wave and earthquake loadings frequencies tend to be in the range 0.1~20 Hz and produce rates of stress increase that are many orders of magnitude greater than is under typical static loading conditions. Hence, the rate-dependency phenomenon cannot be ignored when a wide range of loading frequency is considered. Accordingly, proper understanding of the effects of loading rate on the deformation characteristics of soils has become an important issue.

The results from tests on clay by Graham et al. (1983) indicate that a family of stress-strain curves may be identified, each associated with a specific strain rate, such that a stiffer and stronger response is predicted for higher strain rates. Shibuya et al. (1995) and Kim and Stokoe (1995) showed that in cyclic loading tests, equivalent shear modulus of clay is insensitive to rate of shear straining whereas hysteretic damping increases according to the decrease of shearing rate. Tatsuoka and Kohata (1995), Kim and Stokoe (1995) also showed that elastic Young's modulus (E^e) and damping ratio (h) for very small-amplitude cyclic loading (CL) defined for an single amplitude axial strain $(\varepsilon_a)_{SA} \leq 0.001\%$ are essentially independent of strain rate. For sedimentary soft rock, the undrained elastic Young's modulus E^e is rather insensitive to the change in strain rate when the strain rate is larger than a certain limit. At higher strain levels, however, a stiffer response in the stress-strain characteristics can be observed and the rate effect increases as strain level increases (Kohata et al., 1995). On the other hand, Bolton and Wilson (1989) showed that the rate-dependency plays very little role in the stress-strain response as well as the strength of

granular materials. Most of the previous comprehensive works were performed using simple shear, torsional shear and resonant column apparatuses. A few works using triaxial apparatus (e.g., Tatsuoka and Kohata, 1995) have been reported in the literature.

It is interesting to note that the perceived difference between the static and dynamic moduli has been decreasing as the accuracy of static measurements at very small strains below 0.0005% is increasing. In addition, an understanding is growing that strain amplitude and strain rate are key variables in predicting soil behavior whether the phenomenon is static or dynamic (Burland, 1989; Bolton and Wilson, 1989; Jamiolkowski et al., 1991; Tatsuoka and Shibuya, 1992; Jardine, 1995). The deformation at strains less than about 0.001% is essentially elastic and almost the same elastic deformation modulus can be obtained from static (monotonic and cyclic) and dynamic tests. At strains exceeding the elastic strain limit, however, the stiffness and damping may differ between static and dynamic tests, which should be explained by the differences in strain level, strain rate, number of loading cycles and so on, provided stress and strain measurements are sufficiently accurate.

Described herein is the dependency on loading rate of stiffness (equivalent Young's modulus) and damping ratio of sand evaluated by using triaxial specimens. Loading frequency was varied in the range of 0.005~2.0 Hz. Investigation of E_{eq} and h in the frequency range of 0.5~1.0 Hz has special importance in earthquake engineering. In the 1995 Great Hanshin Awaji earthquake, for instance, a significant damage was caused to buildings with a natural frequency close to 0.5 Hz, even though the ground movements in the surrounding region were quite small.

7.2. Description of the Apparatus

The experimental works were carried out in a modified triaxial apparatus (Fig. 6.1, Chapter 6). The deviator load was measured by a sensitive load cell placed inside the triaxial cell, local axial strains free from bedding errors were measured by a pair of LDTs (LDT1 and LDT2) (Goto et al., 1991) hinged vertically on diametrically opposite sides of a specimen surface, and local radial strains were measured by using three pairs of gap sensors at three levels of height of the specimen. Besides, a gap sensor (GS) was used to measure the displacement of loading cap (i.e., conventional axial strain measurement) of triaxial apparatus. Axial strains evaluated by GS may be

affected by system compliance and bedding error (Jardine et al., 1984; Tatsuoka and Kohata, 1995).

Confining pressure σ_c (=lateral stress σ_r) was applied inside the voids of soil particles by partial vacuum and the deviator load was applied by air pressure through a two-chambered Bellofram cylinder. The upper chamber of the Bellofram cylinder was connected to a static pressure line directly from a house of pressure and accumulator. On the other hand, the bottom chamber was provided with dynamic (or cyclic) air pressure, which is also supplied from the same house of pressure and accumulator, but regulated by a E/P transducer through a function generator or a computer. Anisotropic compression (i.e., axial stress $\sigma_a > \sigma_r$) stress states can be achieved by controlling confining pressure and deviator load through 'static' pressure line. However, to achieve an anisotropic extension stress state ($\sigma_a < \sigma_r$), firstly a zero deviator stress state is assured by applying equal air pressure (greater than atmospheric pressure) into the 'static' and 'dynamic' pressure lines, which is followed by decreasing the pressure in static line compared to that in dynamic line (for details Tatsuoka, 1988). At any stress state, thus acquired, cyclic loading (CL) can be applied by the use of the function generator. In this case, based on the scale of load-amplitude and loading frequency, the function generator controls the dynamic pressure by sending required pressure-equivalent voltage signals to the E/P transducer, which finally materializes the pressure application by allowing the required amount of air to move into or move out of the dynamic pressure line.

Fig. 7.1.a shows the data acquisition (DA) system employed for the principal measuring devices. Load cell and the LDTs possess identical components in the DA system. On the other hand, GSs (both lateral and vertical directions) had its own type dynamic signal conditioner (provided by the manufacturer), while the remaining appliances being the same as LDTs (Fig. 1a). The accuracy of DA systems used for various transducers is very important for static CL tests when CL tests are performed at higher frequency f (say, f=0.5 Hz). This is because in case of high frequency loading (in static tests), the potential error in evaluating damping ratio may come from the time-lag between recorded stress and strain components. That is, if there is any time delay in the recorded responses of loads (hence stresses) and deformations during CL, it will directly influence the measured values of h. However, the influence could be much less severe on the measured values of E_{eq}.

Tests were performed on air-pluviated specimens of Hostun sand. Physical properties are listed in Table 6.1 (Chapter 6). Small specimens (15 cm high and 7.5 cm in diameter) having regular ends with using porous stones at both ends were used in this investigation.

7.3. Testing Procedure and Test Results

Testing program consisted of cyclic loading tests in the axial stress direction (at constant σ_r) at various load or strain amplitudes while varying the loading frequency (f) at each amplitude. Fig. 6.2b shows the definition of E_{eq} and h. Each E_{eq} value was evaluated from the peak-to-peak secant modulus of σ_a~ε_a response of each cycle of CL test, and the evaluation of h needed numerical integration of hysteresis loop for each cycle. Typically 100~120 data points were recorded in each cycle of CL test when $f \leq 0.4$ Hz, whereas for $f > 0.5$ Hz, 20~80 data points were recorded in each cycle. This difference was due to the speed limitation of the computer and the analogue-to-digital card used in the DA system.

Tests were performed on four specimens of Hostun sand: HOSTN2, HOSTN3, HOSTN5, and HOS12. Test conditions are briefly described in Table 7.1. The specimen HOSTN2 had experienced stress histories described in Chapter 8. In brief, the specimen was subjected to stress-controlled TC test from $\sigma_a = \sigma_r = 0.8$ kgf/cm^2 to $\sigma_a = 2.6$ kgf/cm^2 at constant σ_r, followed by unloading to the previous isotropic stress state. This was done to evaluated the deformation characteristics during creep and the small strain stiffness at different stress levels; the results are described in Chapter 8. After that, strain rate dependency of E_{eq} and h was investigated for a single amplitude of cyclic loading, where the single amplitude axial strain $(\varepsilon_a)_{SA}$ was 0.002% and loading frequency was varied from 0.03 to 0.5 Hz. Both sinusoidal and triangular wave-forms load cycles were applied sequentially at a given f. The existence and influences of time-lag were critically examined in the stress-strain responses.

Fig. 7.2a shows some typical relationships between σ_a and ε_a (measured with LDTs) obtained at the tenth cycle at each of different frequencies when the wave-form was sinusoidal. The σ_a~ε_a response for each f was shifted arbitrarily along the ε_a axis in order to differentiate them from each other. Similar results for the use of triangular wave-form are shown in Fig. 7.2b. The stress-strain relations (Figs. 7.2a and b) were nearly linear and the slopes for different f are very

similar to each other, while the variations in the area of hysteresis loops are not visible. Fig. 7.3 shows the variations of E_{eq} and h (evaluated by ε_a of LDTs) with number of the load cycle (N).

On the other hand, the axial strains measured by GS showed noticeably different soil responses as can be observed from Figs. 7.4a and b for sinusoidal and triangular wave-forms of CL tests, respectively. Although the slope (i.e., E_{eq}) did not change largely with f, the area of hysteresis loop grew up drastically with the increase in f. The values of E_{eq} and h (evaluated at the tenth cycle) are plotted against f in Figs. 7.5a and b, respectively. The following trends can be observed.

(a) E_{eq} is rather independent of f and wave-forms for $(\varepsilon_a)_{SA}$= 0.002%.
(b) A large difference is observed between the E_{eq} values obtained based on axial strains measured with LDTs and GS, which can be attributable to the system compliance and bedding error (Tatsuoka and Kohata, 1995; Tatsuoka et al., 1994).
(c) The value of h measured with LDTs is not very sensitive to the changes in f and wave-form. Non-zero values of h indicate that the deformation of sand is not totally elastic even at such small strains.
(d) h values evaluated based on axial strain measured with GS show a very different response, which is not reliable. The reason will be described latter.
(e) By careful observation of the data based on ε_a (LDT), it is seen that with the decrease in f, E_{eq} decreases and h increases at a very small rate. Further, the values of h are slightly larger for sinusoidal wave form than triangular wave form, while the effect on E_{eq} is not visible. Di Benedetto and Tatsuoka (1996) attempted to simulate such features by a three-component rheological model in which a linear spring is connected to Voigt model.

The peculiar strain rate-dependency of h observed based on GS strain (Fig. 7.5b) was resulted from time-lag between the responses of a strain gauge-type load cell and GS (an inductance type sensor). This was confirmed by performing a series of CL tests on a nearly perfect elastic steel spring in place of a sand specimen. Fig. 7.5c shows typical force-displacement relationships obtained from CL tests with $(\varepsilon_a)_{SA}$= 0.03% performed at f= 0.5 and 1.0 Hz. The test results using LDT showed linear relationships, as expected, for the linear elastic material, whereas the responses using GS indicated that the spring behaved as if it were not elastic. The reasons for

the above would be either or both of the following: (a) a GS may be inherently sluggish or fast in response compared to those of the strain gauges used in load cell and LDTs; (b) difference in the data acquisition (DA) systems. The DA systems for LDTs and load cell are exactly identical. That is, it consists of the main signal conditioner (dynamic signal or strain conditioner) with an activated 10 Hz noise cut-off frequency, a DC amplifier, a filter, an analogue-to-digital card, etc. (Fig. 7.1a). On the other hand, an inductance type transducer GS works with the density of magnetic flux. Therefore, the DA system for GS consists of a completely different type of 'main signal conditioner' having different working principles although the rest of the components of the system (Fig. 7.1a) are identical. Therefore, it can be concluded that the electronic measuring devices to measure a pair of corresponding stress and strain must be of having the identical types of DA systems with exactly the identical electrical components in terms of noise cut-off frequency, circuit resistance, circuit capacitance, and so on. Otherwise the difference will be reflected in the acquired data as a time-lag, especially at a higher frequency. Hereafter data obtained with the use of LDTs is represented.

The importance of the use of 32-Hz (cut-off frequency) low-pass filter in the DA system of LDT and load cell (Fig. 7.1a) is verified by performing two series of CL tests on the elastic spring at f=0.1 Hz with $(\varepsilon_a)_{SA}$= 0.035% and 0.067%. In one series, the filters were used, while in the other they were removed before the application of CL. Fig. 7.5d shows the resulting load-displacement relationships. It indicates that the use of such a filter to increase the signal-to-noise ratio in the existing DA system is rather essential for the measurement of both E_{eq} and h.

Dependency of E_{eq} and h on frequency f for very small amplitude axial-strain was investigated at different true virgin stress states in triaxial compression at σ_r= 0.8 kgf/cm^2. Tests were performed on HOS12 specimen. The initially isotropically consolidated specimen (σ_a=σ_r=0.8 kgf/cm^2) was subjected to monotonic axial compression by using an automated (i.e., computer-controlled) load-control system. Deviator load (i.e., axial load in excess to that offered by confining pressure) was applied at a constant rate of axial stress (0.125 kgf/cm^2/min) by increasing the axial stress in very small steps. After reaching the desired stress state, the specimen was allowed to undergo creep while maintaining the constant stress state. When creep rate became negligible (below 0.00001% per minute in the last ten minutes), very small strain amplitude CL tests were performed to evaluated E_{eq} and h about the current stress state as neutral. At each stress

state, f was varied between 0.01 to 2.0 Hz, while $(\varepsilon_a)_{SA}$ was nearly 0.0015%. After completing tests at a given stress state, the next stress state was achieved, which was followed by similar experimental procedure as described above.

Figs. 7.6a and b show the stress-strain relationships of typical cycles at various frequencies obtained when the neutral axial stress was at σ_a=0.8 kgf/cm^2 and σ_a=2.0 kgf/cm^2, respectively. Slope of stress-strain relationship, at a given stress state, seems not to be affected by f, while the hysteresis loop is largely affected by continuous creep, particularly at the lower f. Fig. 7.6c shows the relationships between E^e / $E^e_{f=0.1}$ and f, where $E^e_{f=0.1}$ is the value of E_{eq} (=E^e) at a given axial stress (neutral) evaluated when f=0.1 Hz. $E^e_{f=0.1}$ values at different axial stresses are listed in Fig. 7.6c. The corresponding relationships between damping ratio h and f are shown in Fig. 7.6d. The most of the data sets shown in Figs. 7.6c and d were obtained at virgin states except one, which was obtained at neutral stress state σ_a=1.0 kgf/cm^2 (and σ_r=0.8 kgf/cm^2) after unloading from the maximum value of σ_a. E_{eq} (=E^e) is independent of f, except at lower frequencies (f≤0.05 Hz), where modulus was affected by creep deformation. The higher the neutral stress level, the larger the creep rate (during virgin loading, Chapter 8). Therefore, modulus decreases with the increase in stress level at lower f values. The effects of creep is more severe on h values at lower frequencies. h value increases manifold as the stress level increases with the decrease in frequency, especially when f≤0.05 Hz. At a given stress level, h value tends to increase slightly with the increase in f when f≥0.6 Hz. Very careful observation shows that at a given frequency, h increases very slightly with the increase in stress level although some scatter can also be observed.

Similar behavior was observed from HOSTN3 specimen, which was not 'true virgin' when the investigation was done (see Table 6.1). Figs. 7.6e and f show, respectively, the relations of E_{eq}/f(e) and h with f. CL tests were performed at an anisotropic neutral stress state (σ_a= 1.4 kgf/cm^2, σ_r= 0.8 kgf/cm^2). During CL tests, $(\varepsilon_a)_{SA}$ value was either 0.0012% or 0.0038%, while f was varied between 0.005 Hz to 1.5 Hz. Results were very similar to those shown in Figs. 6.7c and d. However, in this case, because of the previous stress-history (Table 6.1), neither h nor E_{eq} evaluated at f≤0.05 Hz was affected as severely as HOS12 specimen due to creep.

Figs. 7.7a and b show, respectively, the relations of h and E_{eq} with $(\varepsilon_a)_{SA}$ at different frequencies. Tests were performed on specimen HOSTN3. The specimen had previous stress

history of six unload-reload cycles performed with axial stress amplitude from σ_a= 0.8 to 2.0 kgf/cm^2 at constant σ_r= 0.8 kgf/cm^2 (Table 7.1). In the figures, Set A and Set B indicate the configurations of arrangement of principal measuring devices in the analogue-to-digital (A-D) card. In Set A, load cell, GS to measure ε_a, LDT1 and LDT2 were connected serially to the A-D card in the first four channels, while in Set B, the load cell and LDT2 were interchanged, i.e., LDT2, GS, LDT1 and load cell were connected serially. Tests with Set A configuration were performed first and was followed by the tests with Set B configuration. All CL tests were performed symmetrically about the neutral stress at σ_a=1.4 kgf/cm^2 by increasing the amplitude of load cycle in steps, while at each step at least eleven cycles of CL were applied at each frequency of loading. Frequency at each stage was varied in the ascending order from 0.1 to 2.0 Hz before proceeding to the next step. Data at each point in Figs. 7.7a and b is the 10th cycle value obtained at a given stress cycle or $(\varepsilon_a)_{SA}$.

Fig. 7.7b shows that E_{eq} is essentially independent of f for all the values of $(\varepsilon_a)_{SA}$ being investigated with some exceptions. That is, the values of E_{eq} at f=0.1 Hz for relatively larger $(\varepsilon_a)_{SA}$ (i.e., $(\varepsilon_a)_{SA} \geq 0.007\%$) were observed slightly lower (5% at the largest) that those observed at higher frequencies at the same $(\varepsilon_a)_{SA}$. It can also be noticed (Fig. 7.7a) that damping ratio for a given $(\varepsilon_a)_{SA}$ was slightly larger at f=2.0 Hz than those at lower frequencies when $(\varepsilon_a)_{SA}$ was greater than about 0.01%. This could be attributable to the accumulation of slightly larger creep strains in the measured ε_a during CL tests at lower (f=0.1 Hz) frequency. Set A and B arrangements did not show any noticeable differences in the measured values of E_{eq}, while damping ratio at a given $(\varepsilon_a)_{SA}$ varied slightly for Set A and B arrangements. The h value measured with Set B arrangement at a given $(\varepsilon_a)_{SA}$ was lower than that with Set A. It could be because of that the tests with Set B configuration were performed after those with Set A had been done. Therefore, the differences could be due to the effects of previously performed CL tests, but it is not due to the time-lag as described below.

Tests with Set A and B arrangements were performed in order to re-confirm the existence of time-lag, if any, for the arrangements between the responses of LDTs and load cell although they had identical DA systems. While sampling data, the micro-computer does it according to the serial of connections. That is, data of first channel (of A-D card) will be recorded first, which is followed by second, and so forth. That means, the real time responses for all the principal

measuring devices at a given instant can never be recorded by the computer. To minimize the time-lag of this type, it is essential to set the transducers that are directly related to the evaluation of h as close to each other as possible, which was done in this investigation. That means, the larger the gap (in term of serial of connections to A-D card) between the load cell and LDT, for example, larger will be the time-lag. However, time-lag of this type could be a problem only in tests at a high frequency, and the larger the amplitude, the larger will be the problem. The conclusion with this respect cannot be obtained from the results shown in Fig. 7.7a, since the specimen was not at steady state.

The importance of 'steady state conditions' (Bolton and Wilson, 1989) can be realized from the above discussions. 'Steady state conditions' are defined as those prevailing while the soil is repeatedly traversing the same hysteresis loop. Therefore to achieve such a state, the same specimen was then subjected to cyclic prestraining (CP) of a large number of load cycles (40,000 cycles) with nominal axial stress amplitude in the range of σ_a=0.35~1.3 kgf/cm^2. Axial strain at the neutral stress (i.e., σ_a=0.8 kgf/cm^2) was drifted towards extension side for about 0.08% due to CP. After CP, the specimen was observed to traverse the same hysteresis loop without noticeable translation along ε_a axis direction. In Fig. 7.8, such an example is shown for specimen HOSTN3, which will be described later.

Then the test procedure described above (in connection with Figs. 7.7a and b) was repeated with one exception, i.e., stress-amplitude was gradually decreased in steps after starting from the maximum amplitude, which was equal to the stress amplitude (CP_{str}) during CP (i.e., σ_a =0.35~1.3 kgf/cm^2). Fig. 7.9 shows typical σ_a~ε_a relationships during CL tests performed at 2.0 Hz after CP application at the largest axial stress amplitude (i.e., at CP_{str}). Essentially no difference can be noticeable from the responses for Set A and B arrangements. Figs. 7.10a and b show, respectively, the variations of E_{eq} and h with $(\varepsilon_a)_{SA}$ for different f, which was varied as before in the range of 0.1~2.0 Hz in four steps. It can be seen that both E_{eq} and h at a given $(\varepsilon_a)_{SA}$ are independent of loading frequency. Differences in h values at a given $(\varepsilon_a)_{SA}$ for Set A and B arrangements as had seen before were disappeared. Damping ratio increased, as expected, with the increase in $(\varepsilon_a)_{SA}$ and decreased due to CP (Chapter 6; Teachavorasinskun, 1992) especially at larger $(\varepsilon_a)_{SA}$ for a given $(\varepsilon_a)_{SA}$ (as seen by comparing Figs. 7.10a and 7.7a). The values of E_{eq}, on the other hand, decreased with the increase in $(\varepsilon_a)_{SA}$; E_{eq} was not affected by f. These results also

indicate that noticeable time-lag for the arrangement of electronic devices (e.g., for Set A and B arrangements) in DA system did not exist at least within the investigated range of frequency.

As mentioned earlier, Fig. 7.8 shows typical σ_a~ε_a responses from relatively large amplitude CL tests (with axial stress amplitude nominally varying in the range of CP_{str}= 0.8~2.0 kgf/cm^2) performed on the specimen HOSTN3 at virgin stage. A typical characteristics of static (triaxial) CL test can be observed. That is, the response of CL tests were characterized by the drifting of hysteresis loop which tended to stabilize gradually with the number of cycles. 'steady state conditions' (i.e., cessation of drifting) were not obtained after six cycles (Fig. 7.8). Drifting direction was not unique in compression side of ε_a as can be seen in the figure. It rather depends on (a) the location of the neutral stress state of CL, and (b) the magnitude of stress-amplitude. The factors (a) and (b) combinely determines whether a CL test is in the extension bias (i.e., CL in fully triaxial extension stress state) , in the compression bias (i.e., CL in fully triaxial compression stress state), or in combined stress state. With respect to a CL test of combined type, if the shear stress state during symmetric loading comes closer to failure state in TE than in TC, the CL test can be considered as the one in the extension bias, and the drifting of hysteresis loop will occur to the extension side along ε_a axis. Otherwise it can be considered as the one in the compression bias for which the drifting will traverse with translation to the compressive strain direction along ε_a axis. The number of loading cycles that were required to reach steady state conditions varied considerably. The greater the amplitude of load cycle (or, the greater the magnitude of single amplitude axial strain, $(\varepsilon_a)_{SA}$), the greater the number of cycles to achieve steady state conditions. Therefore, to make a comparison of E_{eq} and h values for a certain stress amplitude of a given specimen among different frequencies as well as among different $(\varepsilon_a)_{SA}$, it is necessary to obtain steady state conditions at each given stress-amplitude before doing any CL test with that stress-amplitude. In Fig. 7.8, the σ_a~ε_a responses are shown for CL tests with CP_{str} in the range of σ_a between 0.8 to 2.0 kgf/cm^2 (compression bias) performed on HOSTN3 after application of a large number of axial load cycles (25,000 cycles) at σ_r=0.8 kgf/cm^2. A nearly perfectly steady state conditions was achieved as all the hysteresis loops for eleven cycles traversed the same stress-strain relations without translation in the axial strain direction. During the CP application, the neutral stress state was at σ_a=1.4 kgf/cm^2 and total drift in the axial strain direction was 0.063% (compression). Note that HOSTN5 specimen was also subjected to the similar axial stress load

cycle at CP_{str} for 25000 cycles to attain steady state conditions. In this case, total drift in σ_a direction was 0.98%, which was very large due to the loose specimen.

Steady state conditions having been achieved, HOSTN5 specimen was subjected to multi-stage axial stress CL tests with the neutral axial stress at σ_a=1.4 kgf/cm^2 to evaluate E_{eq} and h values for different $(\varepsilon_a)_{SA}$ by changing the axial stress amplitude in steps. At each step, f was varied in the range of 0.1 to 1.5 Hz in five steps. Fig. 7.11a shows the relationships between E_{eq} and $(\varepsilon_a)_{SA}$, while h~$(\varepsilon_a)_{SA}$ relationships are shown in Fig. 7.11b. Very consistent results, the same as described before, were observed. That is, the E_{eq} value showed little dependency on f, while the damping ratio can be seen to increase slightly with the increase in f (specially when f≥1.0) when $(\varepsilon_a)_{SA}$ was greater than 0.01%.

Subsequently, the same specimen (HOSTN5) was subjected to another series of CP of 40,000 cycles (i.e., in total 65,000 cycles) along the previous CP stress path. E_{eq} and h values were evaluated as before. This time, f was varied in the range of 0.005 to 1.5 Hz in six steps. Figs. 7.12a and b show the E_{eq}~$(\varepsilon_a)_{SA}$ and h~$(\varepsilon_a)_{SA}$ relationships. Identical results can be seen from the point of frequency-dependency of E_{eq} and h.

Apart from the frequency-dependency, the second stage CP application did not bring about noticeable changes in the values of h at a given $(\varepsilon_a)_{SA}$. The E_{eq} value, however, observed to decrease by 4 to 5% at the largest at a given $(\varepsilon_a)_{SA}$, which may be attributable to the effect of 'cyclic prestrain-induced anisotropy' as described in Chapter 6. That is, due to this effect, the stiffness evaluated at axial stress below the peak axial stress during CP can decrease; the degree of decrease is larger as the axial stress level becomes lower.

It was consistently observed that the damping ratio of a prestrained specimen (e.g., HOSTN3) at a relatively larger $(\varepsilon_a)_{SA}$ and a virgin specimen (e.g., HOS12) at even $(\varepsilon_a)_{SA}$≤0.002% increases slightly with the increase in f, especially when f≥1.0 Hz. This finding was not due to any time-lag between the measured axial stress and axial strain. As mentioned earlier, the number of data per cycle at a given stress or strain amplitude that can be recorded with a computer decreases with the increase in f. We recorded 100 to 120 data points per cycle at a lower f (i.e., f≤0.5 Hz), whereas at f= 2.0 Hz, only 20 to 25 data points were recordable for a typical cycle. Since

numerical integration is to be carried out to evaluate h along a closed hysteresis loop of stress-strain response at each cycle (e.g., Fig. 7.1b), naturally a question may arise whether the integration scheme is sensitive to the number of data points per cycle, and if so, it may be more severe for a large stress amplitude load cycle. This point was investigated by considering the axial stress-strain data set of HOSTN5 that had been used to evaluate h and E_{eq} values (i.e., Figs. 7.12a and b) at f= 0.1 Hz as the basic data set. Typically 100 data points per cycle were involved in one cycle at each $(\varepsilon_a)_{SA}$. By using a computer program, a relevant number of data was removed at a regular interval so as to artificially impart the effects (if any) of data points per cycle on the measured h. In that way, additional four sets of data were regenerated, where data points per cycle were varied in a range from 20 to 60. Then by using the same integration scheme, h value for each set of data (including the basic data set) was evaluated. Fig. 7.13 shows the relationships between h and $(\varepsilon_a)_{SA}$. At a given frequency, h is not at all sensitive to the number of data points per cycle at relatively larger stress amplitude, but it may increase slightly with the decrease in the number of data points per cycle at very small $(\varepsilon_a)_{SA}$. Therefore, it can be concluded that the strain rate-dependency of h that was observed at higher frequencies (in Figs. 7.6d, 7.11b and 7.12b) was not due to the difference in the number of data points per cycle used for its evaluation.

The reason for the increase in the h value with the increase in f in physical terms is not understood. This may be explained by a Voigt model, but this model cannot explain the fact that the E_{eq} value was rather insensitive to the changes in f.

7.4. Practical Applications

Firstly we must recognize the limitations of this investigation, in particular, in terms of the range of strain covered (i.e., $(\varepsilon_a)_{SA} \leq 0.04\%$), the soil type being restricted to dry sand, steady state conditions for a certain range stress amplitude and the large number of load cycles applied during CP.

The differences in the response characteristics could be very small between dry and saturated sands for the same strain amplitude and frequency (Wilson, 1985). Tatsuoka and Kohata (1995) showed that the differences in the stiffness values between the drained and undrained states

are merely due to differences in Poisson's ratios. It is likely that the results presented would also be applicable to cases with the presence of pore water in sands under drained condition.

As far as the loading rate-dependency is concerned, the effects of f on E_{eq} can be considered negligible. Due to CP, E_{eq} can changed up to 20% of the value at the virgin state (as described in the previous chapter), which could be either increase or decrease depending on (a) $(\varepsilon_a)_{SA}$ during CP application, (b) $(\varepsilon_a)_{SA}$ at which E_{eq} being measured, and (c) the neutral stress state about which CP was applied symmetrically. Note that in this study, E_{eq} values were obtained by applying cyclic stress symmetrically about the neutral stress state for CP. Damping ratio, on the other hand, decreases always drastically as a result of CP (the previous chapter; Teachavorasinskun, 1992).

The results of this study are applicable to back-analyze the response of ground or soil structures which have been subjected to various types of cyclic loading. Transient loading conditions such as explosions and transient soil states such as cyclic mobility or liquefaction are beyond the scope of this work (specially considering h after CP). Very high frequency (e.g., f=100 Hz) loading that frequently occurs with relatively smaller amplitude tremors during earthquakes are also beyond the scope of this investigation. On the other hand, large stress amplitude earthquake, traffic, machine vibration, wave tend to be in the frequency range of 0.01 to 10 Hz. Structures such as those subjected to traffic loading, those in the zone of high seismicity, offshore gravity type, etc. fall in that category.

7.5. Summaries

(1) Data acquisition systems consisting of various electronic transducers for a pair of corresponding stress and strain must be identical to each other. Otherwise, any difference will be reflected as time-lag in the acquired data, the effects of which will be severe for damping ratio evaluation. For example, damping ratio evaluated with axial strain by gap sensor, which is an inductance type sensor, is found unreliable when used with a strain-gauge type load cell to measure deviator stress, due to the existence of time lag in the data acquisition systems of load cell and gap sensor.

(2) The values of E_{eq} and h were observed to decrease and increase, respectively, with the increase in strain amplitude, as would be expected. The types of cyclic wave-form, triangular or sinusoidal, used during CL to evaluate E_{eq} and h have no influence on the measured values.

(3) The Young's modulus and damping of sand at small strains do not change largely by the change in loading rate except for loading frequency (f) below 0.05 Hz. The viscous effects cannot be totally ignored. In this frequency range (i.e., $f \leq 0.05$ Hz) at a given frequency, damping ratio can be increased manifold and Young's modulus can be decreased by 5 to 10% with the increase in shear stress level.

(4) Before reaching steady state conditions (i.e., at or near virgin state), damping ratio at a given stress amplitude decreases with the number of cyclic loading. The steady state is reached only after a large of cycles of loading.

(5) At steady state conditions and also at the virgin state, E_{eq} is observed independent of f, whereas damping ratio increases slightly with the decrease in f at the virgin state while it increases slightly with the increase in f, especially when $(\varepsilon_a)_{SA}$ is greater than about 0.007% at the steady state conditions.

Table 7.1: List of the specimens with brief description of the tests.

Specimen	$e_{0.8}$	[a] Brief description of tests
HOSTN2	0.70	Pre-sheared at σ_r=0.8 kgf/cm^2; Neutral stress during CL test was at σ_a=σ_r=0.8 kgf/cm^2; $(\varepsilon_a)_{SA}$≈ 0.002%; Wave-form: Sinusoidal and triangular; No cyclic prestraining, Frequency (f) range = 0.03~0.5 Hz.
HOSTN3	0.72	Pre-sheared at σ_r=0.8 kgf/cm^2 (six unload-reload cycles between σ_a= 0.8 to 2.0 kgf/cm^2); Neutral stress during CL tests was at σ_a=σ_r=0.8 kgf/cm^2 ; $(\varepsilon_a)_{SA}$≈ 0.001~0.04%; Sinusoidal wave; f= 0.1~2.0 Hz; Investigation at and before steady state conditions.
HOSTN5	0.81	Evaluation of E_{eq} and h at steady state conditions; Neutral stress at σ_a= 1.4 kgf/cm^2; $(\varepsilon_a)_{SA}$≈ 0.001~0.04%; f= 0.005~1.5 Hz; Sinusoidal wave.
HOS12	0.72	True virgin specimen; Evaluation of E_{eq} and h at various neutral axial stress states at σ_r=0.8 kgf/cm^2; $(\varepsilon_a)_{SA}$≈ 0.0015%; f= 0.01~2 Hz; Sinusoidal wave.

[a]: All tests performed at a constant σ_r (=0.8 kgf/cm^2).

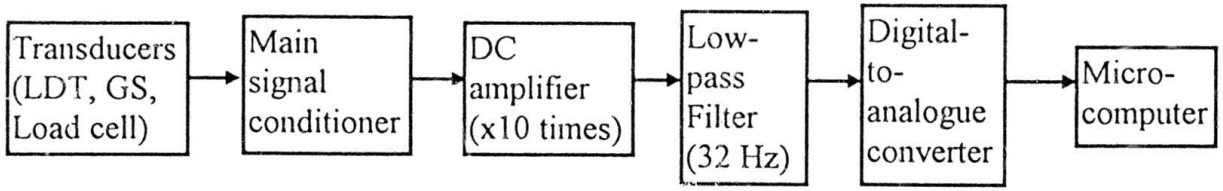

Fig. 7.1: Block diagram of data acquisition system.

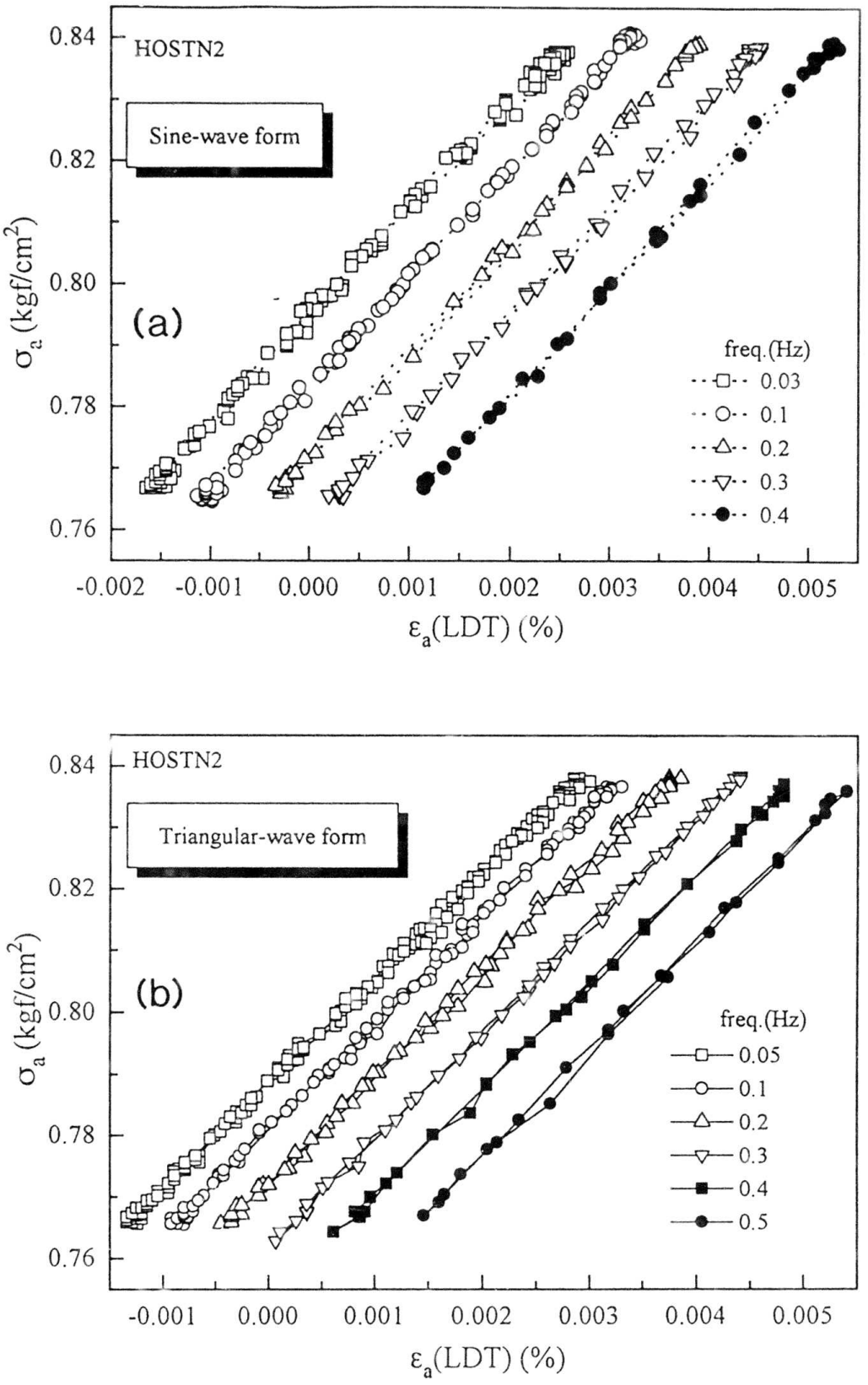

Fig. 7.2: σ_a~ε_a (ε_a measured by LDTs) relations for typical cycles with the use of (a) sine-wave form, (b) triangular wave-form.

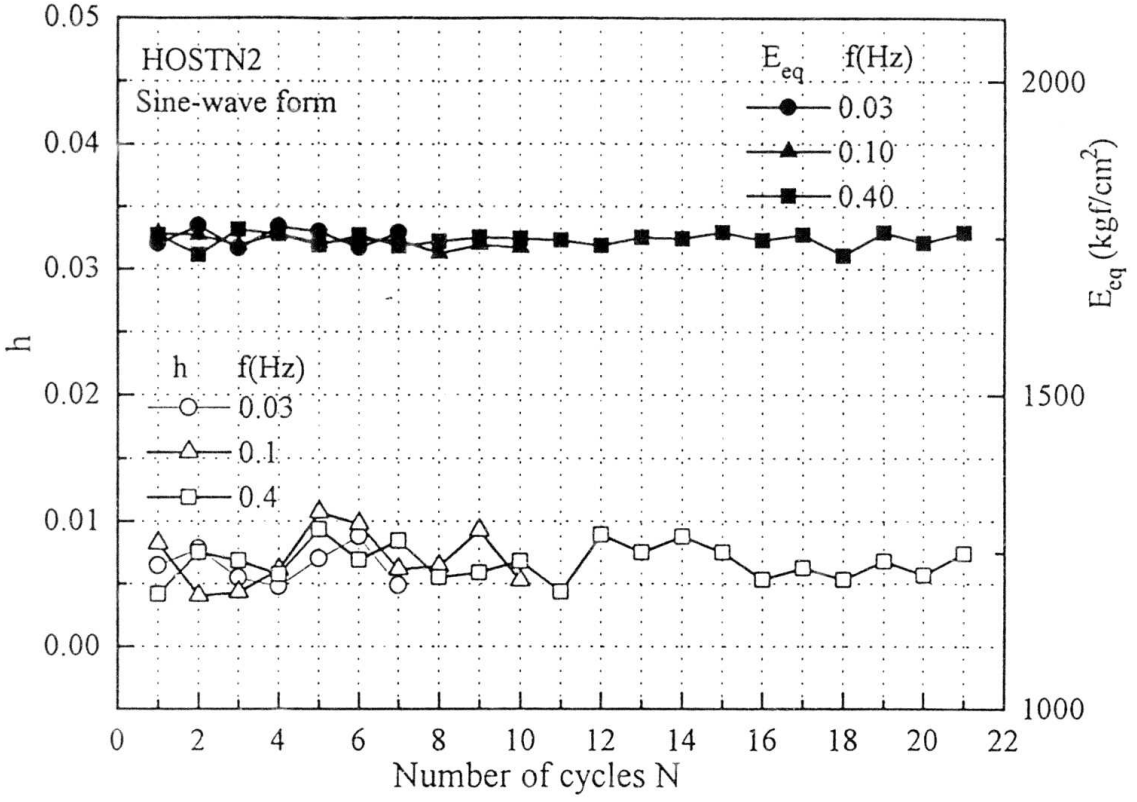

Fig. 7.3: Relations of E_{eq} and h for very small strain (i.e., $(\varepsilon_a)_{SA} \approx 0.002\%$) with the number of load cycles.

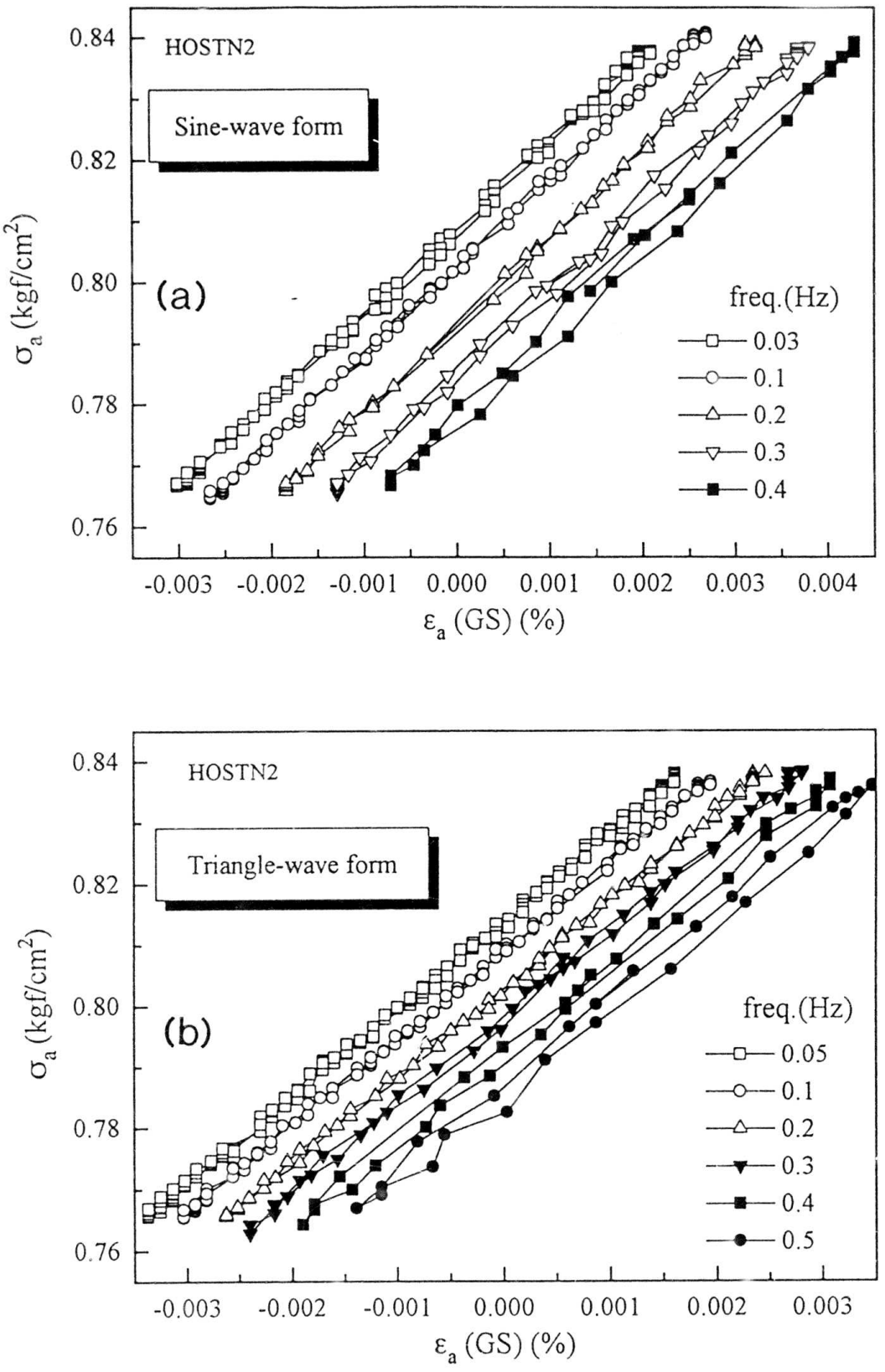

Fig. 7.4: σ_a~ε_a (ε_a measured by GS) relations for typical cycles with the use of (a) sine-wave form, (b) triangular wave-form.

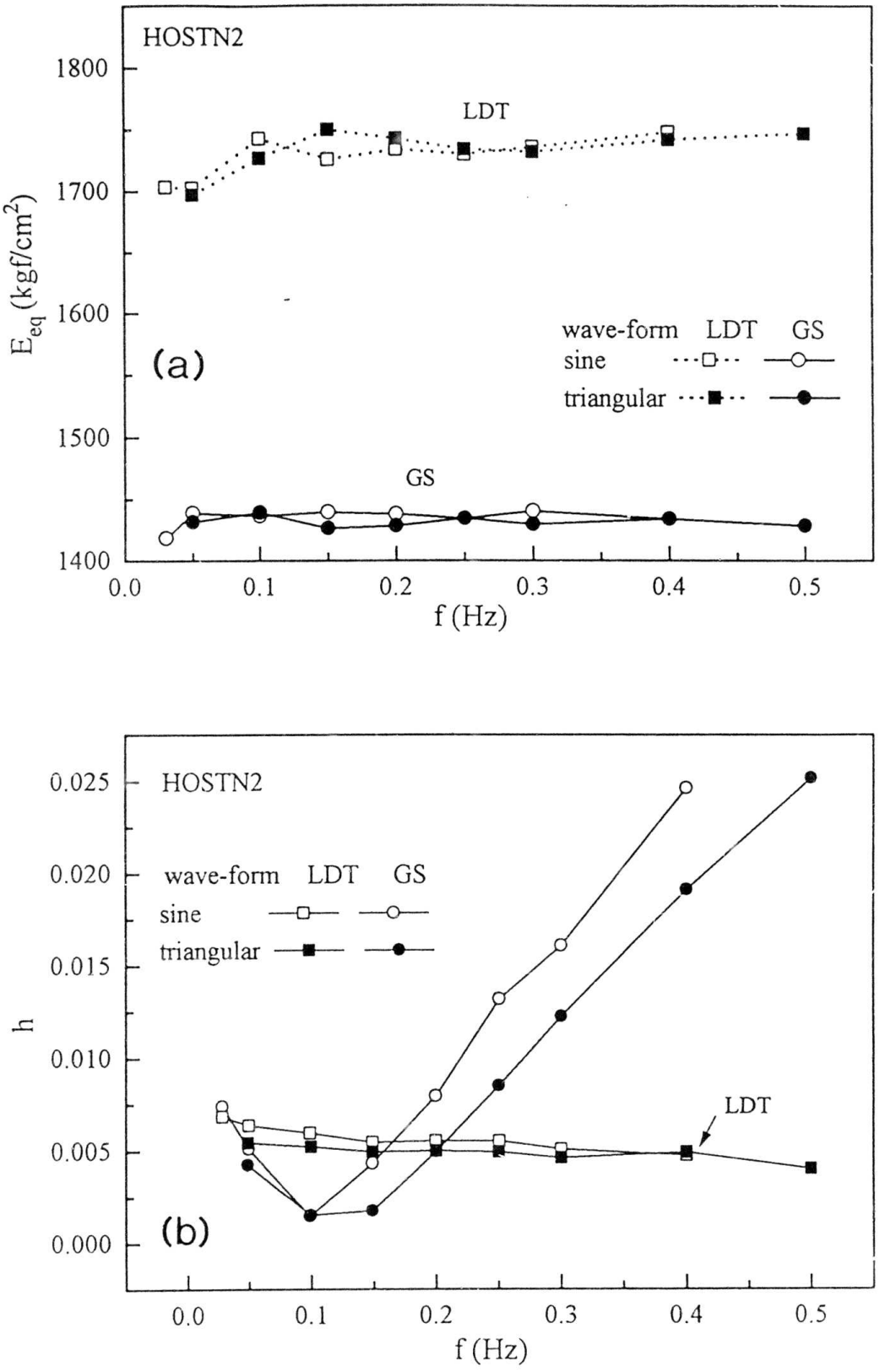

Fig. 7.5: Relationship between (a) E_{eq} and f, (b) h and f at $(\varepsilon_a)_{SA} \simeq 0.002\%$ performed on HOSTN2.

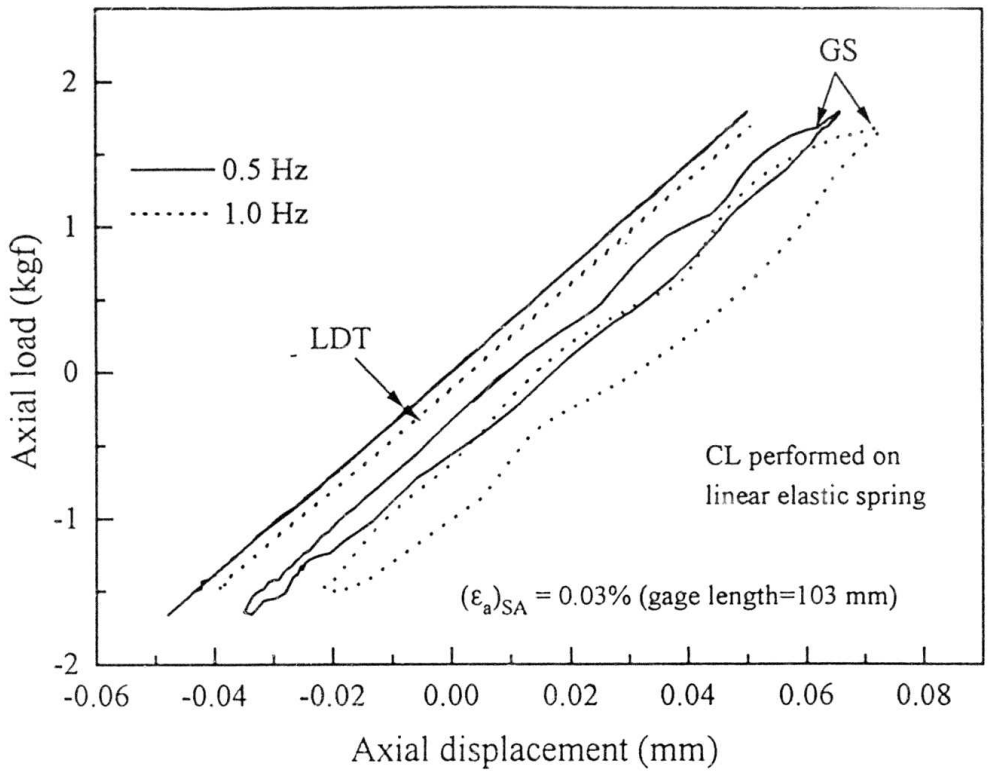

Fig. 7.5c: Typical axial load and axial displacement relationships of elastic spring during CL tests (time-lag concern).

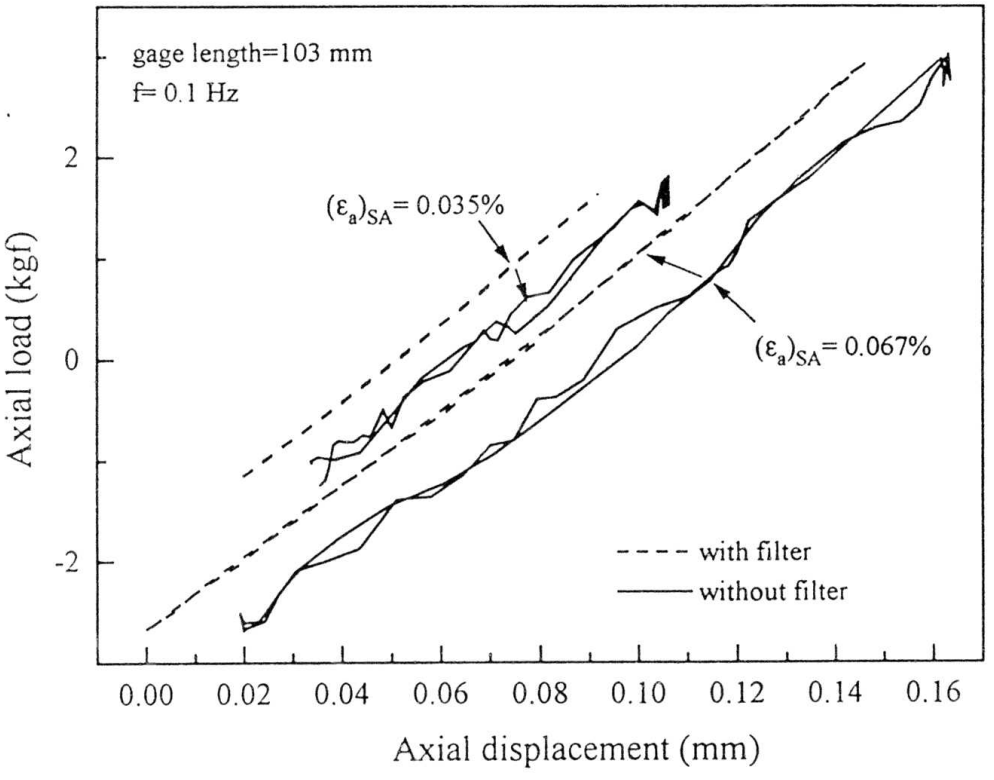

Fig. 7.5d: Typical axial load and displacement relationships of elastic spring during CL tests (filter-concern in the data acquisition system).

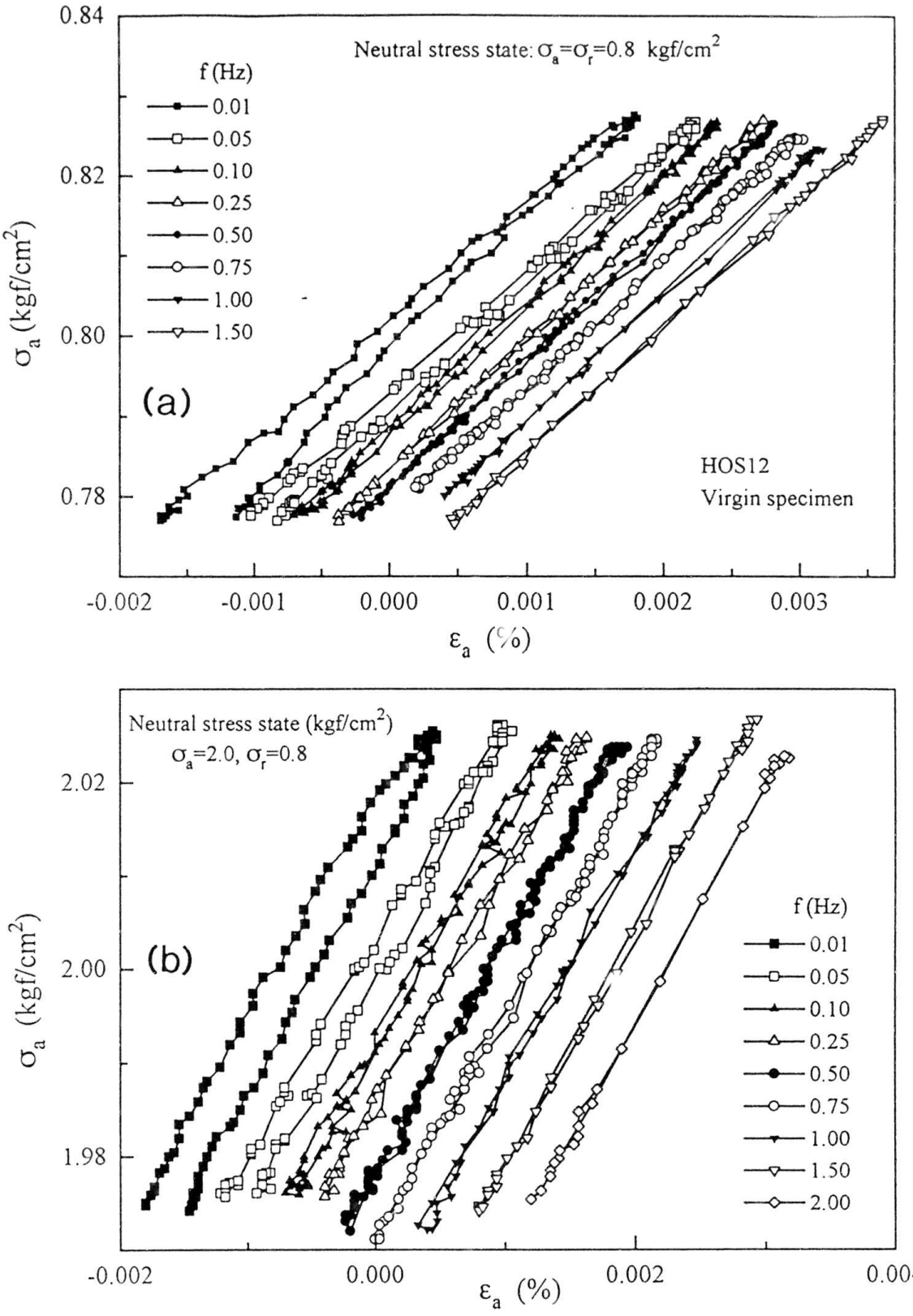

Figs. 7.6: σ_a~ε_a (ε_a measured by LDTs) relations for a typical cycle at each frequency obtained from HOS12 specimen at neutral stress states of (a) $\sigma_a=\sigma_r=0.8$ kgf/cm^2, and (b) $\sigma_a=2.0$ kgf/cm^2, $\sigma_r=0.8$ kgf/cm^2.

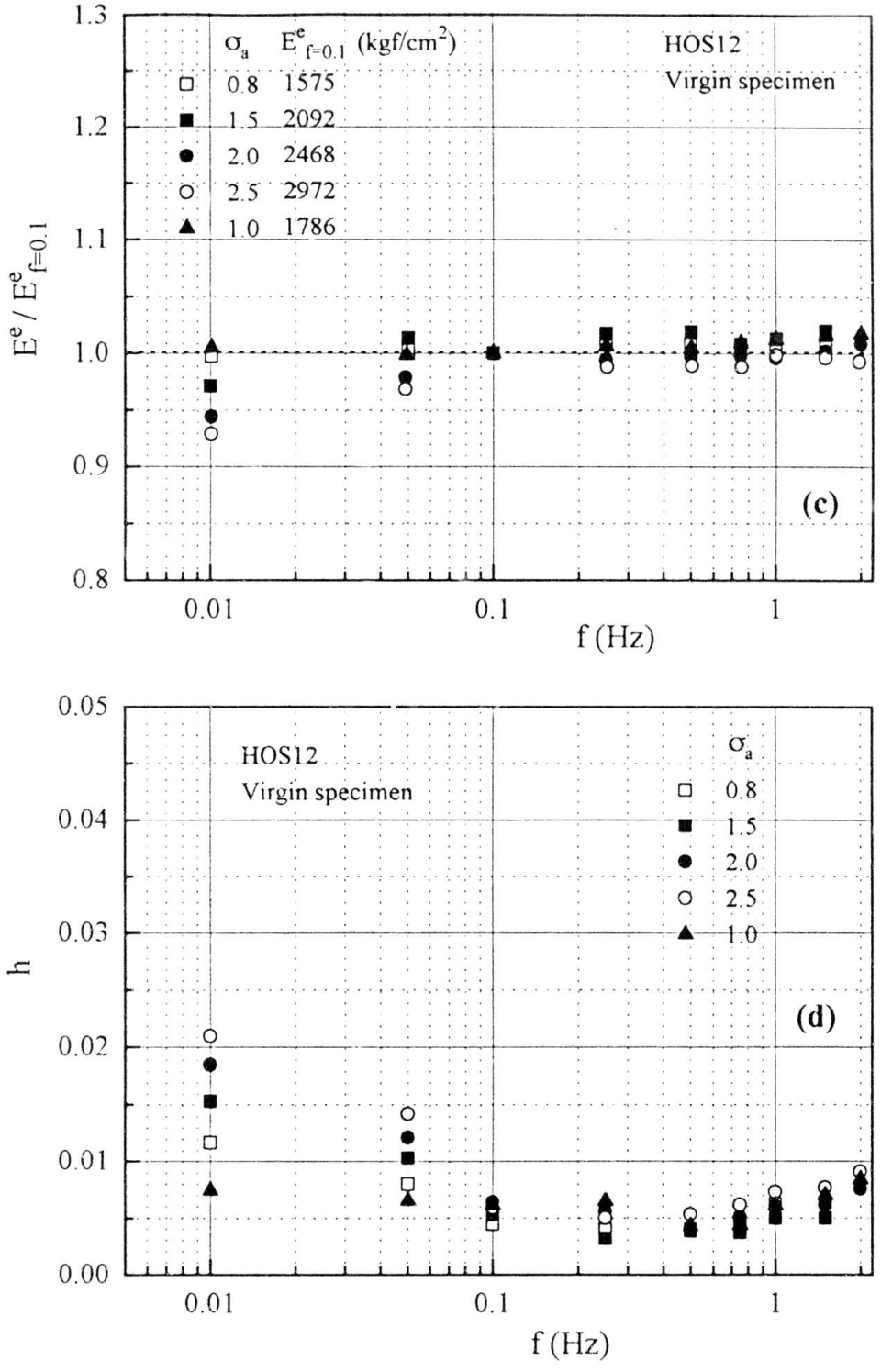

Figs. 7.6: Relationships between (c) $E^e / E^e_{f=0.1}$ and (d) h and f at $(\varepsilon_a)_{SA}$ = 0.0015% performed on HOS12 specimen at diferent neutral axial stress states.

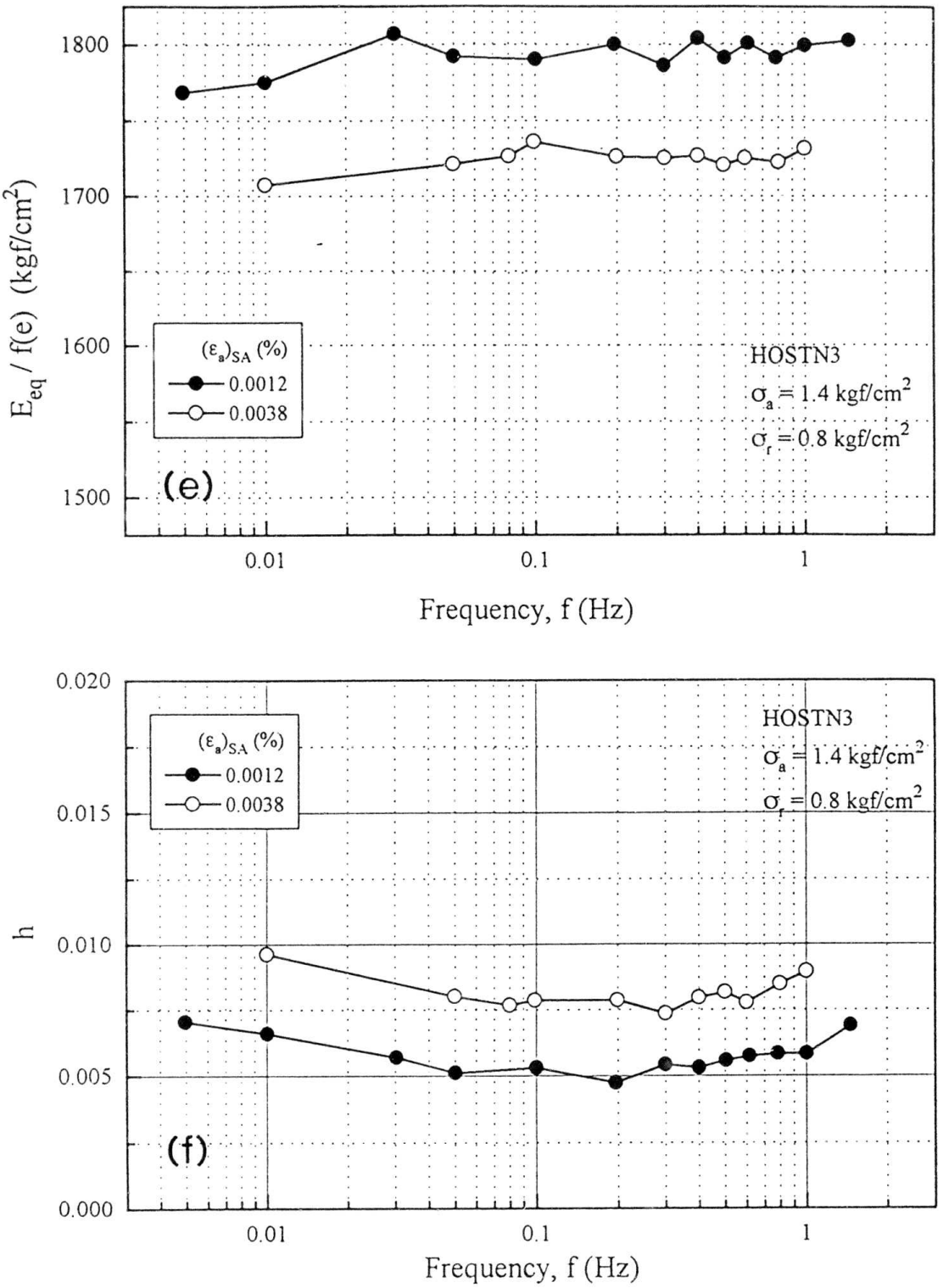

Figs. 7.6: Relationship between (e) E_{eq} /f(e) and f, (f) h and f at $(\varepsilon_a)_{SA}$= 0.0012% and 0.0038% performed on HOSTN3 at a neutral stress state of σ_a=1.4 kgf/cm^2, σ_r=0.8 kgf/cm^2.

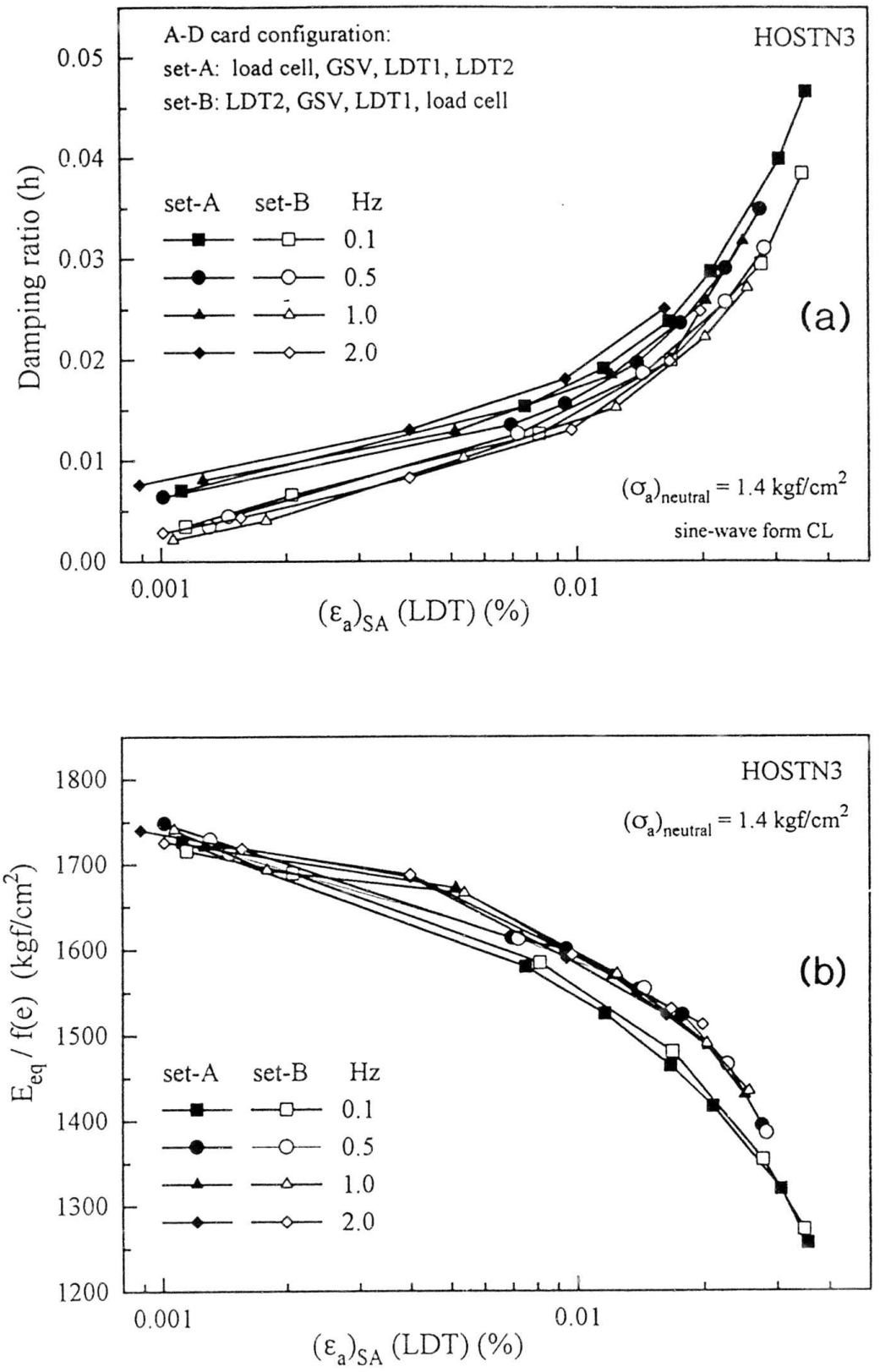

Figs. 7.7: Relationships at near virgin state of HOSTN3 between (a) h and $(\varepsilon_a)_{SA}$, and (b) E_{eq} and $(\varepsilon_a)_{SA}$.

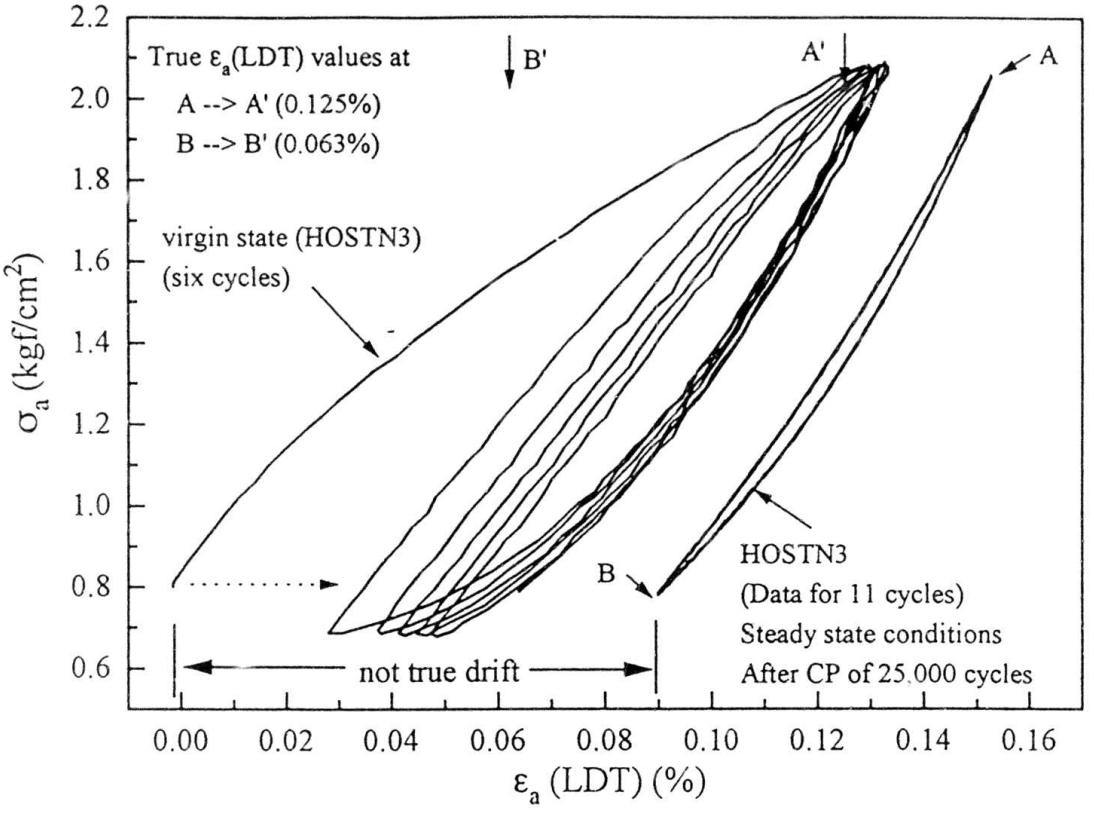

Fig. 7.8: Typical σ_a~ε_a response characteristics during large amplitude axial stress cycles at virgin state and at steady state conditions.

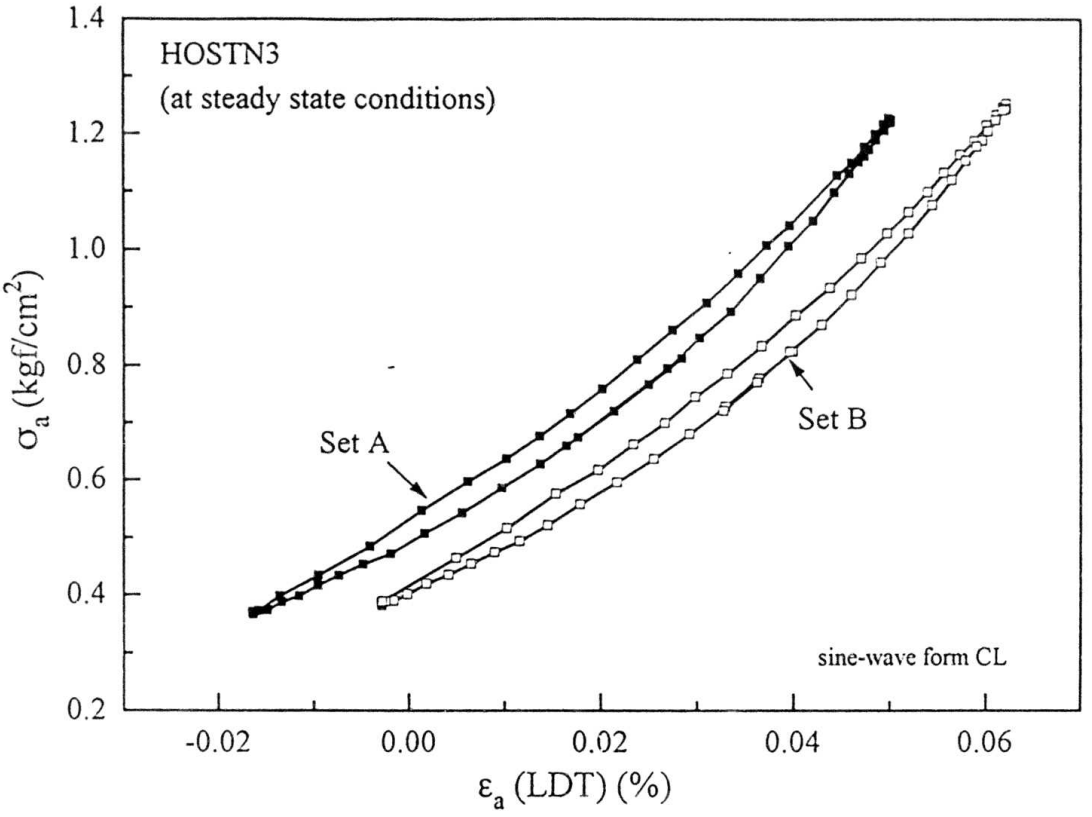

Fig. 7.9: Comparison of σ_a~ε_a responses during large amplitude axial stress cycle between two configurations of arrangement of principal measuring devices at steady state conditions.

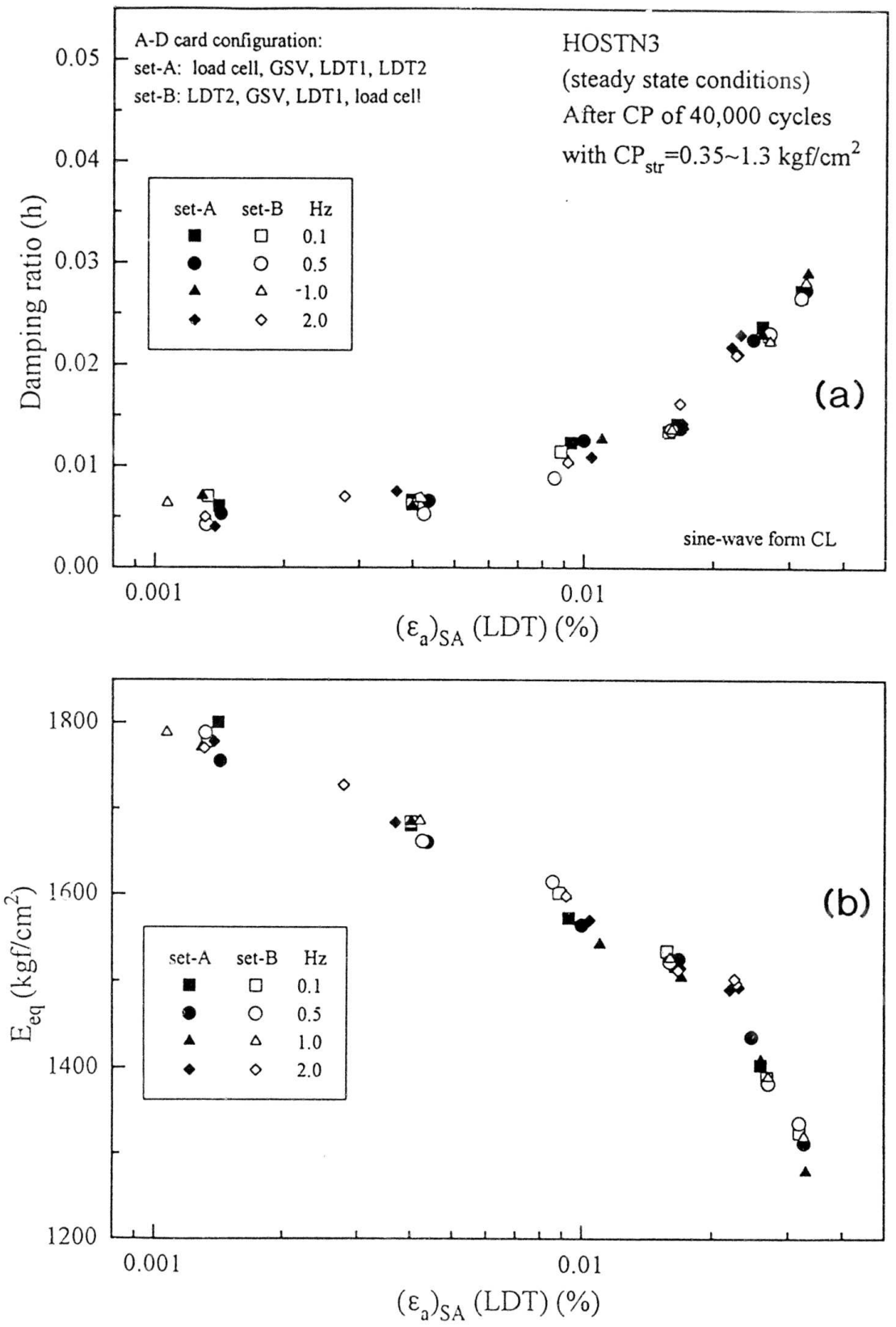

Figs. 7.10: Relationships at steady state conditions of HOSTN3 between (a) h and $(\varepsilon_a)_{SA}$, and (b) E_{eq} and $(\varepsilon_a)_{SA}$.

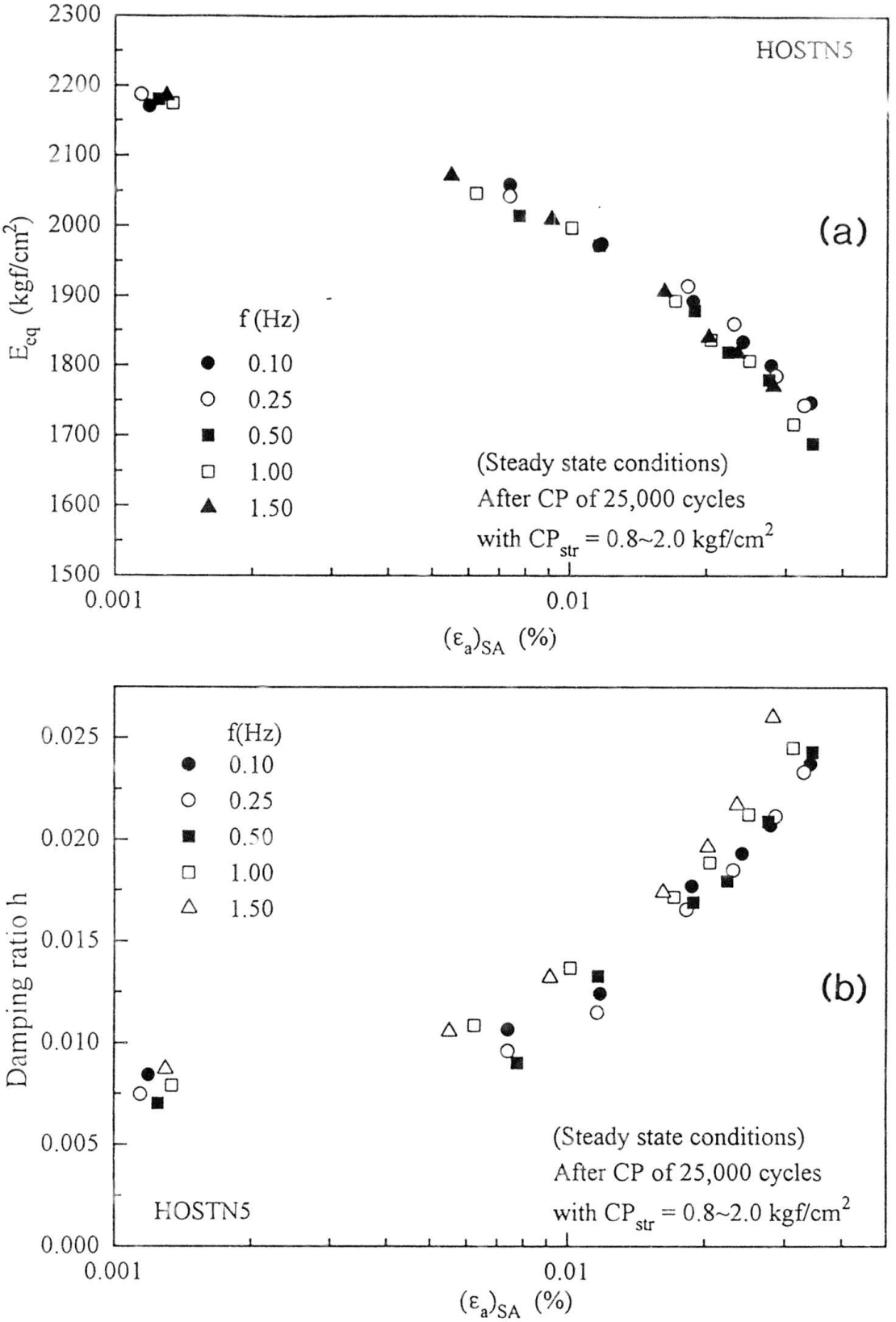

Figs. 7.11: Relationships at steady state conditions (after N=25000 cycles) of HOSTN5 between (a) E_{eq} and $(\varepsilon_a)_{SA}$, and (b) h and $(\varepsilon_a)_{SA}$.

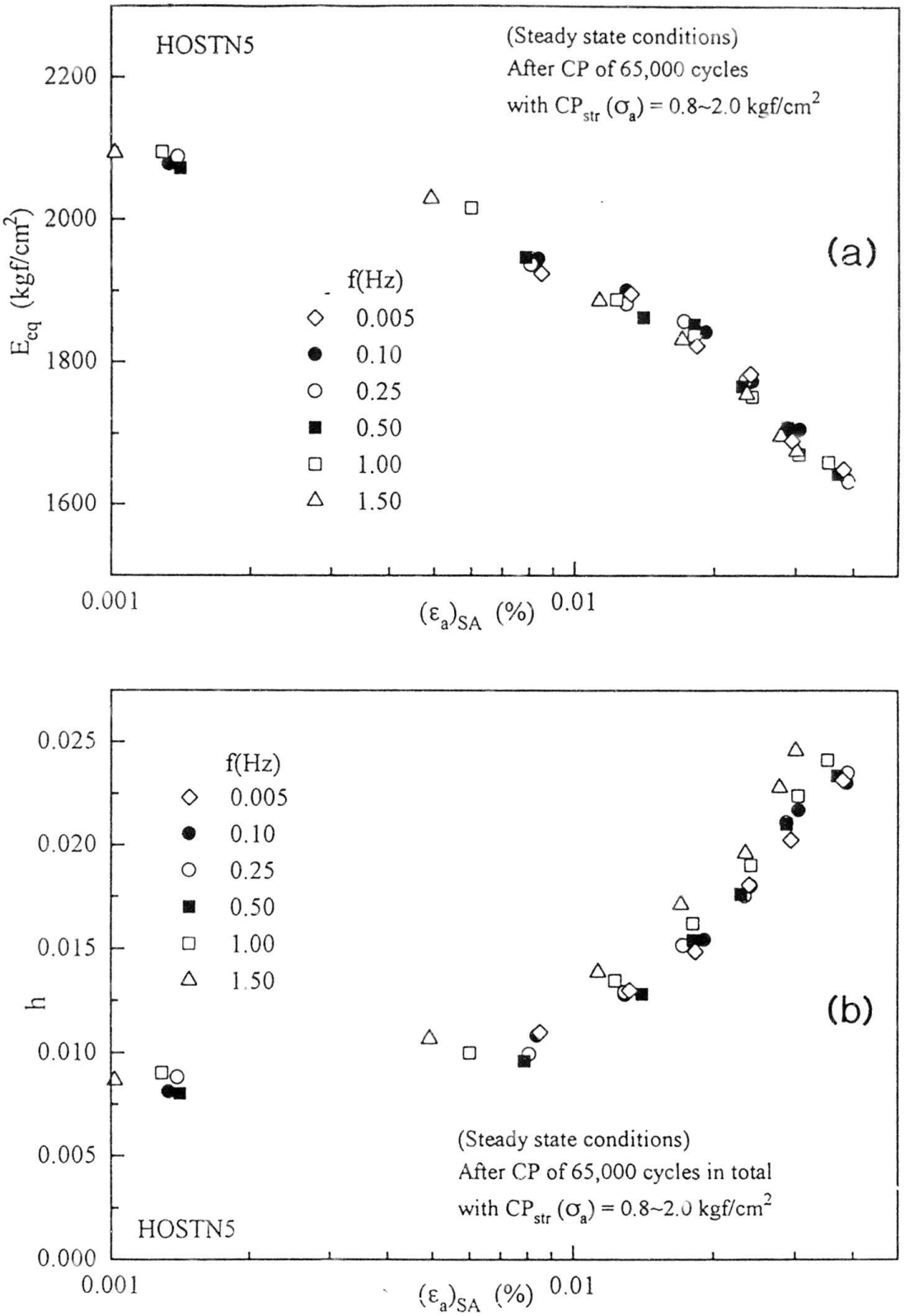

Figs. 7.12: Relationships at steady state conditions (after N=65000 cycles) of HOSTN5 between (a) E_{eq} and $(\varepsilon_a)_{SA}$, and (b) h and $(\varepsilon_a)_{SA}$.

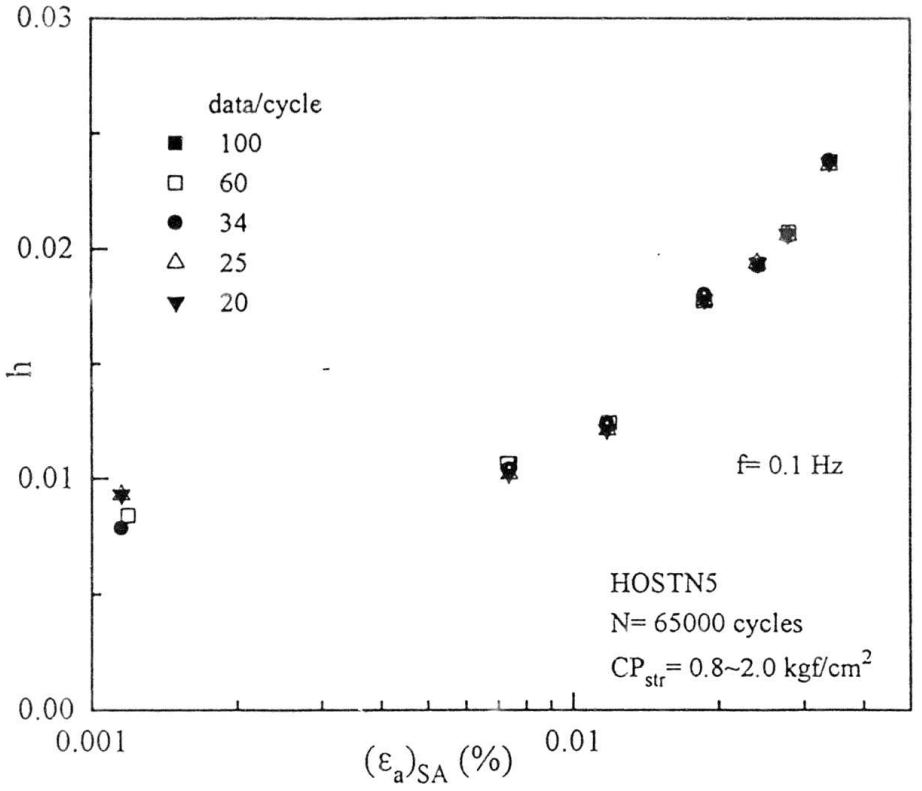

Fig. 7.13: Sensitivity of the number of data points per cycle in the evaluation of h and the resulting relationship between h and $(\varepsilon_a)_{SA}$ at a given frequency.

Chapter 8

Creep behavior of sand in TC test and its effect on the deformation characteristics

8.1. Introduction

A large amount of data presented in Tatsuoka and Shibuya (1992) showed that the deformation of geomaterials measured at strains smaller than about 0.001% in monotonic loading tests is essentially strain rate-independent and recoverable (i.e., elastic), and the initial stiffness values at very small strains determined by static monotonic loading tests are essentially the same with those determined by the corresponding static and dynamic cyclic loading tests. This indicates that a consolidated specimen may exhibit linear elastic deformation at that small strain level, which is independent of the initial stress state; that is, independent of whether the specimen is consolidated isotropically or aniostropically. This feature is best described by a proper kinematic strain hardening model (e.g., Jardine, 1992); i.e., a rather fixed small size of elastic zone always exists around the current stress point on the stress plane and its location is dragged by the current stress point, while the center of the elastic zone is biased towards the direction of the movement of the stress point. From the results of recent static and dynamic works, it can now be understood that the linear elastic range is very small for soft or recent sediments, but may become more significant as a result of compaction, over-consolidation, pre-straining, aging, chemical alteration or diagenesis. The size of the elastic zone increases in clay with the increase in the duration for which the stress state remains at the same point (or with the increase in the creep deformation) (Tatsuoka and Kohata, 1995), and with the increase in the strain rate in the subsequent loading (Mukabi, 1995).

The creep behavior of a granular material, Hostun sand, has been described in this chapter. A particular emphasis is given to investigate the development of elastic deformation properties at various stress states during monotonic loading in TC tests. For that, elastic properties are measured after the creep deformation at a given stress state becoming negligible.

8.2. Test Procedure

Tests were performed on a small cylindrical specimen (D=7.5 cm and H=15 cm) of Hostun sand by using the triaxial testing system described in Chapter 6. Each specimen was reconstituted by the air-pluviation method. Three specimens were tested: two medium-dense specimens, HOSTN2 and HOS12, having a void ratio ($e_{0.8}$) equal to 0.70 and 0.72, respectively, and the other loose specimen (HOSTN4) with $e_{0.8}$=0.882 (the subscript of e indicates the confining pressure in kgf/cm^2 at which the initial void ratio was measured). Each specimen, isotropically consolidated by partial vacuum of $\sigma_a=\sigma_r$=0.8 kgf/cm^2, was subjected to monotonic axial compression by using an automated (i.e., computer-controlled) load-control system. Deviator load (i.e., axial load in excess to that offered by confining pressure) was applied at a constant rate of axial stress equal to 0.125 kgf/cm^2/min by increasing the axial stress in very small steps; the maximum stress level that a specimen experienced in this testing scheme was well below the peak.

Figs. 8.1 to 8.3 show the stress-strain relationships of HOSTN2, HOSTN4 and HOS12, respectively. Of them, Figs. 8.1a, 8.2a and 8.3a show the relationships between the axial stress (σ_a) and the axial strain (ε_a), while Figs. 8.1b, 8.2b and 8.3b show the corresponding relationships between σ_a and radial strain (ε_r). The encircled numbers (e.g., 0, 1, etc.) shown in the figures indicate the stress states at which the specimens were allowed to undergo creep at constant stress state, while the number '0' indicating the initial stress. Each axial stress segment (e.g., stress segment from 0 to 1 or simply 0-1, 1-2, etc. in Fig. 8.1a) generally consisted of the following steps sequentially: (a) shearing up to the next predetermined σ_a level (i.e., loading from '0' to '1', for example); (b) allowing sufficient time to reduce the creep rate to a negligible value, while maintaining the current stress state (i.e., the stress state '1' in the previous example) unchanged within an accuracy of ±0.0025 kgf/cm^2; (c) application of very small-amplitude axial CL to evaluate small strain stiffness; (d) loa to the next predetermined σ_a, and so on.

Besides, a few substeps were included for some specimens in between steps (c) and (d) aforesaid: (i) unloading to a stress state which was always in compression zone (for instance, the segment 2-3 of Fig. 8.1, where σ_a was unloaded from 2 to 3); (ii) allowing creep deformation, if

any, to occur at the over-consolidated stress state after unloading, which hereafter is called delayed rebound, (iii) reloading to a σ_a value, slightly lower than the previously experienced maximum σ_a, with small amplitude axial unload-reload cycles at different stress states (for example, such stress states approximately denoted by 'asteric' symbol along 3-2 segment in Fig. 8.2a). Note that the specimen HOSTN2 (Fig. 8.1a) was not subjected to such small-amplitude unload/reload cycles. Finally, each specimen was sheared to failure from the isotropic stress state $\sigma_a=\sigma_r=0.8$ kgf/cm^2 at a constant rate of axial strain (i.e., 0.14%/min). One virgin specimen (HOSTN7, $e_{0.8}=0.876$) was also sheared to failure at the same loading rate to obtain the reference. Table 8.1 lists some results.

8.3. Test Results and Discussions

8.3.1 Creep Tests and the Deformation Characteristics

Axial strains (ε_a) presented in Figs. 8.1 to 8.3 were those measured by using a pair of LDTs and a gap-sensor (GS). ε_a measured by GS is generally affected by bedding error and system compliances (Tatsuoka and Shibuya, 1992; Tatsuoka and Kohata, 1995), which is clearly reflected in Figs. 8.1a and 8.2a. Hereafter, ε_a measured by LDTs is presented. Radial strains (ε_r) were measured by three pairs of GS.

Fig. 8.4a shows the stress-strains relationships in an enlarged scale for test segments 0-1-2 of Figs. 8.2a and b, and Fig. 8.4b shows the time histories of σ_a, ε_a and ε_r during the same test segments. Similar stress-strain relationships and time histories for test segments 1-2-3-4 of Figs. 8.2a and b are shown in Figs. 8.5a and b, respectively. In the stress-strain relationships shown in Figs. 8.1 to 8.3, the following characteristics can be observed.

(a) Time-dependent deformation (i.e., creep) occurs at a constant virgin stress state along loading (i.e., σ_a increasing) stress path.

(b) Time-dependent deformation also occurs at a constant stress state in an unloading (i.e., σ_a decreasing) stress path, which is also, by definition, creep but which is called here 'delayed

rebound.' It is so named because it is the recovery of strain during unloading that occurred after the completion of unloading.

(c) The sand seems to exhibit elastic behavior at any stress state during monotonic loading after the occurrence of creep deformation at that stress state; the deformation after creep (e.g., loading from point 1 in Fig. 8.1) appears to be similar to that occurs at the initial part of shearing (e.g., shearing from point 0 in Fig. 8.1a).

(d) Over-shooting in the stress-strain relationships (e.g., σ_a versus ε_a and σ_a versus ε_r relationships of Figs. 8.1a and b) during monotonic virgin loading may be observed in some instances during reloading after the occurrence of creep deformation. Here over-shooting means a stiffer response compared to that occurs during monotonic loading (i.e., without allowing creep to occur). In Figs. 8.1a and b, such instances are marked at stress states 1 (to 2) and 2 (to 3), where the corresponding responses without creep are approximated by dotted lines in the respective figures. This behavior (over-shooting) is similar to the results from oedometer tests performed on clay (i.e., e~logp′ relationship, where e is the void ratio at a given effective mean stress p′) (Mukabi, 1995). The reason for this behavior could be attributed to the occurrence of creep deformation that leads to more stabilization of micro-structure by better interlocking. However, the behavior was not always observed within the investigated range of stress state (for example, segments 2-4 in Fig. 8.3a).

Figs. 8.6a to i show the time histories of σ_a, ε_a and ε_r for all creep tests (including delayed rebound) performed on HOSTN4 (Figs. 8.2a and b). The same numerals are used here as in Figs. 8.2a and b for easy identification of each creep test. For example, in Fig. 8.6a, the alphabet 'C' of C1 stands for either creep or delayed rebound test and the numeral '1' stands for the encircled 1 shown in Fig. 8.2a, representing the stress state at which the creep (or delayed rebound) test was performed. The moment when the respective constant σ_a stage (creep test) started is indicated by a horizontal arrow. Similarly, Figs. 8.7a to i show the time histories of σ_a, ε_a and ε_r for all creep tests (including delayed rebound) performed on HOS12 (also see Figs. 8.3a and b), and the corresponding time histories of shear strain γ ($=\varepsilon_a-\varepsilon_r$) and the volumetric strain ε_{vol} ($=\varepsilon_a+2\varepsilon_r$) are

shown in Figs. 8.8a to i. In all the figures, the quantities— elapsed time, σ_a, etc.— are initialized at the beginning of shearing at point 0 of Figs. 8.1 to 8.3. In most of the figures, especially associated with small strain changes such as Figs. 8.6a and 8.7a, time histories of ε_a and ε_r were replaced by average (i.e., smooth) curves. This is because those time histories were perturbed by the bit precision of the analogue-to-digital card, which determines the resolution of the transducers (i.e., LDTS and GS). The following trends can be observed.

(a) Creep rate is quite large at the beginning of each creep stage, gradually decreases with time, and finally dies out.

(b) The creep behavior mentioned above is similar in major and minor principal strains.

(c) With respect to the axial strain ε_a, the direction of creep is always in the direction of the recent deformation. That is, before each creep test, σ_a had been increased and therefore, ε_a (the major principal strain) was compressive during creep. On the other hand, ε_r —the minor principal strain during primary loading in TC— was tensile during creep. However, during creep tests, such as Figs. 8.6a, 8.6b and 8.7a, the creep of ε_r was initially swelling type (i.e., tensile) as would be expected (with the exception of Fig. 8.6a), but after a few minutes the direction changed, and as a result both the increments of ε_a and ε_r occurred in the compressive direction. Fig. 8.6a (for HOSTN4, loose specimen) shows that the creep deformation in ε_r was compressive (i.e., $d\varepsilon_r>0.0$) right from the beginning of the creep test. Because of this behavior, it is obvious that the rate of volumetric creep deformation (ε_{vol}) became gradually larger than that of γ. However, noticeable difference was not observed in the time histories of γ and ε_{vol} as seen from Fig. 8.8a (corresponding to Fig. 8.7a). Rather, they look much more similar than the time histories of ε_a and ε_r. This is due to the relatively small magnitude of ε_r, as seen in Fig. 8.7a, which was only about 10% of ε_a or even less.

(d) The rate of delayed rebound follows the similar behavior as creep does: that is, the rate is initially large, gradually decreases with time, and finally the rate decreases to a negligible value.

However, even at the beginning, the delayed rebound rate is very small compared to that of creep rate at the same stress level.

It has been mentioned that the creep rate is not constant with time. However, for comparison, the average creep rate was estimated based on the total creep deformation that occurred during the first one hour. Fig. 8.9a and b show the relationships of creep rate in axial and radial directions, respectively, with σ_a. The creep rate increases non-linearly with the increase in σ_a; the rate of increase augments with the increase in the axial stress level. At a given stress state, the looser the specimen the larger the creep rate of ε_a. The creep rate of ε_r is insensitive to the void ratio of specimen.

8.3.2. Elastic Deformation Properties

Elastic Young's modulus (E^e) and Poisson's ratio ($\nu=\nu_{vh}$) are evaluated from the responses of very small unload-reload cycles of σ_a at various stress states, which are approximately shown by asteric (*) symbols in Figs. 8.2a and 8.3a. Eleven very small unload-reload cycles were applied at each stress state during overall re-loading (i.e., σ_a increasing) and/or overall re-unloading (i.e., σ_a decreasing) in a given stress segment; this (the application of very small unload/reload cycles during overall reloading and/or overall re-unloading) was done to avoid hampering the rate of creep during primary loading or the rate of delayed rebound during the first overall unloading. Fig. 8.10a shows the relationship between $E^e/f(e)$ and σ_a (i.e., $E^e/f(e)\sim\sigma_a$) of HOSTN4 specimen in full logarithmic scale, while the $\nu\sim\sigma_a/\sigma_r$ relationship is shown in Fig. 8.10b. Similar relationships, i.e., $E^e/f(e)\sim\sigma_a$ and $\nu\sim\sigma_a/\sigma_r$ relations for HOS12 specimen are shown in Figs. 11a and b, respectively. In the figures, the bracketed alphabets in the legend indicate the CL group shown in Figs. 8.2 and 8.3. It can be seen that the elastic Young's modulus can be modeled as a function of σ_a, which was described in Chapters 4 and 6. That is, $E^e= E_1.f(e).\sigma_a^m$, where $E_1=E^e$ at $\sigma_a=1.0$ kgf/cm^2 and $f(e)=1$ (or, $e=0.82$), and the exponent m represents the dependency of E^e on σ_a. The values of E_1 and m, along with the fitted variation (dotted line), are given in the respective figures (i.e., in Figs. 8.10a and 8.11a). On the other hand, the variation of ν can be modeled as a function of stress ratio (σ_a/σ_r), i.e., $\nu= \nu_0.(\sigma_a/\sigma_r)^{m/2}$, where $\nu_0=\nu$ at $\sigma_a/\sigma_r=1.0$ (i.e., at isotropic

stress states). The values of ν_0, E_1 and m are listed in Table 8.1. The way of modeling the elastic parameters is exactly the same that has been described in Chapter 4 and 6. Similar dependency of elastic properties of Hostun sand has been described in Chapter 6. This indicates that preshearing, which is equivalent to over-consolidation in one-dimensional compression, has little effect on the dependency of elastic properties. Note that very small unload-reload cycles were not applied in HOSTN2 specimen.

8.3.3. Existence of Elasticity in any Stress States During Monotonic Loading

The elastic deformation properties always exist at any stress state during monotonic loading. However, it can be observed directly only from the deformation characteristics when the strain level is very small and if the transducers possess sufficient resolutions. At this small strain level, which is usually called the threshold elastic strain, plastic strain component is negligible compared to the elastic component. Beyond this elastic threshold strain, the plastic strain component starts dominating the total strain in a given direction. As the stress level increases and proceeds near failure, the plastic strain component exceeds the elastic component by manifold. This is why, we cannot observe elastic deformation properties directly at any shear stress level except at the beginning of shearing during monotonic loading.

Jardine et al. (1991) shows the existence of elastic zone at any stress state of clay specimens which has experienced creep deformation at that stress-state. On the other hand, the initial stiffness of a consolidated (both isotropic and anisotropic) specimen of granular materials during shearing is found to be similar to the elastic Young's modulus evaluated by static or dynamic cyclic test at the same stress level under otherwise similar conditions (Tatsuoka and Kohata, 1995). This indicates that elastic deformation characteristics can appear at any stress state of granular materials after some creep deformation. That is, after the creep rate reduces to a negligible magnitude at a given stress level, the deformation characteristics after the start of reloading from that stress level may become similar to that of the initial deformation properties.

To investigate whether the deformation during reloading after creep is elastic, the secant Young's modulus (E_{sec}) was evaluated for each reloading test segment (Type 1) (e.g., segment 1-2 of Fig. 8.1a) after initializing σ_a and ε_a at the beginning of each reloading segment. Then, the value of E_{sec} was normalized by the maximum value of E_{sec} (i.e., $(E_{sec})_{max}$) of that segment. The values of $(E_{sec})_{max}$ and the corresponding ν_{sec} values are plotted in Figs. 8.10 and 8.11 with 'x' symbols. Figs. 8.12a, 8.12b and 8.12c show the relationships between E_{sec} / $(E_{sec})_{max}$ and ε_a for HOS12, HOSTN2, and HOSTN4, respectively. Similar analysis was made for the stress-strain curves after overall unloading followed by overall reloading (Type 2 segment) (e.g., segment 2-4 for HOS12). The results are shown in another set of figures (i.e., Figs. 8.13a to d). The relationships obtained from the initial segment (i.e., segment 0-1 of Figs. 8.1 to 8.3) of each specimen were also plotted in the respective figures for comparison. Fig. 8.12d also shows typical relationships between 'normalized' tangent modulus and ε_a for the different segments of HOSTN4 shown in Fig. 8.12c. Tangent modulus (E_{tan}) of a given stress segment was normalized by dividing it with the maximum tangent modulus ($(E_{tan})_{max}$) of that segment.

Figs. 8.10 and 8.11 show that the initial deformation properties at the start of reloading after each creep test are very similar to elastic properties (this is the case for the segments 1-2, 4-5 and 7-8 for HOS12). This point can also be seen from Table 8.2, where E^e, $(E_{eq})_{max}$ and $(E_{tan})_{max}$ values at different stress states are listed. Figs. 8.12a to d also show that the range of elastic deformation characteristics is noticeable in all the investigated segments at least for ε_a=0.001%. Beyond this elastic strain range, the plastic strain component develops at a faster rate as the stress segment (segment 4-5 of Fig. 8.1a, for example) moves farther from the initial consolidated stress state (i.e., from 0). Therefore, after ε_a exceeds the elastic strain range (i.e., $\varepsilon_a \leq 0.001\%$), the decay curve (i..e., normalized E_{sec}~ε_a curve) of segments such as 1-2, 4-5, 7-8, etc. should go below the corresponding relationship for the initial segment (i.e., segment 0-1) of the respective specimen.

In the other cases with overall unloading and reloading in advance, however, this did not happen (for example, segment 2-4 of Figs. 8.13). Because in this case, the particular segment (e.g., segment 2-4) was the continuation of the overall unloading and reloading part of previous segment (i.e., segments 2-3 and 3-2), and therefore, the initial part of segment 2-4 already

included plastic strain component. As a result, the $(E_{sec})_{max}$ value measured at point 2 was much lower than the elastic Young's modulus as can be seen from Table 8.2. The list (i.e., Table 8.2) also shows that $(E_{sec})_{max}$ and $(E_{tan})_{max}$ values evaluated at a given stress state are essentially the same with the elastic Young's modulus E^e (defined for the elastic axial strain) except for those evaluated at stress states, such as '2' of Fig. 8.2a and 8.3a because of the reason described above.

8.3.4. Stress-Dilatancy Relationship

Figs. 8.14a, b and c show the stress-dilatancy relationships of HOS12, HOSTN4, and HOSTN2 specimens, respectively. In these figures, the stress ratio R ($=\sigma_a/\sigma_r$) is plotted against the dilatancy rate D, where D is defined as the ratio of major-to-minor principal plastic strain increments. That is, $D= -2d\varepsilon_r^p / d\varepsilon_a^p$ for loading (i.e., σ_a increasing at constant σ_r), and for unloading (i.e., σ_a decreasing at constant σ_r) $D= - d\varepsilon_a^p / (2d\varepsilon_r^p)$, where $d\varepsilon_a^p$ and $d\varepsilon_r^p$ are the plastic strain increments in axial and radial directions, respectively. The elastic strain increments ($d\varepsilon_a^e$, $d\varepsilon_r^e$) are subtracted from the total strain increments (i.e., $d\varepsilon_a$, $d\varepsilon_r$ in Figs. 8.1 to 8.3) to obtain the plastic strain increments (i.e., $d\varepsilon_a^p$, $d\varepsilon_r^p$). For that purpose, $d\varepsilon_a^e$ and $d\varepsilon_r^e$ were evaluated as $d\varepsilon_a^e= d\sigma_a/E^e$ and $d\varepsilon_r^e= - \nu.d\varepsilon_a^e= -\nu.d\sigma_a/E^e$, respectively. In so doing, the stress-dependency of elastic Young's modulus [that is, $E^e= E_1.f(e).\sigma_a^m$] and the stress ratio-dependency of ν [i.e., $\nu= \nu_0.(\sigma_a/\sigma_r)^{m/2}$] described earlier were considered. The elastic parameters E_1, ν_0, and m listed in Table 8.1 were used for the evaluation. For specimens HOSTN4 and HOS12, these parameters are the measured values (see Figs. 8.10 and 8.11). But for HOSTN2, the exponent m is an assumed value, while E_1 and ν_0 are based on the assumed m and a single pair of E^e and ν values measured at a stress state $\sigma_a=\sigma_r=0.8$ kgf/cm^2 after performing all the tests shown in Fig. 8.1a.

In the figures, for each specimen, the stress-dilatancy relationships are plotted for deformations during: i) virgin (primary) loading from the initial stress point 0 to the maximum σ_a shown in Figs. 8.1 to 8.3; ii) unloading along a typical stress segment (for instance, segment 8-9 of Fig. 8.1a of HOS12); iii) creep tests using loading criteria of D (i.e., $D= -2d\varepsilon_r^p / d\varepsilon_a^p$); and iv) delayed rebound tests using the unloading criteria of D [i.e., $D= -d\varepsilon_a^p / (2d\varepsilon_r^p)$]. During a creep test and a delayed rebound test, it was reasonably assumed that the deformations were fully plastic

(i.e., no elastic strain components). A few deviating data points, which are perhaps owing to lack of reliability, at the start of loading and/or at the start of unloading were discarded; particularly at the start of unloading, the deformation is nearly elastic for relatively a large stress increment, and therefore, the dilatancy data at that stress range is totally unreliable because of the very small values of plastic strain components. From the Figs. 8.14a to c, the following trends can be observed:

(a) For the primary loading, the stress-dilatancy relationship (i.e., R~D) is more-or-less linear for the investigated stress range. That is, Rowe's (1962) stress-dilatancy relation, R= K.D, is valid for Hostun sand specimens with K= 2.6, 2.68 and 3.2 for HOS12, HOSTN2 and HOSTN4, respectively. This indicates that the looser the specimen the higher the value of K. For a given R, the loose specimen is more contractant (i e., small D) than the denser one.

The value of K depends on the kinematics of particle movement as the soil deforms. K= W_i/W_o, where W_i ($=\sigma_a.d\varepsilon_a^p$ for loading in triaxial test) is the plastic work produced by the major principal stress and W_o ($=-2\sigma_r.d\varepsilon_r^p$ for loading in triaxial test) is the output plastic work against minor and intermediate principal stresses. Therefore, the value of energy ratio, K, depends on the percentage of W_i that is dissipated. For energy dissipated by sliding at particle contacts, the value of K depends on the average orientation of sliding contacts, with respect to the principal stress directions, and on the mineral friction angle. When deformation takes place in the way that dissipates the smallest percentage of W_i, the stress-dilatancy coefficient K has its minimum value. The value of K is larger when the shear deformation becomes large, and is the maximum when the material ceases to change volume as it deforms, which is called the critical state. This discussion infers that the value of K is likely to be larger for a looser specimen.

(b) The stress-dilatancy relationship during creep is nearly the same as that for virgin loading. However, some exception can be observed at low stress level, especially in the case of HOSTN4 specimen. Here, the material exhibits relatively larger contractancy (i.e., small D). This behavior (i.e., large contractant at low stress level of loose specimen) is due to the fact that $d\varepsilon_r$ was positive (compressive) during creep at the same stress level (see Figs. 8.6a, b and 8.7a).

(c) During reloading (Fig. 8.14a and b), the deformation, at a given R, becomes more dilatant (i.e., larger D) than that for virgin loading, while the slope K remains more-or-less the similar to that for virgin loading (except the initial points in Fig. 8.14a). However, as R approaches the previous maximum value after which the stess state is virgin, the value of D decreases, and eventually meets the value for virgin loading.

(d) It should be mentioned that the stress-dilatancy relationships for unloading (and for deformations during delayed rebound) in Figs. 8.14a and b are not plotted directly in a comparable form to that of loading (n.b., the creep deformation was also categorized as loading). That is, for unloading, the stress-ratio should be plotted in the inverse way (i..e., 1/R~D). However, it can be easily seen that in such a case all the data points for unloading would fall well below and right to the extended dotted line (up to R=0.4) that assumes the R~D relationship of virgin loading linearly. This indicates that during unloading the deformation is more dilative (i.e., the larger D) than that occur at a given R during loading.

8.3.5. Monotonic TC tests to failure

TC tests to failure were carried out at $\sigma_a=\sigma_r=0.8$ kgf/cm^2 on specimens HOSTN4 and HOSTN2 after the completion of tests shown in Figs. 8.1 and 8.2. For comparison, another TC test was performed under similar conditions on a virgin loose specimen, HOSTN7. Besides, the result of a prestrained specimen HOSTN3 (described earlier in Chapter 6) will be compared. Table 8.3 lists some of the results of each specimen. Fig. 8.15a shows the relationship between the deviator stress q ($=\sigma_a-\sigma_r$) and ε_a (measured by LDTs), and Fig 8.15b shows the relationship between volumetric strain ε_{vol} ($=\varepsilon_a+2.\varepsilon_r$) and ε_a. In the figures, the accumulated strains at the beginning of shearing for all specimens have been trimmed. Like prestrained specimens (described in Chapter 6), specimens HOSTN2 and HOSTN4 were not virgin, rather they have experienced creep deformation at stress levels below the peak, q_{max}. Even though the maximum friction angle (ϕ_{max}) is not affected by this creep deformation (Table 8.3); That is, HOSTN4 exhibited q_{max} value that was similar to that of the virgin specimen HOSTN7 although ε_a of the latter at q_{max} was about

twofold larger than that occurred for specimen HOSTN4. On the other hand, dense specimens HOSTN2 and HOSTN3 having similar void ratios also showed similar peak values. With respect to the volume change characteristics, HOSTN4 became more dilatant than HOSTN7 (Fig. 8.15b) because of the effects of previous stress-histories. Despite substantial difference in void ratios, HOSTN4 and HOSTN2 showed similar volumetric changes during shearing. Having similar void ratio, a prestrained specimen (HOSTN3) exhibits much more dilatant behavior than HOSTN2 which experienced creep deformation. Figs. 8.16a, b and c show the relationships between q and ε_a at small strain levels up to ε_a= 1.0%, 0.1% and 0.005%, respectively. The q~ε_a relationship of prestrained specimen became concave upward at lower strain level due to dominant elastic deformation (Chapter 6). The deformation characteristic of specimens HOSTN2 and HOSTN4 at the same strain levels are similar (i.e., concave downward) to that of a virgin one (HOSTN7). However, previous stress-histories increased the range of linearity in stress-strain relationship compared to that of virgin specimen HOSTN7 (Fig. 8.16c) at a very small strain level.

The secant modulus (E_{sec}) and tangent modulus (E_{tan}) were evaluated for each of the specimens, and were normalized by the corresponding maximum values, i.e., by $(E_{sec})_{max}$ and $(E_{tan})_{max}$, respectively, that occurred at very small strain level. Figs. 8.17a and b show the relationships between the normalized E_{sec} and ε_a, respectively, for the measured full range of ε_a and ε_a=0.5%. Fig. 8.17c shows the relationships between normalized E_{sec} and q/q_{max}. On the other hand, Figs. 18a and b show the relationships between the normalized E_{tan} and ε_a, and q/q_{max}, respectively. Figs. 17 and 18 show that both CP and previous stress-histories (or creep deformation and overall unloading) increased Young's moduli substantially at intermediate stress as well as strain levels although initial stiffness (or elastic Young's modulus E^e) remains unchanged during previous stress-histories (Figs. 8.10a and 8.11a). Teachavorasinskun (1992) observed similar behavior in case of prestrained specimens of granular materials. However, it has been shown in the previous chapter that E^e and hence the initial stiffnesses can be affected by CP. The Young's moduli E^e, $(E_{tan})_{max}$ and $(E_{sec})_{max}$ at $\sigma_a=\sigma_r$=0.8 kgf/cm^2 for each specimen are shown in Table 8.3. The E^e values evaluated by small amplitude axial stress cycle right before TC tests are also listed for comparison. For a given specimen, the three moduli are reasonably similar.

Figs. 8.19a and b show the relationships between E_{tan}/E^e and q/q_{max} corresponding to Fig. 8.18b, where $E^e = E_1.f(e).\sigma_a^m$. Here the respective current E_1 and m values are used, which were obtained immediately before sheaing to failure of each specimen. That is, for HOSTN2 and HOSTN4, E_1 and m values of Table 8.1 were used; for HOSTN3, the values obtained after CP application (listed in Table 6.3, Chapter 6) were used; for HOSTN7, m=0.47 was an assumed value, while E_1 was based on a single measured value of E^e at $\sigma_a=\sigma_r=0.8$ kgf/cm^2. The damage to E^e (Chapter 5) as the stress level approaches near peak was neglected. In all cases, E_{tan}/E^e decreases monotonically with the increase in q/q_{max}, while the pattern of decrease depends on stress-strain histories.

8.4. Summaries

(1) For sand, deformation for a given span of time at a constant stress state, known as creep, is observed to increase with the increase in the shear stress level during monotonic loading. In such a case, rate of creep in the major principal strain is larger for a loose specimen, whereas creep rate in the minor principal strain was observed similar irrespective of void ratio. Direction of creep is always in the direction of the principal strains that occurred during the recently experienced loading.

(2) Similar time-dependent deformations occur at a constant stress state also during unloading (i.e., on an unloaded stress state), which is termed as delayed rebound. However, at a given stress state, the rate of creep during primary loading is much more higher than the rate of delayed rebound.

(3) Creep deformation follows Rowe's stress-dilatancy relationship (i.e., R= K.D.), which is observed during virgin (primary) loading. During unloading (i.e., σ_a decreasing at constant σ_r), material becomes more dilative (i.e., large D) at a given R. Therefore, the stress-dilatancy relationships during loading and unloading are not identical. Dilatancy rate during delayed rebound is more-or-less similar to that occur during unloading at the same stress state.

(4) Elastic deformation properties for granular material is observed to exist at any stress state during monotonic loading. It can be observed at any stress state only after the plastic deformation components (related to creep) are allowed to cease. In conventional TC tests, such deformation properties are masked into relatively very large increments of plastic deformations. This finding explains why the initial stiffness of an isotropically and an anisotropically consolidated specimen during monotonic TC test is similar to that obtained under otherwise similar conditions by small amplitude cyclic loading test.

(5) Elastic deformation properties measured during monotonic loading, unloading, reloading and re-unloading stress paths follow reasonably the same rules about their dependency as that observed in the previous chapters; that is, vertical Young's modulus is a function of axial stress only and the Poisson's ratio ν ($=\nu_{vh}$) is a function of stress ratio ($=\sigma_a/\sigma_r$). Overall unloading and reloading and the previous stress-histories have little affect on E^e and ν.

(6) The elastic Young's modulus (E^e), initial secant modulus (E_{sec}) and the initial tangent modulus (E_{tan}) during monotonic TC tests are essentially similar. As would be expected, the peak strength (i.e., ϕ_{max}) is larger for a denser specimen, is observed unaffected by the previous stress-histories. However as a result of previous stress-histories, the tangent stiffnesses at an intermediate stress (or strain) level are observed to increase substantially.

Table 8.1: List of the elastic parameters.

Specimen	$e_{0.8}$	E_1 (kgf/cm^2)	m	ν_0
HOSTN2	0.70	1920	0.47	0.17
HOSTN4	0.88	1890	0.47	0.23
HOS12	0.72	1800	0.48	0.14

Table 8.2: List of the measured Young's moduli at different stress segments.

Specimen	Stress segments (ref. Figs. 1 to 3)	σ_a at the start of shearing (kgf/cm^2)	E^e (kgf/cm^2)	$(E_{sec})_{max}$ (kgf/cm^2)	$(E_{tan})_{max}$ (kgf/cm^2)
HOSTN2	0 to 1 (0-1)	0.80	1740	1755	1725
	1-2	1.50	2320	2185	2290
	[a]2-4	2.45	2925	1170	1210
HOSTN4	0-1	0.80	1500	1490	1505
	1-2	1.20	1820	1850	1810
	[a]2-4	1.50	2025	870	885
HOS12	0-1	0.80	1980	2080	2010
	1-2	1.20	2400	2320	2460
	[a]2-4	1.50	2670	2200	2190
	4-5	1.75	2880	2745	2770
	[a]5-7	2.00	3070	2990	3030
	7-8	2.25	3250	3205	3270

[a]: Reloading of stress segment 2-4 (for example) did not necessarily start from stress point '2' (Fig. 8.1 a, for example), rather it indicates that it started from any point in between the stress points '2' and '3' for 2-4 segment, or '5' to '6' for segment 5-7, but neither from '2' (for 2-4 segment) nor from '5' (for 5-7 segment).

Table 8.3: List of some results during monotonic TC tests.

Specimen	$e_{0.8}$	ϕ_{max} (degree)	E^e (kgf/cm^2)	$(E_{sec})_{max}$ (kgf/cm^2)	$(E_{tan})_{max}$ (kgf/cm^2)
HOSTN2	0.701	42.8	1720	1630	1685
HOSTN3	0.720	43.0	1610	1595	1585
HOSTN4	0.882	36.0	1515	1495	1525
HOSTN7	0.878	36.6	1480	1495	1505

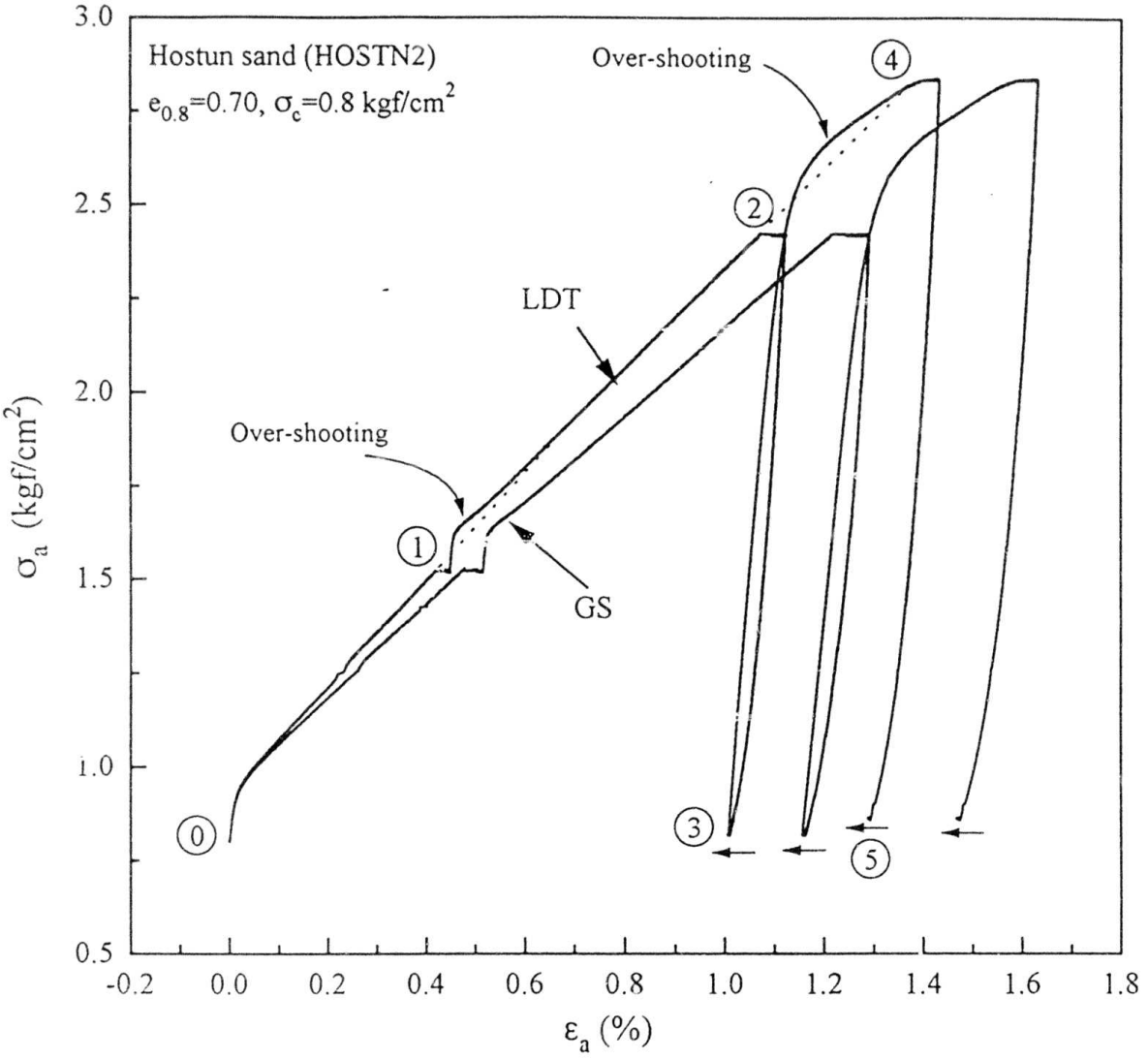

Fig. 8.1a: Relationships between σ_a and ε_a during creep tests performed on HOSTN2 specimen.

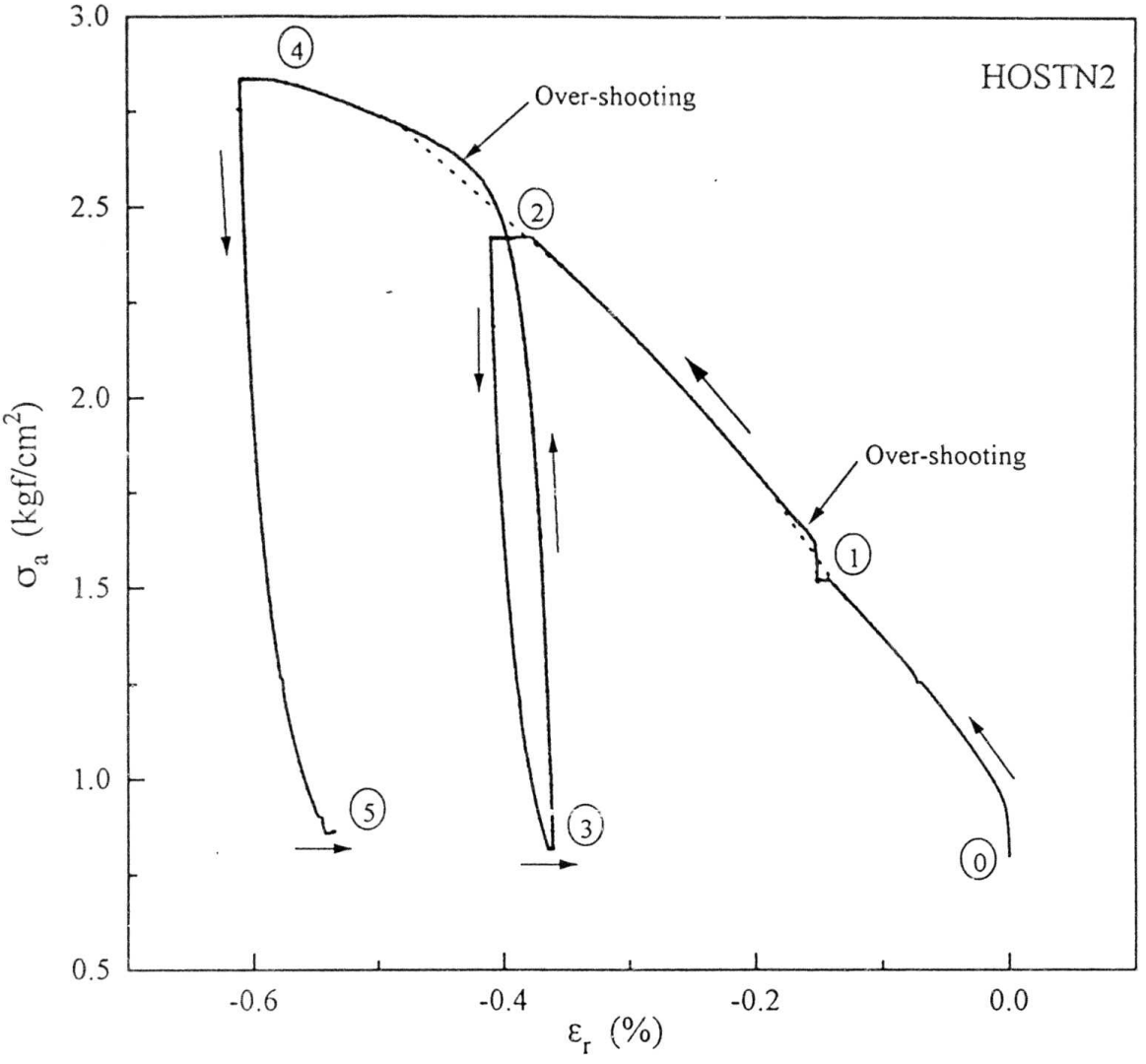

Fig. 8.1b: Relationships between σ_a and ε_r during creep tests performed on HOSTN2 specimen.

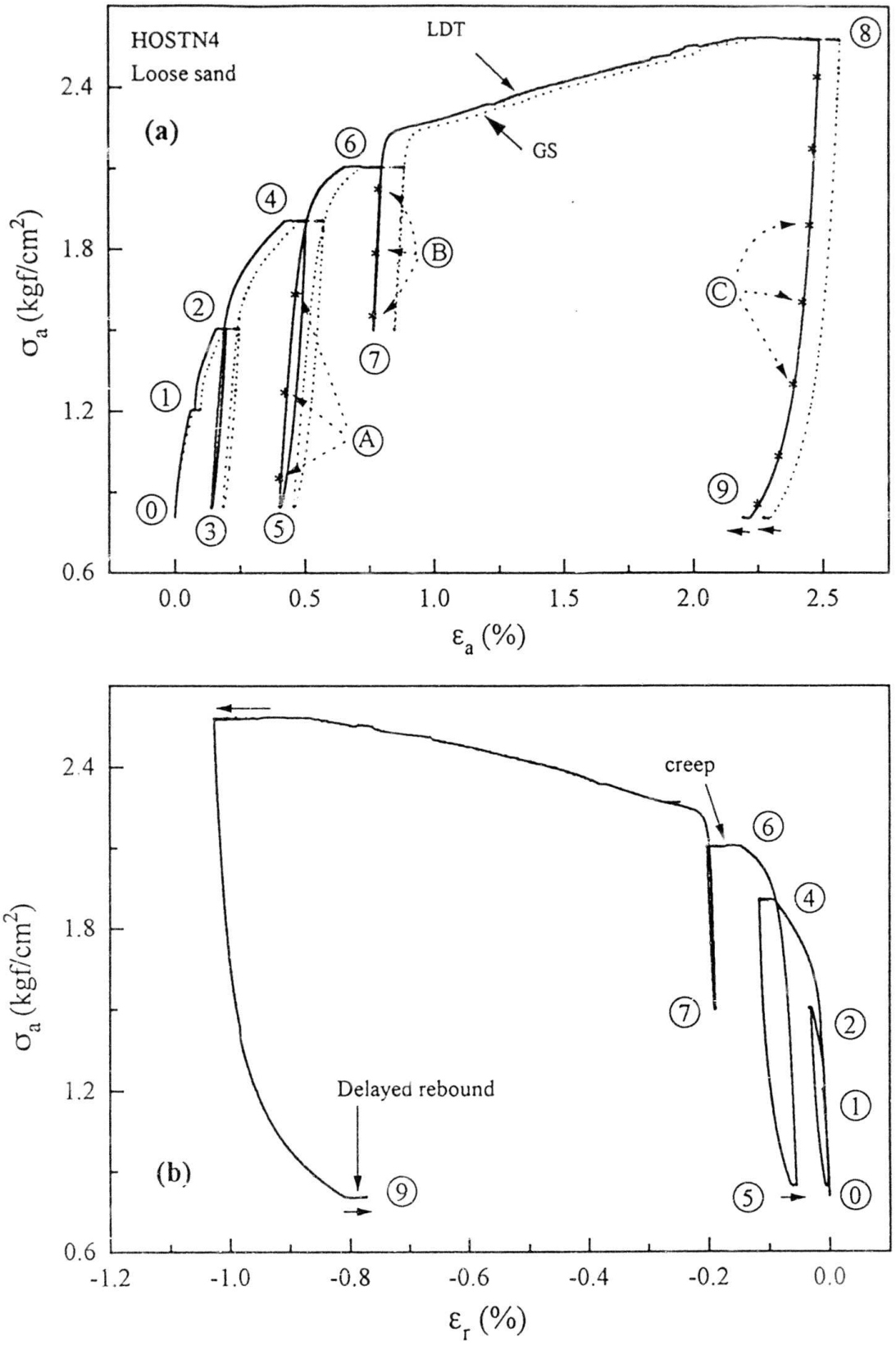

Figs. 8.2: (a) $\sigma_a \sim \varepsilon_a$, and (b) $\sigma_a \sim \varepsilon_r$ relationships during creep tests performed on HOSTN4 specimen.

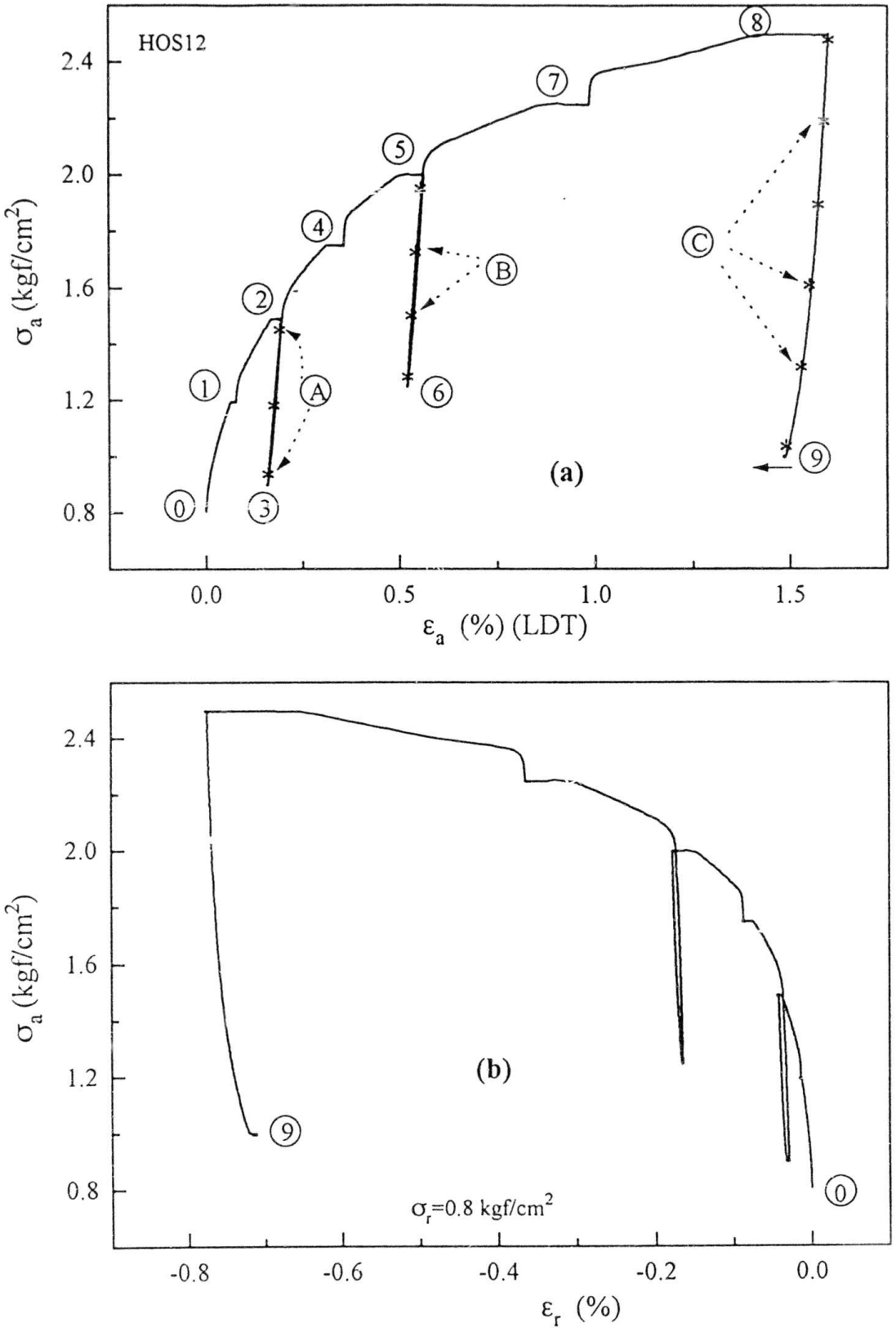

Figs. 8.3: (a) $\sigma_a \sim \varepsilon_a$, and (b) $\sigma_a \sim \varepsilon_r$ relationships during creep tests performed on HOS12 specimen.

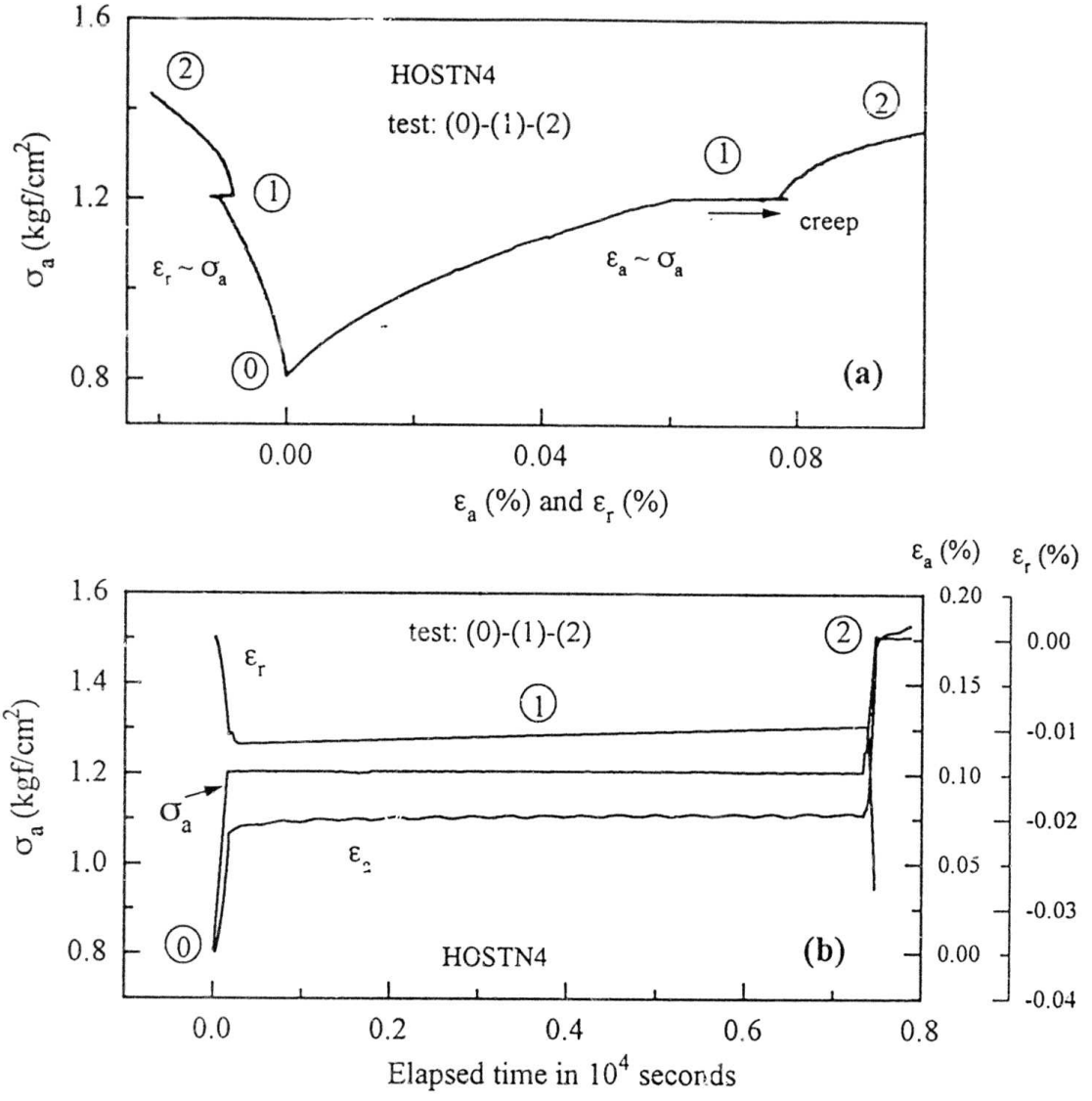

Figs. 8.4: (a) $\sigma_a \sim \varepsilon_a$ and $\sigma_a \sim \varepsilon_r$ relationships, and (b) time histories of σ_a, ε_a and ε_r for the test segments (0)-(1)-(2) performed on HOSTN4 specimen.

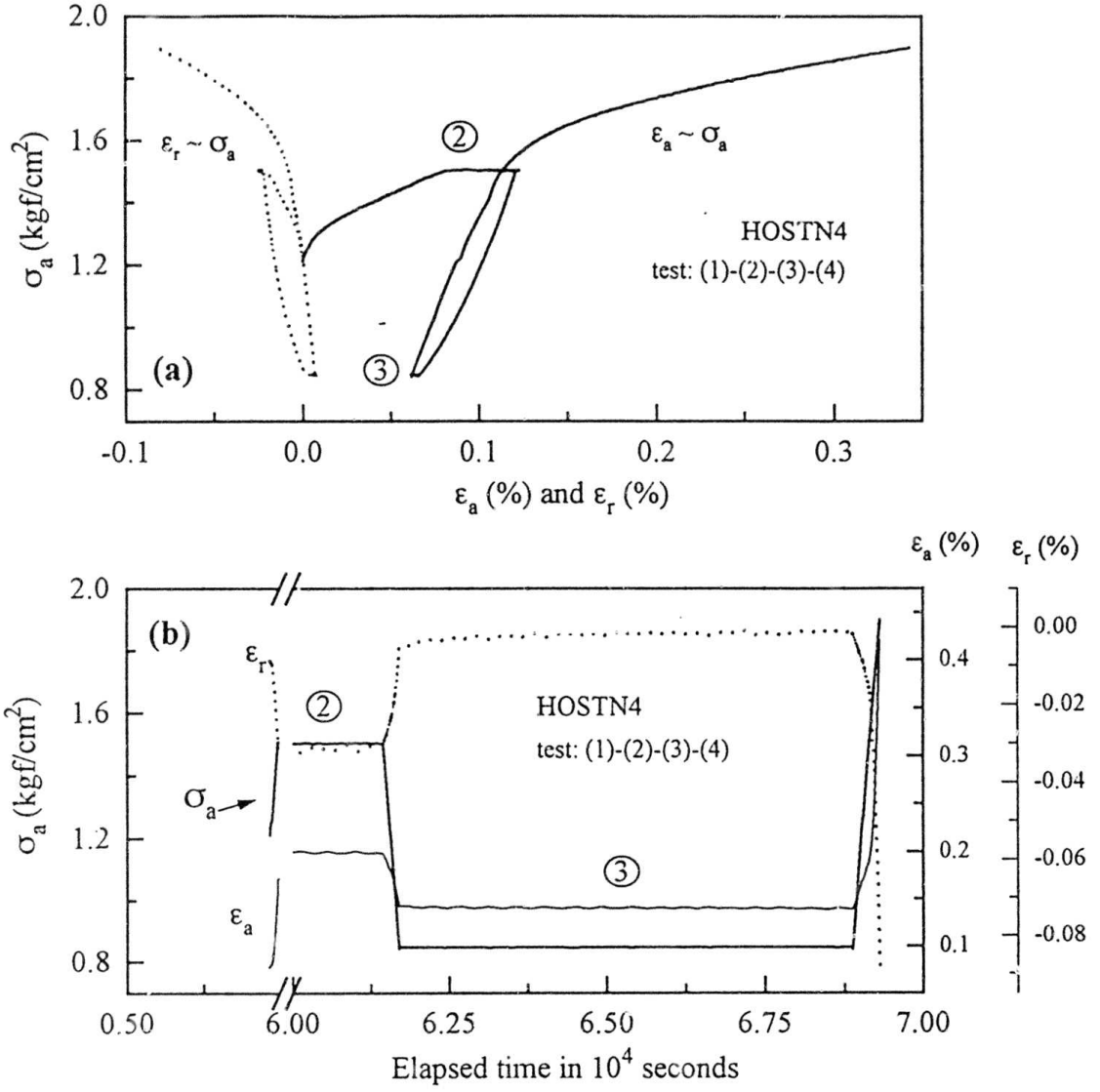

Figs. 8.5: (a) $\sigma_a \sim \varepsilon_a$ and $\sigma_a \sim \varepsilon_r$ relationships, and (b) time histories of σ_a, ε_a and ε_r for the test segments (1)-(2)-(3)-(4) performed on HOSTN4 specimen.

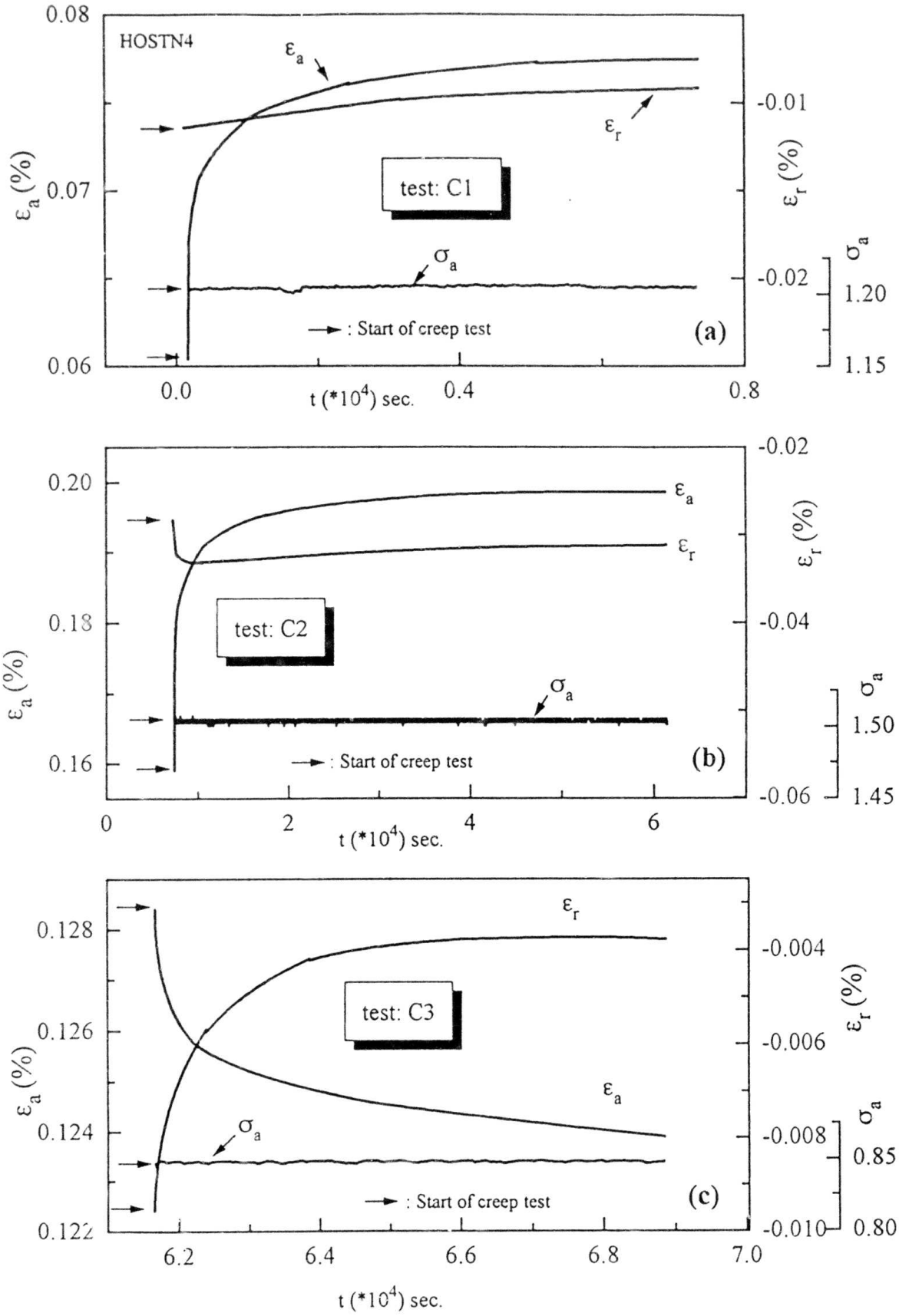

Figs. 8.6: Time histories of the variation of σ_a, ε_a and ε_r during creep tests ((a) Test C1, (b) Test C2, and (c) Test C3) performed at different stress states of HOSTN4 specimen.

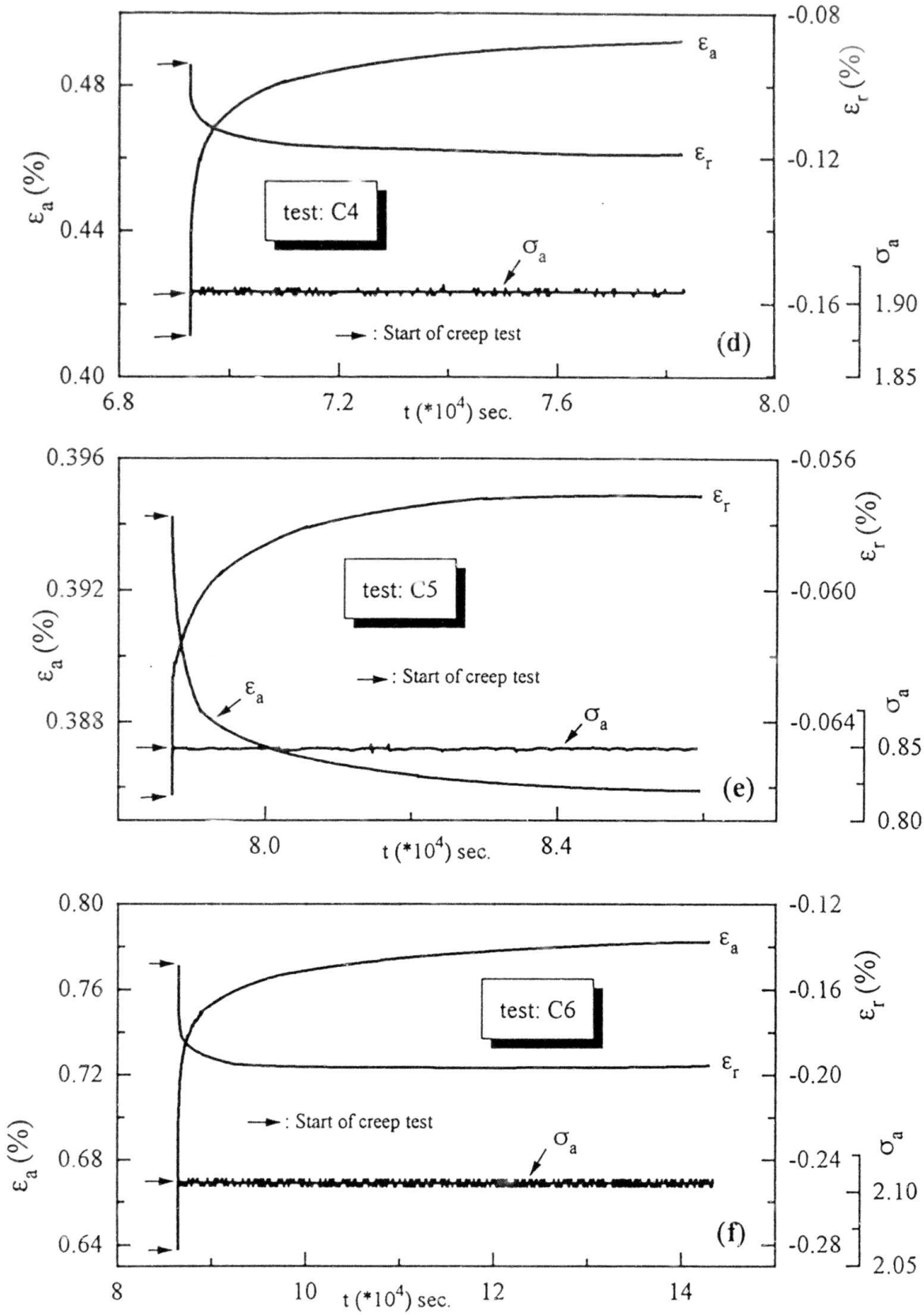

Figs. 8.6: Time histories of the variation of σ_a, ε_a and ε_r during creep tests ((d) Test C4, (e) Test C5, and (f) Test C6) performed at different stress states of HOSTN4 specimen.

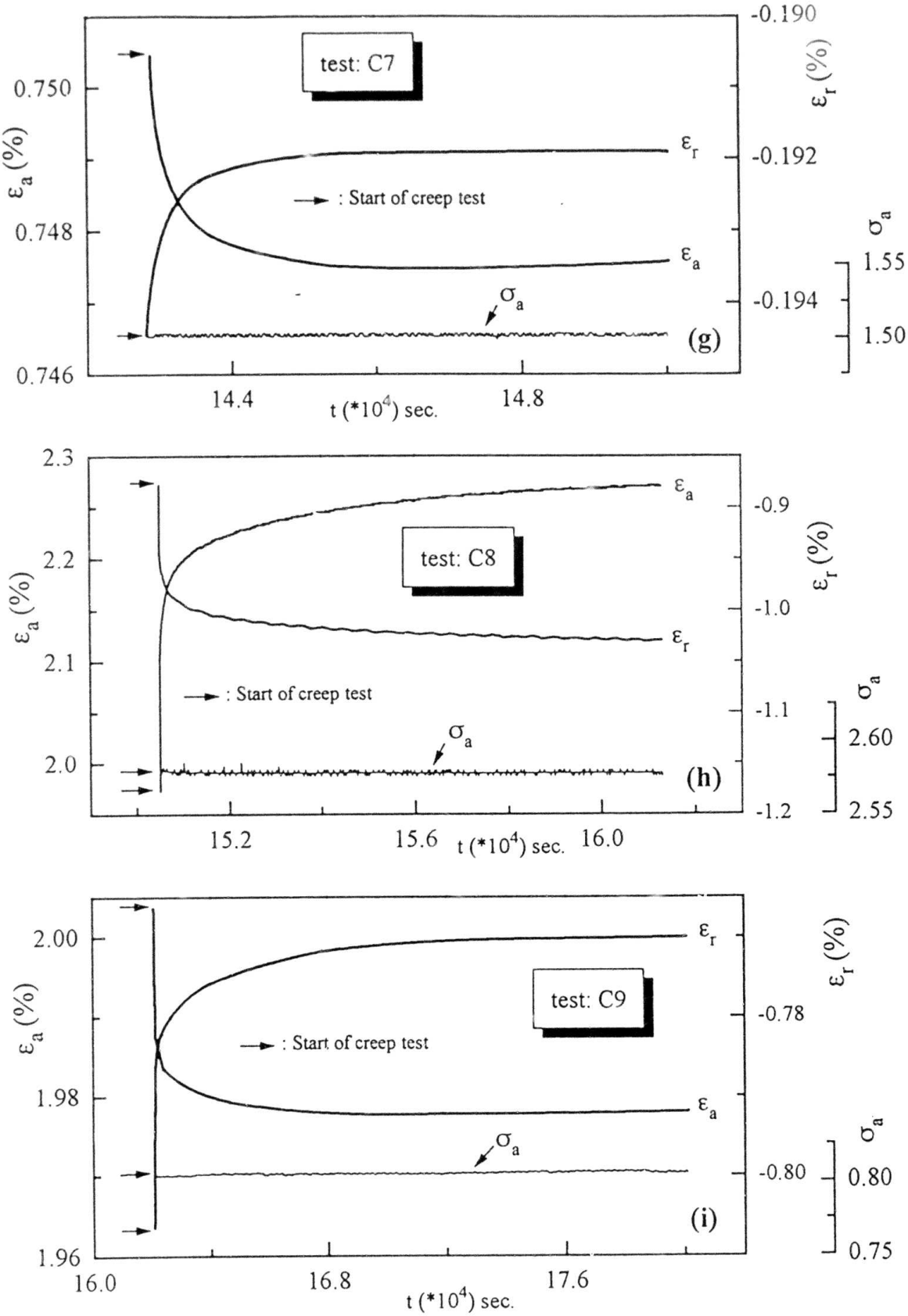

Figs. 8.6: Time histories of the variation of σ_a, ε_a and ε_r during creep tests ((g) Test C7, (h) Test C8, and (i) Test C9) performed at different stress states of HOSTN4 specimen.

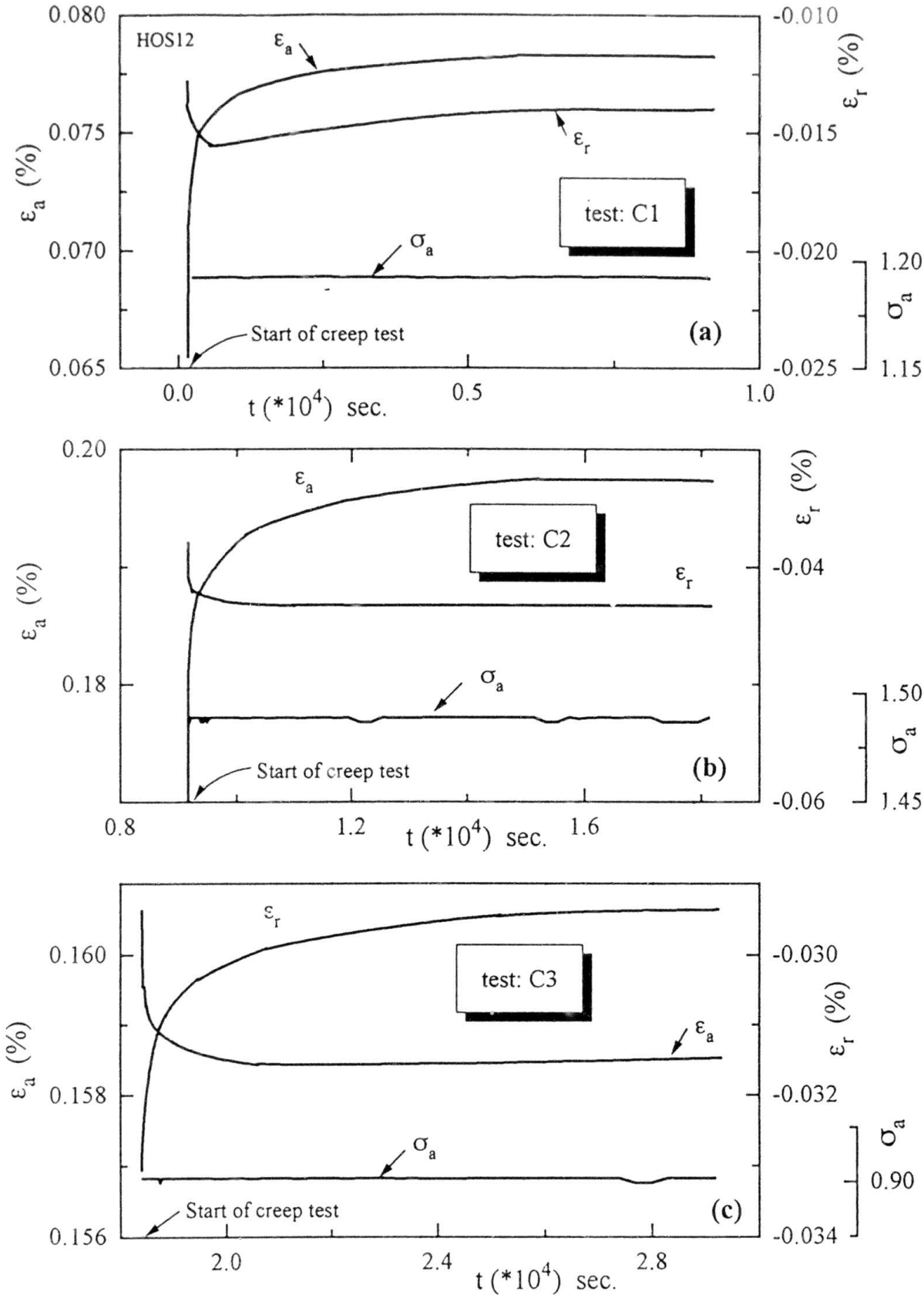

Figs. 8.7: Time histories of the variation of σ_a, ε_a and ε_r during creep tests ((a) Test C1, (b) Test C2, and (c) Test C3) performed at different stress states of HOS12 specimen.

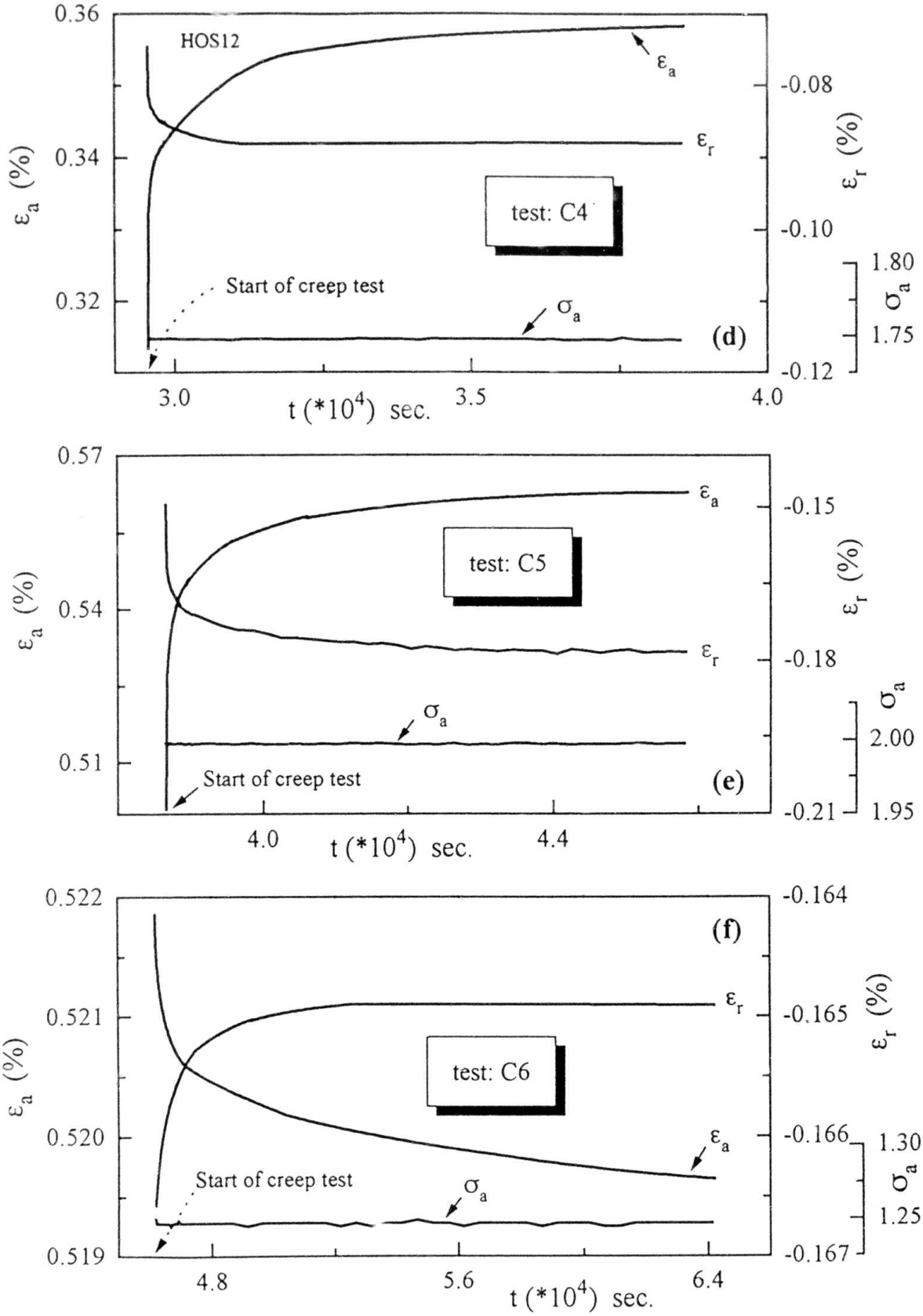

Figs. 8.7: Time histories of the variation of σ_a, ε_a and ε_r during creep tests ((d) Test C4, (e) Test C5, and (f) Test C6) performed at different stress states of HOS12 specimen.

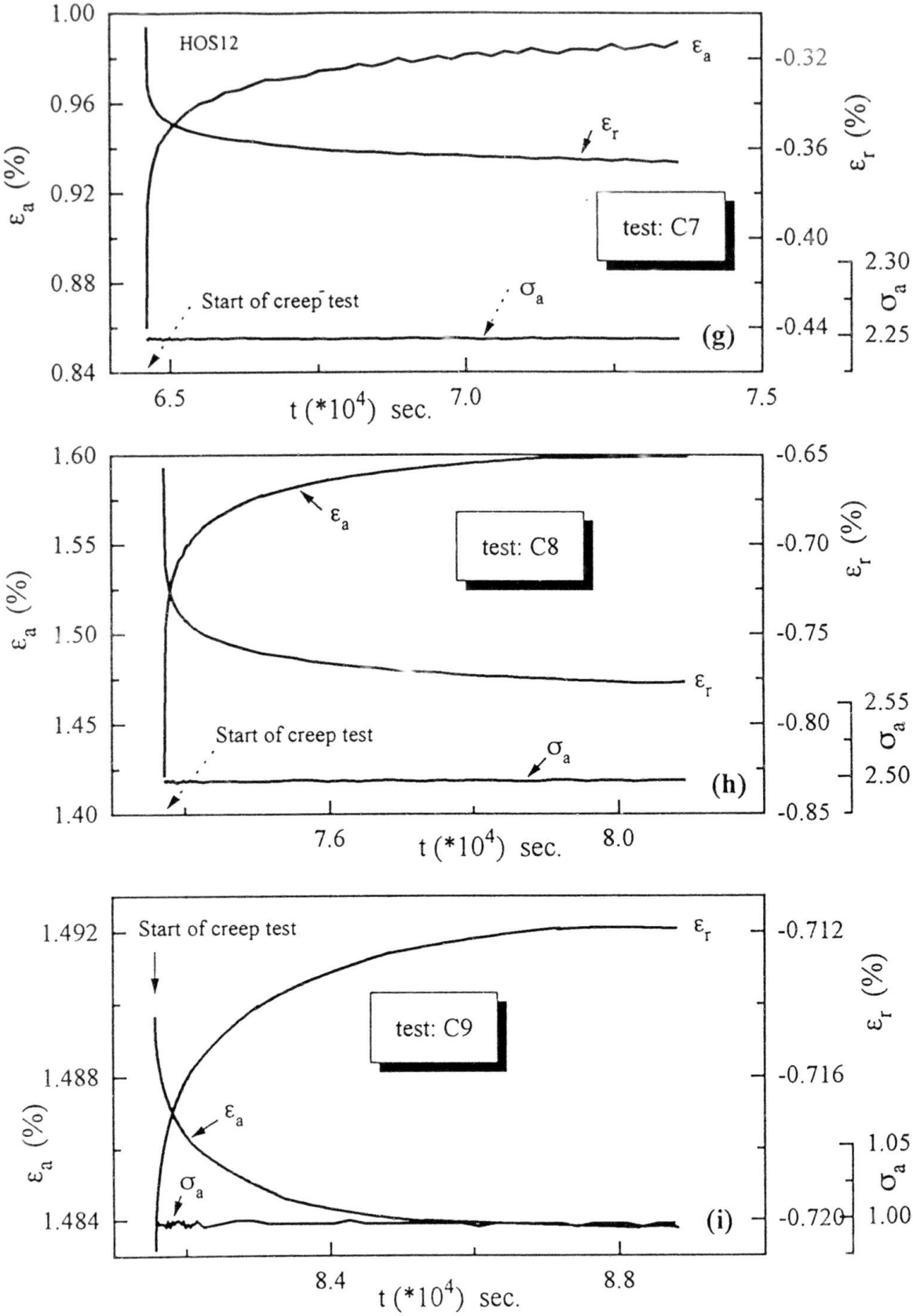

Figs. 8.7: Time histories of the variation of σ_a, ε_a and ε_r during creep tests ((g) Test C7, (h) Test C8, and (i) Test C9) performed at different stress states of HOS12 specimen.

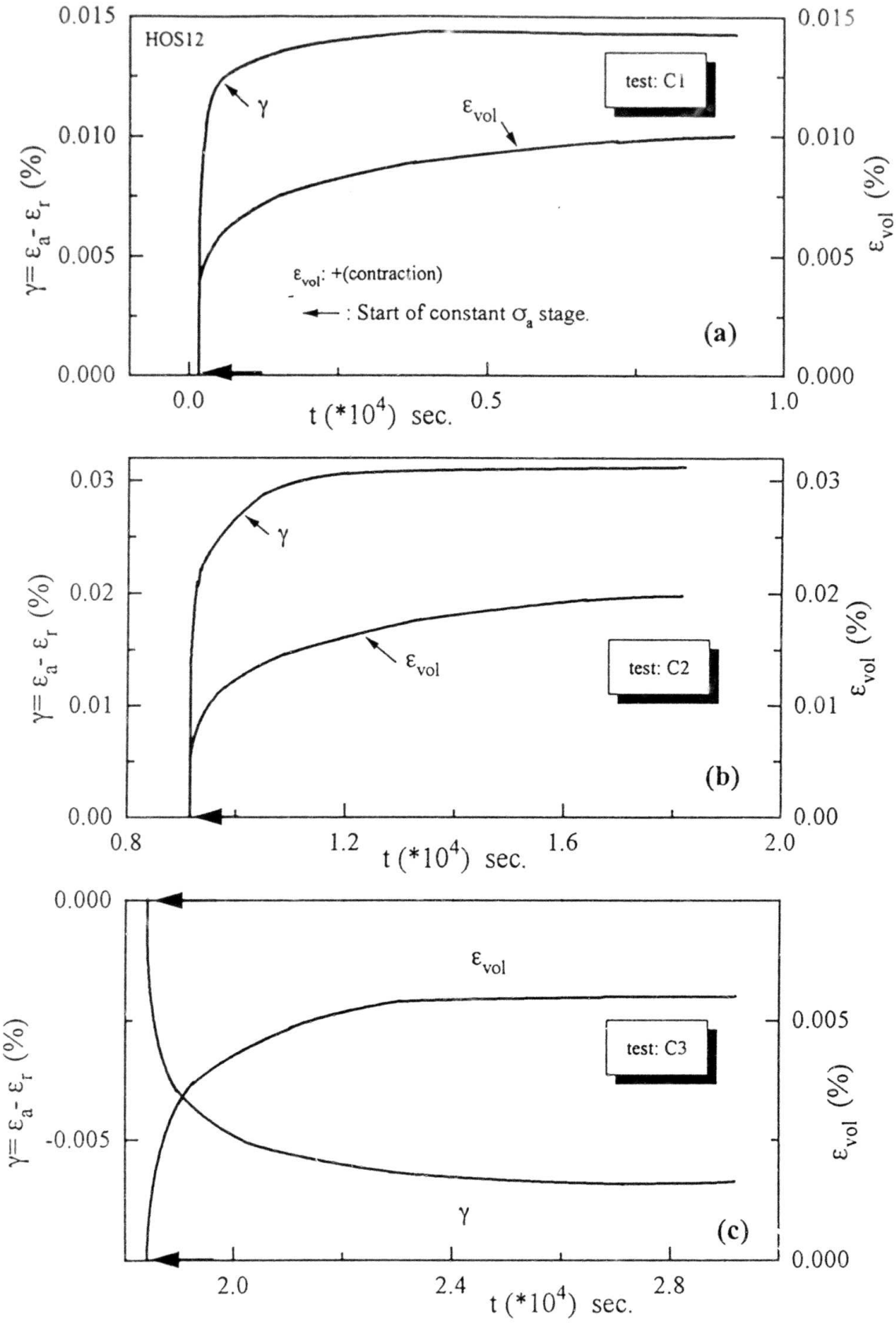

Figs. 8.8: Time histories of the variation of γ and ε_{vol} during creep tests ((a) Test C1, (b) Test C2, and (c) Test C3) performed at different stress states of HOS12 specimen.

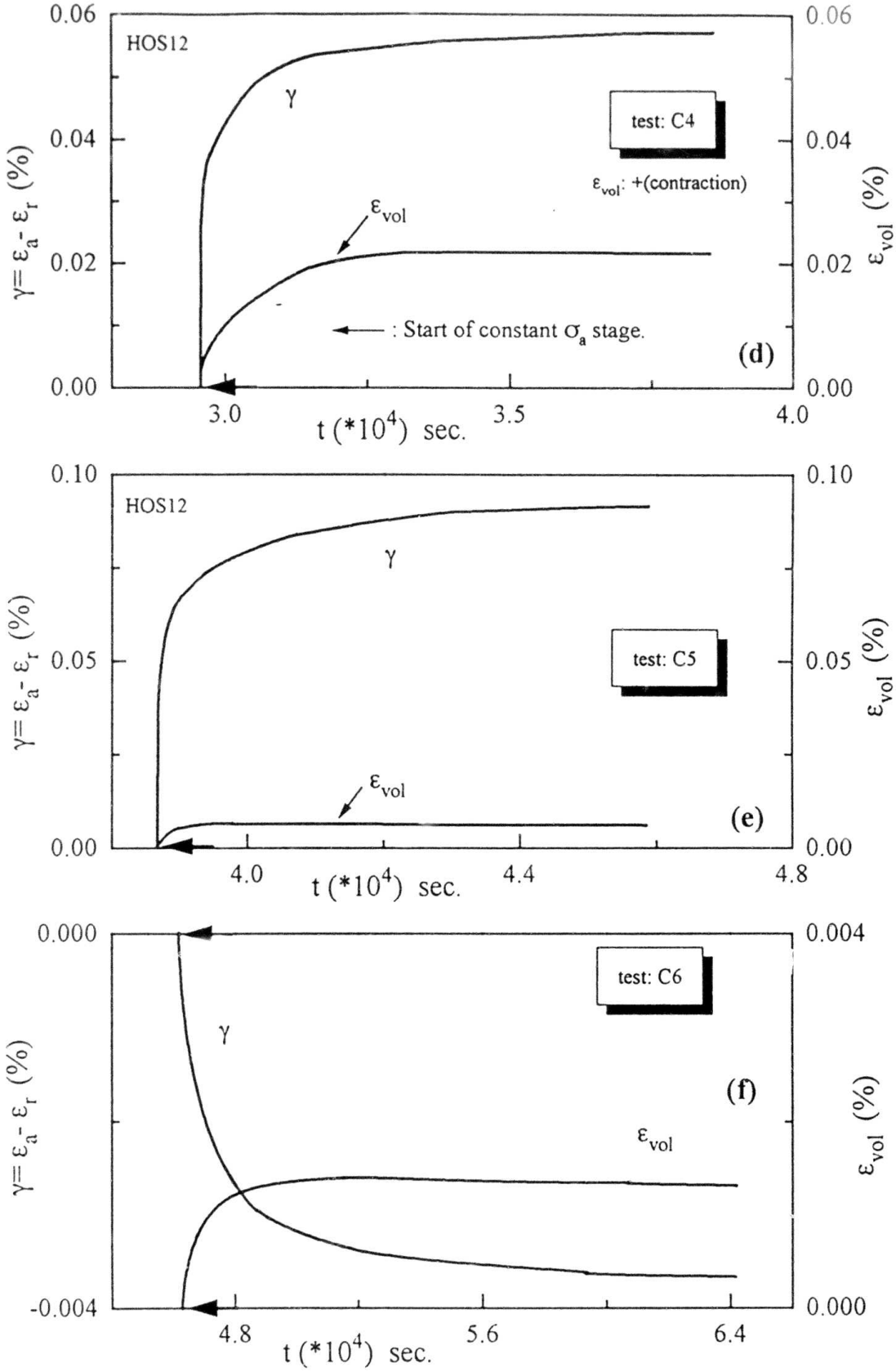

Figs. 8.8: Time histories of the variation of γ and ε_{vol} during creep tests ((d) Test C4, (e) Test C5, and (f) Test C6) performed at different stress states of HOS12 specimen.

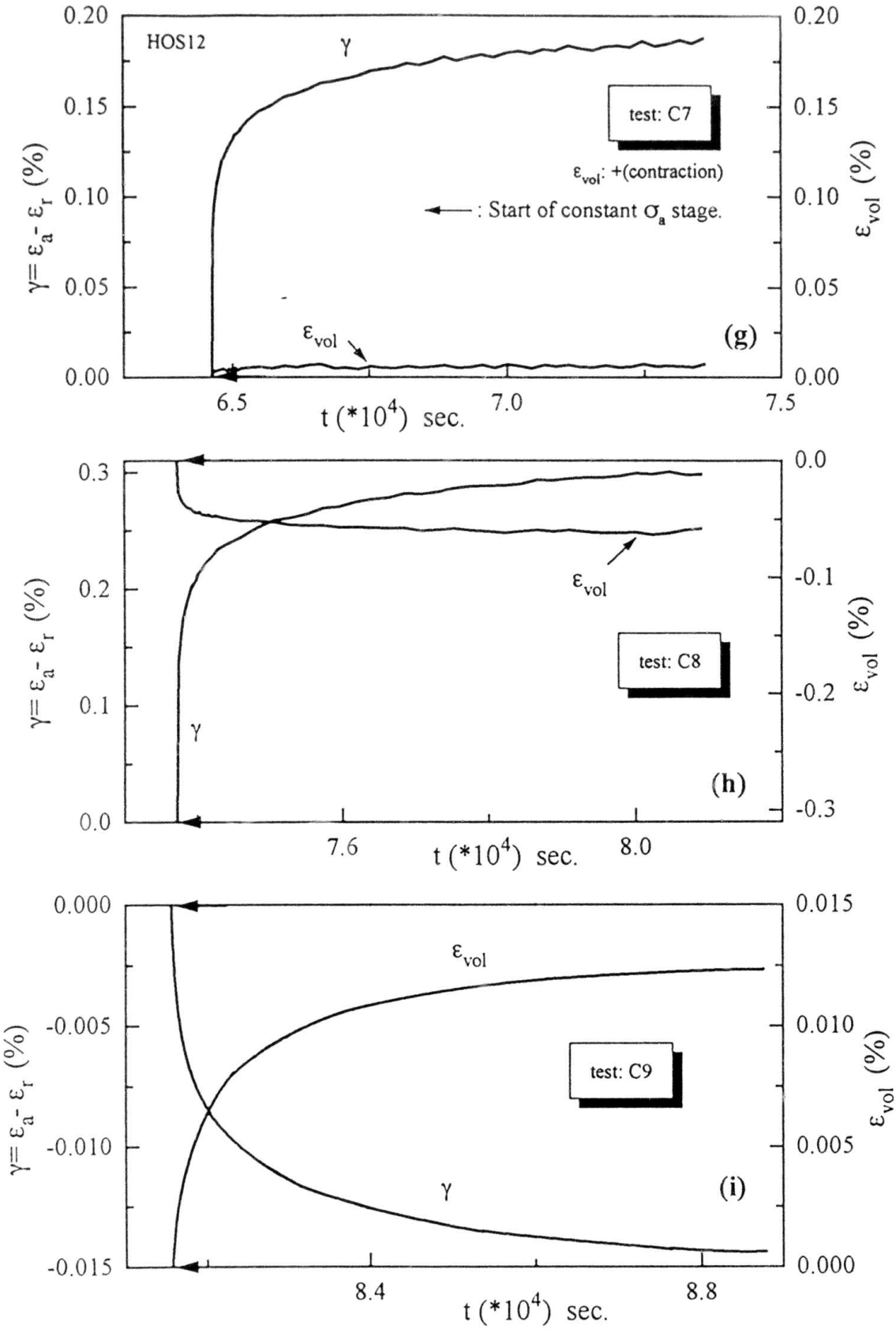

Figs. 8.8: Time histories of the variation of γ and ε_{vol} during creep tests ((g) Test C7, (h) Test C8, and (i) Test C9) performed at different stress states of HOS12 specimen.

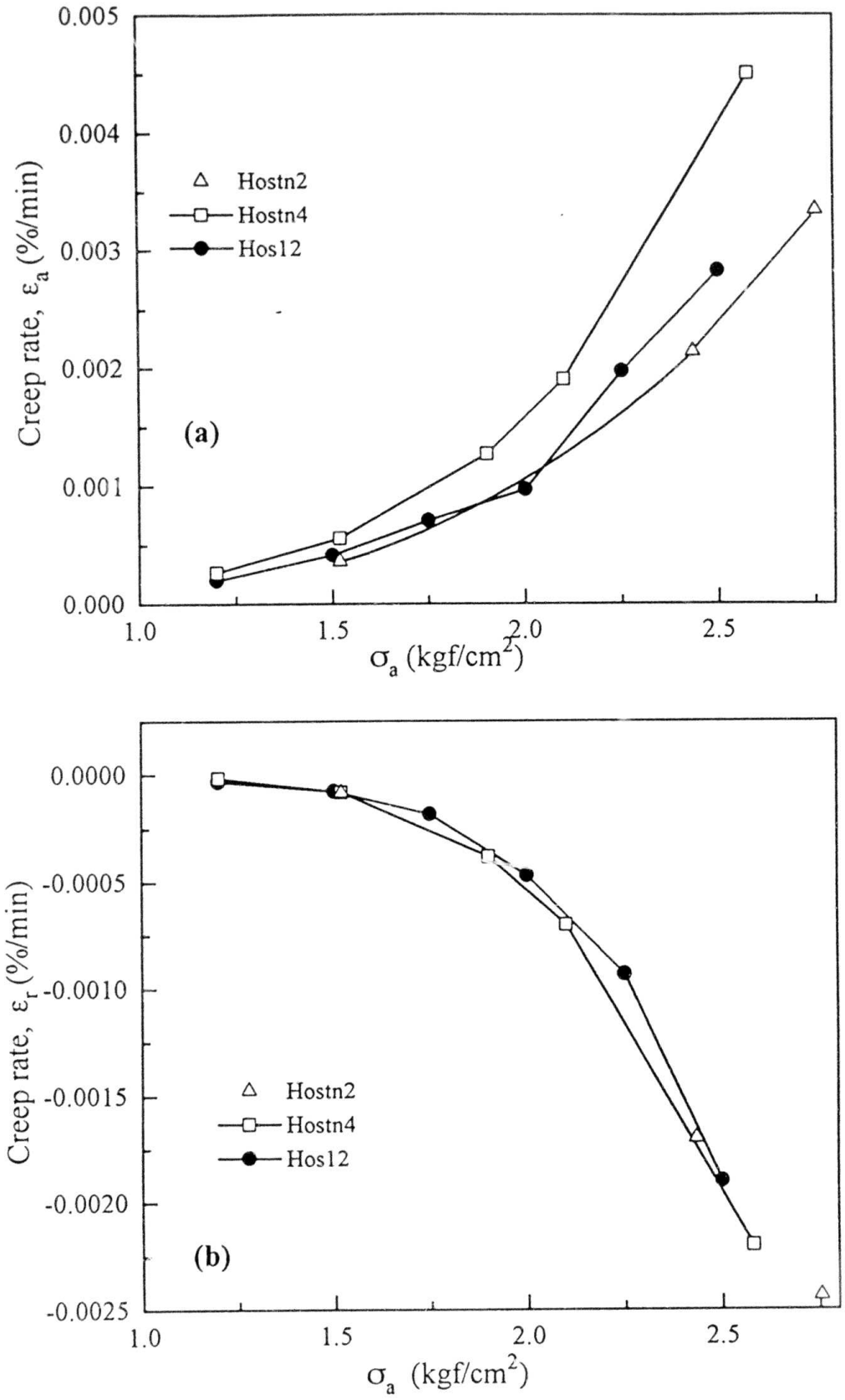

Figs. 8.9: Relationships between σ_a and the creep rate in (a) ε_a, and (b) ε_r for different specimens.

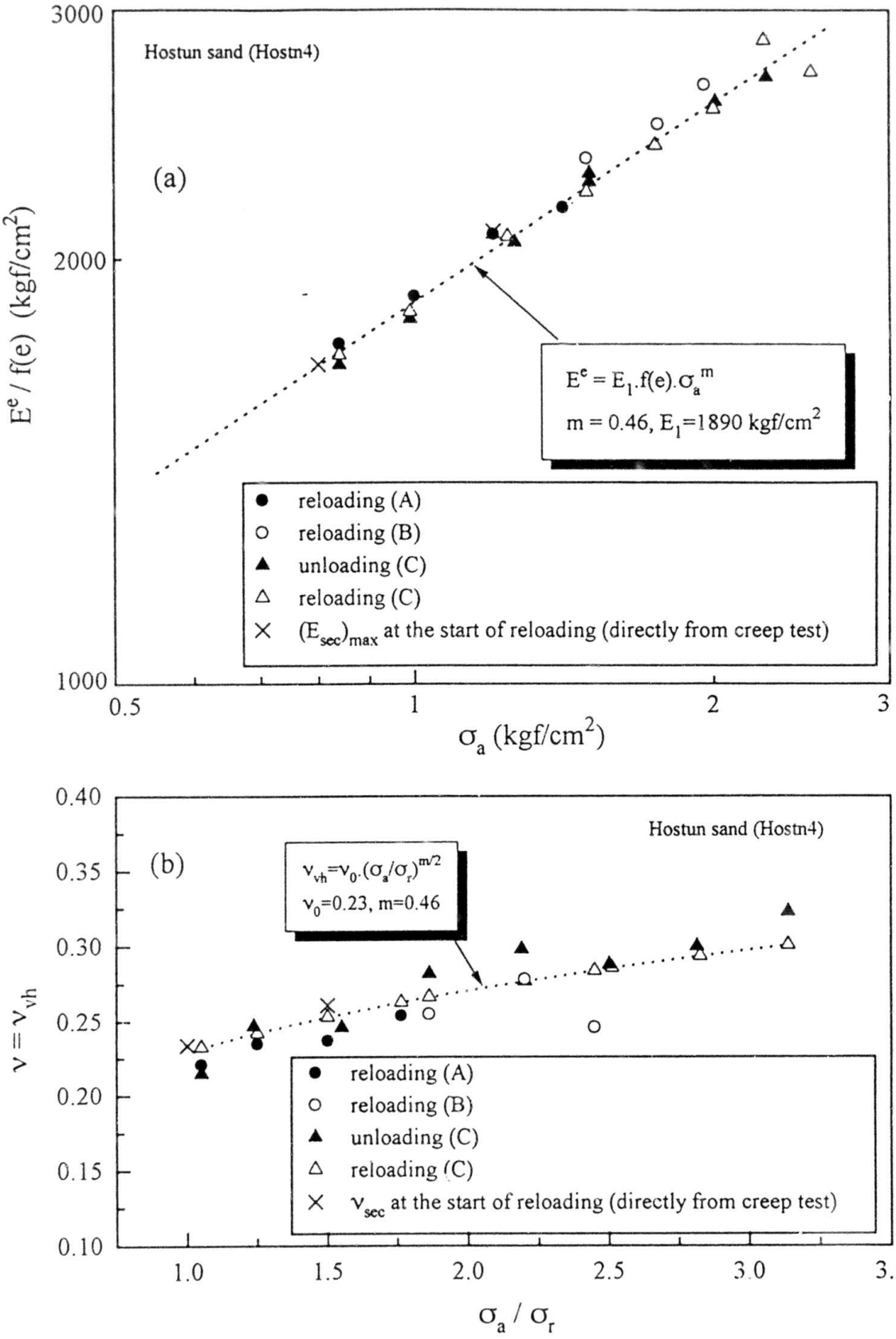

Figs. 8.10: Relationships between (a) $E^e/f(e)$ and σ_a, and (b) ν and σ_a/σ_r of HOSTN4 specimen.

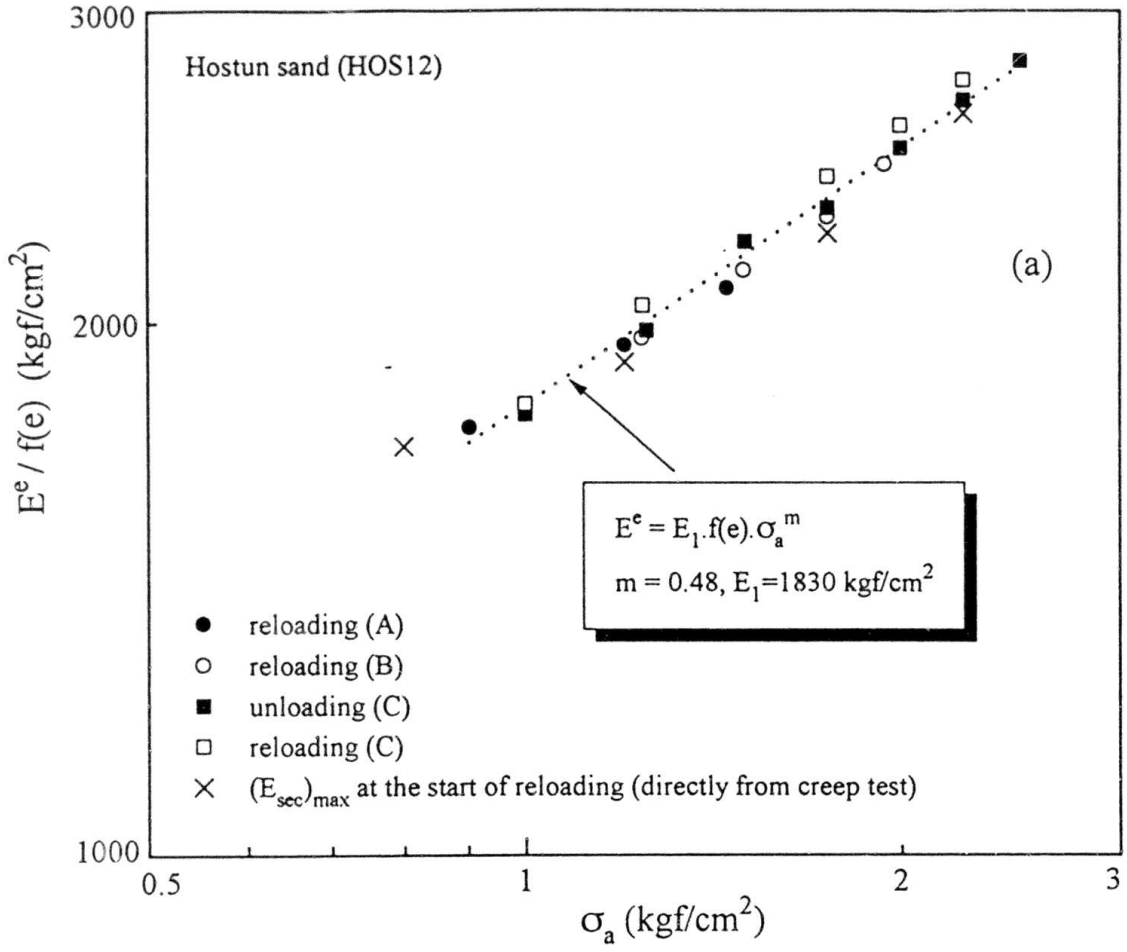

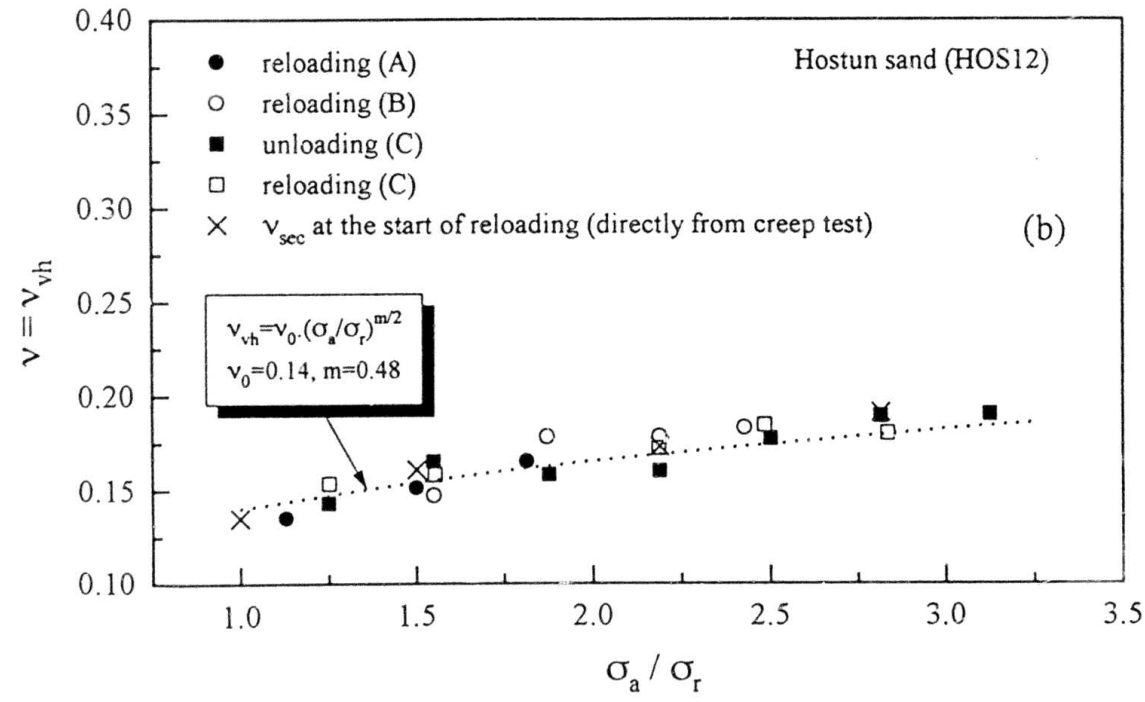

Figs. 8.11: Relationships between (a) $E^e/f(e)$ and σ_a, and (b) ν and σ_a/σ_r of HOS12 specimen.

Fig10.org/creep/D1

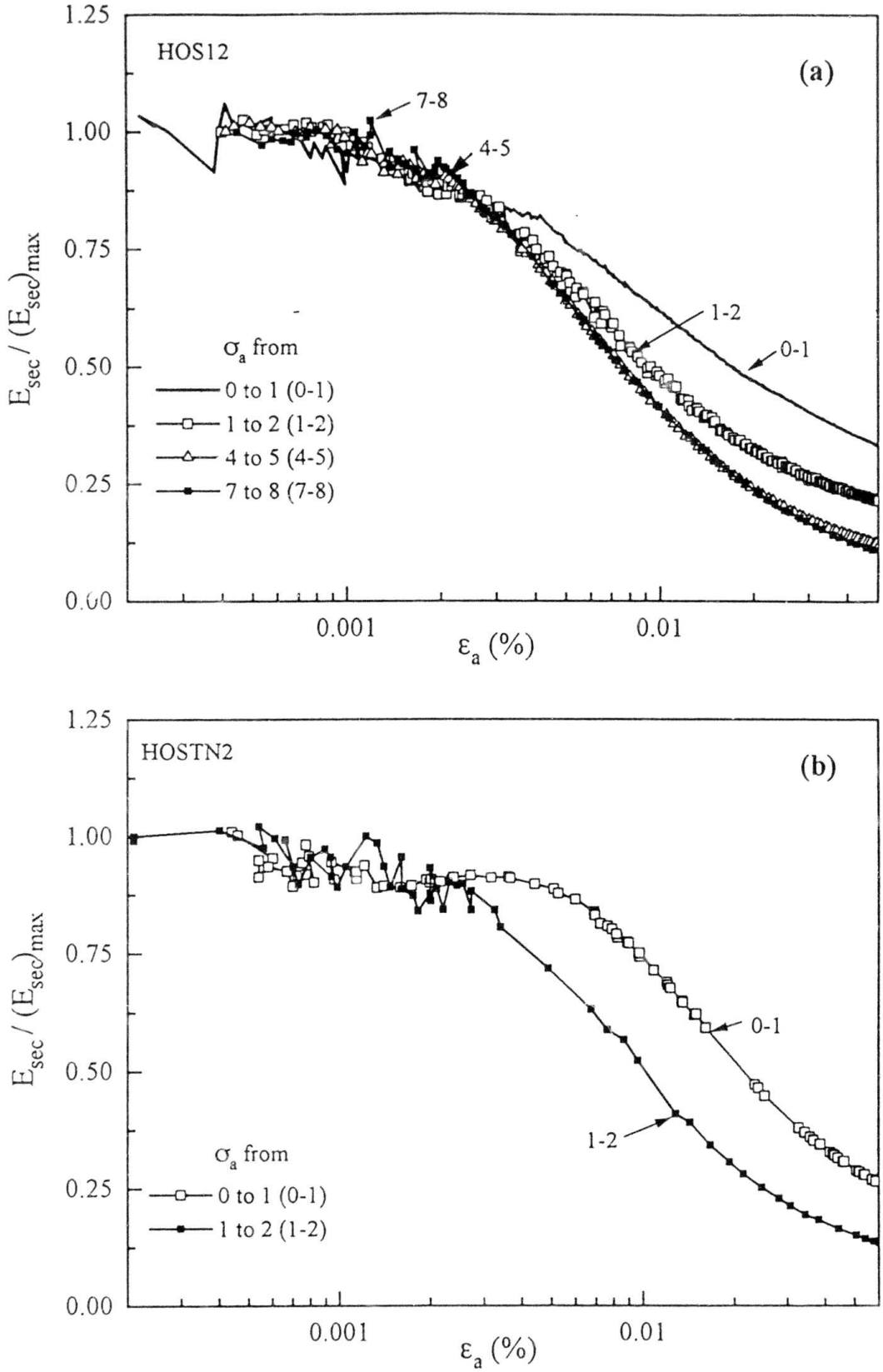

Figs. 8.12: Relationships between $E_{sec}/(E_{sec})_{max}$ and ε_a for different stress segments (Type 1) of specimens (a) HOS12, and (b) HOSTN2.

Fig11.org/creep/D1

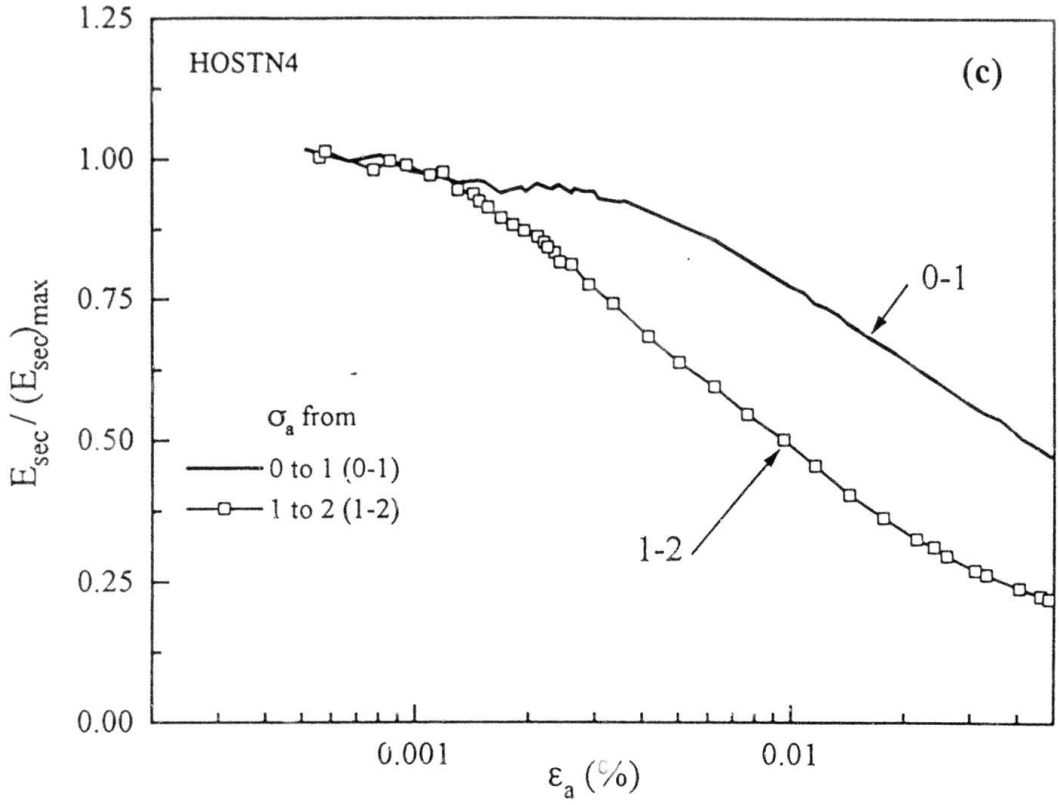

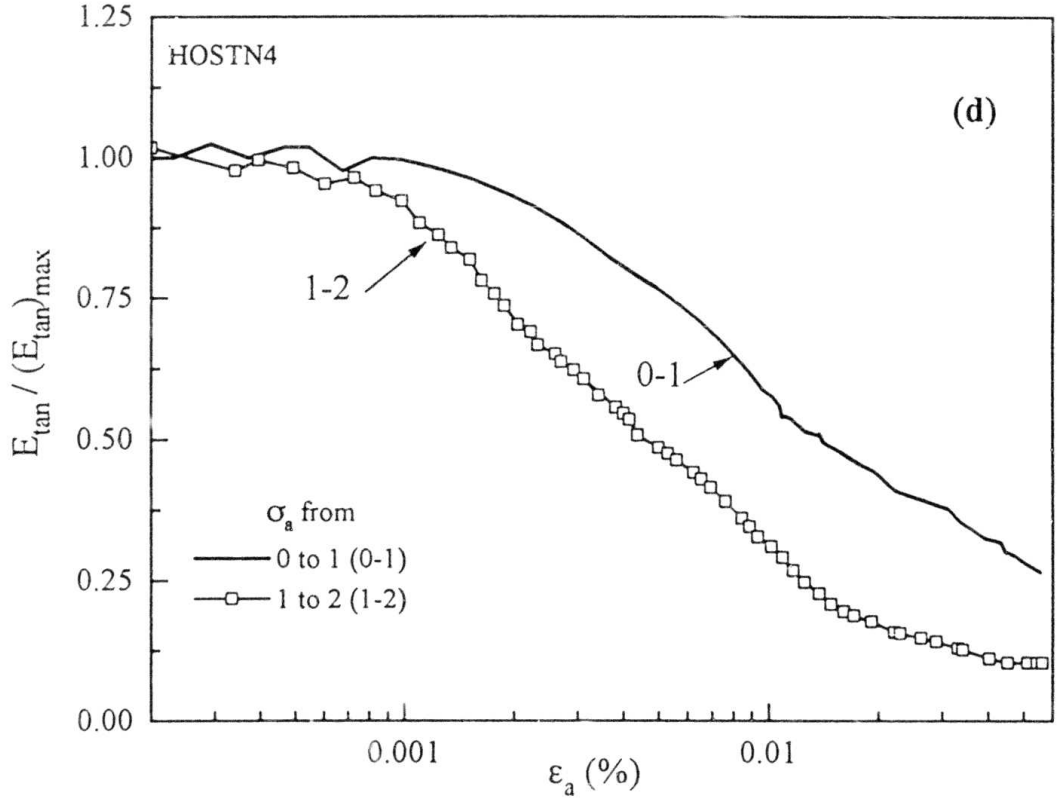

Figs. 8.12: Relationships between (c) $E_{sec}/(E_{sec})_{max}$ and ε_a, and (d) $E_{tan}/(E_{tan})_{max}$ and ε_a for different stress segments (Type 1) of HOSTN4 specimen.

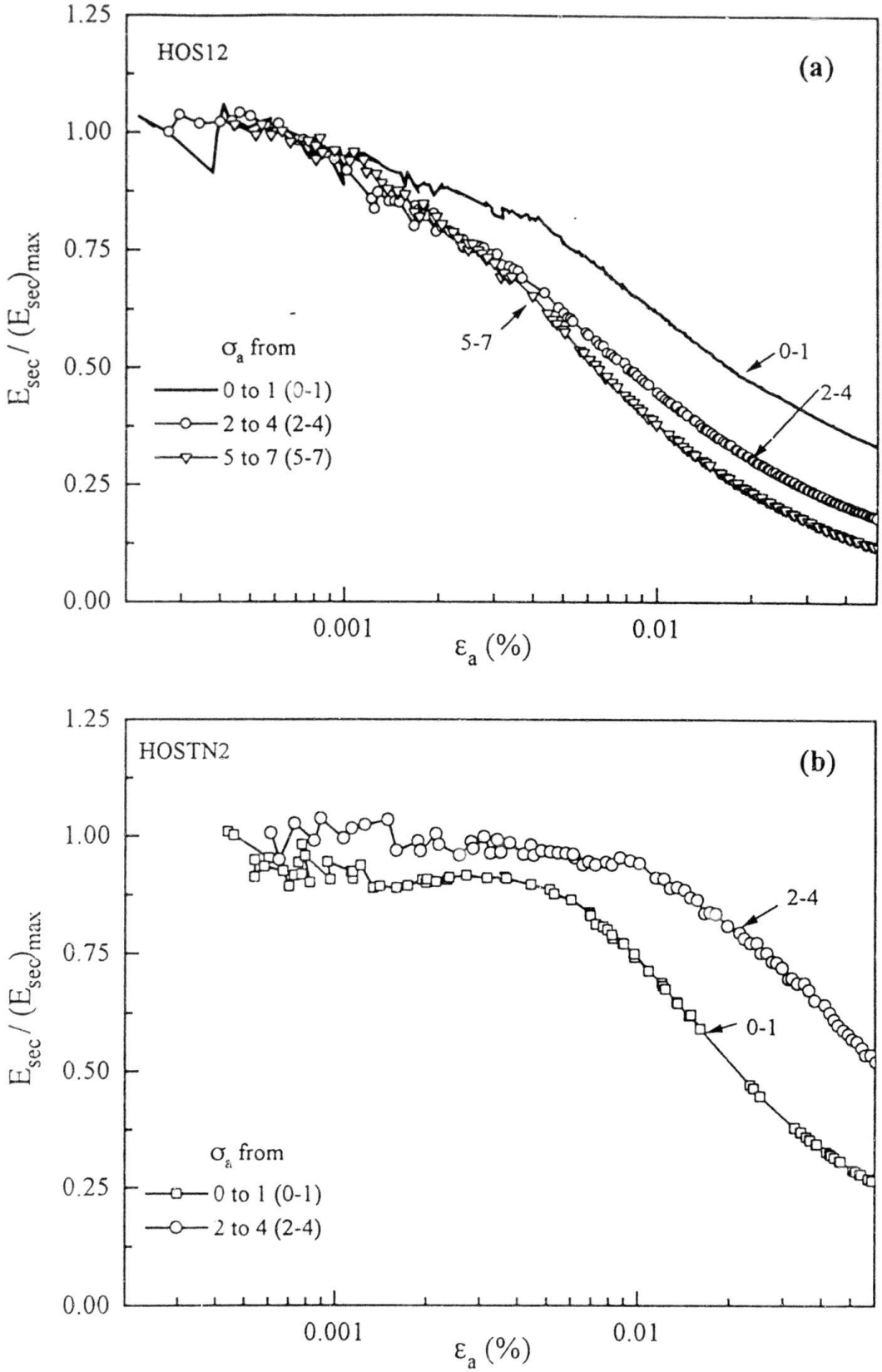

Figs. 8.13: Relationships between $E_{sec}/(E_{sec})_{max}$ and ε_a for different stress segments (Type 2) of specimens (a) HOS12, and (b) HOSTN2.

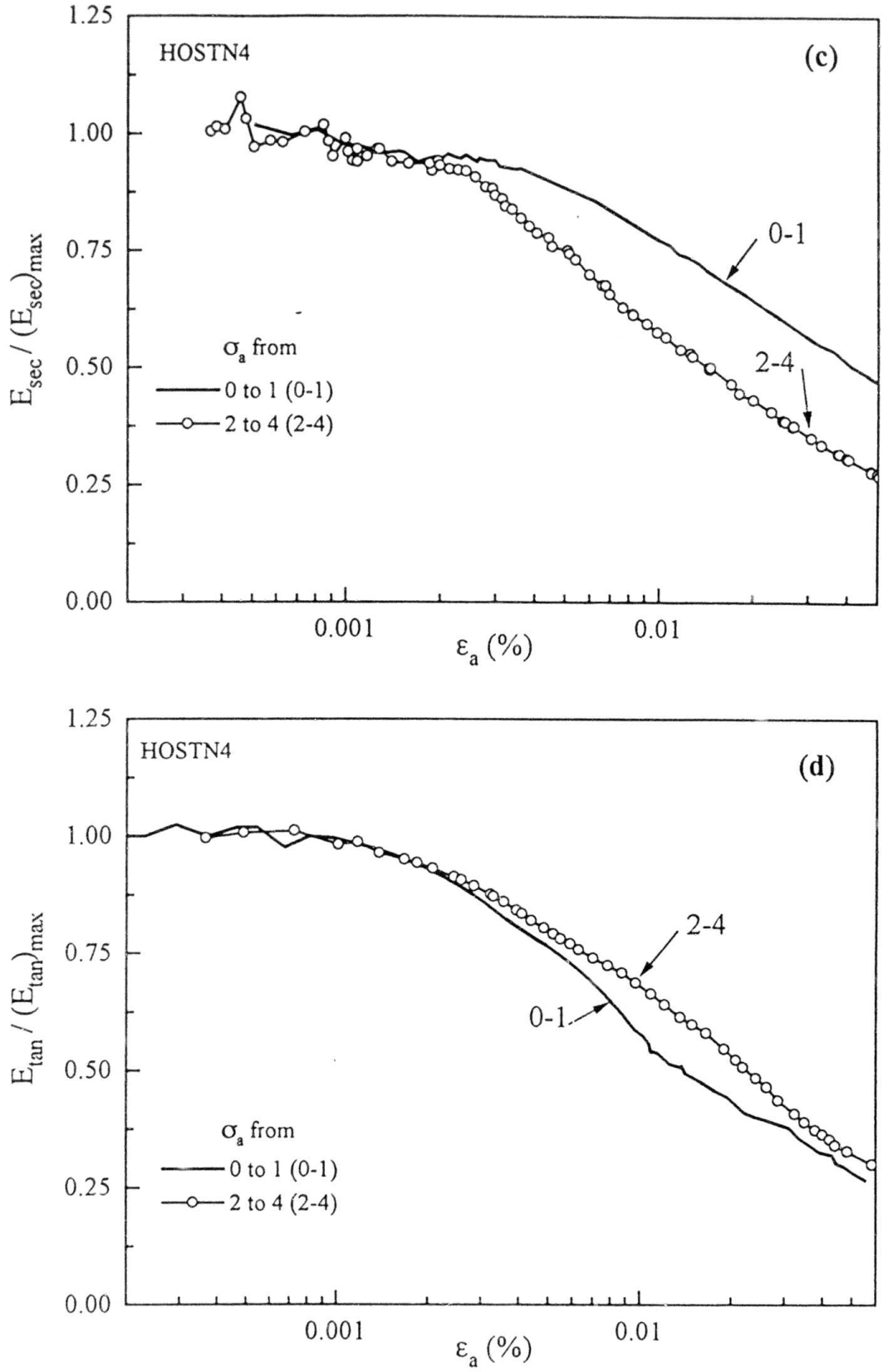

Figs. 8.13: Relationships between (c) $E_{sec}/(E_{sec})_{max}$ and ε_a, and (d) $E_{tan}/(E_{tan})_{max}$ and ε_a for different stress segments (Type 2) of HOSTN4 specimen.

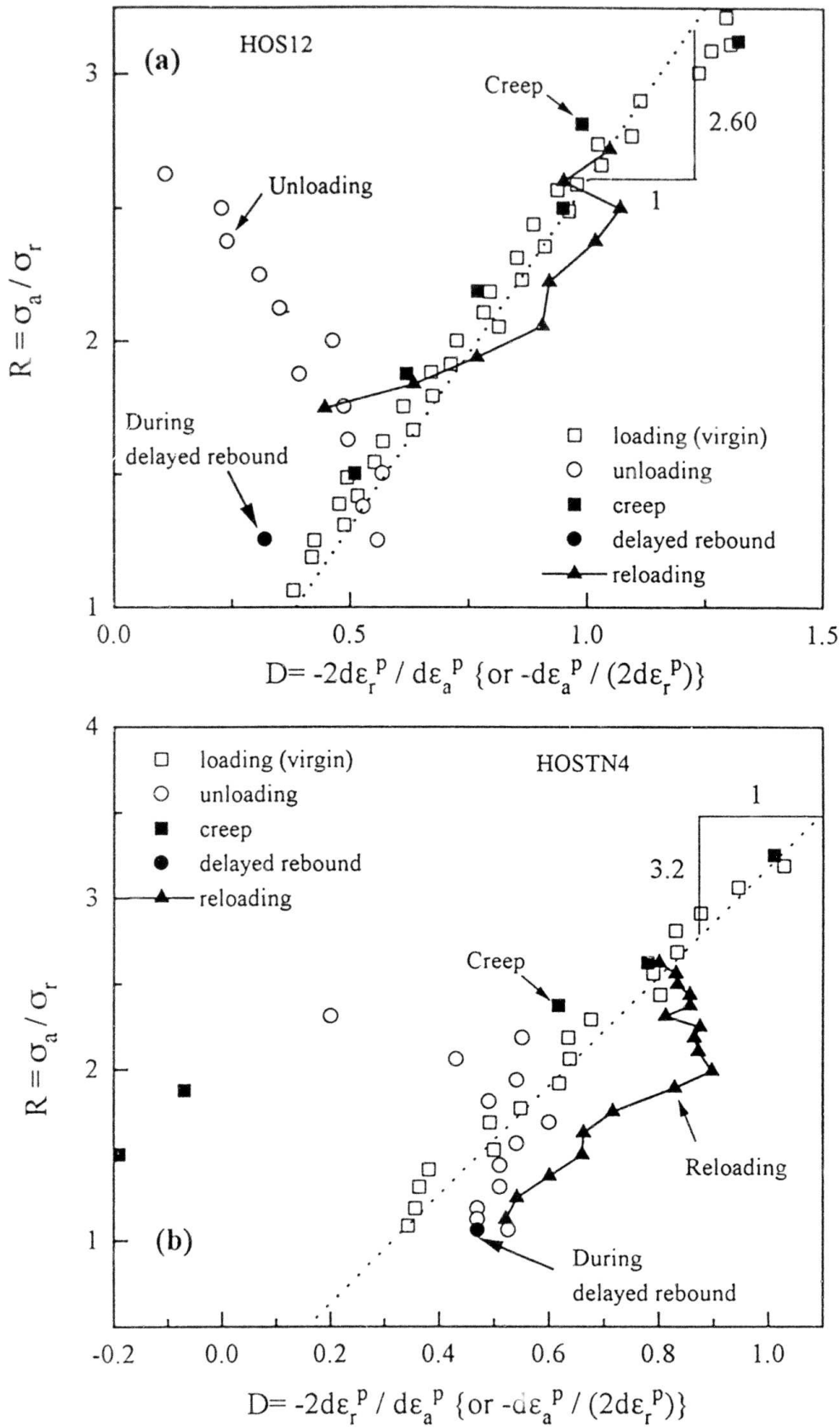

Figs. 8.14: Stress-dilatancy relationships during loading (σ_a increasing), unloading (σ_a decreasing), reloading, creep and delayed rebound for specimens (a) HOS12, and (b) HOSTN4.

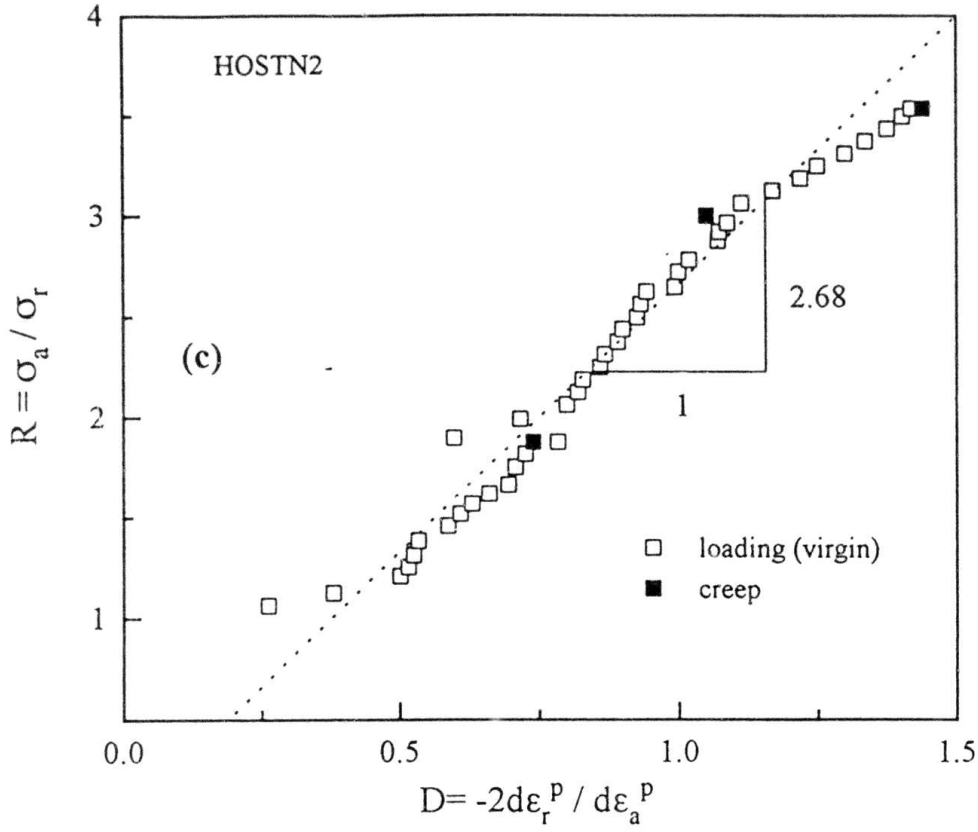

Fig. 8.14c: Stress-dilatancy relationships during loading (σ_a increasing) and creep for HOSTN2 specimen.

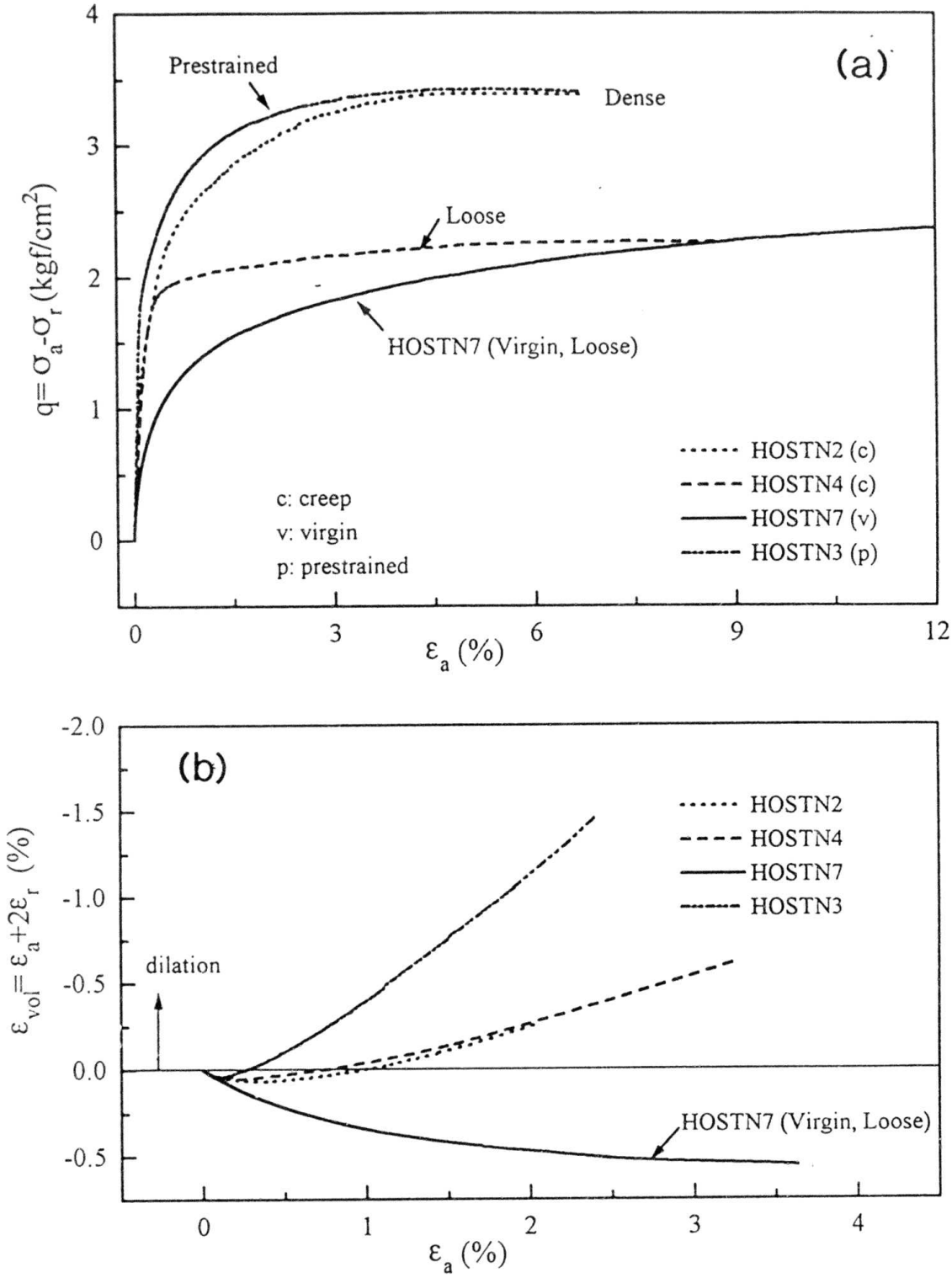

Figs. 8.15: (a) $q \sim \varepsilon_a$ and (b) $\varepsilon_{vol} \sim \varepsilon_a$ relationships of different specimens during TC at $\sigma_a = \sigma_r = 0.8$ kgf/cm^2.

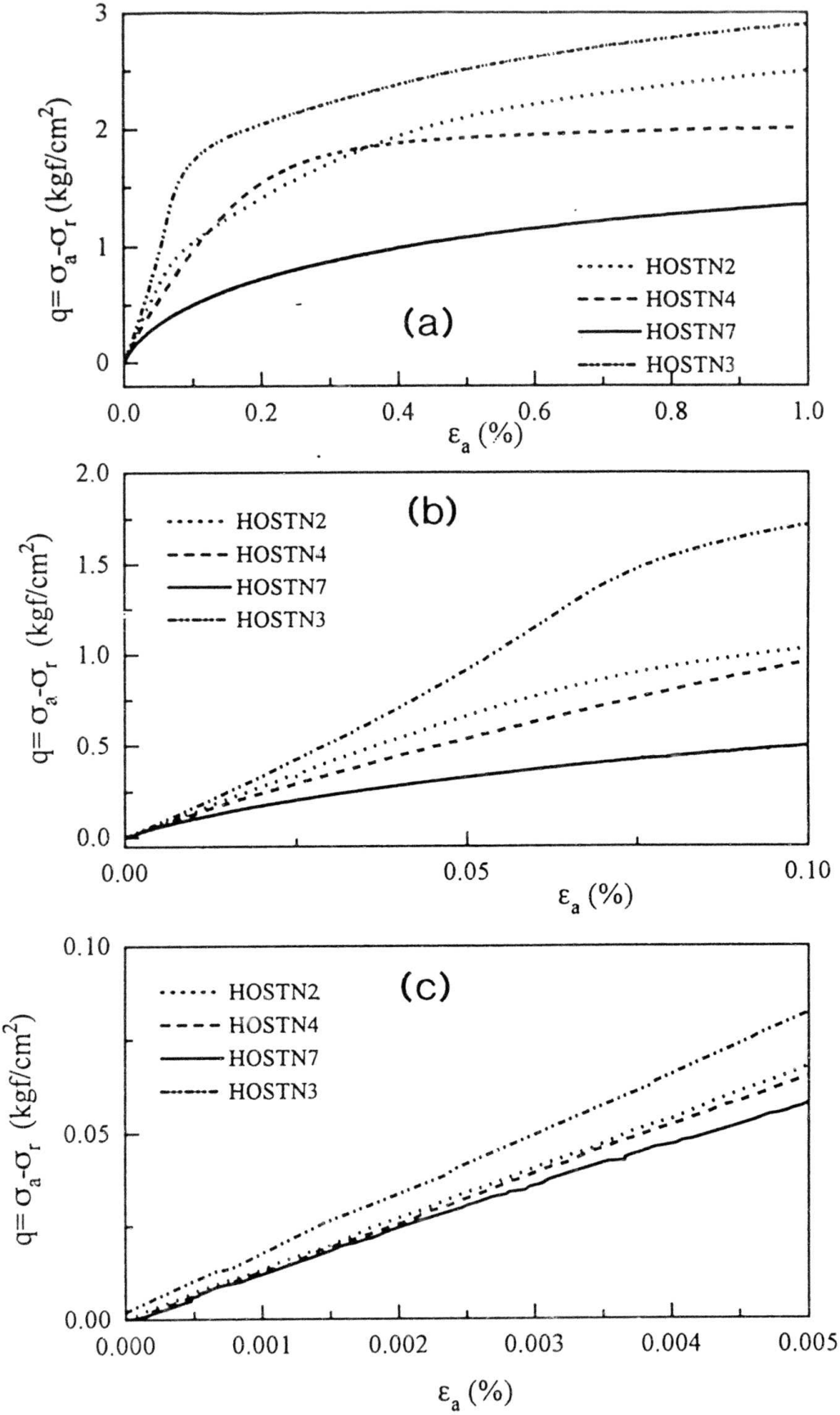

Figs. 8.16: q~ε_a relationships during TC at small strain levels with ε_a up to (a) 1.0%, (b) 0.10% and (c) 0.005%.

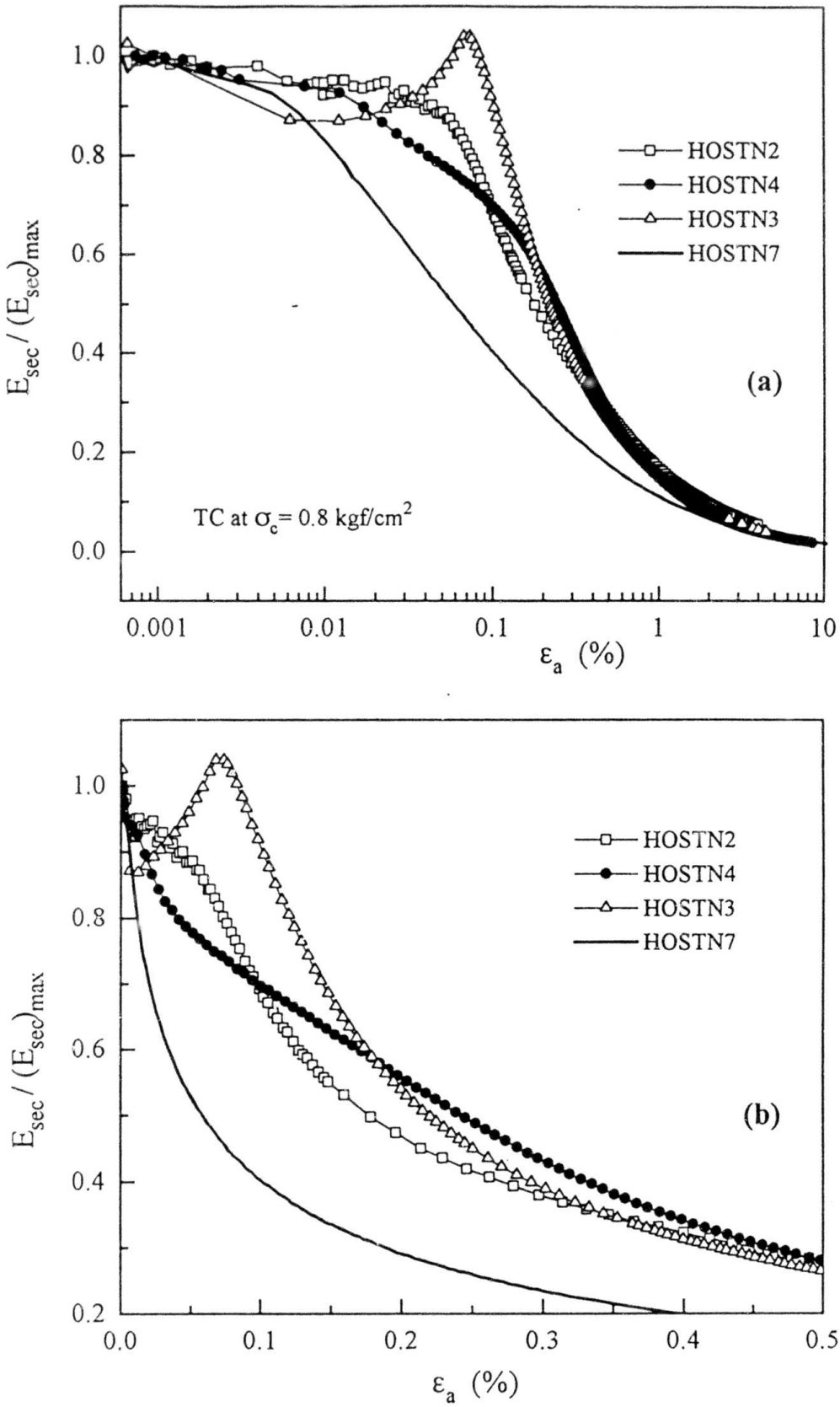

Figs. 8.17: Relationships between $E_{sec}/(E_{sec})_{max}$ and ε_a for different specimens during TC up to (a) the full range of ε_a, and (b) ε_a= 0.5%.

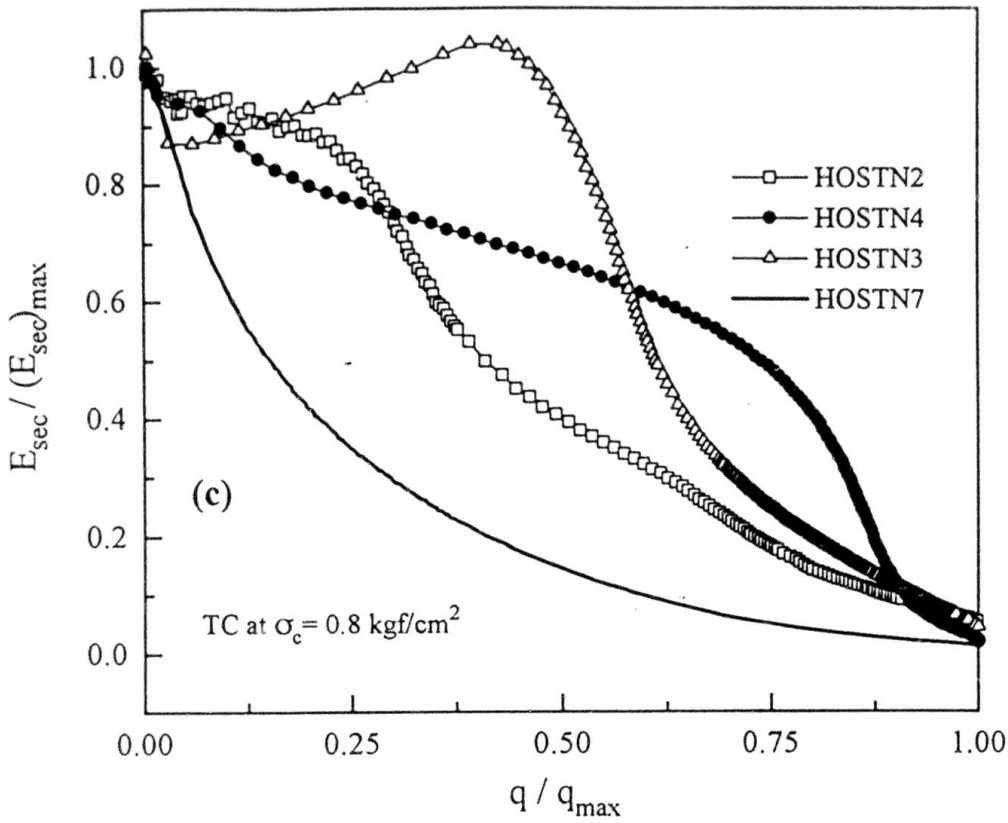

Fig. 8.17c: Relationships between $E_{sec}/(E_{sec})_{max}$ and q/q_{max} for different specimens during TC.

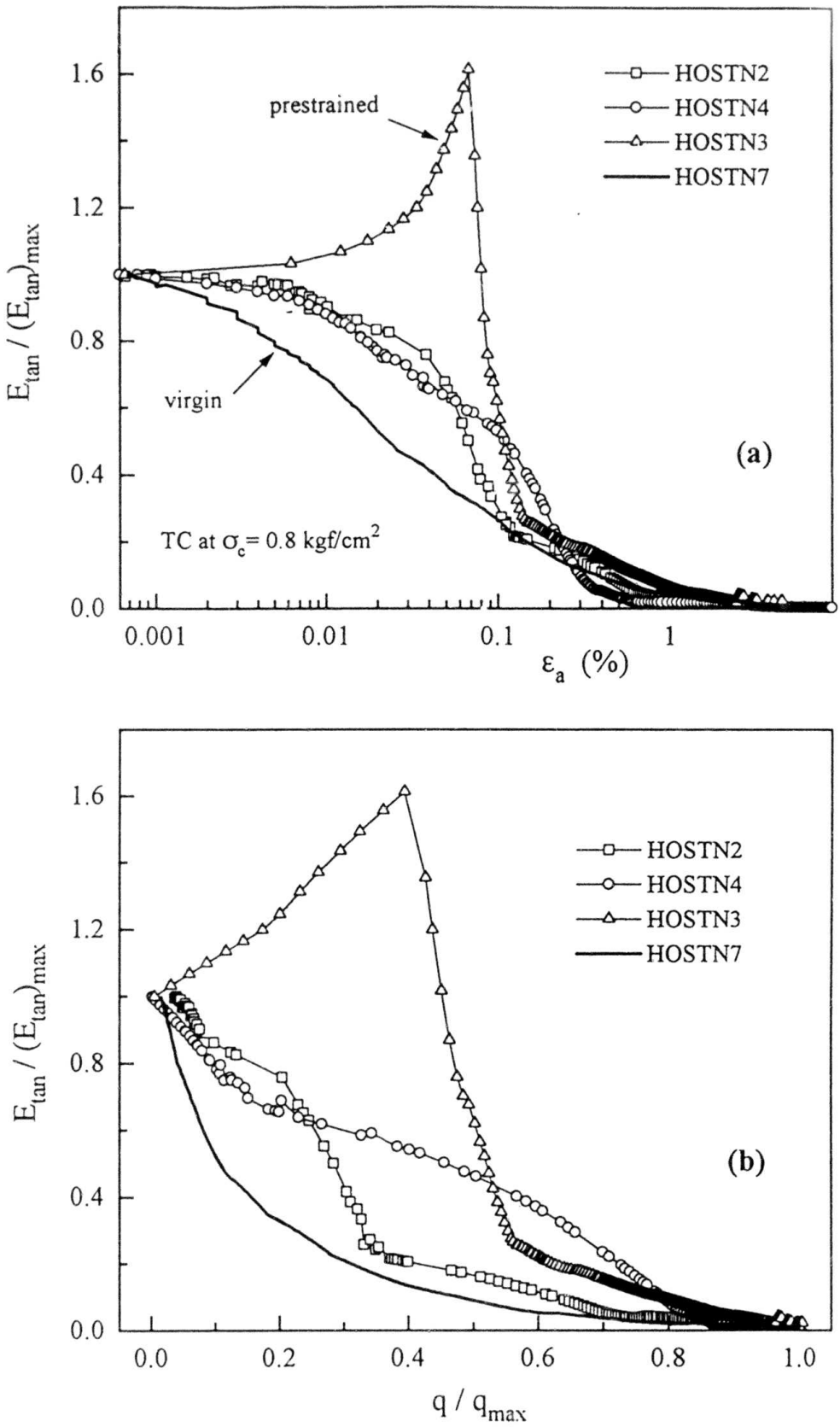

Figs. 8.18: Relationships between (a) $E_{tan}/(E_{tan})_{max}$ and ε_a, and (b) $E_{tan}/(E_{tan})_{max}$ and q/q_{max} for different specimens during TC.

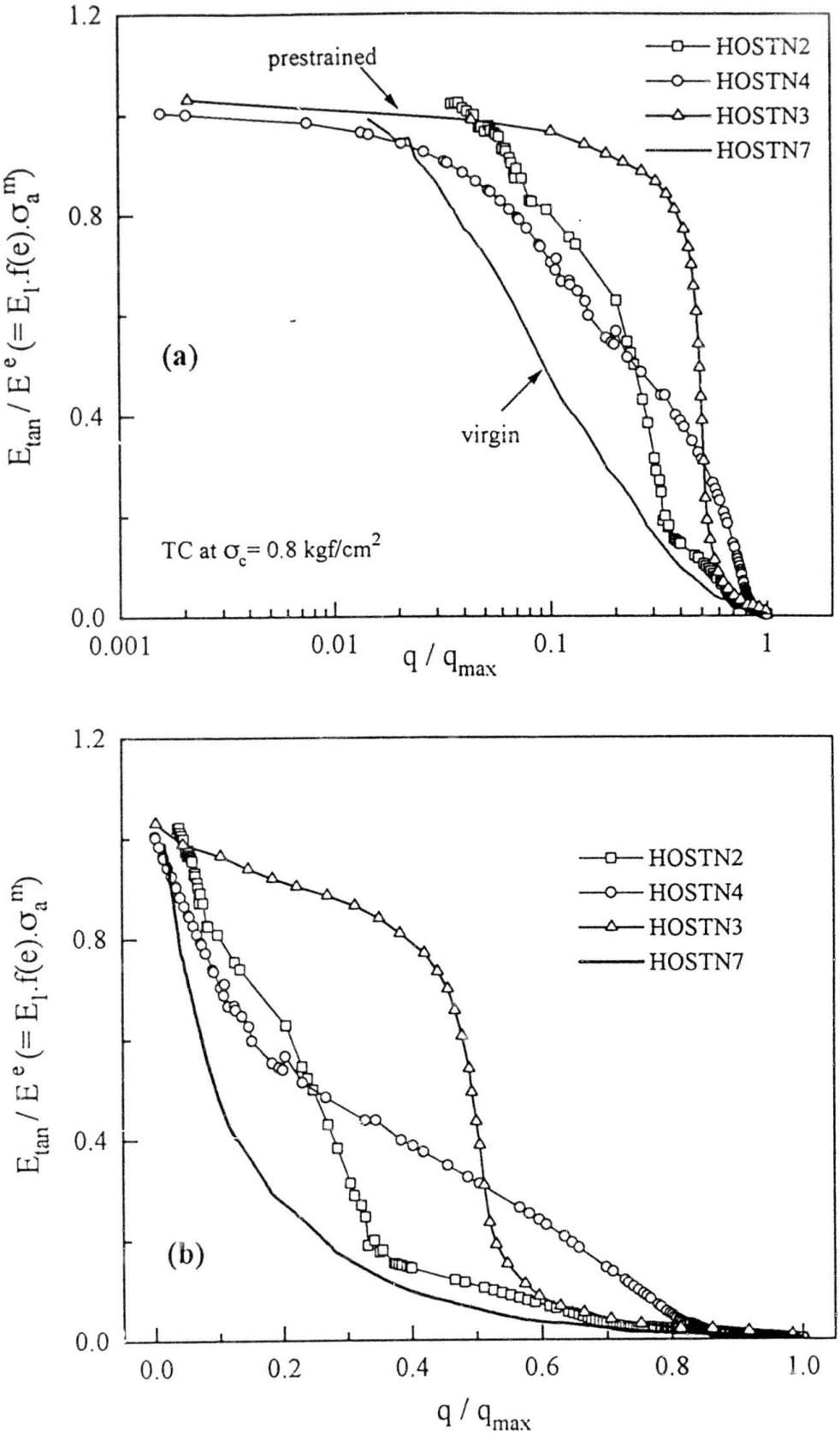

Figs. 19: (a) $E_{tan}/E^e \sim \log(q/q_{max})$, and (b) $E_{tan}/E^e \sim q/q_{max}$ relationships of different specimens during TC.

Chapter 9

Summary, Conclusions, and Recommendations

9.1. Summary

A methodology has been described to characterize anisotropy in small strain moduli by using a large triaxial specimens having a square/rectangular cross section (57 cm x 23 cm x 23 cm). The system utilizes a very high resolution transducer, LDT, to measure local strains in both vertical and lateral directions. An automated loading system was developed for the purpose of present study to control stress states and to apply very small-amplitude cyclic load from which elastic parameters were evaluated. At a given stress state, cyclic loads were applied in either of the principal stress directions, while keeping the stress in the other principal direction constant. To characterize anisotropy in elastic Young's moduli, a stress state was varied along stress paths of isotropic, anisotropic, constant vertical stress, constant horizontal stress, and constant mean stress in a single specimen, while applying vertical and/or horizontal cyclic loading at a number of stress states.

Reliability of this study depends largely on the accurate measurements of stress-strain responses at strains below 0.001%. Particularly, strain measurement below 0.001% is a very sensitive and important issue. Performance of LDTs was investigated critically during the current research. Some of its components were modified to increase resolution and accuracy, as well as to improve hysteretic behavior. Its resolution, accuracy, and workability were investigated. Potential sources of errors, which may affect the measured stiffness, were also examined by providing special attention to creep behavior of LDTs and calibration characteristics.

Effects of cyclic prestraining (CP) on the deformation characteristics of soils were investigated by using small triaxial specimens (each 15 cm high and 7.5 cm diameter). CP was applied with a constant axial stress amplitude for which the single amplitude axial strain was varied in the range from 0.025% to 0.061%. During CP, axial stress was cycled symmetrically about a neutral axis, which was either on an isotropic stress state or on an anisotropic stress state.

For each CP, the number of stress cycle was varied from 25,000 to 120,000 cycles. Effects of CP and long-term consolidation on the deformation characteristics, damping, stress-dependency of small strain stiffness were studied.

The effect of loading frequency on the deformation characteristics of dry sand was investigated by using small triaxial specimens. For that purpose, the performance of the data acquisition system used was evaluated thoroughly to identify time-lag, if exists any, between a pair of measured stress and strain under typical cyclic loading test conditions. The loading frequency was varied from 0.005 Hz to 2.0 Hz, while a single amplitude axial stress during cyclic loading was varied from 0.001% or below to 0.04%. Tests were carried out on both virgin and cyclically prestrained specimens. A specimen was prestrained in order to achieve the steady state condition at which stress-strain relationships at different load cycles traverse along the same hysteresis loop without translation to any strain axis.

Tests were performed on small triaxial specimens to investigate whether a granular material exhibits elastic deformation properties at any stress state during shearing. For that purpose, a specimen was sheared up to a prescribed stress state in triaxial compression at a number of steps. After each step of shearing, the specimen was allowed to undergo creep deformation at a constant stress state for a sufficient period of time until the creep rate became negligible. Loading to the next step of shearing was then restarted. Initial part of the stress-strain relation after the restart of loading was compared with those of elastic deformation at that stress state. For that purpose, current elastic deformation properties were also measured after each creep test.

9.2. Conclusions

9.2.1. Automation and the Performance of LDTs

1. An automated triaxial system has been developed to study into the elastic deformation characteristics in the small strain range (less than 0.001%) of granular materials using a large rectangular-prism specimen. Stress states, in both triaxial extension and compression, can be changed along stress paths with a constant value of axial stress, lateral stress, mean stress, or

stress ratio. Small amplitude vertical or horizontal cyclic loading tests, while keeping the other principal stress constant, can be performed at any stress state to evaluate elastic Young's moduli and Poisson's ratios.

2. Resolution, working range and performance were critically examined with special reference to the evaluation of small strain elastic behavior of soil. LDTs that are able to measure local strains precisely were used successfully to measure lateral strains. LDTs can possess a resolution to measure strains less than 0.0005% (without amplification). It can underestimate the maximum elastic modulus measured during a small unload/reload cycle of a given geomaterial but not more than 2%. LDTs function satisfactorily under submerged conditions into pressurized water for a long duration (at least 41 days).

9.2.2. Inherent Anisotropy in Elastic Deformation Properties

(1) The elastic deformation characteristics of granular materials are anisotropic both i) in small strain stiffnesses with E_v being larger than E_h and ii) in elastic deformation with ε_h being larger than ε_v in isotropic compression. The degree of inherent anisotropy in isotropic compression increases with the increase in stress level.

(2) Anisotropy in small strain stiffness seems to be influenced by particle size, shape, and fabric of particulate materials. Elastic deformation characteristics of coarse grained and subround materials are more anisotropic compared to those of fine grained and subangular materials.

(3) All the materials tested exhibit transverse anisotropy in both small strain stiffness and relatively large deformation. The observations described above are common to both air-pluviated and vibrator-compacted specimens of sand.

(4) Elastic parameters are nearly independent of the frequency of loading (or rate of shear) within the range examined (i.e., f= 0.0066~0.1 Hz).

9.2.3. Cross-Anisotropy in the Small Strain Stiffness

(1) Stress-dependency of elastic Young's modulus is critically examined for three cases: Elastic Young's modulus is a) mean stress-dependent (Case 1), b) directionally stress-dependent (Case 2), and c) dependent on both principal stresses (Case 3).. A large volume of data shows that the elastic Young's modulus is rather a unique function of the normal stress in the direction of the major principal strain increment (Case 2). Case 1 and 3 types of dependency of Young's modulus may underestimate or overestimate true values depending on the stress path being followed and the magnitude of stress states.

(2) Poisson's ratio increases with the increase in stress ratio (σ_v/σ_h) within a relatively small range.

(3) Based on the experimental observation, a cross-anisotropic elastic model has been proposed and evaluated.

(4) Elasticity of granular materials is of hypo-elastic type. Hypo-elasticity, which is the degree of deviation from elasticity, increases in both principal strain directions with the increase in Poisson's ratio at isotropic stress states and m values; it increases in ε_v direction with the increase in I_0, but at the same time it decreases in ε_h direction.

9.2.4. Effects of stress ratio on Young's modulus for elastic strains during shearing

(1) The Young's modulus E_v, defined for the vertical elastic strain increment in a small unload/reload cycle of the vertical stress σ_v, increases as σ_v increases in TC at a constant σ_h, basically following the relation that E_v is a function of σ_v^m (m≈0.49). Similar rule holds for the Young's modulus E_h defined for the lateral elastic strain increment in a small unload/reload cycle of the lateral stress σ_h during TE when σ_h is increasing at a constant σ_v. As the principal stress ratio σ_1/σ_3, which is σ_v/σ_h in TC and σ_h/σ_v in TE, exceeds 3 to 4, particularly as the stress ratio is approaching failure, the value of E_v during TC (or E_h during TE) starts decreasing relatively to the value expected based on the relation described above. This relative reduction of E_v (or E_h) is considered due to the effect of damage to the fabric by shear deformation.

(2) Corresponding to the above, the Young's moduli E_v and E_h are essentially constant when the values of σ_v and σ_h, respectively, are kept constant (e.g., σ_h during TC and σ_v during TE). As σ_1/σ_3 exceeds 3 to 4, the E_h value during TC (or E_v value during TE) also starts decreasing.

(3) In TC (at a constant σ_h), after E_v and E_h start decreasing, the damage to E_v is larger than that to E_h at a given stress ratio, while in TE (at a constant σ_v), the opposite is true.

9.2.5. Cyclic Prestraining and the Elastic Deformation Properties

(1) The elastic deformation characteristics of granular soil become anisotropic as a result of the application of a large amplitude cyclic axial loading with a large number of cycles (as called CP) in addition to the stress system-induced anisotropy. The dependency of E_{max} on σ_a increases by CP. This kind of anisotropy may be called the CP-induced anisotropy.

(2) The ratio of the value E_{max} measured after CP at the neutral stress state (isotropic or anisotropic) of the prestraining stress path to the respective initial value scatters in the range of 0.78~1.20 depending on different stress-strain conditions during CP. Generally, when the cyclic stress is symmetrical about the isotropic stress state, the E_{max} value does not change or decreases. On the other hand, the E_{max} value tends to increase by CP when the cyclic stress is biased to TC stress states.

(3) Even when the E_{max} value changes by CP, the effects of CP on the E_{eq} values measured at larger strains become smaller. Therefore, E_{eq}~$\log((\varepsilon_a)_{SA})$ relationship obtained after CP differs from the corresponding relation obtained immediately before CP. As a result, the shape of the normalized decay curves obtained before and after CP becomes different from each other.

(4) Equivalent Poisson's ratio at relatively large strains decreases as a result of CP, while the Poisson's ratio (ν^e) at very small elastic strains $(\varepsilon_a)_{SA}$ ($\approx 10^{-5}$ or less) is insensitive to CP. Despite CP-induced anisotropy observed in the small strain stiffness, CP does not bring about any change in the dependency of ν^e on stress ratio (σ_a/σ_r).

(5) Damping ratio at strains exceeding the elastic limit strain decreases drastically by the application of a large number of large amplitude axial strain during CP, which leads to the enlargement of the so-called elastic limit; the limit increases with the increase in the number of loading cycles during CP.

(6) When the E_{max} value decreased or increased by CP, a slight increase or decrease in the E_{max} value with elapsed time is observed during post-CP consolidation period, which means a gradual decrease in the effects of CP-induced anisotropy with time. A similar effect is reflected on the E_{eq}~$\log((\varepsilon_a)_{SA})$ relationship. Damping ratio also decreases slightly during the post-CP consolidation period. The E_{max} value increases slightly during pre-CP long-term consolidation period.

(7) The plastic strain increment decreases drastically with cyclic loading along a fixed stress path. However, the deformation does not become totally elastic even after applying a large amount of CP with a relatively large amplitude of axial stress cycle in a fixed stress path. These results suggest that the deformation of sand not be modeled precisely by a simple elasto-plastic model having fixed range of elasto-plastic behavior which is independent of repeated loading. The stress-dilatancy relation is changed by cyclic loading in a complicated manner.

(8) Cyclic prestraining (CP) increases stiffnesses (tangent and secant moduli) largely at intermediate strain (and stress) levels during monotonic triaxial compression (TC) test although the initial stiffness does not change significantly. As a consequence, the E_{tan} value of a cyclically prestrained specimen may increase with the increase in the axial stress in triaxial compression (TC). On the other hand, even for CP specimens, the ratio of E_{tan} to the current elastic Young's modulus always decreases with the increase in the axial stress. CP does not bring about any change in the peak strength.

9.2.6. Loading Rate-Dependency of Deformation Properties

(1) Data acquisition systems, consisting of various electronic transducers, may not record a pair of corresponding stress and strain exactly simultaneously. Any time-lag in the acquired data has severe effects on damping ratio evaluation. For example, damping ratio evaluated with axial

strain by using a gap sensor, which is an inductance type sensor, is found unreliable when deviator stress is measured by using a strain-gauge type load cell, due to time lag in the data acquisition system.

(2) The values of E_{eq} and h were observed to decrease and increase, respectively, with the increase in the strain amplitude, as would be expected. The wave-form, triangular or sinusoidal, of cyclic load used has no influence on the measured values of E_{eq} and h.

(3) The Young's modulus and damping of sand at small strains do not change largely by the change in loading rate except for the loading frequency (f) below 0.05 Hz. The viscous effects cannot be totally ignored at lower frequencies. In the frequency range (i.e., $f \leq 0.005$ Hz) at a given frequency, damping ratio can increase manifold and Young's modulus can decrease by 5 to 10% with the increase in shear stress level.

(4) Before reaching steady state conditions (i.e., at or near the virgin state), damping ratio at a given stress amplitude decreases with the number of cyclic loading. The steady state is reached only after a large number of cycles of loading.

(5) At both virgin and steady state conditions, E_{eq} is independent of f, whereas damping ratio increases slightly with the decrease in f at the virgin state while it increases with the increase in f, especially when $(\varepsilon_a)_{SA}$ is greater than about 0.007%, at the steady state conditions.

9.2.7. Creep Behavior of Sand in TC and its Effect on Deformation Characteristics

(1) For sand, deformation for a given duration at a constant stress state, known as creep, is observed to increase with the increase in the shear stress level. In such a case, the rate of creep in the major principal strain is larger for a loose specimen, whereas the creep rate in the minor principal strain is similar irrespective of void ratio. Creep deformation occurs always in such a way as that the principal strains do during the recently experienced loading increase.

(2) Similar time-dependent deformations occur at a constant stress state also during unloading (i.e., at unloaded stress states), which is termed as delayed rebound (or creep recovery). At a

given stress state, the rate of delayed rebound during primary loading is much lower than the rate of creep.

(3) Creep deformation follows Rowes stress-dilatancy relationship (i.e., R= K.D), which is observed during virgin (primary) loading. During unloading (i.e., σ_a decreasing at constant σ_r), material becomes more dilative (i.e., large D) at a given R. Therefore, the stress-dilatancy relationships during loading and unloading are not identical. Dilatancy rate during delayed rebound is more-or-less similar to that occur during unloading at the same stress state.

(4) Elastic deformation properties for granular material exist after plastic deformation (related to creep) is allowed to occur at any constant stress state during monotonic loading. In conventional TC tests, such deformation properties are masked in relatively very large increments of plastic deformations. This finding explains why the initial stiffness of an isotropically or anisotropically consolidated specimen during monotonic TC test is similar to that obtained by small amplitude cyclic loading tests under otherwise similar conditions.

(5) Elastic deformation properties measured during monotonic loading, unloading, reloading and re-unloading follow nearly the same rules as to their dependency on current stress state; that is, the vertical Young's modulus E^e is a function of axial stress only and the Poisson's ratio ν^e is a function of stress ratio ($=\sigma_a/\sigma_r$). Overall unloading and reloading and the previous stress-histories have little effect on the values of E^e and ν^e.

(6) The elastic Young's modulus (E^e), the initial value of secant modulus (E_{sec}) and the initial value of tangent modulus (E_{tan}) at the start of monotonic TC test are essentially similar to each other. As would be expected, the peak strength (i.e., ϕ_{max}) is larger for a denser specimen, and is observed unaffected by the previous stress-histories. However as a result of previous stress-histories, the tangent stiffnesses at an intermediate stress (or strain) level increases substantially.

9.3. Recommendations for Future Research

The small strain behavior sand has been experimentally studied on clean sands. It will be more realistic if the undisturbed specimen can be tested.

The idea of the CP-induced anisotropy in the small strain stiffness is described without measuring Young's modulus in lateral direction. This can be confirmed by the use of large triaxial apparatus using the automatic control of loading systems described in Chapter 2.

Stiffness degradation curves, i.e., E_{eq}~$(\varepsilon_a)_{SA}$ relationships, are usually obtained based on E_{eq} values evaluated in axial strain direction. In the three-dimensional prediction analysis, the same degradation relationships are used for general stress paths. Its validity can be investigated by constructing similar degradation curve for horizontal direction.

Finally, the author hopes that the huge data and the cross-anisotropic elastic model presented in this study will guide the researchers and the analysts for a better prediction of ground response under working load conditions.

References

Alarcon-Guzman, A., J.L. Chameau, G.A. Leonard and J.D. Frost (1980), "Shear Modulus and Cyclic Undrained Behaviour of Sands," Soils and Foundations, Vol. 20, No. 4, pp. 105-119.

Ampadu, S. and Tatsuoka, F., 1989, "An Automated Stress-Path Control Triaxial System," Geotechnical Testing Journal, GTJODJ, Vol. 12, No. 3, pp. 238-243.

Arthur, J.R.F. and Menzies, B.K. (1972), "Inherent Anisotropy in a Sand," Geotechnique, Vol. 22-1, pp. 115-128.

Atkinson, J. H., 1985, "Simple and Inexpensive Pressure Control Equipment for Conventional and Stress Path Triaxial Testing of Soils," Geotechnique, Vol. 35, No. 1, pp. 61-63.

Bellotti, R., Ghionna, N., Jamiolkowski, M., Robertson, P.K. and Peterson, W. (1989), "Interpretation of Moduli from Self-Boring Pressuremeter Tests on Sand," Geotechnique, Vol. 32, No. 2, pp. 269-293.

Bellotti, R., Jamiolkowski, M., Lo Presti, D.C.F. and O'Neill, D.A. (1994), "Anisotropy of Small Strain Stiffness in Ticino Sand," submitted to Geotechnique.

Bhatia, S.K. and Soliman, A.F. (1990), "Frequency Distribution of Void Ratio of Granular Materials Determined by an Image Analyzer," Soils and Foundations, Vol. 30-1, pp. 1-16.

Bishop, A. W. and Wesley, L. D., 1975, "A Hydraulic Triaxial Apparatus for Controlled Stress Path Testing," Geotechnique, Vol. 25, No. 4, pp. 657-670.

Bolton, M.D. and Wilson, J.M.R. (1989), "An Experimental and Theoretical Comparison between Static and Dynamic Torsional Tests," Geotechnique, 39(4), pp. 585-599.

Burland, J.B. and Symes, M.J. (1982): "A Simple Axial Displacement Gauge for Use in the Triaxial Apparatus," Geotechnique, Vol. 32, No. 1, pp. 62-65.

Burland, J.B. (1989): "Small is Beautiful — the stiffness of Soils st small Strains," Ninth Laurits Bjerrum Memorial Lecture, Canadian Geotechnical Journal, Vol. 26, pp. 499-516.

Chang, C.S. (1994), "Compressibility for Sand Under One-Dimensional Loading Condition," Proceedings of Settlement '94, Geotechnical special publication No. 40, ASCE, Vol. 1, pp. 1298-1311.

Chen, L.S. (1948), "An Investigation of Stress-Strain and Strength Characteristics of Cohesionless Soils by Triaxial Compression Tests," Proc. of second Int. Conf. on Soil Mechanics and Foundation Engg., Rotterdam, Vol. 5, pp. 35-43.

Clayton, C.R.I. and Khatrush, S.A. (1986): "A New Device for Measuring Local Axial Strains on Triaxial Specimens," Geotechnique, Vol. 36, No. 4, pp. 593-597.

Clayton, C.R.I., Khatrush, S.A., Bica, A.V.D. and Siddique, A. (1989): "The Use of Hall Effect Semiconductors in Geotechnical Instrumentation," Geotechnical Testing Journal, ASTM, Vol. 12, No. 1, pp. 69-76.

De Alba, P., K. Baldwin, V. Janoo, G. Roe and B. Celikkol (1984), "Elastic wave velocities and liquefaction potential," Geotechnical Testing Journal, ASTM, Vol. 7, No. 2, pp. 77-87.

Di Benedetto, H. and Tatsuoka, F. (1996), "Small Strain Behavior of Geomaterials: Modelling of Strain Rate Effects," Submitted to Soils and Foundations.

Doroudian, M. and Vucetic, M. (1995): "A Direct Simple Shear Device for Measuring Small-Strain Behavior," Geotechnical Testing Journal, Vol. 18, No. 1, pp. 69-85.

Drnevich, V.P. and F.E. Richart (1970), "Dynamic prestraining of dry sands," J. of Soil Mechanics and Foundation Engg., ASCE, Vol. 96, No. SM2, pp. 451-469.

Drnevich, V.P. (1972), "Undrained Cyclic Shear of Saturated Sand," Journal of SMF Div., ASCE, Vol. 98, No. SM8, pp.807-825.

Drnevich, V.P. (1978), "Resonant Column Testing-Problems and Solutions," Dynamic Geotechnical Testing, ASTM STP 654, ASTM, pp. 384-398.

Drnevich, V.P. and Richart, F.E., Jr. (1970), "Dynamic Prestraining of Dry Sand," Journal of SMF Div., ASCE, Vol. 96, No. SM2, pp.453-469.

Duncan, J.M. and Chang, C.Y. (1970), "Non-Linear Analysis of Stress and Strain Behavior," J. of GE Div., Proc. ASCE, Vol. 96, SM3, pp. 453-469.

El-Hosri, M.S., Biarez, J. and Hicher, P.Y. (1981): "Dynamic Triaxial and Vibratory in-situ Behaviour of Cohesive Soil," Proc. Int. Conf. on Recent Advances in Geotechnical Earthquake Engg. and Soil Dynamics, St. Louis, Vol. II, PP. 585-590.

Flora, A., Jiang, G.L., Kohata, Y. and Tatsuoka, F. (1994), "Small Strain Behaviour of a Gravel along some Triaxial Stress Paths," Proc. Int Symp. on Prefailure Deformation Characteristics of Geomaterials, IS-Hokkaido '94, Balkema, Vol. 1, pp. 279-285.

Germaine, J. T. and Ladd, C. C. (1988): "Triaxial Testing of Saturated Cohesive Soils," Advanced Triaxial Testing of Soil and Rock, ASTM STP 977, R. T. Donaghe, R. C. Chaney, and M. L. Silver, Eds., ASTM, Philadelphia, pp. 421-459.

Goto, S. (1986): "Strength and Deformation Characteristics of Granular Materials in Triaxial Tests," Doctoral Thesis, University of Tokyo.

Goto, S., Tatsuoka, F., Shibuya, S., Kim, Y-S., and Sato, Y., 1991, "A Simple Gauge for Local Small Strain Measurements in the Laboratory," Soils and Foundations, Vol. 31, No. 1, pp. 169-180.

Goto, S., Park, C-S., Tatsuoka, F., and Molenkamp, F., 1993, "Quality of the Lubrication Layer Used in Element Tests on Granular Materials," Soils and Foundations, Vol. 33, No. 2, pp. 47-59.

Graham, J., Crooks, J.H.A. and Bell, A.L. (1983), "Time Effects on the Stress-Strain Behaviour of Soft Clays," Geotechnique, 33(3), pp. 327-340.

Graham, J. and Houlsby, G.T. (1983), "Elastic Anisotropy of Natural Clay," Geotechnique, Vol. 32-2, pp. 165-180.

Hardin, B.O. and Richart, F.E.Jr. (1963), "Elastic Wave Velocities in Granular Soils," J. of SMFD, ASCE, Vol. 89, No. SM1, pp. 33-65.

Hardin, B.O. (1965), "The Nature of Damping in Sands," Journal of SMF Div., ASCE, Vol. 91, No. SM1, pp. 63-97.

Hardin, B.O. and Music, J. (1965), "Apparatus for Vibration of Soil Specimens During the Triaxial Test," Symposium on Instrumentation and Apparatus for Soils and Rocks, ASTM STP 392, ASTM, pp. 55-74.

Hardin, B.O. and Black, W.L. (1968), "Vibration Modulus of Normally Consolidated Clay," Journal of SMF Div., ASCE, Vol. 92, No. SM2, pp. 353-369.

Hardin, B.O. and Drnevich, V.P. (1972), "Shear Modulus and Damping in Soils: Design Equations and Curves," Journal of SMF Div., ASCE, Vol. 98, No. SM7, pp. 667-692.

Hardin, B.O. (1978), "The Nature of Stress-Strain Behavior of Soils," Proc. Geotech. Engg. Div. Specialty Conf. on Earthquake Engg. and Soil Dynamics, ASCE, Vol. 1, Pasadena. pp. 3-90.

Hardin, B.O. and Bladford, G.E. (1989), "Elasticity of Particulate Materials," J. of Geotec. Engg., ASCE, Vol. 115-6, pp. 788-805.

Hird, C. C. and Yung, P. (1987): "Discussion on 'A New Device for Measuring Local Axial Strains on Triaxial Specimens,'" Geotechnique, Vol. 37, No. 3, pp. 413-417.

Hird, C.C. and Yung, C.Y. (1989): "The Use of Proximity Transducers for Local Strain Measurements in Triaxial Tests," Geotechnical Testing Journal, ASTM, Vol. 12, No. 4, pp. 292-296.

Iida, K. (1938), "The Velocity of Elastic Waves in Sands," Bulletin of the Earthquake Research Institute, Tokyo Imperial College, Vol. 16, pp. 131-144.

Iida, K. (1940), "On the Elastic Properties of Soil Particularly in Relation to its Water Contant," Bulletin of The Earthquake Research Institute, Tokyo Imperial College, Vol. 18, pp. 675-690.

Isenhower, W.M. (1979), "Torsional Simple Shear/Resonant Column Properties of San Francisco Bay Mud," Geotechnical Engineering Thesis, GT 80-1, University of Texas, Dec., 307 p.

Ishimoto, M. and Iida, K. (1937), "Determination of Elastic Constants of Soils by Means of Vibration Methods," Bulletin of Earthquake Research Institute, Vol. 16, pp. 67.

Iwasaki, T., Tatsuoka, F. and Takagi, Y. (1978), "Shear Modulus of Sands Under Cyclic Torsional Shear Loading," Soils and Foundations, Vol. 18-1, pp. 39-56.

Jamiolkowski, M., Lerouell, S. and Lo Presti, D.C.F. (1991), "Design Parameters from Theory to Practice," Theme Lecture, Geo-Coast '91, Yokohama, pp. 877-917.

Jardine, R.J., Symes, M.J. and Burland, J.B. (1984), "The Measurement of Soil Stiffness in the Triaxial Apparatus," Geotechnique, Vol. 34, No. 3, pp. 323-340.

Jardine, R.J., St. John, H.D , Hight, D.W. and Potts, D.M. (1991): "Some Practical Applications of a Non-linear Ground Models," Proc. of 10th European Regional Conf. on SMFE, Firenze, Vol. 1, pp. 223-228.

Jardine, R.J. (1995), "One Perspective of the Prefailure Deformation Characteristic of some Geomaterials," Int. Conf. of Pre-Failure Deformation of Geomaterials, Hokkaido, Balkema, Vol. II.

Kim, D. S. and Stokoe, K. H. H. and Roesset, J. M., "Characterization of Material Damping of Soil using Resonant Column and Torsional Shear Tests," Proc. of the 5th Int. Conf. on Soil Dynamics and Earthquake Engineering, Karlsruhe.

Kim, Y.-S. (1992): "Deformation Characteristics of Sedimentary Soft Rocks by Triaxial Compression Tests," Thesis, Doctor of Engg., University of Tokyo.

Kim, D.-S. and Stokoe, K.H.II (1995), "Deformation Characteristics of Soils at Small to Medium Strains," Proc. First Int. Sym. on Earthquake Geotechnical Engg., IS-TOKYO, Balkema, Ishihara edition, Vol.1, pp. 89-94.

King, M.S. (1970), "Static and Dynamic Elastic Moduli of Rocks Under Pressure," Rock-Mechanics: Theory and Practice, Proc. 11th symp. on Rock Mechanics, Berkeley, California. AIME: New York, Somerton, W.H. edition, pp. 329-351.

Kirkpatrick, W.M. and Belshaw, D.J. (1968), "On the Interpretation of the Triaxial Tests," Geotechnique, Vol. 18-3, pp. 336-350.

Knox, D.P., Stokoe, K.H.,II and Kopperman, S.E. (1982), "Effect of State of Stress on Velocity of Low-Amplitude Wave Propagating along Principal Stress Directions in Dry Sand," GR 82-23, Univ. of Texas.

Ko, H.-Y. and Scott, R.F. (1967), "Deformation of Sand in Hydrostatic Compression," J. of SMFD, ASCE, Vol. 93, SM3, pp. 137-156.

Kohata, Y., Tatsuoka, F., Dong, J., Teachavorasinskun, S. and Mizumoto, K. (1994), "Stress States Affecting Elastic Deformation Moduli of Geomaterials," Proc. IS-Hokkaiso, Balkema, Vol. I, pp. 3-11.

Kohata, Y., Tatsuoka, F., Mukabi, J.N. and Suzuki, M. (1995), "Effects of Strain Rate and Drainage on Deformation Characteristics at Small Strain of Geomaterials," Proc. 1st Int. Conf. on Earthquake Geotechnical Engg., Tokyo, Ishihara edition, Balkema, Vol. 1, pp. 151-156.

Lade, P.V. and Nelson, R.V. (1987), "Modeling of Elastic Behavior of Granular Materials," Int. J. for Numerical and Analytical Methods in Geomechanics, vol. 11, pp. 521-542.

Lawrence, F.V., Jr. (1963), "Propagation Velocity of Ultrasonic Waves Through Sand," MIT Research Report, R63-8, March.

Li, X. S., Chan, C. K., and Shen, C. K., 1988, "An Automated Triaxial Testing System," Advanced Triaxial Testing of Soil and Rock, ASTM STP 977, Philadelphia, pp. 95-106.

Lo Presti, D. C. F. and O'Neill, D. A., 1991, "Laboratory Investigation of Small Strain Modulus Anisotropy in Sands," Proc. of Int. Symp. on Calibration Chamber Testing, Clarkson Univ., Potsdam, NY (Huang ed.), Elsevier, pp. 213-224.

Lo Presti, D.C.F., Jamiolkowski, M., Pallara, O., Pisciotta, V. and Ture, S. (1995), "Stress Dependence of Sand Behavior, Proc. 3rd Int. Conf. on Recent Advances in Geotech. Earthquake Engg. and Soil Dynamics, St. Louis, Prakash edition, Vol. I, pp. 71-76.

Lo Presti, D.C.F., Pallara, O., and Puci, I. (1995): "A Modified Commercial Triaxial Testing System for Small Strain Measurements: Preliminary Results on Pisa Clay," Geotechnical Testing Journal, ASTM, Vol. 18, No. 1, pp. 15-31.

Marcuson, W.F.,III and Wahls, H.E. (1972a), "Time Effects on Dynamic Shear Modulus of Clays," Journal of SMF Div., ASCE, Vol. 98, No. SM12, pp. 1359-1373.

Marcuson, W.F.,III and Wahls, H.E. (1972b), "Time Effects on Damping Ratio of Clays," Dynamic Geotechnical Testing, ASTM STP 654, ASTM, pp. 126-147.

Mindlin, R.D. (1949), "Compliance of Elastic Bodies in Contact," Journal of Applied Mechanics, Transactions, ASME, Vol. 71, pp. A-259-268.

Mukabi, J.N. (1995): "Deformation characteristics at small strains of clays in triaxial tests," Thesis, Doctor of Engg., University of Tokyo.

Ni, S.-H. (1987), "Dynamic Properties of Sand Under True Triaxial Stress States from Resonant-Column/Torsional Shear Tests," Ph.D. Dissertation, The University of Texas at Austin, 421 p.

Nishio, S. and Tamaoki, K. (1990), "Stress Dependency of Shear Wave Velocities in Diluvial Gravel Samples During Triaxial Compression Tests," Soils and Foundations, Vol. 30-4, pp. 42-52.

Oda, M. (1972a), "Initial Fabrics and Their Relation to Mechanical Properties of Granular Material," Soils and Foundations, JSSMFE, Vol. 12, No. 1, pp. 18-36.

Oda, M. (1972b), "The Mechanisim of Fabric Changes during Compressional Deformation of Sand," Soils and Foundations, JSSMFE, Vol. 12, No. 2, pp. 1-18.

Oda, M. (1981), "Anisotropic Strength of Cohesionless Sands," J. SMFD, ASCE, 107, GT9, pp. 1219-1231.

Park, C-S. and Tatsuoka, F. (1994), "Anisotropic Strength and Deformation of Sands in Plane Strain Compression," Pros. of 13th Int. Conf. on SMFE, New Delhi, Vol. 1, pp. 1-6.

Parkin, A.K., Gerrard, C.M. and Willoughby, D.R. (1968), "Discussion on Deformation of Sand in Shear," J. SMFD, ASCE 94, SM1, pp. 336-340.

Pickering, D.J. (1970), "Anisotropic Elastic Parameters For Soil," Geotechnique, Vol. 20-3, pp. 271-276.

Pradhan, T.B.S. and Tatsuoka, F. (1989), "On Stress-Dilatancy Equations on Sand Subjected to Cyclic Loading," Soils and Foundations, Vol. 29, No. 1, pp. 65-81.

Pradhan, T. B. S., Tatsuoka, F, Mohri, Y., and Sato, Y., 1989, "An Automated Triaxial Testing System Using a Simple Triaxial Cell for Soils," Soils and Foundations, Vol. 29, No. 1, pp. 151-160.

Richart, J.E.,Jr., Hall, J.R., Jr. and Woods, R.O. (1970), Vibration of Soils and Foundations, Prentice-Hall Inc., Englewood Cliffs, New Jersy, 414 p.

Roesler, S.K. (1979), "Anisotropic Shear Modulus due to Stress Anisotropy," Journal of Geotechnical Engineering Division, ASCE, Vol. 105, No. GT7, pp. 871-880.

Rowe, P.W. (1962), "The Stress-Dilatancy Relation for State Equilibrium of an Assembly of Particles in Contact," Proc. Royal Society, 269A, 500-527.

Rowe, P.W. (1971), "Theoretical Meaning and Observed Values of Deformation Parameters for Soils," Proceeding of Roscoe memorial Sym. on Stress-Strain Behavior of Soils, March, pp. 143-194.

Scholey, G.K., Frost, J.D., Lo Presti, D.C.F., and Jamiolkowski, J. (1995): "A Review of Instrumentation for Measuring Small Strains During Triaxial Testing of Soil Specimens," Geotechnical Testing Journal, ASTM, Vol. 18, No. 2, pp. 137-156.

Sheahan, T.C. and Germaine, J.T., 1992, "Computer Automation of Conventional Triaxial Equipment," Geotechnical Testing Journal, ASTM, Vol. 15, No. 4, pp. 311-322.

Shibuya, S., Mitachi, T., Fukuda, F. and Degoshi, T. (1995), "Strain Rate Effects on Shear Modulus and Damping of Normally Consolidated Clay," Geotechnical Testing Journal, ASTM, Vol. 18, No. 3, pp. 365-375.

Siddiquee, M.S.A. (1994), "FEM Simulations of Deformation and Failure of Stiff Geomaterials Based on Element Test Results," Ph.D. thesis, Tokyo University.

Silver, M.L. and Seed, H.B. (1971), "Deformational Characteristics of Sands under Cyclic Loading," Journal of SMF Div., ASCE, Vol. 97, No. SM8, pp. 1081-1098.

Stokoe, K.H.II and Richart, F.E.Jr. (1973), "In-situ and Laboratory Shear Wave Velocities," Proc. of the 8th Int. Conf. on SMFE, Moscow, Vol. 1.2, pp. 403-409.

Stokoe, K.H.,II and Lodde, P.E. (1978), "Dynamic Response of San Francisco Bay Mud," Proc. Earthquake Engg. and Soil Dynamics Conf., ASCE, Vol. II, pp. 940-959.

Stokoe, K.H.,II, Isenhower, W.M., and Hsu, J.R. (1980), "Dynamic Properties of Offshore Silty Samples," Proc. 1980 Offshore Technology Conf., OTC 3771, Houston, Texas, pp. 289-302.

Stokoe, K. L. II., Lee, J. N. K., and Lee, S. H. H., 1991, "Characterization of Soil in Calibration Chambers with Seismic Waves, "Proc. of Int. Symp. on Calibration Chamber Testing, Clarkson Univ., Potsdam, NY (Huang ed.), Elsevier, pp. 363-376.

Symes, M.J.P.R. (1983), "Rotation of Principal Stresses in Sand," Ph.D. thesis, University of London.

Symes, M.J.P.R. and Burland, J.B. (1984): "Determination of Local Displacement on Soil Samples," Geotechnical Testing Journal, ASTM, Vol. 7, No. 2, pp. 49-59.

Symes, M.J.P.R., Gens, A. and Hight, D.W. (1984), "Undrained Anisotropy and Principal Stress Rotation in Saturated Sand," Geotechnique, 34-1, pp. 11-27.

Tateyama, M., Nishihara, S., Aoki, T. and Tatsuoka, F. (1992), "A FEM Analysis of the Deformation of a Geotextile-Reinforced Soil BridgeAbutment having a Rigid Facing," Proc. 49th Annual Conf. of JSSMFE, Vol. 3, (in Japanese).

Tatsuoka, F. (1985), "Discussion on the paper by Yu and Richart," J. of Geotech. Engg. Div., ASCE, Vol. 111-9, pp. 1155-1157.

Tatsuoka, F., Iwasaki, T. and Takagi, Y. (1978), "Hysteresis Damping of Sands under Cyclic Loading and its Relation to Shear Modulus," Soils and Foundations, JSSMFE, Vol. 18, No. 2, pp. 25-40.

Tatsuoka, F., Iwasaki, T., Fukushima, S., and Sudo, H. (1979), "Stress Conditions and Stress Histories Affecting Shear Modulus and Damping of Sand Under Cyclic Loading," Soils and Foundations, JSSMFE, Vol. 19, No. 2, pp. 29-43.

Tatsuoka, F., 1988, "Some Recent Developments in Triaxial Testing Systems for Cohesionless Soils," Advanced Triaxial Testing of Soil and Rock, STP 977, ASTM, Philadelphia, pp. 7-67.

Tatsuoka, F., Nakamura, S., Huang, C.-C. and Tani, K. (1990), "Strength Anisotropy and Shear Band Direction in Plane Strain Tests of Sand," Soils and Foundations, Vol. 30-1, pp. 35-54.

Tatsuoka, F. and Shibuya, S. (1992), "Deformation characteristics of soils and rocks from field and laboratory tests," Keynote lecture, 9th Asian Regional Conf. on SMFE., Bangkok, Vol. 2, 1992, pp. 101-170.

Tatsouka, F., Sato, T., Park, C.-S., Kim, Y.-S., Mukabi, J.N., and Kohata, Y. (1994a): "Measurements of Elastic Properties of Geomaterials in Laboratory Compression Tests," Geotechnical Testing Journal, ASTM, Vol. 1, pp. 80-94.

Tatsouka, F., Teachavorasinskun, S., Dong, J., Kohata, Y., and Sato, T. (1994b): "Importance of Measuring Local Strains in Cyclic Triaxial Tests on Granular Materials," Dynamic Geotechnical Testing, Vol. 2, ASTM STP 1213, ASTM.

Tatsuoka, F. and Kohata, Y., 1995, "Stiffness of Hard Soils and Soft Soils in Engineering Applications," Report of the Institute of Industrial Science, The University of Tokyo," Vol. 38, Serial No. 242, pp. 135-274.

Tatsuoka, F., Lo Presti, D. C. F. and Kohata, Y., 1995, "Deformation Characteristics of Soils and Rocks under Monotonic and Cyclic Loads and their Relationships," Keynote Lecture, Proc. Int. Conf. on Recent Advances in Geotechnical Earthquake Engineering and Soil Dynamics," St. Louis, Vol. II, pp. 851-879.

Teachavorasinskun, S., 1992, "Deformation Characteristics of Sands at Small Strains," Doctoral thesis," The University of Tokyo.

Tokimatsu, K., T. Yamazaki and Y. Yoshimi (1986), "Soil liquefaction evaluations by elastic shear moduli," Soils and Foundations, Vol. 26, No. 1, pp. 25-35.

Vucetic, M. and Dorby, R. (1991), "Effect of Soil Plasticity on Cyclic Response," Journal of the Geotechnical Engg. Div., ASCE, Vol. 117, No. 1, pp. 89-107.

Weindieck, I. K. (1967), "Zur Strukter Korniger Medien," Bautechnik, Berlin 44, No. 6, pp. 196-199.

Wilson, J.M.R. (1988), "The Dynamic Properties of Soil," M. Phil dissertation, Engineering Department, Cambridge University.

Wu, B., King, M.S. and Hudson, J.A. (1991), "Stress-Induced Ultrasonic Wave Velocity Anisotropy in a Sandstone," Int. J. Rock Mech. Min. Sci. & Geomech. Abstr., Vol. 28, No. 1, pp. 101-107.

Yan, L. and Byrne, P.M. (1991), "Stress State and Stress Ratio Effects in Downhole and Crosshole Shear Wave Velocity Tests on Sands," Proc. second Int. Conf. on Recent Advances in Geotech. Earthquake Engg. and Soil Dynamics, Vol. 1, No. 2.28, St. Lious, Missouri, pp. 229-306.

Yu, P. and Richart, F.E., Jr. (1984), "Stress-Ratio Effects on Shear Modulus of Dry Sands," J. of Geotech. Engg., ASCE, Vol. 110-3, pp. 331-345.